



# Plasticité cristalline à gradients dans un cadre de grandes déformations pour modéliser les effets de taille dans les composants miniaturisés : Application à la localisation des déformations dans les tôles métalliques monocristallines et polycristallines

Lei Cai

## ► To cite this version:

Lei Cai. Plasticité cristalline à gradients dans un cadre de grandes déformations pour modéliser les effets de taille dans les composants miniaturisés : Application à la localisation des déformations dans les tôles métalliques monocristallines et polycristallines. Mécanique des matériaux [physics.class-ph]. HESAM Université, 2021. Français. NNT : 2021HESAE066 . tel-03686637

HAL Id: tel-03686637

<https://pastel.hal.science/tel-03686637>

Submitted on 2 Jun 2022

**HAL** is a multi-disciplinary open access archive for the deposit and dissemination of scientific research documents, whether they are published or not. The documents may come from teaching and research institutions in France or abroad, or from public or private research centers.

L'archive ouverte pluridisciplinaire **HAL**, est destinée au dépôt et à la diffusion de documents scientifiques de niveau recherche, publiés ou non, émanant des établissements d'enseignement et de recherche français ou étrangers, des laboratoires publics ou privés.

**ÉCOLE DOCTORALE SCIENCES DES MÉTIERS DE L'INGÉNIEUR**  
**[Laboratoire d'Étude des Microstructures et de Mécanique des Matériaux**  
**– Campus de Metz]**

# THÈSE

présentée par : **Lei CAI**

soutenue le : **09 Décembre 2021**

pour obtenir le grade de : **Docteur d'HESAM Université**

préparée à : **École Nationale Supérieure d'Arts et Métiers**

Spécialité : **Mécanique et Matériaux**

**Finite deformation strain gradient crystal plasticity framework to model size effects in miniaturized components: Application to strain localization in single- and poly-crystalline metal sheets**

THÈSE dirigée par :  
**M. Farid ABED-MERAIM**

et co-encadrée par :  
**M. Mohamed JEBAHI**

## Jury

**M. Karam SAB**, Professeur, Laboratoire Navier, Ecole Nationale des Ponts et Chaussées  
**M. Samuel FOREST**, Directeur de Recherche CNRS, CDM, Mines ParisTech PSL Univ.  
**Mme. Anne Marie HABRAKEN**, Directrice de Recherche FNRS, MS<sup>2</sup>F, Université de Liège  
**M. Stéphane BERBENNI**, Directeur de Recherche CNRS, LEM3, Université de Lorraine  
**M. Farid ABED-MERAIM**, Professeur, LEM3, ENSAM, Metz  
**M. Mohamed JEBAHI**, Maître de Conférences, LEM3, ENSAM, Metz

Président  
Rapporteur  
Rapporteure  
Examinateur  
Examinateur  
Examinateur

T  
H  
È  
S  
E



# Acknowledgments

First and formost, I would like to express my sincere gratitude to the director of my thesis, Prof. Farid ABED-MERAIM, who kindly gave me this precious opportunity to study in France. I am deeply grateful for his encouragement and invaluable advices during my study. I would like to thank my co-supervisor, Assoc. Prof. Mohamed JEBAHI, for his responsible supervision, meticulous guidance and kind assistance. It is him who brings me into the realm of mechanics, particulary the domain of higher-order plasticity. I will never forget the days we spent together when we disucss the theories, the numerical issues and the papers. Our perseverance finally brings us satisfactory results.

I would like to deeply thank Prof. Karam SAB from Ecole Nationale des Ponts et Chaussées for being the president of my Ph.D. thesis committe. I would like to express my gratidue to two reporters, Prof. Samuel FOREST from Mines ParisTech PSL Univ and Prof. Anne Marie HABRAKEN from Université de Liège, for their insightful comments and academic reports. I am grateful to Prof. Stéphane BERBENNI from Université de Lorraine for accepting the invitation and spending his precious time to attend my thesis defense. I am honored to be able to invite these famous, charming and knowledgeable scholars as the referees. Their insightful, valuable and constructive comments are sincerely appreciated.

I would like to thank the organization-China Scholarship Council (CSC201706280201), who supplied the scholarship to support my study in ENSAM, France.

I would like to thank Boris POITROWSKI and Théophile GROSS for their patient help in dealing with various problems in terms of using the calculation clusters. I also enjoy the days spent with my two friendly colleagues in my office, Christian ADADJA and Médiateur NEMEYUKO, who told me numerous intersting stories in their hometown Africa. In addition, I am happy to meet so many Chinese friends in Metz, with whom I had many happy times together.

Last but not the least, I would like to express my gratitude to my parents for their sacrifices and spiritual support. The encouragement from them is the strength that sustains me thus far.



# Contents

<b>Contents</b>	<b>iii</b>
<b>List of Figures</b>	<b>vii</b>
<b>List of Tables</b>	<b>xv</b>
<b>I English version</b>	<b>1</b>
<b>1 General introduction</b>	<b>3</b>
1.1 Context and objectives . . . . .	3
1.2 Methodology of the thesis . . . . .	7
1.3 Organization of the thesis . . . . .	8
<b>2 State of the art</b>	<b>11</b>
2.1 Definition and classification of size effects . . . . .	12
2.2 Experimental observations of size effects . . . . .	13
2.2.1 First-order extrinsic/intrinsic size effects . . . . .	13
2.2.2 Second-order gradient size effects . . . . .	15
2.3 Numerical modeling of size effects . . . . .	16
2.3.1 Enriched conventional plasticity models . . . . .	17
2.3.2 Surface layer and mesoscopic models . . . . .	18
2.3.3 Gradient-enhanced plasticity models . . . . .	22
2.4 Strain gradient (crystal) plasticity . . . . .	23
2.4.1 Incremental strain gradient (crystal) plasticity models . . . . .	24
2.4.2 Non-incremental strain gradient (crystal) plasticity models . . . . .	24
2.4.3 Discussion . . . . .	27
2.5 Grain boundary models . . . . .	29
2.5.1 Phenomenological GB models . . . . .	30
2.5.2 Crystallography-based GB models . . . . .	31
2.5.3 Discussion . . . . .	31
2.6 Strain localization in crystalline materials . . . . .	32
2.7 Conclusions . . . . .	35
<b>3 Flexible small deformation SGCP</b>	<b>39</b>
3.1 Introduction . . . . .	40

<b>3.2 SGCP model . . . . .</b>	<b>41</b>
3.2.1 Kinematics . . . . .	41
3.2.2 Balance equations . . . . .	42
3.2.3 Dissipation inequality . . . . .	44
3.2.4 Constitutive laws . . . . .	45
3.2.4.1 Energetic constitutive laws . . . . .	45
3.2.4.2 Dissipative constitutive laws . . . . .	46
3.2.5 Flow rules . . . . .	49
3.2.6 Microscopic boundary conditions . . . . .	49
<b>3.3 2D version and numerical implementation . . . . .</b>	<b>50</b>
3.3.1 Simplified 2D SGCP model . . . . .	50
3.3.2 Numerical implementation . . . . .	52
<b>3.4 Assessment and parametric investigation . . . . .</b>	<b>53</b>
3.4.1 Higher-order energetic effects . . . . .	55
3.4.1.1 Energetic length scale . . . . .	56
3.4.1.2 Defect energy index . . . . .	57
3.4.2 Higher-order dissipative effects . . . . .	61
3.4.2.1 Dissipative length scale . . . . .	61
3.4.2.2 Initial higher-order dissipative slip resistance . . . . .	63
3.4.3 Interactions between microscopic stresses . . . . .	65
<b>3.5 Conclusion . . . . .</b>	<b>68</b>
<b>4 Finite deformation extension of the flexible SGCP</b>	<b>71</b>
4.1 Introduction . . . . .	72
4.2 Finite deformation SGCP model . . . . .	72
4.2.1 Kinematics . . . . .	72
4.2.2 Governing equations . . . . .	74
4.2.3 Free energy imbalance . . . . .	75
4.2.4 Constitutive laws . . . . .	75
4.2.4.1 Energetic constitutive laws . . . . .	75
4.2.4.2 Dissipative constitutive laws . . . . .	77
4.2.5 Flow rules . . . . .	78
4.3 2D version and numerical implementation . . . . .	78
4.3.1 Simplified 2D SGCP model . . . . .	79
4.3.2 Integration of constitutive laws . . . . .	80
4.3.3 Weak forms and finite element discretization . . . . .	81
4.4 Model validation . . . . .	83
4.5 Conclusions . . . . .	87
<b>5 Development of finite deformation GB model</b>	<b>89</b>
5.1 Introduction . . . . .	90
5.2 Theoretical formulation . . . . .	91
5.2.1 Finite deformation GB kinematics . . . . .	91
5.2.2 Governing equations . . . . .	93
5.2.3 Free energy imbalance . . . . .	95

5.2.4	Constitutive laws . . . . .	95
5.2.5	Summary of field equations . . . . .	96
5.3	Numerical implementation . . . . .	97
5.3.1	Weak forms . . . . .	97
5.3.2	Finite element discretization . . . . .	98
5.4	Numerical results . . . . .	100
5.4.1	Model validation . . . . .	100
5.4.2	Assessment of the GB model . . . . .	102
5.4.2.1	Influence of GB parameters . . . . .	103
5.4.2.2	Influence of orientation effects . . . . .	105
5.4.3	Application to poly-crystalline materials . . . . .	108
5.5	Conclusions . . . . .	109
<b>6</b>	<b>Application to strain localization</b>	<b>113</b>
6.1	Introduction . . . . .	114
6.2	Strain localization in single crystals . . . . .	114
6.2.1	Regularization of localization bands . . . . .	115
6.2.1.1	Regularization of idealized slip/kink bands . . . . .	115
6.2.1.2	Regularization of general localization bands . . . . .	116
6.2.2	Localization modes in single crystals . . . . .	118
6.2.2.1	Regularization of the mesh-dependence . . . . .	120
6.2.2.2	Conventional CP . . . . .	120
6.2.2.3	Higher-order energetic effects . . . . .	121
6.2.2.4	Higher-order dissipative effects . . . . .	124
6.3	Strain localization in polycrystals . . . . .	125
6.3.1	Grain-induced size effects . . . . .	127
6.3.2	Grain boundary contributions to size effects . . . . .	129
6.3.3	Overall size effects predicted by the SGCP-GB numerical framework . . . . .	133
6.4	Conclusions . . . . .	135
<b>7</b>	<b>Conclusions and perspectives</b>	<b>137</b>
7.1	Conclusions . . . . .	137
7.2	Perspectives and future work . . . . .	139
<b>II</b>	<b>Résumé en français</b>	<b>141</b>
<b>III</b>	<b>Appendices</b>	<b>207</b>
<b>A</b>	<b>Numerical aspects of small deformation SGCP</b>	<b>209</b>
A.1	Overview of the implementation . . . . .	209
A.2	DOF and interpolation functions . . . . .	209
A.3	Regularization function . . . . .	213
A.4	Tangent matrices . . . . .	215
A.5	Shape functions . . . . .	223

<b>B Numerical aspects of large deformation SGCP</b>	<b>225</b>
B.1 DOF and interpolation functions . . . . .	225
B.2 Tangent matrices . . . . .	227
B.3 Shape functions . . . . .	236
<b>C Numerical aspects of grain boundary modeling</b>	<b>237</b>
C.1 Derivation of GB mismatch . . . . .	237
C.2 Regularization function . . . . .	238
C.3 Tangent matrices . . . . .	239
C.4 Shape functions . . . . .	242
<b>Bibliography</b>	<b>245</b>

# List of Figures

1.1 Examples of miniaturized products (from <a href="https://www.picericamic.com">https://www.picericamic.com</a> ). . . . .	4
1.2 Methodology of the thesis. . . . .	9
2.1 Categories of size effects proposed by Vollertsen (2008). . . . .	12
2.2 Illustration of first-order extrinsic size effects on “smaller is weaker”: flow stress of CuNi18Zn20 sheet for different thickness $\lambda$ maintaining the constant grain size (approximately $40\ \mu m$ ) under tensile loading (Kals and Eckstein, 2000). . . . .	14
2.3 Illustrative example of statistical size effects on scatter of flow stress: flow curves for different sheet thicknesses with a constant grain size (Fülöp et al., 2006). . . . .	14
2.4 Illustrative example of intrinsic size effects: True equivalent V.M. stress – V.M. strain curves obtained for cylindrical Ni samples (diameter $10mm$ ) with different averaged grain size (Keller et al., 2015). . . . .	15
2.5 Size dependent material responses for copper wires of diameter $2a$ from $12\mu m$ to $170\mu m$ : (a) true stress $\sigma$ vs logarithmic strain $\varepsilon$ tension (b) torsional response displayed in the form $Q/a^3$ vs $\kappa a$ where $Q$ is the torque, $a$ the wire radius and $\kappa$ the twist per unit length (Fleck et al., 1994). . . . .	16
2.6 Illustration of geometrically necessary dislocations in a plastically bent beam: (a) a periodic array of dislocations with Burgers vector $b$ and spacing $L$ will generate a lattice curvature as $b/L^2$ (b) a schematic view of geometrically necessary dislocations in a plastically bent lattice (Gao and Huang, 2003). . . . .	16
2.7 Basic idea of surface layer model initially proposed by Engel and Eckstein (2002): share of surface grains with the change of diameter of a cylindrical billet and grain size. . . . .	18
2.8 Numerical predictions by mesoscopic model Geiger et al. (2007): flat upsetting test of cylindrical specimens made by CuZn15 with a diameter of $0.5\ mm$ and length $3\ mm$ for different mean grain sizes $\bar{d}$ . . . . .	21
2.9 Comparison between predictions of SGP theory (Aifantis, 1999) and experiment results for twisted Cu wires in terms of $Q/\alpha^3$ v.s. $\gamma_s$ where $Q$ is the torque, $\alpha$ is the wire radius and $\gamma_s$ is the surface shear strain of the wire. . . . .	22
2.10 Illustration of elastic gaps following application of passivation predicted by the non-incremental (Gudmundson, 2004; Gurtin and Anand, 2009) and incremental (Fleck and Hutchinson, 2001) theories (Fleck et al., 2014). . . . .	27
2.11 Illustration of grain boundary: the microstructure image is taken from Lei et al. (2016) of solution-treated as-received Fe-17Cr-6Ni austenitic stainless steel. . . . .	29
2.12 Illustrative example of strain localization: experimentally observed shear band for aluminum AA6111 under uniaxial tensile test (Duan et al., 2005). . . . .	32
2.13 Illustration of slip and kink bands within a single crystal having only one slip system. .	33

2.14 Illustration of mesh-dependence pathology: (a) profiles of local effective plastic strain (b) stress-strain curves with different mesh size under classical plasticity model (Song and Voyatzis, 2020). . . . .	34
3.1 2D crystalline strip with two active slip systems, symmetrically tilted by $\theta_1 = 60^\circ$ and $\theta_2 = -60^\circ$ with respect to $e_1$ direction, for shear test simulations. . . . .	55
3.2 Influence of the energetic length scale $l_{en}$ under proportional loading conditions in the absence of higher-order dissipative effects: comparison between the present and Gurtin et al. (2007) results ( $n = 2$ , $l_{dis} = 0$ , $H_\pi = 0$ ). . . . .	56
3.3 Stress-strain responses under proportional and non-proportional loading conditions for different values of the defect energy index $n$ in the range of $n < 2$ and different values of the energetic length scale $l_{en}$ ( $l_{dis} = 0$ , $H_\pi = 0$ ). . . . .	57
3.4 Stress-strain curves and plastic slip distributions at different loading stages, obtained under first proportional and non-proportional loading to a macroscopic shear strain $\Gamma = 0.02$ followed by a complete loading cycle $\Gamma = 0.02 \rightarrow -0.02 \rightarrow 0.02$ ( $n = 1.3$ , $l_{en} = h$ , $l_{dis} = 0$ , $H_\pi = 0$ ). . . . .	59
3.5 Stress-strain responses for different values of the defect energy index $n$ in the range of $n \geq 2$ and different values of the energetic length scale $l_{en}$ , obtained under proportional and non-proportional loading conditions ( $l_{dis} = 0$ , $H_\pi = 0$ ). . . . .	60
3.6 Experimental evidence of the nonlinear kinematic hardening after one loading cycle in a large-grained Fe–Cr alloy aged at 923 K for 72 h (Reproduced from Taillard and Pineau (1982)). . . . .	61
3.7 Plastic shear strain distributions along $e_2$ direction for different values of the defect energy order-controlling index $n$ and different values of the energetic length scale $l_{en}$ , obtained under proportional loading ( $l_{dis} = 0$ , $H_\pi = 0$ ). . . . .	61
3.8 Influence of the dissipative length scale $l_{dis}$ in the absence of higher-order energetic effects under proportional loading conditions: comparison between the present and Gurtin et al. (2007) results ( $l_{en} = 0$ , $S_{\xi 0} = 50$ MPa, $H_\pi = 0$ , $H_\xi = 0$ ). . . . .	62
3.9 Influence of the higher-order hardening modulus $H_\xi$ in the absence of higher-order energetic effects ( $l_{en} = 0$ , $l_{dis} = h$ , $S_{\xi 0} = 50$ MPa, $H_\pi = 0$ ). . . . .	63
3.10 Comparison between the plastic shear strain profiles obtained using the present model and those obtained by Shu et al. (2001) using discrete dislocation plasticity at different values of applied shear strain $\Gamma$ under proportional loading conditions ( $l_{en} = 0$ , $l_{dis} =$ $0.3 h$ , $S_{\pi 0} = 15$ MPa, $S_{\xi 0} = 3$ MPa, $H_\pi = 0$ , $H_\xi = 200$ MPa). . . . .	64
3.11 Influence of the initial higher-order dissipative slip resistance $S_{\xi 0}$ on the elastic gap under proportional and non-proportional loading conditions ( $l_{en} = 0$ , $l_{dis} = h$ , $H_\pi = 0$ , $H_\xi = 100$ MPa). . . . .	66
3.12 Influence of the initial higher-order slip resistance $S_{\xi 0}$ on the moment-curvature re- sponse of the considered strip under pure bending with microfree conditions followed by top and bottom edges passivation and continued bending ( $l_{en} = 0$ , $l_{dis} = h$ , $H_\pi = 0$ , $H_\xi = 100$ MPa) . . . . .	66
3.13 Interaction between the different stresses involved in the proposed SGCP model under proportional loading ( $n = 2$ , $S_{\xi 0} = 50$ MPa). . . . .	67

4.1	Illustration of multiplicative decomposition of deformation gradient: Kröner-Lee decomposition (Kröner, 1959; Lee, 1964) . . . . .	73
4.2	Finite element used in the present work. . . . .	82
4.3	Simple shear of a constrained strip with two active slip systems. . . . .	84
4.4	Small shear loading results for different energetic and dissipative parameters: comparison between the small and finite deformation models. . . . .	85
4.5	Large shear loading results: comparison between the present model and the model of Kuroda and Tvergaard (2008a) for different values of $l_{en}/H$ . . . . .	86
5.1	A domain consisting of two grains A and B separated by grain boundary $\mathcal{G}$ in the reference configuration. . . . .	91
5.2	Illustration of bulk material element and grain boundary element used in this work. . . . .	99
5.3	A bi-crystal example for the validation and assessment of the proposed finite deformation grain boundary model. . . . .	100
5.4	Results of energetic GB parameter $\kappa = 10^3 \text{ N m}^{-1}$ using three combinations of bulk and grain boundary constitutive frameworks under shear loading $\Gamma = 0.04$ with $l_{en}/W = 10, S_{GB_0} = 0, H_{GB} = 0$ . . . . .	102
5.5	Results of dissipative GB parameter $S_{GB_0} = 40 \text{ N m}^{-1}$ using three combinations of bulk and grain boundary constitutive frameworks under shear loading $\Gamma = 0.04$ with $l_{en}/W = 10, \kappa = 0, H_{GB} = 0$ . . . . .	102
5.6	Influence of only GB energetic parameter $\kappa$ under cyclic loading ( $l_{en}/W = 10, S_{GB_0} = 0, H_{GB} = 0$ ). . . . .	103
5.7	Influence of only GB dissipative parameter $S_{GB_0}$ under cyclic loading ( $l_{en}/W = 10, \kappa = 0, H_{GB} = 0$ ). . . . .	104
5.8	Influence of GB dissipative hardening $H_{GB}$ under cyclic loading ( $l_{en}/W = 10, \kappa = 0, S_{GB_0} = 40 \text{ N m}^{-1}$ ). . . . .	104
5.9	Stress-strain responses under five complete cyclic loadings with $H_{GB} = 1e4 \text{ N m}^{-1}$ ( $l_{en}/W = 10, \kappa = 0, S_{GB_0} = 40 \text{ N m}^{-1}$ ). . . . .	105
5.10	Influence of energetic length scale $l_{en}$ under cyclic loading with only grain boundary dissipative effects ( $W = 1 \mu\text{m}, \kappa = 0, S_{GB_0} = 80 \text{ N m}^{-1}, H_{GB} = 0$ ). . . . .	106
5.11	Influence of geometry size effects $W$ under cyclic loading with only grain boundary dissipative effects ( $l_{en} = 10 \mu\text{m}, \kappa = 0, S_{GB_0} = 40 \text{ N m}^{-1}, H_{GB} = 0$ ). . . . .	106
5.12	Apparent initial yield stress $\sigma_{12}^0$ as a function of $1/W$ with only grain boundary dissipative effects ( $l_{en} = 10 \mu\text{m}, \kappa = 0, S_{GB_0} = 40 \text{ N m}^{-1}, H_{GB} = 0$ ). . . . .	107
5.13	Influence of grain misorientation $\theta_M$ under cyclic shear loading ( $l_{en}/W = 10, \kappa = 0, S_{GB_0} = 40 \text{ N m}^{-1}, H_{GB} = 0$ ) with a fixed grain boundary orientation angle $\theta_{GB} = 0^\circ$ . . . . .	107
5.14	Influence of grain boundary orientation $\theta_{GB}$ under cyclic shear loading ( $l_{en}/W = 10, \kappa = 0, S_{GB_0} = 40 \text{ N m}^{-1}, H_{GB} = 0$ ) with a constant grain misorientation $\theta_M = 20^\circ$ . . . . .	108
5.15	A poly-crystalline square plate of randomly distributed grains with two slip systems in each grain. . . . .	109
5.16	Stress-strain responses of polycrystalline plate under cyclic non-proportional and proportional loading with dissipative GB constitutive parameters for different geometry size ( $l_{en} = 10 \mu\text{m}, \kappa = 0, S_{GB_0} = 5 \text{ N m}^{-1}, H_{GB} = 0$ ). . . . .	110

6.1 Stress-strain curves and distributions of plastic scalar variable $\gamma$ along $x_2$ -direction in the case of horizontal slip at $\Gamma = 0.0032$ for different mesh refinements ( $l_{en}/H = 0.1$ , $l_{dis} = 0$ , $H_\pi = -500$ MPa, $n = 2$ ). . . . .	115
6.2 Stress-strain curves and distributions of plastic scalar variable $\gamma$ along $x_2$ -direction in the case of vertical slip at $\Gamma = 0.01$ for different mesh refinements ( $l_{en}/H = 0.1$ , $l_{dis} = 0$ , $H_\pi = -500$ MPa, $n = 2$ ). . . . .	116
6.3 Uniaxial tension of a single crystal plate with two slip systems symmetrically oriented with respect to the tension direction. . . . .	117
6.4 Nominal stress-strain curves and accumulated plastic slip variable distributions along $x_2$ -direction at nominal strain $\Delta L/L_0 = 0.1$ for different mesh refinements ( $l_{en}/W = 0.2$ , $l_{dis} = 0$ , $H_\pi = -500$ MPa). . . . .	119
6.5 Deformed meshes and contours of accumulated plastic slip variable $\gamma_{acc}$ at nominal strain $\Delta L/L_0 = 0.1$ for different mesh refinements ( $l_{en}/W = 0.2$ , $l_{dis} = 0$ , $H_\pi = -500$ MPa). . . . .	119
6.6 Uniaxial tension results obtained using conventional CP (CP: $l_{en} = l_{dis} = 0$ ), SGCP including only higher-order energetic effects (SGCP-EN: $l_{en}/W = 0.25$ , $l_{dis} = 0$ ) and SGCP including only higher-order dissipative effects (SGCP-DIS: $l_{en} = 0$ , $l_{dis}/W = 0.25$ ) for different meshes, with $S_{\xi 0} = 60.84$ MPa and $H_\xi = 0$ . . . . .	121
6.7 Evolution of plastic slip variable $\gamma$ and lattice rotation angle $\theta$ at different nominal tensile strains predicted by conventional CP ( $l_{en} = l_{dis} = 0$ ). . . . .	122
6.8 Evolution of plastic slip variable $\gamma$ and lattice rotation angle $\theta$ at different nominal tensile strains predicted by SGCP including only higher-order energetic effects ( $l_{en}/W = 0.25$ , $l_{dis} = 0$ ). . . . .	123
6.9 Influence of energetic length scale $l_{en}$ on the formation of the kink bands at the beginning of straining $\Delta L/L_0 = 0.006$ ( $l_{dis} = 0$ ). . . . .	124
6.10 Influence of energetic length scale $l_{en}$ on the nominal stress-strain responses and distribution of plastic slip variable $\gamma$ along $x_2$ direction at $\Delta L/L_0 = 0.2$ ( $l_{dis} = 0$ ). . . . .	125
6.11 Evolution of plastic slip variable $\gamma$ and lattice rotation angle $\theta$ at different nominal tensile strains predicted by SGCP including only higher-order dissipative effects with nonzero initial higher-order slip resistance $S_{\xi 0}$ ( $l_{en} = 0$ , $l_{dis}/W = 0.25$ , $S_{\xi 0} = 60.84$ MPa, $H_\xi = 60.84$ MPa) . . . . .	126
6.12 Influence of dissipative length scale $l_{dis}$ on tensile nominal stress-strain response and the distribution of plastic slip variable $\gamma$ along $x_2$ direction at $\Delta L/L_0 = 0.4$ ( $l_{en} = 0$ , $S_{\xi 0} = 60.84$ MPa, $H_\xi = 60.84$ MPa). . . . .	127
6.13 Poly-crystalline plates composed of several grains having two slip systems and different grain sizes . . . . .	128
6.14 Nominal stress-strain curves obtained using CCP in the grains ( $l_{en} = l_{dis} = 0$ ) and micro-free conditions at the grain boundaries ( $\kappa = 0$ , $S_{GB0} = 0$ , $H_{GB} = 0$ ), for different randomly generated grain orientations and different grain sizes. . . . .	130
6.15 Accumulated plastic slip variable $\gamma_{acc}$ contours within 40-grain plates at the end of loading obtained using CCP in the grains ( $l_{en} = l_{dis} = 0$ ) and micro-free conditions at the grain boundaries ( $\kappa = 0$ , $S_{GB0} = 0$ , $H_{GB} = 0$ ), for different randomly generated grain orientations. . . . .	131

6.16 Accumulated plastic slip variable $\gamma_{acc}$ contours within 40-grain plate with grain orientation “0” at different loading stages obtained using CCP in the grains ( $l_{en} = l_{dis} = 0$ ) and micro-free conditions at the grain boundaries ( $\kappa = 0, S_{GB_0} = 0, H_{GB} = 0$ ). . . . .	131
6.17 Influence of higher-order energetic and dissipative effects on the nominal tensile stress-strain response of 40-grain plate with grain orientation “0”, using micro-free GB conditions ( $\kappa = 0, S_{GB_0} = 0, H_{GB} = 0$ ). . . . .	132
6.18 Accumulated plastic slip variable $\gamma_{acc}$ contours within 40-grain plate with grain orientation “0” at the end of loading using different higher-order energetic and dissipative length scales and micro-free GB conditions ( $\kappa = 0, S_{GB} = 0, H_{GB} = 0$ ). . . . .	132
6.19 Influence of purely GB energetic and purely GB dissipative effects on nominal stress-strain response of 40-grain poly-crystalline plate with grain orientation “0”, obtained using $l_{en}/W = 0.25, l_{dis} = 0$ . . . . .	133
6.20 Deformed contours of accumulated plastic slip variable $\gamma_{acc}$ at the end of loading using different GB energetic coefficient $\kappa$ ( $S_{GB} = 0, H_{GB} = 0, l_{en}/W = 0.25, l_{dis} = 0$ ) and dissipative initial resistance $S_{GB_0}$ ( $\kappa = 0, H_{GB} = 0, l_{en}/W = 0.25, l_{dis} = 0$ ) for plate with 40 grains using grain orientation “0” . . . . .	134
6.21 An illustrative example of the overall size effects for different values of geometry size $W$ in terms of nominal stress-strain curves using SGCP constitutive parameters ( $l_{en} = l_{dis} = 2 \mu\text{m}, S_{\xi_0} = 60.84 \text{ MPa}, H_{\xi} = 60.84 \text{ MPa}$ ) in the bulk and GB parameters ( $\kappa = 1e2 \text{ N m}^{-1}, S_{GB_0} = 5 \text{ N m}^{-1}, H_{GB} = 1e3 \text{ N m}^{-1}$ ). . . . .	134
6.22 Relation between nominal critical stress and strain at the onset of strain localization with respect to the inverse of geometry horizontal dimension $1/W$ using both SGCP ( $l_{en} = l_{dis} = 2 \mu\text{m}, S_{\xi_0} = 60.84 \text{ MPa}, H_{\xi} = 60.84 \text{ MPa}$ ) and GB parameters ( $\kappa = 1e2 \text{ N m}^{-1}, S_{GB_0} = 5 \text{ N m}^{-1}, H_{GB} = 1e3 \text{ N m}^{-1}$ ). . . . .	135
7.1 Exemples de produits miniaturisés (de <a href="https://www.piceramic.com">https://www.piceramic.com</a> ). . . . .	144
7.2 Méthodologie de la thèse. . . . .	149
7.3 Catégories d’effets de taille proposées par Vollertsen (2008) . . . . .	152
7.4 Illustration des effets de taille extrinsèques de premier ordre sur le principe "plus petit, c’est plus faible" (Kals and Eckstein, 2000). . . . .	154
7.5 Exemple illustratif des effets de la taille statistique sur la dispersion de la contrainte d’écoulement : courbes d’écoulement pour différentes épaisseurs de feuilles avec une taille de grain constante (Fülöp et al., 2006). . . . .	154
7.6 Réponses contrainte-déformation dans des conditions de chargement proportionnel et non proportionnel pour différentes valeurs de l’indice d’énergie des défauts $n$ dans la gamme $n < 2$ et différentes valeurs de l’échelle de longueur énergétique $l_{en}$ ( $l_{dis} = 0, H_{\pi} = 0$ ). . . . .	165
7.7 Influence de la résistance initiale au glissement dissipatif d’ordre supérieur $S_{\xi_0}$ sur l’écart élastique dans des conditions de chargement proportionnel et non proportionnel ( $l_{en} = 0, l_{dis} = h, H_{\pi} = 0, H_{\xi} = 100 \text{ MPa}$ ). . . . .	167
7.8 Influence de la résistance initiale au glissement d’ordre supérieur $S_{\xi_0}$ sur la réponse moment-courbure de la bande considérée en flexion pure avec des conditions de microflexion, suivie d’une passivation des bords supérieurs et inférieurs et d’une flexion continue ( $l_{en} = 0, l_{dis} = h, H_{\pi} = 0, H_{\xi} = 100 \text{ MPa}$ ). . . . .	167

7.9	Illustration de la décomposition multiplicative du gradient de déformation : Décomposition de Kröner-Lee (Kröner, 1959; Lee, 1964). . . . .	170
7.10	Résultats des charges de petit cisaillement pour différents paramètres énergétiques et dissipatifs : comparaison entre le modèle de petite déformation et le modèle de déformation finie. . . . .	174
7.11	Résultats des charges de grand cisaillement : comparaison entre le présent modèle et le modèle de Kuroda and Tvergaard (2008a) pour différentes valeurs de $l_{en}/H$ . . . . .	175
7.12	Un domaine constitué de deux grains A et B séparés par un joint de grain $\mathcal{G}$ dans la configuration de référence. . . . .	179
7.13	Influence du seul paramètre énergétique GB $\kappa$ sous chargement cyclique ( $l_{en}/W = 10$ , $S_{GB_0} = 0$ , $H_{GB} = 0$ ). . . . .	182
7.14	Influence du seul paramètre dissipatif $S_{GB_0}$ sous chargement cyclique ( $l_{en}/W = 10$ , $\kappa = 0$ , $H_{GB} = 0$ ). . . . .	183
7.15	Une plaque carrée polycristalline dont les grains sont répartis de manière aléatoire et qui présente deux systèmes de glissement dans chaque grain. . . . .	183
7.16	Réponses contrainte-déformation d'une plaque polycristalline sous chargement cyclique non proportionnel et proportionnel avec des paramètres constitutifs GB dissipatifs pour différentes tailles géométriques ( $l_{en} = 10$ , $\kappa = 0$ , $S_{GB} = 5$ , $H_{GB} = 0$ ). . . . .	184
7.17	Courbes de contrainte-déformation et distributions de la variable scalaire plastique $\gamma$ le long de la direction $x_2$ dans le cas d'un glissement horizontal à $\Gamma = 0.0032$ pour différents raffinements de maillage ( $l_{en}/H = 0.1$ , $l_{dis} = 0$ , $H_\pi = -500$ MPa, $n = 2$ ). . . . .	189
7.18	Courbes de contrainte-déformation et distributions de la variable scalaire plastique $\gamma$ le long de la direction $x_2$ dans le cas d'un glissement vertical à $\Gamma = 0.01$ pour différents raffinements de maillage ( $l_{en}/H = 0.1$ , $l_{dis} = 0$ , $H_\pi = -500$ MPa, $n = 2$ ). . . . .	189
7.19	Courbes de contrainte-déformation nominales et distributions des variables de glissement plastique cumulé le long de la direction $x_2$ à la déformation nominale $\Delta L/L_0 = 0.1$ pour différents raffinements de maillage ( $l_{en}/W = 0.2$ , $l_{dis} = 0$ , $H_\pi = -500$ MPa). . . . .	191
7.20	Maillages déformés et contours de la variable de glissement plastique cumulé $\gamma_{acc}$ à la déformation nominale $\Delta L/L_0 = 0.1$ pour différents raffinements de maillage ( $l_{en}/W = 0.2$ , $l_{dis} = 0$ , $H_\pi = -500$ MPa). . . . .	191
7.21	Résultats de traction uniaxiale obtenus en utilisant la CP conventionnelle (CP: $l_{en} = l_{dis} = 0$ ), la SGCP incluant seulement les effets énergétiques d'ordre supérieur (SGCP-EN: $l_{en}/W = 0.25$ , $l_{dis} = 0$ ) et SGCP incluant uniquement les effets dissipatifs d'ordre supérieur (SGCP-DIS: $l_{en} = 0$ , $l_{dis}/W = 0.25$ ) pour différentes maillages, avec $S_{\xi_0} = 60.84$ MPa et $H_\xi = 0$ . . . . .	192
7.22	Plaque polycristalline constituée de trois différents nombres de grains avec deux systèmes de glissement dans chaque grain. . . . .	193
7.23	Courbes de contrainte-déformation nominales utilisant la CP conventionnelle ( $l_{en} = l_{dis} = 0$ ) avec des orientations de grains aléatoires adoptant des conditions de GB micro-libre ( $\kappa = 0$ , $S_{GB_0} = 0$ , $H_{GB} = 0$ ) pour différents nombres de grains. . . . .	195
7.24	Influence des effets énergétiques d'ordre supérieur ( $l_{dis} = 0$ ) et dissipatifs ( $l_{en} = 0$ , $S_{\xi_0} = 60.84$ MPa, $H_\xi = 60.84$ MPa) sur les réponses nominales traction-déformation avec une condition de GB micro-libre ( $\kappa = 0$ , $S_{GB_0} = 0$ , $H_{GB} = 0$ ) pour une plaque à 40 grains avec une orientation de grain "0". . . . .	196

7.25 Influence des effets énergétiques ( $S_{GB_0} = 0, H_{GB} = 0$ ) et dissipatifs ( $\kappa = 0, H_{GB} = 0$ ) de GB sur les réponses traction-déformation nominales avec seulement des effets énergétiques d'ordre supérieur ( $l_{en}/W = 0.25, l_{dis} = 0$ ) dans les cristaux massifs pour une plaque à 40 grains avec une orientation de grain "0". . . . .	197
7.26 Contours déformés de la variable de glissement plastique cumulé $\gamma_{acc}$ à la fin du chargement en utilisant différents coefficients énergétiques GB $\kappa$ ( $S_{GB} = 0, H_{GB} = 0, l_{en}/W = 0.25, l_{dis} = 0$ ) et résistance initiale dissipative $S_{GB_0}$ ( $\kappa = 0, H_{GB} = 0, l_{en}/W = 0.25, l_{dis} = 0$ ) pour une plaque à 40 grains avec une orientation de grain "0". . . . .	197
7.27 Exemple illustratif des effets de taille globaux pour différentes tailles de géométrie $W$ en termes de courbes de contrainte-déformation nominales utilisant les paramètres constitutifs SGCP ( $l_{en} = l_{dis} = 2 \mu\text{m}, S_{\xi_0} = 60.84 \text{ MPa}, H_{\xi} = 60.84 \text{ MPa}$ ) dans la masse et les paramètres GB ( $\kappa = 1e2 \text{ N m}^{-1}, S_{GB_0} = 5 \text{ N m}^{-1}, H_{GB} = 1e3 \text{ N m}^{-1}$ ). . . . .	198
7.28 Relation entre la contrainte et la déformation critiques nominales au début de la localisation des déformations par rapport à l'inverse de la dimension horizontale de la géométrie $1/W$ en utilisant à la fois les paramètres SGCP ( $l_{en} = l_{dis} = 2 \mu\text{m}, S_{\xi_0} = 60.84 \text{ MPa}, H_{\xi} = 60.84 \text{ MPa}$ ) et les paramètres GB ( $\kappa = 1e2 \text{ N m}^{-1}, S_{GB_0} = 5 \text{ N m}^{-1}, H_{GB} = 1e3 \text{ N m}^{-1}$ ). . . . .	198
A.1 Flow chart of numerical implementation. . . . .	210
A.2 The quadratic quadrilateral element with natural coordinates. . . . .	224



# List of Tables

3.1	Material parameters implied in system (3.70): the values of the fixed parameters are taken from Gurtin et al. (2007), for comparison purposes. . . . .	55
4.1	Material parameters implied for simple shear of constrained layer undergoing finite deformation, inspired by Kuroda and Tvergaard (2008a). . . . .	86
5.1	Material parameters implied for simple shear of periodic bi-crystal plate, inspired by Peirce et al. (1983); Kuroda (2011). . . . .	101
6.1	Material parameters implied for uniaxial tension of single crystal plate, inspired by Peirce et al. (1983); Kuroda (2011). . . . .	118
6.2	Material parameters implied for uniaxial tension of poly-crystalline plates, the bulk is inspired by Peirce et al. (1983); Kuroda (2011). . . . .	128
A.1	Gauss points for quadratic quadrilateral element. . . . .	223
B.1	Gauss points for element in finite deformation example. . . . .	236
C.1	Gauss points for one-dimensional line element in finite deformation example. . . . .	243



# **Part I**

## **English version**



# Chapter 1

## General introduction

### 1.1 Context and objectives

Over the past few decades, the significant developments in micro-electronics and micro-electro-mechanical systems (MEMS) have led to a dramatically increasing demand for miniaturized products. The size of these products generally ranges from a few micrometers to a few millimeters. Examples of such products are given in Fig. 1.1. The manufacture of miniaturized components is often a challenging task due to the presence of size effects, which render simple similarity-based rules for down-scaling conventional forming processes inapplicable (Vollertsen et al., 2006). In micro-forming processes, size effects may influence both material and process parameters and must be carefully considered (Engel and Eckstein, 2002). These effects have received a strong scientific interest in recent years, making them one of the major research concerns of today. When the geometrical dimensions of components down-scale from conventional (macroscopic) to microscopic level, the associated material behaviors become no longer size-independent. Several material properties, *e.g.*, flow stress, hardening and anisotropy, are altered owing to geometrical miniaturization. This may, in turn, influence the forming process parameters, such as forming forces, friction and scatter of the results. It is therefore necessary to properly consider size effects on miniaturized components. This will make it possible to optimize the micro-forming processes used to obtain these components. Consequently, micro-scale products with enhanced machinability and operating performance can be obtained.

Several classifications of size effects can be found in the literature (Vollertsen et al., 2006; Vollertsen, 2008; Geers et al., 2006; Liu et al., 2012), according to either their sources or impacts. Among them, the order-based classification proposed by Geers et al. (2006), which classifies size effects into first- and second-order effects, seems to be more general and attractive in the context of poly-crystalline metallic materials. In this classification, first-order size effects cover all microstructure (intrinsic) and statistical (extrinsic) size effects resulting from the discrete granular anisotropic nature of the microstructure, however excluding effects due deformation gradients. Second-order size effects cover the gradient effects within grains and those caused by boundaries (external surfaces, material interfaces, and grain boundaries). The order-based classification can cover most of size effects experimentally observed within poly-crystalline metallic materials. For instance, phenomena such as decrease of flow stress and increase of flow stress scatter by decreasing geometrical size correspond to first-order grain statistical (extrinsic) size effects (Fülöp et al., 2006; Kals and Eckstein, 2000; Chan et al., 2011). Strengthening phenomenon as a result of grain

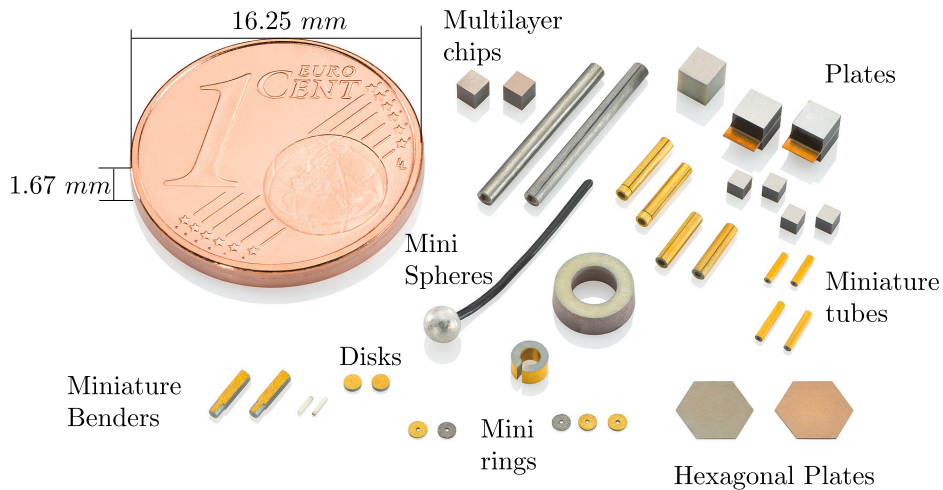


**Fig. 1.1.** Examples of miniaturized products (from <https://www.picericamic.com>).

refinement is a first-order microstructure (intrinsic) size effect (Janssen et al., 2006). On the contrary, strengthening due lattice curvature is a typical second-order (gradient) size effect, leading to “smaller is stronger” phenomenon as reported by several researches (Fleck et al., 1994; Liu et al., 2013; Dahlberg et al., 2017). With identical geometrical proportions, down-scaling a component naturally leads to an increase of strain gradients which have to be geometrically accommodated by curvature. The latter, which is limited by the lattice structure, is accommodated by the formation of geometrically necessary dislocations (GNDs; Ashby, 1970). As for classical dislocations, GNDs act as obstacles to plastic slips, leading to further strengthening and/or hardening. Strengthening phenomena due to external surfaces and grain boundaries are second-order effects.

Classical plasticity theories cannot predict size effects, due to the lack of size-dependent parameters. To account for these effects, several investigations have proposed enriched constitutive laws which include information on the size of interest using size-dependent factors, *e.g.*, geometry size, average grain size, *etc.* (Kim et al., 2007; Leu, 2009; Meng and Fu, 2015). The additional size-dependent factors are generally calibrated based on experimental micro-scale tests for specific specimens. Inspired by the fact that surface proportions, and then their effects, are more important in miniaturized components than in conventional (macroscopic) ones, multipart material behavior models, *i.e.*, including different material descriptions in different regions, have been developed. One typical multipart model is the surface layer model proposed by Engel and Eckstein (2002), in which the studied material is subdivided into surface and inner grains with different modeling assumptions. Due to the slight grain boundary influence on grains near the surface, these grains are considered as single crystals, while average poly-crystalline behavior is adopted for the inner grains. The overall behavior is obtained by summing up the surface and inner contributions multiplied by their respective percentages. However, the resulting behavior ignores any smooth transition between the contributions. Regarding this deficiency, Geiger et al. (2007) have developed a mesoscopic model where the studied material is subdivided into single grains with individual properties, depending on the size and position of each grain within the material. This model requires the creation of synthetic microstructure close to the real one in the studied material. Compared to conventional models with artificial inclusion of size-dependent factors within the constitutive laws, surface layer and mesoscopic models represent a non-trivial progress towards the accurate

modeling of size effects. Involving single-crystal plasticity, these models show good capabilities in capturing first-order size effects, as reported by several authors in the literature (Lai et al., 2008; Yun et al., 2010; Wang et al., 2013; Ran et al., 2013).

First-order size effects, whether extrinsic or intrinsic, are closely related to the microstructure of miniaturized products. Conventional crystal plasticity theories, which describe plastic deformation based on individual plastic slips on specific slip systems, enable covering this kind of size effects in a natural manner. However, as these theories are based on the principle of local action and do not include internal length scales, they cannot capture second-order size effects induced by deformation gradients. To overcome limitations of local theories, several enhanced plasticity approaches have been developed during the past few decades with the aim of properly accounting for nonlocal deformation mechanisms, *e.g.*, Cosserat theories (Forest et al., 1997), micromorphic theories (Forest, 2009) and strain gradient plasticity (SGP) theories (Aifantis, 1987). Thanks to their attractive features in capturing second-order effects, SGP theories have received a strong scientific interest in recent years, leading to the development of various SGP models for small and finite deformation micro-scale problems (Aifantis, 1999; Fleck and Hutchinson, 1997, 2001; Gudmundson, 2004; Martínez-Pañeda et al., 2016, 2017, 2019). These models have first been developed for poly-crystalline structures (Aifantis, 1987), and then extended to single-crystals Gurtin (2000). Capable of capturing local single-crystal features and deformation gradients, single-crystal SGP models, which will be referred to hereafter as strain gradient crystal plasticity (SGCP) models, provide an excellent framework to capture both first- and second-order size effects within single crystals. However, several issues related to their theoretical formulations, such as accurate description of defect and dissipation energies and flexibility in controlling some important higher-order mechanisms, still need to be considered for a realistic prediction of these effects. One of the PhD objectives consists in corroborating the existing works on these issues, with the aim of developing a flexible finite deformation SGCP model allowing for an easy control of some predicted higher-order effects.

Formulated at the scale of single-crystals, SGCP models are not devoted to provide precise description of second-order grain boundary (GB) effects, which become significant with decreasing the geometry size. To capture the latter effects, it is necessary to couple these models with GB formulations that account for the interaction mechanisms between dislocations and grain boundaries. In the framework of enhanced continua, simple micro-free (fully transparent) or micro-hard (fully opaque) grain boundary conditions have widely been used in studies for which GB contributions are not of central interest (Geers et al., 2006; Yalçinkaya et al., 2017). These conditions represent limiting cases for real GB behaviors which rely on complex interaction mechanisms between dislocations and grain boundaries (GBs), including dislocation pile-ups, absorption, emission and reflection at the GBs (Bayerschen et al., 2016). Attempts to develop more elaborate GB models with respect to these interaction mechanisms can be found in the literature (Cermelli and Gurtin, 2002; Aifantis and Willis, 2005; Aifantis et al., 2006; Fredriksson and Gudmundson, 2007; Bayerschen et al., 2015; Bayerschen and Böhlke, 2016; Bayerschen et al., 2016; Wulffinghoff et al., 2013; Wulffinghoff, 2017). The simplest of these models have been formulated based on simplified phenomenological constitutive laws for GBs (Gudmundson, 2004; Aifantis and Willis, 2005; Aifantis et al., 2006; Fredriksson and Gudmundson, 2007). Both small and finite deformation variations of such models can be found in the literature. Although successfully applied to predict interesting GB mechanisms, these models do not account for some important geometrical and crystallographic features, like grain and grain boundary orientations, which can have significant influence on GB

behaviors.

To overcome limitations of phenomenological GB approaches, GB models based on kinematic control variables accounting for geometrical and crystallographic effects have been proposed. In this context, models of [Evers et al. \(2004b\)](#) and [Gurtin \(2008b\)](#) can particularly be cited. Both these models include grain misorientation and grain boundary orientation effects. They are respectively proposed within dislocation-density-based (*i.e.*, with dislocation densities as primary variables) and plastic-slip-based (*i.e.*, with plastic slips as primary variables) frameworks. Based on [Klusemann et al. \(2012\)](#), these frameworks generally provide similar results for similar problems. However, plastic-slip-based framework seems to present some advantages in calculating plastic slips and constraining dislocation flow at boundaries. Indeed, there is no need for local integration scheme to obtain plastic slips (considered as primary variables) from dislocation densities. Furthermore, dislocation flow at boundaries can easily be controlled by directly constraining plastic slips rather than their gradients. This framework is retained for the developments of the present PhD project. However, further investigation is needed to better understand the difference between the two frameworks.

In the context of plastic-slip-based approaches, the interesting features of the [Gurtin \(2008b\)](#) model have inspired the development of several Gurtin-type GB models which rely on geometrical and crystallographic considerations. Most of these models have been proposed for small deformation problems ([van Beers et al., 2013](#); [Gottschalk et al., 2016](#)). Only few works extending [Gurtin \(2008b\)](#) model to finite deformation exist in the literature. [McBride et al. \(2016\)](#) have proposed a finite deformation Gurtin-type GB model formulated using Eulerian description, which is not widely used in the context of strain gradient continua. Another finite deformation Gurtin-type GB model can be found in [Peng et al. \(2019\)](#). Although developed using Lagrangian description, this model is based on a simplifying assumption that the undistorted lattice resides in the reference (material) space and not in the structural one. Furthermore, no plastic distortion of the lattice is considered. These assumptions lead to a GB formulation which is identical to that proposed by [Gurtin \(2008b\)](#) in small deformation context, making it unsuitable for problems involving large deformations at GBs. As the Lagrangian description is widely used in the context of strain gradient plasticity, development of a Lagrangian finite deformation extension of the [Gurtin \(2008b\)](#) model, while accounting properly for plastic lattice distortion, would be very helpful. Indeed, several applications involving miniaturized products activate large deformation effects even at the grain boundaries.

In spite of extensive scientific efforts made in the direction of accurate modeling of size effects, realistic and precise description of these effects still faces various challenging issues. These issues prevent the development of a comprehensive numerical tool capable of capturing all kinds of size effects characterizing poly-crystalline structures. These include first- and second-order effects within individual grains and at grain boundaries. With the ever growing demand for miniaturized products in various engineering areas, this numerical tool is eagerly awaited as it will allow for optimizing the micro-forming processes used to obtain these products. In this context, the present PhD project aims at corroborating existing works on the development of such a numerical tool. Inspired by [Gurtin et al. \(2007\)](#), a flexible finite deformation strain gradient crystal plasticity (SGCP) model will be developed. This model will be used to predict first- and second-order size effects within single crystals. To capture finite deformation size effects due to grain boundaries, a finite deformation extension of the grain boundary (GB) model of [Gurtin \(2008b\)](#) will be performed using fully Lagrangian description, which is most commonly used in the context on gradient-enhanced continua. As an application, the proposed finite deformation SGCP and GB models will be applied

to study size effects on one of the most challenging finite deformation problems characterizing micro-forming processes: localization in single- and poly-crystalline structures.

## 1.2 Methodology of the thesis

Fig. 1.2 presents the methodology followed in this work to achieve the overall objectives of the PhD project, which are the development of flexible numerical framework capable of capturing different kinds of poly-crystalline size effects and the application of this framework to study localization phenomena within single- and poly-crystalline structures.

An extensive literature review was first done to better understand size effects within polycrystals as well as the modeling techniques used to predict them. Based on this literature review, mainly three classes of size effects can be distinguished: first- and second-order grain effects and grain boundary (GB) effects. Strain gradient crystal plasticity (SGCP) theories present interesting capabilities in reproducing the first two classes of size effects. The latter class can be modeled using adapted grain boundary (GB) formulation accounting for complex interaction mechanisms between dislocations at grain boundaries. A coupling between SGCP and GB models is then required to accurately reproduce major poly-crystalline size effects. Such a coupling represents the backbone of the intended flexible numerical framework. The choice of the SGCP and GB formulations to be coupled can highly affect the effectiveness of this framework and considerable attention must be given to this task.

Despite the strong scientific effort made on SGCP theories, some challenging issues related to their theoretical formulations still need to be addressed. Most of them are concerned with the definition of energetic and dissipative higher-order processes. Energetic processes are pragmatically described using quadratic forms of defect energy. As pointed out by several authors (*e.g.*, Cordero et al., 2010; Forest and Guéninchault, 2013), quadratic forms are unusual in classical dislocation theories and can be very simple to correctly reflect the real nature of energetic higher-order processes. Other forms of defect energy have been tested, *e.g.* linear (Ohno and Okumura, 2007; Hurtado and Ortiz, 2013; Wulffinghoff et al., 2015) and logarithmic (Forest, 2013; Wulffinghoff et al., 2015) defect energy. Depending on the adopted form of defect energy, different size effects have been obtained. As for dissipative processes, in almost all existing SGCP models, such processes are described using coupling effective strain measures implying plastic strains and their gradients in a coupled manner. This choice relies on a constraining assumption that dissipative processes due to plastic strains and their gradients are coupled. Such an assumption, although not confirmed experimentally, highly constrains the control of dissipative effects. With the aim of developing a flexible SGCP model as a part of the intended numerical framework, the first objective of the present PhD work is to corroborate existing studies on SGCP issues. Based on the work of Gurtin et al. (2007), a flexible Gurtin-type model based on generalized defect energy, with order-controlling index, and uncoupled dissipation assumption was developed. A small deformation version of the model was first proposed to perform a comprehensive investigation of higher-order parameters in the absence of large strain effects. Then, a finite deformation extension was proposed for problems involving large strain effects, such as localization problems. This version was formulated using fully Lagrangian description. Small and finite deformation versions of the model were implemented within the commercial finite element code Abaqus/Standard via User-Element (UEL) subroutines.

The proposed small and finite deformation Gurtin-type SGCP variations make it possible to

capture first- and second-order single-crystal size effects within small and finite deformation frameworks. To depict GB effects in poly-crystalline materials, these variations must be coupled with appropriate GB formulations. Several grain boundary models have been proposed in the literature ([Gudmundson, 2004](#); [Fredriksson and Gudmundson, 2007](#); [Aifantis and Willis, 2005](#); [Wulffinghoff, 2017](#); [Gurtin, 2008b](#); [van Beers et al., 2013](#); [Gottschalk et al., 2016](#)). Among them, the [Gurtin \(2008b\)](#) model presents promising capabilities in capturing different kinds of GB size effects, including those due to grain and grain boundary orientations. Therefore, it was chosen in this work as basis for the modeling of GB size effects. This model which has been proposed in small deformation framework was implemented in this work within Abaqus/Standard and coupled with the small deformation version of the proposed SGCP model. For large deformation applications, a new extension of this model based on fully Lagrangian description was formulated and implemented within Abaqus/Standard. After validation of the model implementation, this extension was applied to conduct a comprehensive investigation on the influence of major GB parameters on the prediction of GB size effects.

The coupling between the proposed SGCP and GB models provides a flexible numerical tool capable of capturing different kinds of size effects within poly-crystalline structures under small and large deformation conditions. As an application of this numerical tool, it was applied to take a first step in the investigation of size effects on localization phenomena. Single crystals were first considered to study the capabilities of SGCP in capturing different kinds of localization bands, including slip, kink and complex bands. Then, an initiation into localization within poly-crystalline structures was provided. Considering the time required to prepare the input files for poly-crystalline simulations, an advanced python tool allowing for automating this task was developed. This tool will be used in future work to conduct a complete study of size effects on localization phenomena and formability of small-scale sheet metals.

### 1.3 Organization of the thesis

Following the general introduction, the remaining parts of the thesis are organized as follows:

- In Chapter 2: A literature review related to the objectives of this thesis will be given. Definition and classifications of major size effects in poly-crystalline structures will first be discussed. Next, some common numerical approaches used to reproduce such effects will briefly be presented and compared. Then, an emphasis will be placed on gradient-enhanced theories and some major related issues, as they are the basis of the PhD developments. Finally, the current progress on the investigation of strain localization phenomena using these theories will be discussed.
- In Chapter 3: A flexible small deformation Gurtin-type SGCP model will be developed based on a generalized non-quadratic defect energy and uncoupled constitutive assumption for dissipative processes. A two-dimensional version of the proposed model will be implemented and validated using examples from the literature. Systematic assessment of the model will be performed using both proportional and non-proportional shear loading conditions.
- In Chapter 4: The flexible small deformation SGCP model will be extended to finite deformation using fully Lagrangian description. A two-dimensional version of the finite deformation

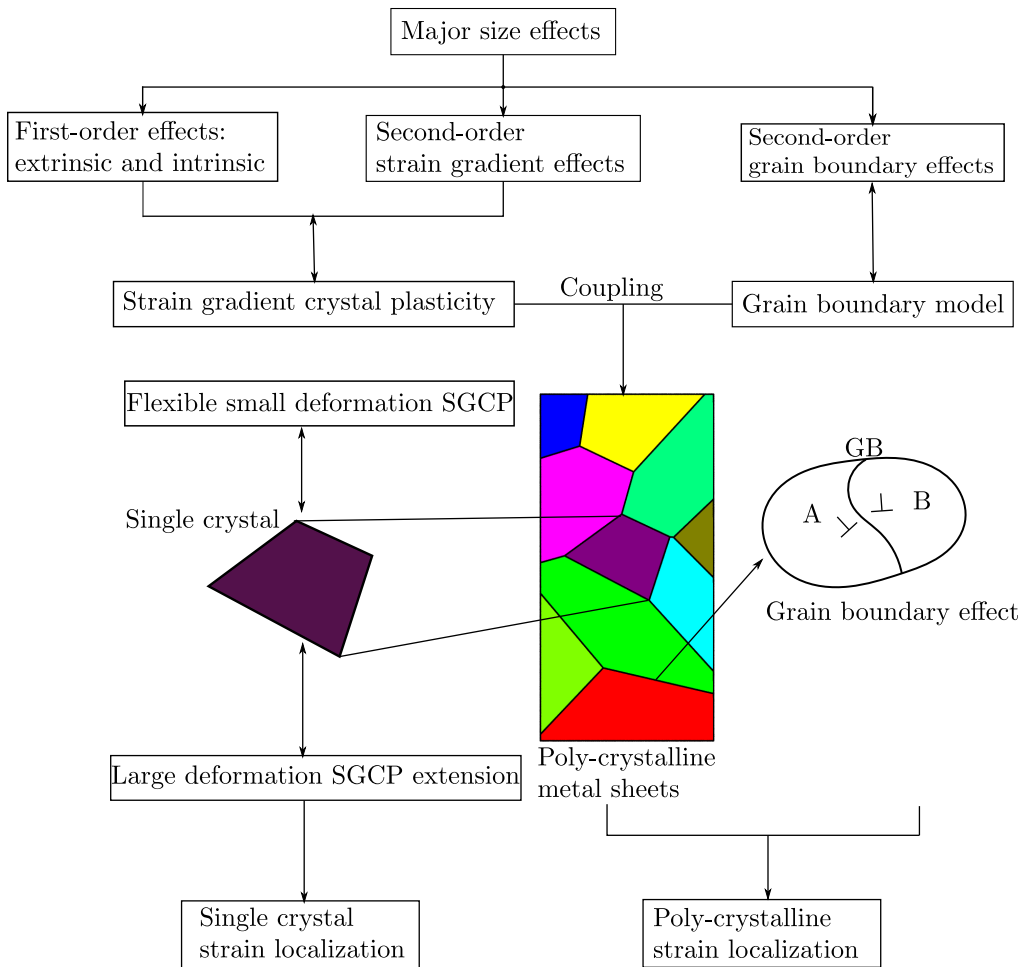


## **Fig. 1.2.** Methodology of the thesis.

model will be implemented and validated by comparison with small deformation results and with finite deformation ones from the literature.

- In Chapter 5: A new finite deformation extension of the GB model of [Gurtin \(2008b\)](#) will be formulated using fully Lagrangian description. This model will be implemented and coupled with the finite deformation version of the proposed flexible SGCP model. The model implementation will be validated by comparing the associated results with those obtained using the [Gurtin \(2008b\)](#) model. Finally, influence of major GB parameters involved in this model will investigated.
  - In Chapter 6: The developed SGCP and GB models will be coupled and applied to study strain localization in single- and poly-crystalline metal sheets. The purposes of the strain localization study in single crystals is to provide an in-depth investigation of the capabilities and limitations of the finite deformation SGCP model in predicting different kinds of localization modes. Strain localization investigation in poly-crystalline metal sheets will then be performed.
  - Finally, the thesis will end up with several conclusions and perspectives.



# **Chapter 2**

## **State of the art**

### **Abstract**

This chapter provides a literature review of important aspects related to each objective of the thesis. An overview of size effects will be given first from the perspectives of their definition, classification and influence. Next, major numerical models developed in the continuum domain to capture these effects will briefly be presented, in which the choice of the gradient-enhanced crystal plasticity as basis for the development of the numerical framework will be discussed. In addition, strain gradient plasticity will be briefly reviewed by demonstrating incremental and non-incremental models. Then, grain boundary models based gradient-enhanced plasticity will be reviewed. Finally, important localization aspects within crystalline materials associated with the application of the numerical tool developed in the thesis will be discussed.

## 2.1 Definition and classification of size effects

With the development of micro-electro-mechanical systems (MEMS), a great demand in miniaturized products has emerged. Due to their microscopic dimensions, these products present a size-dependent material behavior. Generally speaking, size effects come along with up- or down-scaling of an object and were discovered and depicted for up-scaling processes (Vollertsen, 2008). With the dramatically increasing demand for miniaturized products during the last few decades, various kinds of size effects are frequently observed during the manufacturing process of these products. Size effects can be literally interpreted as, the unexpected deviations due to changing the dimensions of a structure. Referring to Vollertsen (2008), a more precise definition of size effects can be given as those deviations from intrinsic (intensive) values or expected changes in extrinsic (extensive) values of a process after scaling the geometrical dimensions. Intrinsic variables represent those which do not change with mass (or size) of an object, *e.g.*, density. Extrinsic variables are directly related to the amount of material of an object, *e.g.*, volume.

The systematic categories of size effects have been proposed by Vollertsen (2008) including density size effects, shape size effects and microstructure size effects, as illustrated in Fig. 2.1. The density size effects occur when the density of a geometry is held constant. As a result, features such as point defects (*e.g.* small pores), line defects (*e.g.* dislocation lines) or interface areas (*e.g.* grain boundaries) will normally decrease in the considered geometry, which will lead to strengthening and scatter in flow stress (Armstrong, 1961). Obviously, the density variable in this category corresponds to “intensive values” as prescribed in size effects definition. Shape size effects will occur if the value of interest (*e.g.*, surface grains and interior grains) depends on the ratio between the total surface area and volume. This ratio increases while reducing geometry size proportionally. One typical example is the decrease of flow stress with decreased geometry size as reported by several works (Chan et al., 2011; Liu et al., 2011a). The shape variable here corresponds to the “extensive values”. The microstructure size effects take place when the microstructure features (*e.g.*, grain size or precipitates and surface roughness) are remained constant while decreasing geometry size.

Geers et al. (2006) proposed a more universal classification of size effects, viz. first-order effects and second-order effects exclusive to crystalline materials. Regarding first-order effects, they cover all effects stemming from the discrete granular anisotropic nature of the microstructure.

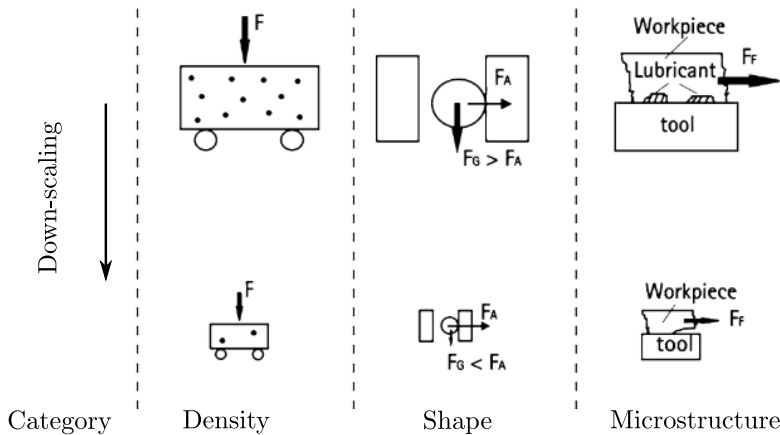


**Fig. 2.1.** Categories of size effects proposed by Vollertsen (2008).

The second-order size effects comprise contributions due to lattice curvature effects (gradients of deformation, *e.g.*, strain gradients, slip gradients, *etc.*) and boundary effects (*e.g.*, grain boundary effects and external boundary effects).

[Fu and Wang \(2021\)](#) classified size effects into three categories by their manifestations: smaller is stronger (SS) effects, smaller is weaker (SW) effects and those between SS and SW. The first one, SS effects, refer to the increase of material property (*e.g.*, material strength, flow stress and hardness, *etc.*) as the geometry decreases. For the SW effects, it is the opposite case compared to SS. The intermediate effects show a varied tendency between SS and SW. For instance, [Kals \(1999\)](#) discovered a switching trend from SW effects to SS effects through bending cases of aluminum alloy.

In fact, the aforementioned categories of size effects have several overlaps. For instance, density size effects of [Vollertsen \(2008\)](#) lead to the scatter in flow stress which corresponds to first-order extrinsic size effects defined by [Geers et al. \(2006\)](#). One manifestation of shape size effects discussed in [Vollertsen \(2008\)](#) is the decrease of flow stress with smaller geometry. It coincides with the example in first-order extrinsic size effects ([Geers et al., 2006](#)) showing a decrease of flow stress as geometrical dimension diminishes. Meanwhile, it is equivalent to the SW category proposed by [Fu and Wang \(2021\)](#). The strain gradient effects regarded as the category of microstructure size effects ([Vollertsen, 2008](#)) is equivalent to the second-order effects ([Geers et al., 2006](#)) due to gradients of deformation.

With respect to crystalline metallic miniaturized structures, the order-based classification ([Geers et al., 2006](#)) of size effects seems more appropriate to embrace various size effects in an organized manner. This manner attempts to classify size effects into lower-order (local effects caused by microstructure) and higher-order (non-local ones caused by gradient effects in addition with boundary effects) ones according to the sources generating size effects. It is a more flexible manner compared to the classification by [Fu and Wang \(2021\)](#), which can be regarded as a phenomenon-oriented manner (*i.e.*, classifying size effects referring to their resulting phenomenon such as “smaller is stronger” and “smaller is weaker”). Hence, the order-based classification of size effects will be adopted in this thesis and frequently mentioned hereafter. In what follows, experimental observations of size effects on the basis of first- and second-order classification will be presented.

## 2.2 Experimental observations of size effects

### 2.2.1 First-order extrinsic/intrinsic size effects

According to [Geers et al. \(2006\)](#), first-order size effects are mainly reflected by two ways, *i.e.*, statistical (extrinsic) size effects and microstructure (intrinsic) size effects. The statistical effects usually result in a decrease of mean flow stress and an increase of scatter on flow stress. Fig. 2.2 presents an example of the decreased flow stress along with miniaturization, through a tensile test of CuNi18Zn20 sheet performed by [Kals and Eckstein \(2000\)](#). The miniaturization measure is defined by reducing specimen thickness  $\lambda$ , while keeping an approximately constant grain size ( $d = 40 \mu\text{m}$ ). It is clearly shown in Fig. 2.2 that a thinner sheet has a lower flow stress. The decrease of flow stress is generally denoted as “smaller is weaker” phenomenon, a typical feature for first-order extrinsic size effects. The “smaller is weaker” phenomenon has been widely recognized as a result of different material behaviors of surface and inner grains due to miniaturization. The surface

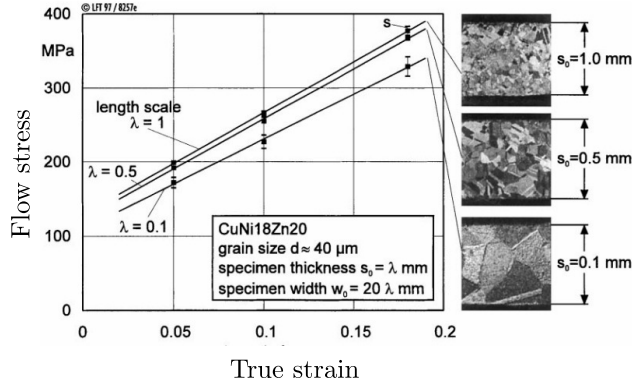


**Fig. 2.2.** Illustration of first-order extrinsic size effects on “smaller is weaker”: flow stress of CuNi18Zn20 sheet for different thickness  $\lambda$  maintaining the constant grain size (approximately  $40 \mu\text{m}$ ) under tensile loading (Kals and Eckstein, 2000).

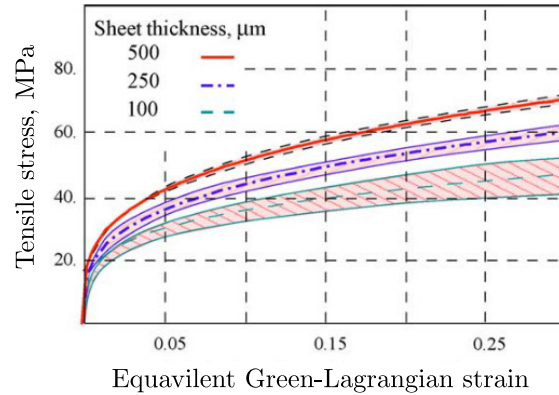


**Fig. 2.3.** Illustrative example of statistical size effects on scatter of flow stress: flow curves for different sheet thicknesses with a constant grain size (Fülop et al., 2006).

grains exert less constraints compared to inner ones (Miyazaki et al., 1979), thus have a lower flow stress behavior. With miniaturizing (shown in Fig. 2.2 right side), the proportion of surface grains over the total grains enlarges. Hence, the overall flow stress, which is composed by surface and inner contributions, decreases for a thinner sheet thickness in Fig. 2.2. Similar experimental tests showing “smaller is weaker” can also be found in tensile tests of different material sheet foils (Peng et al., 2007; Liu et al., 2011a) and compression tests of cylindrical specimens (Chan et al., 2011; Xu et al., 2015) with different diameter.

Another manifestation of first-order statistical (extrinsic) size effects is the scatter of flow stress. An example can be found by a tensile example of aluminum sheets in Fig. 2.3. For each sheet thickness in Fig. 2.3, five samples with random microstructure and constant mean grain size ( $100 \mu\text{m}$ ) are adopted. For thinner specimens, a smaller flow stress was obtained which indicates the “smaller is weaker” effect. A larger spread over the flow stress occurs while decreasing sheet thickness. The scatter of flow stress is the distinctive feature of extrinsic size effects. With reduction of thickness, individual grains become manifest and the anisotropic behaviors appear obvious. Influence of individual grain orientation becomes more significant with fewer grains in the section of sheets.

First-order intrinsic size effects can also be denoted as grain size effects or microstructure size

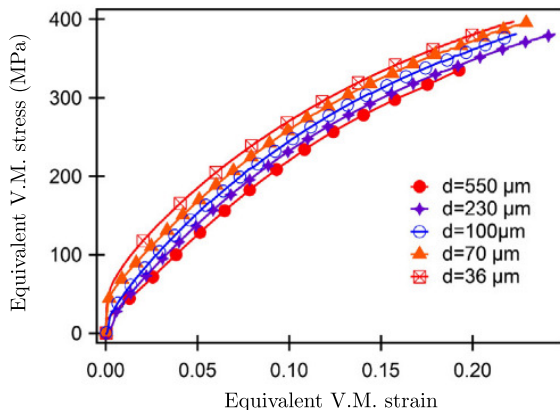


**Fig. 2.4.** Illustrative example of intrinsic size effects: True equivalent V.M. stress – V.M. strain curves obtained for cylindrical Ni samples (diameter 10mm) with different averaged grain size (Keller et al., 2015).

effects (Geers et al., 2006). One common example is the grain size refinement strengthening by reducing grain size such as through heat treatment. Several experimental evidences can be found in (Kals and Eckstein, 2000; Janssen et al., 2006; Hug and Keller, 2010; Hug et al., 2014; Keller et al., 2015). The strengthening effects caused by intrinsic size effects can be explained as the increase of dislocation interactions across grain boundaries. Fig. 2.4 provides experimental evidence for grain intrinsic size effects by tensile tests on cylindrical Ni sample (constant cylindrical diameter 10mm) using different grain sizes  $d$  (Keller et al., 2015). With a refined grain size, material strengthening can be discovered.

## 2.2.2 Second-order gradient size effects

Second-order gradient size effects occur with the presence of deformation gradients which have been revealed by several small scale experiments. One typical experiment was performed by Fleck et al. (1994) on the tension and torsion of cooper wires as shown in Fig. 2.5. Both tension and torsion cases of the copper wires show size-dependent material responses, *i.e.*, a smaller diameter exhibits a larger yield and hardening. The size-dependent material responses are more pronounced for the torsion loading. A similar study of thin wires torsion was also reported by Liu et al. (2012). Several different experiments, such as micro-indentation (Nix and Gao, 1998; McElhaney et al., 1998; Ma et al., 2012; Sarac et al., 2016; Dahlberg et al., 2017), micro-bending of thin foils (Stölken and Evans, 1998; Hayashi et al., 2011), and micro-pillar compression (Greer and Nix, 2005) have shown gradient size effects as well.

The second-order size effects in the aforementioned experiments for small dimensional structures can be attributed to the presence of strain gradients (Fleck et al., 1994). During plastic deformation for metallic materials, dislocations will be generated, moved and stored. Two types of dislocations exist during dislocation movement, one is statistically stored dislocations (SSDs), which trap each other in a random way, the other named as geometrically necessary dislocations (GNDs), which are required for compatible deformation of various parts of the crystalline materials (Ashby, 1970). The concept of GNDs can be explained by a bending example, as illustrated in Fig. 2.6 by a bent beam. Due to non-uniform plastic deformation, certain dislocations are required to

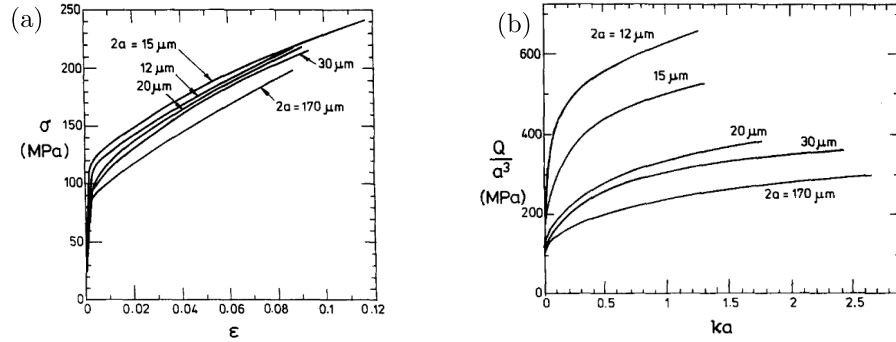


**Fig. 2.5.** Size dependent material responses for copper wires of diameter  $2a$  from  $12 \mu\text{m}$  to  $170 \mu\text{m}$ : (a) true stress  $\sigma$  vs logarithmic strain  $\epsilon$  tension (b) torsional response displayed in the form  $Q/a^3$  vs  $\kappa a$  where  $Q$  is the torque,  $a$  the wire radius and  $\kappa$  the twist per unit length (Fleck et al., 1994).

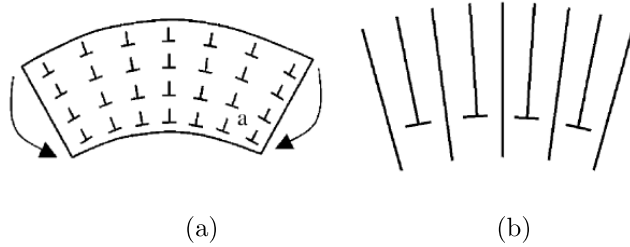


**Fig. 2.6.** Illustration of geometrically necessary dislocations in a plastically bent beam: (a) a periodic array of dislocations with Burgers vector  $b$  and spacing  $L$  will generate a lattice curvature as  $b/L^2$  (b) a schematic view of geometrically necessary dislocations in a plastically bent lattice (Gao and Huang, 2003).

accommodate the lattice curvature. GNDs are generally accompanied by inhomogeneous plastic deformation leading to material hardening by acting as obstacles to the motion of other SSDs. The GNDs, which are associated with plastic strain gradients will manifest their effects when the characteristic length of deformation becomes sufficiently small (Gao and Huang, 2003). This explains the correlation between the smaller is stronger in aforementioned experiments and the presence of strain gradients.

## 2.3 Numerical modeling of size effects

The first- and second-order size effects, as detailed in the previous subsection, are treated as the major size effects for miniaturized components. It is essential to take into account the major size effects in the constitutive framework aiming to obtain accurate predictions by numerical simulations. Hence, in this subsection, numerical modeling techniques associated with size effects will be reviewed firstly. Weighing the pros and cons of these techniques, the choice of numerical models in this work will be discussed.

### 2.3.1 Enriched conventional plasticity models

Conventional plasticity theories fail to predict size dependence of material responses in micro-scale, as a result of lacking size-dependent variables. To overcome this deficiency, many researchers have made efforts to capture size effects by extending conventional plasticity theories, such as adding extra parameters associated with geometry size. Various investigations have been devoted to capturing size effects by adding variables associated with size effects into constitutive laws. These parameters linked to size effects description are generally calibrated through experiments in micro-scale. In what follows, several attempts will be summarized.

[Kim et al. \(2007\)](#) proposed a modified Hall-Petch relation by introducing two parameters  $\alpha$  and  $\beta$  for describing specimen size and grain size. The classical Hall-Petch relation is formulated as ([Armstrong et al., 1962](#)):

$$\sigma = \sigma_0 + \frac{k}{\sqrt{d}} \quad (2.1)$$

where  $\sigma_0$  and  $k$  are material constants,  $d$  represents the grain size. The material constant  $\sigma_0$  is related to resolved shear stress  $\tau$  so the Hall-Petch relation can be reformulated as ([Armstrong et al., 1962](#)):

$$\sigma = M\tau + \frac{k}{\sqrt{d}} \quad (2.2)$$

with  $\tau$  the resolved shear stress and  $M$  the orientation factor. The model proposed by [Kim et al. \(2007\)](#) can be considered as an enhancement of the Hall-Petch relation which is expressed as:

$$\sigma = M^\alpha \tau + \frac{k}{\sqrt{d}} \beta \quad (2.3)$$

where the exponent  $\alpha$  and  $\beta$  are scaling parameters. Note that parameters  $M, \alpha, \beta$  in this model need to be calibrated through experimental data. It is possible to simulate single and poly-crystals by different setup of the scaling parameters. The model showed a good agreement with different experimental results. However, this model is only limited to equiaxed grains and homogeneous material behavior ([Kim et al., 2007](#)).

[Chen and Ngan \(2011\)](#) proposed a model for Ag micro-wires in which the overall material strength is divided into three parts involved respectively by grain size  $d$ , specimen size  $t$  and the ratio  $t/d$ :

$$\sigma = \sigma_1(t) + \sigma_2(t/d) + \frac{k}{\sqrt{d}} \quad (2.4)$$

where  $\sigma_1(t)$  represents specimen size effects,  $\sigma_2(t/d)$  describes shape effects and  $\frac{k}{\sqrt{d}}$  is the usual Hall-Petch dependence. Results predicted by this model showed significant shape size effect and grain size effect. Interestingly, results also indicated the existence of strengthening effect with decreasing specimen size  $t$  when the shape effects factor  $t/d$  is in the range of less than 3.

[Meng and Fu \(2015\)](#) proposed a modified Swift constitutive model in order to consider surface roughness induced by size effects. The modified model introduced a coefficient associated with thickness non-uniform feature as follows:

$$\sigma = \frac{K(\varepsilon + \varepsilon_0)^n}{\xi_{sf}} \quad (2.5)$$

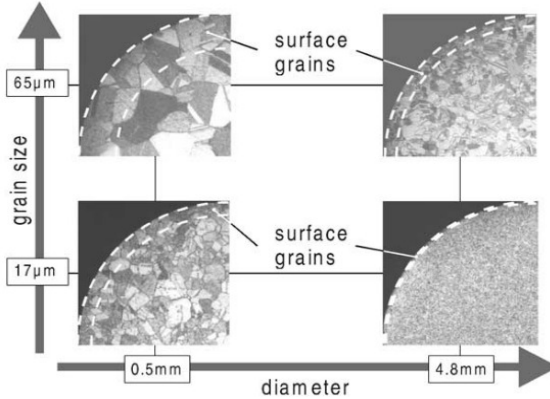


**Fig. 2.7.** Basic idea of surface layer model initially proposed by Engel and Eckstein (2002): share of surface grains with the change of diameter of a cylindrical billet and grain size.

where  $K$ ,  $n$ ,  $\varepsilon_0$  are the strength coefficient, strain hardening exponent and initial strain respectively.  $\xi_{sf}$  is the non-uniform coefficient which enables qualitatively modeling of surface roughening with the decrease of geometry size. Several different modifications can also be found in Peng et al. (2007); Leu (2009, 2015) on the basis of introducing size-associated parameters into conventional constitutive laws.

For the attempts made by conventional plasticity models augmented with various size-associated factors, it is only possible to cover size-dependent material response, e.g., “smaller is weaker” phenomenon. The introduction of several size-associated factors seems to be made quite artificially and intentionally. In addition, it is not convenient to perform parameter identification whenever a new size-dependent parameter is added. One advantage of this approach is that these models are generally based on well-known constitutive laws, which is not difficult for beginners.

### 2.3.2 Surface layer and mesoscopic models

As discussed in 2.2.1, the “smaller is weaker” is due to different material properties of surface and inner grains in a miniaturized structure. Additionally, the percentage of surface grains among the overall geometry enlarges with the reduction of geometry. Motivated by these, Engel and Eckstein (2002) proposed the concept of surface layer model holding the idea that free surface grains show less hardening compared to the inner volume grains, as illustrated in Fig. 2.7 by a cylindrical billet. Mathematically, surface layer model can be formulated as:

$$\sigma = p_s \sigma_s + p_i \sigma_i \quad (2.6)$$

where  $\sigma$  is the overall flow stress,  $\sigma_s$  and  $p_s$  represent flow stress and proportion of surface grains,  $\sigma_i$  and  $p_i$  represent flow stress and proportion of inner grains.

The surface layer model requires specific descriptions of surface and inner grains behavior. Lai et al. (2008) proposed a mixed description in which surface grains behave as single crystals and inner grains as polycrystals. Referring to Lai et al. (2008), the flow stress of surface grains  $\sigma_s$  in (2.6) can be modeled as:

$$\sigma_s = m\tau \quad (2.7)$$

where  $m$  is the orientation factor for single crystal. Regarding the behavior of inner grains, the Hall-Petch relation extended by Armstrong et al. (1962) is adopted as expressed in (2.2). To summarize, the surface layer model proposed by Lai et al. (2008) can be written as:

$$\begin{cases} \sigma = p_s \sigma_s + p_i \sigma_i \\ \sigma_s = m\tau \\ \sigma_i = M\tau + \frac{k}{\sqrt{d}} \\ 1 = p_s + p_i \end{cases} \quad (2.8)$$

Based on this idea, many enhanced surface layer models have been proposed with the inclusion of specific parameters. Several are listed in what follows, without being exhaustive. Wang et al. (2013) enhanced the surface layer model by taking into account the contributions of constrained grains restricted by external boundaries. Compared to (2.6), an extra contribution to the overall flow stress, resulting from external constrained grains, has been added as (Wang et al., 2013):

$$\sigma = p_s \sigma_s + p_i \sigma_i + p_c \sigma_c \quad (2.9)$$

where  $\sigma_c$  and  $p_c$  represent the flow stress and fraction of surface constrained grains.

A combined surface layer and grain boundary strengthening model was proposed by Li et al. (2017) to study deformation and ductile fracture behavior in micro-scale deformation. The difference between Li et al. (2017) and surface layer model is the description of inner grains which are assumed to have different material behaviors, *i.e.*, grain boundary and grain interior for inner grains. The flow stress of a specimen proposed in Li et al. (2017) can be written as:

$$\sigma = p_s \sigma_s + p_{gb} \sigma_{gb} + p_{gi} \sigma_{gi} \quad (2.10)$$

where  $\sigma_{gb}$  and  $p_{gb}$  represent the flow stress and fraction of grain boundary for inner grains,  $\sigma_{gi}$  and  $p_{gi}$  represent the flow stress and fraction of interior material for inner grains.

In terms of experimental investigations, Chan et al. (2011) performed micro-cylindrical and micro-ring compression tests and verified the established surface layer models. Ran et al. (2013) investigated the influence of size effects on ductile fracture based on the surface layer model proposed by Lai et al. (2008). With an ad-hoc assumption, Molotnikov et al. (2008) formulated a constitutive model considering the effect of the thickness of copper sheet by modeling surface and interior proportions separately. In this model, the strength of surface grains is governed by dislocation image forces, while that of interior grains is determined by dislocation cell structure.

However, one deficiency in surface layer model is that it ignores the transition between surface grains and interior grains, which is described in a discontinuous manner (*i.e.*, the mathematical superposition of surface and inner grains flow stress multiplied by their fractions). To remedy this, a mesoscopic model was proposed by Geiger et al. (2007) which takes into account the size effects occurring at the micro-scale. The influences of grain size and its position are taken into account by creating a synthetic material structure and the calculation of individual material properties for each of the synthetic grains. According to the general formulation of Hall-Petch relation in (2.1), for shear stress  $\tau$  it yields:

$$\tau = \tau_0 + \frac{k}{\sqrt{d}} \quad (2.11)$$

with  $\tau_0$  the critical shear stress. Taking into account the influence of neighboring grains on the mechanical properties of a single grain  $n$ , (2.11) becomes:

$$\tau_n = \tau_n^0 + \frac{m_{1,2}\tau_n^c\sqrt{\delta}}{\sqrt{d_n}} \quad (2.12)$$

where  $m_{1,2}$  represents a transformation matrix regarding the different sliding systems in adjacent grains,  $\tau_n^0$  is the critical shear stress in the considered grain  $n$ ,  $\delta$  represents the distance between the pile-up source and the dislocation. The stress  $\tau_n^c$  is a threshold value to determine whether dislocation sources will be activated in neighboring grains. When the stress at the grain boundary exceeds the threshold  $\tau_n^c$ , dislocation sources are activated. A Hall-Ph factor  $K_n$  for single grain is denoted as:

$$K_n = m_{1,2}\tau_n^c\sqrt{\delta} \quad (2.13)$$

The considered single crystal should be integrated on the overall domain, yielding the relation:

$$K_n = K\xi_n \quad (2.14)$$

where  $\xi_n$  represents the amount of dislocation pile-up at the grain boundary region for the considered single crystal. It is defined as:

$$\xi_n = \frac{1}{\sigma_G} \frac{1}{\alpha_G} \sum \alpha_c \sigma_{Gn} \quad (2.15)$$

where  $\sigma_G$  represents the averaged yield stress of an individual grain,  $\sigma_{Gn}$  is the yield stress of the neighboring grains,  $\alpha_G$  and  $\alpha_c$  represent the overall grain boundary area and real contact length, respectively. Then, the shear stress of an individual grain taking into account influences of neighboring grains through the parameter  $\xi_n$  can be written as:

$$\tau_n = \tau_n^0 + \frac{K\xi_n}{\sqrt{d_n}} \quad (2.16)$$

The overall stress can be calculated as:

$$\tau = \sum_{n=1}^N \tau_n \quad (2.17)$$

with  $N$  the total number of grains in the considered geometry.

The mesoscopic model can cover most of features of surface layer model in a more natural manner. For example, in case of surface grains,  $\xi_n$  will normally decrease as a result of free surfaces for the surface grains resulting in a lower flow stress. This corresponds to the behavior of surface grains which are considered less constrained and exhibit lower flow stress. Additionally, the interactions between the grains are considered. Numerical simulations using the mesoscopic model have been performed through a flat upsetting test as shown in Fig. 2.8. The mean forming force predicted by the mesoscopic model reached a good agreement with experimental results. The scatter of process factors can also be obtained as shown in Fig. 2.8.

A notable progress has been made by the surface layer model which tries to model the material behavior from a deeper viewpoint compared to the previous ones, namely, surface and inner

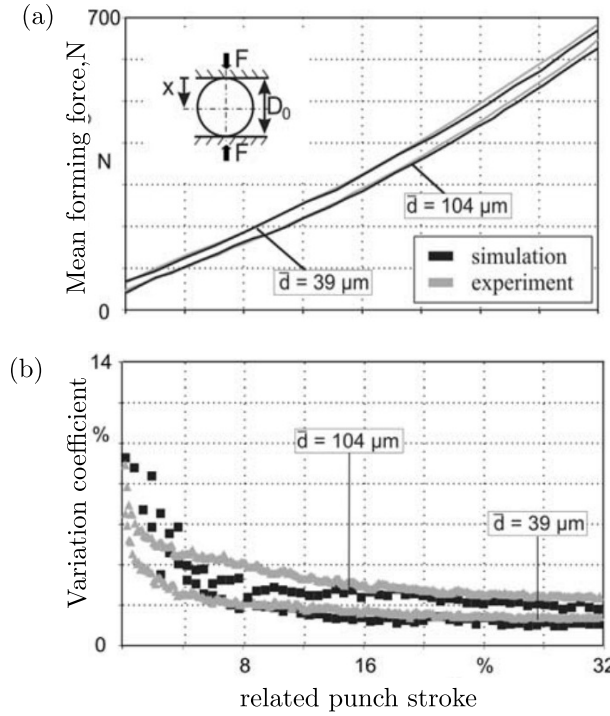


**Fig. 2.8.** Numerical predictions by mesoscopic model Geiger et al. (2007): flat upsetting test of cylindrical specimens made by CuZn15 with a diameter of 0.5 mm and length 3 mm for different mean grain sizes  $\bar{d}$ .

grains. Compared to enriched conventional plasticity models, surface layer model treats the considered domain as surface and inner parts which have different mechanical behaviors. However, the simple superposition of surface and inner grains multiplied with their percentages overlooks the interactions between inner and surface grains. The identification of the parameters in surface layer model is quite inconvenient and inaccurate. For example, determination of the proportions of surface grains needs digital image processing technique (Li et al., 2017). Mesoscopic model is an enhancement based on surface layer model taking into account the transitions between surface and inner grains. It can predict first-order size effects including “smaller is weaker” phenomenon and the scatter of flow stress. Behaviors of individual grains and their positions are considered compared to the treatment of surface and inner grains adopted in the surface layer model. However, the data identification is much more complicated than surface layer model due to the fact that each grain should be treated solely. In addition, microstructure descriptions are not modeled in a nature way.

However, the “smaller is stronger” phenomenon which is widely observed in micro-scale experiments (Fleck et al., 1994; Nix and Gao, 1998; Stölken and Evans, 1998; Greer and Nix, 2005) cannot be reproduced by the aforementioned methods (enriched plasticity, surface/mesoscopic). This is due to the fact that no non-local ingredients (*e.g.*, strain gradients), which are the sources of “smaller is stronger” effects, are taken into account in these methods. Gradient-enhanced plasticity theories remedy this deficiency. Therefore, gradient-enhances plasticity models will be introduced as follows.

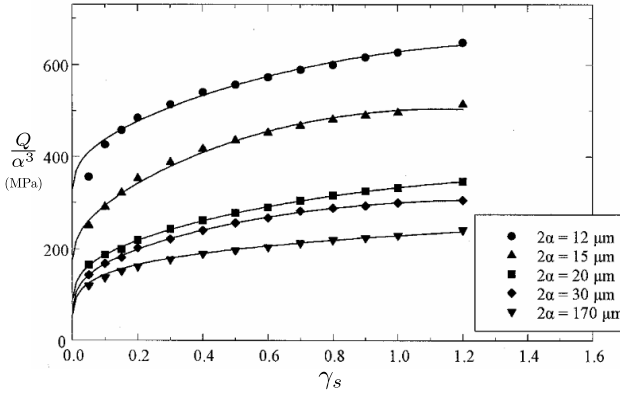


**Fig. 2.9.** Comparison between predictions of SGP theory (Aifantis, 1999) and experiment results for twisted Cu wires in terms of  $Q/\alpha^3$  v.s.  $\gamma_s$  where  $Q$  is the torque,  $\alpha$  is the wire radius and  $\gamma_s$  is the surface shear strain of the wire.

### 2.3.3 Gradient-enhanced plasticity models

Aifantis (1984, 1987) conducted the pioneering works of strain gradient plasticity in which strain gradient ingredients were added into the conventional yield function initially intended for regularizing thickness of localization regions. In Aifantis (1984), a modified flow rule augmented with gradient terms reads:

$$\sigma^{eq} = \sigma(\varepsilon_p^{eq}) - c\nabla^2\varepsilon_p^{eq} \quad (2.18)$$

where  $\sigma^{eq}$  is the equivalent stress calculated by  $\sigma^{eq} = \sqrt{\frac{1}{2}\boldsymbol{\sigma}^{dev} : \boldsymbol{\sigma}^{dev}}$  with  $\boldsymbol{\sigma}^{dev}$  the deviatoric stress tensor,  $\varepsilon_p^{eq}$  is the equivalent plastic strain evolved as  $\varepsilon_p^{eq} = \int_0^t \dot{\varepsilon}_p^{eq} dt$  with equivalent plastic strain rate  $\dot{\varepsilon}_p^{eq} = \sqrt{2\dot{\varepsilon}_p : \dot{\varepsilon}_p}$ ,  $\sigma(\varepsilon_p^{eq})$  represents the conventional homogeneous part of the flow resistance,  $c$  is a positive material constant and  $\nabla^2$  represents the Laplacian operator. The material constant  $c$  is assumed as (Aifantis, 1984),  $c = Hl^2$ , with  $H$  a generalized hardening modulus and  $l$  the internal length scale.

Based on their early works (Aifantis, 1984, 1987), the SGP theory has been extended to study various problems by Aifantis and his co-workers, *e.g.*, shear bands problem (Zbib and Aifantis, 1988; Aifantis, 1999), size effects (Tsagarakis et al., 2003; Zbib and Aifantis, 2003), fracture (Aifantis, 1996), . It is worthy noting that strain gradient plasticity can well predict second-order gradient effects. Aifantis (1999) compared numerical predictions by SGP theory and experimental results for wire torsion with different diameters  $2\alpha$  as shown in Fig. 2.9 and obtained good agreement on both results. This proves the good capability of capturing second-order gradient size effects by gradient-enhanced plasticity models. When coupled with crystal plasticity framework, the SGP model can capture both first-order size effects (by the crystallographic settings) and second-order gradient effects (by gradient ingredients). The SGP theory coupled with crystal plasticity framework is generally denoted as strain gradient crystal plasticity (SGCP) theory. Several investigations in size effects employing strain gradient crystal plasticity models can be found in Keller et al. (2012b,a).

The strain gradient crystal plasticity framework will be chosen as the backbone in the development of numerical tool of this thesis aiming at capturing first-order size effects and second-order

gradient effects. Since [Aifantis \(1984\)](#), numerous researchers have constantly contributed to the SGP domain in terms of theoretical, numerical and experimental aspects. In the following section, a detailed overview of SGP theory will be given following a manner of presenting different classes of SGP models and several open issues related to these models.

## 2.4 Strain gradient (crystal) plasticity

Strain gradient plasticity theories can be classified into several categories in terms of different manners. For instance, according to the manner of capturing strain gradients, these theories can be grouped as lower-order ([Acharya and Bassani, 2000](#); [Bassani, 2001](#); [Evers et al., 2002](#); [Acharya et al., 2004](#); [Huang et al., 2004](#)) and higher-order gradient theories ([Gudmundson, 2004](#); [Fleck and Hutchinson, 2001](#); [Gurtin, 2000, 2002](#); [Voyiadjis and Deliktas, 2009b](#)). [Hutchinson \(2012\)](#) proposed a more attractive classification according to how increments of higher-order stresses are related to increments of strain gradients, *i.e.*, incremental models in which increments of higher-order stresses are related to increments of strain gradients, and non-incremental models in which the higher-order stresses themselves are expressed in terms of increments of strain gradients. In what follows, incremental and non-incremental SGP models will be introduced.

To start with, a unified formulations of strain gradient plasticity framework will be established within small deformation. The principle of virtual power within an arbitrary domain  $V$  can be written as:

$$\int_V \boldsymbol{\sigma} : \delta \dot{\boldsymbol{\varepsilon}}_e + \pi \delta \dot{\varepsilon}_p^{eff} + \boldsymbol{\xi} \cdot \delta \nabla \dot{\varepsilon}_p^{eff} dV = \int_S \mathbf{t} \cdot \delta \dot{\mathbf{u}} + \chi \delta \dot{\varepsilon}_p^{eff} dS \quad (2.19)$$

where  $\boldsymbol{\sigma}$  is the Cauchy stress tensor power-conjugate to elastic strain tensor rate  $\dot{\boldsymbol{\varepsilon}}_e$ ,  $\pi$  is a scalar stress power-conjugate to the effective plastic strain rate  $\dot{\varepsilon}_p^{eff} = \sqrt{\frac{2}{3} \dot{\boldsymbol{\varepsilon}}_p : \dot{\boldsymbol{\varepsilon}}_p}$ ,  $\boldsymbol{\xi}$  is a vectorial stress power-conjugate to the gradient of  $\dot{\varepsilon}_p^{eff}$ ,  $\mathbf{t}$  and  $\chi$  are traction quantities expending power on the surface  $S$ .

To derive force balance equations, a conventional plastic flow condition is assumed as according to [Fleck and Hutchinson \(2001\)](#) for plastic loading condition:

$$\dot{\boldsymbol{\varepsilon}}_p = \dot{\varepsilon}_p^{eff} \mathbf{m} \quad (2.20)$$

where  $\mathbf{m}$  is a tensor prescribes the direction of plastic strain increment. It can be obtained by the relation  $\mathbf{m} = \frac{3}{2} \frac{\boldsymbol{\sigma}^{dev}}{\sigma^{eff}}$  with  $\sigma^{eff} = \sqrt{\frac{3}{2} \boldsymbol{\sigma}^{dev} : \boldsymbol{\sigma}^{dev}}$  the conventional effective stress. By setting  $\delta \dot{\varepsilon}_p^{eff} = 0$  in 2.19, the macroscopic force balance with macroscopic traction condition can be obtained:

$$\begin{cases} \nabla \cdot \boldsymbol{\sigma} = 0 & \text{in } V \\ \boldsymbol{\sigma} \cdot \mathbf{n} = \mathbf{t} & \text{on } S \end{cases} \quad (2.21)$$

By setting  $\delta \dot{\mathbf{u}}$  and with the help of 2.20, the microscopic force balance with microscopic traction condition can be written as:

$$\begin{cases} \nabla \cdot \boldsymbol{\xi} + \sigma^{eff} - \pi = 0 & \text{in } V \\ \boldsymbol{\xi} \cdot \mathbf{n} = \chi & \text{on } S \end{cases} \quad (2.22)$$

A generalized effective strain measure is defined as:

$$E_p = \sqrt{\dot{\varepsilon}_p^{eff2} + l^2 |\nabla \dot{\varepsilon}_p^{eff}|^2} \quad (2.23)$$

with  $l$  an internal length scale.

### 2.4.1 Incremental strain gradient (crystal) plasticity models

Fleck and Hutchinson (2001) have proposed a phenomenological higher-order SGP model with the purpose of generalizing the classical  $J_2$  flow theory to account for gradient effects at small scales. Both higher-order stresses and additional boundary conditions are considered and more than one material length scale parameters are covered in this model. The increments of stresses are defined in Fleck and Hutchinson (2001) as follows:

$$\dot{\sigma} = \mathbb{C} : (\dot{\varepsilon} - \dot{\varepsilon}_p^{eff} \mathbf{m}) \quad (2.24)$$

$$\dot{\pi} = h(E_p) \dot{\varepsilon}_p^{eff} \quad (2.25)$$

$$\dot{\xi} = l^2 h(E_p) \nabla \dot{\varepsilon}_p^{eff} \quad (2.26)$$

where  $\mathbb{C}$  is fourth-order elasticity modulus,  $h(E_p)$  is the tangent hardening modulus.

The notion of “incremental SGP model” can be well demonstrated in 2.26, where increment of higher-order stress  $\dot{\xi}$  is a function of increment of effective strain measure  $\nabla \dot{\varepsilon}_p^{eff}$ .

However, the compatibility of incremental model with the thermodynamic dissipation requirements (*i.e.*, nonnegative dissipation) has not been addressed by the authors (Fleck and Hutchinson, 2001; Hutchinson, 2012). Gudmundson (2004) has pointed out that the nonnegative dissipation cannot always be guaranteed by this model. Later, the work of Gurtin and Anand (2009) has shown that this model is incompatible with thermodynamics unless the nonlocal terms are dropped. A modified version of this model in which the higher-order stresses are assumed to be fully energetic is proposed by Hutchinson (2012) to ensure its thermodynamic consistency. The assumption of no higher-order contributions to dissipation has been used in subsequent works to develop thermodynamically-acceptable incremental models (*e.g.*, Fleck et al., 2015; Nelleman et al., 2017, 2018). However, the consistency of this assumption with the current understanding of dislocation physics is questioned. Until now, there are no acceptable recipes for an incremental model including higher-order dissipative stresses (Fleck et al., 2015).

### 2.4.2 Non-incremental strain gradient (crystal) plasticity models

To overcome the thermodynamic deficiency of the above class of models, while considering higher-order contributions to dissipation, several authors have proposed models in which the higher-order stresses are expressed in terms of increments of plastic strain gradients, *i.e.*, the non-incremental

models according to the classification of [Hutchinson \(2012\)](#). Various non-incremental models can be found in a series works of [Gurtin \(2002\)](#); [Gudmundson \(2004\)](#); [Gurtin \(2004\)](#).

In order to derive the constitutive equations, principle of second thermodynamics are employed following the work of [Gurtin \(2002\)](#). The second law of thermodynamics require that the temporal increase in free energy of any subregion  $\mathcal{V}$  is less than or equal to the external power expended on this subregion, which can be expressed as:

$$\overline{\int_{\mathcal{V}} \dot{\psi} dv} \leq \mathcal{P}_{ext}. \quad (2.27)$$

Using (2.19) and considering the arbitrariness of the subregion  $\mathcal{V}$ , the local free energy imbalance can be written as:

$$\boldsymbol{\sigma} : \dot{\boldsymbol{\varepsilon}}_e + \pi \dot{\varepsilon}_p^{eff} + \boldsymbol{\xi} \cdot \nabla \dot{\varepsilon}_p^{eff} - \dot{\psi} \geq 0. \quad (2.28)$$

The local free energy imbalance along with the prescription of free energy  $\psi$  give birth to constitutive laws. In [Gudmundson \(2004\)](#), the free energy is assumed as a function of  $\boldsymbol{\varepsilon}_e$ ,  $\varepsilon_p^{eff}$  and  $\nabla \varepsilon_p^{eff}$ :

$$\psi = \psi(\boldsymbol{\varepsilon}_e, \varepsilon_p^{eff}, \nabla \varepsilon_p^{eff}) \quad (2.29)$$

The local free energy imbalance can be rewritten as:

$$\left( \boldsymbol{\sigma} - \frac{\partial \psi}{\partial \boldsymbol{\varepsilon}_e} \right) : \dot{\boldsymbol{\varepsilon}}_e + \left( \pi - \frac{\partial \psi}{\partial \varepsilon_p^{eff}} \right) \dot{\varepsilon}_p^{eff} + \left( \boldsymbol{\xi} - \frac{\partial \psi}{\partial \nabla \varepsilon_p^{eff}} \right) \cdot \nabla \dot{\varepsilon}_p^{eff} \geq 0.$$

The stress  $\boldsymbol{\sigma}$  is assumed to be fully energetic then it has the relation as:

$$\boldsymbol{\sigma} = \frac{\partial \psi}{\partial \boldsymbol{\varepsilon}_e}. \quad (2.30)$$

The microscopic stresses  $\pi$  and  $\boldsymbol{\xi}$  can decomposed into be energetic and dissipative parts:

$$\pi = \pi_{en} + \pi_{dis}, \quad \boldsymbol{\xi} = \boldsymbol{\xi}_{en} + \boldsymbol{\xi}_{dis} \quad (2.31)$$

with

$$\boldsymbol{\pi}_{en} = \frac{\partial \psi}{\partial \varepsilon_p^{eff}}, \quad \boldsymbol{\xi}_{en}^{\alpha} = \frac{\partial \psi}{\partial \nabla \varepsilon_p^{eff}}. \quad (2.32)$$

The inequality (2.28) can be rewritten as:

$$\pi_{dis} \dot{\varepsilon}_p^{eff} + \boldsymbol{\xi}_{dis} \cdot \nabla \dot{\varepsilon}_p^{eff} \geq 0.$$

The key step in constructing a non-negative dissipation in the models of [Gudmundson \(2004\)](#) and [Gurtin \(2004\)](#) is to define a generalized stress  $\boldsymbol{\Sigma}_{dis}$  and a co-directional plastic strain rate  $\dot{\mathbf{E}}_p$  vectors. Referring to [Hutchinson \(2012\)](#); [Reddy \(2011\)](#); [Fleck et al. \(2014\)](#), the generalized dissipative stress  $\boldsymbol{\Sigma}_{dis}$  and plastic strain  $\dot{\mathbf{E}}_p$  vectors can be given as:

$$\boldsymbol{\Sigma}_{dis} = (\pi_{dis}, l_{dis}^{-1} \boldsymbol{\xi}_{dis}), \quad \dot{\mathbf{E}}_p = (\dot{\varepsilon}_p^{eff}, l_{dis} \nabla \dot{\varepsilon}_p^{eff}) \quad (2.33)$$

with their magnitudes defined as:

$$|\Sigma| = \sqrt{\pi_{dis}^2 + l_{dis}^{-2} \boldsymbol{\xi}_{dis} \cdot \boldsymbol{\xi}_{dis}} \quad (2.34)$$

$$|\dot{\mathbf{E}}_p| = \sqrt{\left(\dot{\varepsilon}_p^{eff}\right)^2 + l_{dis}^2 \nabla \dot{\varepsilon}_p^{eff} \cdot \nabla \dot{\varepsilon}_p^{eff}} \quad (2.35)$$

where  $l_{dis}$  is the dissipative length scale. Then, the dissipation inequality can be written as:

$$\pi_{dis} \dot{\varepsilon}_p^{eff} + \boldsymbol{\xi}_{dis} \cdot \nabla \dot{\varepsilon}_p^{eff} = \Sigma_{dis} \cdot \dot{\mathbf{E}}_p \quad (2.36)$$

Assume  $\Sigma$  is co-directional to  $\dot{\mathbf{E}}_p$ , this always leads to non-negative dissipation, *i.e.*, the inequality:

$$\pi_{dis} \dot{\varepsilon}_p^{eff} + \boldsymbol{\xi}_{dis} \cdot \nabla \dot{\varepsilon}_p^{eff} = |\Sigma| |\dot{\mathbf{E}}_p| \geq 0$$

holds true with the co-directional assumption. To keep a uniformed formulation as the incremental models, a specific choice of [Fleck and Willis \(2009\)](#) regarding the generalized stress  $\Sigma_{dis}$  is employed:

$$\Sigma_{dis} = \sigma_0(E_p) \frac{\dot{\mathbf{E}}_p}{|\dot{\mathbf{E}}_p|} \quad (2.37)$$

Denote the dissipation as:

$$\varphi = \Sigma_{dis} \cdot \dot{\mathbf{E}}_p = \sigma_0(E_p) |\dot{\mathbf{E}}_p|, \quad (2.38)$$

and the non-negative requirement  $\varphi = \sigma_0(E_p) |\dot{\mathbf{E}}_p| \geq 0$  is fulfilled. The dissipative forces can be derived as:

$$\boldsymbol{\pi}_{dis} = \frac{\partial \varphi}{\partial \dot{\varepsilon}_p^{eff}} = \sigma_0(E_p) \frac{\dot{\varepsilon}_p^{eff}}{|\dot{\mathbf{E}}_p|} \quad (2.39)$$

$$\boldsymbol{\xi}_{dis} = \frac{\partial \varphi}{\partial \nabla \dot{\varepsilon}_p^{eff}} = l_{dis}^2 \sigma_0(E_p) \frac{\nabla \dot{\varepsilon}_p^{eff}}{|\dot{\mathbf{E}}_p|} \quad (2.40)$$

The higher-order stress  $\boldsymbol{\xi}_{dis}$  is expressed as a function of plastic strain gradient in rate form as shown in (2.40). Compared to the class of incremental models, the present one always satisfies the thermodynamic requirements of nonnegative dissipation. However, as pointed out by several authors (*e.g.*, [Hutchinson, 2012](#); [Fleck et al., 2014, 2015](#)), it may lead in some cases to likely unacceptable results related to finite stress variation under infinitesimal loading change. One commonly discussed phenomenon is the so-called “elastic gaps” (an example is presented in Fig. 2.10 performed by [Fleck et al. \(2014\)](#)) for non-proportional loading.

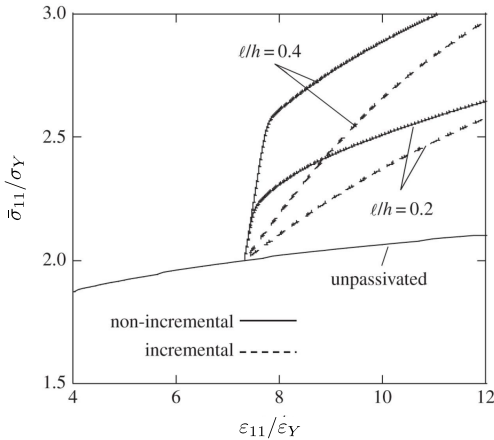


**Fig. 2.10.** Illustration of elastic gaps following application of passivation predicted by the non-incremental (Gudmundson, 2004; Gurtin and Anand, 2009) and incremental (Fleck and Hutchinson, 2001) theories (Fleck et al., 2014).

### 2.4.3 Discussion

Both incremental and non-incremental SGP models have deficiencies. The incremental models represented by Fleck and Hutchinson (2001) cannot satisfy the thermodynamic requirement under certain loading cases as demonstrated by Gudmundson (2004). Later work of Gurtin and Anand (2009) has shown that this model is incompatible with thermodynamics unless the nonlocal terms are dropped. A modified version of Fleck and Hutchinson (2001) in which the higher-order stresses are assumed to be fully energetic is proposed by Hutchinson (2012) to ensure its thermodynamic consistency. The assumption of no higher-order contributions to dissipation has been used in subsequent works to develop thermodynamically-acceptable incremental models (*e.g.*, Fleck et al. (2015); Nellemann et al. (2017, 2018)). However, from a physical viewpoint, part of work associated with higher-order stresses should be dissipative (Hutchinson, 2012). In addition, several recent experiments (Motz et al., 2005; Kiener et al., 2010) provides evidence of dissipative strain gradient effects in promoting strengthening phenomenon for micro-scale structures. It indicates the necessity of accounting for high-order dissipative stresses in SGP models. Until now, there are no acceptable recipes for an incremental model including higher-order dissipative stresses (Fleck et al., 2015). It is a contradiction between the necessity of including higher-order dissipative effects for physical needs and the requirement of non-negative dissipation by removing higher-order dissipative stresses, which makes this type of SGP model not suitable for our development. Regarding non-incremental SGP models, the thermodynamic deficiency is always assured with higher-order contributions to dissipation. Hence, the non-incremental SGP framework will be chosen for the constitutive framework development.

Despite the strong scientific effort on SGP theories, several related difficulties remain to be addressed. One of them is how to define the defect energy which conditions the higher-order energetic effects. In most existing SGP models, this energy is pragmatically assumed to be quadratic in plastic strain gradients (Gurtin, 2002, 2004; Gurtin et al., 2007; Panteghini and Bardella, 2016). Using this assumption, Gurtin et al. (2007) have shown that the energetic length scale effects have only influence on the rate of the classical kinematic hardening, but not on the material strengthening. Although this statement is widely recognized when using quadratic defect energy, Bardella

and Panteghini (2015) have recently shown that accounting for plastic spin in this energy can lead to strengthening effects even if quadratic form is chosen. Despite their widespread use, quadratic forms are not usual in classical dislocation theories and several investigations have shown their inadequacy in the context of SGP (*e.g.*, Cordero et al., 2010; Forest, 2013). Motivated by line tension arguments, rank-one (linear) defect energy has been used by several authors (*e.g.*, Ohno and Okumura, 2007; Hurtado and Ortiz, 2013; Wulffinghoff et al., 2015). In most cases, this form shows strengthening effects of the energetic length scale. Bardella (2010) has studied the effects of the defect energy nonlinearity with quadratic and non-quadratic formulations involving plastic spin. Results by the author confirm the strengthening effects of the energetic length scale when using non-quadratic defect energy. Inspired by the statistical dislocation theory of Groma et al. (2003), Forest (2013) and Wulffinghoff et al. (2015) have proposed logarithmic form of defect energy. To overcome the problem of non-smoothness and non-convexity of this form, a quadratic regularization at small dislocation densities has been used (Wulffinghoff et al., 2015; Wulffinghoff and Böhlke, 2015). El-Naaman et al. (2016) have investigated two defect energy formulations with the aim of improving the microstructural response predicted by SGP theories. A more complete investigation of these formulations using cyclic loading, as well as an interesting discussion about the origins of the strengthening effects of the energetic length scale, have very recently been published by the authors (El-Naaman et al., 2019). In almost all existing works on the subject, the higher-order energetic effects are studied using only proportional loading. It is necessary to corroborate these works by proposing a comprehensive investigation of these effects under both proportional and non-proportional loading conditions. To this end, a generalized power-law defect energy formulation, with adjustable order-controlling index  $n$ , as a function of dislocation densities will be proposed.

Another issue related to SGP theories is how to describe the dissipative processes. In almost all existing strain gradient works, these processes are considered to be coupled and described with the help of generalized effective plastic strain measures, which imply plastic strains and their gradients in a coupled manner (*e.g.*, Fleck and Hutchinson, 2001; Gurtin et al., 2007; Gurtin and Anand, 2009; Hutchinson, 2012; Fleck et al., 2015; Nelleman et al., 2017, 2018), as the generalized effective strain measure defined in (2.23). This kind of measures makes the issue of proposing robust and flexible dissipation formulations and the control of important dissipative effects difficult. Using coupled measures, it is not easy to control, for example, the elastic gaps at initial yield or at the occurrence of non-proportional loading sources. However, in most cases, the coupling between dissipative processes in the description of dissipation is only used by assumption. The existence of such a coupling in reality appears not to be physically confirmed. Based on the current understanding of dislocation physics, there exist no physical obstacles to assuming uncoupled dissipative processes. This can be confirmed by the contributions of Forest et al. (1997, 2000) and Forest and Sedláček (2003). These authors have already adopted and extensively discussed uncoupling assumptions for the description of dissipative processes associated with force-stress and couple-stress quantities in the context of Cosserat plasticity theories. The resulting uncoupled-dissipation-based models are referred to in the literature as multi-surface or multi-criterion models. In the context of phenomenological strain gradient theories, Fleck et al. (2015) have also proposed uncoupled formulations for the description of dissipative processes associated with first- and higher-order stresses. In the same context, the very recent model proposed by Panteghini et al. (2019) can also be seen as a multi-criterion model. Indeed, several independent yield surfaces are introduced to describe the higher-order dissipation, which is considered to be independent of the first-order one. With

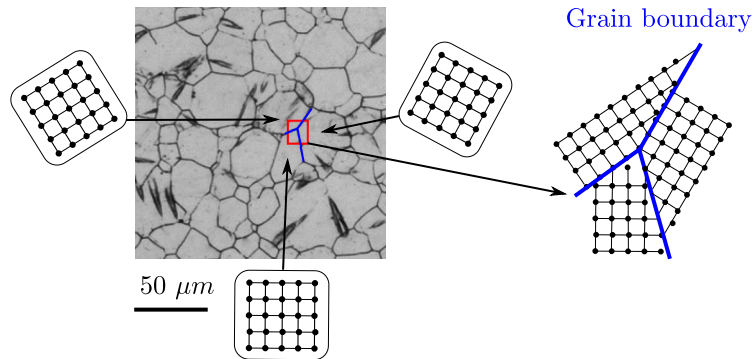


**Fig. 2.11.** Illustration of grain boundary: the microstructure image is taken from [Lei et al. \(2016\)](#) of solution-treated as-received Fe-17Cr-6Ni austenitic stainless steel.

the aim of extending these works, and more particularly the work of [Fleck et al. \(2015\)](#), to strain gradient crystal plasticity, the present thesis will propose a flexible uncoupled dissipation assumption to describe dissipative processes due to plastic slips and their gradients. These processes are assumed to be derived from a pseudo-potential which is expressed as a sum of two independent functions of plastic slips and plastic slip gradients. Conclusions about the physical consistency of this assumption will be drawn by comparing the associated results with others from the literature obtained using coupled dissipation.

These issues related to non-incremental SGP models will be investigated in chapter 3 within a small deformation assumption. The contribution of this chapter will be the proposal of a flexible SGP model allowing for controlling these higher-order effects. Then, the flexible small deformation SGP model will be extended to finite deformation aiming at studying severe plastic deformation cases. However, the SGP model is formulated within single-crystals. They are not devoted to capture the precise description of grain boundary effects, which are particularly significant for miniaturized structures. As a result, it is indispensable to model grain boundary behavior within the proposed flexible SGCP framework. To this end, a review of current development in grain boundary modeling employing enhanced-plasticity as bulk description will be presented in the next section.

## 2.5 Grain boundary models

Grain boundaries (GBs) are generally considered as interfaces between two grains or crystalline structures characterized with different crystallographic features in polycrystalline materials. Fig. 2.11 gives an illustration of grain boundary based on microstructure image ([Lei et al., 2016](#)). Different slip system orientations can be found in each grain near a grain boundary.

Taking into account the effects of GBs in the deformation of polycrystalline materials is indispensable due to different impacts of dislocation interactions of adjacent grains at the GBs. GBs may act as obstacles to dislocation movement, resulting in pile-ups of dislocations at GBs leading to strengthening of the materials. Apart from blocking dislocation transmission by GBs, dislocations interact with GBs by several different mechanisms, *e.g.*, sink or absorption of dislocations, emission of dislocations and reflection of dislocations, . A review on grain boundary mechanisms can be found in [Bayerschen et al. \(2016\)](#). The miniaturized structures usually have size-dependent

effects which have been captured by gradient enhanced continuum theories ([Aifantis, 1984](#); [Fleck et al., 1994](#); [Gurtin, 2002](#); [Gurtin et al., 2007](#); [Gurtin, 2008a](#)). For polycrystalline materials within micro or nano dimension range, the proportion of GBs with respect to the overall volume is effectively increased compared to that in normal dimension range. As a result, depicting the grain boundary behavior accurately for small-scale polycrystalline structures becomes as essential as introducing internal length scales for the bulk crystals. One common manner is to introduce grain boundary contributions into strain gradient plasticity models.

### 2.5.1 Phenomenological GB models

A large majority of the investigations for polycrystalline materials adopt micro-free or micro-hard grain boundaries ([Shu and Fleck, 1999](#); [Evers et al., 2004b](#); [Ekh et al., 2007](#); [Yalçinkaya et al., 2018](#)) due to its simplicity. It allows for zero power (work) expenditure at grain boundaries resulting in the micro-free GBs across which dislocations can freely flow, the micro-hard GBs at which dislocations are totally hindered acting as an impenetrable internal surface. The two limiting boundary conditions for GBs fail to capture complex dislocation interactions in the vicinity of GBs due to lack of necessary grain boundary associated factors, *e.g.*, grain misorientation of adjacent grains, grain boundary type and dislocation interaction mechanisms ([Alipour et al., 2020](#)).

Consequently, various grain boundary models have been proposed so as to depict different grain boundary mechanisms. Based on a phenomenological strain gradient plasticity model, [Gudmundson \(2004\)](#) proposed an interface model in which the surface energy depends on plastic strains at each side of the interface. Following this framework, [Fredriksson and Gudmundson \(2007\)](#) developed two interface models: one has a purely energetic surface energy and the other has a purely dissipative one. These models were employed to study the behavior of a thin film subject to bi-axial strain. [Aifantis and Willis \(2005\)](#) introduced an interfacial energy into a deformation-theory version of strain gradient plasticity which is able to penalize the build-up of plastic strains at interfaces. However, the plastic strain across the interface is assumed to be continuous which may be considered as over-constraint. It was further developed by [Aifantis et al. \(2006\)](#) with an interfacial yield condition which can capture interface yielding and dislocations penetrating these interfaces. [Wulffinghoff et al. \(2013\)](#) proposed an interface yield condition based on gradient plasticity model which enables accounting for the resistance of grain boundaries against plastic flow. An enhanced grain boundary yield criterion was then developed by [Wulffinghoff \(2017\)](#) in which grain boundary isotropic and kinematic hardening were augmented. [Alipour et al. \(2019\)](#) developed a grain boundary model motivated by the grain boundary flow yield criterion ([Wulffinghoff, 2017](#)) in finite deformation framework aiming at improving single crystal models.

The aforementioned interface (grain boundary) models are not suitable for investigation of polycrystalline materials owing to lack of variables accounting for crystallographic factors, *e.g.*, slip systems, grain misorientation and grain boundary types, . One possible solution is the inclusion of crystallographic-like variables into these constitutive models. For instance, the grain boundary theory within strain gradient plasticity proposed by [Voyadjis et al. \(2014\)](#) treats the accumulated plastic strain at each side of the grain boundary as the measure which ensembles the mismatch of Schmid-orientation tensor in [Gurtin \(2008b\)](#). A corresponding grain boundary flow rule is then needed and its parameters require identification by means of the conventional micro-scale experiments. Similarly, [Alipour et al. \(2020\)](#) extended their previous grain boundary model ([Alipour et al., 2019](#)) which is incapable of capturing orientations effects by adding a geometrical transmis-

sibility parameter based on the geometric criterion (Werner and Prantl, 1990). The inclusion of the parameter aims to evaluate the dislocation transmission at the GBs which yet only considers grain misorientation of adjacent grains. However, these attempts to containing crystallographic factors into constitutive laws are not comprehensive. A more effective manner is to adopt crystallographic constitutive frameworks such as strain gradient crystal plasticity models and to introduce crystallographic information into grain boundary constitutive laws.

## 2.5.2 Crystallography-based GB models

One of the pertinent works was presented by Cermelli and Gurtin (2002) who proposed a grain boundary framework based on a strain gradient crystal plasticity model. Microscopic internal forces of the GBs conjugate to plastic slip rates are introduced and linked to flow rule by higher-order micro-traction. The unique feature of this model lies in the description of orientational variables for grain boundary. A constitutive function composed by a grain boundary normal, grain misorientation and a slip-orientation pair is embedded in grain boundary microscopic forces. With the help of viscoplastic yield conditions for the grain boundary, experimental results of Shu and Fleck (1999) are likely to be obtained. Analogous to Burgers tensor in the bulk (Cermelli and Gurtin, 2001), Gurtin and Needleman (2005) proposed a Burgers-vector density of the grain boundary and introduced an internal tensorial force distributed over grain boundary which is power-conjugate to Burgers-vector flow. The notion of grain boundary Burgers-vector density was further employed by Gurtin (2008b) in a theory of GBs that accounts automatically for grain misorientation and grain-boundary orientation under infinitesimal deformation framework. The crystallographic factors, which are interpreted as inter-grain and intra-grain slip interaction moduli, are derived from the magnitude of grain boundary Burgers tensor. Both energetic and dissipative grain boundary microscopic forces depend on grain boundary Burgers tensor and its rate. van Beers et al. (2013) developed a grain boundary model within infinitesimal strain gradient crystal plasticity framework (Evers et al., 2004a; Bayley et al., 2006) using the so-called “interface normal slip” vectors to measure mismatch at the GBs. As shown by Gottschalk et al. (2016), the grain boundary model of van Beers et al. (2013) is equivalent to the general theory of Gurtin (2008b) in terms of description of grain boundary mismatch under planar restrictions. McBride et al. (2016) extended the Gurtin (2008b) strain gradient crystal plasticity based grain boundary model to the finite deformation regime using the plastic distortion tensor in the observed configuration. Their work emphasized on three alternative thermodynamically consistent plastic flow relations on the grain boundary and the comparisons of these relations using a series of numerical experiments. However, the GBs are assumed from the onset to be fully dissipative. Very recently, Peng et al. (2019) proposed a grain boundary model by considering slip transmission at GBs within the framework of a finite strain gradient crystal plasticity. They introduced a grain boundary residual defects quantity to describe slip transmissions between adjacent grains in the intermediate configuration. This quantity is indeed equivalent to the grain boundary Burgers tensor of Gurtin (2008b).

## 2.5.3 Discussion

Focused on small-scale structures in current work, microstructure influences due to crystallographic factors cannot be overlooked. The phenomenological GB models, which do not introduce crystallographic parameters into constitutive framework, seem not appropriate for capturing grain boundary

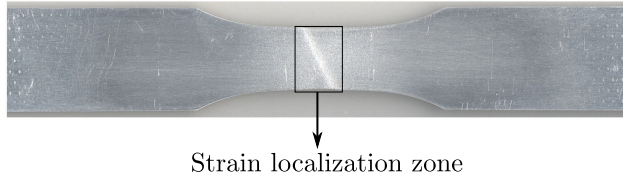


**Fig. 2.12.** Illustrative example of strain localization: experimentally observed shear band for aluminum AA6111 under uniaxial tensile test ([Duan et al., 2005](#)).

effects in the present constitutive framework. A large majority of GB models are designated on the basis of strain gradient crystal plasticity framework in the bulk ([Cermelli and Gurtin, 2002](#); [Gurtin, 2008b](#); [van Beers et al., 2013](#); [Gottschalk et al., 2016](#); [McBride et al., 2016](#); [Peng et al., 2019](#)), allowing for depicting orientation effects (*e.g.*, grain misorientation and grain boundary orientation effects) in natural manner. Under this circumstances, crystallographic-based GB models will be employed in the current numerical framework.

Among the above grain boundary models which are capable of capturing crystallographic factors, most of them are depicted in small deformation framework and only a few ones are targeted to finite deformation ([McBride et al., 2016](#); [Peng et al., 2019](#)). This inspires the present work to develop a GB model under finite deformation framework. The coupling of the flexible finite deformation SGCP model and GB model described adopting Lagrangian description enables the numerical framework to capture both first- and second-order size effects, particularly for severe plastic deformation. In addition, the GB model can be introduced into a series of investigations for polycrystals ([Cordero et al., 2012](#); [Berbenni et al., 2020](#)) in which simple grain boundary behavior is assumed.

As an application of the numerical tool, strain localization problems in crystalline materials will be investigated. To this end, a review of strain localization issues employing gradient-enhanced plasticity theories will be presented in the next section.

## 2.6 Strain localization in crystalline materials

Strain localization is an important plastic instability process occurring prior to fracture. It is usually observed in the form of narrow bands of intense plastic shear strain in deformed bodies undergoing severe inhomogeneous deformation. This process has received a strong scientific interest since the pioneering work of [Considère \(1885\)](#) and numerous studies have been published on the subject ([Hill, 1952](#); [Rice, 1976](#); [Asaro and Rice, 1977](#); [Forest and Cailletaud, 1995](#); [Forest, 1998](#); [Forest and Lorentz, 2004](#); [Marano et al., 2019, 2021](#)). Fig. 2.12 shows an experimentally observed example for shear localization by uniaxial tensile test on aluminum specimen ([Duan et al., 2005](#)). A tilting shear band located approximately near the center of the specimen can be seen. Shear band is a generalized macroscopic notion related to strain localization phenomenon.

Depending on the material microstructure, several types of localization modes have been revealed. Considering a single crystal with multiple activated slip systems, it has been shown that strain localization may occur along general shear bands, which can have an arbitrary orientation with respect to the crystallographic directions ([Rice, 1976](#); [Needleman and Tvergaard, 1992](#); [Kuroda, 2011](#)). When only one slip system is activated, two types of shear bands, known as slip and

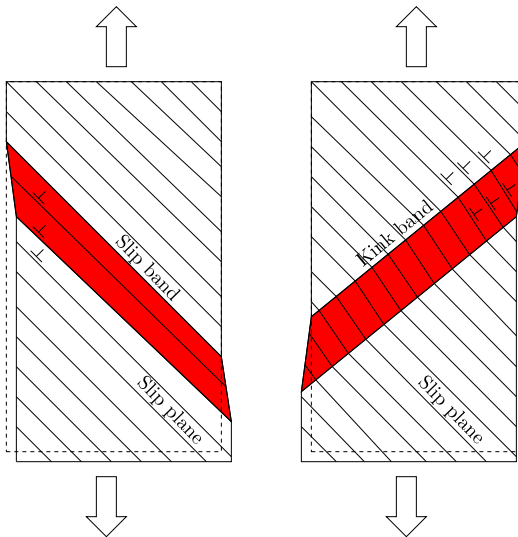


**Fig. 2.13.** Illustration of slip and kink bands within a single crystal having only one slip system.

kink bands illustrated in Fig. 2.13, may occur at incipient plasticity according to the seminal work of [Asaro and Rice \(1977\)](#) based on bifurcation analysis. Slip bands correspond to slip localization along a crystallographic slip plane, whereas kink bands are orthogonal to the slip direction.

Slip bands are sharp structures formed by intense dislocation slip on a few neighboring crystallographic planes. They are parallel to the active slip plane and correspond to main signature of plastic slip in single crystals. Kink bands, which have been first observed by [Orowan \(1942\)](#), are localization bands orthogonal to the slip direction. They are accompanied by a strong lattice rotation in the bands compared to the surrounding regions. These bands are bounded by high lattice curvature boundaries formed by geometrically necessary dislocations (GNDs) walls. These bands present much larger width than slip bands. They are known to occur when strain incompatibility arises and there are not enough slip systems available to accommodate this incompatibility. According to the experimental evidence of [Di Gioacchino and Quinta Da Fonseca \(2015\)](#), such bands are characterized by the presence of a dense distribution of short slip bands along the slip plane normal direction. An interesting discussion about the occurrence of these bands can be found in [Marano et al. \(2021\)](#).

Conventional crystal plasticity (CCP) theories have widely been applied in the literature to study strain localization within single crystals ([Peirce et al., 1982, 1983](#); [Forest and Cailletaud, 1995](#); [Zhang et al., 2010](#); [Takagi et al., 2019](#)). Although these theories are able to capture several kinds of localization modes including slip and kink bands, they present mesh-dependence difficulties demonstrated in Fig. 2.14. A finer mesh leads to a thinner shear band width (Fig. 2.14 a) and a lower stress-strain response (Fig. 2.14 b). Localization bands obtained using such theories present mesh-dependent widths and plastic slip peak values ([Needleman, 1988](#); [Forest, 1998](#)).

In addition, CCP theories identically predict slip and kink bands which appear in this framework as equivalent bifurcation modes. This result has been demonstrated by [Asaro and Rice \(1977\)](#) using bifurcation analysis for single crystals undergoing single slip. A confirmation of such results for poly-crystals has recently been provided by [Marano et al. \(2019\)](#) using Fast Fourier Transform (FFT) poly-crystal simulations. In these simulations, systematically comparable distributions of slip and kink bands have been obtained. This seems not to be in accordance with strain localiza-

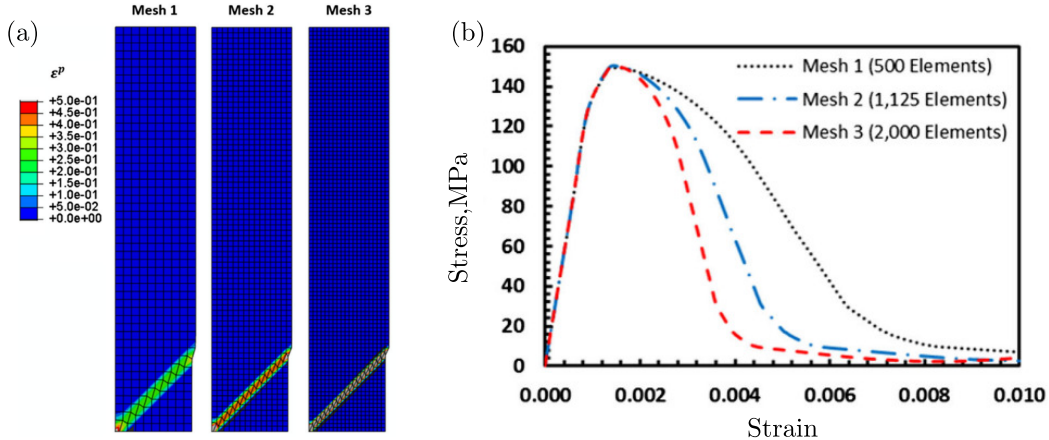


**Fig. 2.14.** Illustration of mesh-dependence pathology: (a) profiles of local effective plastic strain (b) stress-strain curves with different mesh size under classical plasticity model (Song and Voyatzis, 2020).

tion in real materials where overwhelming dominant slip bands are commonly observed. In the context of CCP theories, selection between slip and kink bands is only due to structural effects. From a physical point of view, the equivalence between these bands is questioned as they rely on quite different formation processes. Compared to slip bands, much more dislocation sources are generally required to form kink bands. Consequently, CCP theories are not suitable to study localization phenomena in single crystals. These theories include no internal length scale(s) allowing for stabilizing localization which theoretically will occur in a set of zero measure.

A solution to overcome limitations of the aforementioned theories consists in applying non-local plasticity approaches. Including internal length scale(s), these approaches provide a natural framework to capture nonlocal effects. Their promising features have motivated the development of various nonlocal models for both single and poly-crystal structures in the last two decades (Aifantis, 1984; Forest, 1998; Acharya and Bassani, 2000; Gurtin, 2002; Pouria and Xu, 2015; Wulffinghoff and Böhlke, 2015; Kuroda and Needleman, 2019; Marano et al., 2019; Berbenni et al., 2020; Jebahi and Forest, 2021). Although most of these models have been developed to investigate size effects at small scales, a few works applying them to localization problems exist in the literature. In the context of single crystals, Forest (1998) has proposed a small deformation Cosserat crystal plasticity model to investigate the formation of slip and kink bands. Taking into account lattice rotation, the proposed model allows for breaking the equivalence between the two bands. Furthermore, it enables regularization of kink bands which present a finite width. However, this is not the case for slip bands which are not necessarily accompanied by lattice curvature. Recently, a reduced micromorphic crystal plasticity model relying on the gradient of a cumulative scalar slip variable has been proposed by Ling et al. (2018). This model presents the unique feature of regularizing both slip and kink bands. However, the same internal length scale is involved in the regularization of these bands, which could be problematic considering their different physical features and formation processes. Application of the proposed model to study strain localization within single crystals undergoing single slip has revealed a complex localization behavior with competition between kink and slip bands. Experimental evidence of this behavior can be found in Takagi et al. (2019).

Another class of nonlocal approaches, which presents auspicious features to capture localiza-

tion phenomena in single crystals, is the class of strain gradient crystal plasticity (SGCP) theories. This class has been the subject of a large number of recent works mostly focusing on size effects (Acharya et al., 2003; Kuroda, 2011; Liu et al., 2011b; Pouriyayevali and Xu, 2015; Bittencourt, 2018, 2019; Jebahi et al., 2020). However, only few works applying SGCP theories to study localization phenomena can be found in the literature. Using a finite deformation SGCP model, Kuroda (2011) has investigated the effects of the finite element type on the formation of localization bands within single crystals. Scherer et al. (2019) have proposed a reduced SGCP model based on the work of Ling et al. (2018) to study the formation of localization bands in voided irradiated materials. This model relies on the gradient of a cumulative scalar slip variable and it has been implemented using an approach combining micromorphic and Lagrange multiplier methods. Very recently, a more elaborate SGCP model based on the full GND density tensor has been proposed by Marano et al. (2021) to study the influence of strain gradient plasticity on the modeling of localization bands within poly-crystalline solids.

In almost all existing studies of localization phenomena in single crystals, only higher-order energetic effects have been considered. Higher-order dissipative effects on these phenomena have not yet been explored. Furthermore, there exist no works providing a comprehensive investigation of the abilities of SGCP theories in capturing different kinds of localization modes within single crystals, particularly the competition between slip and kind bands. From single crystalline to polycrystalline, extra contributions to the overall material response originate from interactions between grains in the polycrystalline materials. The precision of constitutive modeling for polycrystalline materials plays a decisive role in capturing more realistic strain localization phenomena. Strain localization in polycrystalline sheet metals will then be studied using the developed constitutive numerical tool in this thesis.

## 2.7 Conclusions

In this chapter, state of the art related to the objectives of the thesis has been reviewed. Definition and classification of size effects have been discussed in the first place. Regarding crystalline metallic miniaturized structures, the order-based size effects classification (Geers et al., 2006) seems more appropriate to account for various size effects in a well-organized manner. Then, various numerical modeling methods devoted to capturing size effects are discussed. Through analyzing the features of these models, the choice of gradient-enhanced crystal plasticity model, which can cover first-order size effects and second-order gradient effects, has been determined. To capture second-order grain boundary effects, grain boundary model will be coupled with the gradient-enhanced crystal plasticity model. Progresses on various GB models have been reviewed. Finally, strain localization aspects for crystalline metallic material has been discussed.

Aspects of size effects have been discussed in section 2.1 firstly. The general definition of size effects has been given and several different kinds of classifications of size effects are presented. Among them, first- and second-order size effects classification provides us a more organized category. First-order size effects are composed of extrinsic and intrinsic ones mainly sourced from the underlying microstructure. For second-order size effects, one originates from deformation gradients, and the other one includes grain boundary effects and external boundary effects. Following the order-based classification of size effects, experimental observations of size effects have been presented in section 2.2. The first-order extrinsic size effects give rise to the “smaller is weaker”

phenomenon and the scatter of flow stress. The “smaller is weaker” is attributed to the less constrained surface grains and an increased proportion of surface grains with decreasing geometry size. Another effect related to microstructure is the grain size strengthening which is usually generated by grain size refinement. The well-known Hall-Petch relation is one typical example of grain size strengthening. Second-order gradient size effects are commonly recognized with the presence of deformation gradient for miniaturized structures leading to the commonly observed “smaller is stronger” phenomenon for micro-scale experiments. For polycrystalline materials, grain boundary effects play an important role in deformation behaviors. Grain boundaries in polycrystalline material impact dislocation interactions between adjacent grains.

In order to predict plastic deformation of miniaturized products, numerical models should take into account both the first- and second-order size effects in a proper manner. The current progresses of numerical modeling of size effects within continuum domain have been detailed in section 2.3. Several attempts have been made on conventional plasticity models, denoted as enriched conventional plasticity models, by introducing various sorts of size-dependent parameters. It can merely predict the “smaller is weaker” size effects among the first-order category. In addition, the inclusion of size-dependent parameters seems quite intentionally and parametric calibration is complicated and time-consuming. A non-trivial progress has been made by surface layer model, in which material behaviors of a part is modeled by surface and inner grains respectively. The combination of surface and inner grains is performed in a discontinuous manner, *i.e.*, a simple superposition of these two multiplied by their percentages with respect to the overall volume. Mesoscopic model solves this deficiency by considering each grain and covering the influences from its neighboring grains. The mesoscopic model enables modeling first-order size effects, *i.e.*, both the “smaller is weaker” and scatter of flow stress. However, the parameter identification for mesoscopic model is rather complicated and time-consuming which restricts its wide applications. Gradient-enhanced plasticity models can capture the “smaller is stronger” effects by taking into account strain gradient. When coupled with crystal plasticity framework, it enables modeling both first-order size effects and second-order gradient effects. Motivated by these reasons, the gradient-enhanced plasticity models coupled with crystal plasticity will be chosen as the backbone of the numerical development for the thesis.

In section 2.4, strain gradient (crystal) plasticity is reviewed starting with a comparison of incremental and non-incremental SGP models. One issue related to incremental models, in which increments of higher-order stresses are formulated by increments of strain gradients, is that non-negative dissipation cannot be assured at any kind of loading cases. For non-incremental models, higher-order stresses are formulated by increments of strain gradients. This type of models always satisfy non-negative dissipation requirement. As a result, non-incremental type of SGP models has been chosen for the numerical development in this thesis. Yet, several issues still remain to be discussed, *e.g.*, formation of defect energy and description of dissipation processes. These problems will be studied in chapter 3 by proposing a flexible strain gradient plasticity model within small deformation framework. Then, the flexible model will be extended to finite deformation in chapter 4 so as to simulate severe plastic deformation problems.

In section 2.5, developments of grain boundary modeling based on gradient plasticity is detailed. The two limiting grain boundary conditions, micro-free and micro-hard, are far enough to capture the precise behaviors between grains and grain boundaries. Within the framework of gradient plasticity, two types of grain boundary models have been developed in the literature according to their purposes. One type of grain boundary models aims to demonstrate the grain boundary

mechanisms (*e.g.*, grain boundary hardening, grain boundary contribution to overall flow stress, *etc.*). In general, these formulations emphasize the interfacial behaviors while ignore crystallographic factors (*e.g.*, grain misorientation and grain boundary orientation). A natural manner of introducing crystallographic parameters is to adopt crystal plasticity description of the bulk material. As a result, grain boundary model based on description of the bulk by strain gradient crystal plasticity seems appropriate. Focused on grain boundary models oriented on the scope of strain gradient crystal plasticity, most of the existing models are developed for small deformation. Few finite deformation grain boundary models can be found in the literature. Furthermore, the strain localization study application of the set of numerical tools developed in this thesis requests a finite deformation framework of both the bulk and grain boundary material behaviors. To this end, a finite deformation grain boundary model will be developed in chapter 5.

In section 2.6, a brief introduction of strain localization investigations for crystalline metallic structures using strain gradient plasticity theories has been presented. Conventional crystal plasticity models cannot predict mesh-independent strain localization phenomenon due to lack of internal length scales. In addition, they can not distinguish slip and kink band formation which usually occur at the onset of plasticity. Higher-order gradient plasticity theories can solve these deficiencies. However, few strain localization investigations have employed strain gradient crystal plasticity theories. For miniaturized structures, grain boundary contributions to the overall plastic deformation are of vital importance. Unfortunately, few works on strain localization attempt to take into account size effects induced by both bulk crystals and the grain boundary, which can be modeled by the numerical framework developed in this thesis. Inspired by this, the capabilities and limitations of the flexible strain gradient crystal plasticity will be assessed on several topics associated with strain localization problems for single crystals, *e.g.*, mesh sensitivity, evolution and competition of slip and kink bands and size effects on localization behaviors, *etc.* Then poly-crystalline examples will be studied in which size effects originated from the bulk material (modeled by the flexible strain gradient crystal plasticity) and from grain boundaries captured by the proposed grain boundary theory. The investigation will be presented in chapter 6 focused on strain localization problems for sheet metals.



# **Chapter 3**

## **Development of flexible Gurtin-type strain gradient crystal plasticity model at small deformation**

### **Abstract**

Based on the work of [Gurtin et al. \(2007\)](#), this chapter aims at developing a flexible strain gradient crystal plasticity model in small deformation framework. To ensure flexible control of some major higher-order effects, the proposed model will be formulated based on generalized form of defect energy, with order-controlling index  $n$ , and new uncoupling assumption regarding dissipative processes. After model implementation and validation, the model will be applied to investigate the influence of its major parameters on the prediction of size effects.

### 3.1 Introduction

Among approaches used to model size effects, strain gradient crystal plasticity (SGCP) theories are very promising and allow for capturing both first- and second-order effects within crystalline structure. However, despite the strong scientific efforts made on these theories, some issues related to their theoretical formulations remain to be addressed. With the aim of corroborating such efforts, the present chapter tries to develop a SGCP model allowing for flexible control of major higher-order energetic and dissipative effects. To ensure its thermodynamic consistency, the proposed model will be formulated within the framework of non-incremental approaches based on the model of [Gurtin et al. \(2007\)](#).

To model higher-order energetic effects, [Gurtin et al. \(2007\)](#) have proposed a quadratic form of defect energy as a function of dislocation densities associated with slip systems. Although widely used, quadratic forms are not common in classical dislocation theories. Several authors have pointed out limitations of these forms in reproducing effectively realistic higher-order energetic processes ([Cordero et al., 2010](#); [Forest and Guéninchault, 2013](#)). To overcome these limitations, other forms of defect energy have been proposed, *e.g.*, linear ([Ohno and Okumura, 2007](#)) and logarithmic ([Wulffinghoff et al., 2015](#)) defect energy. Different predictions of higher-order energetic effects have been obtained depending on the applied form of defect energy. In the absence of experimental studies on the subject, a power-law defect energy, with order-controlling index, will be adopted in this chapter. This choice allows for easily varying the order of the defect energy to investigate its influence on the higher-order energetic size effects. The adopted defect energy form will be used to perform an in-depth investigation of these effects under proportional and non-proportional loading conditions.

In almost all existing thermodynamically-consistent strain gradient (crystal) plasticity theories, the description of higher-order dissipative processes is done based on effective plastic strain measures which involve plastic strains and their gradients in a coupled manner ([Fleck and Hutchinson, 2001](#); [Gurtin et al., 2007](#); [Hutchinson, 2012](#); [Fleck et al., 2015](#); [Nelleman et al., 2017, 2018](#)). However, no works proving the physical nature of such a coupling exist in the literature. Furthermore, this coupling makes it difficult to control some major higher-order dissipative effects. For instance, using coupled dissipation, it is difficult to deal with elastic gaps which are usually observed under certain non-proportional loading conditions ([Hutchinson, 2012](#); [Fleck et al., 2014, 2015](#)). Inspired by multi-criterion approaches from the literature ([Forest and Sedláček, 2003](#); [Fleck et al., 2015](#); [Panteghini et al., 2019](#)), a new constitutive assumption of uncoupled first- and higher-order dissipative processes will be proposed in this chapter. Effects of this uncoupling assumption on the prediction of higher-order dissipative effects, particularly elastic gaps, will be investigated under proportional and non-proportional loading conditions.

After this introduction, the present chapter is organized as follows. Section 3.2 presents the proposed Gurtin-type SGCP model, which is formulated in small deformation based on generalized non-quadratic defect energy and uncoupling dissipation assumption. Section 3.3 discusses the implementation of a simplified two-dimensional (2D) version of the proposed model. This version is used to investigate, in a simple manner, the effects of the model constitutive parameters on the global response of a crystalline strip subjected to proportional and non-proportional shear loading conditions. Results of this investigation and discussions are presented in Section 3.4. Section 3.5 presents some concluding remarks.

## 3.2 Strain gradient crystal plasticity (SGCP) model

In this section, a Gurtin-type strain gradient crystal plasticity (SGCP) model is developed based on generalized non-quadratic defect energy and uncoupled dissipation, within the framework of small deformation.

### 3.2.1 Kinematics

Let  $\mathbf{u}(\mathbf{x}, t)$  denotes the displacement at time  $t$  of an arbitrary material point identified by  $\mathbf{x}$  in a subregion  $\mathcal{V}$  of the considered continuum. In the framework of small deformation, the displacement gradient  $\nabla \mathbf{u}$  can be additively split into elastic and plastic parts:

$$\nabla \mathbf{u} = \mathbf{H}_e + \mathbf{H}_p \quad (3.1)$$

where  $\mathbf{H}_e$  and  $\mathbf{H}_p$  represent respectively the elastic distortion, due to stretch and rotation of the underlying lattice, and the plastic distortion, due to plastic flow. Their symmetric parts define respectively the elastic and plastic strain tensors, and their skew-symmetric parts give respectively the elastic and plastic rotation tensors:

$$\boldsymbol{\varepsilon}_e = \frac{1}{2} [\mathbf{H}_e + \mathbf{H}_e^T], \quad \boldsymbol{\varepsilon}_p = \frac{1}{2} [\mathbf{H}_p + \mathbf{H}_p^T], \quad \boldsymbol{\omega}_e = \frac{1}{2} [\mathbf{H}_e - \mathbf{H}_e^T], \quad \boldsymbol{\omega}_p = \frac{1}{2} [\mathbf{H}_p - \mathbf{H}_p^T] \quad (3.2)$$

In single-crystal plasticity framework, it is widely acknowledged that plastic flow occurs through slip on prescribed slip systems, with each system  $\alpha$  defined by a slip direction  $\mathbf{s}^\alpha$  and a slip-plane normal  $\mathbf{m}^\alpha$  unit vectors. With this description of plastic flow, the rate of  $\mathbf{H}_p$  can be expressed as:

$$\dot{\mathbf{H}}_p = \sum_{\alpha=1}^q \dot{\gamma}^\alpha [\mathbf{s}^\alpha \otimes \mathbf{m}^\alpha] \quad (3.3)$$

where  $\dot{\gamma}^\alpha$  is the rate of plastic slip on slip system  $\alpha$ ,  $q$  is the total number of slip systems, and “ $\otimes$ ” is the tensor product operator. Using this expression, the plastic strain rate tensor  $\dot{\boldsymbol{\varepsilon}}_p$  can be written as:

$$\dot{\boldsymbol{\varepsilon}}_p = \sum_{\alpha=1}^q \dot{\gamma}^\alpha \mathbf{P}^\alpha \quad (3.4)$$

where  $\mathbf{P}^\alpha$  is the symmetrized Schmid tensor associated with slip system  $\alpha$ :

$$\mathbf{P}^\alpha = \frac{1}{2} (\mathbf{s}^\alpha \otimes \mathbf{m}^\alpha + \mathbf{m}^\alpha \otimes \mathbf{s}^\alpha) \quad (3.5)$$

Equation (3.3), together with (3.1) and (3.2), can also be used to obtain a relation between  $\dot{\mathbf{u}}$ ,  $\dot{\boldsymbol{\varepsilon}}_e$ ,  $\dot{\boldsymbol{\omega}}_e$  and  $\dot{\gamma}^\alpha$ :

$$\nabla \dot{\mathbf{u}} = \dot{\boldsymbol{\varepsilon}}_e + \dot{\boldsymbol{\omega}}_e + \sum_{\alpha=1}^q \dot{\gamma}^\alpha \mathbf{s}^\alpha \otimes \mathbf{m}^\alpha \quad (3.6)$$

In what follows,  $\boldsymbol{\gamma}$  and  $\dot{\boldsymbol{\gamma}}$  (in bold) will be used to designate the list of plastic slips and their rates, respectively:

$$\boldsymbol{\gamma} = (\gamma^1, \gamma^2, \dots, \gamma^q), \quad \dot{\boldsymbol{\gamma}} = (\dot{\gamma}^1, \dot{\gamma}^2, \dots, \dot{\gamma}^q) \quad (3.7)$$

### 3.2.2 Balance equations

The balance equations of the proposed strain gradient crystal plasticity (SGCP) model will be derived based on a generalization of the virtual power density of internal forces. In the present enhanced continuum, both displacement and plastic slip fields are considered as primary and controllable variables. As a consequence, the rates of these variables and their gradients will be involved in the definition of the virtual power density of internal forces:

$$\{\dot{\mathbf{u}}, \nabla \dot{\mathbf{u}}, \dot{\boldsymbol{\gamma}}, \nabla \dot{\boldsymbol{\gamma}}\} \quad (3.8)$$

The internal virtual power expended within a subregion  $\mathcal{V}$  of the considered continuum is computed by means of density  $p_{int}$  that is assumed to depend linearly on all the virtual variations of the modeling variables given by (3.8):

$$p_{int} = \mathbf{f}_i \cdot \delta \dot{\mathbf{u}} + \boldsymbol{\sigma} : \delta \nabla \dot{\mathbf{u}} + \sum_{\alpha=1}^q \kappa^\alpha \delta \dot{\gamma}^\alpha + \sum_{\alpha=1}^q \boldsymbol{\xi}^\alpha \cdot \delta \nabla \dot{\gamma}^\alpha \quad (3.9)$$

where  $\mathbf{f}_i$  is internal volumetric force,  $\boldsymbol{\sigma}$  is macroscopic stress tensor,  $\kappa^\alpha$  and  $\boldsymbol{\xi}^\alpha$  are respectively microscopic stress scalar (work-conjugate to  $\dot{\gamma}^\alpha$ ) and microscopic stress vector (work-conjugate to  $\nabla \dot{\gamma}^\alpha$ ) associated with slip system  $\alpha$ , and “:” is the double-dot product operator. The introduced microscopic stress scalar and vector are referred to hereafter as first- and higher-order microscopic stresses, respectively. Since the virtual power density of internal forces must be objective (*i.e.*, independent of the frame in which the virtual variations are expressed),  $\mathbf{f}_i$  must be zero and  $\boldsymbol{\sigma}$  must be symmetric (Germain, 1973). By using (3.6), it is then easy to demonstrate that:

$$p_{int} = \boldsymbol{\sigma} : \delta \dot{\boldsymbol{\epsilon}}_e + \sum_{\alpha=1}^q (\kappa^\alpha + \tau^\alpha) \delta \dot{\gamma}^\alpha + \sum_{\alpha=1}^q \boldsymbol{\xi}^\alpha \cdot \delta \nabla \dot{\gamma}^\alpha \quad (3.10)$$

where  $\tau^\alpha$  is resolved shear stress on slip system  $\alpha$  defined by  $\tau^\alpha = \boldsymbol{\sigma} : (\mathbf{s}^\alpha \otimes \mathbf{m}^\alpha)$ . Introducing a new first-order microscopic stress scalar  $\pi^\alpha$  such that  $\pi^\alpha = \kappa^\alpha + \tau^\alpha$ , a more compact form of  $p_{int}$ , which is similar to that used by Gurtin et al. (2007), can be obtained:

$$p_{int} = \boldsymbol{\sigma} : \delta \dot{\boldsymbol{\epsilon}}_e + \sum_{\alpha=1}^q \pi^\alpha \delta \dot{\gamma}^\alpha + \sum_{\alpha=1}^q \boldsymbol{\xi}^\alpha \cdot \delta \nabla \dot{\gamma}^\alpha \quad (3.11)$$

Considering this expression of  $p_{int}$ , the internal virtual power expended within the subregion  $\mathcal{V}$  can be expressed as follows:

$$\mathcal{P}_{int} = \int_{\mathcal{V}} \boldsymbol{\sigma} : \delta \dot{\boldsymbol{\epsilon}}_e dv + \sum_{\alpha=1}^q \int_{\mathcal{V}} \pi^\alpha \delta \dot{\gamma}^\alpha dv + \sum_{\alpha=1}^q \int_{\mathcal{V}} \boldsymbol{\xi}^\alpha \cdot \delta \nabla \dot{\gamma}^\alpha dv \quad (3.12)$$

Assuming that no external body forces act on the subregion  $\mathcal{V}$  and the contact forces acting on its boundary  $\mathcal{S}$  can be represented by a macroscopic traction vector  $\mathbf{t}$  and a microscopic traction scalar  $\chi^\alpha$  on each slip system  $\alpha$ , the external virtual power expended on  $\mathcal{V}$  can be expressed as:

$$\mathcal{P}_{ext} = \int_{\mathcal{S}} \mathbf{t} \cdot \delta \dot{\mathbf{u}} ds + \sum_{\alpha=1}^q \int_{\mathcal{S}} \chi^\alpha \delta \dot{\gamma}^\alpha ds \quad (3.13)$$

Application of the virtual power principle, which postulates that the internal and external virtual powers are balanced for any subregion  $\mathcal{V}$  and virtual variations of the modeling variables, leads to two kinds of balance equations (since two kinds of primary variables are used). Macroscopic balance equations can be obtained by setting:

$$\delta\dot{\gamma} = \mathbf{0} \quad (\text{i.e., } \delta\nabla\dot{\mathbf{u}} = \delta\dot{\boldsymbol{\varepsilon}}_e + \delta\dot{\boldsymbol{\omega}}_e) \quad (3.14)$$

Considering the symmetry of the stress tensor  $\boldsymbol{\sigma}$ , after application of the Gauss (divergence) theorem, the virtual power balance becomes:

$$\int_{\mathcal{V}} (\nabla \cdot \boldsymbol{\sigma}) \cdot \delta\dot{\mathbf{u}} \, dv = \int_{\mathcal{S}} (\boldsymbol{\sigma} \cdot \mathbf{n} - \mathbf{t}) \cdot \delta\dot{\mathbf{u}} \, ds \quad (3.15)$$

which is valid for any arbitrary subregion  $\mathcal{V}$  and virtual variations of the modeling variables. This leads to the classical balance equations (static case) and the well-known traction conditions:

$$\begin{cases} \nabla \cdot \boldsymbol{\sigma} = \mathbf{0} & \text{in } \mathcal{V} \\ \boldsymbol{\sigma} \cdot \mathbf{n} = \mathbf{t} & \text{on } \mathcal{S} \end{cases} \quad (3.16)$$

with  $\mathbf{n}$  the outward unit normal to  $\mathcal{S}$ . The microscopic counterparts of these balance equations and boundary conditions can be obtained by setting:

$$\delta\dot{\mathbf{u}} = \mathbf{0} \quad (\text{i.e., } \delta\dot{\boldsymbol{\varepsilon}}_e + \delta\dot{\boldsymbol{\omega}}_e = - \sum_{\alpha=1}^q \delta\dot{\gamma}^\alpha \mathbf{s}^\alpha \otimes \mathbf{m}^\alpha) \quad (3.17)$$

Considering (3.17), it can be demonstrated that:

$$\boldsymbol{\sigma} : \delta\dot{\boldsymbol{\varepsilon}}_e = - \sum_{\alpha=1}^q \tau^\alpha \delta\dot{\gamma}^\alpha \quad (3.18)$$

which leads, after application of the Gauss theorem, to the following form of the virtual power balance:

$$\sum_{\alpha=1}^q \int_{\mathcal{V}} (\tau^\alpha + \nabla \cdot \boldsymbol{\xi}^\alpha - \pi^\alpha) \delta\dot{\gamma}^\alpha \, dv = \sum_{\alpha=1}^q \int_{\mathcal{S}} (\boldsymbol{\xi}^\alpha \cdot \mathbf{n} - \chi^\alpha) \delta\dot{\gamma}^\alpha \, ds = 0 \quad (3.19)$$

Since (3.19) is valid for any arbitrary subregion  $\mathcal{V}$  and virtual variations of the modeling variables, the microscopic balance equation (static case) and the microscopic traction condition on each slip system  $\alpha$  can be obtained:

$$\begin{cases} \tau^\alpha + \nabla \cdot \boldsymbol{\xi}^\alpha - \pi^\alpha = 0 & \text{in } \mathcal{V} \\ \boldsymbol{\xi}^\alpha \cdot \mathbf{n} = \chi^\alpha & \text{on } \mathcal{S} \end{cases} \quad (3.20)$$

### 3.2.3 Dissipation inequality

The dissipation inequality in local form will be derived based on the second law of thermodynamics. In a mechanical perspective, this law can be expressed as follows: the temporal increase in free energy of any subregion  $\mathcal{V}$  is less than or equal to the external power expended on this subregion. Mathematically, this means:

$$\overline{\int_{\mathcal{V}} \dot{\psi} dv} \leq \mathcal{P}_{ext} \quad (3.21)$$

where  $\psi$  is free energy per unit volume, which is assumed to be controlled by the following set of state variables:  $\{\boldsymbol{\varepsilon}_e, \boldsymbol{\gamma}, \nabla \boldsymbol{\gamma}\}$ , as usually done in the framework of strain gradient crystal plasticity.

$$\psi = \psi(\boldsymbol{\varepsilon}_e, \boldsymbol{\gamma}, \nabla \boldsymbol{\gamma}) \quad (3.22)$$

Considering the identity  $\mathcal{P}_{int} = \mathcal{P}_{ext}$ , the above inequality can be rewritten in terms of internal power components as follows:

$$\int_{\mathcal{V}} \left( \dot{\psi} - \boldsymbol{\sigma} : \dot{\boldsymbol{\varepsilon}}_e - \sum_{\alpha=1}^q \pi^\alpha \dot{\gamma}^\alpha - \sum_{\alpha=1}^q \boldsymbol{\xi}^\alpha \cdot \nabla \dot{\gamma}^\alpha \right) dv \leq 0 \quad (3.23)$$

with

$$\dot{\psi}(\boldsymbol{\varepsilon}_e, \boldsymbol{\gamma}, \nabla \boldsymbol{\gamma}) = \frac{\partial \psi}{\partial \boldsymbol{\varepsilon}_e} : \dot{\boldsymbol{\varepsilon}}_e + \sum_{\alpha=1}^q \frac{\partial \psi}{\partial \gamma^\alpha} \dot{\gamma}^\alpha + \sum_{\alpha=1}^q \frac{\partial \psi}{\partial \nabla \gamma^\alpha} \cdot \nabla \dot{\gamma}^\alpha \quad (3.24)$$

Since  $\mathcal{V}$  is arbitrary, (3.23) yields the local dissipation inequality (also called local free energy imbalance):

$$\mathcal{D} = \boldsymbol{\sigma} : \dot{\boldsymbol{\varepsilon}}_e + \sum_{\alpha=1}^q \pi^\alpha \dot{\gamma}^\alpha + \sum_{\alpha=1}^q \boldsymbol{\xi}^\alpha \cdot \nabla \dot{\gamma}^\alpha - \dot{\psi} \geq 0 \quad (3.25)$$

Replacing  $\dot{\psi}$  by its expression (3.24), this local inequality can be rewritten as follows:

$$\mathcal{D} = \left( \boldsymbol{\sigma} - \frac{\partial \psi}{\partial \boldsymbol{\varepsilon}_e} \right) : \dot{\boldsymbol{\varepsilon}}_e + \sum_{\alpha=1}^q \left( \pi^\alpha - \frac{\partial \psi}{\partial \gamma^\alpha} \right) \dot{\gamma}^\alpha + \sum_{\alpha=1}^q \left( \boldsymbol{\xi}^\alpha - \frac{\partial \psi}{\partial \nabla \gamma^\alpha} \right) \cdot \nabla \dot{\gamma}^\alpha \geq 0. \quad (3.26)$$

In the present SGCP model, the macroscopic stress  $\boldsymbol{\sigma}$  is regarded as energetic quantity having no contribution to dissipation:

$$\boldsymbol{\sigma} = \frac{\partial \psi}{\partial \boldsymbol{\varepsilon}_e} \quad (3.27)$$

whereas the microscopic stresses  $\pi^\alpha$  and  $\xi^\alpha$  on each slip system  $\alpha$  may possibly be divided into energetic and dissipative parts:

$$\pi^\alpha = \pi_{en}^\alpha + \pi_{dis}^\alpha, \quad \xi^\alpha = \xi_{en}^\alpha + \xi_{dis}^\alpha \quad (3.28)$$

with

$$\pi_{en}^\alpha = \frac{\partial \psi}{\partial \gamma^\alpha}, \quad \xi_{en}^\alpha = \frac{\partial \psi}{\partial \nabla \gamma^\alpha} \quad (3.29)$$

It should be noted that higher-order dissipation in the context of strain gradient (crystal) plasticity theories still remains an open question. Although ignored in some works, several authors consider this kind of dissipation in their models ([Gurtin et al., 2007](#); [Voyiadjis and Deliktas, 2009b](#); [Fleck and Willis, 2009](#); [Gurtin, 2010](#)). As reported by [Fleck and Willis \(2009\)](#), direct experimental measurement shows that the core energy of dislocations stored during plastic deformation is much smaller than the plastic work dissipated in dislocation motion. Consequently, both statistically stored and geometrically necessary dislocations would contribute more to plastic dissipation than to a change in free energy. The source of dissipation process can be attributed to the motion of the mobile dislocations. Motion of dislocations yields energy dissipation which, in turn, results in resistance to the dislocation motion and increase in the yield strength due to size effects ([Voyiadjis and Deliktas, 2009a](#)). Considering (3.29), the local dissipation inequality can be simplified as follows:

$$\mathcal{D} = \sum_{\alpha=1}^q \pi_{dis}^\alpha \dot{\gamma}^\alpha + \sum_{\alpha=1}^q \xi_{dis}^\alpha \cdot \nabla \dot{\gamma}^\alpha \geq 0 \quad (3.30)$$

This inequality will be considered in the definition of suitable constitutive laws for the dissipative microscopic stresses  $\pi_{dis}^\alpha$  and  $\xi_{dis}^\alpha$  on each slip system  $\alpha$ .

### 3.2.4 Constitutive laws

Constitutive relations are derived in this subsection to describe the evolution of the macroscopic and microscopic stresses involved in the balance equations (3.16)<sub>1</sub> and (3.20)<sub>1</sub>, and then to reproduce the mechanical behavior of the considered continuum. This behavior is assumed to be governed by energetic and dissipative processes.

#### 3.2.4.1 Energetic constitutive laws

The energetic processes are represented by the density of free energy  $\psi$ . In this work, the classical decomposition of  $\psi$  into an elastic strain energy  $\psi_e$  and a defect energy  $\psi_p$  is adopted. The elastic part  $\psi_e$  is assumed to be a quadratic function of  $\varepsilon_e$ :

$$\psi_e(\varepsilon_e) = \frac{1}{2} \varepsilon_e : \mathbf{C} : \varepsilon_e \quad (3.31)$$

where  $\mathbf{C}$  is the elasticity tensor, which is assumed to be symmetric and positive-definite. Building on the work of [Gurtin et al. \(2007\)](#),  $\psi_p$  is assumed to be function of dislocation densities:

$$\boldsymbol{\rho} = (\rho_{\vdash}^1, \rho_{\vdash}^2, \dots, \rho_{\vdash}^q, \rho_{\circlearrowleft}^1, \rho_{\circlearrowleft}^2, \dots, \rho_{\circlearrowleft}^q) \quad (3.32)$$

where  $\rho_{\text{F}}^{\alpha}$  and  $\rho_{\odot}^{\alpha}$  denote respectively edge and screw dislocation densities on slip system  $\alpha$ . As shown by [Arsenlis and Parks \(1999\)](#), these quantities can be calculated by:

$$\rho_{\text{F}}^{\alpha} = -\mathbf{s}^{\alpha} \cdot \nabla \gamma^{\alpha}, \quad \rho_{\odot}^{\alpha} = \mathbf{l}^{\alpha} \cdot \nabla \gamma^{\alpha} \quad (3.33)$$

where  $\mathbf{l}^{\alpha}$  is the line direction of dislocation distribution defined by  $\mathbf{l}^{\alpha} = \mathbf{m}^{\alpha} \times \mathbf{s}^{\alpha}$  (“ $\times$ ” is cross product operator). However, contrary to the work of [Gurtin et al. \(2007\)](#), in the present work,  $\psi_p$  is assumed to be non-quadratic in these densities. A power-law form, with adjustable order-controlling index  $n$ , is applied to define this energy:

$$\psi_p(\boldsymbol{\rho}) = \frac{1}{n} X_0 l_{en}^n \sum_{\alpha=1}^q [|\rho_{\text{F}}^{\alpha}|^n + |\rho_{\odot}^{\alpha}|^n] \quad (3.34)$$

where  $X_0$  is a constant representing the energetic slip resistance, and  $l_{en}$  is an energetic length scale. To ensure the convexity of  $\psi_p$ , the defect energy index  $n$  must be greater than or equal to 1 ( $n \geq 1$ ). Using (3.31) and (3.34), the free energy density can be expressed as:

$$\psi(\boldsymbol{\varepsilon}_e, \boldsymbol{\rho}) = \frac{1}{2} \boldsymbol{\varepsilon}_e : \mathbf{C} : \boldsymbol{\varepsilon}_e + \frac{1}{n} X_0 l_{en}^n \sum_{\alpha=1}^q [|\rho_{\text{F}}^{\alpha}|^n + |\rho_{\odot}^{\alpha}|^n] \quad (3.35)$$

The partial derivatives of this expression with respect to the state variables presented in (3.22) provide the energetic constitutive laws that describe the evolution of the energetic stresses involved in the balance equations (3.16)<sub>1</sub> and (3.20)<sub>1</sub>. The (energetic) macroscopic stress tensor  $\boldsymbol{\sigma}$  can be expressed as:

$$\boldsymbol{\sigma} = \frac{\partial \psi}{\partial \boldsymbol{\varepsilon}_e} = \mathbf{C} : \boldsymbol{\varepsilon}_e \quad (3.36)$$

Since there is no explicit dependence between the assumed form of  $\psi$  and  $\gamma$ , the energetic part of the microscopic stress scalar  $\pi_{en}^{\alpha}$  is zero for any slip system  $\alpha$ :

$$\pi_{en}^{\alpha} = \frac{\partial \psi}{\partial \gamma^{\alpha}} = 0 \quad (3.37)$$

The energetic microscopic stress vector  $\boldsymbol{\xi}_{en}^{\alpha}$  on slip system  $\alpha$  can be expressed as:

$$\boldsymbol{\xi}_{en}^{\alpha} = \frac{\partial \psi(\boldsymbol{\varepsilon}_e, \boldsymbol{\rho})}{\partial \nabla \gamma^{\alpha}} = X_0 l_{en}^n [|\mathbf{s}^{\alpha} \cdot \nabla \gamma^{\alpha}|^{n-2} \mathbf{s}^{\alpha} \otimes \mathbf{s}^{\alpha} + |\mathbf{l}^{\alpha} \cdot \nabla \gamma^{\alpha}|^{n-2} \mathbf{l}^{\alpha} \otimes \mathbf{l}^{\alpha}] \cdot \nabla \gamma^{\alpha} \quad (3.38)$$

### 3.2.4.2 Dissipative constitutive laws

As discussed in the introduction, in almost all existing strain gradient theories involving both first- and higher-order dissipative microscopic stresses, the evolution of the latter is described using constitutive equations based on generalized effective plastic strain measures, which imply plastic strains and their gradients in a coupled manner (*e.g.*, [Fleck and Hutchinson, 2001](#); [Gurtin et al., 2007](#); [Gurtin and Anand, 2009](#); [Hutchinson, 2012](#); [Fleck et al., 2015](#); [Nellemann et al., 2017, 2018](#)). An example of these measures is:

$$\dot{E}_p = \sqrt{\|\dot{\boldsymbol{\varepsilon}}_p\|^2 + l_{dis}^2 \|\nabla \dot{\boldsymbol{\varepsilon}}_p\|^2}, \quad E_p = \int \dot{E}_p dt \quad (3.39)$$

where  $l_{dis}$  is a dissipative length scale. However, the use of such coupled measures to define the dissipative constitutive equations largely restricts their flexibility and makes the control of some numerically noticed unusual behaviors, *e.g.*, the elastic gap at initial yield (Hutchinson, 2012; Fleck et al., 2015), difficult. Actually, in most cases, these coupled measures are only used by assumption, as the coupling between first- and higher-order dissipative processes is hitherto not physically confirmed.

To allow for more flexible control of major dissipative effects, in present work, the dissipative microscopic stresses are derived from a dissipation functional  $\varphi$ , which is postulated based on the assumption of uncoupled dissipative contributions from plastic slips and plastic slip gradients. In spirit of multi-criterion approaches available in the literature (Forest and Sedláček, 2003; Fleck et al., 2015; Panteghini et al., 2019), this functional is assumed to be divided into two independent parts: one part, which describes first-order dissipative effects, is only function of plastic slips and their rates; and the other part, which describes higher-order dissipative effects, depends only on gradients of plastic slips and their rates. Note that similar (uncoupling) assumption was applied in the recent contribution of Fleck et al. (2015) to describe first- and higher-order dissipative effects in the context of phenomenological strain gradient plasticity. Therefore, the present work can be seen as an extension of this contribution to strain gradient crystal plasticity.

Define independent first- and higher-order effective plastic strains for each slip system  $\alpha$  ( $e_\pi^\alpha$  and  $e_\xi^\alpha$ , respectively) as follows:

$$\dot{e}_\pi^\alpha = |\dot{\gamma}^\alpha| = \sqrt{(\dot{\gamma}^\alpha)^2}, \quad e_\pi^\alpha = \int \dot{e}_\pi^\alpha dt \quad (3.40)$$

$$\dot{e}_\xi^\alpha = \|l_{dis} \nabla^\alpha \dot{\gamma}^\alpha\| = l_{dis} \sqrt{(\nabla^\alpha \dot{\gamma}^\alpha)^2}, \quad e_\xi^\alpha = \int \dot{e}_\xi^\alpha dt \quad (3.41)$$

where  $\nabla^\alpha$  is the projection of  $\nabla$  onto slip system  $\alpha$ :

$$\nabla^\alpha \phi = (\mathbf{s}^\alpha \cdot \nabla \phi) \mathbf{s}^\alpha + (\mathbf{l}^\alpha \cdot \nabla \phi) \mathbf{l}^\alpha \quad (3.42)$$

The proposed uncoupled dissipation functional can be expressed as:

$$\varphi(\dot{\mathbf{e}}_i, \mathbf{e}_i, \dot{\mathbf{e}}_\pi, \mathbf{e}_\pi, \dot{\mathbf{e}}_\xi, \mathbf{e}_\xi) = \varphi_\pi(\dot{\mathbf{e}}_\pi, \mathbf{e}_\pi) + \varphi_\xi(\dot{\mathbf{e}}_\xi, \mathbf{e}_\xi) \quad (3.43)$$

with

$$\dot{\mathbf{e}}_i = (\dot{e}_\pi^1, \dot{e}_\pi^2, \dots, \dot{e}_\pi^q), \quad \mathbf{e}_i = (e_\pi^1, e_\pi^2, \dots, e_\pi^q), \quad \dot{\mathbf{e}}_\pi = (\dot{e}_\xi^1, \dot{e}_\xi^2, \dots, \dot{e}_\xi^q), \quad \mathbf{e}_\xi = (e_\xi^1, e_\xi^2, \dots, e_\xi^q) \quad (3.44)$$

For comparison purposes, expressions of  $\varphi_\pi$  and  $\varphi_\xi$  are postulated in such a way as to obtain dissipative microscopic stresses having forms close to those proposed by Gurtin et al. (2007):

$$\varphi_i(\dot{\mathbf{e}}_i, \mathbf{e}_i) = \sum_{\alpha=1}^q S_i^\alpha \frac{\dot{\gamma}_0^\alpha}{m+1} \left[ \frac{\dot{e}_i^\alpha}{\dot{\gamma}_0^\alpha} \right]^{m+1} \quad (3.45)$$

where the subscript  $i$  takes as value  $\pi$  or  $\xi$  in reference to first- or higher-order dissipative microscopic stresses,  $\dot{\gamma}_0^\alpha > 0$  is a constant strain rate representative of the flow rates of interest,  $m > 0$

is a constant characterizing the rate-sensitivity of the considered material, and  $S_i^\alpha$  ( $i \in \{\pi, \xi\}$ ) are stress-dimensional internal state variables ( $S_\pi^\alpha > 0$  and  $S_\xi^\alpha \geq 0$ ). These variables are referred to hereafter as dissipative slip resistances and their evolutions are assumed to be governed by:

$$\dot{S}_i^\alpha = \sum_{\beta=1}^q h_i^{\alpha\beta} \left( S_i^\beta \right) \dot{e}_i^\beta \quad \text{with} \quad S_i^\alpha(0) = S_{i0} \quad (3.46)$$

$S_{i0}$  ( $i \in \{\pi, \xi\}$ ) are initial dissipative slip resistances (with  $S_{\pi0} > 0$  and  $S_{\xi0} \geq 0$ ), and  $h_i^{\alpha\beta}$  ( $i \in \{\pi, \xi\}$ ) are positive hardening moduli assumed to evolve according to:

$$h_i^{\alpha\beta} \left( S_i^\beta \right) = \underbrace{s^{\alpha\beta} h_i \left( S_i^\beta \right)}_{\text{Self hardening}} + \underbrace{l^{\alpha\beta} h_i \left( S_i^\beta \right)}_{\text{Latent hardening}} \quad (3.47)$$

$s^{\alpha\beta}$  is self hardening parameter marking coplanar slip planes and is defined by:

$$s^{\alpha\beta} = \begin{cases} 1 & \text{if } \mathbf{m}^\alpha \wedge \mathbf{m}^\beta = \mathbf{0} \\ 0 & \text{otherwise} \end{cases} \quad (3.48)$$

and  $l^{\alpha\beta}$  is latent hardening parameter defined in this work as:

$$l^{\alpha\beta} = |\mathbf{s}^\alpha \cdot \mathbf{s}^\beta| \|\mathbf{m}^\alpha \wedge \mathbf{m}^\beta\| \quad (3.49)$$

to take into account the influence of the relative misorientation of slip planes on the hardening moduli.  $h_i$  ( $i \in \{\pi, \xi\}$ ) are self-hardening functions which, motivated by several works from the literature (e.g., [Kalidindi et al., 1992](#); [Gurtin et al., 2007](#)), are assumed to be defined as:

$$h_i \left( S_i^\beta \right) = \begin{cases} H_i \left( 1 - \frac{S_i^\beta}{S_{iF}} \right)^a & \text{for } S_{i0} \leq S_i^\beta < S_{iF} \\ 0 & \text{for } S_i^\beta \geq S_{iF} \end{cases} \quad (3.50)$$

with  $S_{iF} > S_{i0}$ ,  $a \geq 1$  and  $H_i \geq 0$ .

Based on the above definitions of the ingredients of the proposed dissipation functional  $\varphi$ , it can easily be verified that this functional is nonnegative and convex in  $\dot{\gamma}^\alpha$  and  $\nabla \dot{\gamma}^\alpha$ , which guarantees a priori satisfaction of the second principle of thermodynamics (nonnegative dissipation). The partial derivatives of  $\varphi$  with respect to  $\dot{\gamma}^\alpha$  and  $\nabla \dot{\gamma}^\alpha$  give the expressions of the dissipative stress scalar  $\pi_{dis}^\alpha$  and vector  $\boldsymbol{\xi}_{dis}^\alpha$  on slip system  $\alpha$ :

$$\pi_{dis}^\alpha = \frac{\partial \varphi}{\partial \dot{\gamma}^\alpha} = S_\pi^\alpha \left[ \frac{\dot{e}_\pi^\alpha}{\dot{e}_0^\alpha} \right]^m \frac{\dot{\gamma}^\alpha}{\dot{e}_\pi^\alpha} \quad (3.51)$$

$$\boldsymbol{\xi}_{dis}^\alpha = \frac{\partial \varphi}{\partial \nabla \dot{\gamma}^\alpha} = S_\xi^\alpha l_{dis}^2 \left[ \frac{\dot{e}_\xi^\alpha}{\dot{e}_0^\alpha} \right]^m \frac{\nabla^\alpha \dot{\gamma}^\alpha}{\dot{e}_\xi^\alpha} \quad (3.52)$$

As mentioned above, the dissipation functional proposed in this work  $\varphi$  leads to dissipative microscopic stresses close to those postulated by [Gurtin et al. \(2007\)](#) based on the normality rule. The latter can be obtained from (3.51) and (3.52) by replacing the first- and higher-order effective plastic strains by a coupled one defined by:

$$\dot{d}^\alpha = \sqrt{(\dot{e}_\pi^\alpha)^2 + (\dot{e}_\xi^\alpha)^2}, \quad d^\alpha = \int \dot{d}^\alpha dt \quad (3.53)$$

and by replacing  $S_\pi^\alpha$  and  $S_\xi^\alpha$  by a single strictly positive slip resistance  $S^\alpha$  calculated based on  $\dot{d}^\alpha$ .

### 3.2.5 Flow rules

Based on the expressions of the microscopic stresses, the microscopic balance equation associated with slip system  $\alpha$  (3.20)<sub>1</sub> can be reformulated as follows:

$$\tau^\alpha + \nabla \cdot \xi_{en}^\alpha + \nabla \cdot \xi_{dis}^\alpha - \pi_{dis}^\alpha = 0 \quad (3.54)$$

When augmented by the microscopic constitutive laws (7.8), (3.51) and (3.52), this equation acts as a flow rule associated with slip system  $\alpha$ :

$$\tau^\alpha + \nabla \cdot \xi_{en}^\alpha + \nabla \cdot \left\{ S_\xi^\alpha l_{dis}^2 \left[ \frac{\dot{e}_\xi^\alpha}{\dot{\gamma}_0^\alpha} \right]^m \frac{\nabla^\alpha \dot{\gamma}^\alpha}{\dot{e}_\xi^\alpha} \right\} - S_\pi^\alpha \left[ \frac{\dot{e}_\pi^\alpha}{\dot{\gamma}_0^\alpha} \right]^m \frac{\dot{\gamma}^\alpha}{\dot{e}_\pi^\alpha} = 0 \quad (3.55)$$

Bearing in mind (3.38),  $\nabla \cdot \xi_{en}^\alpha$  can be expressed as:

$$\nabla \cdot \xi_{en}^\alpha = \mathbf{A}^{\alpha\alpha} : \nabla \nabla \gamma^\alpha \quad (3.56)$$

with

$$\mathbf{A}^{\alpha\alpha} = (n-1) X_0 l_{en}^n [| \mathbf{s}^\alpha \cdot \nabla \gamma^\alpha |^{n-2} \mathbf{s}^\alpha \otimes \mathbf{s}^\alpha + | \mathbf{l}^\alpha \cdot \nabla \gamma^\alpha |^{n-2} \mathbf{l}^\alpha \otimes \mathbf{l}^\alpha] \quad (3.57)$$

Using (3.56), the flow rule (3.55) becomes:

$$\tau^\alpha + \mathbf{A}^{\alpha\alpha} : \nabla \nabla \gamma^\alpha + \nabla \cdot \left\{ S_\xi^\alpha l_{dis}^2 \left[ \frac{\dot{e}_\xi^\alpha}{\dot{\gamma}_0^\alpha} \right]^m \frac{\nabla^\alpha \dot{\gamma}^\alpha}{\dot{e}_\xi^\alpha} \right\} - S_\pi^\alpha \left[ \frac{\dot{e}_\pi^\alpha}{\dot{\gamma}_0^\alpha} \right]^m \frac{\dot{\gamma}^\alpha}{\dot{e}_\pi^\alpha} = 0. \quad (3.58)$$

The second term in the above equation, being energetic, represents the negative of a backstress, leading to Bauschinger effects in the flow rule. The last two terms of this equation are dissipative (resulting from the dissipation functional). A reversal of the flow direction ( $\dot{\gamma}^\alpha \rightarrow -\dot{\gamma}^\alpha$ ) simply changes their sign. Therefore, these terms represent dissipative (isotropic-like) hardening. The flow rule (3.58) can then be written in a more convenient form as:

$$\begin{aligned} \tau^\alpha - \underbrace{(-\mathbf{A}^{\alpha\alpha} : \nabla \nabla \gamma^\alpha)}_{\text{Energetic backstress}} &= \underbrace{S_\pi^\alpha \left[ \frac{\dot{e}_\pi^\alpha}{\dot{\gamma}_0^\alpha} \right]^m \frac{\dot{\gamma}^\alpha}{\dot{e}_\pi^\alpha} - \nabla \cdot \left\{ S_\xi^\alpha l_{dis}^2 \left[ \frac{\dot{e}_\xi^\alpha}{\dot{\gamma}_0^\alpha} \right]^m \frac{\nabla^\alpha \dot{\gamma}^\alpha}{\dot{e}_\xi^\alpha} \right\}}_{\text{Dissipative hardening}} \end{aligned} \quad (3.59)$$

### 3.2.6 Microscopic boundary conditions

Within the framework of higher-order gradient theories, the presence of higher-order stresses can result in an expenditure of microscopic power on the boundary of the studied domain ( $\mathcal{S}$ ). For each slip system  $\alpha$ , the microscopic power expended, per unit area, on this boundary is given by:

$$(\xi^\alpha \cdot \mathbf{n}) \dot{\gamma}^\alpha \quad (3.60)$$

The present work focuses on simple microscopic boundary conditions (BCs) that result in a null power expenditure on  $\mathcal{S}$ :

$$(\xi^\alpha \cdot \mathbf{n}) \dot{\gamma}^\alpha = 0 \quad \text{on } \mathcal{S} \quad (3.61)$$

Specifically, two limit cases of microscopic BCs are considered in this work:

$$\begin{aligned}\dot{\gamma}^\alpha &= 0 \quad \text{on } \mathcal{S}_\gamma^\alpha \\ \boldsymbol{\xi}^\alpha \cdot \mathbf{n} &= 0 \quad \text{on } \mathcal{S}_\chi^\alpha\end{aligned}\tag{3.62}$$

with  $\mathcal{S}_\gamma^\alpha$  and  $\mathcal{S}_\chi^\alpha$  complementary subsurfaces of  $\mathcal{S}$ . The micro-hard BCs (3.62)<sub>1</sub> correspond to impenetrable surfaces with no slip, whereas the micro-free BCs (3.62)<sub>2</sub> represent free surfaces without slip resistance.

### 3.3 Simplified two-dimensional version of the SGCP model and numerical implementation

In this section, a simplified two-dimensional (2D) version of the proposed SGCP model is derived and implemented to investigate, in a simple manner, the influence of the constitutive parameters and the uncoupled dissipation functional on the global response of the considered continuum.

#### 3.3.1 Simplified 2D SGCP model

The plane strain condition is adopted for the 2D model. Under this condition, the displacement field can be degenerated as:

$$\mathbf{u}(\mathbf{x}, t) = u_1(x_1, x_2, t) \mathbf{e}_1 + u_2(x_1, x_2, t) \mathbf{e}_2\tag{3.63}$$

which results in a displacement gradient  $\nabla \mathbf{u}$  that is independent of  $x_3$ . Furthermore, attention is restricted to planar slip systems, *i.e.*, slip systems satisfying:

$$\mathbf{s}^\alpha \cdot \mathbf{e}_3 = 0, \quad \mathbf{m}^\alpha \cdot \mathbf{e}_3 = 0, \quad \mathbf{s}^\alpha \times \mathbf{m}^\alpha = \mathbf{e}_3\tag{3.64}$$

with slips  $\gamma^\alpha$  independent of  $x_3$ . All other slip systems are ignored. This approximate assumption is widely used in the literature under plane strain, as it allows for constructing simple 2D constitutive models. Using this assumption, it can be shown that:

$$\mathbf{e}_3 \cdot \nabla \gamma^\alpha = 0 \quad \text{and} \quad \mathbf{l}^\alpha = \mathbf{m}^\alpha \times \mathbf{s}^\alpha = -\mathbf{e}_3\tag{3.65}$$

which implies that screw dislocations vanish:

$$\rho_{\odot}^\alpha = \mathbf{l}^\alpha \cdot \nabla \gamma^\alpha = 0, \quad \forall \alpha \in \{1, 2, \dots, q\}\tag{3.66}$$

Ignoring the crystalline elastic anisotropy and using the proposed form of defect energy (3.34), with only edge dislocation densities, the energetic macroscopic and microscopic stresses involved in the simplified model can be expressed as:

$$\begin{aligned}\boldsymbol{\sigma} &= \lambda \operatorname{tr}(\boldsymbol{\varepsilon}_e) \mathbf{I} + 2\mu \boldsymbol{\varepsilon}_e \\ \pi_{en}^\alpha &= 0 \\ \boldsymbol{\xi}_{en}^\alpha &= X_0 l_{en}^n [|\mathbf{s}^\alpha \cdot \nabla \gamma^\alpha|^{n-2} \mathbf{s}^\alpha \otimes \mathbf{s}^\alpha] \cdot \nabla \gamma^\alpha\end{aligned}\tag{3.67}$$

where  $\lambda$  and  $\mu$  are the first and second Lamé elastic moduli. Concerning the dissipative microscopic stresses, simplified equations obtained from (3.51) and (3.52), with the slip resistances  $S_\pi^\alpha$  and  $S_\xi^\alpha$  assumed to evolve linearly with the effective plastic strains, are used to define these stresses:

$$\begin{aligned}\pi_{dis}^\alpha &= S_\pi^\alpha \left[ \frac{\dot{e}_\pi^\alpha}{\dot{\gamma}_0^\alpha} \right]^m \frac{\dot{\gamma}^\alpha}{\dot{e}_\pi^\alpha} \\ \xi_{dis}^\alpha &= S_\xi^\alpha l_{dis}^2 \left[ \frac{\dot{e}_\xi^\alpha}{\dot{\gamma}_0^\alpha} \right]^m \frac{\nabla^\alpha \dot{\gamma}^\alpha}{\dot{e}_\xi^\alpha}\end{aligned}\quad (3.68)$$

where, for  $i \in \{\pi, \xi\}$ :

$$\dot{S}_i^\alpha = \sum_{\beta=1}^q H_i \dot{e}_i^\beta \quad \text{with} \quad S_i^\alpha(0) = S_{i0}, \quad H_i = \text{constant} \geq 0 \quad (3.69)$$

Note that  $S_{\pi0} > 0$  and  $S_{\xi0} \geq 0$ .

In summary, the overall constitutive equations of the simplified 2D SGCP model are:

$$\left\{ \begin{array}{l} \boldsymbol{\sigma} = \lambda \operatorname{tr}(\boldsymbol{\varepsilon}_e) \mathbf{I} + 2\mu \boldsymbol{\varepsilon}_e \\ \boldsymbol{\xi}^\alpha = X_0 l_{en}^n [| \mathbf{s}^\alpha \cdot \nabla \gamma^\alpha |^{n-2} \mathbf{s}^\alpha \otimes \mathbf{s}^\alpha] \cdot \nabla \gamma^\alpha + S_\xi^\alpha l_{dis}^2 \left[ \frac{\dot{e}_\xi^\alpha}{\dot{\gamma}_0^\alpha} \right]^m \frac{\nabla^\alpha \dot{\gamma}^\alpha}{\dot{e}_\xi^\alpha} \\ \pi^\alpha = S_\pi^\alpha \left[ \frac{\dot{e}_\pi^\alpha}{\dot{\gamma}_0^\alpha} \right]^m \frac{\dot{\gamma}^\alpha}{\dot{e}_\pi^\alpha} \\ \dot{S}_\pi^\alpha = \sum_{\beta=1}^q H_\pi \dot{e}_\pi^\beta, \quad S_\pi^\alpha(0) = S_{\pi0} > 0 \\ \dot{S}_\xi^\alpha = \sum_{\beta=1}^q H_\xi \dot{e}_\xi^\beta, \quad S_\xi^\alpha(0) = S_{\xi0} \geq 0 \\ \dot{e}_\pi^\alpha = |\dot{\gamma}^\alpha|, \quad \dot{e}_\xi^\alpha = \|l_{dis} \nabla^\alpha \dot{\gamma}^\alpha\| \\ \alpha = 1, 2, \dots, q \end{array} \right. \quad (3.70)$$

These equations are solved numerically within the framework of finite element method. Several methods are used in the literature to solve these equations. Among them, one can cite the approach proposed by Scherer et al. (2020) combining the advantages of micromorphic and Lagrange multiplier methods. In this approach, a scalar micromorphic variable is linked to a cumulative plastic slip measure by a Lagrange multiplier to ensure uncoupling between constitutive nonlinearity and spatial nonlocality. Other methods based on an independent thermodynamic variable for each slip system can be found, allowing for more flexible control of gliding on the slip systems. Two common examples of these methods can be cited:  $\rho$ -method (Kuroda and Tvergaard, 2008a; Kuroda, 2011; Klusemann et al., 2012; Pouriayevali and Xu, 2017; Peng et al., 2018) and  $\gamma$ -method (Gurtin et al., 2007; Borg, 2007; Jebahi et al., 2020). The former considers dislocation densities or their rates as primary variables (additional degrees of freedom), whereas plastic slips or plastic slip rates are considered as primary variables in the latter. According to Klusemann et al. (2012), the two methods generally lead to similar results. However,  $\gamma$ -methods provide more flexibility in constraining the dislocation flow on the boundaries. Furthermore, it does not require a local loop (at the integration points) to calculate the plastic slip rates  $\dot{\gamma}^\alpha$ , which are given by solving the global system of equations. This method is chosen in the present work. A brief presentation of the numerical procedure is presented in the next subsection.

### 3.3.2 Numerical implementation

The weak forms of the macroscopic and microscopic balance equations (3.16)<sub>1</sub> and (3.20)<sub>1</sub> may be formulated using the virtual power relations given in section 3.2. Here, the virtual fields  $\delta\dot{\mathbf{u}}$  and  $\delta\dot{\gamma}$ , which are referred to as test fields, are assumed to be kinematically admissible to  $\mathbf{0}$  on the portions of the boundary of the studied domain on which Dirichlet (essential) boundary conditions are imposed. The macroscopic and microscopic weak forms can then be respectively expressed as:

$$\begin{aligned} G_u &= \int_{\mathcal{V}} \delta\dot{\varepsilon} : \boldsymbol{\sigma} dv - \int_{\mathcal{S}_t} \delta\dot{\mathbf{u}} \cdot \mathbf{t} ds \\ G_\gamma &= \sum_{\alpha=1}^q \int_{\mathcal{V}} \nabla \delta\dot{\gamma}^\alpha \cdot \boldsymbol{\xi}^\alpha dv + \sum_{\alpha=1}^q \int_{\mathcal{V}} \delta\dot{\gamma}^\alpha \pi^\alpha dv - \sum_{\alpha=1}^q \int_{\mathcal{V}} \delta\dot{\gamma}^\alpha \mathbf{P}^\alpha : \boldsymbol{\sigma} dv - \sum_{\alpha=1}^q \int_{\mathcal{S}_\chi^\alpha} \delta\dot{\gamma}^\alpha \chi^\alpha ds \end{aligned} \quad (3.71)$$

where  $\mathcal{S}_t$  and  $\mathcal{S}_\chi^\alpha$  are respectively the portions of the domain boundary on which macroscopic and microscopic traction forces, respectively noted as  $\mathbf{t}$  and  $\chi^\alpha$ , are imposed.

To numerically solve these weak forms, a User-Element (UEL) subroutine is implemented within the commercial finite element package ABAQUS/Standard. Both displacement and plastic slip fields ( $\mathbf{u}$  and  $\gamma$ ) are considered as degrees of freedom in the UEL. Isoparametric two-dimensional eight-node quadratic elements are used. Integration within these elements is carried out using 9-point Gaussian technique. In each element, displacement fields  $u_i$  ( $i \in \{1, 2\}$ ) and plastic slip fields  $\gamma^\alpha$  ( $\alpha \in \{1, 2, \dots, q\}$ ) are approximated based on nodal values as follows:

$$u_i(x_1, x_2) = \sum_{k=1}^8 N_k(x_1, x_2) U_i^k, \quad \gamma^\alpha(x_1, x_2) = \sum_{k=1}^8 N_k(x_1, x_2) \Gamma_k^\alpha \quad (3.72)$$

where  $U_i^k$  and  $\Gamma_k^\alpha$  are respectively the nodal values of displacement  $u_i$  and plastic slip  $\gamma^\alpha$ , and  $N_k$  are the interpolation (shape) functions, which are assumed to be the same for both displacement and plastic slip fields. Using these field approximations, the above weak forms can be written, in matrix form, within a representative finite element as:

$$\begin{aligned} G_u^e &= (\delta\dot{\underline{U}}^e)^T \cdot \left( \int_{\mathcal{V}^e} \underline{\underline{B}}_u^T \cdot \underline{\underline{\sigma}} dv - \int_{\mathcal{S}_t^e} \underline{\underline{N}}_u^T \cdot \underline{\underline{t}} ds \right) \\ G_\gamma^e &= (\delta\dot{\underline{\Gamma}}^e)^T \cdot \left( \int_{\mathcal{V}^e} \underline{\underline{B}}_\gamma^T \cdot \underline{\xi} dv + \int_{\mathcal{V}^e} \underline{\underline{N}}_\gamma^T \cdot \underline{\pi} dv - \int_{\mathcal{V}^e} \underline{\underline{N}}_\gamma^T \cdot \underline{\tau} dv - \int_{\mathcal{S}_\chi^e} \underline{\underline{N}}_\gamma^T \cdot \underline{\chi} ds \right) \end{aligned} \quad (3.73)$$

where  $\underline{\underline{\sigma}}$ ,  $\underline{\pi}$  and  $\underline{\xi}$  are vector representations of the macroscopic stress and the microscopic stresses on all slip systems,  $\underline{\tau}$  is a vector containing the resolved shear stresses on all slip systems,  $\underline{\underline{t}}$  is the macroscopic traction vector,  $\underline{\chi}$  is a vector containing the microscopic tractions on all slip systems,  $\underline{\underline{N}}_u$  and  $\underline{\underline{B}}_u$  are interpolation and gradient matrices associated with the displacement field, and  $\underline{\underline{N}}_\gamma$  and  $\underline{\underline{B}}_\gamma$  are interpolation and gradient matrices associated with the plastic slip fields. Expressions of these vector and matrix quantities are long and not revealing, they are not presented in this work.

The principle of virtual power implies that  $G_u^e$  and  $G_\gamma^e$  are zero for any virtual variations of the element nodal variables  $\delta\dot{\underline{U}}^e$  and  $\delta\dot{\underline{\Gamma}}^e$ . Therefore:

$$\begin{aligned}\underline{R}_u^e &= \int_{\mathcal{V}^e} \underline{\underline{B}}_u^T \cdot \underline{\underline{\sigma}} dv - \int_{S_t^e} \underline{\underline{N}}_u^T \cdot \underline{\underline{t}} ds = 0 \\ \underline{R}_\gamma^e &= \int_{\mathcal{V}^e} \underline{\underline{B}}_\gamma^T \cdot \underline{\underline{\xi}} dv + \int_{\mathcal{V}^e} \underline{\underline{N}}_\gamma^T \cdot \underline{\underline{\pi}} dv - \int_{\mathcal{V}^e} \underline{\underline{N}}_\gamma^T \cdot \underline{\underline{\tau}} dv - \int_{S_x^e} \underline{\underline{N}}_\gamma^T \cdot \underline{\underline{\chi}} ds = 0\end{aligned}\quad (3.74)$$

These equations are linearized with respect to the variations of the element nodal variables  $\underline{U}^e$  and  $\underline{\Gamma}^e$ , which results in an elementary system of linear equations that can be presented in matrix form as follows:

$$\begin{bmatrix} \underline{\underline{K}}_{uu}^e & \underline{\underline{K}}_{u\gamma}^e \\ \underline{\underline{K}}_{\gamma u}^e & \underline{\underline{K}}_{\gamma\gamma}^e \end{bmatrix} \begin{bmatrix} \Delta \underline{U}^e \\ \Delta \underline{\Gamma}^e \end{bmatrix} = \begin{bmatrix} -\underline{R}_u^e \\ -\underline{R}_\gamma^e \end{bmatrix} \quad (3.75)$$

where:

$$\underline{\underline{K}}_{uu}^e = \frac{\partial \underline{R}_u^e}{\partial \underline{U}^e}, \quad \underline{\underline{K}}_{u\gamma}^e = \frac{\partial \underline{R}_u^e}{\partial \underline{\Gamma}^e}, \quad \underline{\underline{K}}_{\gamma u}^e = \frac{\partial \underline{R}_\gamma^e}{\partial \underline{U}^e}, \quad \underline{\underline{K}}_{\gamma\gamma}^e = \frac{\partial \underline{R}_\gamma^e}{\partial \underline{\Gamma}^e} \quad (3.76)$$

The global system of linear equations can be obtained by assembling all the elementary systems associated with the overall finite elements. This system is solved by means of a Newton-Raphson iterative solution scheme for the overall increments of the displacement and plastic slip fields ( $\Delta \underline{U}$  and  $\Delta \underline{\Gamma}$ , respectively). At each iteration, updated values of these increments are obtained and used to numerically solve the constitutive equations (3.70) at the Gauss points (algorithm 3.1). A detailed numerical implementation can be found in the Appendix A.

## 3.4 Assessment and parametric investigation of the SGCP model

To investigate the influence of the major constitutive parameters involved in the proposed SGCP model, the simplified 2D version of this model is applied to simulate simple 2D shear tests. These tests have been widely treated by existing strain gradient plasticity models and interesting comparison results related to these tests exist in the literature (e.g., Shu et al., 2001; Bittencourt et al., 2003; Niordson and Hutchinson, 2003; Gurtin et al., 2007; Nelleman et al., 2017). A 2D crystalline strip of height  $h$  and width  $w$  is considered, with two active slip systems symmetrically oriented with respect to  $e_1$  direction ( $\theta_1 = -\theta_2 = 60^\circ$ ), as illustrated in Fig. 3.1. This strip is discretized using 100 quadratic finite elements, which represents a good compromise between results accuracy and computation cost. To model the infinite length of the strip in  $e_1$  direction, the following periodic conditions are imposed on the left and right edges:

$$\begin{aligned}u_i(0, x_2, t) &= u_i(w, x_2, t), \quad \text{for } i = 1, 2 \\ \gamma^\alpha(0, x_2, t) &= \gamma^\alpha(w, x_2, t), \quad \text{for } \alpha = 1, 2\end{aligned}\quad (3.77)$$

In addition, the bottom edge is subject to macro-clamped displacement boundary conditions and the top edge is subject to a loading-unloading cycle of displacement in  $e_1$  direction:

$$u_1(x_1, 0, t) = u_2(x_1, 0, t) = 0, \quad u_1(x_1, h, t) = h\Gamma(t), \quad \text{and } u_2(x_1, h, t) = 0 \quad (3.78)$$

**Algorithm 3.1** Time integration of the SGCP constitutive equations

---

**Inputs:**  $\Delta t, \Delta \mathbf{u}, \Delta \boldsymbol{\gamma}, \mathbf{u}, \boldsymbol{\gamma}, \boldsymbol{\varepsilon}, \boldsymbol{\varepsilon}_e, \boldsymbol{\varepsilon}_p, \boldsymbol{\sigma}, S_\pi^\alpha, S_\xi^\alpha, \pi^\alpha, \boldsymbol{\xi}^\alpha$

**Compute:**  $\Delta \boldsymbol{\varepsilon} = [\nabla(\Delta \mathbf{u})]_{sym}, \quad \Delta \boldsymbol{\varepsilon}_p = \sum_{\alpha=1}^q \Delta \gamma^\alpha \boldsymbol{P}^\alpha, \quad \Delta \boldsymbol{\varepsilon}_e = \Delta \boldsymbol{\varepsilon} - \Delta \boldsymbol{\varepsilon}_p$

**Update:**  $\mathbf{u} \leftarrow \mathbf{u} + \Delta \mathbf{u}, \quad \boldsymbol{\gamma} \leftarrow \boldsymbol{\gamma} + \Delta \boldsymbol{\gamma}, \quad \boldsymbol{\varepsilon} \leftarrow \boldsymbol{\varepsilon} + \Delta \boldsymbol{\varepsilon}, \quad \boldsymbol{\varepsilon}_e \leftarrow \boldsymbol{\varepsilon}_e + \Delta \boldsymbol{\varepsilon}_e, \quad \boldsymbol{\varepsilon}_p \leftarrow \boldsymbol{\varepsilon}_p + \Delta \boldsymbol{\varepsilon}_p$

**Compute:**  $\boldsymbol{\sigma} = \lambda \text{tr}(\boldsymbol{\varepsilon}_e) \mathbf{I} + 2\mu \boldsymbol{\varepsilon}_e$

**for**  $\alpha=1$  **to**  $q$  **do**

**Compute:**  $\Delta e_\pi^\alpha = |\Delta \gamma^\alpha|, \quad \Delta e_\xi^\alpha = \|l_{dis} \boldsymbol{\nabla}^\alpha(\Delta \gamma^\alpha)\|$

**end for**

**for**  $\alpha=1$  **to**  $q$  **do**

**Compute:**  $\Delta S_\pi^\alpha = \sum_{\beta=1}^q H_\pi \Delta e_\pi^\beta, \quad \Delta S_\xi^\alpha = \sum_{\beta=1}^q H_\xi \Delta e_\xi^\beta$

**Update:**  $S_\pi^\alpha \leftarrow S_\pi^\alpha + \Delta S_\pi^\alpha, \quad S_\xi^\alpha \leftarrow S_\xi^\alpha + \Delta S_\xi^\alpha$

**Compute:**  $\pi^\alpha = S_\pi^\alpha \left[ \frac{\Delta e_\pi^\alpha}{\dot{\gamma}_0^\alpha \Delta t} \right]^m \frac{\Delta \gamma^\alpha}{\Delta e_\pi^\alpha}$

**Compute:**  $\boldsymbol{\xi}^\alpha = X_0 l_{en}^n [|\mathbf{s}^\alpha \cdot \boldsymbol{\nabla} \boldsymbol{\gamma}^\alpha|^{n-2} \mathbf{s}^\alpha \otimes \mathbf{s}^\alpha] \cdot \boldsymbol{\nabla} \boldsymbol{\gamma}^\alpha + S_\xi^\alpha l_{dis}^2 \left[ \frac{\Delta e_\xi^\alpha}{\dot{\gamma}_0^\alpha \Delta t} \right]^m \frac{\boldsymbol{\nabla}^\alpha(\Delta \gamma^\alpha)}{\Delta e_\xi^\alpha}$

**end for**

---

where  $\Gamma(t)$  is the prescribed shear strain, going from 0 to 0.02 and back to 0. In order to establish proportional and non-proportional loading conditions, which are necessary to better investigate certain SGCP aspects, two types of microscopic (slip) boundary conditions are also considered on the top and bottom edges. In the case of proportional loading, both the edges are passivated from the beginning to the end of the simulation:

$$\gamma^\alpha(x_1, 0, t) = \gamma^\alpha(x_1, h, t) = 0, \quad \text{for } \alpha = 1, 2 \quad (3.79)$$

However, in the case of non-proportional loading, only the bottom edge is passivated over the entire simulation. The top edge is assumed to be unpassivated until a certain value of the prescribed shear strain in the plastic range ( $\Gamma = 0.01$ ) and then passivated until the end of the simulation:

$$\gamma^\alpha(x_1, 0, t) = 0, \quad \dot{\gamma}^\alpha(x_1, h, t > t_0) = 0, \quad \text{for } \alpha = 1, 2 \quad (3.80)$$

where  $t_0$  is the passivation time, *i.e.*, time at which  $\Gamma(t_0) = 0.01$ . Note that, in the considered case of non-proportional loading, nonuniform plastic strain distribution develops within the strip before the non-proportional loading source (top edge passivation) occurs. As will be seen later, this allows for a more complete investigation of the higher-order energetic and dissipative effects under non-proportional loading conditions.

Results in terms of macroscopic stress-strain curves and plastic shear strain distributions in  $e_2$  direction are adopted to investigate the influence of the major constitutive parameters on the global response of the considered material, with a focus on those implied in the definition of the higher-order energetic and dissipative stresses. The stress-strain curves are generated based on the average shear stress within the strip (simply noted  $\sigma_{12}$  hereafter) as a function of the prescribed shear strain  $\Gamma$ . For the plastic shear strain distribution in  $e_2$  direction, the engineering plastic shear

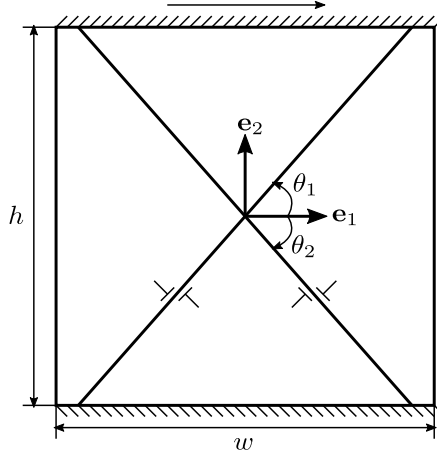


**Fig. 3.1.** 2D crystalline strip with two active slip systems, symmetrically tilted by  $\theta_1 = 60^\circ$  and  $\theta_2 = -60^\circ$  with respect to  $e_1$  direction, for shear test simulations.

**Tab. 3.1.** Material parameters implied in system (3.70): the values of the fixed parameters are taken from [Gurtin et al. \(2007\)](#), for comparison purposes.

Material parameter name	Symbol	Value	Unit
First Lamé elastic modulus	$\lambda$	150	GPa
Second Lamé elastic modulus	$\mu$	100	GPa
Reference slip rate	$\dot{\gamma}_0^\alpha$	0.04	$s^{-1}$
Rate-sensitivity parameter	$m$	0.05	—
Higher-order energetic slip resistance	$X_0$	50	MPa
Initial first-order dissipative slip resistance	$S_{\pi 0}$	50	MPa
Initial higher-order dissipative slip resistance	$S_{\xi 0}$	case study	MPa
First-order hardening modulus	$H_\pi$	case study	MPa
Higher-order hardening modulus	$H_\xi$	case study	MPa
Energetic length scale	$l_{en}$	case study	$\mu m$
Dissipative length scale	$l_{dis}$	case study	$\mu m$
Defect energy index	$n$	case study	—

strain  $\gamma_{12}^p = 2\varepsilon_{12}^p$  is employed. These results are mainly discussed with respect to the results of [Gurtin et al. \(2007\)](#), whose theory is used as basis of the present one. Therefore, the material parameters that are not concerned by the parametric investigation in system (3.70) are set equal to those used by [Gurtin et al. \(2007\)](#), as illustrated in Tab. 3.1.

### 3.4.1 Influence of higher-order energetic stress parameters

In this subsection, the influence of the main higher-order energetic stress parameters, specifically the energetic length scale  $l_{en}$  and the defect energy index  $n$ , and the interaction between them are investigated in the absence of dissipative effects. For this purpose, the dissipative length scale  $l_{dis}$  and the first-order hardening modulus  $H_\pi$  are set to zero.

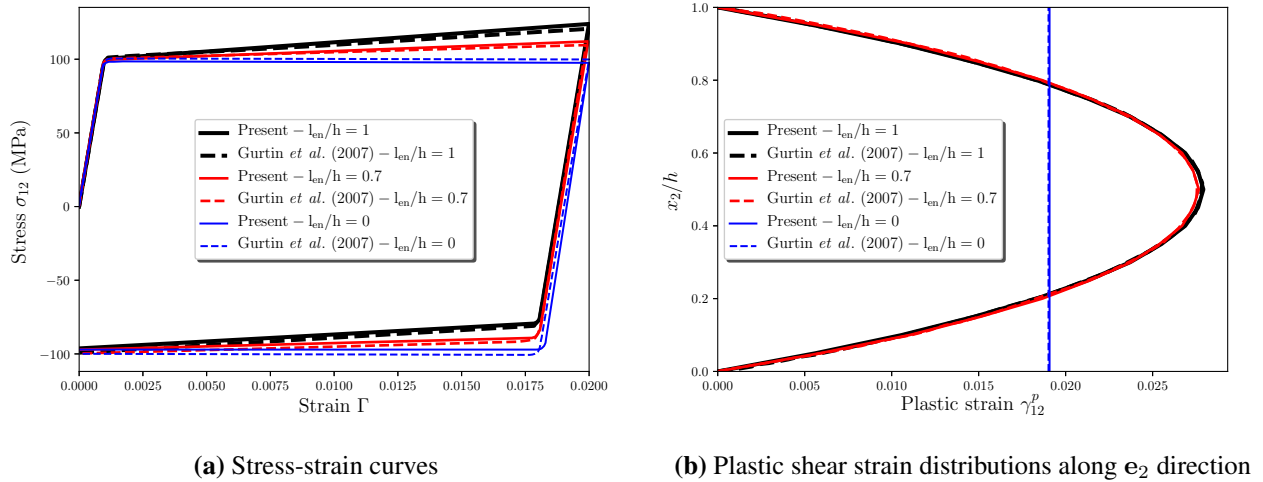


**Fig. 3.2.** Influence of the energetic length scale  $l_{en}$  under proportional loading conditions in the absence of higher-order dissipative effects: comparison between the present and Gurtin et al. (2007) results ( $n = 2$ ,  $l_{dis} = 0$ ,  $H_\pi = 0$ ).

### 3.4.1.1 Energetic length scale $l_{en}$ : validation of the model implementation

Using  $l_{dis} = 0$ , the higher-order effective plastic strain rates  $\dot{e}_\xi^\alpha$  (3.41) vanish and the first-order counterparts  $\dot{e}_\pi^\alpha$  (3.40) coincide with the coupled measures proposed by Gurtin et al. (2007):

$$\dot{d}^\alpha = \sqrt{(\dot{e}_\pi^\alpha)^2 + (\dot{e}_\xi^\alpha)^2} = \dot{e}_\pi^\alpha, \quad \text{for } \alpha = 1, 2 \quad (3.81)$$

Therefore, by using the same values of constitutive parameters, the present model becomes equivalent to the Gurtin et al. (2007) model. Comparison between the results of the two models in this case allows for validation of the numerical implementation of present one. Fig. 3.2 presents the comparison results for different values of  $l_{en}$ , obtained using quadratic defect energy ( $n = 2$ ) and proportional loading. The present results are in very good agreement with the results of Gurtin et al. (2007), regardless of the  $l_{en}$  value. The very small differences between the results would be due to the use of different types of finite elements and different mesh refinements. As mentioned earlier, 8-node quadratic elements are used in this work, whereas 9-node quadratic elements are adopted in the work of Gurtin et al. (2007). As expected, for quadratic defect energy ( $n = 2$ ) and proportional loading conditions, the energetic length scale  $l_{en}$  contributes to hardening but not to strengthening. By varying  $l_{en}$ , only the hardening rate after yielding changes, the plastic regime always starts from the same yield point (Fig. 3.2a). The case of  $l_{en} = 0$  corresponds to the classical crystal plasticity (CP) with no hardening. This case, which will simply be designated by “Perfect CP” in subsequent figures, leads to a flat stress-strain curve with no hardening after yielding and to a uniform plastic shear strain distribution through the strip thickness. For  $l_{en} = 0.7 h$  and  $l_{en} = h$ , kinematic hardening occurs, leading to classical Bauschinger effects which become more marked with increasing  $l_{en}$ . The associated plastic shear strain distributions along the strip thickness present a quadratic form (Fig. 3.2b).

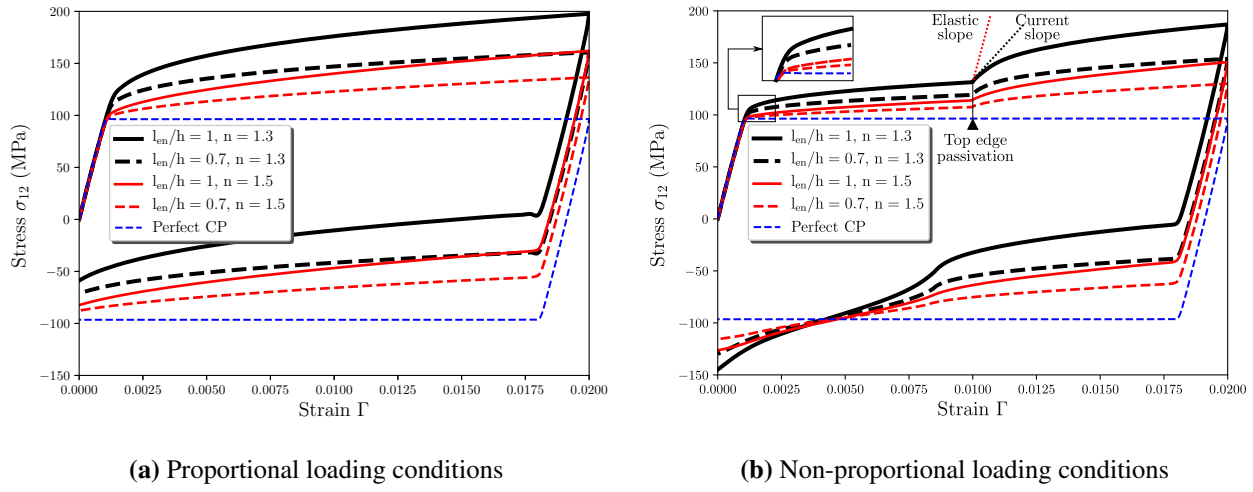


**Fig. 3.3.** Stress-strain responses under proportional and non-proportional loading conditions for different values of the defect energy index  $n$  in the range of  $n < 2$  and different values of the energetic length scale  $l_{en}$  ( $l_{dis} = 0$ ,  $H_\pi = 0$ ).

### 3.4.1.2 Defect energy index $n$ : investigation under proportional and non-proportional loading conditions

In the above  $l_{en}$  investigation, quadratic defect energy is employed ( $n = 2$ ) with only proportional loading conditions. The obtained results confirm a common belief that  $l_{en}$  only contributes to material hardening (Gurtin et al., 2007). However, it has recently been demonstrated that this belief is not necessarily true for other forms of defect energy (Fleck and Willis, 2015; Wulffinghoff et al., 2015). Using two different defect energy formulations, El-Naaman et al. (2019) have recently conducted an interesting investigation into the interaction between the energetic length scale effects and the form of the defect energy. The obtained results highlight the complex nonlinear hardening effects of  $l_{en}$  in the case of non-quadratic defect energy, resulting in an apparent material strengthening under monotonic loading. However, only proportional loading conditions are used in their investigation. Hereafter, it is proposed to extend this investigation by considering both proportional and non-proportional loading conditions.

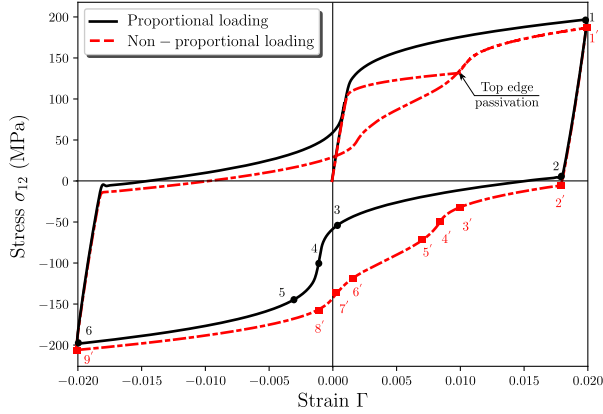
Fig. 3.3 presents the stress-strain curves for different values of  $n < 2$  and  $l_{en}$ , obtained under the proportional and non-proportional loading conditions introduced at the beginning of the section. By analyzing only the loading part of the results,  $l_{en}$  seems to contribute to material strengthening. Strengthening (elastic gap at initial yield) is observed in both the proportional and non-proportional loading cases. The smaller the value of  $n$  (i.e.,  $n$  approaches 1), the larger are the gaps. Under the considered non-proportional loading conditions, the obtained elastic gaps at initial yield are less marked than those obtained under proportional loading conditions. Moreover, at the occurrence of the non-proportional loading source (passivation of the top edge), no further elastic gaps are observed, there is only a short rapid rise in the average stress with a slope much smaller than the elastic slope (Fig. 3.3b). With only the bottom edge passivated from the beginning, lower plastic strain gradients develop within the strip, which explains the smaller elastic gaps at initial yield. After yielding, the plastic strain gradients continue to develop over a large part of the strip and their

existence prior to the top edge passivation prevents the occurrence of further gaps. Considering now the entire loading-unloading results, two striking features can be noticed. The first feature, which is concerned with both the proportional and non-proportional loading cases, is the concave form of the unloading curves. The second feature, which is concerned with only the non-proportional loading case, is the presence of inflection points at the middle of the associated unloading curves. Interestingly, these inflection points seem to occur at approximately the same plastic states at which the top edge was passivated, even though no modification is made to the unloading conditions.

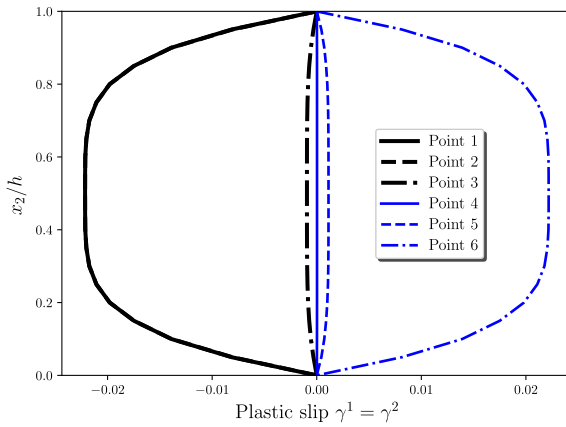
To better understand these features, more complete simulations under proportional and non-proportional loading conditions were performed, using  $n = 1.3$  and  $l_{en} = h$ . In these simulations, after a first (proportional or non-proportional) loading to a macroscopic shear strain  $\Gamma = 0.02$ , a complete loading cycle is applied, such that  $\Gamma$  goes from 0.02 to  $-0.02$  and back to 0.02 (*i.e.*, the simple unloading  $\Gamma = 0.02 \rightarrow 0$  is replaced by a complete cycle  $\Gamma = 0.02 \rightarrow -0.02 \rightarrow 0.02$ ). Fig. 3.4 presents the associated results in terms of stress-strain responses and plastic slip distributions at key stages of the loading cycle. The stress-strain response associated with the proportional case shows that the material only experienced an unusual pure nonlinear kinematic hardening with steep-sloped inflection points (Fig. 3.4a). These inflection points occur at zero plastic slips where the plastic slip gradients vanish (Stage 4 in Fig. 3.4b). They are caused by a rapid increase followed by a rapid decrease in the evolution rate of the higher-order energetic stresses  $\xi_{en}^\alpha$  as the latter approach their singularity at zero plastic slip gradients. The obtained stress-strain response under proportional loading confirms the results of El-Naaman et al. (2019). Further discussion on this response can be found in their paper. For the non-proportional case, more complex stress-strain response is obtained with additional inflection points (Fig. 3.4a). Each of the (steep-sloped) inflection points observed in the proportional case is split into two moderate-sloped ones. As can be noted from Fig. 3.4c, one of these moderate-sloped inflection points takes place at plastic slips in the vicinity of the top edge equivalent to those measured at this edge at its passivation, reflecting a loading history memory-like effect of  $l_{en}$ . This point corresponds to nearly zero plastic slip gradients in the upper half of the studied strip (Stage 4' in Fig. 3.4c). The other moderate-sloped inflection point occurs at zero plastic slips in the vicinity of the bottom edge where nearly zero plastic slip gradients occur in the lower half of the strip (Stage 7' in Fig. 3.4c). With different passivation conditions applied on the top and bottom edges, the plastic slip gradients do not vanish at the same time in the upper and lower strip halves, leading to two distinct and smoother inflection points.

The nonlinear kinematic hardening with inflection points, which is observed under proportional and non-proportional loading conditions, is largely controlled by the defect energy index  $n$  (Fig. 3.3). It becomes less and less marked as  $n$  approaches 2. From  $n = 2$ , this hardening type disappears and is replaced by the classical kinematic hardening with no apparent inflection points (Fig. 3.5). In this case,  $l_{en}$  has no longer any contribution to material strengthening, neither under proportional loading nor under non-proportional loading. For the latter type of loading, the top edge passivation is only marked by a change in the hardening rate to match that corresponding to proportional loading with the top and bottom edges passivated from the beginning. In the range of  $n \geq 2$ ,  $l_{en}$  has only effects on the rate of the classical kinematic hardening, which decrease with increasing  $n$ . A large value of  $n$  can even cancel these effects of  $l_{en}$  (case of  $n = 4$  in Fig. 3.5).

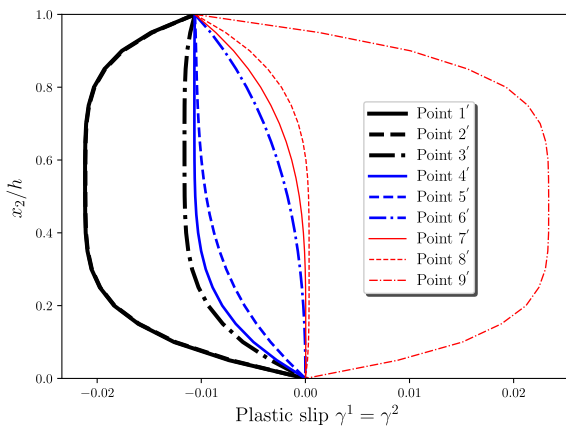
In the framework of SGCP, the unusual nonlinear kinematic hardening, at least that obtained under proportional loading, was first reported by Ohno et al. (2008), using rank-one defect energy. However, the authors did not recognize the physical origin of this phenomenon. Instead, they



(a) Stress-strain curves



(b) Plastic slip distributions at stages 1 to 6 in Fig. 3.4a



(c) Plastic slip distributions at stages 1' to 9' in Fig. 3.4a

**Fig. 3.4.** Stress-strain curves and plastic slip distributions at different loading stages, obtained under first proportional and non-proportional loading to a macroscopic shear strain  $\Gamma = 0.02$  followed by a complete loading cycle  $\Gamma = 0.02 \rightarrow -0.02 \rightarrow 0.02$  ( $n = 1.3$ ,  $l_{en} = h$ ,  $l_{dis} = 0$ ,  $H_\pi = 0$ ).

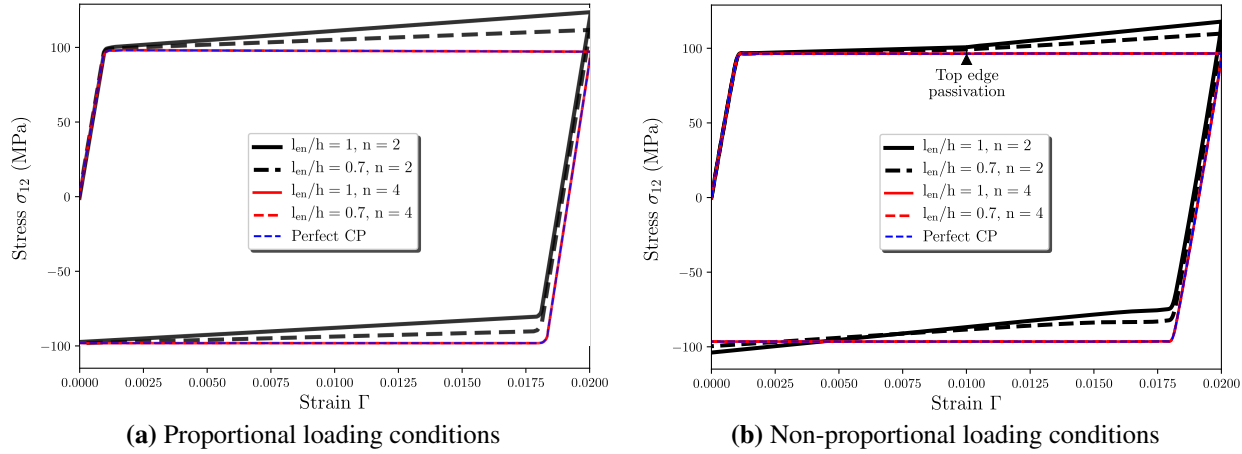


**Fig. 3.5.** Stress-strain responses for different values of the defect energy index  $n$  in the range of  $n \geq 2$  and different values of the energetic length scale  $l_{en}$ , obtained under proportional and non-proportional loading conditions ( $l_{dis} = 0, H_\pi = 0$ ).

further developed their model to replace the rank-one defect energy by a dissipative formulation removing the inflection points. More recently, this phenomenon was also obtained by several authors using other forms of defect energy (Wulffinghoff et al., 2015; El-Naaman et al., 2019). Wulffinghoff et al. (2015) were the first to provide a physical explanation to the phenomenon in the context of SGCP. According to them, it corresponds to the kinematic hardening type III (KIII) of Asaro (1975). This type is associated with a “first in/last out” sequence of dislocation motion and represents the most perfect form of recovery of plastic memory. Although uncommon, experimental evidence of the obtained nonlinear kinematic hardening exists in the literature. Unusual stress-strain hysteresis loops with inflection points have already been observed in some Al-Cu-Mg and Fe-Cr polycrystalline alloys (Stoltz and Pelloux, 1976; Taillard and Pineau, 1982). An illustration of these loops, which is obtained by Taillard and Pineau (1982) in a large-grained Fe-Cu alloy aged at 923 K for 72 h after one loading cycle, is given in Fig. 3.6. TEM observations by Stoltz and Pelloux (1976) and Taillard and Pineau (1982) show that the inflected loops are caused by the piling-up of dislocations at the precipitates and their possible destruction under reverse loading. These experimentally observed mechanisms are analogous to the piling-up and unpiling-up of dislocations at the passivated edges in the present simulations. The use of non-quadratic defect energy with  $n < 2$  seems to provide an accurate continuum description of the piling-up and unpiling-up phenomena. This results in plastic shear strain distributions more in consistency with small scale predictions using dislocation mechanics (e.g., Shu et al., 2001). Fig. 3.7a gives the plastic shear strain profiles along the strip thickness for different values of  $n$ , obtained using proportional loading. Using  $n < 2$ , obvious boundary layers develop in the vicinity of the top and bottom boundaries with nearly uniform plastic shear strain distribution outside these layers, as generally predicted using discrete dislocation mechanics (e.g., Shu et al., 2001). This would constitute another argument in favor of defect energy formulations with order-controlling index  $n < 2$ .

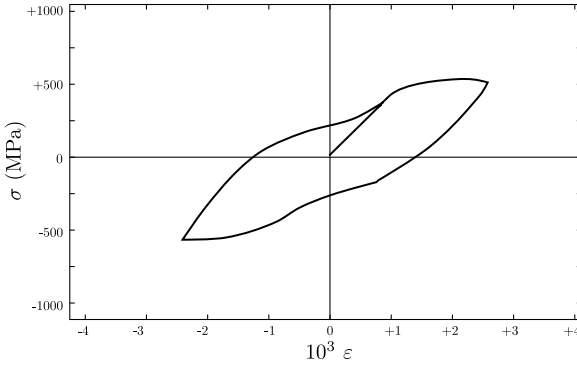


**Fig. 3.6.** Experimental evidence of the nonlinear kinematic hardening after one loading cycle in a large-grained Fe–Cr alloy aged at 923 K for 72 h (Reproduced from Taillard and Pineau (1982)).

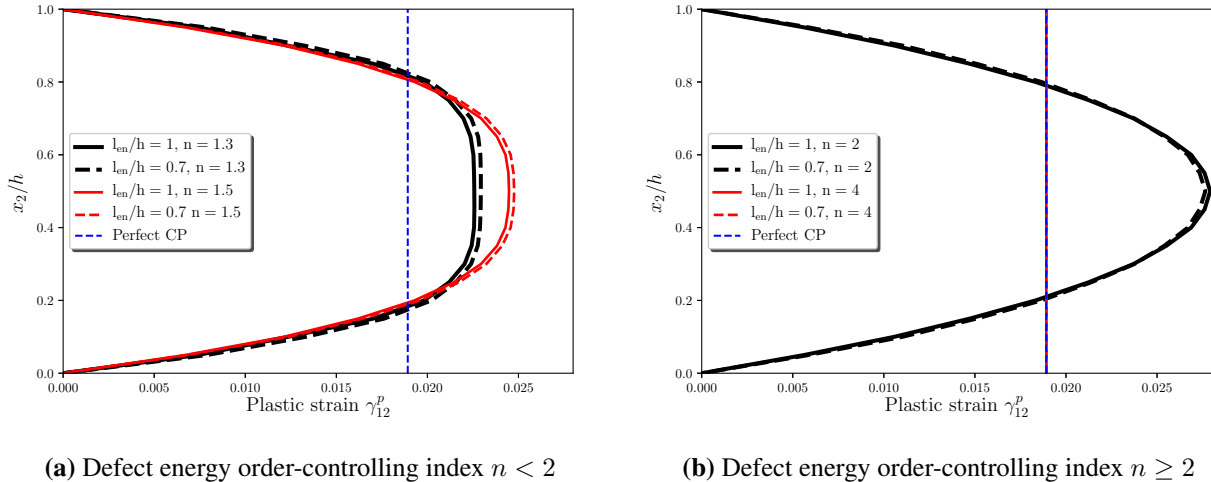


**Fig. 3.7.** Plastic shear strain distributions along  $e_2$  direction for different values of the defect energy order-controlling index  $n$  and different values of the energetic length scale  $l_{en}$ , obtained under proportional loading ( $l_{dis} = 0$ ,  $H_\pi = 0$ ).

### 3.4.2 Influence of higher-order dissipative stress parameters

In this subsection, the main higher-order dissipative stress parameters are investigated in the framework of uncoupled dissipation. For a better analysis of these parameters, the energetic and first-order hardening effects are ignored (*i.e.*,  $l_{en} = 0$  and  $H_\pi = 0$ ).

#### 3.4.2.1 Dissipative length scale $l_{dis}$ : investigation of the uncoupled dissipation assumption

In this investigation, the initial higher-order dissipative slip resistance is set equal to the first-order one ( $S_{\xi 0} = S_{\pi 0}$ ). Moreover, the higher-order hardening effects are first ignored ( $H_\xi = H_\pi = 0$ ). By doing so, the only difference between the present and [Gurtin et al. \(2007\)](#) models lies in the way the effective plastic strain measures are calculated. Comparison between the results of the models in this case makes it possible to underscore the influence of the uncoupled dissipation assumption adopted in this work. Fig. 3.8 gives the comparison results for different values of

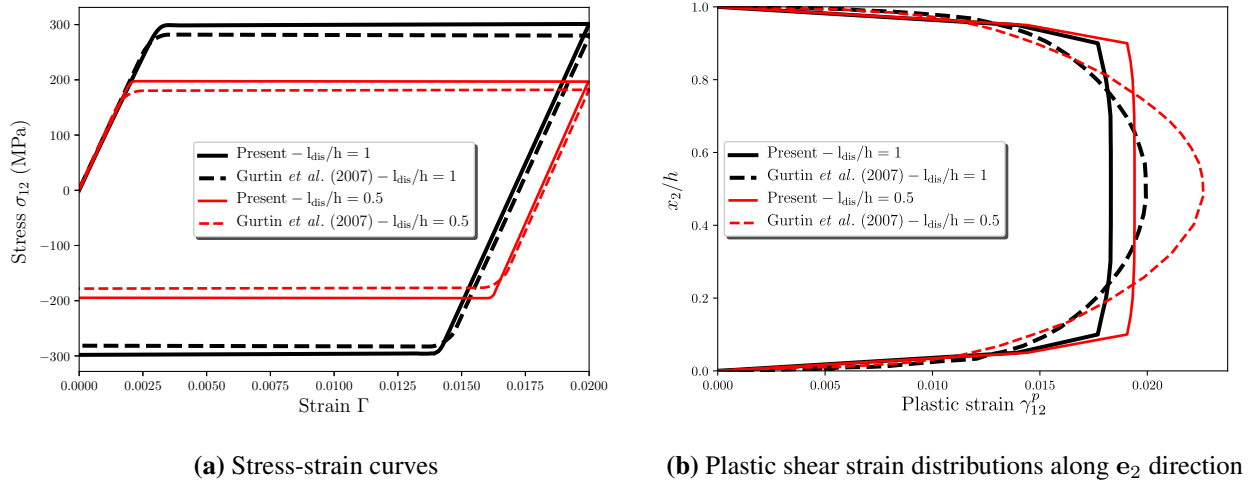


**Fig. 3.8.** Influence of the dissipative length scale  $l_{dis}$  in the absence of higher-order energetic effects under proportional loading conditions: comparison between the present and [Gurtin et al. \(2007\)](#) results ( $l_{en} = 0$ ,  $S_{\xi 0} = 50$  MPa,  $H_\pi = 0$ ,  $H_\xi = 0$ ).

dissipative length scale, obtained under proportional loading. These results are achieved by setting  $S_{\xi 0} = S_{\pi 0} = 50$  MPa, which corresponds to the initial slip resistance used by [Gurtin et al. \(2007\)](#) in their study of  $l_{dis}$ . As can be seen in Fig. 3.8a, in terms of stress-strain response, the results are not particularly sensitive to the use of coupled or uncoupled formulation for the dissipation processes. Both the formulations lead to the same conclusions about the influence of  $l_{dis}$  on the material response. The parameter  $l_{dis}$  influences the yield strength, which increases with increasing  $l_{dis}$ , but not the strain hardening after yielding. A slight overestimation of the yield strength as predicted by the present SGCP model can however be reported. This overestimation is due to the fact that the uncoupled plastic strain measures lead to slightly smaller values, compared to those which can be obtained using coupled ones ([Gurtin et al., 2007](#)). This results in overestimating the higher-order dissipative stresses and then the energetic macroscopic stress  $\sigma$  via the flow rule (3.59).

Although leading to close results in terms of stress-strain curves, the assumption of uncoupled dissipation has a strong influence on the distribution of the plastic shear strain across the thickness. As illustrated in Fig. 3.8b, the plastic shear strain profiles obtained in this work are quite different from those obtained by [Gurtin et al. \(2007\)](#) using coupled dissipation. The latter profiles have always smooth parabolic forms with more or less sharp gradients in the vicinity of the top and bottom boundaries. With the hypothesis of uncoupled dissipation, more clearly distinguishable boundary layers develop in the vicinity of the top and bottom boundaries; beyond these layers, the plastic shear strain becomes near-uniform with a plateau-shaped distribution (Fig. 3.8b). With no higher-order hardening ( $H_\xi = 0$ ), these layers present a very small thickness, which is in very good agreement with the results of [Gurtin et al. \(2007\)](#). The thickness of such layers can, however, be controlled by the higher-order hardening modulus  $H_\xi$ . Fig. 3.9 compares the stress-strain results and the associated plastic shear strain profiles with and without higher-order hardening ( $H_\xi = 0, 100, 200$  MPa), obtained using proportional loading. The thickness of the obtained boundary layers depends on  $H_\xi$ . The larger this parameter, the thicker are the boundary layers (Fig. 3.9b).

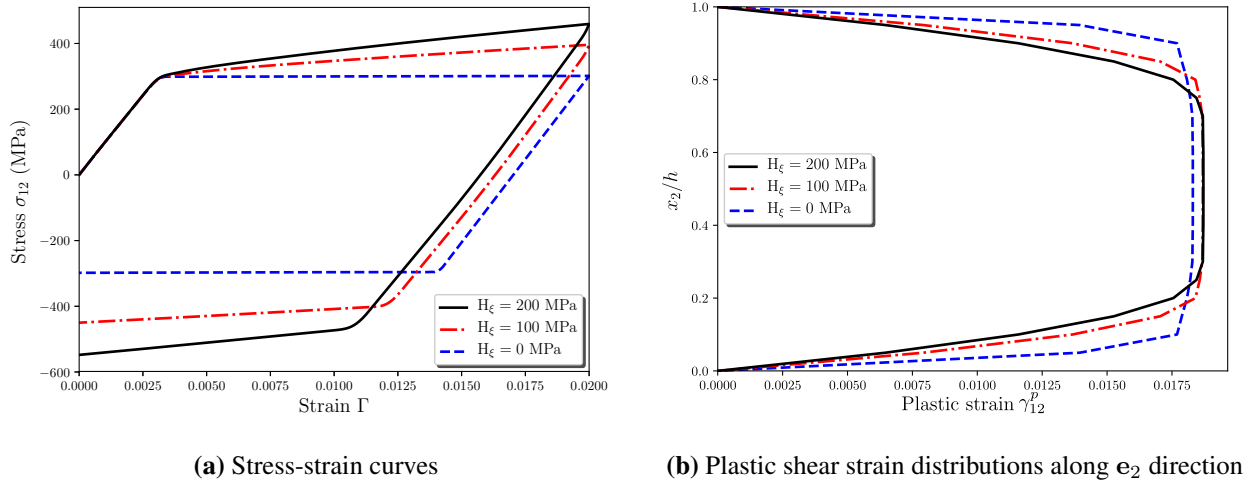


**Fig. 3.9.** Influence of the higher-order hardening modulus  $H_\xi$  in the absence of higher-order energetic effects ( $l_{en} = 0$ ,  $l_{dis} = h$ ,  $S_{\xi 0} = 50$  MPa,  $H_\pi = 0$ ).

Such a parameter generates isotropic hardening effects of more or less standard type (Fig. 3.9a).

The plastic shear strain distributions obtained in this work using uncoupled dissipation seem to be more in consistency with small scale numerical predictions (e.g., Bittencourt et al., 2003; Shu et al., 2001). Fig. 3.10 compares the plastic shear strain profiles predicted by the present model with those predicted by Shu et al. (2001) using discrete dislocation plasticity, for different values of applied shear strain  $\Gamma$  under proportional conditions. The material parameters used to obtain the present profiles are determined by identification procedure considering only dissipative stresses:  $l_{en} = 0$ ,  $S_{\pi 0} = 15$  MPa,  $H_\pi = 0$ ,  $l_{dis} = 0.3 h$ ,  $S_{\xi 0} = 3$  MPa, and  $H_\xi = 200$  MPa. The obtained results are in good agreement with the results of Shu et al. (2001). The small differences between the results in the boundary layers at large applied shear strains  $\Gamma$  are due to the asymmetry of the discrete dislocation profiles, which is caused by the fluctuations in the plastic strains.

### 3.4.2.2 Initial higher-order dissipative slip resistance $S_{\xi 0}$ : towards a more flexible control of elastic gaps

In the above  $l_{dis}$  study, the initial higher-order dissipative slip resistance is fixed at  $S_{\xi 0} = S_{\pi 0} = 50$  MPa and only proportional loading is applied. The obtained results highlight the contribution of  $l_{dis}$  to material strengthening which increases with increasing  $l_{dis}$  (Fig. 3.8a), as noted in the literature using coupled dissipation. Further investigation into  $l_{dis}$  effects under varying  $S_{\xi 0}$  is given hereafter, using proportional and non-proportional loading conditions.

Starting with the proportional loading conditions, Fig. 3.11a displays the associated stress-strain results for different values of  $S_{\xi 0}$ , with  $l_{dis} = h$  and  $H_\xi = 100$  MPa. At fixed  $l_{dis}$ , elastic gaps at initial yield are largely controlled by  $S_{\xi 0}$ . The smaller this parameter, the smaller are the gaps, which can also be removed by setting  $S_{\xi 0} = 0$  (in practice, a small value must be used instead of 0 to avoid excessively small time steps for convergence). Using  $S_{\xi 0} = 0.01$  MPa, no apparent elastic gaps are obtained at initial yield. This is in accordance with the outcomes of Fleck et al. (2015) and can be explained by zero (nearly zero) higher-order dissipative stresses  $\xi_{dis}^\alpha$  at the onset

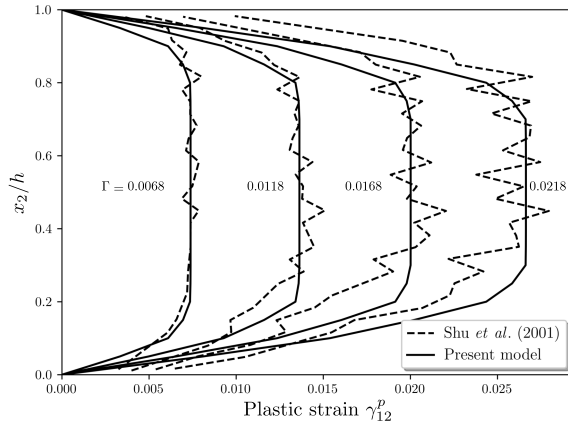


**Fig. 3.10.** Comparison between the plastic shear strain profiles obtained using the present model and those obtained by Shu et al. (2001) using discrete dislocation plasticity at different values of applied shear strain  $\Gamma$  under proportional loading conditions ( $l_{en} = 0$ ,  $l_{dis} = 0.3 h$ ,  $S_{\pi 0} = 15$  MPa,  $S_{\xi 0} = 3$  MPa,  $H_\pi = 0$ ,  $H_\xi = 200$  MPa).

of yield. It is worth recalling that, with the assumption of uncoupled dissipation, the higher-order dissipative stresses  $\xi_{dis}^\alpha$  depend only on plastic slip gradients and their rates, and then they continue to be zero after any uniform plastic straining. Therefore, the proposed model allows for avoiding elastic gaps not only at initial yield but also after any uniform plastic straining.

Concerning the non-proportional loading conditions, Fig. 3.11b presents the corresponding results obtained using different values of  $S_{\xi 0}$ , with  $l_{dis} = h$  and  $H_\xi = 100$  MPa. This figure shows that, unlike  $l_{en}$ , the dissipative length scale  $l_{dis}$  can lead to elastic gaps not only at initial yield but also at the passivation of the top edge. For nonzero  $S_{\xi 0}$ , the gaps observed at initial yield under proportional loading conditions, with both edges passivated from the beginning, are divided into two parts. One part occurs at initial yield, where only the bottom edge is passivated; and the other part occurs at the passivation of the top edge. For zero (nearly zero)  $S_{\xi 0}$ , no apparent elastic gaps are observed, neither at initial yield nor at the occurrence of the non-proportional loading source. If the absence of elastic gaps at initial yield can be explained in the same way as beforehand, their absence at the passivation of the top edge is more difficult to explain. Indeed, under the considered non-proportional loading conditions, nonuniform plastic strains develop within the studied strip before passivation of the top edge, making the current higher-order slip resistances  $S_\xi^\alpha$  (and then  $\xi_{dis}^\alpha$ ) under evolution within the studied strip. To better explain the absence of elastic gaps in this case, the rate-sensitivity terms, which are only used for regularization, will be ignored hereafter. In the rate-independent limit, avoidance of elastic gaps at the occurrence of a non-proportional loading source translates the existence of nonzero plastic slip rates  $\dot{\gamma}^\alpha$  that satisfy the microscopic balance equations (first line of system (3.20)). Assuming, for simplicity, that the boundary conditions are such that either  $\dot{\gamma}^\alpha = 0$  or  $\chi^\alpha = 0$  on the boundary, in the absence of higher-order energetic stresses, these equations can be written, in weak form, as:

$$G_\gamma = \sum_{\alpha=1}^q \int_V [(|\tau^\alpha| - S_\pi^\alpha) \dot{e}_\pi^\alpha - S_\xi^\alpha \dot{e}_\xi^\alpha] dv = 0 \quad (3.82)$$

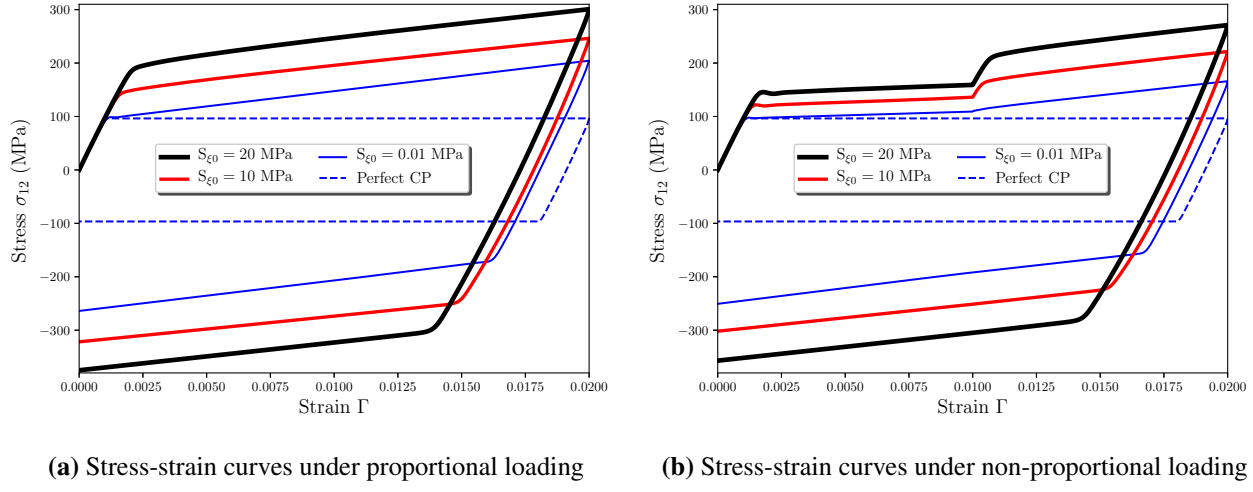
For this expression to have nonzero  $\dot{\gamma}^\alpha$  solutions at the occurrence of a non-proportional loading

source, the latter must not significantly alter the ratio between  $\dot{e}_\pi^\alpha$  and  $\dot{e}_\xi^\alpha$  in the regions where the higher-order dissipative stresses  $\xi_{dis}^\alpha$  are activated ( $S_\xi^\alpha \neq 0$ ). Otherwise, the plastic flow is interrupted until the resolved shear stresses  $\tau^\alpha$  (evolving elastically) reach sufficient values to offset the disproportionate variations between terms of (3.82). By passivating only the bottom edge, plastic strain gradients develop only within the lower half of the studied strip (the plastic slip profiles are similar to those obtained at stage 4' in Fig. 3.4c). Using  $S_{\xi 0} = 0$ , after yielding, the stresses  $\xi_{dis}^\alpha$  are continuously activated (from 0) in this part of the strip and remain inactive otherwise. The occurrence of the top edge passivation modifies the plastic slip distributions only within the upper half of the studied strip, where the stresses  $\xi_{dis}^\alpha$  are not yet activated. This explains the absence of elastic gaps at the passivation of this edge.

By assuming uncoupled dissipation with  $S_{\xi 0} = 0$ , two important mechanisms generating or amplifying elastic gaps in conventional Gurtin-type models have been disabled. The first mechanism is due to the nonzero higher-order dissipative stresses  $\xi_{dis}^\alpha$  at their activation, and the second mechanism is due to the possible evolution of the current higher-order slip resistances  $S_\xi^\alpha$  under uniform plastic straining. Disabling these mechanisms, the proposed model has allowed elastic gaps to be removed under the considered non-proportional loading conditions. However, this model is not completely gap-free in the sense that it cannot avoid gaps for any non-proportional loading conditions. Indeed, application of a loading source generating large variation in the plastic slip gradients within regions with activated higher-order dissipative stresses  $\xi_{dis}^\alpha$  can lead to elastic gaps. This would be the case if the studied strip is submitted to pure bending into the plastic range with microfree conditions followed by both edges passivation and continued bending (Fig. 3.12). In this case, the model can remove gaps only at initial yield. At the occurrence of the edges passivation,  $S_{\xi 0}$  has only influence on the amplitude of the generated gaps but does not remove them. To the authors' knowledge, to date, there is no gap-free model including thermodynamically-consistent higher-order dissipative stresses in the literature, except for the very recent model of [Panteghini et al. \(2019\)](#) in which dissipation is implicitly embedded within the definition of the defect energy. It should be noted that the attitude taken here is rather agnostic on the occurrence of elastic gaps in reality. Some authors link these gaps to the size-dependence capabilities of gradient-based theories, whereas others see no physical reasons for their occurrence within a single crystal. Keeping with the latter opinion, [Wulffinghoff and Böhlke \(2013\)](#) have proposed a SGCP approach with no elastic gaps (in effect, the involved higher-order stresses are assumed to be fully energetic and to stem from quadratic defect energy) for polycrystalline solids, in which the size-dependence effects are embedded within a grain boundary constitutive model. In the absence of experimental data for ruling on the existence of elastic gaps in reality, development of a model allowing for a more flexible control of these gaps, while explicitly including higher-order dissipative processes, would be very worthwhile.

### 3.4.3 Interactions between microscopic stresses: recommendations for material parameters identification

Interaction between the different stresses involved in the SGCP model, including both first- and higher-order microscopic stresses, is presented in Fig. 3.13. Although only proportional loading conditions are applied for this figure, the following discussion is also valid for non-proportional loading conditions. At small scales, the global response of the considered material is (not surprisingly) more sensitive to the higher-order energetic and dissipative stresses. The energetic ones have



(a) Stress-strain curves under proportional loading

(b) Stress-strain curves under non-proportional loading

**Fig. 3.11.** Influence of the initial higher-order dissipative slip resistance  $S_{\xi_0}$  on the elastic gap under proportional and non-proportional loading conditions ( $l_{en} = 0$ ,  $l_{dis} = h$ ,  $H_\pi = 0$ ,  $H_\xi = 100$  MPa).

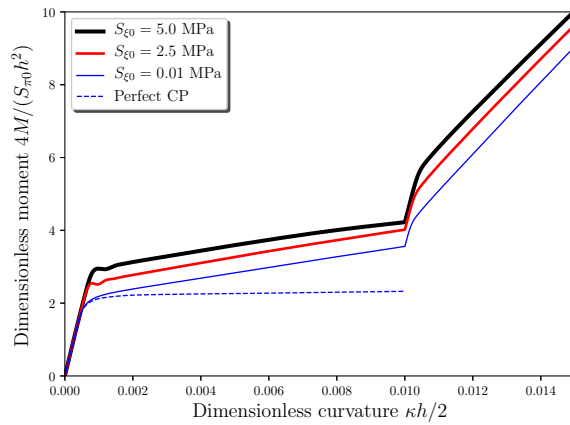


**Fig. 3.12.** Influence of the initial higher-order slip resistance  $S_{\xi_0}$  on the moment-curvature response of the considered strip under pure bending with microfree conditions followed by top and bottom edges passivation and continued bending ( $l_{en} = 0$ ,  $l_{dis} = h$ ,  $H_\pi = 0$ ,  $H_\xi = 100$  MPa)

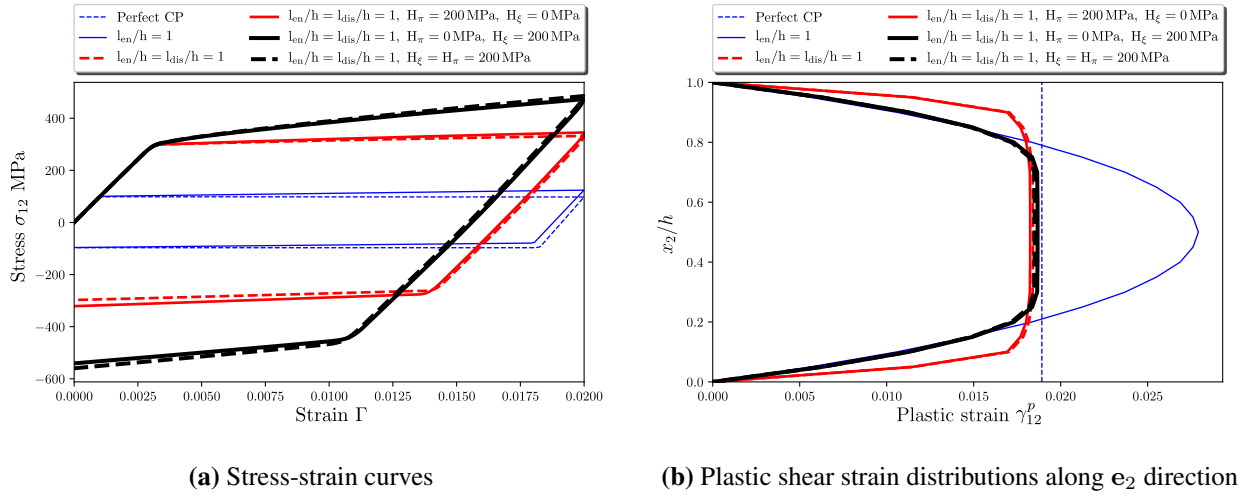


**Fig. 3.13.** Interaction between the different stresses involved in the proposed SGCP model under proportional loading ( $n = 2, S_{\xi_0} = 50 \text{ MPa}$ ).

mainly kinematic hardening effects, whereas the dissipative counterparts have isotropic hardening effects. The first-order dissipative stresses can also lead to isotropic hardening effects. However, compared to those generated by the higher-order ones, these effects have only small impact on the global material response. Using these observations, recommendations to identify the major model parameters for a real material are given hereafter. It is noteworthy, however, that, with the current understanding of dislocation physics, it is still early to confirm which small scale mechanisms must be considered in this model to correctly reproduce the small scale behavior of real materials. The great flexibility offered by the proposed model, thanks to the assumption of uncoupled dissipation, in controlling a wide selection of these mechanisms makes the task of switching between them relatively easy.

Using the dissipation uncoupling assumption, the constitutive equations of the first-order dissipative stresses correspond exactly to those classically used to describe the evolution of the resolved shear stresses in the context of conventional crystal plasticity. It is then suggested to separately identify the parameters of these equations in such a way as to reproduce the behavior of the considered material in the absence of size effects. This allows for application of the model on large specimens in which size effects are negligible. To this end, experimental results obtained using relatively large samples with sufficient number of grains must be used for the identification of these parameters. Note that such parameters can also be found in literature for several common materials. To model size effects at small scales, the higher-order constitutive parameters must then be included and identified. Preliminary experimental tests under cyclic loading would be necessary to determine which higher-order parameters are required. If only kinematic hardening is obtained, parameters associated with higher-order dissipative stresses can be neglected ( $l_{dis} = 0$ ). On the contrary, if mainly isotropic hardening is found, parameters associated with higher-order energetic stresses may be ignored ( $l_{en} = 0$ ). If combined hardening is obtained, all higher-order parameters need to be taken into consideration. The retained parameters can finally be identified based on further experimental tests implying small specimens with different grain sizes to find out about the elastic gaps. In the case of higher-order energetic stresses, these gaps can be controlled by  $n < 2$ .

and  $l_{en}$ . Although not treated in this work, the higher-order energetic slip resistance  $X_0$  can also influence such gaps in the range of  $n < 2$ . According to expressions of higher-order energetic stresses, this parameter behaves as  $l_{en}^n$  and may be used to control the range in which  $l_{en}$  contributes to material hardening and/or strengthening. In the case of higher-order dissipative stresses, the elastic gaps can be controlled by  $S_{\xi 0}$  and  $l_{dis}$ . Depending on the number of retained constitutive parameters to be identified, robust identification algorithms can be applied to simplify this task ([Chtourou et al., 2017](#)). However, it should be noted that these algorithms are generally based on mathematical optimization and do not necessarily lead to a unique set of optimized parameters.

### 3.5 Conclusion

A flexible Gurtin-type strain gradient crystal plasticity (SGCP) model was developed in small deformation, based on non-quadratic defect energy and uncoupled dissipation assumption. Both energetic (recoverable) and dissipative (unrecoverable) microscopic stresses are considered in this model. To evaluate the proposed SGCP model and to investigate the influence of its major constitutive parameters, a simplified two-dimensional (2D) version of this model was derived and implemented within the commercial finite element package Abaqus/Standard, using a User-EElement (UEL) subroutine. This version was then applied to simulate the classical 2D simple shear problem of a constrained crystalline strip submitted to proportional and non-proportional loading conditions. Major simulation results and conclusions are recalled hereafter.

Starting with the energetic length scale effects, it was found that these effects depend on the value of the order-controlling index  $n$ . Two cases can be distinguished:  $n < 2$  and  $n \geq 2$ . In the range of  $n < 2$ , the energetic length scale  $l_{en}$  leads to unusual nonlinear kinematic hardening, resulting in an apparent increase of the yield strength (strengthening) under monotonic loading. This is in accordance with results from the literature (e.g., [Fleck and Willis, 2015](#); [Wulffinghoff et al., 2015](#); [El-Naaman et al., 2019](#)). Under non-proportional loading conditions, more complex kinematic hardening with additional inflection points is obtained. Interestingly, these additional points take place at approximately the same plastic state at which the non-proportional loading source occurred, revealing new loading history memory-like effects of  $l_{en}$ . The unusual nonlinear kinematic hardening with inflection points, at least that obtained under proportional loading conditions, complies with the kinematic hardening type III (KIII) of [Asaro \(1975\)](#). It corresponds to a “first in/last out” sequence of dislocation motion and represents the most perfect form of recovery of plastic memory. Although uncommon, this phenomenon has already been observed experimentally in some polycrystalline materials, such as Fe-Cr alloys ([Taillard and Pineau, 1982](#)). For  $n < 2$ , KIII type hardening is the only active hardening mechanism, allowing for accurate continuum description of the piling-up and unpiling-up phenomena. Increasing  $n$  (i.e.,  $n$  approaching 2), this hardening type becomes less and less marked and vanishes at  $n = 2$  to be replaced by the classical kinematic hardening (KI type hardening, in the terminology of [Asaro \(1975\)](#)). From  $n = 2$ , regardless of loading type,  $l_{en}$  has only influence on the rate of hardening after yielding but not on the material strengthening, as widely recognized in the literature.

Concerning dissipation aspects, in terms of stress-strain response, the assumption of uncoupled dissipation has no significant impact. It leads to a slight overestimation of the yield strength, compared to the results of [Gurtin et al. \(2007\)](#), which are obtained using coupled dissipation. This overestimation is due to the fact that the uncoupled plastic strain measures used in the present model

predict slightly smaller values, compared to those which can be obtained using coupled measures ([Gurtin et al., 2007](#)). This results in overestimating the dissipative microscopic stresses and then the energetic macroscopic stress  $\sigma$  via the flow rule (3.59). However, in terms of plastic shear strain distributions across the thickness of the studied strip, quite different results were obtained depending on whether coupled or uncoupled dissipation is adopted. Using the assumption of uncoupled dissipation, obvious boundary layers develop in the vicinity of the top and bottom edges of the studied strip. Beyond these layers, the plastic shear strain becomes near-uniform with a plateau-shaped distribution. On the contrary, using coupled dissipation, the plastic shear strain distributions obtained by [Gurtin et al. \(2007\)](#) have always near-quadratic forms, even outside the boundary layers. The distributions of plastic shear strain obtained in this work, with obvious boundary layers and a plateau outside the layers, seem to be more in accordance with those produced by discrete dislocation simulations in the work of [Shu et al. \(2001\)](#) and [Bittencourt et al. \(2003\)](#). Accurately capturing boundary layer effects is essential since they represent important nonlocal (size) effects that emerge at small scales. The thickness of these layers can easily be controlled by the higher-order hardening modulus  $H_\xi$ . Another advantage of using uncoupled dissipation is the flexible control of some important dissipative effects, such as elastic gaps which can easily be controlled by varying the initial higher-order slip resistance  $S_{\xi 0}$ . By canceling the latter parameter, a variant of the proposed model allowing for removing such gaps under certain circumstances, *e.g.* at initial yield or, in a general manner, when a non-proportional loading source does not significantly variate the plastic slip gradients within regions in which the higher-order dissipative stresses are activated, can be obtained.

Although it is still early to confirm which small scale mechanisms must be considered to correctly reproduce the small scale behavior of real materials, the proposed model, with its energetic and dissipative parts, offers a great flexibility in monitoring major of these mechanisms. This makes the task of switching between them relatively easy. The next chapter deals with the extension of this model to finite deformation. This will allow for studying size effects on large strain phenomena, particularly localization in crystalline structures.



# **Chapter 4**

## **Finite deformation extension of the flexible Gurtin-type strain gradient crystal plasticity model**

### **Abstract**

This chapter aims at extending the flexible small deformation Gurtin-type strain gradient crystal plasticity model to finite deformation using Lagrangian description. As in [Gurtin \(2002\)](#), this model is derived based on finite deformation kinematics assuming multiplicative decomposition of the deformation gradient. A simplified two-dimensional (2D) version of this model will be implemented and validated by comparison with small deformation results obtained in the previous chapter and with some finite deformation results available in the literature.

## 4.1 Introduction

The development of the small deformation SGCP model in the previous chapter allows for capturing size effects within crystalline structures in the absence of large deformation mechanisms. However, several complex small scale problems require the latter mechanisms to be correctly considered for a better prediction of size effects. Among them, localization problems within miniaturized components can particularly be cited. Indeed, localization phenomena must correctly be considered to characterize the formability of micro-scaled products and to optimize the micro-forming processes used to obtain them.

To allow for applying of the proposed Gurtin-type model to problems involving large strain effects, it will be extended in this chapter to finite deformation framework following the procedure detailed in [Gurtin \(2002\)](#). The model extension is formulated using Lagrangian description and is based on multiplicative decomposition of the deformation gradient. Using this description, the small deformation constitutive laws presented in the previous chapter will be rewritten in the Lagrangian configuration considering large deformation mechanisms. A two-dimensional (2D) version of the extended model will be implemented in the commercial finite element software Abaqus/Standard. To validate the model implementation, it will be applied to simulate a simple shear problem of a constrained layer under plane strain conditions. The obtained results will be compared with small deformation results obtained in the previous chapter and with others available in the literature for specific constitutive choices.

Following this introduction, the chapter is organized as follows. Section 4.2 details the theoretical formulation of the proposed finite deformation SGCP model, which is derived following the procedure of [Gurtin \(2002\)](#). Section 4.3 discusses the implementation of a two-dimensional (2D) version of this model. Section 4.4 is devoted to the validation of the model implementation. Section 4.5 provides some concluding remarks.

## 4.2 Finite deformation SGCP model

In this section, the small deformation SGCP model proposed in chapter 3, based on generalized defect energy and uncoupled dissipation, is extended to finite deformation framework. Following [Gurtin \(2002\)](#), the finite deformation model is formulated with respect to the reference configuration to simplify its numerical implementation.

### 4.2.1 Kinematics and single crystal hypothesis

Following [Gurtin \(2002\)](#), the finite deformation elastic-plastic kinematics is described by multiplicative (Kröner-Lee) decomposition of the deformation gradient  $\mathbf{F}$  ([Kröner, 1959](#); [Lee, 1964](#)) as illustrated by Fig. 4.1:

$$\mathbf{F} = \mathbf{F}^e \mathbf{F}^p \quad (4.1)$$

where  $\mathbf{F}^e$  represents the elastic distortion including stretch and rotation of the lattice and  $\mathbf{F}^p$  represents the plastic distortion due to plastic deformation caused by the flow of defects. The plastic incompressibility is also assumed with  $\det(\mathbf{F}^p) = 1$ . Considering (4.1), the velocity gradient tensor

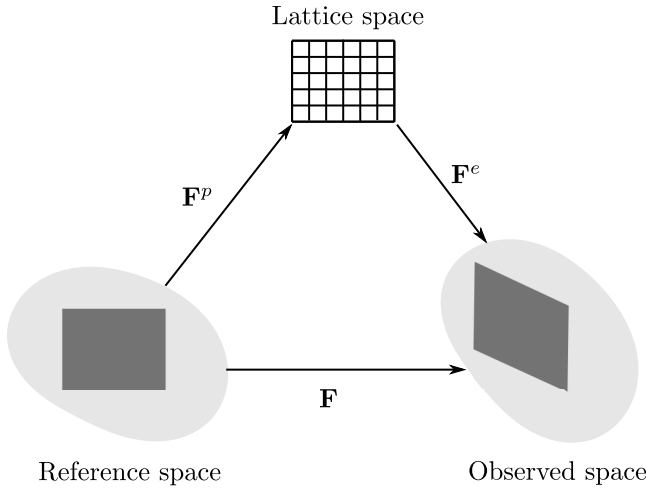


**Fig. 4.1.** Illustration of multiplicative decomposition of deformation gradient: Kröner-Lee decomposition (Kröner, 1959; Lee, 1964).

can be written:

$$\mathbf{L} = \dot{\mathbf{F}}\mathbf{F}^{-1} = \mathbf{L}^e + \mathbf{F}^e\mathbf{L}^p\mathbf{F}^{e-1} \quad (4.2)$$

with the elastic and plastic distortion rate tensors  $\mathbf{L}^e$  and  $\mathbf{L}^p$  defined by:

$$\mathbf{L}^e = \dot{\mathbf{F}}^e\mathbf{F}^{-e} \quad \text{and} \quad \mathbf{L}^p = \dot{\mathbf{F}}^p\mathbf{F}^{p-1} \quad (4.3)$$

The single crystal hypothesis requires  $\mathbf{L}^p$  to be governed by slip rates on the individual slip systems. Two view points can be found in the literature to define these systems in large deformation crystalline framework. Some authors introduce these systems in the reference configuration, meaning that the undistorted lattice resides in this configuration (*i.e.*, lattice is considered as material) (Lubarda, 2007; Ling, 2018; Marano et al., 2019; Peng et al., 2019). In this case, isoclinic mapping from reference to lattice space, *i.e.*, with no lattice rotation, is required. Indeed, from a physical point of view, a flow of dislocations involves a flow of material relative to the undistorted lattice. However, according to Gurtin et al. (2010), the introduction of slip systems in the reference configuration would be a misconception. Pursuant to their reasoning (Gurtin et al., 2010; Gurtin and Reddy, 2016), lattice vectors cannot be material and must be introduced in the lattice (intermediate) space (Fig. 4.1). As our work is based on those of Gurtin and co-workers, the last point of view is adopted in the following. This point of view seems to be confirmed by experimental observations (Kazantseva et al., 2015).

As in Gurtin (2008a), the slip systems are defined in the intermediate space, in which slip and slip plane normal directions associated with a slip system  $\alpha$ , denoted respectively by  $\mathbf{s}^\alpha$  and  $\mathbf{m}^\alpha$ , are constant lattice vectors:

$$\mathbf{s}^\alpha \cdot \mathbf{m}^\alpha = 0 \quad \text{and} \quad |\mathbf{s}^\alpha| = |\mathbf{m}^\alpha| = 1 \quad (4.4)$$

These vectors as well as the glide direction vector ( $\mathbf{l}^\alpha = \mathbf{m}^\alpha \wedge \mathbf{s}^\alpha$ ) are expressed in the reference configuration as (Gurtin, 2006):

$$\mathbf{s}_r^\alpha = \mathbf{F}^{p-1}\mathbf{s}^\alpha, \quad \mathbf{m}_r^\alpha = \mathbf{F}^{pT}\mathbf{m}^\alpha, \quad \mathbf{l}_r^\alpha = \mathbf{F}^{p-1}\mathbf{l}^\alpha \quad (4.5)$$

Using single crystal hypothesis, the plastic distortion rate tensor  $\mathbf{L}^p$  can be written within the intermediate space as:

$$\mathbf{L}^p = \sum_{\alpha=1}^q \dot{\gamma}^\alpha \mathbb{S}^\alpha \quad (4.6)$$

where  $\mathbb{S}^\alpha = \mathbf{s}^\alpha \otimes \mathbf{m}^\alpha$  denotes the Schmid tensor associated with the slip system  $\alpha$ ,  $\dot{\gamma}^\alpha$  represents the plastic slip rate on this system, and  $q$  is the number of slip systems. For the sake of consistency with the small deformation SGCP model presented in chapter 3, the same symbol ( $\dot{\gamma}^\alpha$ ) is used to designate plastic slip rate on slip system  $\alpha$ . However, within finite deformation framework,  $\dot{\gamma}^\alpha$  cannot be interpreted as material time derivative of a physically-meaningful field variable  $\gamma^\alpha$ . Indeed, slips (as fields on individual slip systems) are not in general well-defined quantities from a physical point of view (Gurtin, 2008a).

## 4.2.2 Principle of virtual power and governing equations

Considering the generalized power density of internal forces (Forest and Aifantis, 2010; Forest, 2011), the internal and external virtual power expenditures within an arbitrary subregion  $V_0$  of boundary  $S_0$  in the reference configuration can be expressed as (neglecting body forces):

$$\mathcal{P}_{int} = \int_{V_0} \mathbf{P} : \dot{\mathbf{F}} dv_0 + \sum_{\alpha=1}^q \int_{V_0} \kappa^\alpha \dot{\gamma}^\alpha dv_0 + \sum_{\alpha=1}^q \int_{V_0} \boldsymbol{\xi}^\alpha \cdot \mathbf{grad}_X(\dot{\gamma}^\alpha) dv_0 \quad (4.7)$$

$$\mathcal{P}_{ext} = \int_{S_0} \mathbf{t} \cdot \dot{\mathbf{u}} ds_0 + \sum_{\alpha=1}^q \int_{S_0} \chi^\alpha \dot{\gamma}^\alpha ds_0 \quad (4.8)$$

where  $\mathbf{P} = J\boldsymbol{\sigma}\mathbf{F}^{T-1}$  is the first Piola-Kirchhoff stress tensor (power-conjugate to  $\dot{\mathbf{F}}$ ),  $J = \det(\mathbf{F})$  is the volumetric Jacobian,  $\boldsymbol{\sigma}$  is the Cauchy stress tensor,  $\kappa^\alpha$  is a scalar microscopic stress (power-conjugate to  $\dot{\gamma}^\alpha$ ),  $\boldsymbol{\xi}^\alpha$  is a vector microscopic stress (power-conjugate to  $\mathbf{grad}_X(\dot{\gamma}^\alpha)$ ),  $\mathbf{t}$  is a macroscopic surface traction,  $\chi^\alpha$  is a microscopic surface traction, and  $\mathbf{grad}_X(\bullet)$  is the Lagrangian gradient operator (*i.e.*, w.r.t. the Lagrangian coordinates). This operator can be related to the lattice gradient operator  $\mathbf{grad}_\#(\bullet)$  and the Eulerian gradient operator  $\mathbf{grad}_x(\bullet)$  by:

$$\mathbf{grad}_\#(\bullet) = \mathbf{grad}_X(\bullet) \cdot \mathbf{F}^{p-1} = \mathbf{grad}_x(\bullet) \cdot \mathbf{F}^e \quad (4.9)$$

Introducing the first and second Piola elastic stress tensors, which are respectively defined by:

$$\mathbf{P}^e = J\boldsymbol{\sigma}\mathbf{F}^{eT-1} \quad \text{and} \quad \mathbf{S}^e = J\mathbf{F}^{e-1} \cdot \boldsymbol{\sigma} \cdot \mathbf{F}^{eT-1} \quad (4.10)$$

and defining the resolved shear (Schmid) stress  $\tau^\alpha$  as:

$$\tau^\alpha = \mathbf{C}^e \mathbf{S}^e : \mathbb{S}^\alpha$$

where  $\mathbf{C}^e = \mathbf{F}^{eT} \mathbf{F}^e$  is the right Cauchy-Green elastic deformation tensor, the term  $\mathbf{P} : \dot{\mathbf{F}}$  in the expression of  $\mathcal{P}_{int}$  (4.7) can be rewritten as:

$$\mathbf{P} : \dot{\mathbf{F}} = \mathbf{P}^e : \dot{\mathbf{F}}^e + \sum_{\alpha=1}^q \tau^\alpha \dot{\gamma}^\alpha \quad (4.11)$$

This leads to:

$$\mathcal{P}_{int} = \int_{V_0} \mathbf{P}^e : \dot{\mathbf{F}}^e dv_0 + \sum_{\alpha=1}^q \int_{V_0} [\pi^\alpha \dot{\gamma}^\alpha + \boldsymbol{\xi}^\alpha \cdot \mathbf{grad}_X(\dot{\gamma}^\alpha)] dv_0$$

with the scalar microscopic stress  $\pi^\alpha = \kappa^\alpha + \tau^\alpha$ . Application of the generalized principle of virtual power (Forest, 2009) results in the following macroscopic and microscopic balance equations and boundary conditions:

$$\begin{aligned} \mathbf{div}_X(\mathbf{P}) &= \mathbf{0} && \text{in } V_0 \\ \mathbf{P} \cdot \mathbf{n}_0 &= \mathbf{t} && \text{on } S_0 \end{aligned} \quad (4.12)$$

$$\begin{aligned} \mathbf{div}_X(\boldsymbol{\xi}^\alpha) + \tau^\alpha - \pi^\alpha &= 0 && \text{in } V_0 \\ \boldsymbol{\xi}^\alpha \cdot \mathbf{n}_0 &= \chi^\alpha && \text{on } S_0 \end{aligned} \quad (4.13)$$

with  $\mathbf{n}_0$  the outward unit normal to  $S_0$  and  $\mathbf{div}_X(\bullet)$  the Lagrangian divergence operator.

### 4.2.3 Free energy imbalance

The free energy imbalance (second thermodynamic law) requires that the temporal increase of free energy in an arbitrary subregion  $V_0$  be less than or equal to the external power expended on  $V_0$ . Mathematically, this can be formulated as:

$$\int_{V_0} \dot{\Psi} dv_0 - \int_{V_0} \left\{ \mathbf{P}^e : \dot{\mathbf{F}}^e + \sum_{\alpha=1}^q (\pi^\alpha \dot{\gamma}^\alpha + \boldsymbol{\xi}^\alpha \cdot \mathbf{grad}_X(\dot{\gamma}^\alpha)) \right\} dv_0 \leq 0 \quad (4.14)$$

where  $\Psi$  denotes the free energy per unit volume measured in the reference configuration. Defining the elastic Green-Lagrange strain tensor  $\mathbf{E}^e$  as:

$$\mathbf{E}^e = \frac{1}{2} (\mathbf{C}^e - \mathbf{I}) \quad (4.15)$$

it can easily be shown that  $\mathbf{P}^e : \dot{\mathbf{F}}^e = \mathbf{S}^e : \dot{\mathbf{E}}^e$ . Since  $V_0$  is arbitrary, the local free energy imbalance can be obtained:

$$\dot{\Psi} - \mathbf{S}^e : \dot{\mathbf{E}}^e - \sum_{\alpha=1}^q (\pi^\alpha \dot{\gamma}^\alpha + \boldsymbol{\xi}^\alpha \cdot \mathbf{grad}_X(\dot{\gamma}^\alpha)) \leq 0 \quad (4.16)$$

### 4.2.4 Constitutive laws

#### 4.2.4.1 Energetic constitutive laws

The free energy in (4.16) consists of an elastic strain energy  $\Psi^e$  and a defect energy  $\Psi^\rho$ . Building on the work of Gurtin (2008b),  $\Psi^\rho$  is assumed to be function of dislocation densities:

$$\boldsymbol{\rho} = \{\rho_-^1 \cdots \rho_-^q, \rho_\odot^1 \cdots \rho_\odot^q\}$$

where  $\rho_{\Gamma}^{\alpha}$  and  $\rho_{\odot}^{\alpha}$  are respectively the edge and screw dislocation densities associated with the slip system  $\alpha$ , which are respectively defined by:

$$\dot{\rho}_{\Gamma}^{\alpha} = -\mathbf{s}^{\alpha} \cdot \mathbf{grad}_{\#}(\dot{\gamma}^{\alpha}) \quad \text{and} \quad \dot{\rho}_{\odot}^{\alpha} = \mathbf{l}^{\alpha} \cdot \mathbf{grad}_{\#}(\dot{\gamma}^{\alpha}) \quad (4.17)$$

These densities are in units of  $length^{-1}$  and may be positive or negative. Bearing in mind equations (4.5) and (4.9), it can easily be demonstrated that:

$$\dot{\rho}_{\Gamma}^{\alpha} = -\mathbf{s}_r^{\alpha} \cdot \mathbf{grad}_X(\dot{\gamma}^{\alpha}) \quad \text{and} \quad \dot{\rho}_{\odot}^{\alpha} = \mathbf{l}_r^{\alpha} \cdot \mathbf{grad}_X(\dot{\gamma}^{\alpha}) \quad (4.18)$$

The elastic strain energy  $\Psi^e$  is assumed to be a quadratic form of  $\mathbf{E}^e$ :

$$\Psi^e = \frac{1}{2} \mathbf{E}^e : \mathbb{C} : \mathbf{E}^e$$

where  $\mathbb{C}$  is a symmetric and positive-definite elasticity tensor. In rate form, this quantity can be written as:

$$\dot{\Psi}^e = \frac{\partial \Psi^e}{\partial \mathbf{E}^e} : \dot{\mathbf{E}}^e \quad (4.19)$$

As for defect energy, similar form as that used in the previous chapter is adopted to describe this energy:

$$\Psi^{\rho} = \frac{1}{n} X_0 l_{en}^n \sum_{\alpha=1}^q (|\rho_{\Gamma}^{\alpha}|^n + |\rho_{\odot}^{\alpha}|^n) \quad (4.20)$$

where  $X_0$  is a constant representing the energetic slip resistance, and  $l_{en}$  is an energetic length scale. To ensure the convexity of  $\Psi^{\rho}$ , the defect energy index  $n$  must be greater than or equal to 1 ( $n \geq 1$ ). Its rate form is given by:

$$\begin{aligned} \dot{\Psi}^{\rho} &= \sum_{\alpha=1}^q \left( \frac{\partial \Psi^{\rho}}{\partial \rho_{\Gamma}^{\alpha}} \dot{\rho}_{\Gamma}^{\alpha} + \frac{\partial \Psi^{\rho}}{\partial \rho_{\odot}^{\alpha}} \dot{\rho}_{\odot}^{\alpha} \right) \\ &= X_0 l_{en}^n \sum_{\alpha=1}^q \left( -|\rho_{\Gamma}^{\alpha}|^{n-2} \rho_{\Gamma}^{\alpha} \mathbf{s}_r^{\alpha} + |\rho_{\odot}^{\alpha}|^{n-2} \rho_{\odot}^{\alpha} \mathbf{l}_r^{\alpha} \right) \cdot \mathbf{grad}_X(\dot{\gamma}^{\alpha}) \end{aligned} \quad (4.21)$$

Substituting (4.19) and (4.21) into (4.16), the local free energy imbalance can be rewritten as:

$$\begin{aligned} \left( \frac{\partial \Psi^e}{\partial \mathbf{E}^e} - \mathbf{S}^e \right) : \dot{\mathbf{E}}^e + \sum_{\alpha=1}^q \left[ X_0 l_{en}^n \left( -|\rho_{\Gamma}^{\alpha}|^{n-2} \rho_{\Gamma}^{\alpha} \mathbf{s}_r^{\alpha} + |\rho_{\odot}^{\alpha}|^{n-2} \rho_{\odot}^{\alpha} \mathbf{l}_r^{\alpha} \right) - \boldsymbol{\xi}^{\alpha} \right] \cdot \mathbf{grad}_X(\dot{\gamma}^{\alpha}) \\ - \sum_{\alpha=1}^q \pi^{\alpha} \dot{\gamma}^{\alpha} \leq 0 \end{aligned} \quad (4.22)$$

In the following, it is assumed that  $\mathbf{S}^e$  is fully energetic,  $\pi^{\alpha}$  is fully dissipative, and  $\boldsymbol{\xi}^{\alpha}$  is divided into energetic and dissipative parts:

$$\mathbf{S}^e = \frac{\partial \Psi^e}{\partial \mathbf{E}^e}, \quad \pi^{\alpha} = \pi_{dis}^{\alpha}, \quad \text{and} \quad \boldsymbol{\xi}^{\alpha} = \boldsymbol{\xi}_{en}^{\alpha} + \boldsymbol{\xi}_{dis}^{\alpha}$$

It should be noted that higher-order dissipation in the context of strain gradient (crystal) plasticity theories still remains an open question. Although ignored in some works, several authors consider this kind of dissipation in their models (Gurtin et al., 2007; Voyadjis and Delikta, 2009b; Fleck and Willis, 2009; Gurtin, 2010; Jebahi et al., 2020). As reported by Fleck and Willis (2009), direct experimental measurement shows that the core energy of dislocations stored during plastic deformation is much smaller than the plastic work dissipated in dislocation motion. Consequently, both statistically stored and geometrically necessary dislocations would contribute more to plastic dissipation than to a change in free energy. The source of dissipation process can be attributed to the motion of the mobile dislocations. Motion of dislocations yields energy dissipation which, in turn, results in resistance to the dislocation motion and increase in the yield strength due to size effects (Voyadjis and Delikta, 2009b).

The energetic constitutive laws can then be obtained:

$$\begin{aligned} \mathbf{S}^e &= \mathbb{C} : \mathbf{E}^e \\ \boldsymbol{\xi}_{en}^\alpha &= X_0 l_{en}^n \left( -|\rho_F^\alpha|^{n-2} \rho_F^\alpha \mathbf{s}_r^\alpha + |\rho_\odot^\alpha|^{n-2} \rho_\odot^\alpha \mathbf{l}_r^\alpha \right) \end{aligned} \quad (4.23)$$

It can be verified from  $(4.23)_2$  that the energetic microscopic stress  $\boldsymbol{\xi}_{en}^\alpha$  is tangent to the  $\alpha^{\text{th}}$  slip plane. Using  $(4.23)$ , the dissipation inequality becomes:

$$\sum_{\alpha=1}^q (\pi_{dis}^\alpha \dot{\gamma}^\alpha + \boldsymbol{\xi}_{dis}^\alpha \cdot \mathbf{grad}_X(\dot{\gamma}^\alpha)) \geq 0 \quad (4.24)$$

$\boldsymbol{\xi}_{dis}^\alpha$  characterizes the dissipative microscopic forces associated with the evolution of dislocations in the  $\alpha^{\text{th}}$  slip plane. As the motion of such dislocations is tangent to this plane,  $\boldsymbol{\xi}_{dis}^\alpha$  is also required to be tangential. Therefore, without losing generality, the gradient term in  $(4.24)$  can be replaced by the corresponding tangential gradient defined by:

$$\mathbf{grad}_X^\alpha(\dot{\gamma}^\alpha) = (\mathbf{I} - \bar{\mathbf{m}}_r^\alpha \otimes \bar{\mathbf{m}}_r^\alpha) \cdot \mathbf{grad}_X(\dot{\gamma}^\alpha), \quad \text{with } \bar{\mathbf{m}}_r^\alpha = \frac{\mathbf{m}_r^\alpha}{|\mathbf{m}_r^\alpha|}$$

This yields:

$$\sum_{\alpha=1}^q (\pi_{dis}^\alpha \dot{\gamma}^\alpha + \boldsymbol{\xi}_{dis}^\alpha \cdot \mathbf{grad}_X^\alpha(\dot{\gamma}^\alpha)) \geq 0 \quad (4.25)$$

#### 4.2.4.2 Dissipative constitutive laws

Referring to the description of dissipative processes defined in small deformation SGCP model presented in chapter 3, uncoupled effective plastic strain measures are used to describe the first- and higher-order dissipative effects. These measures, which are referred to hereafter as first- and higher-order measures, are respectively defined by:

$$\begin{aligned} \dot{e}_\pi^\alpha &= |\dot{\gamma}^\alpha|, \quad e_\pi^\alpha = \int \dot{e}_\pi^\alpha dt \\ \dot{e}_\xi^\alpha &= l_{dis} \|\mathbf{grad}_X^\alpha(\dot{\gamma}^\alpha)\|, \quad e_\xi^\alpha = \int \dot{e}_\xi^\alpha dt \end{aligned}$$

where  $l_{dis}$  is dissipative internal length scale. To ensure positive dissipation, the scalar and vector dissipative stresses associated with slip system  $\alpha$  are taken as:

$$\pi_{dis}^\alpha = S_\pi^\alpha \left( \frac{\dot{e}_\pi^\alpha}{\dot{\gamma}_0^\alpha} \right)^m \frac{\dot{\gamma}^\alpha}{\dot{e}_\pi^\alpha} \quad (4.26)$$

$$\boldsymbol{\xi}_{dis}^\alpha = S_\xi^\alpha l_{dis}^2 \left( \frac{\dot{e}_\xi^\alpha}{\dot{\gamma}_0^\alpha} \right)^m \frac{\mathbf{grad}_X^\alpha(\dot{\gamma}^\alpha)}{\dot{e}_\xi^\alpha} \quad (4.27)$$

where  $\dot{\gamma}_0^\alpha > 0$  is a constant strain rate representative of the flow rates of interest,  $m > 0$  is a constant characterizing the rate-sensitivity of the considered material, and  $S_i^\alpha$  ( $i \in \{\pi, \xi\}$ ) are stress-dimensional internal state variables ( $S_\pi^\alpha > 0$  and  $S_\xi^\alpha \geq 0$ ). These variables are called hereafter dissipative slip resistances. Their evolutions are assumed to be governed by:

$$\dot{S}_i^\alpha = \sum_{\beta=1}^q h_i^{\alpha\beta} \left( S_i^\beta \right) \dot{e}_i^\beta \quad \text{with} \quad S_i^\alpha(0) = S_{i0} \quad (4.28)$$

$S_{i0}$  ( $i \in \{\pi, \xi\}$ ) are initial dissipative slip resistances ( $S_{\pi0} > 0$  and  $S_{\xi0} \geq 0$ ), and  $h_i^{\alpha\beta}$  ( $i \in \{\pi, \xi\}$ ) are positive hardening moduli.

## 4.2.5 Flow rules

Based on the expressions of the microscopic stresses, the microscopic balance equation associated with slip system  $\alpha$  can be reformulated as follows:

$$\tau^\alpha + \mathbf{div}_X(\boldsymbol{\xi}_{en}^\alpha) + \mathbf{div}_X(\boldsymbol{\xi}_{dis}^\alpha) - \pi_{dis}^\alpha = 0 \quad (4.29)$$

Substituting (4.23)<sub>2</sub>, (4.26) and (4.27) into (4.29), the flow rule associated with slip system  $\alpha$  can be obtained:

$$\underbrace{\tau^\alpha - X_0 l_{en}^n \mathbf{div}_X \left( |\rho_-^\alpha|^{n-2} \rho_-^\alpha \mathbf{s}_r^\alpha - |\rho_+^\alpha|^{n-2} \rho_+^\alpha \mathbf{l}_r^\alpha \right)}_{\text{I}} = \underbrace{S_\pi^\alpha \left( \frac{\dot{e}_\pi^\alpha}{\dot{\gamma}_0^\alpha} \right)^m \frac{\dot{\gamma}^\alpha}{\dot{e}_\pi^\alpha}}_{\text{II}} - \underbrace{\mathbf{div}_X \left( S_\xi^\alpha l_{dis}^2 \left( \frac{\dot{e}_\xi^\alpha}{\dot{\gamma}_0^\alpha} \right)^m \frac{\mathbf{grad}_X^\alpha(\dot{\gamma}^\alpha)}{\dot{e}_\xi^\alpha} \right)}_{\text{III}} \quad (4.30)$$

Term I in the above equation, being energetic, represents a backstress, leading to kinematic hardening (Bauschinger) effects. Terms II and III are dissipative and lead to dissipative (isotropic-like) hardening effects.

## 4.3 Simplified two-dimensional version of the SGCP model and numerical implementation

In this section, a two-dimensional (2D) version of the finite deformation SGCP model is implemented under plane strain conditions with planar slip systems, using a total Lagrangian finite element formulation. Extension to generalized three-dimensional case can easily be derived.

### 4.3.1 Simplified 2D SGCP model

Assuming plane strain conditions with planar slip systems, it can easily be demonstrated that screw dislocation densities vanish (Gurtin et al., 2007; Gurtin and Ohno, 2011; Jebahi et al., 2020):

$$\dot{\rho}_\odot^\alpha = \mathbf{l}^\alpha \cdot \mathbf{grad}_\#(\dot{\gamma}^\alpha) = 0 \quad (4.31)$$

Therefore, the energetic microscopic stresses become:

$$\boldsymbol{\xi}_{en}^\alpha = -X_0 l_{en}^n (|\rho_\vdash^\alpha|^{n-2} \rho_\vdash^\alpha \mathbf{s}_r^\alpha).$$

The dissipative microscopic stresses are given by (4.26) and (4.27), with the slip resistances  $S_\pi^\alpha$  and  $S_\xi^\alpha$  assumed hereafter to evolve linearly with the effective plastic strain measures:

$$\dot{S}_i^\alpha = \sum_{\beta=1}^q H_i \dot{e}_i^\beta \quad \text{with} \quad S_i^\alpha(0) = S_{i0}, \quad H_i = \text{constant} \geq 0 \quad (4.32)$$

Note that  $i \in \{\pi, \xi\}$ ,  $S_{\pi0} > 0$  and  $S_{\xi0} \geq 0$ . Using the above expressions of the microscopic stresses, a simplified form of the flow rule (4.30) can be obtained:

$$\tau^\alpha - X_0 l_{en}^n \operatorname{div}_X (|\rho_\vdash^\alpha|^{n-2} \rho_\vdash^\alpha \mathbf{s}_r^\alpha) = S_\pi^\alpha \left( \frac{\dot{e}_\pi^\alpha}{\dot{\gamma}_0^\alpha} \right)^m \frac{\dot{\gamma}^\alpha}{\dot{e}_\pi^\alpha} - \operatorname{div}_X \left( S_\xi^\alpha l_{dis}^2 \left( \frac{\dot{e}_\xi^\alpha}{\dot{\gamma}_0^\alpha} \right)^m \frac{\mathbf{grad}_X^\alpha(\dot{\gamma}^\alpha)}{\dot{e}_\xi^\alpha} \right) \quad (4.33)$$

In summary, key equations characterizing the simplified two-dimensional SGCP model are recalled hereafter:

$$\left\{ \begin{array}{l} \mathbf{F} = \mathbf{F}^e \mathbf{F}^p, \quad \mathbf{L}^p = \sum_{\alpha=1}^q \dot{\gamma}^\alpha \mathbb{S}^\alpha, \quad \mathbb{S}^\alpha = \mathbf{s}^\alpha \otimes \mathbf{m}^\alpha \\ \dot{\mathbf{F}}^p = \mathbf{L}^p \mathbf{F}^p, \quad \mathbf{F}^e = \mathbf{F} \mathbf{F}^{p-1}, \quad \mathbf{C}^e = \mathbf{F}^{eT} \mathbf{F}^e, \quad \mathbf{E}^e = \frac{1}{2} (\mathbf{C}^e - \mathbf{I}) \\ \mathbf{S}^e = \mathbb{C} : \mathbf{E}^e, \quad \mathbf{P} = \mathbf{F}^e \mathbf{S}^e \mathbf{F}^{pT-1}, \quad \boldsymbol{\sigma} = J^{-1} \mathbf{F}^e \mathbf{S}^e \mathbf{F}^{eT} \\ \pi_{dis}^\alpha = S_\pi^\alpha \left( \frac{\dot{e}_\pi^\alpha}{\dot{\gamma}_0^\alpha} \right)^m \frac{\dot{\gamma}^\alpha}{\dot{e}_\pi^\alpha} \\ \boldsymbol{\xi}^\alpha = X_0 l_{en}^n (-|\rho_\vdash^\alpha|^{n-2} \rho_\vdash^\alpha \mathbf{s}_r^\alpha) + S_\xi^\alpha l_{dis}^2 \left( \frac{\dot{e}_\xi^\alpha}{\dot{\gamma}_0^\alpha} \right)^m \frac{\mathbf{grad}_X^\alpha(\dot{\gamma}^\alpha)}{\dot{e}_\xi^\alpha} \\ \dot{S}_\pi^\alpha = \sum_{\beta=1}^q H_\pi (S_\pi^\beta) \dot{e}_\pi^\beta, \quad S_{\pi0} > 0 \\ \dot{S}_\xi^\alpha = \sum_{\beta=1}^q H_\xi (S_\xi^\beta) \dot{e}_\xi^\beta, \quad S_{\xi0} \geq 0 \\ \dot{\rho}_\vdash^\alpha = -\mathbf{s}_r^\alpha \cdot \mathbf{grad}_X(\dot{\gamma}^\alpha) \\ \dot{e}_\pi^\alpha = |\dot{\gamma}^\alpha|, \quad \dot{e}_\xi^\alpha = l_{dis} \|\mathbf{grad}_X^\alpha(\dot{\gamma}^\alpha)\| \end{array} \right. \quad (4.34)$$

These equations will be solved numerically within a total Lagrangian finite element framework. To this end,  $\gamma$ -method (Gurtin et al., 2007; Borg, 2007; Jebahi et al., 2020) will be adopted as in

chapter 3. In addition to the displacement field  $\mathbf{u}$ , the scalar field variables defined on each slip system  $\alpha$  by:

$$\gamma^\alpha = \int_0^t \dot{\gamma}^\alpha dt, \quad \text{with} \quad \gamma^\alpha(t=0) = 0 \quad (4.35)$$

are taken as primary variables, in consistency with the implemented small deformation version of the proposed SGCP model. It is worth recalling that these variables, which can be interpreted in small deformation as plastic slips on the slip systems, have no real physical interpretation in finite deformation (only their increments are physically relevant). As will be seen in the validation section, this choice of primary variables has no impact on the numerical results, as the integration of the constitutive laws is only based on the increments of these variables.

### 4.3.2 Integration of constitutive laws

Numerical integration of constitutive laws consists in updating the values of stresses and internal variables, given the increments of kinematic variables. Knowing the increments of the primary field variables ( $\Delta\mathbf{u}$  and  $\Delta\gamma^\alpha$ ), the displacement, the deformation gradient and the plastic distortion rate quantities can be calculated at a given point as:

$$\mathbf{u}_{n+1} = \mathbf{u}_n + \Delta\mathbf{u}, \quad \mathbf{F}_{n+1} = \mathbf{grad}_X(\mathbf{u}_{n+1}) + \mathbf{I}, \quad \text{and} \quad \mathbf{L}_{n+1}^p = \sum_{\alpha=1}^q \left( \frac{\Delta\gamma^\alpha}{\Delta t} \mathbb{S}^\alpha \right) \quad (4.36)$$

with  $\mathbf{I}$  the second-order unity tensor. Two approaches can be used to calculate the plastic distortion tensor based on equation (4.3)<sub>2</sub>. Using explicit method, (4.3)<sub>2</sub> can be approximated by:

$$\mathbf{F}_{n+1}^p - \mathbf{F}_n^p = \left[ \sum_{\alpha} \Delta\gamma^\alpha \mathbb{S}^\alpha \right] \mathbf{F}_n^p \quad (4.37)$$

This gives :

$$\mathbf{F}_{n+1}^p = \left[ \mathbf{I} + \sum_{\alpha} \Delta\gamma^\alpha \mathbb{S}^\alpha \right] \mathbf{F}_n^p \quad (4.38)$$

Using implicit approach, (4.3)<sub>2</sub> can be approximated by:

$$\mathbf{F}_{n+1}^p - \mathbf{F}_n^p = \left[ \sum_{\alpha=1}^q \Delta\gamma^\alpha \mathbb{S}^\alpha \right] \mathbf{F}_{n+1}^p \quad (4.39)$$

which leads to:

$$\mathbf{F}_{n+1}^{p-1} = \mathbf{F}_n^{p-1} \left[ \mathbf{I} - \sum_{\alpha=1}^q \Delta\gamma^\alpha \mathbb{S}^\alpha \right] \quad (4.40)$$

As only  $\mathbf{F}^{p-1}$  is involved in the constitutive laws, the latter approach, which allows for directly determining this quantity, will be adopted in this work. Note that equation (4.40) does not guarantee

plastic incompressibility, which can be done by imposing  $\det \mathbf{F}^p = 1$ . Therefore, unimodular operator is applied to the term between brackets in the above equation ([Erdle and Böhlke, 2017](#)):

$$\mathbf{F}_{n+1}^{p-1} = \mathbf{F}_n^{p-1} \text{uni} \left( \mathbf{I} - \sum_{\alpha=1}^q \Delta \gamma^\alpha \mathbb{S}^\alpha \right) \quad (4.41)$$

where, for a second order tensor  $\mathbf{A}$ , the term  $\text{uni}(\mathbf{A})$  is defined by:

$$\text{uni}(\mathbf{A}) = [\det(\mathbf{A})]^{-\frac{1}{3}} \mathbf{A} \quad (4.42)$$

Considering (4.1), the elastic part of deformation gradient is calculated by:

$$\mathbf{F}_{n+1}^e = \mathbf{F}_{n+1} \mathbf{F}_{n+1}^{p-1}. \quad (4.43)$$

and then the elastic Green-Lagrange strain tensor  $\mathbf{E}_{n+1}^e$  can be obtained:

$$\mathbf{E}_{n+1}^e = \frac{1}{2} (\mathbf{C}_{n+1}^e - \mathbf{I}), \quad \text{with} \quad \mathbf{C}_{n+1}^e = \mathbf{F}_{n+1}^{eT} \mathbf{F}_{n+1}^e \quad (4.44)$$

Knowing the updated kinematic quantities, the stresses and internal variables can be updated. Alg. 4.1 summarizes the steps of integration of constitutive laws, where the subscripts “ $n$ ” and “ $n + 1$ ” are omitted for clarity.

---

**Algorithm 4.1** Integration of constitutive equations

---

**Inputs:**  $\mathbf{u}$ ,  $\mathbf{F}^p$ ,  $\rho_F^\alpha$ ,  $\Delta \mathbf{u}$ ,  $\Delta \gamma^\alpha$ ,

**Update:**  $\mathbf{u} \leftarrow \mathbf{u} + \Delta \mathbf{u}$

**Calculate:**  $\mathbf{F}$ ,  $\mathbf{F}^{-p}$ ,  $\mathbf{F}^e$ ,  $\mathbf{C}^e$  and  $\mathbf{E}^e$

**Calculate:**  $J = \det(\mathbf{F})$

**Calculate:**  $\mathbf{S}^e = \mathbb{C} : \mathbf{E}^e$ ,  $\mathbf{P} = \mathbf{F}^e \cdot \mathbf{S}^e \cdot \mathbf{F}^{pT-1}$ ,  $\boldsymbol{\sigma} = J^{-1} \mathbf{F}^e \cdot \mathbf{S}^e \cdot \mathbf{F}^{eT}$

**Do**  $\alpha = 1$  **to**  $q$ :

**Calculate:**  $\Delta e_\pi^\alpha = |\Delta \gamma^\alpha|$ ,  $\Delta e_\xi^\alpha = l_{dis} \|\mathbf{grad}_X^\alpha(\Delta \gamma^\alpha)\|$

**end do**

**Do**  $\alpha = 1$  **to**  $q$ :

**Calculate:**  $\Delta \rho_F^\alpha = -\mathbf{s}_r^\alpha \cdot \mathbf{grad}_X^\alpha(\Delta \gamma^\alpha)$ ,  $\Delta S_\pi^\alpha = \sum_{\beta=1}^q H_\pi \Delta e_\pi^\beta$ ,  $\Delta S_\xi^\alpha = \sum_{\beta=1}^q H_\xi \Delta e_\xi^\beta$

**Update:**  $\rho_F^\alpha \leftarrow \rho_F^\alpha + \Delta \rho_F^\alpha$ ,  $S_\pi^\alpha \leftarrow S_\pi^\alpha + \Delta S_\pi^\alpha$ ,  $S_\xi^\alpha \leftarrow S_\xi^\alpha + \Delta S_\xi^\alpha$

**Calculate:**  $\pi_{dis}^\alpha = S_\pi^\alpha \left( \frac{\Delta e_\pi^\alpha}{\dot{\gamma}_0^\alpha \Delta t} \right)^m \frac{\Delta \gamma^\alpha}{\Delta e_\pi^\alpha}$

**Calculate:**  $\xi_{n+1}^\alpha = X_0 l_{en}^n (-|\rho_F^\alpha|^{n-2} \rho_F^\alpha \mathbf{s}_r^\alpha) + S_\xi^\alpha l_{dis}^2 \left( \frac{\Delta e_\xi^\alpha}{\dot{\gamma}_0^\alpha \Delta t} \right)^m \frac{\mathbf{grad}_X^\alpha(\Delta \gamma^\alpha)}{\Delta e_\xi^\alpha}$

**end do**

---

### 4.3.3 Weak forms and finite element discretization

Assume the virtual fields  $\delta \dot{\mathbf{u}}$  and  $\delta \dot{\gamma}^\alpha$  which are kinematically admissible to zero on the portions of the boundary of the studied domain on which macroscopic and microscopic Dirichlet boundary

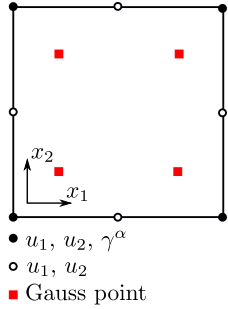


**Fig. 4.2.** Finite element used in the present work.

conditions are respectively imposed. The weak forms of the macroscopic and microscopic balance equations (4.12)<sub>1</sub> and (4.13)<sub>1</sub> can be obtained as follows:

$$\begin{aligned} G_u &= \int_{V_0} \mathbf{grad}_X(\delta \dot{\mathbf{u}}) : \mathbf{P} dv - \int_{S_0^t} \delta \dot{\mathbf{u}} \cdot \mathbf{t} ds \\ G_\gamma &= \sum_{\alpha=1}^q \left( \int_{V_0} \mathbf{grad}_X(\delta \dot{\gamma}^\alpha) \cdot \boldsymbol{\xi}^\alpha dv + \int_{V_0} \delta \dot{\gamma}^\alpha \pi^\alpha dv - \int_{V_0} \delta \dot{\gamma}^\alpha \tau^\alpha dv \right) - \sum_{\alpha=1}^q \int_{S_0^{\chi^\alpha}} \delta \dot{\gamma}^\alpha \chi^\alpha ds \end{aligned} \quad (4.45)$$

where  $S_0^t$  and  $S_0^{\chi^\alpha}$  are the portions of the domain boundary on which macroscopic and microscopic traction forces, noted respectively as  $\mathbf{t}$  and  $\chi^\alpha$ , are imposed. These weak forms are solved numerically using total Lagrangian finite element method. To this end, a User-Element (UEL) subroutine is implemented within the commercial finite element package ABAQUS/Standard. In this UEL, displacement and plastic scalar fields ( $\mathbf{u}$  and  $\gamma^\alpha$ ) are considered as primary variables (degrees of freedom). Several finite element types can be used to approximate these fields. In this work, an element type employing eight-noded (quadratic) interpolation of  $\mathbf{u}$ , four-noded (linear) interpolation of  $\gamma^\alpha$  and  $2 \times 2$  Gauss integration is adopted (Fig. 4.2). Based on Kuroda (2011), this element type is well suited to study localization problems with more affordable computation time. Within each element, displacements  $u_i$  ( $i = 1, 2$ ) and plastic scalar variables  $\gamma^\alpha$  ( $\alpha = 1, 2, \dots, q$ ) can be approximated based on the associated nodal values as follows:

$$u^i = \sum_{k=1}^8 N_u^k U_k^i, \quad \gamma^\alpha = \sum_{k=1}^4 N_\gamma^k \Gamma_k^\alpha \quad (4.46)$$

where  $U_k^i$  and  $\Gamma_k^\alpha$  are nodal values of displacements and plastic scalar variables, and  $N_u^k$  and  $N_\gamma^k$  are the associated interpolation functions.

Using the above field approximations, the macroscopic and microscopic weak forms can be written within a representative finite element, in a simplified matrix form, as follows:

$$\begin{aligned} G_u^e &= (\delta \dot{\underline{U}}^e)^T \cdot \left( \int_{V_{e0}} \underline{\underline{B}}_u^T \cdot \underline{\underline{P}} dv - \int_{S_{e0}^t} \underline{\underline{N}}_u^T \cdot \underline{\mathbf{t}} ds \right) \\ G_\gamma^e &= (\delta \dot{\underline{\underline{\Gamma}}}^e)^T \cdot \left( \int_{V_{e0}} \underline{\underline{B}}_\gamma^T \cdot \underline{\xi} dv + \int_{V_{e0}} \underline{\underline{N}}_\gamma^T \cdot \underline{\pi} dv - \int_{V_{e0}} \underline{\underline{N}}_\gamma^T \cdot \underline{\tau} dv - \int_{S_{e0}^\chi} \underline{\underline{N}}_\gamma^T \cdot \underline{\chi} ds \right) \end{aligned} \quad (4.47)$$

where  $\underline{N}$  and  $\underline{B}$  are the interpolation and gradient matrices associated with the displacement field,  $\underline{\underline{N}}_\gamma$  and  $\underline{\underline{B}}_\gamma$  are the interpolation and gradient matrices associated with the plastic scalar fields,  $\underline{P}$ ,  $\underline{\xi}$ ,  $\underline{\pi}$  are vector representations of the macroscopic stress and microscopic stresses on all slip systems,  $\underline{\tau}$  is vector of resolved shear stresses on all slip systems,  $\underline{t}$  and  $\underline{\chi}$  are vectors of macroscopic and microscopic traction forces.

Considering the principle of virtual power ( $G_u^e = 0$  and  $G_\gamma^e = 0$ , for any arbitrary  $\delta \underline{U}^e$  and  $\delta \dot{\underline{\Gamma}}^e$ ), the associated residuals can be written:

$$\begin{aligned} \underline{R}_u^e &= \int_{V_{e0}} \underline{\underline{B}}_u^T \cdot \underline{P} dv - \int_{S_{e0}^t} \underline{\underline{N}}_u^T \cdot \underline{t} ds = 0 \\ \underline{R}_\gamma^e &= \int_{V_{e0}} \underline{\underline{B}}_\gamma^T \cdot \underline{\xi} dv + \int_{V_{e0}} \underline{\underline{N}}_\gamma^T \cdot \underline{\pi} dv - \int_{V_{e0}} \underline{\underline{N}}_\gamma^T \cdot \underline{\tau} dv - \int_{S_{e0}^\chi} \underline{\underline{N}}_\gamma^T \cdot \underline{\chi} ds = 0 \end{aligned} \quad (4.48)$$

Linearization of these equations with respect to small variations of  $\underline{U}^e$  and  $\underline{\Gamma}^e$  leads to an elementary system of equations, which can be written in matrix form as:

$$\begin{bmatrix} \underline{\underline{K}}_{uu}^e & \underline{\underline{K}}_{u\gamma}^e \\ \underline{\underline{K}}_{\gamma u}^e & \underline{\underline{K}}_{\gamma\gamma}^e \end{bmatrix} \begin{bmatrix} \Delta U^e \\ \Delta \Gamma^e \end{bmatrix} = - \begin{bmatrix} \underline{R}_u^e \\ \underline{R}_\gamma^e \end{bmatrix} \quad (4.49)$$

with

$$\underline{\underline{K}}_{uu} = \frac{\partial \underline{R}_u^e}{\partial \Delta U^e}, \quad \underline{\underline{K}}_{u\gamma} = \frac{\partial \underline{R}_u^e}{\partial \Delta \Gamma^e}, \quad \underline{\underline{K}}_{\gamma u} = \frac{\partial \underline{R}_\gamma^e}{\partial \Delta U^e}, \text{ and } \underline{\underline{K}}_{\gamma\gamma} = \frac{\partial \underline{R}_\gamma^e}{\partial \Delta \Gamma^e} \quad (4.50)$$

The global system of linear equations can be obtained by assembling all the elementary systems of equations associated with the overall finite elements. This system is solved by means of a Newton-Raphson iterative solution scheme. At each iteration, updated values of the overall increments of the displacement and plastic scalar fields ( $\Delta U$  and  $\Delta \Gamma$ , respectively) are obtained and used to numerically solve the constitutive equations at the Gauss points (algorithm 4.1). A detailed numerical implementation can be found in Appendix B.

## 4.4 Validation of the model implementation

The present section aims to validate the numerical implementation of the proposed finite deformation SGCP model. To this end, it is applied to simulate a simple shear problem of a constrained layer under plane strain conditions. The considered layer is first subjected to small shear loading, allowing for comparison with the small deformation version of the proposed model in chapter 3. This makes it possible to draw conclusions about the effectiveness of the present model version in reproducing correctly different energetic and dissipative size effects, for which large deformation results are not necessarily available in the literature. Then, large shear loading is applied for a particular case of quadratic defect energy ( $n = 2$ ) with no higher-order dissipation ( $l_{dis} = 0$ ). For this case, the proposed model is equivalent to the model of Kuroda and Tvergaard (2008a), for which large deformation shear results are available. These results are used to assess the ability of the present model to capture finite deformation effects.

Figure 4.3 presents the geometrical model used in this section. A strip of infinite width in  $x_1$ -direction and height  $H$  in  $x_2$ -direction is subjected to simple shear loading under plane strain

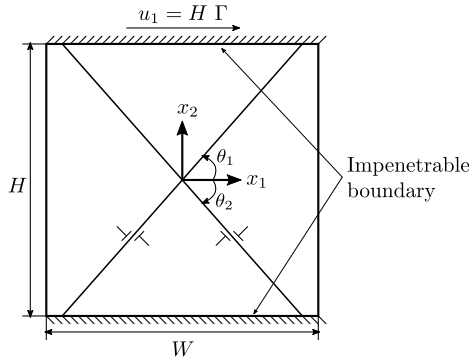


**Fig. 4.3.** Simple shear of a constrained strip with two active slip systems.

conditions. Two slip systems symmetrically oriented with respect to  $x_1$ -direction ( $\theta_1 = 60^\circ$  and  $\theta_2 = -60^\circ$ ) are considered. The macroscopic boundary conditions are given by:

$$\left. \begin{array}{l} u_1 = 0, \quad u_2 = 0 \quad \text{along} \quad x_2 = 0 \\ u_1 = H \Gamma, \quad u_2 = 0 \quad \text{along} \quad x_2 = H \end{array} \right\} \quad (4.51)$$

where  $\Gamma$  is the prescribed shear strain. Micro-hard boundary conditions are imposed on the top and bottom edges to hinder dislocation flow at them (impenetrable to dislocations):

$$\dot{\gamma}^1 = \dot{\gamma}^2 = 0 \quad \text{along} \quad x_2 = 0, H$$

To model the infinite width of the strip, periodic boundary conditions are imposed at its left and right edges:

$$\left. \begin{array}{l} u_i(0, x_2, t) = u_i(W, x_2, t) \quad \text{for} \quad i = 1, 2 \\ \gamma^\alpha(0, x_2, t) = \gamma^\alpha(W, x_2, t) \quad \text{for} \quad \alpha = 1, 2 \end{array} \right\}$$

With these conditions, the strip width  $W$  does not affect the results and can arbitrarily be chosen. To save computation time,  $W$  is chosen to have only one finite element along  $x_1$ -direction. A numerical sample consisting of a column of 100 finite elements in  $x_2$ -direction is then adopted.

For the case of small shear loading, a complete loading cycle is imposed (*i.e.*,  $0 \rightarrow \Gamma \rightarrow -\Gamma \rightarrow \Gamma$ ), with the prescribed shear strain restricted to  $\Gamma = 0.02$ . The material parameters are chosen as in small deformation SGCP model as presented in Tab. 3.1. Fig. 4.4 compares the associated results obtained using the present finite deformation model with those obtained using the small deformation one, for different energetic and dissipative parameters. Solid line curves correspond to the finite deformation results and those with markers correspond to the small deformation ones. For comparison purposes, results obtained using conventional small and finite deformation crystal plasticity with no hardening ( $H_\pi = 0$ ) are also presented in Fig. 4.4 (curves named ‘Perfect CP’). It can be seen that the stress-strain responses obtained using the finite deformation formulation show very good agreement with those obtained using the small deformation one. Note that the stress-strain curves obtained using  $n = 1.7$  present inflection points, reflecting nonlinear kinematic hardening type III (KIII) of Asaro (1975) as discussed in section (3.4.1.2). Applying small shear loading, the nonlinear geometrical effects are insignificant. In this case, the small and finite deformation formulations must lead to similar results, which is the case according to Fig. 4.4. This

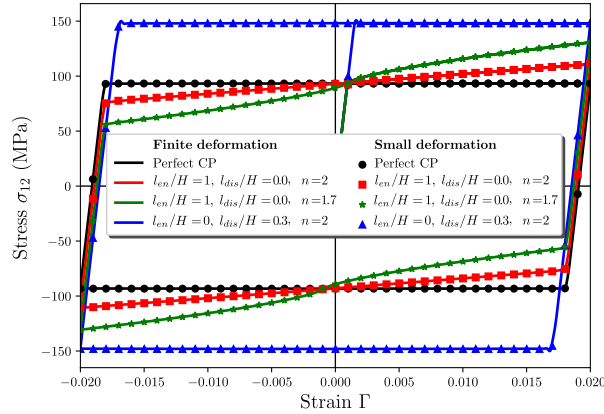


**Fig. 4.4.** Small shear loading results for different energetic and dissipative parameters: comparison between the small and finite deformation models.

validates the capabilities of the implemented finite deformation model in reproducing correctly the energetic and dissipative effects, at least in the range of the prescribed shear loading.

To examine the effectiveness of the present model implementation with regard to nonlinear geometrical effects, the simple shear example of Kuroda and Tvergaard (2008a) which implies large shear loading is reproduced in this work. In this example, the same geometrical sample as in Fig. 4.3 is used, with imposed shear loading  $\Gamma = 0.24$ . The defect energy index and the dissipative length scale are set as  $n = 2$  and  $l_{dis} = 0$ , respectively. With these choices, the present finite deformation model is equivalent to that of Kuroda and Tvergaard (2008a), in which only energetic backstress is considered. The other material parameters, which are taken from Kuroda and Tvergaard (2008a), are presented in Tab. 4.1. Fig. 4.5 compares results of the present model with those obtained by Kuroda and Tvergaard (2008a) for two values of energetic length scale  $l_{en}$ . Very good agreement between the results is obtained, regardless of the value of  $l_{en}$ . This shows the ability of the present model implementation to correctly reproduce finite deformation effects. As can be seen from Fig. 4.5a, in the range of small shear strains, until approximately  $\Gamma = 0.025$ , nonlinear geometrical effects are insignificant and the shear stress  $\sigma_{12}$  increases almost linearly with  $\Gamma$  after yielding. Beyond approximately  $\Gamma = 0.025$ , nonlinear stress-strain dependence takes place and becomes more striking at larger strains, due to nonlinear geometrical effects. Fig. 4.5b presents the distributions of the total plastic variables  $\gamma^\alpha$  associated with the considered slip systems along  $x_2$ -direction, as obtained using the present and the Kuroda and Tvergaard (2008a) models. As shown, the nonlinear geometrical effects lead to asymmetric evolution of these variables, despite the initial symmetry of the slip systems with respect to the loading direction. A distinct deviation between the  $\gamma^1$  and  $\gamma^2$  profiles, which coincide with those obtained by Kuroda and Tvergaard (2008a), is observed. Such a deviation was also reported by Bittencourt (2018) using similar simple shear problem under monotonic large shear loading. It can be explained by an apparent hardening increase in one system and an apparent hardening decrease in the other system due to lattice rotation effects (Kuroda and Tvergaard, 2008a; Bittencourt, 2018).

**Tab. 4.1.** Material parameters implied for simple shear of constrained layer undergoing finite deformation, inspired by [Kuroda and Tvergaard \(2008a\)](#).

Material parameter name	Symbol	Value	Unit
Young's modulus	$E$	130	GPa
Poisson's ratio	$\nu$	0.3	—
Reference slip rate	$\dot{\gamma}_0^\alpha$	0.001	$s^{-1}$
Rate-sensitivity parameter	$m$	0.02	—
Higher-order energetic slip resistance	$X_0$	50	MPa
Initial first-order dissipative slip resistance	$S_{\pi 0}$	50	MPa
Initial higher-order dissipative slip resistance	$S_{\xi 0}$	50	MPa
First-order hardening modulus	$H_\pi$	250	MPa
Higher-order hardening modulus	$H_\xi$	0	MPa
Energetic length scale	$l_{en}$	case study	$\mu m$
Dissipative length scale	$l_{dis}$	0	$\mu m$
Defect energy index	$n$	2	—

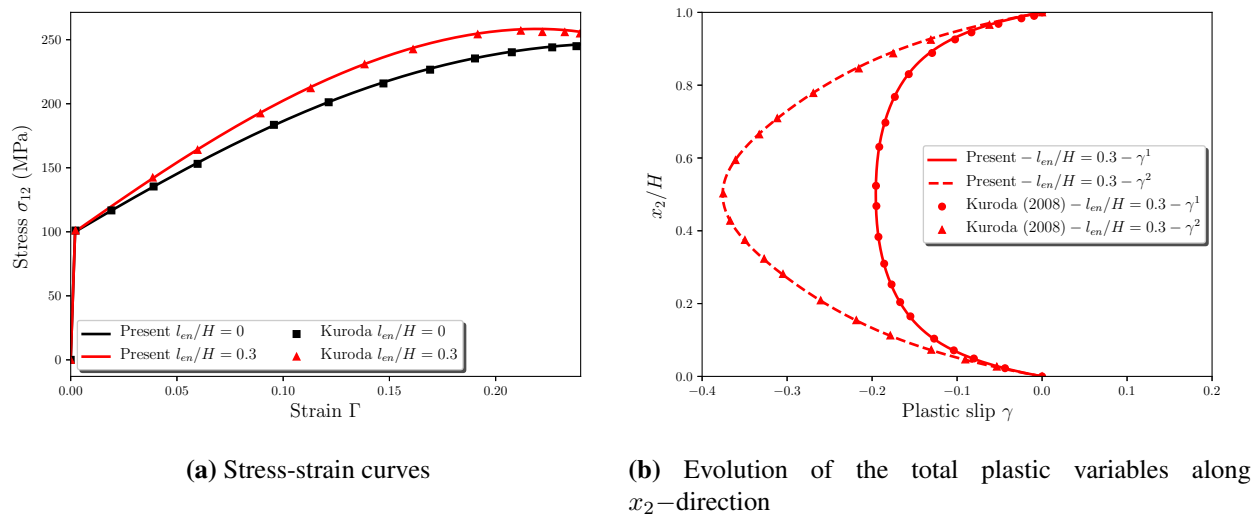


**Fig. 4.5.** Large shear loading results: comparison between the present model and the model of [Kuroda and Tvergaard \(2008a\)](#) for different values of  $l_{en}/H$ .

## 4.5 Conclusions

The present chapter dealt with the extension of the small deformation SGCP model presented in the previous chapter to finite deformation following the procedure of [Gurtin \(2002, 2008a\)](#). The extended model was formulated within the reference configuration using  $\gamma$ -based approach. As in [Gurtin et al. \(2010\)](#), the kinematics of finite deformation single-crystal is described based on the assumption that the undistorted lattice resides within the lattice configuration and not in the reference one. This assumption allows for capturing effects of lattice plastic distortion and seems to be more in accordance with experimental observations ([Gurtin and Reddy, 2016](#)). A simplified two-dimensional version of this model was implemented within the commercial finite element package Abaqus/Standard through a User-Element (UEL) subroutine.

To validate the model implementation, it was applied to simulate a simple shear problem of a constrained layer under plane strain conditions. The considered layer was first subjected to small shear loading, allowing for comparison with the small deformation version of the model. This comparison was intended to assess the model effectiveness in reproducing different energetic and dissipative size effects, for which large deformation results are not available in the literature. Large shear loading is then applied for a particular case of quadratic defect energy ( $n = 2$ ) with no higher-order dissipation ( $l_{dis} = 0$ ). For this case, the proposed model is equivalent to the model of ([Kuroda and Tvergaard, 2008a](#)), for which large deformation results are available. These results were used to assess the ability of the proposed model to correctly predict large deformation effects. For both loading cases, results obtained using the proposed model are in very good agreement with the comparison ones.



# **Chapter 5**

## **Development of finite deformation grain boundary model**

### **Abstract**

The present chapter aims at extending the small deformation grain boundary model of [Gurtin \(2008b\)](#) to finite deformation framework. The extended model will be derived within the reference configuration considering the lattice plastic distortion. The objective is to allow for a more realistic description of finite deformation interactions between neighboring grains by considering the effects of the mismatch between grains and the orientation of the grain boundary.

## 5.1 Introduction

The finite deformation SGCP model developed in chapter 4 makes it possible to capture first- and second-order size effects within single crystals. Application of this model to predict size effects within poly-crystalline structures is only possible in the limiting cases of micro-free (fully transparent) and micro-hard (fully-opaque) grain boundary (GB) conditions. However, such limiting cases are too much simplified to accurately reproduce the GB contributions to the overall behavior of poly-crystalline structures. Indeed, the dislocation interactions across the grain boundaries (GBs) can have much more complex forms, including dislocation pile-ups, absorption, transmission and reflection, *etc.* (Bayerschen et al., 2016). With decreasing the geometrical size, the GB proportions become more significant and their contributions to the overall material behavior should be dealt with precisely. This concern has motivated the work of the present chapter which aims at shedding light on the modeling of finite deformation GB behaviors.

Several works related to GBs have been performed and various GB models have been developed in the literature (Cermelli and Gurtin, 2002; Gudmundson, 2004; Aifantis and Willis, 2005; Aifantis et al., 2006; Wulffinghoff et al., 2013; Bayerschen et al., 2015; Wulffinghoff, 2017). The first GB models have been formulated based on simplified phenomenological constitutive laws ignoring the crystallographic orientations at the interfaces between grains. These models have been successfully applied to reproduce some important GB phenomena, *e.g.*, GB hardening. However, they are not adapted to capture effects due to mismatch between grains and grain boundary orientation. To account for the latter effects, Gurtin (2008b) have proposed a small deformation crystallography-based GB model, which is of particular interest in our work as it is formulated using plastic-slip-based approach. The interesting features of this model have motivated several works proposing enhancements of such a model regarding some GB aspects (Gottschalk et al., 2016; Özdemir and Yalçinkaya, 2014; Voyiadjis et al., 2014). However, only few of them have been developed in finite deformation framework.

McBride et al. (2016) have proposed a finite deformation extension of the Gurtin (2008b) model using the plastic distortion rate tensor  $L^p$  to describe the mismatch between adjacent grains. This model has been formulated using Eulerian description, which is not widely used in the context of strain gradient continua. Peng et al. (2019) have developed a finite deformation GB model using the same  $L^p$  tensor to describe the GB mismatch. This model has been formulated within Lagrangian configuration using the assumption that the undistorted lattice resides in the reference (material) space with no lattice plastic distortion. According to Gurtin et al. (2010), this assumption is not relevant from a physical point of view as discussed in subsection 4.2.1. The present chapter aims at extending the GB model of Gurtin (2008b) using the same finite deformation description of single-crystal kinematics as in the previous chapter. This allows for easily coupling it with the finite deformation SGCP model discussed earlier in order to model size effects within poly-crystals.

The outline of this chapter is as follows. In Section 5.2, a new extension of the Gurtin (2008b) GB model to finite deformation will be derived using Lagrangian description. This model will be used to describe the interaction between grains whose material response will be described using the finite deformation SGCP model developed in chapter 4. Section 5.3 details the implementation of the extended GB model within the commercial finite element package Abaqus/Standard. Validation and assessment of this model are discussed in Section 5.4. Finally, some concluding remarks are given in Section 4.5.

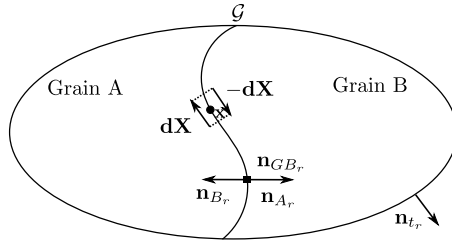


**Fig. 5.1.** A domain consisting of two grains A and B separated by grain boundary  $\mathcal{G}$  in the reference configuration.

## 5.2 Theoretical formulation

The present section details a new formulation of a finite deformation GB model proposed within fully Lagrangian framework. This model will be used to describe the interaction between grains considering the crystallographic orientations at the grain boundaries. The behavior within each grain is described using the finite deformation SGCP model presented in Chapter 4.

### 5.2.1 Finite deformation grain boundary kinematics

Consider a domain composed of two grains A and B separated by grain boundary  $\mathcal{G}$  (Fig. 5.1). In the reference configuration, the external surface unit normal vector is denoted by  $\mathbf{n}_{t_r}$ . Furthermore, the outward unit normal vectors associated with grains A and B at the grain boundary  $\mathcal{G}$  are respectively denoted by  $\mathbf{n}_{A_r}$  and  $\mathbf{n}_{B_r}$ . Let  $\mathbf{n}_{GB_r}$  denotes the unit normal vector at the grain boundary  $\mathcal{G}$  directed outward from grain A:

$$\mathbf{n}_{GB_r} = \mathbf{n}_{A_r} = -\mathbf{n}_{B_r} \quad (5.1)$$

Given an arbitrary field  $\phi$  in the considered domain, this field is assumed to be smooth in each grain and continuous up to the grain boundary  $\mathcal{G}$  from either grain. The jump of  $\phi$  across  $\mathcal{G}$  is given by:

$$\mathbb{G} = [\![\phi]\!] = \phi_B - \phi_A \quad (5.2)$$

The choice of the field  $\phi$  to control the interaction between grains represents the main difference between existing GB models.

Within small deformation framework, [Gurtin \(2008b\)](#) have proposed to use the grain boundary Burgers tensor to describe the mismatch between adjacent grains:

$$\mathbb{G}_{\text{Gurtin}} = [\![\mathbf{H}_B^p - \mathbf{H}_A^p]\!] (\mathbf{n}_{GB_r} \times) = [\![\mathbf{H}^p]\!] (\mathbf{n}_{GB_r} \times) \quad (5.3)$$

where  $\mathbf{H}^p$  represents the plastic distortion tensor and, for any vector  $\mathbf{v}$ , the quantity  $(\mathbf{v} \times)$  is a second-order tensor defined by  $(\mathbf{v} \times)_{ij} = \varepsilon_{ikj} v_k$ , with  $\varepsilon_{ikj}$  the permutation (Levi-Civita) symbol. This control field allows for considering both grain and grain boundary orientation effects. To the best of the authors' knowledge, finite deformation extensions of the [Gurtin \(2008b\)](#) GB model including both these effects can only be found in [McBride et al. \(2016\)](#) and [Peng et al. \(2019\)](#). The formulation of [McBride et al. \(2016\)](#) has been developed using Eulerian description within the current configuration. The geometrical GB mismatch is characterized by the spatial plastic

distortion rate tensor defined by  $\mathbf{L}_c^p = \mathbf{F}^e \mathbf{L}^p \mathbf{F}^{e-1}$ , with  $\mathbf{F}^e$  the elastic distortion tensor (4.1) and  $\mathbf{L}^p$  the lattice plastic distortion rate tensor (4.6):

$$\dot{\mathbb{G}}_{\text{McBride}} = [\mathbf{L}_{B_c}^p - \mathbf{L}_{A_c}^p] (\mathbf{n}_{GB_r} \times) = \llbracket \mathbf{L}_c^p \rrbracket (\mathbf{n}_{GB_c} \times), \quad \mathbb{G}_{\text{McBride}} = \int_0^t \dot{\mathbb{G}}_{\text{McBride}} dt \quad (5.4)$$

$\mathbf{n}_{GB_c}$  represents the GB unit normal expressed in the current configuration. Based on the assumption that the undistorted lattice resides in the reference (material) space, with isoclinic mapping from this space to the lattice one, a simplified version of the GB model of Peng et al. (2019) implies the following incompatibility tensor:

$$\dot{\mathbb{G}}_{\text{Peng}} = [\mathbf{L}_{B_r}^p - \mathbf{L}_{A_r}^p] (\mathbf{n}_{GB_r} \times) = \llbracket \mathbf{L}_r^p \rrbracket (\mathbf{n}_{GB_r} \times), \quad \mathbb{G}_{\text{Peng}} = \int_0^t \dot{\mathbb{G}}_{\text{Peng}} dt \quad (5.5)$$

with  $\mathbf{L}_r^p = \mathbf{L}^p$  (the lattice vectors are assumed to remain constant when going from the reference to the lattice configuration). Although used in several gradient-enhanced finite deformation works, the assumption on which relies the model of Peng et al. (2019) seems not physically relevant according to Gurtin et al. (2010) who state that the lattice vectors cannot be material.

Following similar procedure as in Gurtin (2008b), a finite deformation counterpart of (5.3) is derived hereafter within Lagrangian framework. In the present GB derivation, the lattice is assumed to be defined in the structural configuration (Gurtin et al., 2010). Consider an arbitrary point  $\mathbf{X}$  on the grain boundary  $\mathcal{G}$  and an arbitrary line vector  $d\mathbf{X}$  at this point tangent to  $\mathcal{G}$ . Let  $d\Gamma$  be an infinitesimal circuit consisting of  $d\mathbf{X}$  in grain A and  $-d\mathbf{X}$  in grain B (Fig. 5.1). The Burgers vector associated with  $d\Gamma$  can be defined in finite deformation as (Cermelli and Gurtin, 2001):

$$\mathbf{b}_r(d\Gamma) = \int_{d\Gamma} \mathbf{F}^p d\mathbf{X} = \int_{dS_\Gamma} \operatorname{curl}(\mathbf{F}^p)^T \mathbf{n}_r d\mathbf{X} \quad (5.6)$$

where  $dS_\Gamma$  is a surface element bounded by  $d\Gamma$ . Note that  $\operatorname{curl}(\mathbf{F}^p)^T = \mathbf{0}$  for any compatible plastic deformation (*i.e.*, gradient of a vector field). This tensor provides a measure of the plastic deformation incompatibility. With the considered infinitesimal circuit, the following relation can be obtained:

$$\int_{d\Gamma} \mathbf{F}^p d\mathbf{X} = -[\mathbf{F}_B^p - \mathbf{F}_A^p] \cdot d\mathbf{X} = -\llbracket \mathbf{F}^p \rrbracket \cdot d\mathbf{X} \quad (5.7)$$

Since the vector  $d\mathbf{X}$  is tangent to  $\mathcal{G}$ , it can be replaced by its projection on  $\mathcal{G}$  without loss in generality:

$$-\llbracket \mathbf{F}^p \rrbracket d\mathbf{X} = -\llbracket \mathbf{F}^p \rrbracket (\mathbf{I} - \mathbf{n}_{GB_r} \otimes \mathbf{n}_{GB_r}) d\mathbf{X} \quad (5.8)$$

The above equation can further be reformulated using the following identity relation:

$$\mathbf{I} - \mathbf{n}_{GB_r} \otimes \mathbf{n}_{GB_r} = -(\mathbf{n}_{GB_r} \times) (\mathbf{n}_{GB_r} \times) \quad (5.9)$$

which gives:

$$-\llbracket \mathbf{F}^p \rrbracket d\mathbf{X} = \llbracket \mathbf{F}^p \rrbracket (\mathbf{n}_{GB_r} \times) (\mathbf{n}_{GB_r} \times) d\mathbf{X} = (\llbracket \mathbf{F}^p \rrbracket (\mathbf{n}_{GB_r} \times)) (\mathbf{n}_{GB_r} \times d\mathbf{X}) \quad (5.10)$$

Note that  $-\mathbf{n}_{GB_r} \times d\mathbf{X}$  represents an area element directed orthogonal to  $dS_\Gamma$  (surface element bounded by  $d\Gamma$ ) and tangent to the grain boundary. The minus sign is added to obtain right-handed normal direction with respect to the orientation of  $d\Gamma$  (Fig. 5.1). The tensor defined by:

$$\mathbb{G} = [\![\mathbf{F}^p]\!] (\mathbf{n}_{GB_r} \times) \quad (5.11)$$

can be viewed as a generalization of (5.3) in finite deformation. This tensor will be referred to hereafter as GB Burgers tensor. Its rate form is given by:

$$\dot{\mathbb{G}} = [\![\dot{\mathbf{F}}^p]\!] (\mathbf{n}_{GB_r} \times) \quad (5.12)$$

and can be interpreted as the Burgers vector flow out of the grain boundary  $\mathcal{G}$  from the grains or also the Burgers vector production within the grain boundary.  $\dot{\mathbb{G}}$  provides a rate-like measure of the kinematic and geometric mismatch at the grain boundary in finite deformation and will be used in the following to develop a finite deformation GB model based on Lagrangian description. As in Gurtin (2008b), this model is based on the assumption that no displacement jump occurs at the grain boundaries, i.e. no grain boundary sliding or opening takes place. For GB models involving GB sliding within strain gradient plasticity framework, the reader can refer to the works of Cermelli and Gurtin (2002) and Gurtin and Anand (2008).

### 5.2.2 Principle of virtual power and governing equations

The domain of Fig. 5.1, which consists of two grains, is considered in this subsection to derive the principle of virtual power. However, the following developments are also valid for domains with multiple grains. Consider a subregion  $V_0$  of boundary  $S_0$  ( $S_0 = \partial V_0$ ) containing two grain portions separated by grain boundary  $S_{GB}$ . The internal and external power expenditures in this subregion can be written as (in static case and neglecting body forces):

$$\mathcal{P}_{int} = \int_{V_0} \mathbf{P}^e : \dot{\mathbf{F}}^e dv_0 + \sum_{\alpha=1}^q \int_{V_0} [\pi^\alpha \dot{\gamma}^\alpha + \boldsymbol{\xi}^\alpha \cdot \mathbf{grad}_X(\dot{\gamma}^\alpha)] dv_0 + \int_{S_{GB}} \dot{\phi}_{GB} ds_0 \quad (5.13)$$

$$\mathcal{P}_{ext} = \int_{S_0} \mathbf{t} \cdot \dot{\mathbf{u}} ds_0 + \sum_{\alpha=1}^q \int_{S_0} \chi^\alpha \dot{\gamma}^\alpha ds_0 \quad (5.14)$$

where  $\mathbf{P}^e$  represents the first elastic Piola-Kirchhoff stress tensor (power-conjugate to  $\dot{\mathbf{F}}^e$ ),  $\pi^\alpha$  is a scalar microscopic stress (power-conjugate to  $\dot{\gamma}^\alpha$ ),  $\boldsymbol{\xi}^\alpha$  is a vector microscopic stress (power-conjugate to  $\mathbf{grad}_X(\dot{\gamma}^\alpha)$ ),  $\mathbf{t}$  is a macroscopic surface traction,  $\chi^\alpha$  is a microscopic surface traction, and  $\mathbf{grad}_X(\bullet)$  is the Lagrangian gradient operator (i.e., w.r.t. the Lagrangian coordinates). The field  $\dot{\phi}_{GB}$  is a grain boundary field that accounts for power expenditure due to GB mechanisms. With the assumption of no displacement jump across the grain boundaries, this field depends only on microscopic GB mechanisms and can be defined as:

$$\dot{\phi}_{GB} = \mathbb{K} : \dot{\mathbb{G}} = \mathbb{K} : [\![\dot{\mathbf{F}}^p]\!] (\mathbf{n}_{GB_r} \times) = \mathbb{K} : [\dot{\mathbf{F}}_B^p (\mathbf{n}_{GB_r} \times) - \dot{\mathbf{F}}_A^p (\mathbf{n}_{GB_r} \times)] \quad (5.15)$$

where  $\mathbb{K}$  is an internal GB microscopic stress tensor (power-conjugate to  $\dot{\mathbb{G}}$ ). Using (4.3) and (4.6), the above relation (5.15) can be rewritten as:

$$\dot{\phi}_{GB} = \sum_{\alpha=1}^q \dot{\gamma}^\alpha \mathbb{K} : [\mathbb{N}_B^\alpha - \mathbb{N}_A^\alpha] \quad (5.16)$$

where, for  $J \in \{A, B\}$ ,  $\mathbb{N}_J^\alpha$  is defined by:

$$\mathbb{N}_J^\alpha = \mathbb{S}_J^\alpha \mathbf{F}_J^p (\mathbf{n}_{GBr} \times) = \mathbf{s}_J^\alpha \otimes \left( \mathbf{F}_J^{pT} \mathbf{m}_J^\alpha \times \mathbf{n}_{GBr} \right) \quad (5.17)$$

Application of the generalized principle of virtual power (Forest, 2009) yields to:

$$\begin{aligned} \int_{V_0} \mathbf{P}^e : \dot{\mathbf{F}}^e dv_0 + \sum_{\alpha=1}^q \int_{V_0} [\pi^\alpha \dot{\gamma}^\alpha + \boldsymbol{\xi}^\alpha \cdot \mathbf{grad}_X(\dot{\gamma}^\alpha)] dv_0 + \sum_{\alpha=1}^q \int_{S_{GB}} \dot{\gamma}^\alpha \mathbb{K} : [\mathbb{N}_B^\alpha - \mathbb{N}_A^\alpha] ds_0 \\ = \int_{S_0} \mathbf{t} \cdot \dot{\mathbf{u}} ds_0 + \sum_{\alpha=1}^q \int_{S_0} \chi^\alpha \dot{\gamma}^\alpha ds_0 \end{aligned} \quad (5.18)$$

Bearing in mind (4.11), by setting  $\dot{\gamma}^\alpha = 0$ , the above equation reduces to:

$$\int_{S_0} (\mathbf{P} \mathbf{n}) \cdot \dot{\mathbf{u}} ds_0 - \int_{V_0} \mathbf{div}_X(\mathbf{P}) : \dot{\mathbf{u}} dv_0 = \int_{S_0} \mathbf{t} \cdot \dot{\mathbf{u}} ds_0$$

and the macroscopic balance equations along with the macroscopic boundary conditions can be derived as:

$$\begin{aligned} \mathbf{div}_X(\mathbf{P}) = \mathbf{0} & \quad \text{in } V_0 \\ \mathbf{P} \mathbf{n}_{tr} = \mathbf{t} & \quad \text{on } S_0 \end{aligned} \quad (5.19)$$

Assuming  $\dot{\mathbf{u}} = \mathbf{0}$  and using (4.11), the principle of virtual power (5.18) becomes:

$$\begin{aligned} \sum_{\alpha=1}^q \int_{V_0} [\pi^\alpha \dot{\gamma}^\alpha - \tau^\alpha \dot{\gamma}^\alpha - \mathbf{div}_X(\boldsymbol{\xi}^\alpha) \dot{\gamma}^\alpha] dv_0 + \sum_{\alpha=1}^q \int_{S_0} \boldsymbol{\xi}^\alpha \cdot \mathbf{n}_0 \dot{\gamma}^\alpha ds_0 - \sum_{\alpha=1}^q \int_{S_0} \chi^\alpha \dot{\gamma}^\alpha ds_0 \\ = \sum_{\alpha=1}^q \int_{S_{GB}} (\boldsymbol{\xi}_B^\alpha \cdot \mathbf{n}_{GBr} \dot{\gamma}_B^\alpha - \boldsymbol{\xi}_A^\alpha \cdot \mathbf{n}_{GBr} \dot{\gamma}_A^\alpha) ds_0 - \sum_{\alpha=1}^q \int_{S_{GB}} \dot{\gamma}^\alpha \mathbb{K} : [\mathbb{N}_B^\alpha - \mathbb{N}_A^\alpha] ds_0 \end{aligned} \quad (5.20)$$

Therefore, the microscopic balance equations and the associated boundary and interface conditions can be derived as:

$$\begin{aligned} \mathbf{div}_X(\boldsymbol{\xi}^\alpha) + \tau^\alpha - \pi^\alpha &= 0 \quad \text{in } V_0 \\ \boldsymbol{\xi}^\alpha \cdot \mathbf{n}_{tr} &= \chi^\alpha \quad \text{on } S_0 \\ \boldsymbol{\xi}_A^\alpha \cdot \mathbf{n}_{GBr} &= \mathbb{K} : \mathbb{N}_A^\alpha \quad \text{on } S_{GB} \\ \boldsymbol{\xi}_B^\alpha \cdot \mathbf{n}_{GBr} &= \mathbb{K} : \mathbb{N}_B^\alpha \quad \text{on } S_{GB} \end{aligned} \quad (5.21)$$

### 5.2.3 Free energy imbalance

The free energy imbalance (second thermodynamic law) requires that the temporal increase of the free energy in an arbitrary subregion  $V_0$  be less than or equal to the external power expended on  $V_0$ . Introducing the free energy per unit volume in the bulk  $\Psi_{Bulk}$  and the free energy per unit area at the grain boundary  $\Psi_{GB}$ , this can mathematically be formulated as follows:

$$\int_{V_0} \left\{ \dot{\Psi}_{Bulk} - \mathbf{P}^e : \dot{\mathbf{F}}^e - \sum_{\alpha=1}^q (\pi^\alpha \dot{\gamma}^\alpha + \boldsymbol{\xi}^\alpha \cdot \mathbf{grad}_X(\dot{\gamma}^\alpha)) \right\} dv_0 + \int_{S_{GB}} \left\{ \dot{\Psi}_{GB} - \mathbb{K} : \dot{\mathbb{G}} \right\} ds_0 \leq 0 \quad (5.22)$$

As  $V_0$  is an arbitrary subregion, the local free energy imbalance in the bulk and at the grain boundary can be obtained as (noting that  $\mathbf{P}^e : \dot{\mathbf{F}}^e = \mathbf{S}^e : \dot{\mathbf{E}}^e$ ):

$$\dot{\Psi}_{Bulk} - \mathbf{S}^e : \dot{\mathbf{E}}^e - \sum_{\alpha=1}^q (\pi^\alpha \dot{\gamma}^\alpha + \boldsymbol{\xi}^\alpha \cdot \mathbf{grad}_X(\dot{\gamma}^\alpha)) \leq 0 \quad (5.23)$$

$$\dot{\Psi}_{GB} - \mathbb{K} : \dot{\mathbb{G}} \leq 0 \quad (5.24)$$

with  $\mathbf{S}^e$  the second Piola elastic stress tensor (4.10) and  $\dot{\mathbf{E}}^e$  the elastic Green-Lagrange strain tensor (4.15).

### 5.2.4 Constitutive laws

The constitutive laws in the bulk material, including both energetic and dissipative contributions, are identical to those derived in Subsection 4.2.4. The present subsection focuses on the derivation of the constitutive laws at the grain boundary. The free energy arising from GB is assumed to be a quadratic function of the Burgers tensor given by (5.11):

$$\Psi_{GB} = \Psi_{GB}(\mathbb{G}) = \frac{1}{2} \kappa \|\mathbb{G}\|^2 \quad (5.25)$$

where  $\kappa > 0$  is a material constant for grain boundary. In the rate form, this energy can be written:

$$\dot{\Psi}_{GB} = \frac{\partial \Psi_{GB}}{\partial \mathbb{G}} : \dot{\mathbb{G}} \quad (5.26)$$

Substituting (5.26) into (5.24), the GB local free energy imbalance becomes:

$$\left( \mathbb{K} - \frac{\partial \Psi_{GB}}{\partial \mathbb{G}} \right) : \dot{\mathbb{G}} \geq 0 \quad (5.27)$$

In order to model both energetic and dissipative effects at the GBs,  $\mathbb{K}$  is assumed to be divided into energetic and dissipative parts ( $\mathbb{K} = \mathbb{K}_{en} + \mathbb{K}_{dis}$ ).  $\mathbb{K}_{en}$  can be obtained as:

$$\mathbb{K}_{en} = \frac{\partial \Psi_{GB}}{\partial \mathbb{G}} = \kappa \mathbb{G} \quad (5.28)$$

which leads to the following reduced GB dissipation inequality:

$$\mathcal{D} = \mathbb{K}_{dis} : \dot{\mathbb{G}} \geq 0 \quad (5.29)$$

To model  $\mathbb{K}_{dis}$ , an accumulated GB defectiveness defined by

$$\dot{\Delta} = \|\dot{\mathbb{G}}\|, \quad \Delta = \int \dot{\Delta} dt \quad (5.30)$$

is introduced, representing the impermeability of GBs to the flow of Burgers vector. Inspired by (Gurtin and Needleman, 2005; Gurtin, 2008b), the GB dissipative stress tensor is assumed to be described as:

$$\mathbb{K}_{dis} = S_{GB} \left( \frac{\dot{\Delta}}{\dot{G}_0} \right)^d \frac{\dot{\mathbb{G}}}{\dot{\Delta}} \quad (5.31)$$

where  $S_{GB} > 0$  represents a dissipative hardening function at the GBs,  $d > 0$  a sensitivity parameter for GB, and  $\dot{G}_0 > 0$  is a scalar reference rate of GB Burgers tensor. To model GB hardening,  $S_{GB}$  is assumed to evolve according to:

$$\dot{S}_{GB} = H_{GB} \dot{\Delta} \quad \text{with} \quad S_{GB}(0) = S_{GB_0} \geq 0 \quad (5.32)$$

where  $H_{GB}$  is GB hardening modulus and  $S_{GB_0}$  is the initial grain boundary defectiveness resistance.

## 5.2.5 Summary of field equations

The basic equations involved in the proposed theory, considering both the bulk and grain boundary, can be summarized as:

- kinematical equations:

$$\mathbf{F} = \mathbf{F}^e \mathbf{F}^p, \quad \mathbf{L}^p = \sum_{\alpha} \dot{\gamma}^{\alpha} \mathbb{S}^{\alpha}$$

$$\mathbb{G} = [\![\mathbf{F}^p]\!] (\mathbf{n}_{GB_r} \times)$$

- macroscopic balance equations along with macroscopic boundary conditions:

$$\begin{aligned} \operatorname{div}_X(\mathbf{P}) &= \mathbf{0} && \text{in } V_0 \\ \mathbf{P} \mathbf{n}_{tr} &= \mathbf{t} && \text{on } S_0 \end{aligned} \quad (5.33)$$

- microscopic balance equations along with microscopic boundary and interface conditions:

$$\begin{aligned} \operatorname{div}_X(\boldsymbol{\xi}^{\alpha}) + \tau^{\alpha} - \pi^{\alpha} &= 0 && \text{in } V_0 \\ \boldsymbol{\xi}^{\alpha} \cdot \mathbf{n}_{tr} &= \chi^{\alpha} && \text{on } S_0 \\ \boldsymbol{\xi}_B^{\alpha} \cdot \mathbf{n}_{GB_r} &= \mathbb{K} : [\mathbb{S}_B^{\alpha} \mathbf{F}_B^p (\mathbf{n}_{GB_r} \times)] && \text{on } S_{GB} \\ \boldsymbol{\xi}_A^{\alpha} \cdot \mathbf{n}_{GB_r} &= \mathbb{K} : [\mathbb{S}_A^{\alpha} \mathbf{F}_A^p (\mathbf{n}_{GB_r} \times)] && \text{on } S_{GB} \end{aligned}$$

- constitutive equations in the bulk:

$$\begin{aligned}\mathbf{S}^e &= \mathbb{C} : \mathbf{E}^e \\ \pi_{dis}^\alpha &= S_\pi^\alpha \left( \frac{\dot{\epsilon}_\pi^\alpha}{\dot{\gamma}_0^\alpha} \right)^m \frac{\dot{\gamma}^\alpha}{\dot{\epsilon}_\pi^\alpha} \\ \boldsymbol{\xi}_{en}^\alpha &= X_0 l_{en}^n \left( -|\rho_\vdash^\alpha|^{n-2} \rho_\vdash^\alpha \mathbf{s}_r^\alpha + |\rho_\odot^\alpha|^{n-2} \rho_\odot^\alpha \mathbf{l}_r^\alpha \right) \\ \boldsymbol{\xi}_{dis}^\alpha &= S_\xi^\alpha l_{dis}^2 \left( \frac{\dot{\epsilon}_\xi^\alpha}{\dot{\gamma}_0^\alpha} \right)^m \frac{\mathbf{grad}_X^\alpha(\dot{\gamma}^\alpha)}{\dot{\epsilon}_\xi^\alpha}\end{aligned}$$

- constitutive equations at the GB:

$$\begin{aligned}\mathbb{K}_{en} &= \kappa \mathbb{G} \\ \mathbb{K}_{dis} &= S_{GB} \left( \frac{\dot{\Delta}}{\dot{G}_0} \right)^d \frac{\dot{\mathbb{G}}}{\dot{\Delta}}, \quad \dot{S}_{GB} = H_{GB} \dot{\Delta}\end{aligned}$$

## 5.3 Numerical implementation

In this section, the proposed finite deformation GB model will be implemented using Lagrangian description within the framework of the two-dimensional version of the SGCP model presented in Chapter 4. It is worth recalling that both displacement and plastic scalar fields ( $\mathbf{u}$  and  $\gamma^\alpha$ ) are considered as primary variables (degrees of freedom). Although the weak forms will be provided for both the bulk and the grain boundary, numerical details will only be given for the GB contributions to the overall system of equations associated with the studied problem.

### 5.3.1 Weak forms

Assume the virtual fields  $\delta\dot{\mathbf{u}}$  and  $\delta\dot{\gamma}^\alpha$  which are kinematically admissible to zero on the portions of the boundary of the studied domain on which macroscopic and microscopic Dirichlet boundary conditions are respectively imposed. The weak forms of the macroscopic (5.19)<sub>1</sub> and microscopic (5.21)<sub>1</sub> balance equations can be obtained as:

$$G_u = \int_{V_0} \mathbf{grad}_X(\delta\dot{\mathbf{u}}) : \mathbf{P} dv_0 - \int_{S_0^t} \delta\dot{\mathbf{u}} \cdot \mathbf{t} ds_0 \quad (5.34)$$

$$\begin{aligned}G_\gamma = \sum_{\alpha=1}^q &\left( \int_{V_0} \mathbf{grad}_X(\delta\dot{\gamma}^\alpha) \cdot \boldsymbol{\xi}^\alpha dv_0 + \int_{V_0} \delta\dot{\gamma}^\alpha \pi^\alpha dv - \int_{V_0} \delta\dot{\gamma}^\alpha \tau^\alpha dv_0 \right) \\ &- \sum_{\alpha=1}^q \int_{S_0^{\chi^\alpha}} \delta\dot{\gamma}^\alpha \chi^\alpha ds_0 - \sum_{\alpha=1}^q \int_{S_{GB}} \boldsymbol{\xi}_A^\alpha \cdot \mathbf{n}_{A_r} \dot{\gamma}_A^\alpha + \boldsymbol{\xi}_B^\alpha \cdot \mathbf{n}_{B_r} \dot{\gamma}_B^\alpha ds_0\end{aligned} \quad (5.35)$$

where  $S_0^t$  and  $S_0^{\chi^\alpha}$  are the portions of the domain boundary on which macroscopic and microscopic traction forces, noted respectively as  $\mathbf{t}$  and  $\chi^\alpha$ , are imposed. The last term of (5.35) represents the GB contribution and will be noted as  $G_\gamma^{\text{GB}}$ :

$$G_\gamma^{\text{GB}} = - \sum_{\alpha=1}^q \int_{S_{GB}} \boldsymbol{\xi}_A^\alpha \cdot \mathbf{n}_{A_r} \dot{\gamma}_A^\alpha + \boldsymbol{\xi}_B^\alpha \cdot \mathbf{n}_{B_r} \dot{\gamma}_B^\alpha ds_0 \quad (5.36)$$

Using the GB equilibrium equations (5.21)<sub>3,4</sub>, together with the convention of the GB normal direction (5.1),  $G_\gamma^{\text{GB}}$  can be rewritten as:

$$\begin{aligned} G_\gamma^{\text{GB}} &= \sum_{\alpha=1}^q \int_{S_{GB}} \mathbb{N}_B^\alpha : \mathbb{K} \delta \dot{\gamma}_B^\alpha - \mathbb{N}_A^\alpha : \mathbb{K} \delta \dot{\gamma}_A^\alpha ds_0 \\ &= \sum_{\alpha=1}^q \int_{S_{GB}} \Pi_B^\alpha \delta \dot{\gamma}_B^\alpha - \Pi_A^\alpha \delta \dot{\gamma}_A^\alpha ds_0 \end{aligned} \quad (5.37)$$

with  $\Pi_A^\alpha = \mathbb{N}_A^\alpha : \mathbb{K}$  and  $\Pi_B^\alpha = \mathbb{N}_B^\alpha : \mathbb{K}$

### 5.3.2 Finite element discretization

The finite elements for the bulk and the grain boundary are illustrated in Fig. 5.2. For the bulk material, eight-noded (quadratic) interpolation of  $\mathbf{u}$ , four-noded (linear) interpolation of  $\gamma^\alpha$  and  $2 \times 2$  Gauss integration is adopted, as explained in Chapter 4. Within each bulk finite element, the displacements  $u_i$  ( $i = 1, 2$ ) and plastic scalar variables  $\gamma^\alpha$  ( $\alpha = 1, 2, \dots, q$ ) can be approximated based on the associated nodal values as follows:

$$u^i = \sum_{k=1}^8 N_u^k U_k^i, \quad \gamma^\alpha = \sum_{k=1}^4 N_\gamma^k \Gamma_k^\alpha \quad (5.38)$$

where  $U_k^i$  and  $\Gamma_k^\alpha$  are nodal values of displacements and plastic scalar variables, and  $N_u^k$  and  $N_\gamma^k$  are the associated interpolation functions.

Several techniques can be found in the literature to model grain boundaries. One of these techniques consists in using the same finite element type as in the bulk part while discretizing the GB region using sufficiently thin elements (McBride et al., 2016; Gottschalk et al., 2016). As stated by (Gottschalk et al., 2016), the GB is usually only 1 – 2 atoms thick compared to the bulk phase. In this technique, penalty approach is applied to control the displacement jump across the GB. In the present work, the GB is modeled by zero-thickness finite elements which are obtained by duplicating interface nodes of adjacent bulk elements when separated by the GB. Fig. 5.2 presents an example of a GB element where the duplicated nodes from grain A and B are distanced for clarity (nodes at the interface edge of grain B are duplicated from those of the interface edge of grain A). This GB discretization technique is most commonly used in the literature (van Beers et al., 2013; Özdemir and Yalçinkaya, 2016; McBride et al., 2016; Peng et al., 2019). Simultaneously, to ensure the displacement continuity at the GB, the displacements of duplicated nodes are forced to be equivalent using kinematic constraints (*i.e.*,  $\mathbf{u}_3 = \mathbf{u}_{12}$ ,  $\mathbf{u}_6 = \mathbf{u}_{16}$ ,  $\mathbf{u}_2 = \mathbf{u}_9$  in the example of Fig. 5.2). The two adjacent edges of the bulk elements form a zero-thickness grain boundary element following a counter-clockwise node numbering order: 9, 12, 3, 2, 16, 6. Two-noded line element with 2-point Gauss integration is chosen to interpolate the plastic scalar variables  $\gamma^\alpha$  at the grain boundary.

Within each GB element, plastic slip fields from grain A and B are interpolated by:

$$\begin{bmatrix} \gamma_A^\alpha \\ \gamma_B^\alpha \end{bmatrix} = \begin{bmatrix} 0 & 0 & N_\gamma^1 & N_\gamma^2 \\ N_\gamma^2 & N_\gamma^1 & 0 & 0 \end{bmatrix} \begin{bmatrix} \Gamma_9^\alpha \\ \Gamma_{12}^\alpha \\ \Gamma_3^\alpha \\ \Gamma_2^\alpha \end{bmatrix} = \begin{bmatrix} N_{\gamma_A}^\alpha \\ N_{\gamma_B}^\alpha \end{bmatrix} \begin{bmatrix} \Gamma_9^\alpha \\ \Gamma_{12}^\alpha \\ \Gamma_3^\alpha \\ \Gamma_2^\alpha \end{bmatrix} \quad (5.39)$$

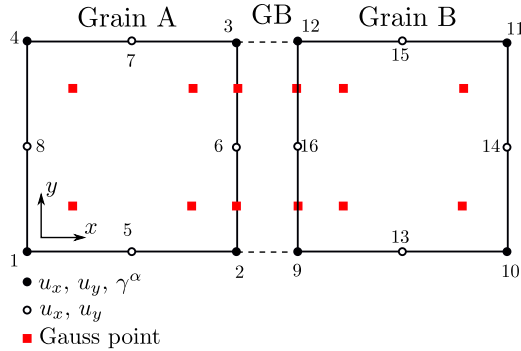


**Fig. 5.2.** Illustration of bulk material element and grain boundary element used in this work.

where  $\Gamma_k^\alpha$  are nodal values of plastic scalar variables, and  $N_\gamma^1$  and  $N_\gamma^2$  are the associated interpolation functions defined in the GB. Using the GB field approximation (5.39), the GB contribution to the weak form (5.35) can be rewritten as:

$$G_{\gamma_{GB}}^e = \left( \delta \underline{\underline{\Gamma}}^e \right)^T \int_{S_{GB}} \underline{\underline{N}}_{\gamma_B}^T \cdot \underline{\underline{\Pi}}_B - \underline{\underline{N}}_{\gamma_A}^T \cdot \underline{\underline{\Pi}}_A ds_0$$

where  $\underline{\underline{N}}_{\gamma_A}$  and  $\underline{\underline{N}}_{\gamma_B}$  are the interpolation matrices associated with the plastic scalar fields from grain A and B respectively, and  $\underline{\underline{\Pi}}_A$  and  $\underline{\underline{\Pi}}_B$  are vector representations of the microscopic grain boundary induced stresses on all slip systems. The GB residual can then be expressed as:

$$\underline{R}_{\gamma_{GB}}^e = \int_{S_{GB}} \underline{\underline{N}}_{\gamma_B}^T \cdot \underline{\underline{\Pi}}_B - \underline{\underline{N}}_{\gamma_A}^T \cdot \underline{\underline{\Pi}}_A ds_0 \quad (5.40)$$

and the corresponding tangent matrix is given by:

$$\begin{aligned} \underline{\underline{K}}_{\gamma\gamma_{GB}}^e &= \frac{\partial \underline{R}_{\gamma_{GB}}^e}{\partial \Delta \underline{\underline{\Gamma}}} \\ &= \int_{S_{GB}} \left( \underline{\underline{N}}_{\gamma_B}^T \frac{\partial \underline{\underline{\Pi}}_B}{\partial \Delta \underline{\underline{\Gamma}}} - \underline{\underline{N}}_{\gamma_A}^T \frac{\partial \underline{\underline{\Pi}}_A}{\partial \Delta \underline{\underline{\Gamma}}} \right) ds_0 \\ &= \int_{S_{GB}} \left\{ \underline{\underline{N}}_{\gamma_B}^T \left( \frac{\partial \underline{\underline{\Pi}}_B}{\partial \Delta \underline{\underline{\gamma}}_B} \underline{\underline{N}}_{\gamma_B} + \frac{\partial \underline{\underline{\Pi}}_B}{\partial \Delta \underline{\underline{\gamma}}_A} \underline{\underline{N}}_{\gamma_A} \right) - \underline{\underline{N}}_{\gamma_A}^T \left( \frac{\partial \underline{\underline{\Pi}}_A}{\partial \Delta \underline{\underline{\gamma}}_A} \underline{\underline{N}}_{\gamma_A} + \frac{\partial \underline{\underline{\Pi}}_A}{\partial \Delta \underline{\underline{\gamma}}_B} \underline{\underline{N}}_{\gamma_B} \right) \right\} ds_0 \end{aligned} \quad (5.41)$$

Detailed derivation of (5.41) is presented in Appendix C.3.

Considering the GB contributions, the overall linearized system of equations associated with the global studied problem presents the following form:

$$\begin{bmatrix} \underline{\underline{K}}_{uu} & \underline{\underline{K}}_{u\gamma} \\ \underline{\underline{K}}_{\gamma u} & \underline{\underline{K}}_{\gamma\gamma} + \underline{\underline{K}}_{\gamma\gamma_{GB}} \end{bmatrix} \begin{bmatrix} \Delta \underline{\underline{U}} \\ \Delta \underline{\underline{\Gamma}} \end{bmatrix} = - \begin{bmatrix} \underline{R}_u \\ \underline{R}_\gamma + \underline{R}_{\gamma_{GB}} \end{bmatrix} \quad (5.42)$$

where  $\underline{\underline{K}}_{uu}$ ,  $\underline{\underline{K}}_{u\gamma}$ ,  $\underline{\underline{K}}_{\gamma u}$ ,  $\underline{\underline{K}}_{\gamma\gamma}$ ,  $\underline{R}_u$  and  $\underline{R}_\gamma$  are obtained by assembling the elementary systems of equations in the bulk material given by (4.49), and  $\underline{\underline{K}}_{\gamma\gamma_{GB}}$  and  $\underline{R}_{\gamma_{GB}}$  are obtained by assembling the elementary systems of equations at the grain boundaries. The GB element has been implemented within the commercial finite element package ABAQUS/Standard using a separate User-EElement (UEL) subroutine. For comparison purposes, the small deformation GB element of Gurtin (2008b) has also been implemented within Abaqus/Standard using the same GB element type.

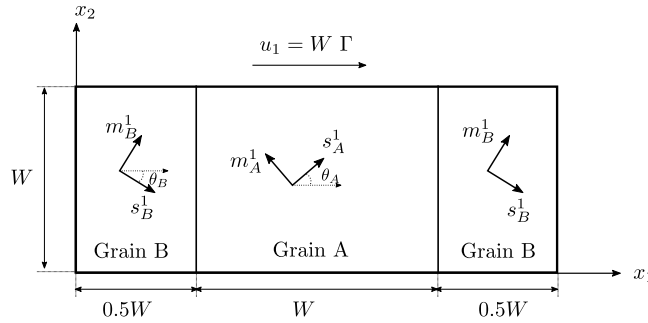


**Fig. 5.3.** A bi-crystal example for the validation and assessment of the proposed finite deformation grain boundary model.

## 5.4 Numerical results

This section aims at validating and assessing the proposed finite deformation GB model. For the validation of the model and the investigation of the model parameters, a 2D periodic bi-crystal plate subjected to monotonic and cyclic simple shear loading conditions is used. The model is then applied to study the mechanical response of a poly-crystalline square plate with randomly distributed grains under proportional and non-proportional shear loading conditions. To investigate the possible formation of elastic gaps due to GB effects, only energetic effects with quadratic defect energy is applied in the grains. This choice prevents formation of elastic gaps due to bulk effects as discussed in Chapter 3.

### 5.4.1 Validation of the GB model

The geometrical model used in this subsection is presented in Fig. 5.3. It consists of periodic bi-crystal in  $x_1$  and  $x_2$  directions. Grains A and B composing this bi-crystal present the same dimensions  $W \times W$ . For each grain, single slip system is considered with orientation  $\theta_A$  in grain A and  $\theta_B$  in grain B with respect to  $x_1$  direction (Fig. 5.3). Following van Beers et al. (2013), the grain misorientation and grain boundary orientation are respectively quantified using:

$$\theta_M = \theta_A - \theta_B \quad \text{and} \quad \theta_{GB} = \frac{1}{2} (\theta_A + \theta_B) \quad (5.43)$$

In the present subsection, the slip system orientations are chosen such that  $\theta_A = -\theta_B = 10^\circ$  (*i.e.*,  $\theta_M = 20^\circ$  and  $\theta_{GB} = 0^\circ$ ).

The macroscopic boundary conditions are given by:

$$\left. \begin{array}{l} u_1 = 0 \quad \text{along} \quad x_2 = 0 \\ u_1 = W \Gamma \quad \text{along} \quad x_2 = W \end{array} \right\} \quad (5.44)$$

where  $\Gamma = 0.04$  is the prescribed shear strain. Furthermore, to avoid rigid body displacement along  $x_2$  direction, the left-bottom corner is fixed:  $u_2(0, 0, t) = 0$ . Additional boundary conditions are

**Tab. 5.1.** Material parameters implied for simple shear of periodic bi-crystal plate, inspired by Peirce et al. (1983); Kuroda (2011).

Material parameter name	Symbol	Value	Unit
Young's modulus	$E$	60.84	GPa
Poisson's ratio	$\nu$	0.3	—
Reference slip rate for bulk	$\dot{\gamma}_0^\alpha$	0.001	$s^{-1}$
Rate-sensitivity parameter for bulk	$m$	0.05	—
Higher-order energetic slip resistance	$X_0$	60.84	MPa
Initial first-order dissipative slip resistance	$S_{\pi 0}$	60.84	MPa
Initial higher-order dissipative slip resistance	$S_{\xi 0}$	Not used	MPa
First-order hardening modulus	$H_\pi$	0	MPa
Second-order hardening modulus	$H_\xi$	Not used	MPa
Energetic length scale	$l_{en}$	case study	$\mu m$
Dissipative length scale	$l_{dis}$	0	$\mu m$
Defect energy index	$n$	2	—
Reference flow rate for GB	$\dot{G}_0$	0.001	$s^{-1}$
Rate-sensitivity parameter for GB	$d$	0.05	—
Energetic coefficient for GB	$\kappa$	case study	$N m^{-1}$
Dissipative initial slip resistance for GB	$S_{GB_0}$	case study	$N m^{-1}$
Dissipative hardening modulus for GB	$H_{GB}$	case study	$N m^{-1}$

also imposed on the model edges to ensure  $x_1$  and  $x_2$  periodicity:

$$\left. \begin{array}{l} \mathbf{u}(0, x_2, t) = \mathbf{u}(2W, x_2, t) \\ \mathbf{u}(x_1, 0, t) = \mathbf{u}(x_1, W, t) \\ \gamma(0, x_2, t) = \gamma(2W, x_2, t) \\ \gamma(x_1, 0, t) = \gamma(x_1, W, t) \end{array} \right\} \quad (5.45)$$

Concerning the material parameters, the same bulk parameters are used in the two grains as presented in Tab. 5.1, which is inspired by Peirce et al. (1983) and Kuroda (2011). In the grains, only energetic effects with quadratic defect energy are considered ( $l_{dis} = 0$  and  $n = 2$ ) and no first-order hardening is assumed ( $H_\pi = 0$ ). The GB parameters are also given in Tab. 5.1. The GB reference flow rate and the rate-sensitivity parameters ( $\dot{G}_0$  and  $d$ ) are assumed to be the same as their bulk counterparts ( $\dot{\gamma}_0^\alpha$  and  $m$ ).

Fig. 5.4 and 5.5 present results of stress-strain curves and grain boundary defectiveness  $\dot{\Delta}$  considering only energetic GB effects ( $\kappa = 10^3 N m^{-1}$  and  $S_{GB_0} = 0$ ) and only dissipative GB effects ( $\kappa = 0$  and  $S_{GB_0} = 40 N m^{-1}$ ), for three combinations of constitutive frameworks. These combinations include: small deformation bulk - small deformation GB, large deformation bulk - small deformation GB, and large deformation bulk - large deformation GB. At small strain range (until  $\Gamma = 0.02$  approximately), results of the three constitutive combinations show very good agreement. Beyond approximately  $\Gamma = 0.02$ , slight differences can be noted between curves associated with small deformation bulk and large deformation bulk, regardless of the GB setting. These differences, which become more obvious with increasing  $\Gamma$ , are due to finite deformation effects. Considering the case of finite deformation bulk, comparison between results associated with small deformation GB and large deformation GB suggests that the grain boundary also contributes to these effects.

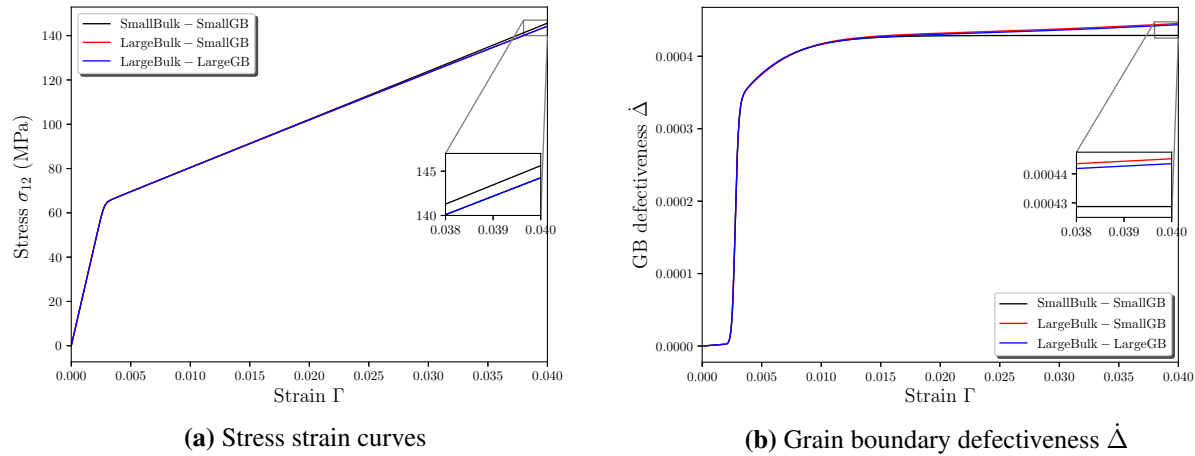


**Fig. 5.4.** Results of energetic GB parameter  $\kappa = 10^3 \text{ N m}^{-1}$  using three combinations of bulk and grain boundary constitutive frameworks under shear loading  $\Gamma = 0.04$  with  $l_{en}/W = 10$ ,  $S_{GB_0} = 0$ ,  $H_{GB} = 0$ .

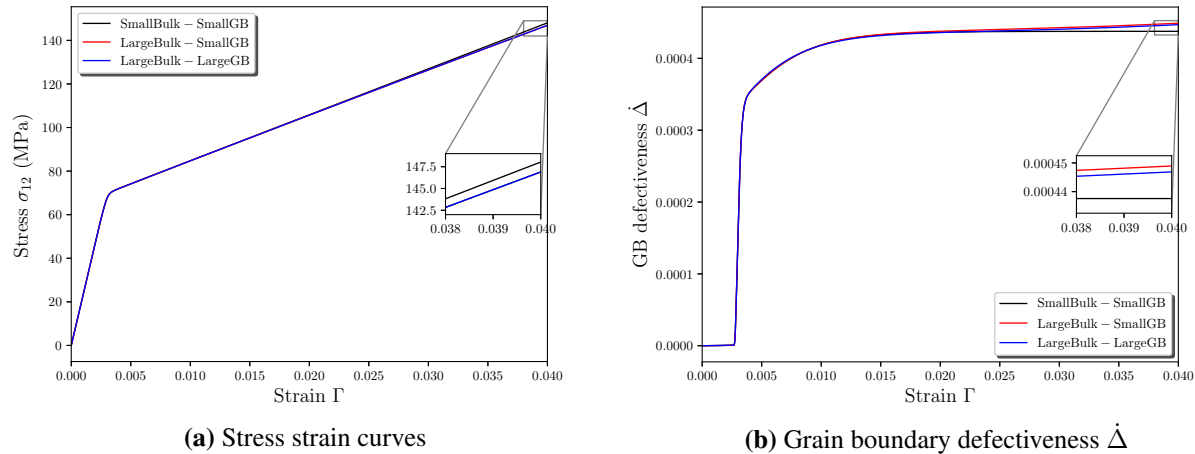


**Fig. 5.5.** Results of dissipative GB parameter  $S_{GB_0} = 40 \text{ N m}^{-1}$  using three combinations of bulk and grain boundary constitutive frameworks under shear loading  $\Gamma = 0.04$  with  $l_{en}/W = 10$ ,  $\kappa = 0$ ,  $H_{GB} = 0$ .

Finite deformation contributions of GB are more obvious on the GB defectiveness curves (Figs. 5.4b and 5.5b). However, these contributions remain small compared to those of the bulk.

#### 5.4.2 Assessment of the GB model

The periodic bi-crystal of Fig. 5.3 is used in this subsection to investigate the proposed finite deformation GB model. The monotonic shear loading is replaced by a complete cycle of loading (*i.e.*,  $0 \rightarrow \Gamma \rightarrow -\Gamma \rightarrow \Gamma$ ). Influence of energetic and dissipative grain boundary parameters will

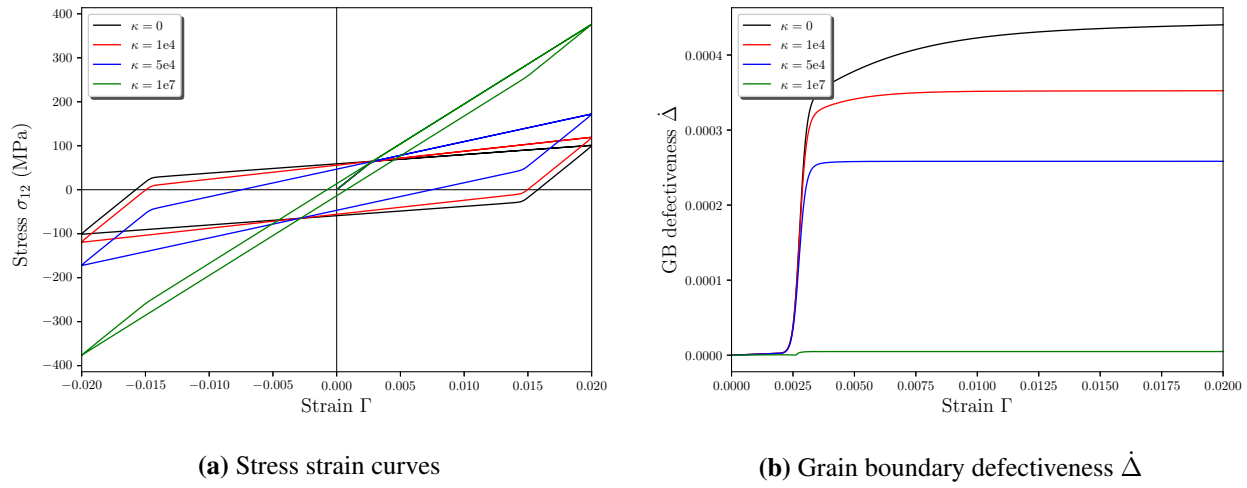


**Fig. 5.6.** Influence of only GB energetic parameter  $\kappa$  under cyclic loading ( $l_{en}/W = 10$ ,  $S_{GB_0} = 0$ ,  $H_{GB} = 0$ ).

first be addressed. Then, geometrical orientation effects including grain misorientation and GB orientation will be discussed.

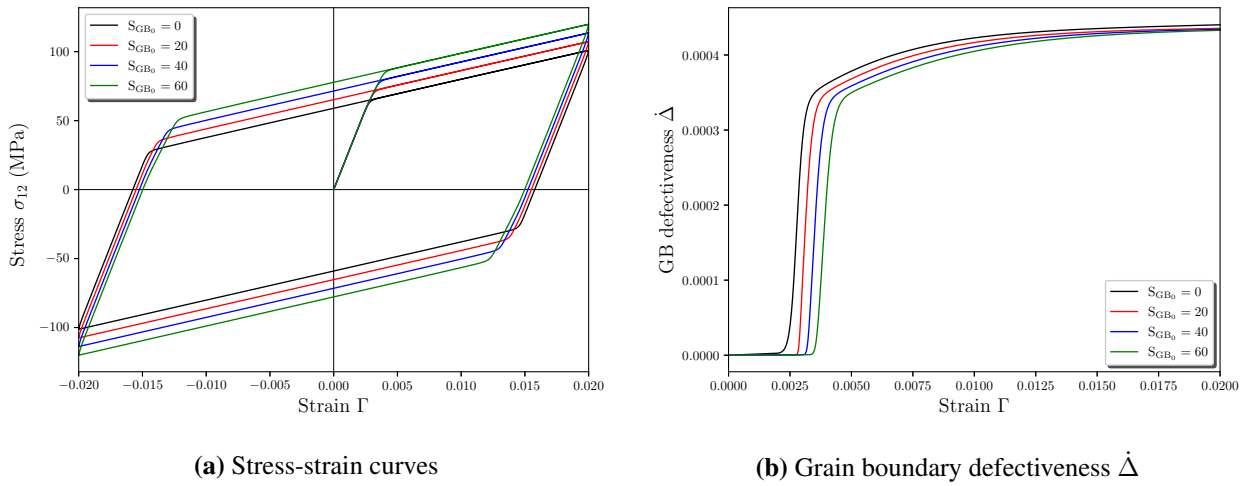
#### 5.4.2.1 Influence of GB parameters

To better investigate the effects of energetic and dissipative GB parameters, the energetic length scale  $l_{en}$  in the grains is first set to a high value ( $l_{en} = 10 W$ ). This choice of  $l_{en}$  leads to high energetic effects in the grains, allowing for better assessment of the role of the GB on these effects.

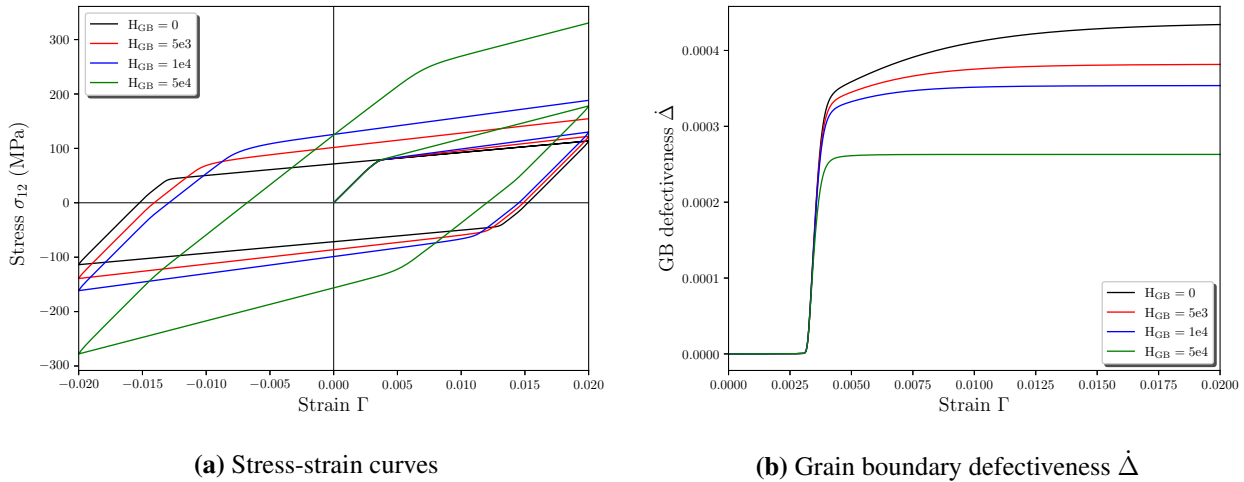
Fig. 5.6 presents the effects of the GB energetic coefficient  $\kappa$ , while ignoring GB dissipation. As shown in Fig. 5.6a, this coefficient leads to kinematic hardening and only influences the hardening slope after yielding. Regardless of the  $\kappa$  value, no effects on the initial yield are observed. However, larger value of  $\kappa$  leads to steeper kinematic hardening slope. Analysis of  $\dot{\Delta}$  curves shows no  $\kappa$  influence on the GB activation, which occurs at the same imposed shear strain (Fig. 5.6b). After GB activation,  $\dot{\Delta}$  presents nearly plateau-shaped evolution for which the maximum value decreases with increasing  $\kappa$ . The case of  $\kappa = 1e7 \text{ N m}^{-1}$  yields nearly zero GB defectiveness ( $\dot{\Delta} \approx 0$ ) and corresponds to nearly opaque GB (micro-hard GB conditions).

Fig. 5.7 shows the effects of the GB dissipative initial slip resistance  $S_{GB_0}$ , while ignoring GB energetic effects ( $\kappa = 0$ ) and GB dissipative hardening ( $H_{GB} = 0$ ). The stress-strain curves in Fig. 5.7a show an apparent strengthening effect of  $S_{GB_0}$  (*i.e.*, increase of the apparent initial yield  $\sigma_{12}^0$  beyond which the plastic deformation increases drastically). As shown in Fig. 5.7b, the increase of  $S_{GB_0}$  delays the GB activation, which occurs at later imposed shear strain, leading to an apparent strengthening. After GB activation, the GB defectiveness  $\dot{\Delta}$  evolves towards a plateau-shaped form with an asymptotic value which corresponds to micro-free GB ( $S_{GB_0} = 0$ ), as shown by Fig. 5.7b. The obtained results are in accordance with those obtained by van Beers et al. (2013) and Peng et al. (2019).

Fig. 5.8 provides the effects of the dissipative GB hardening parameter  $H_{GB}$ , for  $\kappa = 0$  and  $S_{GB_0} = 40 \text{ N m}^{-1}$ . This parameter leads to further dissipative (isotropic-like) hardening after



**Fig. 5.7.** Influence of only GB dissipative parameter  $S_{GB_0}$  under cyclic loading ( $l_{en}/W = 10$ ,  $\kappa = 0$ ,  $H_{GB} = 0$ ).



**Fig. 5.8.** Influence of GB dissipative hardening  $H_{GB}$  under cyclic loading ( $l_{en}/W = 10$ ,  $\kappa = 0$ ,  $S_{GB_0} = 40 \text{ N m}^{-1}$ ).

yielding, resulting in smaller asymptotic value of  $\dot{\Delta}$  after GB activation. Fig. 5.9 presents the stress-strain response of the considered bi-crystal under several cycles of shear loading, for  $H_{GB} = 1e4 \text{ N m}^{-1}$  and  $S_{GB_0} = 40 \text{ N m}^{-1}$ . For nonzero  $H_{GB}$ , the current GB dissipative slip resistance  $S_{GB}$  increases with the cumulative GB defectiveness  $\Delta$ . As a consequence, for each cycle, the GB activation occurs in a smaller region compared to the former cycle. The cyclic response converges towards a response for which GB activation is no longer possible. The obtained results are in accordance with those obtained by Alipour et al. (2019) using phenomenological GB model.

The above investigation of GB parameters has been performed using constant dimension size  $W$  and higher order energetic length scale  $l_{en} = 10 W$ . To investigate the capabilities of the GB

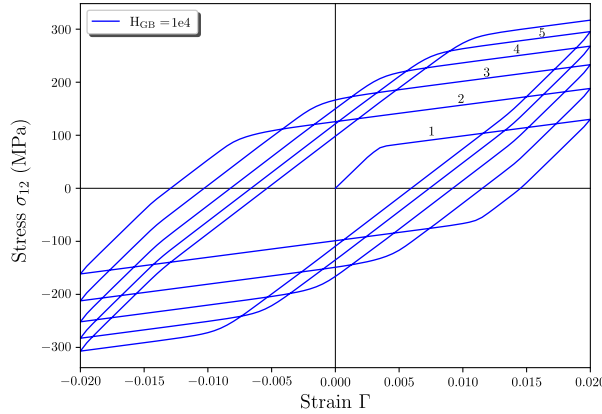


**Fig. 5.9.** Stress-strain responses under five complete cyclic loadings with  $H_{GB} = 1e4 \text{ N m}^{-1}$  ( $l_{en}/W = 10$ ,  $\kappa = 0$ ,  $S_{GB_0} = 40 \text{ N m}^{-1}$ ).

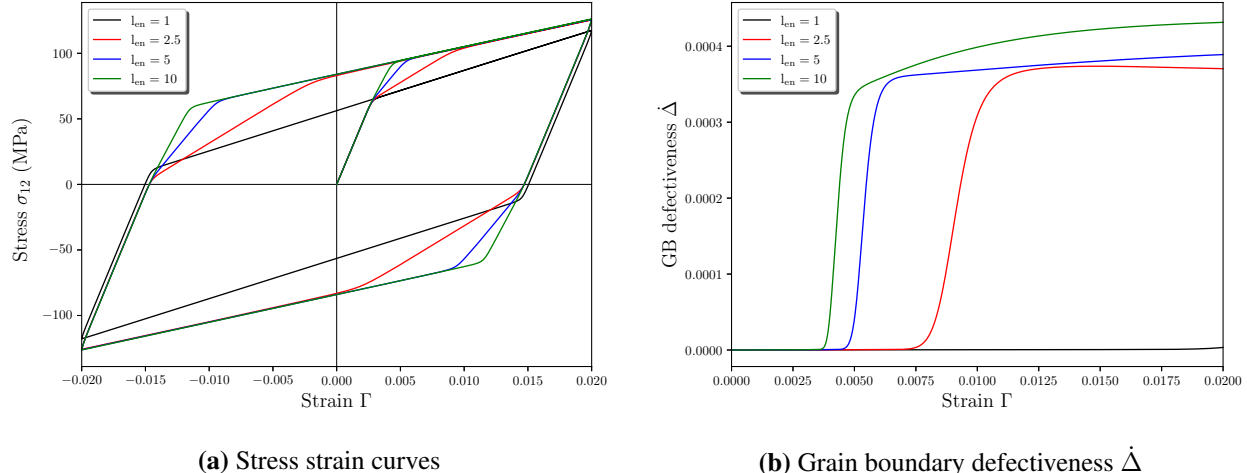
model in capturing GB size effects, different values of  $l_{en}/W$  are tested first by varying  $l_{en}$  and then by changing  $W$ . Only GB dissipative effects with no GB hardening are considered in this investigation ( $\kappa = 0$  and  $H_{GB} = 0$ ). Fig. 5.10 presents the effects of  $l_{en}$  in the grains, for  $W = 1 \mu\text{m}$  and  $S_{GB} = 80 \text{ N m}^{-1}$ . It can be shown from this figure that larger  $l_{en}$  leads to earlier GB activation. Interestingly, when the GB is activated, no further influence of this parameter is obtained, at least for the considered example. Similar conclusions have been reported by Alipour et al. (2019) using phenomenological GB model. Fig. 5.11 presents the effects of  $W$ , for  $l_{en} = 10 \mu\text{m}$  and  $S_{GB_0} = 40 \text{ N m}^{-1}$ . Obvious size effects can be observed in this figure. The apparent initial yield  $\sigma_{12}^0$  increases with decreasing  $W$ , which is in accordance with experimental observations of size effects at the scale of interest. Fig. 5.12 shows that  $\sigma_{12}^0$  increases linearly with  $1/W$ . It is worth recalling that the bulk parameters are chosen such that no contribution to strengthening comes from grains. The observed strengthening is only caused by the GB behavior.

#### 5.4.2.2 Influence of grain and grain boundary orientations

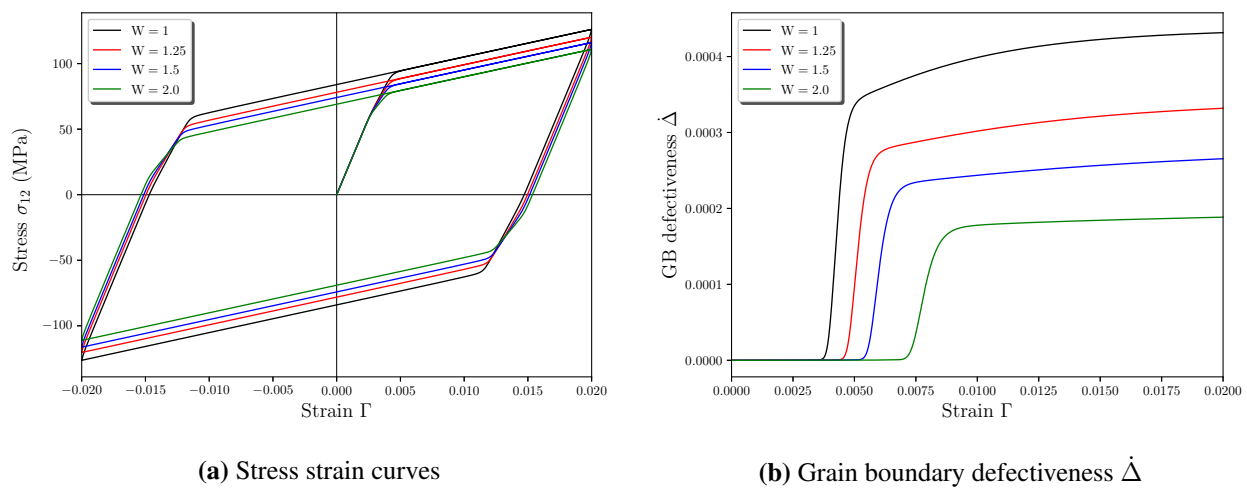
As based on the GB approach of (Gurtin, 2008b), the present GB model naturally accounts for effects due to grain and grain boundary orientations. The present subsection aims at illustrating these effects, using  $l_{en}/W = 10$ ,  $\kappa = 0$ ,  $S_{GB_0} = 40$  and  $H_{GB} = 0$ .

Fig. 5.13 presents the effects of grain misorientation  $\theta_M$ , for constant GB orientation  $\theta_{GB} = 0^\circ$ . As shown in Fig. 5.13a, larger grain misorientation increases the yield strength and strain hardening. It can be shown from Fig. 5.13b that increasing  $\theta_M$  delays GB activation and leads to higher steady-state value of  $\dot{\Delta}$ . The case  $\theta_M = 0^\circ$  represents a coherent slip system configuration for grain A and B, resulting in zero GB defectiveness ( $\dot{\Delta} = 0$ ) as presented in Fig. 5.13b. In this case, the bi-crystal behaves as a single-crystal with no role for the grain boundary.

Fig. 5.14 presents the influence of the GB orientation  $\theta_{GB}$ , for constant grain misorientation ( $\theta_M = 20^\circ$ ). Similarly to what has been obtained for  $\theta_M$ , larger GB orientation  $\theta_{GB}$  results in larger yield strength and strain hardening (Fig. 5.14b). A nonzero GB orientation  $\theta_{GB}$  results in unsymmetrical slip systems in the grains with respect to the shear direction. As a consequence, unsymmetrical evolution of the plastic slips takes place in these grains, leading to more complex



**Fig. 5.10.** Influence of energetic length scale  $l_{en}$  under cyclic loading with only grain boundary dissipative effects ( $W = 1 \mu\text{m}$ ,  $\kappa = 0$ ,  $S_{GB0} = 80 \text{ N m}^{-1}$ ,  $H_{GB} = 0$ ).



**Fig. 5.11.** Influence of geometry size effects  $W$  under cyclic loading with only grain boundary dissipative effects ( $l_{en} = 10 \mu\text{m}$ ,  $\kappa = 0$ ,  $S_{GB0} = 40 \text{ N m}^{-1}$ ,  $H_{GB} = 0$ ).

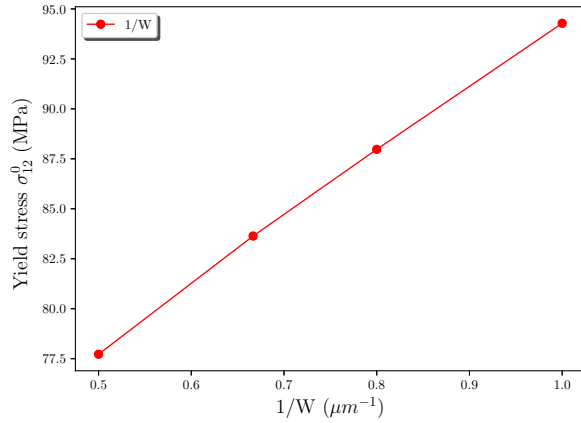


**Fig. 5.12.** Apparent initial yield stress  $\sigma_{12}^0$  as a function of  $1/W$  with only grain boundary dissipative effects ( $l_{en} = 10 \mu\text{m}$ ,  $\kappa = 0$ ,  $S_{GB_0} = 40 \text{ N m}^{-1}$ ,  $H_{GB} = 0$ ).

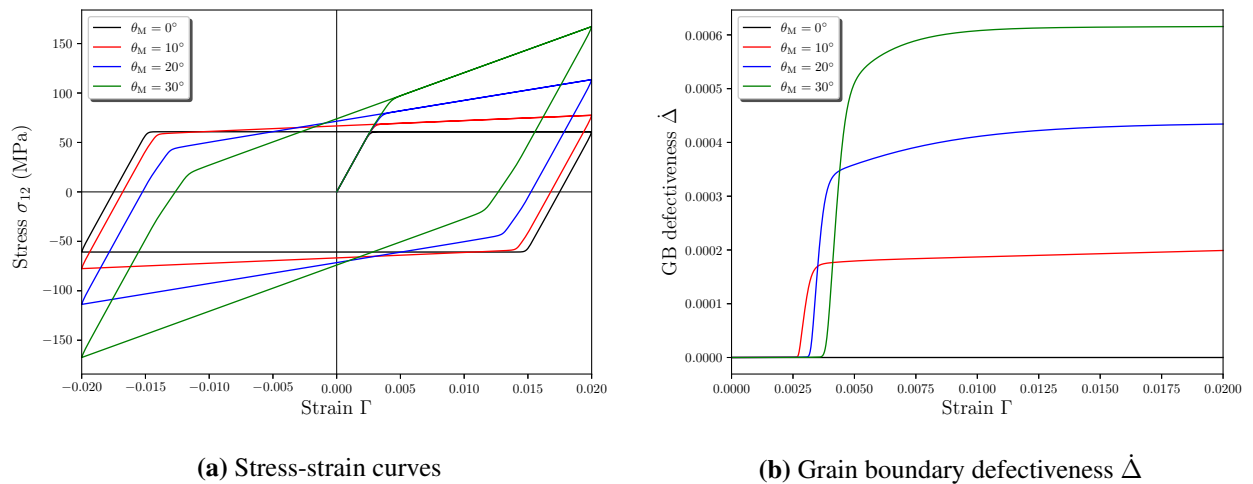


**Fig. 5.13.** Influence of grain misorientation  $\theta_M$  under cyclic shear loading ( $l_{en}/W = 10$ ,  $\kappa = 0$ ,  $S_{GB_0} = 40 \text{ N m}^{-1}$ ,  $H_{GB} = 0$ ) with a fixed grain boundary orientation angle  $\theta_{GB} = 0^\circ$ .

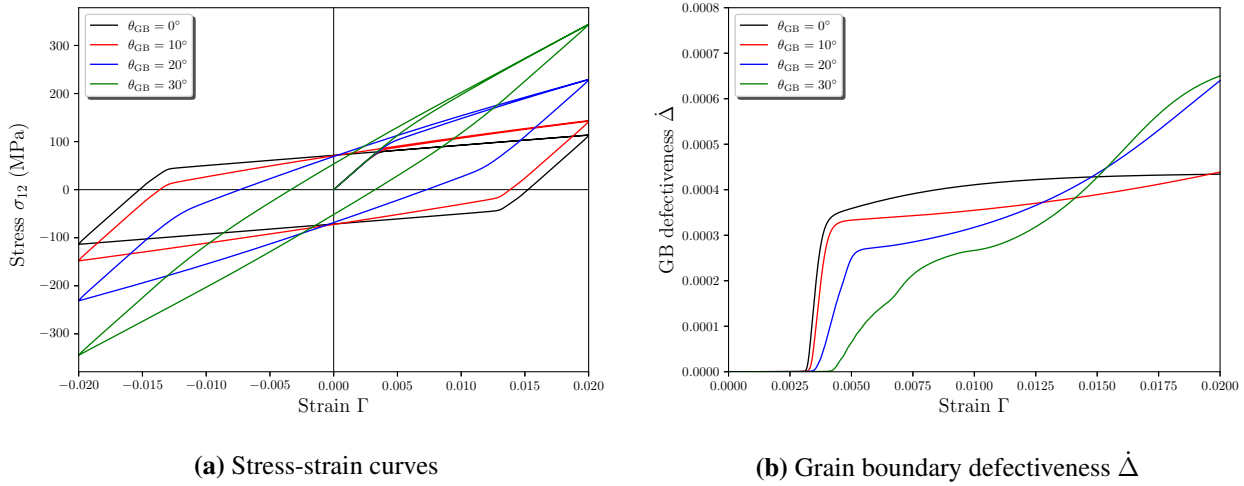


**Fig. 5.14.** Influence of grain boundary orientation  $\theta_{GB}$  under cyclic shear loading ( $l_{en}/W = 10$ ,  $\kappa = 0$ ,  $S_{GB0} = 40 \text{ N m}^{-1}$ ,  $H_{GB} = 0$ ) with a constant grain misorientation  $\theta_M = 20^\circ$ .

evolution of GB defectiveness (Fig. 5.14b).

### 5.4.3 Poly-crystalline material response under proportional and non-proportional loading conditions

It has been shown in subsection 5.4.2 that the material response of the considered bi-crystal depends on the grain size  $W$ . The overall yield strength of the bi-crystal depends linearly on  $1/W$  (Fig. 5.12). The present subsection aims at investigating this dependence using a more realistic poly-crystalline structure. A poly-crystalline square plate of dimensions  $W \times W$  composed of randomly distributed grains is considered, as shown in Fig. 5.15. Each grain is assumed to have two slip systems with an angle  $\theta = 60^\circ$  between them. The macroscopic boundary conditions are set as:

$$\left. \begin{array}{l} u_1 = 0, \quad u_2 = 0 \quad \text{along} \quad x_2 = 0 \\ u_1 = W\Gamma, \quad u_2 = 0 \quad \text{along} \quad x_2 = W \end{array} \right\} \quad (5.46)$$

where  $\Gamma = 0.003$  is the prescribed shear strain. In order to establish proportional and non-proportional loading conditions, two types of microscopic boundary conditions are used. In proportional loading case, all the plate edges are assumed to be micro-free during the entire simulation. In non-proportional loading case, the previous microscopic conditions are applied until a prescribed shear strain  $\Gamma = 0.0015$ , and then passivation conditions are applied on the top and bottom edges till the end of the simulation:

$$\dot{\gamma}^1 = \dot{\gamma}^2 = 0 \quad \text{along} \quad x_2 = 0, W \quad (5.47)$$

Additional periodic (macroscopic and microscopic) boundary conditions are also imposed on the left and right edges to ensure infinite length of the plate in  $x_1$ -direction:

$$\left. \begin{array}{l} u_i(0, x_2, t) = u_i(W, x_2, t) \quad \text{for} \quad i = 1, 2 \\ \gamma^\alpha(0, x_2, t) = \gamma^\alpha(W, x_2, t) \quad \text{for} \quad \alpha = 1, 2 \end{array} \right\}$$

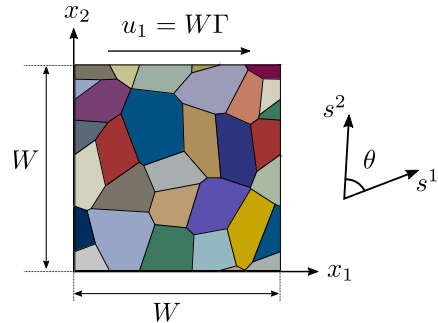


**Fig. 5.15.** A poly-crystalline square plate of randomly distributed grains with two slip systems in each grain.

It should be noted that the grains composing the considered plate are generated based on periodic Voronoï diagram to ensure geometrical periodicity and to simplify application of periodic boundary conditions. The material properties used in the present study are the same as those presented in Tab. 5.1.

Fig. 5.16a presents stress-strain responses for different values of the geometry size  $W$  under loading-unloading cycle of proportional and non-proportional conditions. This figure shows obvious size effects in terms of yield strength and strain hardening which increase with decreasing  $W$ . As shown by Fig. 5.16b, the yield strength increases linearly with the inverse of geometry size  $1/W$ . Analysis of the non-proportional loading results shows that the occurrence of the non-proportional loading source (passivation of the top and bottom edges) only influences the strain hardening which increases after top and bottom edges passivation (Fig. 5.16a). However, the latter does not lead to formation of “elastic gaps”. This result could be interesting from a physical point of view as it can reinforce the hypothesis that elastic gaps are not physical. As discussed in chapter 3, existence of these gaps in reality is subject of extensive discussion within the strain gradient plasticity community. It is worth recalling that using almost all existing SGCP approaches including thermodynamically-consistent higher-order dissipation in single crystal, the passivation step is accompanied by the formation of an elastic gap. Furthermore, the SGCP model proposed in chapter 3 allows for avoiding these gaps only if they are not preceded by activation of gradient effects, which is not the case in the present example. Due to different grain orientations, plastic strain is first activated in favorably oriented grains leading to plastic gradients within the poly-crystalline structure.

## 5.5 Conclusions

The novelty of the work lies in the development of a finite deformation extension of the GB model of (Gurtin, 2008b), considering lattice plastic distortion. Using similar procedure as in (Gurtin, 2008b), the extended model is derived based on a GB Burgers tensor expressed in terms of plastic distortion  $F^p$ . Both GB energetic and dissipative processes are considered in this model, which was implemented within the commercial finite element package Abaqus/Standard using UEL subroutine. The implementation technique is based on zero-thickness GB finite elements. For comparison purposes, the small deformation GB model of Gurtin (2008b) was also implemented within Abaqus/Standard using the same technique.

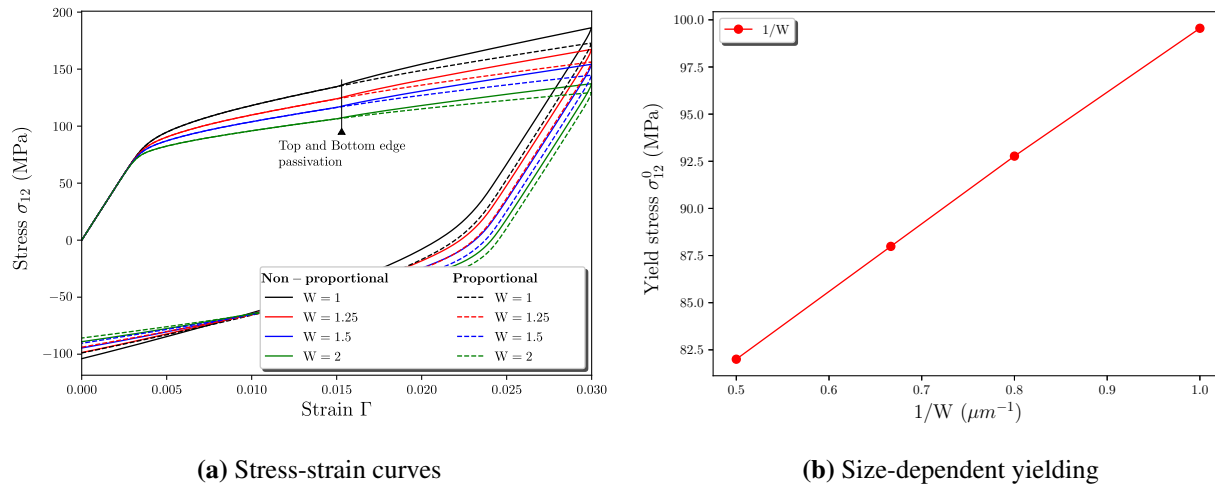


**Fig. 5.16.** Stress-strain responses of polycrystalline plate under cyclic non-proportional and proportional loading with dissipative GB constitutive parameters for different geometry size ( $l_{en} = 10\mu\text{m}$ ,  $\kappa = 0$ ,  $S_{GB0} = 5\text{ N m}^{-1}$ ,  $H_{GB} = 0$ ).

To validate the model implementation, a periodic bi-crystal subjected to simple shear loading was simulated using three constitutive settings: small deformation bulk - small deformation GB, large deformation bulk - small deformation GB, and large deformation bulk - large deformation GB. At small imposed shear strain  $\Gamma$ , the obtained results are in very good agreement. Beyond a certain value of  $\Gamma$ , differences between curves associated with small deformation bulk and large deformation bulk appear, regardless of the GB setting. These differences, which become more obvious with increasing  $\Gamma$ , are due to finite deformation effects. Considering the case of finite deformation bulk, comparison between results associated with small deformation GB and large deformation GB suggests that the GB also contributes to these effects. Finite deformation contributions of GB are more obvious on the GB defectiveness curves (Figs. 5.4b and 5.5b). However, these contributions remain small compared to those of the bulk.

The bi-crystal test under simple shear was also used to assess the GB parameters. The material parameters in the grains were chosen in such a way as to avoid strengthening effects due to bulk response. Furthermore, large energetic length scale was adopted in these grains. In terms of stress-strain responses, the assessment results are consistent with some existing works in the literature, such as [van Beers et al. \(2013\)](#) and [Peng et al. \(2019\)](#). However, some differences arise regarding grain boundary defectiveness due to distinctive formulation of the proposed model. It was found that energetic GB effects only influence the overall strain hardening after yielding but not the yield strength. GB dissipative effects can influence both strain hardening and strengthening. In the presence of the latter effects, size-dependent yield strength was obtained, which depends linearly on the inverse of the geometrical size.

The latter result motivated application of the GB model on more realistic poly-crystalline structure with randomly oriented grains under proportional and non-proportional shear loading conditions. The obtained results confirm the linear dependence between the yield strength and the inverse of the geometrical size. Interestingly, although strengthening effects were captured, no traces of elastic gaps at the occurrence of the non-proportional source were obtained. This could be inter-

esting from a physical point of view, as it can reinforce that hypothesis that elastic gaps are not physical.



# **Chapter 6**

## **Application to strain localization in single- and poly-crystalline metal sheets**

### **Abstract**

In this chapter, the finite deformation strain gradient crystal plasticity (SGCP) and grain boundary (GB) models presented in the previous chapters will be applied to take a first step into the investigation of size effects on localization phenomena. Capabilities of the SGCP model to capture different kinds of localization bands will first be revisited considering single-crystal structures. Then, an initiation into the investigation of size effects on the localization phenomena within poly-crystalline structures will be provided.

## 6.1 Introduction

As an important plastic instability phenomenon, strain localization within single- and poly-crystalline structures has received a strong scientific interest in the last decades and numerous works have been published on the subject (Rice, 1976; Asaro and Rice, 1977; Needleman and Tvergaard, 1992; Forest, 1998; Marano et al., 2019, 2021). Using multiple slip systems, it has been shown that strain localization may occur along narrow shear bands, which can be arbitrarily oriented with respect to the initial crystallographic directions (Rice, 1976; Needleman and Tvergaard, 1992; Kuroda, 2011). In the case of a single slip system, two types of shear bands, known as slip and kink bands, can take place (Asaro and Rice, 1977).

Due to lack of internal length scale(s), conventional crystal plasticity theories are not able to correctly capture localization bands. As an alternative, Forest (1998) has applied a small deformation Cosserat single crystal plasticity theory to investigate the formation of slip and kink bands within single crystals. As shown by the author, this theory allows for regularizing kink bands that will have a finite thickness. However, it does not regularize slip bands which are not necessarily associated with lattice curvature (Forest, 1998; Forest et al., 2001). Although not well investigated in the literature, SGCP theories, which are classically based on GND densities, are also expected to present difficulties in regularizing idealized slip bands. Indeed, a slip gradient along the normal to the slip planes does not result in the storage of GNDs. Recently, Ling et al. (2018) have proposed a finite deformation micromorphic crystal plasticity model which is capable of regularizing both kink and slip bands. Application of this model to strain localization in single crystals presenting one slip system has brought to light complex localization behavior with competition between kink and slip bands. The capabilities of SGCP theories in predicting such a complex localization behavior has very recently been investigated by Marano et al. (2021) using a small deformation version of the SGCP model of Gurtin (2002). Only higher-order energetic effects are considered in this investigation. As a first step, the present chapter aims at extending this investigation using the finite deformation SGCP model presented in chapter 4, which accounts for both higher-order energetic and dissipative effects. Particular focus will be given to the ability of such a model to reproduce the competition between slip and kink bands. Then, an initiation into the investigation of size effects on the localization phenomena within poly-crystalline structures will be provided.

After this introduction, the chapter is organized as follows. Section 6.2 discusses the capabilities of the proposed SGCP model in regularizing different kinds of localization bands in single-crystal structures. Section 6.3 presents preliminary results regarding size effects on the localization phenomena within poly-crystalline structures. Some concluding remarks are given in section 6.4.

## 6.2 Strain localization in single crystals

The proposed finite deformation SGCP model will be applied in this section to conduct a comprehensive investigation of localization phenomena within single-crystalline structures, considering both higher-order energetic and dissipative effects.

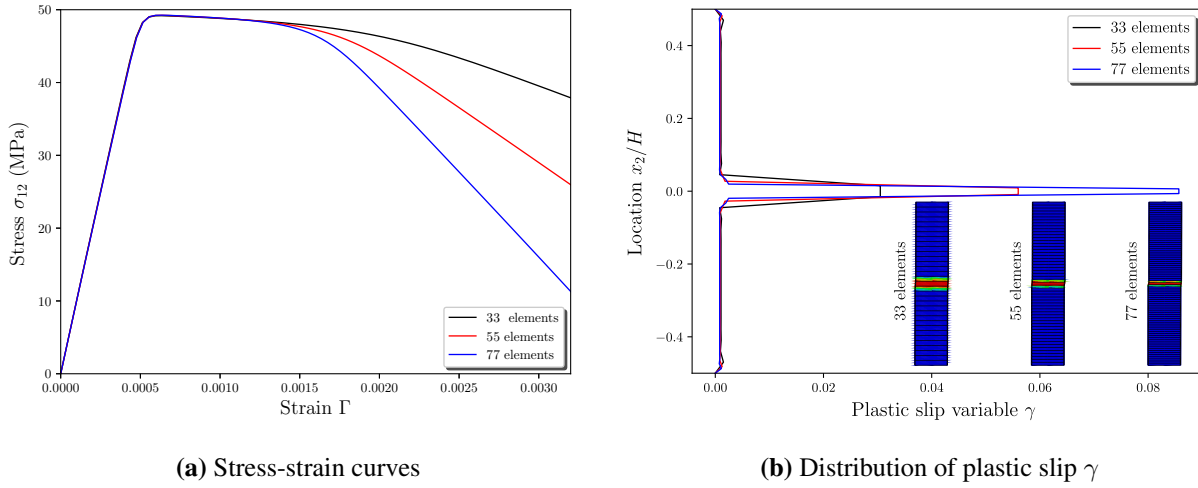


**Fig. 6.1.** Stress-strain curves and distributions of plastic scalar variable  $\gamma$  along  $x_2$ -direction in the case of horizontal slip at  $\Gamma = 0.0032$  for different mesh refinements ( $l_{en}/H = 0.1$ ,  $l_{dis} = 0$ ,  $H_\pi = -500$  MPa,  $n = 2$ ).

## 6.2.1 Regularization of different kinds of localization bands

Capabilities of the proposed SGCP model in regularizing different kinds of localization bands, including idealized slip and kink bands as well as general shear bands (*i.e.*, with no particular orientation with respect to the crystallographic directions), will be revisited hereafter.

### 6.2.1.1 Simple shear with single slip system: regularization of idealized slip/kink bands

Simple shear simulations using single crystals with single slip are performed. The geometrical model used in these simulations is similar to that presented in Fig. 4.3, except for the slip systems, which are replaced by only one system. To obtain idealized slip and kink bands, this system is oriented such that the slip plane is either parallel (horizontal slip case) or normal (vertical slip case) to the shear direction. The same microscopic and macroscopic boundary conditions as in Fig. 4.3 are assumed. The applied material parameters are similar to those presented in Tab. 3.1, except for  $H_\pi$  which is taken as  $H_\pi = -500$  MPa to model softening. To trigger strain localization, a material imperfection is considered in a small central region of height  $H/11$ . In this region, the initial first-order slip resistance  $S_{\pi 0}$  is linearly decreased to  $0.9 S_{\pi 0}$  at the center.

Considering the case of horizontal slip, Fig. 6.1 presents the associated results in terms of stress-strain curves and distributions of plastic scalar variable  $\gamma$  along  $x_2$ -direction for different mesh refinements. Although these results are obtained considering only higher-order energetic effects ( $l_{en}/H = 0.1$  and  $l_{dis} = 0$ ), it has been verified that activation of higher-order dissipative effects ( $l_{dis} \neq 0$ ) does not affect them. The SGCP model failed to regularize the obtained idealized slip band, which shows mesh-dependence. As can be seen in Fig. 6.1b, the width of the obtained band is set by the mesh spacing and decreases with increasing the number of finite elements. For the considered slip configuration, the present SGCP model behaves as a conventional crystal plasticity model. Indeed, slip gradients in the direction normal to the slip plane do not correspond to GNDs (Forest, 1998; Gurtin et al., 2007; Gurtin, 2008a). Consequently, no size effects are predicted by

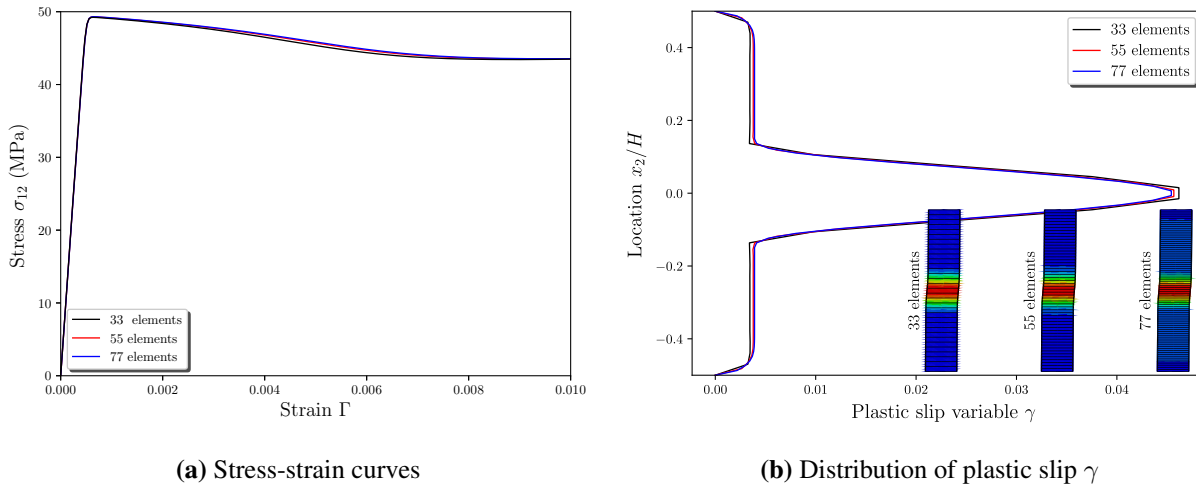


**Fig. 6.2.** Stress-strain curves and distributions of plastic scalar variable  $\gamma$  along  $x_2$ -direction in the case of vertical slip at  $\Gamma = 0.01$  for different mesh refinements ( $l_{en}/H = 0.1$ ,  $l_{dis} = 0$ ,  $H_\pi = -500$  MPa,  $n = 2$ ).

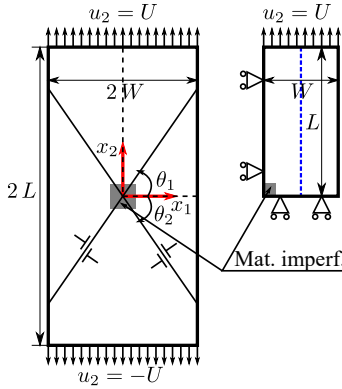
GND-based SGCP theories for the development of such normal slip gradients. This is also the case for Cosserat crystal plasticity theories in which size effects are only triggered by lattice curvature (Forest, 1998).

Fig. 6.2 presents the shear results associated with the case of vertical slip in terms of stress-strain responses and distributions of plastic scalar variable  $\gamma$  along  $x_2$ -direction for different mesh refinements. Using sufficiently fine mesh, the stress-strain response becomes nearly mesh-independent (Fig. 6.2a). Note that the slope inversion and the plateau-shaped form observed on the stress-strain curves beyond  $\Gamma = 0.008$  is due to the competition between softening caused by negative  $H_\pi$  and hardening caused by higher-order energetic effects ( $l_{en} \neq 0$ ). As shown in Fig. 6.2b, thick kink bands which spread over several finite elements are obtained. For relatively fine mesh, the thickness of these bands is nearly mesh-insensitive.

As for Cosserat crystal plasticity models (Forest, 1998), the proposed SGCP model enables mesh-independent simulation of kink bands which imply slip gradients in the slip direction. On the contrary, it fails to regularize idealized slip bands which are not accompanied by the development of GNDs. However, the idealized slip conditions used to obtain the latter bands are not commonly encountered in real material deformation. The following subsection discusses the ability of the present SGCP model to correctly capture strain localization within a more practical problem, for which shear bands have not necessarily particular orientations with respect to the initial crystallographic directions.

### 6.2.1.2 Uniaxial tension with two slip systems: regularization of general localization bands

A uniaxial tension problem with two slip systems symmetrically oriented with respect to the tension direction is considered in this subsection. Fig. 6.3 presents the associated geometrical model, which is a plate of dimensions  $2L \times 2W = 20 \times 10$  mm having two slip systems inclined at  $60^\circ$  from both sides of  $x_1$ -direction ( $\theta_1 = -\theta_2 = 60^\circ$ ). For this problem, according to bifurcation analysis



**Fig. 6.3.** Uniaxial tension of a single crystal plate with two slip systems symmetrically oriented with respect to the tension direction.

(Rice, 1976; Needleman and Tvergaard, 1992), it is expected that localization will occur along two crossed shear bands whose orientations are close to those of the slip planes. Due to symmetry, only one quarter (upper right part) of the plate is analyzed. The macroscopic boundary conditions applied on this portion of the plate are set as:

$$\begin{cases} u_1 = 0 & \text{for } x_1 = 0 \\ u_2 = 0 & \text{for } x_2 = 0 \\ u_2 = U & \text{for } x_2 = L \end{cases} \quad (6.1)$$

Furthermore, all the edges of this plate portion are assumed to be micro-free (transparent to dislocations). As in the previous simple shear problem,  $H_\pi$  is assumed to be negative to model softening ( $H_\pi = -500$  MPa). The other material constants are given in Tab. 6.1. To trigger localization, a material imperfection is considered within a square region of 0.25 mm side located at bottom left-hand corner of the considered plate portion (Fig. 6.3). In this region, the initial first-order slip resistance  $S_{\pi 0}$  is replaced by 0.9  $S_{\pi 0}$ . To quantify strain localization, the accumulated plastic slip variable defined by  $\gamma_{acc} = \sum_\alpha |\gamma^\alpha|$  is adopted.

Fig. 6.4 presents the associated results in terms of nominal stress-strain curves and accumulated plastic slip variable distributions along  $x_2$ -direction for different mesh refinements. The nominal stress is calculated as the reaction force  $F$  on the top edge over the initial width  $W_0$  of the studied plate portion (the thickness is assumed to be 1) and the nominal strain as the ratio between the elongation  $\Delta L$  and the initial length  $L_0$ . The values of  $\gamma_{acc}$  in Fig. 6.4b are determined at nodes belonging to the vertical center line of the studied portion of the plate (dashed blue line in Fig. 6.3). Fig. 6.5 presents the deformed meshes and contours of accumulated plastic slip variable  $\gamma_{acc}$  for different mesh refinements. Concerning the nominal stress-strain response, mesh convergence is obtained as soon as a sufficiently fine mesh is applied (Fig. 6.4a). In terms of strain localization, it seems that finer meshes lead to a larger  $\gamma_{acc}$  peak value in the obtained shear band. However, this band presents a finite width which converges towards an intrinsic value covering several finite elements. Based on Fig. 6.5, such a band is oriented at an angle of approximately  $54^\circ$  with respect to  $x_1$ -direction, which is slightly smaller than the angle of the first slip direction ( $\theta_1 = 60^\circ$ ). This is in agreement with the bifurcation and numerical results of Kuroda (2011). Using similar configuration of activated slip systems with  $\theta_1 = 54.7^\circ$ , these authors have shown that strain lo-

**Tab. 6.1.** Material parameters implied for uniaxial tension of single crystal plate, inspired by [Peirce et al. \(1983\)](#); [Kuroda \(2011\)](#).

Material parameter name	Symbol	Value	Unit
Young's modulus	$E$	60.84	GPa
Poisson's ratio	$\nu$	0.3	—
Reference slip rate	$\dot{\gamma}_0^\alpha$	0.001	$s^{-1}$
Rate-sensitivity parameter	$m$	0.005	—
Higher-order energetic slip resistance	$X_0$	60.84	MPa
Initial first-order dissipative slip resistance	$S_{\pi 0}$	60.84	MPa
Initial higher-order dissipative slip resistance	$S_{\xi 0}$	case study	MPa
First-order hardening modulus	$H_\pi$	case study	MPa
Higher-order hardening modulus	$H_\xi$	case study	MPa
Energetic length scale	$l_{en}$	case study	$\mu m$
Dissipative length scale	$l_{dis}$	case study	$\mu m$
Defect energy index	$n$	2	—

calization occurs along a line inclined at approximately  $49^\circ$  from  $x_1$ -direction. To better analyze the obtained results, the lattice rotation is approximated based on the polar decomposition of the elastic deformation gradient  $\mathbf{F}^e = \mathbf{R}^e \mathbf{U}^e$ , where  $\mathbf{R}^e$  and  $\mathbf{U}^e$  are respectively the elastic rotation and elastic stretch tensors. Neglecting the elastic distortion described by  $\mathbf{U}^e$ ,  $\mathbf{R}^e$  can be interpreted as the lattice rotation and the corresponding angle  $\theta$  is calculated using [Marano et al. \(2019\)](#):

$$\theta = \arccos \left[ \frac{1}{2} (\text{tr } \mathbf{R}^e - 1) \right] \quad (6.2)$$

The angle sign is determined considering the sign of the off-diagonal terms of  $\mathbf{R}^e$ . By doing so, it is found that strain localization is accompanied by a lattice rotation of approximately  $-5.5^\circ$ . Therefore, the localization band obtained in the considered portion of the plate is not an idealized slip band, as it is associated with lattice curvature, which explains its regularization by the present SGCP model. However, the obtained band could be considered as a slip band since it is nearly parallel to the rotated first slip direction within the band ( $60^\circ - 5.5^\circ = 54.5^\circ$ ).

Although GND-based SGCP theories fail to regularize idealized slip bands, the present investigation shows that they are capable of regularizing general localization bands. The next subsection aims at investigating the ability of such theories to correctly capture complex localization behaviors with competition between kink and slip bands.

## 6.2.2 Competition between slip and kink bands in single crystals undergoing single slip

The proposed finite deformation SGCP model is applied hereafter to reproduce the uniaxial tension problem of a single crystal undergoing single slip, which has been studied by [Ling et al. \(2018\)](#) using a micromorphic crystal plasticity approach. This problem is characterized by complex localization behavior with competition between kink and slip bands. The geometrical model is similar

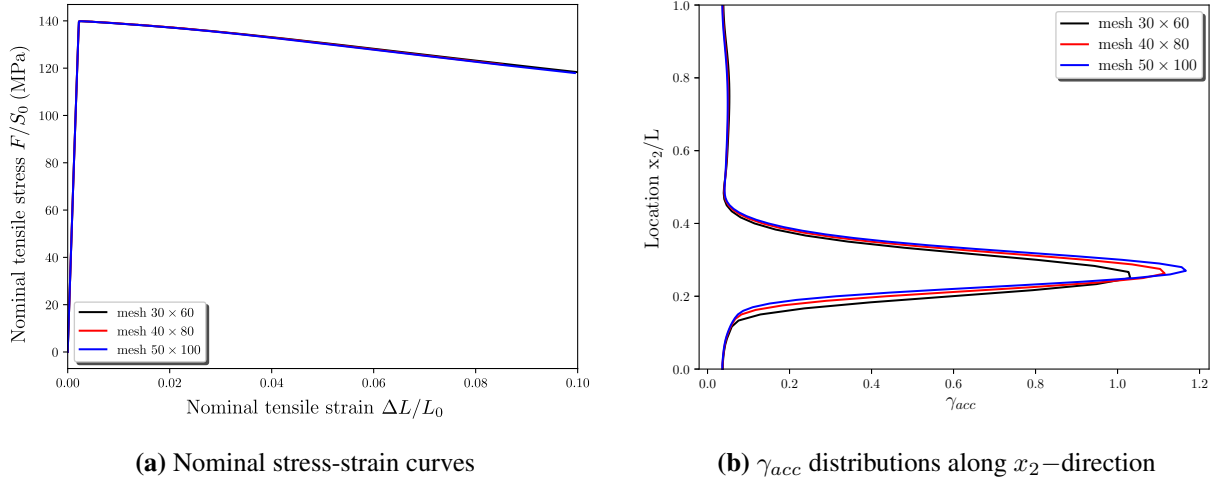


**Fig. 6.4.** Nominal stress-strain curves and accumulated plastic slip variable distributions along  $x_2$ -direction at nominal strain  $\Delta L/L_0 = 0.1$  for different mesh refinements ( $l_{en}/W = 0.2$ ,  $l_{dis} = 0$ ,  $H_\pi = -500$  MPa ).

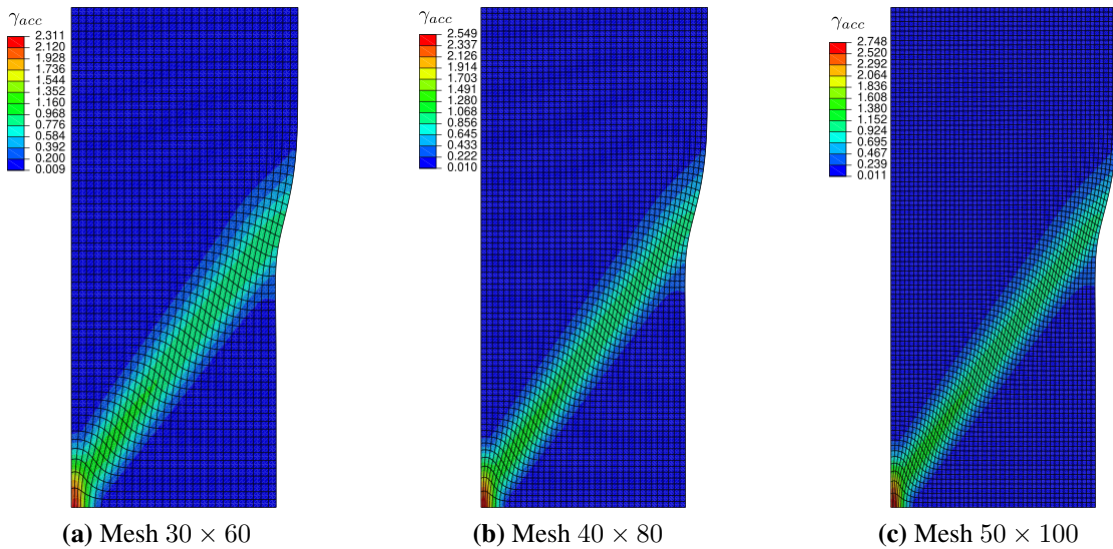


**Fig. 6.5.** Deformed meshes and contours of accumulated plastic slip variable  $\gamma_{acc}$  at nominal strain  $\Delta L/L_0 = 0.1$  for different mesh refinements ( $l_{en}/W = 0.2$ ,  $l_{dis} = 0$ ,  $H_\pi = -500$  MPa).

to that used by Ling et al. (2018). It consists of a single crystal plate of dimensions  $W$  and  $L$  in respectively  $x_1$ - and  $x_2$ -directions with an aspect ratio of  $L/W = 6$  and a single slip system oriented to an angle of  $\theta = -33.7^\circ$  with respect to  $x_1$ -direction. This plate is subjected to the following macroscopic boundary conditions:

$$\left. \begin{array}{ll} u_1 = 0, u_2 = 0 & \text{for } x_2 = 0 \\ u_1 = 0, u_2 = \varepsilon_l L & \text{for } x_2 = L \end{array} \right\} \quad (6.3)$$

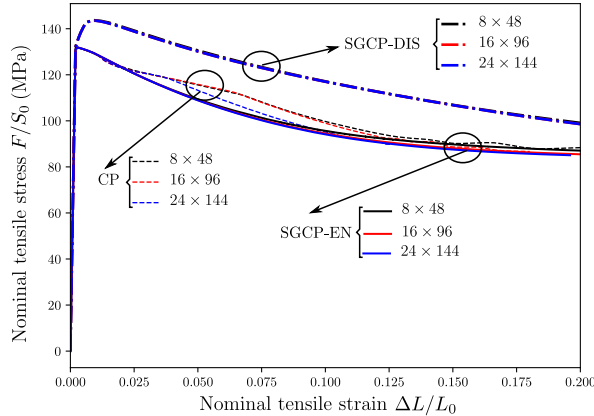
with the imposed tensile strain  $\varepsilon_l = 0.2$ . Furthermore, all the plate edges are assumed to be micro-free (transparent to dislocations). The material parameters are the same as those used in the previous uniaxial tension problem (Tab. 6.1), except for  $H_\pi$  which is set to a small positive value ( $H_\pi = 1$  MPa). For this problem, it is not needed to introduce material softening or imperfection to trigger strain localization. Indeed, the latter can occur due to geometrical softening induced by cross-section reduction and lattice rotation. Although the material parameters used in the present and Ling et al. (2018) investigations are not the same, comparison between the associated results is possible from a qualitative point of view, which is sufficient to meet the objectives of this subsection. As in Ling et al. (2018), the plastic scalar variable defined by (4.35) on the considered slip system is adopted to investigate strain localization and formation of slip and kink bands. Since the main difference between these bands is that kink bands are accompanied by a lot of lattice rotation, the lattice rotation angle (7.52) is used to detect the presence of the latter bands.

### 6.2.2.1 Regularization of the mesh-dependence of the stress-strain response

To check the mesh-regularization capability of the present SGCP model regarding the stress-strain response, different mesh refinements are considered:  $8 \times 48$ ,  $16 \times 96$  and  $24 \times 144$  meshes. Fig. 6.6 presents the associated results obtained using different constitutive configurations. In this figure, CP, SGCP-EN and SGCP-DIS curves are respectively associated with conventional CP ( $l_{en} = l_{dis} = 0$ ), SGCP including only higher-order energetic effects ( $l_{en}/W = 0.25$  and  $l_{dis}/W = 0$ ) and SGCP including only higher-order dissipative effects ( $l_{en}/W = 0$  and  $l_{dis}/W = 0.25$ ). For conventional crystal plasticity, results are highly mesh-dependent and display spurious oscillations. Similar results have been obtained by Ling et al. (2018). Activation of higher-order effects, regardless of their energetic or dissipative nature, allows for overcoming these mesh difficulties. No spurious oscillations are observed for the results associated with SGCP-EN and SGCP-DIS cases. Furthermore, mesh convergence is obtained for both cases as soon as a sufficiently refined mesh is used. Results associated with  $16 \times 96$  and  $24 \times 144$  meshes are in very close agreement for both these cases. The apparent increase of yield stress obtained for the SGCP-DIS case is due to the strengthening effects of the dissipative length scale  $l_{dis}$ , as widely recognized in the literature (Gurtin et al., 2007; Jebahi et al., 2020). In the following subsections, the considered plate is discretized using  $24 \times 144$  mesh.

### 6.2.2.2 Localization modes using conventional crystal plasticity

For comparison purposes, localization modes in the considered plate are first revisited using conventional CP ( $l_{en} = l_{dis} = 0$ ). Fig. 6.7a shows the evolution of the plastic slip variable  $\gamma$  (4.35) within this plate at different nominal strains. To investigate the formation of kink bands, evolution of the lattice rotation angle within the plate is presented in Fig. 6.7b. At the beginning of straining

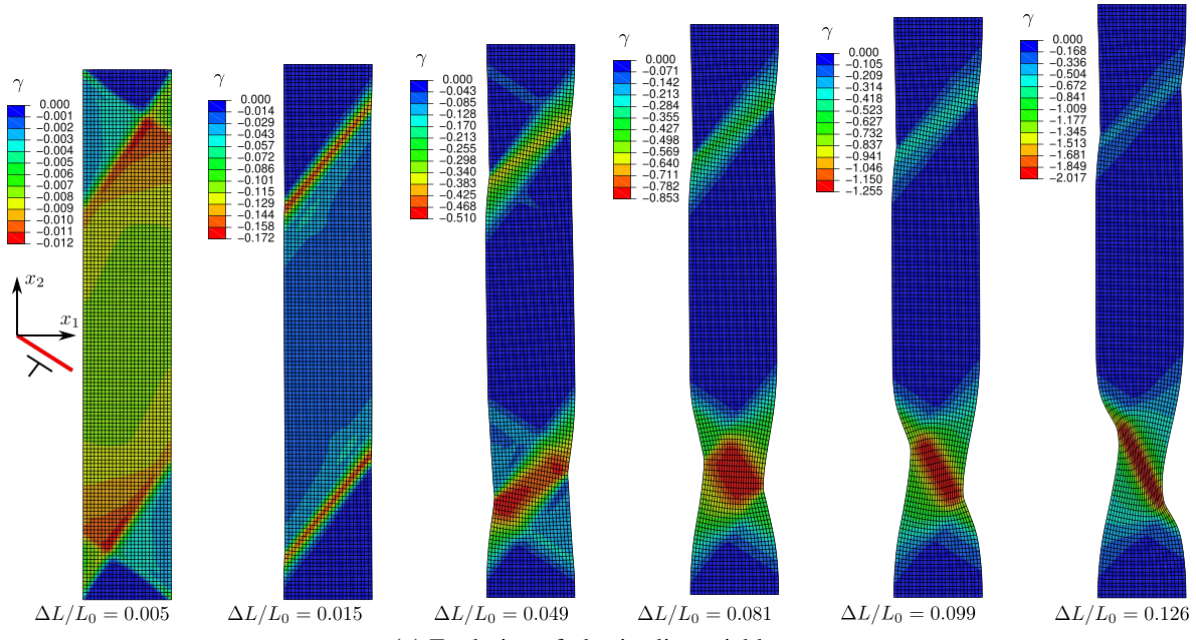
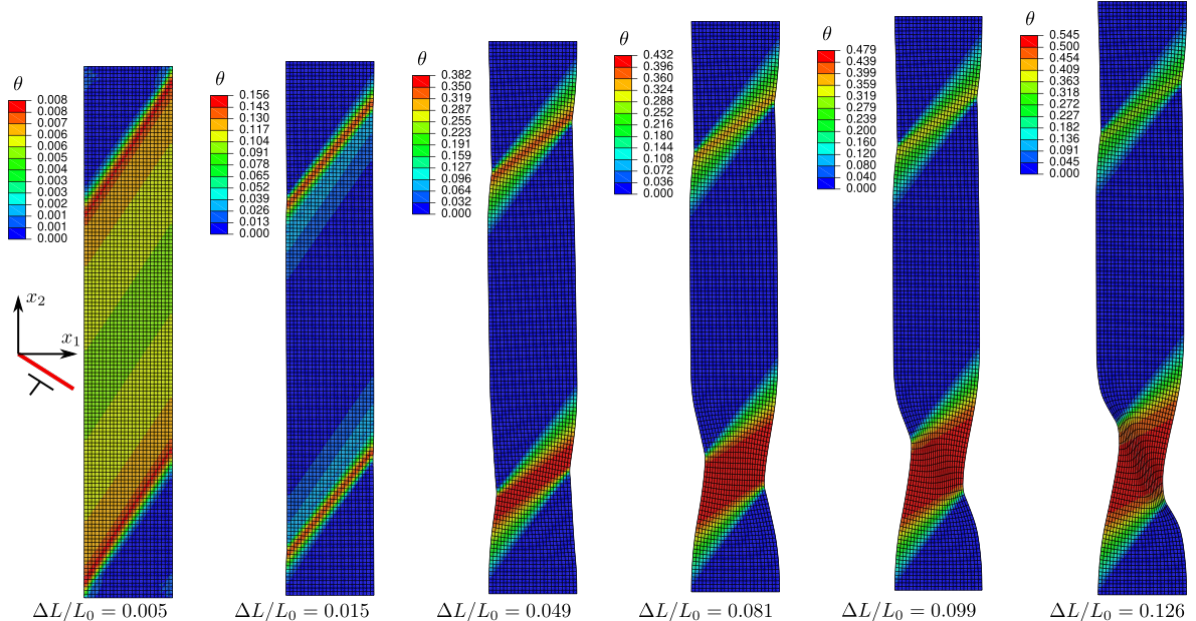


**Fig. 6.6.** Uniaxial tension results obtained using conventional CP (CP:  $l_{en} = l_{dis} = 0$ ), SGCP including only higher-order energetic effects (SGCP-EN:  $l_{en}/W = 0.25$ ,  $l_{dis} = 0$ ) and SGCP including only higher-order dissipative effects (SGCP-DIS:  $l_{en} = 0$ ,  $l_{dis}/W = 0.25$ ) for different meshes, with  $S_{\xi 0} = 60.84$  MPa and  $H_{\xi} = 0$ .

( $\Delta L/L_0 \approx 0.005$ ), both slip and kink bands start to emerge (crossed bands near the top and bottom edges of the plate). This would be in agreement with the bifurcation analysis of Asaro and Rice (1977). According to this analysis, slip and kink bands can simultaneously appear at incipient plasticity when using conventional CP. By increasing  $\Delta L/L_0$ , kinking phenomenon becomes dominant, leading to formation of two pronounced kink bands. These bands are accompanied by considerable lattice rotation, which results in local increase of the Schmid factor and then local decrease of the resolved shear stress (RSS) for the considered slip system. This geometrical softening mechanism acting in the kink regions promotes the development of kink bands. As straining increases, strain localizes in the kink band located near the bottom edge of the plate. In addition, the direction of localization starts to shift gradually, which is due to formation of a slip band crossing the initial kink region. Due to hardening effects, the RSS in the kink region increases and can reach a level for which the glide along the “unrotated” slip direction becomes easier, hence the appearance of the slip band. It can be observed from Fig. 6.7b that formation of this band does not give rise to lattice rotation. Finally, the formed slip band intensifies with straining, leading to final necking of the plate.

### 6.2.2.3 Localization modes using purely higher-order energetic effects

The above complex localization behavior is studied hereafter using the present SGCP model with only higher-order energetic effects. Figs. 6.8a and 6.8b present the contours of the plastic slip variable  $\gamma$  and the lattice rotation angle  $\theta$  within the studied plate at different nominal strains, with the energetic length scale  $l_{en} = 0.25 W$ . Compared to conventional crystal plasticity results, two broader kink bands appear at the beginning of straining ( $\Delta L/L_0 = 0.006$  in Fig. 6.8a). These bands rapidly aggregate to form a larger kink region with concentrated lattice rotation at the center of the studied plate. In the meanwhile, a central slip band appears and starts to interact with this region as shown at straining  $\Delta L/L_0 = 0.015$ . The kink-slip transition region shows a much smoother form compared to that obtained using conventional CP (Fig. 6.7a). As straining increases, the formed slip

(a) Evolution of plastic slip variable  $\gamma$ .(b) Evolution of lattice rotation angle  $\theta$  in radians.

**Fig. 6.7.** Evolution of plastic slip variable  $\gamma$  and lattice rotation angle  $\theta$  at different nominal tensile strains predicted by conventional CP ( $l_{en} = l_{dis} = 0$ ).

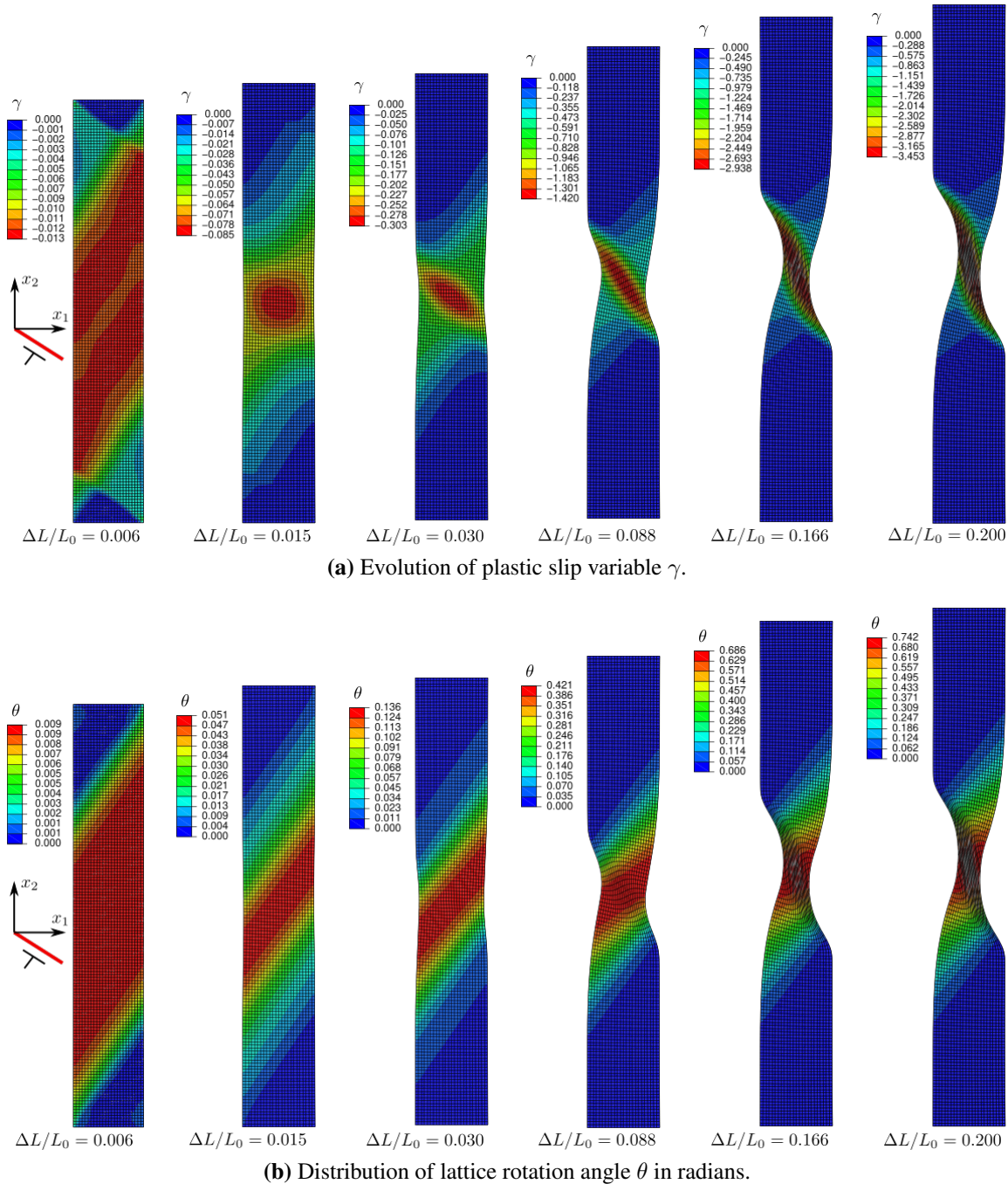


**Fig. 6.8.** Evolution of plastic slip variable  $\gamma$  and lattice rotation angle  $\theta$  at different nominal tensile strains predicted by SGCP including only higher-order energetic effects ( $l_{en}/W = 0.25$ ,  $l_{dis} = 0$ ).

band becomes more and more intensified, leading to final necking of the plate.

To investigate the influence of the higher-order energetic effects on the present localization behavior, different values of  $l_{en}$  are tested. Fig. 6.9 presents the associated results in terms of plastic slip contours in the studied plate at straining  $\Delta L/L = 0.006$ , which corresponds to emergence of kink bands. The width of the obtained bands as well as the distance between them are function of

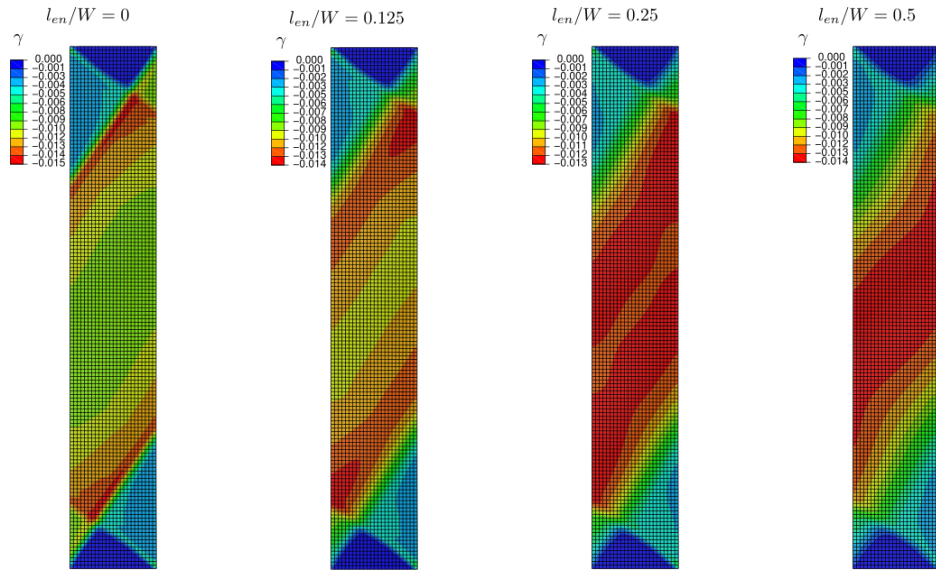


**Fig. 6.9.** Influence of energetic length scale  $l_{en}$  on the formation of the kink bands at the beginning of straining  $\Delta L/L_0 = 0.006$  ( $l_{dis} = 0$ ).

$l_{en}$ . By increasing this parameter, larger and closer kink bands are obtained. For sufficiently large  $l_{en}$ , single kink band located at the center of the considered plate is formed. Fig. 6.10 presents the nominal tensile stress-strain curves and the plastic slip variable distributions along the plate length direction for different energetic length scales. Although no change in initial yield is observed, the stress level after yielding increases with increasing  $l_{en}$  due to strain gradient hardening effects (Fig. 6.10a). In addition, larger  $l_{en}$  leads to larger final localization band with lower peak value of plastic slip  $\gamma$  in this band (Fig. 6.10b). This is in accordance with several investigations based on nonlocal approaches (Sluys and Estrin, 2000; Niordson and Redanz, 2004; Borg, 2007; Ling et al., 2018; Kuroda and Needleman, 2019). The energetic length scale behaves as a “localization limiter” and governs the width of localization bands.

#### 6.2.2.4 Localization modes using purely higher-order dissipative effects

The present subsection aims at investigating the higher-order dissipative effects on the localization behavior in the considered plate, while neglecting the higher-order energetic effects ( $l_{en} = 0$ ). One distinctive feature of the present SGCP model is that the higher-order dissipative effects are uncoupled from the first-order ones. The advantages of this uncoupled constitutive assumption have already been discussed in Jebahi et al. (2020). It is worth recalling here that such an assumption makes it possible to flexibly choose the initial value of the higher-order dissipative slip resistance  $S_{\xi 0}$ . This parameter can also be set to zero in order to obtain progressive activation of the higher-order dissipative effects, as for the energetic ones involved in the previous subsection. In this case, a nonzero higher-order hardening modulus  $H_{\xi}$  is necessary to activate such effects according to (4.32). Using  $S_{\xi 0} = 0$  and  $H_{\xi} = 60.84$  MPa, the obtained results (not presented in the paper) are qualitatively quite similar to those obtained in the above subsection.

Applying nonzero  $S_{\xi 0}$ , finite higher-order dissipative stresses take place and instantaneously activate with the emergence of strain gradients. Influence of these stresses is investigated hereafter

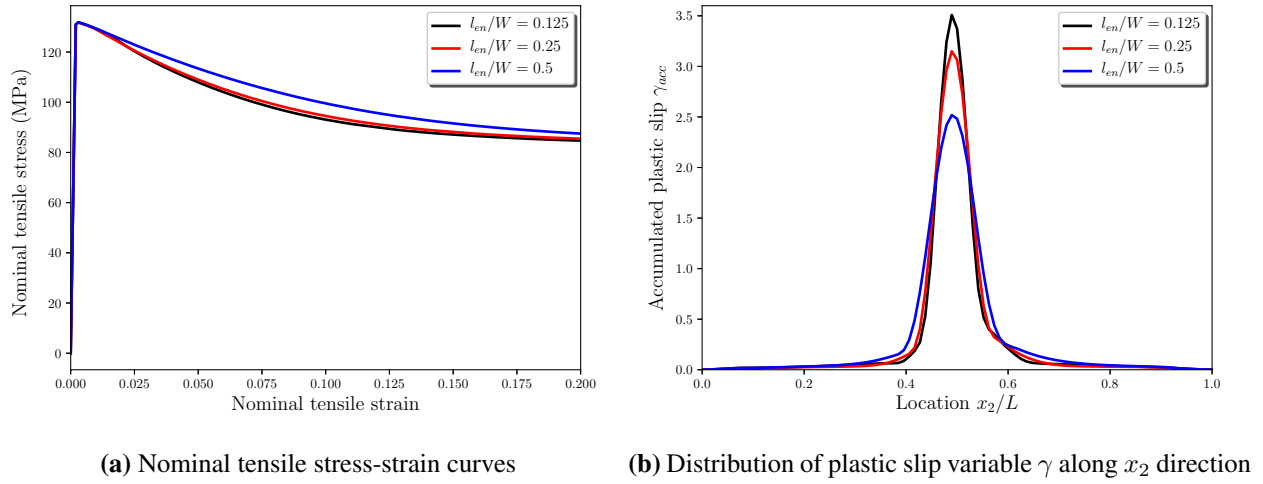


**Fig. 6.10.** Influence of energetic length scale  $l_{en}$  on the nominal stress-strain responses and distribution of plastic slip variable  $\gamma$  along  $x_2$  direction at  $\Delta L/L_0 = 0.2$  ( $l_{dis} = 0$ ).

assuming  $S_{\xi 0} = S_{\pi 0} = 60.84$  MPa, as in classical SGCP theories with coupled dissipation, while keeping  $H_\xi = 60.84$  MPa. Figs. 6.11a and 6.11b present the associated results in terms of plastic slip variable and lattice rotation distributions in the plate at different nominal tensile strains. These results are quite different from those obtained using conventional CP and SGCP including progressive activation of higher-order effects. Instead of two kink bands, a large central region parallel to the slip direction appears at the beginning of straining ( $\Delta L/L_0 = 0.0035$ ) with nearly plateau-shaped distribution of  $\gamma$ . The width of this region progressively decreases with straining. In the meanwhile, less pronounced kink region appears at the plate center and interacts with the initial slip region, as can be shown by analyzing the lattice rotation distributions in the plate (Fig. 6.11b). The width of both these regions continues to reduce with increasing  $\Delta L/L_0$  until final necking of the plate. The final localization band is oriented to an angle close to that of the slip direction. Compared to those obtained in the previous subsections, this band is much more diffuse. Using higher-order dissipative effects with nonzero  $S_{\xi 0}$ , slip localization seems to outweigh kinking, although the latter phenomenon is not completely removed.

Effects of  $l_{dis}$  on the localization response of the considered plate are given in Fig. 6.12, which is obtained assuming  $S_{\xi 0} = S_{\pi 0} = 60.84$  MPa and  $H_\xi = 60.84$  MPa. This parameter leads to similar effects as for  $l_{en}$  regarding the increase of hardening after yielding and the growth of the width of the final localization band. In addition to these effects,  $l_{dis}$  presents strengthening effects which are illustrated by an increase of the initial yield.

### 6.3 Application to strain localization in poly-crystals

In the previous section, capabilities and limitations of the finite deformation SGCP model in capturing localization phenomena in single crystals have been demonstrated by a series of elementary numerical examples. The present section aims at extending this investigation by considering poly-crystalline structures. To this end, the proposed finite deformation SGCP and GB models are

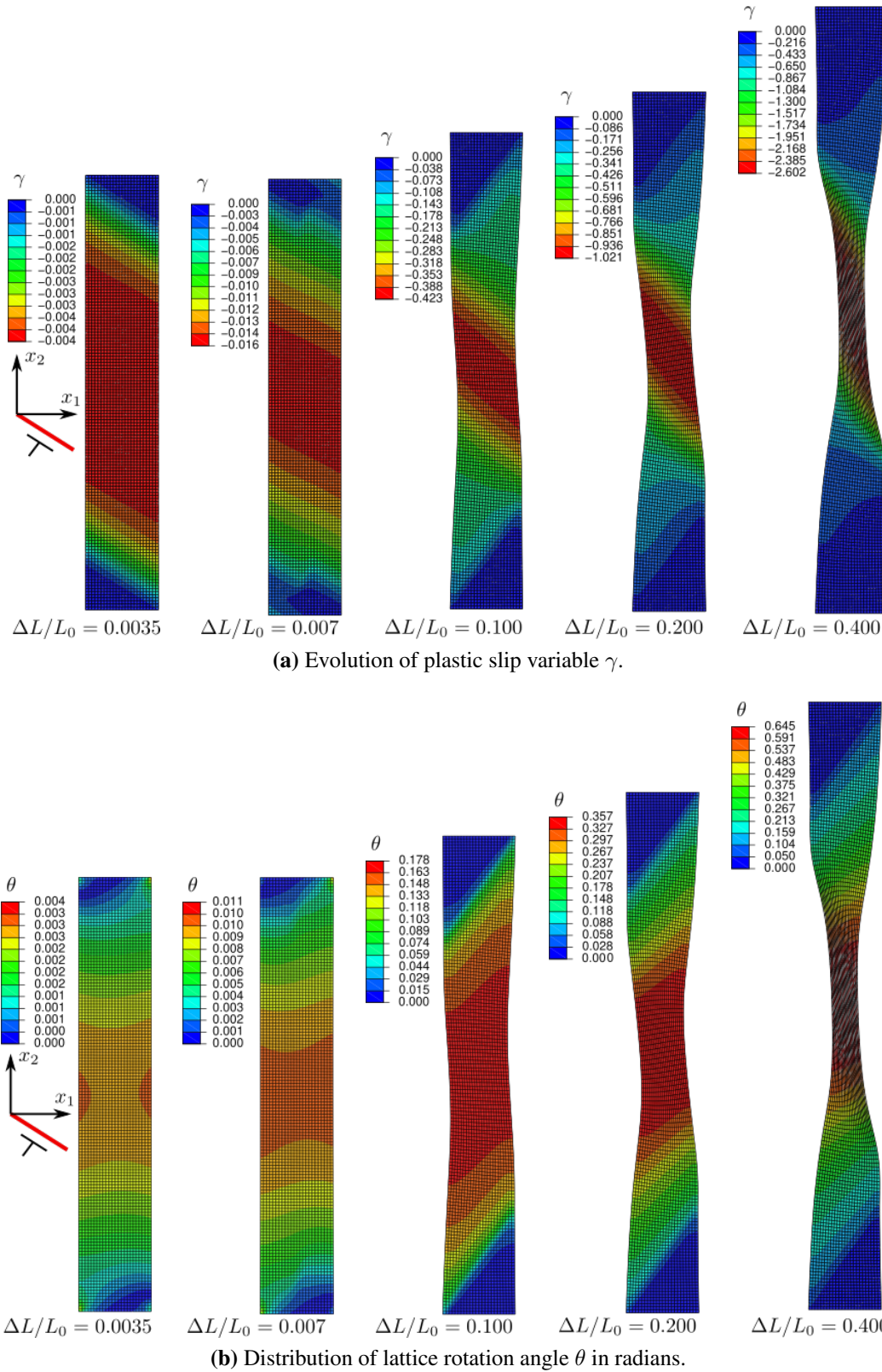


**Fig. 6.11.** Evolution of plastic slip variable  $\gamma$  and lattice rotation angle  $\theta$  at different nominal tensile strains predicted by SGCP including only higher-order dissipative effects with nonzero initial higher-order slip resistance  $S_{\xi 0}$  ( $l_{en} = 0$ ,  $l_{dis}/W = 0.25$ ,  $S_{\xi 0} = 60.84$  MPa,  $H_{\xi} = 60.84$  MPa)

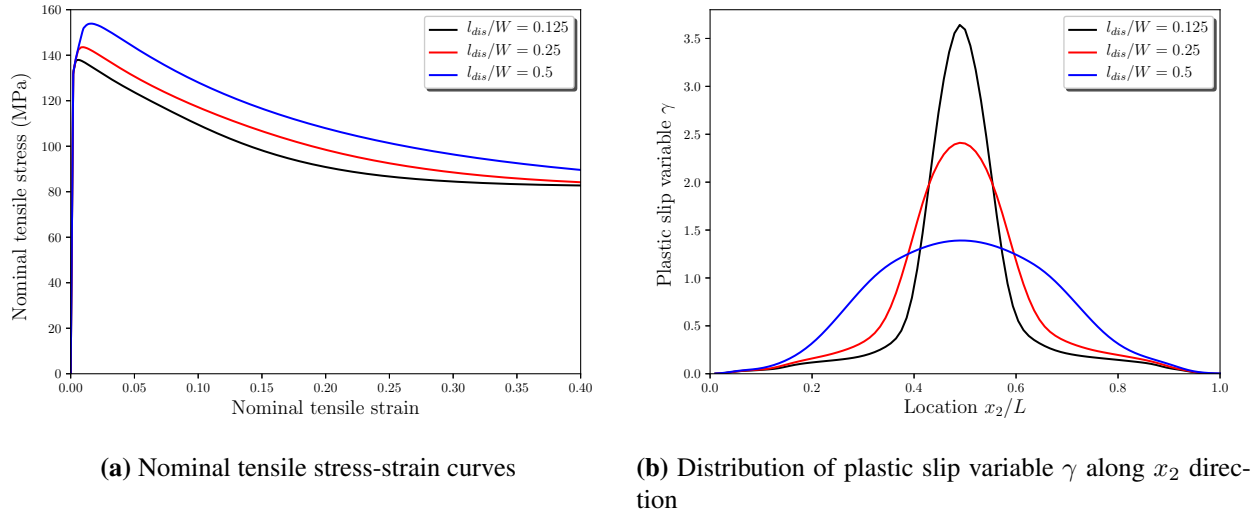


**Fig. 6.12.** Influence of dissipative length scale  $l_{dis}$  on tensile nominal stress-strain response and the distribution of plastic slip variable  $\gamma$  along  $x_2$  direction at  $\Delta L/L_0 = 0.4$  ( $l_{en} = 0$ ,  $S_{\xi 0} = 60.84$  MPa,  $H_\xi = 60.84$  MPa).

applied to simulate uniaxial tensile response of poly-crystalline plates having the same geometrical dimensions as those used in the single-crystal uniaxial tension simulations. To study grain size effects, three poly-crystalline plates with different grain sizes are prepared based on the Voronoï technique as shown in Fig. 6.13. Each grain is assumed to have two slip systems with an angle  $\theta = 60^\circ$  between them. The grains, which are assumed to be randomly oriented, are supposed to have the same material parameters as in the single-crystal uniaxial tension simulation. These parameters as well as those applied at the grain boundaries are presented in Tab. 6.2. Furthermore, the same microscopic and macroscopic boundary conditions are applied. All the boundaries are assumed to be micro-free and the top and bottom boundaries are subject to the following displacement conditions:

$$\left. \begin{array}{ll} u_1 = 0, & u_2 = 0 \quad \text{for } x_2 = 0 \\ u_1 = 0, & u_2 = \varepsilon_l L \quad \text{for } x_2 = L \end{array} \right\} \quad (6.4)$$

with the imposed tensile strain  $\varepsilon_l = 0.2$ .

### 6.3.1 Grain-induced size effects

Grain contributions to size effects on the poly-crystalline localization phenomena are studied in this subsection assuming micro-free GB conditions ( $\kappa = 0$ ,  $S_{GB0} = 0$ ,  $H_{GB} = 0$ ). For comparison purposes, results associated with conventional crystal plasticity (CCP) applied within the grains will first be analyzed ( $l_{en} = l_{dis} = 0$ ). Then, the influence of higher-order energetic and dissipative grain effects will be discussed.

Considering the case of CCP simulations, to study the effects of the random distribution of the grain orientations, five poly-crystalline plates with randomly distributed grains are prepared for each grain size. Fig. 6.14 presents the associated results in terms of nominal stress-strain curves.

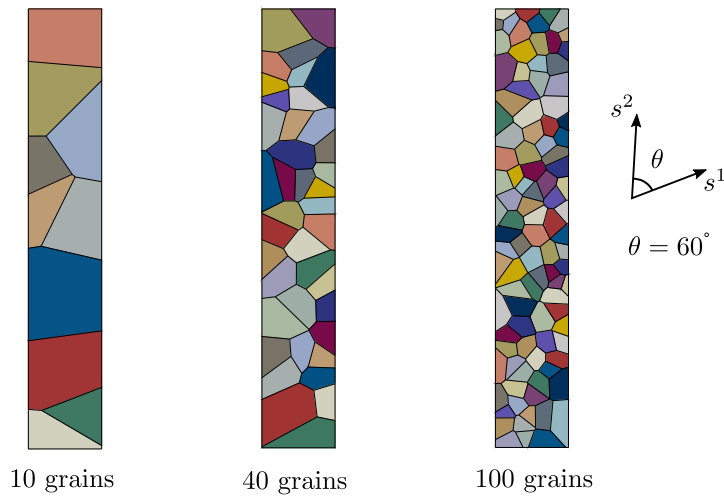


**Fig. 6.13.** Poly-crystalline plates composed of several grains having two slip systems and different grain sizes

**Tab. 6.2.** Material parameters implied for uniaxial tension of poly-crystalline plates, the bulk is inspired by Peirce et al. (1983); Kuroda (2011).

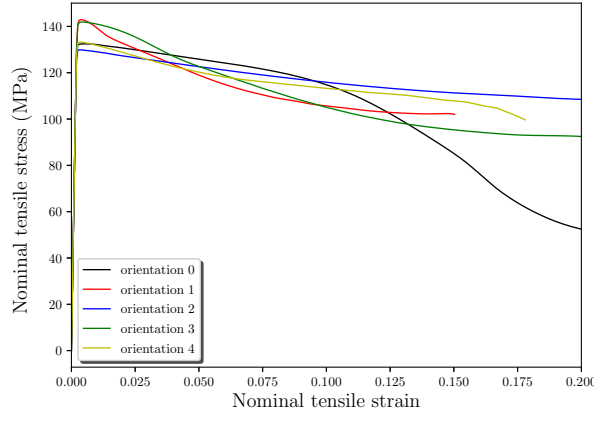
Material parameter name	Symbol	Value	Unit
Young's modulus	$E$	60.84	GPa
Poisson's ratio	$\nu$	0.3	—
Reference slip rate for bulk	$\dot{\gamma}_0^\alpha$	0.001	$\text{s}^{-1}$
Rate-sensitivity parameter for bulk	$m$	0.005	—
Higher-order energetic slip resistance	$X_0$	60.84	MPa
Initial first-order dissipative slip resistance	$S_{\pi 0}$	60.84	MPa
Initial higher-order dissipative slip resistance	$S_{\xi 0}$	case study	MPa
First-order hardening modulus	$H_\pi$	case study	MPa
Second-order hardening modulus	$H_\xi$	case study	MPa
Energetic length scale	$l_{en}$	case study	$\mu\text{m}$
Dissipative length scale	$l_{dis}$	case study	$\mu\text{m}$
Defect energy index	$n$	2	—
Reference flow rate for GB	$\dot{G}_0$	0.001	$\text{s}^{-1}$
Rate-sensitivity parameter for GB	$d$	0.005	—
Energetic coefficient for GB	$\kappa$	case study	$\text{N m}^{-1}$
Dissipative initial slip resistance for GB	$S_{GB_0}$	case study	$\text{N m}^{-1}$
Dissipative hardening modulus for GB	$H_{GB}$	case study	$\text{N m}^{-1}$

For a given grain size, the stress-strain response depends on the distribution of grain orientations. The latter influences both the yield strength and the strain hardening. These effects, which can be classified as first-order extrinsic size effects, have been reported in several works from the literature (Geers et al., 2006; Yalçinkaya et al., 2018). The scatter of results at small imposed tensile strain ( $\varepsilon_l < 0.05$ ) decreases with increasing the number of grains (*i.e.*, decreasing the grain size) and become negligible for the case of 100 grains (Fig. 6.14c). By increasing the number of grains, the anisotropic and individual grain effects become less pronounced, reducing the scatter of the homogeneous results. However, after localization, large scatter is obtained even in the case of 100 grains (Fig. 6.14). Contrary to the homogeneous tensile behavior which is more sensitive to the number of grains in the tensile direction, the localization behavior is also sensitive to the small number of grains in the transverse direction. Fig. 6.15 shows the accumulated plastic variable  $\gamma_{acc}$  contours at the end of tensile loading ( $\varepsilon_l = 0.2$ ) obtained using 40 grains with five different random distributions of grain orientations. Different positions of localized strains are obtained, depending on the random position of the grain having the most favorable orientation for localization. The steps of localization are illustrated in Fig. 6.16 for a given distribution of grain orientations (orientation “0”). The obtained localization behavior shares some similarities with that obtained within a single crystal subjected to the same loading conditions (Fig. 6.7a). At incipient plasticity, two localization regions appear in the plate. As straining increases, strain localizes in one of these regions located near the bottom edge. However, the localization regions do not have the form of narrow bands as in the case of a single crystal. It should be noted that, although not presented, the poly-crystalline stress-strain responses obtained using CCP in the grains show mesh-dependence pathology, due to the lack of internal length scale(s).

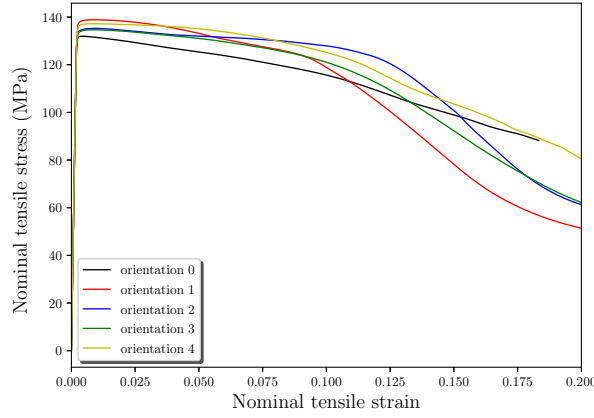
To study the influence of higher-order effects, the 40-grain plate with grain orientation “0” is considered in the following, while always assuming micro-free boundary conditions. Fig. 6.17 shows the associated nominal stress-strain responses obtained using different higher-order energetic and dissipative length scales. As illustrated in Fig. 6.17a, the energetic length scale  $l_{en}$  not only increases the strain hardening but also affects the beginning of the stress drop, which marks the beginning of strain localization. Larger  $l_{en}$  yields earlier onset of localization which occurs at smaller imposed tensile strain. The single crystal example in Fig. 6.10a shows only a strain hardening effect of  $l_{en}$ . Concerning dissipative length scale effects (Fig. 6.17b),  $l_{dis}$  leads to obvious strengthening as in the case of single crystal (Fig. 6.12a). Contrary to  $l_{en}$ ,  $l_{dis}$  seems to present a delaying effect on the onset of localization which occurs at slightly larger imposed tensile strain. However, this effect is not as obvious as that of  $l_{en}$ . The accumulated plastic slip variable  $\gamma_{acc}$  contours at the end of loading are presented in Fig. 6.17, for different energetic and dissipative length scales. Comparison of these contours with that obtained using CCP with grain orientation “0” (Fig. 6.15) shows that both  $l_{en}$  and  $l_{dis}$  significantly affect the localization behavior.

### 6.3.2 Grain boundary contributions to size effects

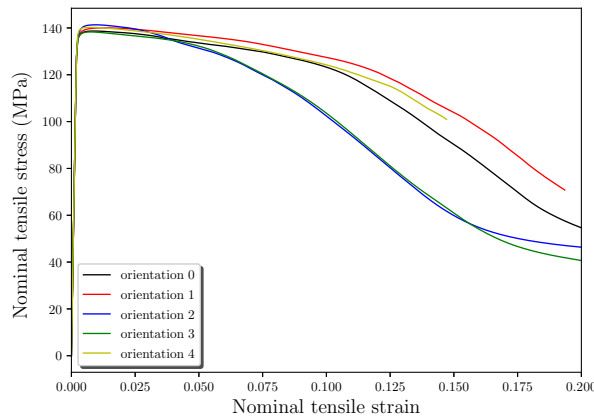
The GB effects on the poly-crystalline localization behavior are investigated in this subsection, using 40-grain plate with grain orientation “0”. For simplicity, only higher-order energetic effects are activated in the grains. ( $l_{en}/W = 0.25$ ,  $l_{dis} = 0$ ). Fig. 6.19 shows the nominal stress-strain curves obtained using purely energetic GB effects ( $S_{GB_0} = 0$ ,  $H_{GB} = 0$ ) and purely dissipative GB effects with no GB hardening ( $\kappa = 0$ ,  $H_{GB} = 0$ ). It can be shown from Fig. 6.19a that larger GB energetic coefficient  $\kappa$  leads to larger strain hardening, which is in accordance with



(a) 10 grains



(b) 40 grains



(c) 100 grains

**Fig. 6.14.** Nominal stress-strain curves obtained using CCP in the grains ( $l_{en} = l_{dis} = 0$ ) and micro-free conditions at the grain boundaries ( $\kappa = 0, S_{GB_0} = 0, H_{GB} = 0$ ), for different randomly generated grain orientations and different grain sizes.

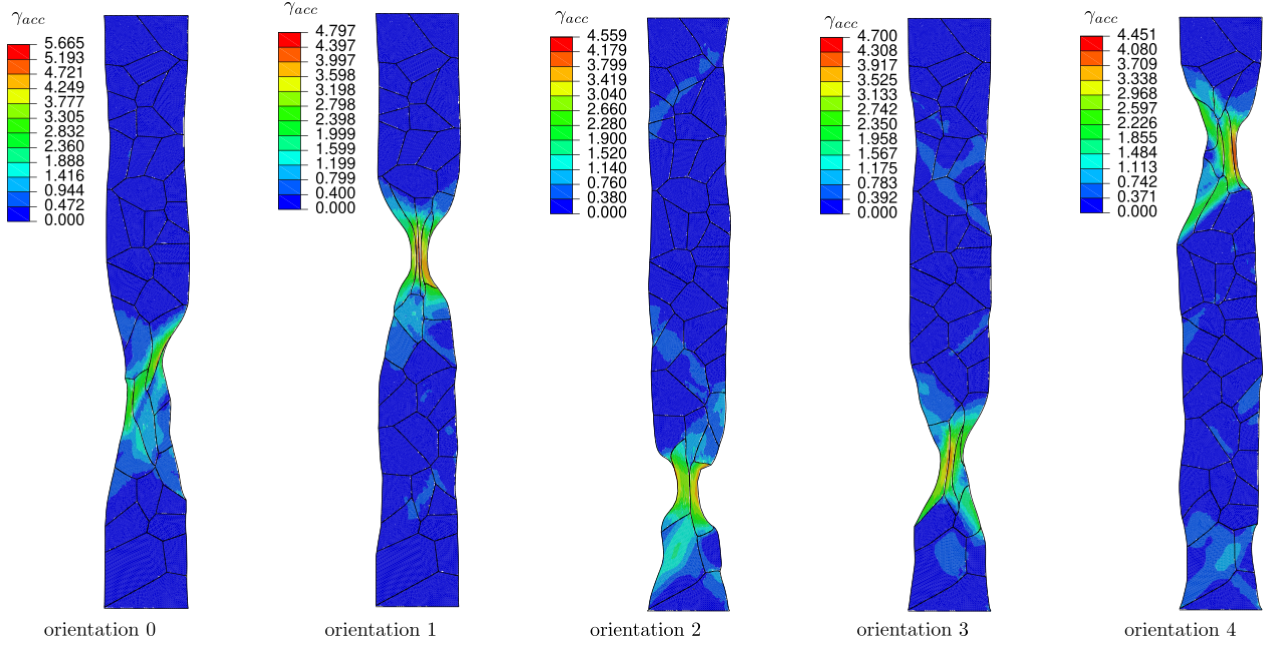


**Fig. 6.15.** Accumulated plastic slip variable  $\gamma_{acc}$  contours within 40-grain plates at the end of loading obtained using CCP in the grains ( $l_{en} = l_{dis} = 0$ ) and micro-free conditions at the grain boundaries ( $\kappa = 0, S_{GB_0} = 0, H_{GB} = 0$ ), for different randomly generated grain orientations.

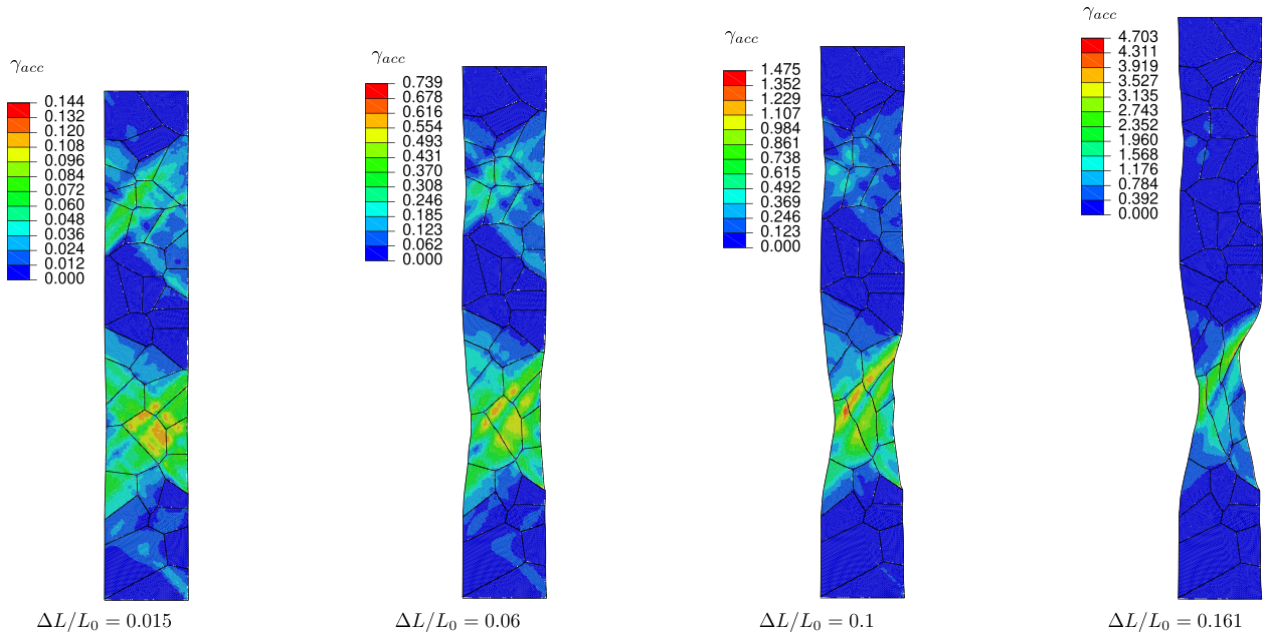


**Fig. 6.16.** Accumulated plastic slip variable  $\gamma_{acc}$  contours within 40-grain plate with grain orientation "0" at different loading stages obtained using CCP in the grains ( $l_{en} = l_{dis} = 0$ ) and micro-free conditions at the grain boundaries ( $\kappa = 0, S_{GB_0} = 0, H_{GB} = 0$ ).

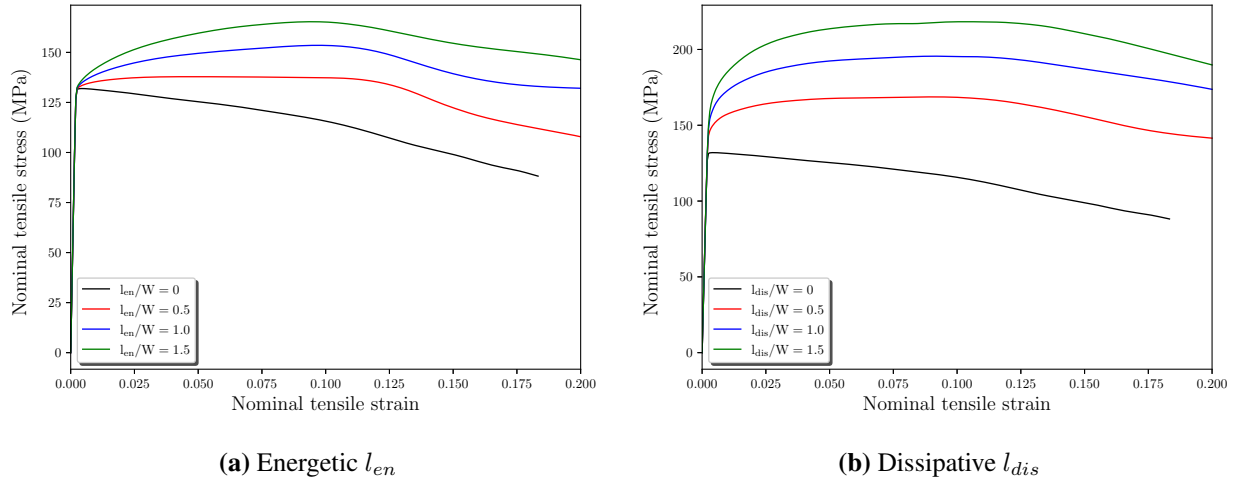


**Fig. 6.17.** Influence of higher-order energetic and dissipative effects on the nominal tensile stress-strain response of 40-grain plate with grain orientation “0”, using micro-free GB conditions ( $\kappa = 0, S_{GB_0} = 0, H_{GB} = 0$ ).

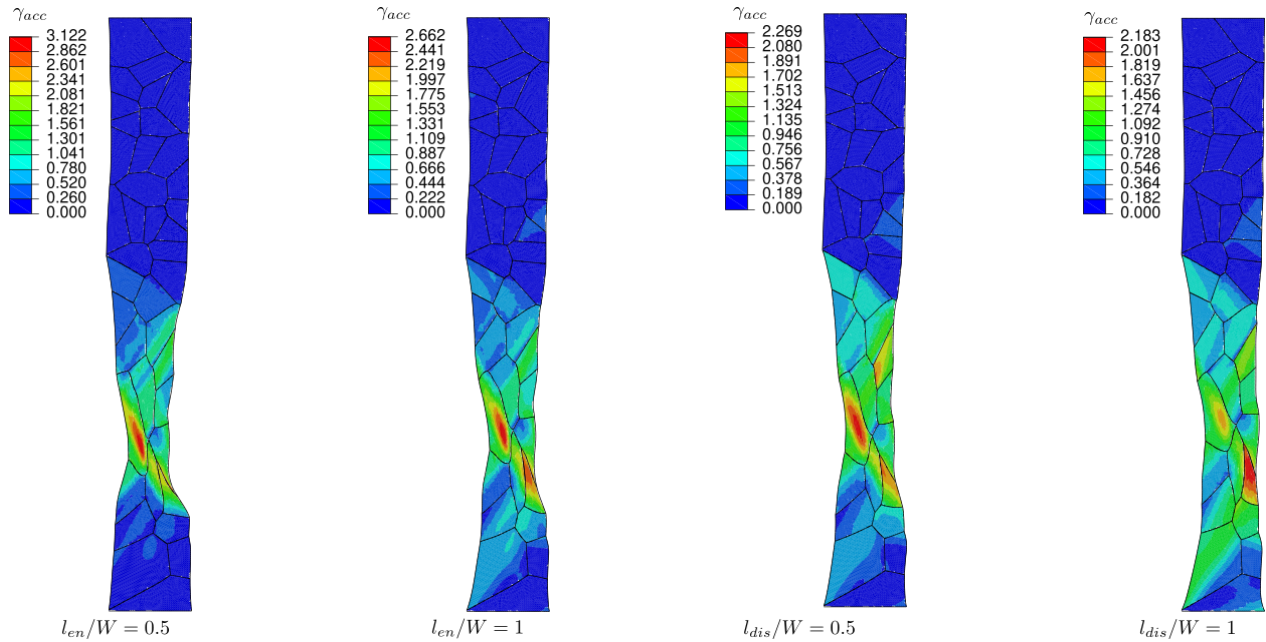


**Fig. 6.18.** Accumulated plastic slip variable  $\gamma_{acc}$  contours within 40-grain plate with grain orientation “0” at the end of loading using different higher-order energetic and dissipative length scales and micro-free GB conditions ( $\kappa = 0, S_{GB} = 0, H_{GB} = 0$ ).

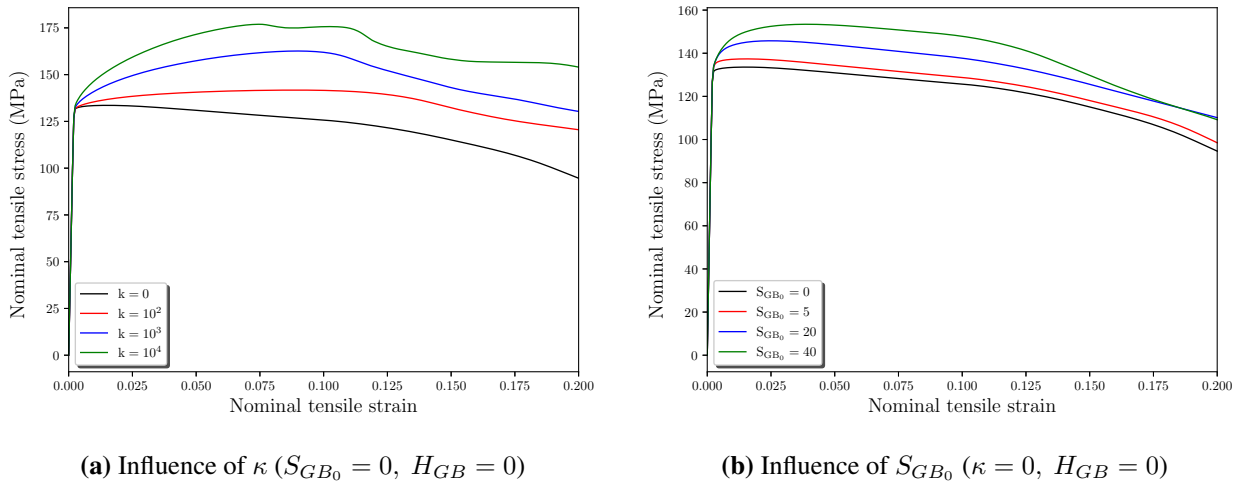


**Fig. 6.19.** Influence of purely GB energetic and purely GB dissipative effects on nominal stress-strain response of 40-grain poly-crystalline plate with grain orientation “0”, obtained using  $l_{en}/W = 0.25$ ,  $l_{dis} = 0$ .

the bi-crystal assessment results presented in subsection 5.4.2. In addition, as for the energetic length scale  $l_{en}$ , this parameter presents an accelerating effect on the onset of localization, which occurs at smaller imposed tensile strain when increasing  $\kappa$ . Regarding the influence of initial GB dissipative resistance  $S_{GB_0}$ , larger values increase the yield stress as shown in 6.19b. Analysis of the  $\gamma_{acc}$  contours at the end of loading for energetic and dissipative GB parameters shows the strong influence of the grain boundary settings on the final localization pattern (Fig. 6.20). This result highlights the necessity of correctly considering GB phenomena in the investigation of the formability of miniaturized structures.

### 6.3.3 Overall size effects predicted by the SGCP-GB numerical framework

Both first- and second-order size effects may take place during deformation of miniaturized structures. An example considering all the capabilities of the SGCP-GB numerical framework in capturing these effects is presented hereafter. For illustrative purposes, the higher-order grain parameters are set as:  $l_{en} = l_{dis} = 2 \mu\text{m}$ ,  $S_{\xi 0} = 60.84 \text{ MPa}$ ,  $H_{\xi} = 60.84 \text{ MPa}$ . Furthermore, the GB parameters are chosen as:  $\kappa = 1e2 \text{ N m}^{-1}$ ,  $S_{GB_0} = 5 \text{ N m}^{-1}$ ,  $H_{GB} = 1e3 \text{ N m}^{-1}$ . It should be noted that these parameters may not refer to any specific materials, but for demonstrating intentions. To study size effects on the overall poly-crystalline localization behavior, three poly-crystalline plates with different geometrical dimensions are used. These plates are obtained by applying two-dimensional scaling of the 40-grain plate with grain orientation “0”, which is used in the previous subsections, while preserving the ratio between the plate length  $L$  and width  $W$  (*i.e.*, constant  $L/W = 6$ ). The width  $W$  ( $= L/6$ ) is used to characterize the geometry size in the following.

Fig. 6.21 presents the obtained results in terms of nominal stress-strain responses, obtained for different geometry sizes  $W$ . The peculiar phenomenon “smaller is stronger” can clearly be observed in this figure, where larger yield strength is obtained for smaller  $W$ . To investigate the relation between strain localization and geometry size, the critical points (corresponding the onset

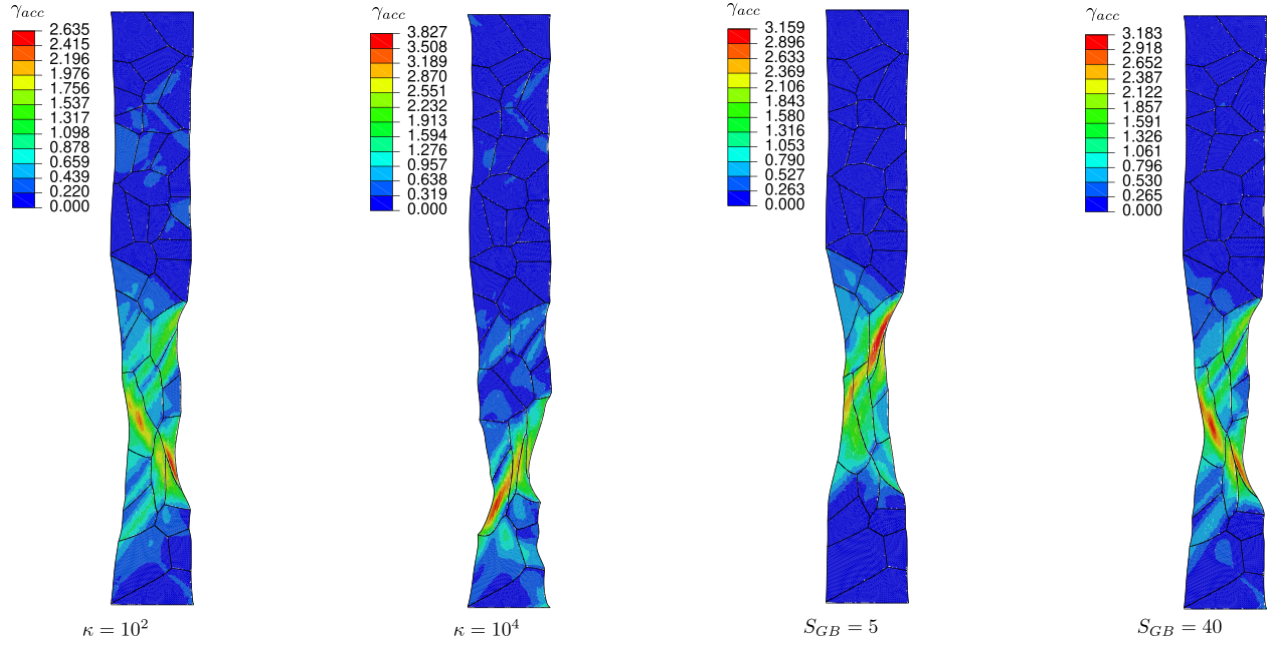


**Fig. 6.20.** Deformed contours of accumulated plastic slip variable  $\gamma_{acc}$  at the end of loading using different GB energetic coefficient  $\kappa$  ( $S_{GB} = 0$ ,  $H_{GB} = 0$ ,  $l_{en}/W = 0.25$ ,  $l_{dis} = 0$ ) and dissipative initial resistance  $S_{GB_0}$  ( $\kappa = 0$ ,  $H_{GB} = 0$ ,  $l_{en}/W = 0.25$ ,  $l_{dis} = 0$ ) for plate with 40 grains using grain orientation “0” .

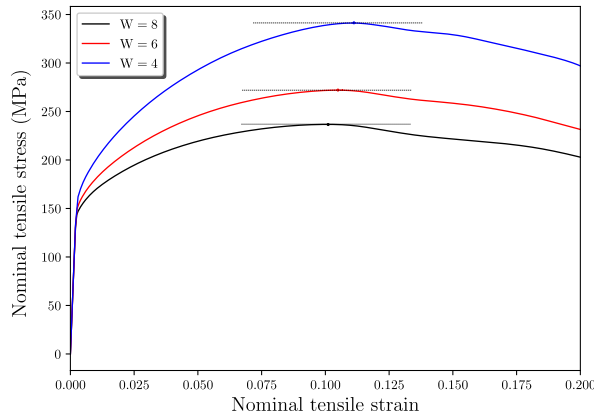


**Fig. 6.21.** An illustrative example of the overall size effects for different values of geometry size  $W$  in terms of nominal stress-strain curves using SGCP constitutive parameters ( $l_{en} = l_{dis} = 2 \mu\text{m}$ ,  $S_{\xi 0} = 60.84 \text{ MPa}$ ,  $H_{\xi} = 60.84 \text{ MPa}$ ) in the bulk and GB parameters ( $\kappa = 1e2 \text{ N m}^{-1}$ ,  $S_{GB_0} = 5 \text{ N m}^{-1}$ ,  $H_{GB} = 1e3 \text{ N m}^{-1}$ ).

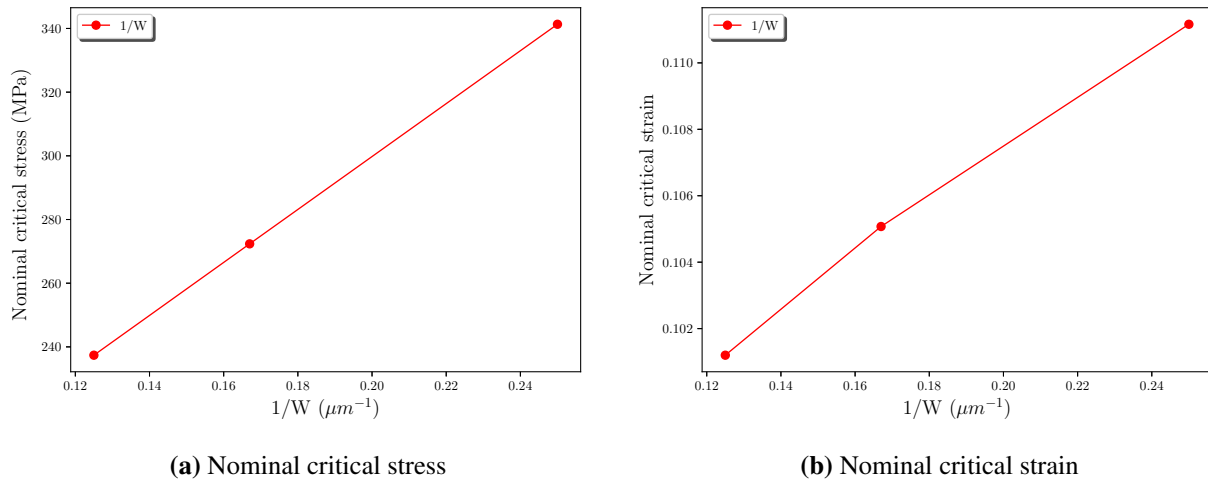


**Fig. 6.22.** Relation between nominal critical stress and strain at the onset of strain localization with respect to the inverse of geometry horizontal dimension  $1/W$  using both SGCP ( $l_{en} = l_{dis} = 2 \mu\text{m}$ ,  $S_{\xi_0} = 60.84 \text{ MPa}$ ,  $H_\xi = 60.84 \text{ MPa}$ ) and GB parameters ( $\kappa = 1e2 \text{ N m}^{-1}$ ,  $S_{GB_0} = 5 \text{ N m}^{-1}$ ,  $H_{GB} = 1e3 \text{ N m}^{-1}$ ).

of strain localization referring to the maximum force criterion) are determined in Fig. 6.21 and the associated critical strains and stresses are obtained. As can be seen in Fig. 6.17, the latter quantities increase nearly linearly with the inverse of the geometry size ( $1/W$ ). Considering energetic and dissipative effects in the grains and at the grain boundaries, smaller geometry size seems to delays the onset of localization. The points in Fig. 6.22b can be linked with specific points in the forming limit diagrams associated with the considered plates. Using the proposed SGCP-GB numerical framework, future work will focus on the determination of these diagrams for different geometry sizes to study size effects on the formability of ultra-thin sheet metals.

## 6.4 Conclusions

The present chapter focused on the application of the finite deformation SGCP-GB numerical tool to study localization phenomena within single- and poly-crystalline structures. The capabilities of the proposed finite deformation SGCP model in regularizing different kinds of localization bands were first revisited using several elementary localization tests. It was shown that only idealized slip bands, which are not quite common in real problems, cannot be regularized by the applied model. This is due to the fact that slip gradients in the direction normal to the slip plane do not correspond to GNDs and no size effects are predicted for the development of such normal slip gradients. With regard to idealized slip bands, the present SGCP model behaves as a conventional crystal plasticity model. This is also the case for Cosserat crystal plasticity models in which size effects are only triggered by lattice curvature (Forest, 1998).

The good capabilities of the SGCP model in dealing with general localization bands motivated the application of this model to study the complex localization behavior with competition between slip and kink bands, which is encountered within single crystals undergoing single slip. This behav-

ior has already been studied by [Ling et al. \(2018\)](#) using reduced micromorphic approach. To this end, a uniaxial tension problem of a single crystal plate having single slip system was simulated using the present SGCP model. Different constitutive configurations, including purely higher-order energetic effects and purely higher-order dissipative effects, are considered. Simulations using conventional crystal plasticity (CCP) were also performed for comparison purposes. Results associated with the latter simulations show mesh-dependence pathology. It was shown that this pathology can be removed by including higher-order effects, either energetic or dissipative. Depending on the nature of the higher-order effects, different localization behaviors were obtained. Application of higher-order energetic effects results in a localization behavior with competition between slip and kink bands. The obtained results are in good agreement with those obtained by ([Ling et al., 2018](#)) using micromorphic approach. Application of higher-order dissipative effects with nonzero higher-order initial slip resistance leads to a localization behavior which is overwhelmingly dominated by slip banding, although analysis of lattice rotation during localization shows the coexistence of kinking.

After application of the SGCP model to capture localization phenomena in single crystals, the this model as well as the GB model were applied to study size effects on the localization response of poly-crystalline structures. The interesting features of the SGCP-GB numerical framework in capturing different kinds of first- and second-order size effects on the poly-crystalline localization phenomena were shown through this study. It was shown that higher-order energetic effects (both in the grains and at the grain boundaries) act as accelerators for strain localization. On the contrary, higher-order dissipative effects have tendency to delay this phenomenon.

# Chapter 7

## Conclusions and perspectives

### 7.1 Conclusions

The strong demand on miniaturized products has motivated numerous investigations aiming at the accurate manufacture of high-quality products in small scales. Among these works, modeling the material behavior in small scale has become a hot topic due to the occurrence of the so-called size effects with miniaturization. Compared to experimental studies concerning size effects, numerical modeling analysis reduces significantly the costs and improves the efficiency effectively. Therefore, numerical models which can cover size effects in a comprehensive perspective are highly required. Oriented on the numerical modeling demand for miniaturized products, this thesis aims to develop a flexible numerical tool which can consider several common size effects. To achieve this goal, the following aspects have been investigated.

A panorama related to several important aspects of this thesis has been presented in chapter 2. A comprehensive literature review has been done associated with size effects has been done in terms of the definition, classification and experimental observations. The focus of this work has been paid to first-order size effects, second-order gradient effects and grain boundary effects. Among several numerical models, strain gradient crystal plasticity (SGCP) model coupled with grain boundary (GB) model are the most appropriate manners in terms of capturing these size effects. With the help of a review of SGCP and GB models, several issues related to the thesis topic have been discovered. Regarding the SGCP theories, two open issues exist, *i.e.*, descriptions of defect energy and dissipation processes. For GB models enabling taking into account the grain misorientation and GB orientation effects, few are intended for finite deformation framework. Therefore, these issues will be studied in this work.

In chapter 3, a flexible SGCP model at small deformation has been proposed. This model is based on a Gurtin-type ([Gurtin et al., 2007](#)) SGCP theory with new features in a generalized non-quadratic defect energy and a uncoupled constitutive assumption for dissipative processes. A power-law defect energy, with adjustable order-controlling index  $n$ , is proposed to provide a comprehensive investigation concerning the higher-order energetic effects under proportional and non-proportional loading conditions. Results of this investigation reveal quite different effects of the energetic length scale, depending on the value of  $n$  and the type of loading. For  $n \geq 2$ , regardless of the loading type, the energetic length scale has only influence on the rate of the classical kinematic hardening. However, in the range of  $n < 2$ , this parameter leads to unusual nonlinear kinematic hardening effects with inflection points in the macroscopic mechanical response, result-

ing in an apparent increase of the yield strength under monotonic loading. More complex effects, with additional inflection points, are obtained under non-proportional loading conditions, revealing new loading history memory-like effects of the energetic length scale. Concerning dissipation, to make the dissipative effects more easily controllable, dissipative processes due to plastic strains and their gradients are assumed to be uncoupled. Separate formulations, expressed using different effective plastic strain measures, are proposed to describe such processes. Results obtained using these formulations show the great flexibility of the proposed model in controlling some major dissipative effects, such as elastic gaps. A simple way to remove these gaps under certain non-proportional loading conditions is provided. Application of the proposed uncoupled formulations to simulate the mechanical response of a sheared strip has led to accurate prediction of the plastic strain distributions, which compare very favorably with those predicted using discrete dislocation mechanics.

In chapter 4, the flexible small deformation SGCP model is extended to finite deformation. The finite deformation extension is intended for further applications to strain localization analysis, which is generally involved with severe plastic deformation. The constitutive equations of the finite deformation version are developed in the reference configuration to facilitate numerical implementation. A two-dimensional version of the flexible SGCP model has been summarized and implemented numerically. To validate the numerical implementation, it is firstly applied to a simple shear problem in small strain range and systematically compared to results of small deformation version in chapter 3. Then, the model is assessed in large deformation and compared to several results from the literature to examine its capability in capturing geometrical effects. The finite deformation results in this chapter showed good agreement with both small and large deformation results.

In chapter 5, a finite deformation GB model, which can naturally be coupled with the flexible SGCP in finite deformation, has been proposed. The novelty of the proposed GB model lies in the description of GB mismatch compared to the existing ones in the literature (Gurtin, 2008b). A description of GB Burgers tensor which is analogous to its counterpart in the bulk has been proposed and employed as the measure of GB mismatch. Both energetic and dissipative GB processes are proposed based on the GB mismatch. Additionally, the influences of grain misorientation and GB orientation are introduced into GB constitutive laws with the help of the proposed GB measurement. Based on the framework of finite deformation SGCP for the bulk crystal, the GB model is implemented introducing a zero-thickness element for GB. The GB model is well-validated by comparison with results from the literature. The model is then assessed systematically by a bi-crystal periodic simple shear example under cyclic loading conditions. The influences of GB constitutive parameters present good qualitative agreements with existing works. The GB model is then applied on a poly-crystalline structure under proportional and non-proportional loading conditions. The linear dependence between yield stress and the inverse of geometry size has been obtained by the results. When non-proportional loading source occurred, no traces of elastic gaps arise. This could evidence the viewpoint that elastic gaps are not physical.

In chapter 6, the set of numerical framework composed by the flexible finite deformation SGCP coupled with the finite deformation GB model is employed to investigate strain localization problems in single- and poly-crystalline sheet metals. To have an in-depth understanding of different localization modes, single-crystalline example is adopted to show the capabilities and limitations of the finite deformation SGCP model in dealing with strain localization problems. Within a simple shear example, it has been proved that the finite deformation SGCP model enables the regulariza-

tion of general localization bands. Only idealized slip bands cannot be regularized by the present model which are not very common in real material deformation. The model is then applied to a uniaxial tension of a single-crystalline plate to investigate the complex localization modes, which is done here for the first time using a SGCP model. Different constitutive configurations have been performed such as conventional crystal plasticity (CP), only higher-order energetic effects and only higher-order dissipative effects. Conventional CP predicted mesh-dependent results in terms of stress-strain responses, while they were regularized with the help of internal length scales (energetic or dissipative). Evolution and competition of slip and kink bands have been revealed in these constitutive settings. The good capability of the finite deformation SGCP in predicting deformation behavior for single crystals laid a reliable foundation when coupling with GB model. The single-crystalline uniaxial tension example is then extended to polycrystalline case using Voronoi tessellation. The capability of the SGCP coupled with GB model was verified by activating different constitutive parameters. It was demonstrated that the numerical tool consisting of finite deformation SGCP and GB model is able to capture the major size effects.

## 7.2 Perspectives and future work

This thesis aimed at the development a set of numerical framework that can cover the major size effects for miniaturized products, specialized for the investigation of strain localization phenomenon within both single- and poly-crystalline frameworks. The development of the numerical tool is composed by the contributions in each chapter. Several feasible perspectives emerge in each chapter and can be investigated in future works.

The major size effects as detailed in chapter 2 can be viewed as internal originated ones. For instance, first-order extrinsic/intrinsic size effects are due to the underlying microstructure of materials which can be regarded as the internal sources. Second-order gradient effects are caused by deformation gradients which are related to accumulation of GNDs inside of materials. Grain boundaries are internal boundaries, which obviously belong to this category (internal originated sources). With the decrease of geometry size, the free surface to volume ratio also increases. Here, the free surface refers to those without imposing external boundary conditions. In this thesis, the free surfaces are taken as dislocation free, representing null microscopic power expenditures. However, several experiments ([Shan et al., 2008](#); [Oh et al., 2009](#)) show that surfaces may also act as, e.g., dislocation sources and sinks which are similar to grain boundary. This leads to extra microscopic power (work) expenditure due to these dislocation interactions with surfaces. As a result, surface effects are equally important as first- and second-order size effects which should be considered into constitutive laws. Very recently, [Peng and Huang \(2015, 2017\)](#) have proposed constitutive models capturing both energetic and dissipative surface effects, within the framework of SGCP theory. It has been reported that surface effects significantly influence the plastic behavior. Motivated by their work ([Peng and Huang, 2015, 2017](#)), one promising future work may focus on the enrichment of the developed numerical framework to cover surface effects.

As mentioned in chapter 3, flexible control of the “elastic gap” has become an open issue in strain gradient plasticity theories for non-incremental types. This thesis attempts to control the elastic gap by proposing an uncoupled dissipation process. Inspired by the investigations on elastic gap problems using non-proportional loading examples, another possible solution has come up with. It is well-known that total strain  $\varepsilon$  can be additively decomposed into elastic part  $\varepsilon_e$  and

plastic part  $\varepsilon_p$  within infinitesimal strain framework. It is believed that this decomposition is likely to be applicable to higher-order strain, *i.e.*, gradient of plastic slip  $\nabla\gamma$  can be decomposed into elastic part  $\nabla\gamma_e$  and plastic part  $\nabla\gamma_p$ . The idea of higher-order strain decomposition may be helpful in controlling elastic gaps under non-proportional loading. It is noticed that very recently, a series of experimental results and equipments have been reported by [Hua et al. \(2021\)](#). However, non-proportional loading has not been reported. Other numerical methods, such as discrete dislocation dynamics (DDD) are also helpful in understanding the mechanism in elastic gap phenomenon. The idea of higher-order strain decomposition can be investigated in future work.

As discussed in chapter 3, two methods exist with respect to numerical modeling of SGCP, *i.e.*,  $\rho$ -method and  $\gamma$ -method. The difference between these two modeling manners is the selection of primary state variables. It has been reported by [Klusemann et al. \(2012\)](#) that the two models generally predict nearly identical results for single crystals within small deformation framework. The differences arise near the external boundaries due to how boundary conditions are imposed by the two formulations. A recent work of [Carlsson et al. \(2017\)](#) compared both methods for a tri-crystal plate with micro-hard GB condition and obvious differences have been reported. Motivated by this, it is urgent to confirm that whether these two methods will lead to differences for the GB model ( $\rho$ -method GB modeling can be found in [van Beers et al. \(2013\)](#); [Peng et al. \(2019\)](#) and  $\gamma$ -method such as [Özdemir and Yalçinkaya \(2014\)](#); [Gottschalk et al. \(2016\)](#); [Yalçinkaya et al. \(2018\)](#)). Therefore, it is promising to compare between  $\gamma$ - and  $\rho$ -methods coupled with GB model in future work.

The GB model as proposed in chapter 5 assumes null power (work) expenditure in displacement jumps across GB, *i.e.*, displacement is assumed as continuous across GB. In fact, during severe plastic deformation in large strain framework, GB sliding and opening are likely to happen. The present finite deformation GB model can introduce these effects in an efficient way. Several related models including GB sliding can be found in [Gurtin \(2008b\)](#) and [Gurtin and Anand \(2008\)](#). Much complex extensions, such as GB opening, require cohesive zone technique ([Shawish et al., 2013](#); [Rezaei et al., 2020](#)).

The illustrative example of polycrystalline plate in chapter 6 shows the capability of the numerical tool in depicting concerned size effects. Yet, a three dimensional extension is highly required, which will facilitate its application to real engineering examples. Another promising work will focus on the prediction of forming limit diagrams (FLDs) using the SGCP and GB model, which enables capturing the influences of major size effects on the ductility limit of metal sheets.

## **Part II**

### **Résumé en français**



# Introduction générale

## Contexte et objectifs

Au cours des dernières décennies, les développements significatifs de la microélectronique et des systèmes micro-électromécaniques (MEMS) ont conduit à une augmentation spectaculaire de la demande en produits miniaturisés. La taille de ces produits varie généralement de quelques micromètres à quelques millimètres. Des exemples de tels produits sont donnés dans la Fig. 7.1. La fabrication de composants miniaturisés est souvent une tâche difficile en raison de la présence d'effets de taille, qui rendent inapplicables les règles simples basées sur la similarité pour réduire l'échelle des procédés de formage conventionnels (Vollertsen et al., 2006). Dans les procédés de microformage, les effets de taille peuvent influencer les paramètres des matériaux et des procédés et doivent être soigneusement pris en compte (Engel and Eckstein, 2002). Ces effets ont fait l'objet d'un vif intérêt scientifique ces dernières années, ce qui en fait l'une des principales préoccupations de la recherche actuelle. Lorsque les dimensions géométriques des composants passent du niveau conventionnel (macroscopique) au niveau microscopique, les comportements des matériaux associés ne sont plus indépendants de la taille. Plusieurs propriétés des matériaux, par exemple la contrainte d'écoulement, le durcissement et l'anisotropie, sont modifiées en raison de la miniaturisation géométrique. Cela peut à son tour influencer les paramètres du processus de formage, tels que les forces de formage, le frottement et la dispersion des résultats. Il est donc nécessaire de considérer correctement les effets de taille sur les composants miniaturisés. Cela permettra d'optimiser les procédés de microformage utilisés pour obtenir ces composants. Par conséquent, il sera possible d'obtenir des produits à micro-échelle dont la fabrication et les performances de fonctionnement seront améliorées.

Plusieurs classifications des effets de taille peuvent être trouvées dans la littérature (Vollertsen et al., 2006; Vollertsen, 2008; Geers et al., 2006; Liu et al., 2012), selon leurs sources ou leurs impacts. Parmi elles, la classification basée sur l'ordre proposée par Geers et al. (2006), qui classe les effets de taille en effets de premier et de second ordre, semble être plus générale et attrayante dans le contexte des matériaux métalliques polycristallins. Dans cette classification, les effets de taille de premier ordre couvrent tous les effets de taille de microstructure (intrinsèques) et statistiques (extrinsèques) résultant de la nature anisotrope granulaire discrète de la microstructure, excluant toutefois les effets dus aux gradients de déformation. Les effets de taille de second ordre couvrent les effets de gradient et ceux causés par les frontières (surfaces externes, interfaces de matériaux et joints de grains). La classification basée sur l'ordre peut couvrir la plupart des effets de taille observés expérimentalement dans les matériaux métalliques polycristallins. Par exemple, des phénomènes tels que la diminution de la contrainte d'écoulement et l'augmentation de la dispersion de la contrainte d'écoulement par la diminution de la taille géométrique correspondent

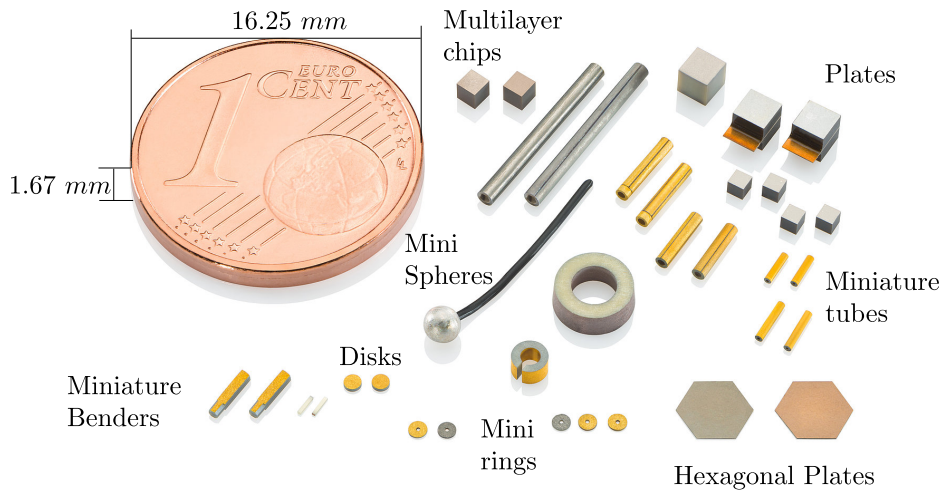


**Fig. 7.1.** Exemples de produits miniaturisés (de <https://www.picericamic.com>).

à des effets de taille statistique de grain (extrinsèque) de premier ordre (Fülöp et al., 2006; Kals and Eckstein, 2000; Chan et al., 2011). Le phénomène d'augmentation de résistance due au raffinement des grains est un effet de taille de microstructure (intrinsèque) du premier ordre (Janssen et al., 2006). Au contraire, l'augmentation de résistance due à la courbure du réseau est un effet de taille typique de second ordre (gradient), conduisant au phénomène "plus petit, plus fort", comme le rapportent plusieurs recherches (Fleck et al., 1994; Liu et al., 2013; Dahlberg et al., 2017). A proportions géométriques identiques, la réduction d'échelle d'un composant conduit naturellement à une augmentation des gradients de déformation qui doivent être géométriquement accommodés par la courbure. Cette dernière, qui est limitée par la structure du réseau, est accommodée par la formation de dislocations géométriquement nécessaires (GNDs; Ashby, 1970). Comme pour les dislocations classiques, les GNDs agissent comme des obstacles aux glissements plastiques, conduisant à une augmentation de résistance et/ou un durcissement. Les phénomènes d'augmentation de résistance dus aux surfaces externes et aux joints de grains sont des effets de second ordre.

Les théories classiques de la plasticité ne peuvent pas prédire les effets de taille, en raison du manque de paramètres dépendant de la taille. Pour tenir compte de ces effets, plusieurs recherches ont proposé des lois constitutives enrichies qui incluent des informations sur la taille d'intérêt en utilisant des facteurs dépendants de la taille, par exemple, la taille de la géométrie, la taille moyenne des grains, etc. (Kim et al., 2007; Leu, 2009; Meng and Fu, 2015). Les facteurs additionnels dépendant de la taille sont généralement calibrés sur la base d'essais expérimentaux à micro-échelle pour des spécimens spécifiques. Inspirés par le fait que les proportions de surface, et donc leurs effets, sont plus importants dans les composants miniaturisés que dans les composants conventionnels (macroscopiques), des modèles de comportement de matériaux de types multi-zones, c'est-à-dire incluant différentes descriptions de matériaux dans différentes régions, ont été développés. Un modèle multi-zone typique est le modèle de couche de surface proposé par Engel and Eckstein (2002), dans lequel le matériau étudié est subdivisé en grains de surface et grains internes avec différentes hypothèses de modélisation. En raison de la faible influence des joints de grains sur les grains proches de la surface, ces grains sont considérés comme des monocristaux, tandis qu'un comportement polycristallin moyen est adopté pour les grains internes. Le comportement global est obtenu en additionnant les contributions de la surface et de l'intérieur, multipliées par leurs

pourcentages respectifs. Cependant, le comportement résultant ne permet pas une transition douce entre les contributions. Pour remédier à cette lacune, Geiger et al. (2007) ont développé un modèle mésoscopique où le matériau étudié est subdivisé en grains individuels ayant des propriétés individuelles, dépendant de la taille et de la position de chaque grain dans le matériau. Ce modèle nécessite la création d'une microstructure synthétique proche de la microstructure réelle dans le matériau étudié. Par rapport aux modèles conventionnels avec inclusion artificielle de facteurs dépendant de la taille dans les lois constitutives, les modèles à couche de surface et mésoscopique représentent un progrès non négligeable vers la modélisation précise des effets de taille. Utilisant la plasticité cristalline, ces modèles montrent de bonnes capacités à capter les effets de taille de premier ordre, comme le rapportent plusieurs auteurs dans la littérature (Lai et al., 2008; Yun et al., 2010; Wang et al., 2013; Ran et al., 2013).

Les effets de taille de premier ordre, qu'ils soient extrinsèques ou intrinsèques, sont étroitement liés à la microstructure des produits miniaturisés. Les théories conventionnelles de plasticité cristalline, qui décrivent la déformation plastique sur la base de glissements plastiques individuels sur des systèmes de glissement spécifiques, permettent de couvrir ce type d'effets de taille d'une manière naturelle. Cependant, comme ces théories sont basées sur le principe de l'action locale et n'incluent pas les échelles de longueurs internes, elles ne peuvent pas capter les effets de taille de second ordre induits par les gradients de déformation. Pour surmonter les limitations des théories locales, plusieurs approches améliorées de plasticité ont été développées au cours des dernières décennies dans le but de rendre compte correctement des mécanismes non locaux de déformation, par exemple les théories de Cosserat (Forest et al., 1997), les théories micromorphes (Forest, 2009) et les théories de plasticité à gradient de déformation (SGP) (Aifantis, 1987). Grâce à leurs propriétés attractives à capter les effets de second ordre, les théories SGP ont reçu un fort intérêt scientifique ces dernières années, ce qui a conduit au développement de divers modèles SGP pour les problèmes de micro-échelle en petites ou grandes déformations (Aifantis, 1999; Fleck and Hutchinson, 1997, 2001; Gudmundson, 2004; Martínez-Pañeda et al., 2016, 2017, 2019). Ces modèles ont d'abord été développés pour des structures polycristallines (Aifantis, 1987), puis étendus aux monocristaux Gurtin (2000). Capables de capter les caractéristiques monocrystallines locales et les gradients de déformation, les modèles SGP monocrystallins, qui seront appelés ci-après modèles de plasticité cristalline à gradient de déformation (SGCP), fournissent un excellent cadre pour capter les effets de taille de premier et second ordre au sein des monocristaux. Cependant, plusieurs questions liées à leurs formulations théoriques, telles que la description précise des énergies de défaut et de dissipation et la flexibilité dans le contrôle de certains mécanismes importants d'ordre supérieur, doivent encore être prises en compte pour une prédition réaliste de ces effets. Un des objectifs de la thèse consiste à corroborer les travaux existants sur ces questions, dans le but de développer un modèle SGCP flexible en grandes déformations permettant un contrôle aisément de certains effets prédisposés d'ordre supérieur.

Formulés à l'échelle des monocristaux, les modèles SGCP ne sont pas voués à fournir une description précise des effets de second ordre des joints de grains (GB), qui deviennent significatifs lorsque la taille de la géométrie diminue. Pour capter ces derniers effets, il est nécessaire de coupler ces modèles avec des formulations GB qui tiennent compte des mécanismes d'interaction entre les dislocations et les joints de grains. Dans le cadre des modèles généralisés (non locaux) de comportement, de simples conditions de joints de grains micro-libre (totalement transparents) ou micro-dur (totalement opaques) ont été largement utilisées dans les études pour lesquelles les contributions des GB ne sont pas d'un intérêt central (Geers et al., 2006; Yalçinkaya et al., 2017).

Ces deux conditions extrêmes représentent des cas limites pour les comportements réels des GB qui reposent sur des mécanismes complexes d’interaction entre les dislocations et les joints de grains (GB), notamment les empilements de dislocations, l’absorption, l’émission et la réflexion au niveau des GB (Bayerschen et al., 2016). Des tentatives de développement de modèles de GB plus élaborés concernant ces mécanismes d’interaction peuvent être trouvées dans la littérature (Cermelli and Gurtin, 2002; Aifantis and Willis, 2005; Aifantis et al., 2006; Fredriksson and Gudmundson, 2007; Bayerschen et al., 2015; Bayerschen and Böhlke, 2016; Bayerschen et al., 2016; Wulfinghoff et al., 2013; Wulfinghoff, 2017). Les plus simples de ces modèles ont été formulés sur la base de lois constitutives phénoménologiques simplifiées pour les GB (Gudmundson, 2004; Aifantis and Willis, 2005; Aifantis et al., 2006; Fredriksson and Gudmundson, 2007). On trouve dans la littérature des variantes de ces modèles, tant pour les petites déformations que pour les grandes déformations. Bien qu’ils aient été appliqués avec succès pour prédire des mécanismes intéressants de GB, ces modèles ne tiennent pas compte de certaines caractéristiques géométriques et cristallographiques importantes, comme les orientations des grains et des joints de grains, qui peuvent avoir une influence significative sur le comportement des GB.

Pour surmonter les limitations des approches phénoménologiques des GB, des modèles de GB basés sur des variables de contrôle cinématiques tenant compte des effets géométriques et cristallographiques ont été proposés. Dans ce contexte, les modèles d’Evers et al. (2004b) et de Gurtin (2008b) peuvent être particulièrement cités. Ces deux modèles incluent les effets de désorientation des grains et d’orientation des joints de grains. Ils sont respectivement proposés dans des cadres basés sur la densité de dislocation (c’est-à-dire avec les densités de dislocation comme variables primaires) et sur les glissements plastiques (c’est-à-dire avec les glissements plastiques comme variables primaires). D’après Klusemann et al. (2012), ces cadres fournissent généralement des résultats semblables pour des problèmes similaires. Cependant, le cadre basé sur les glissements plastiques semble présenter certains avantages pour le calcul des glissements plastiques et pour contraindre le flux de dislocation aux frontières. En effet, il n’est pas nécessaire de recourir à un schéma d’intégration locale pour obtenir les glissements plastiques (considérés comme des variables primaires) à partir des densités de dislocation. De plus, le flux de dislocation aux frontières peut facilement être contrôlé en contraignant directement les glissements plastiques plutôt que leurs gradients. Ce cadre est retenu pour les développements du présent projet de thèse. Cependant, des recherches supplémentaires sont nécessaires pour mieux comprendre la différence entre les deux cadres de modélisation.

Dans le contexte des approches basées sur le glissement plastique, les caractéristiques intéressantes du modèle de Gurtin (2008b) ont inspiré le développement de plusieurs modèles de GB de type Gurtin incluant des considérations géométriques et cristallographiques. La plupart de ces modèles ont été proposés pour des problèmes de petites déformations (van Beers et al., 2013; Gottschalk et al., 2016). Seuls quelques travaux étendant le modèle de Gurtin (2008b) aux grandes déformations existent dans la littérature. McBride et al. (2016) ont proposé un modèle de GB de type Gurtin en grandes déformations formulé à l’aide d’une description eulérienne, cette dernière description n’étant pas beaucoup utilisée dans le contexte des modèles à gradient de déformation. Un autre modèle de GB de type Gurtin en grandes déformations se trouve dans Peng et al. (2019). Bien que développé à l’aide d’une description lagrangienne, ce modèle est basé sur une hypothèse simplificatrice selon laquelle le réseau non déformé réside dans l’espace (matériel) de référence et non dans l’espace structurel. En outre, aucune déformation plastique du réseau n’est prise en compte. Ces hypothèses conduisent à une formulation des GB qui est identique à celle

proposée par [Gurtin \(2008b\)](#) dans le contexte des petites déformations, ce qui la rend inadaptée aux problèmes impliquant de grandes déformations aux GB. Comme la description lagrangienne est largement utilisée dans le contexte de la plasticité à gradient de déformation, le développement d'une extension lagrangienne en grandes déformations du modèle de [Gurtin \(2008b\)](#), tout en tenant compte correctement de la distorsion du réseau, serait très utile. En effet, plusieurs applications utilisant des produits miniaturisés entraînent des effets de grandes déformations, y compris aux joints de grains.

Malgré les efforts scientifiques considérables déployés dans le sens d'une modélisation précise des effets de taille, une description réaliste et précise de ces effets se heurte encore à divers obstacles. Ces derniers empêchent le développement d'un outil numérique complet capable de capter tous les types d'effets de taille caractérisant les structures polycristallines. Il s'agit notamment des effets de premier et de second ordre à l'intérieur des grains individuels et aux joints de grains. Avec la demande toujours croissante de produits miniaturisés dans divers domaines de l'ingénierie, cet outil numérique est très attendu car il permettra d'optimiser les procédés de microformage utilisés pour obtenir ces produits. Dans ce contexte, le présent projet de thèse vise à corroborer les travaux existants sur le développement d'un tel outil numérique. Inspiré par [Gurtin et al. \(2007\)](#), un modèle flexible de plasticité cristalline à gradient de déformation (SGCP) sera développé dans le cadre des grandes déformations. Ce modèle sera utilisé pour prédire les effets de taille de premier et de second ordre dans les monocristaux. Pour capter les effets de taille en grandes déformations dus aux joints de grains, une extension aux grandes déformations du modèle de joints de grains (GB) de [Gurtin \(2008b\)](#) sera réalisée en utilisant une description entièrement lagrangienne, qui est le plus souvent utilisée dans le contexte des milieux généralisés à gradient. En guise d'application, les modèles SGCP et GB ainsi développés en grandes déformations seront appliqués pour étudier les effets de taille dans un problème d'intérêt majeur impliquant de grandes déformations : à savoir la localisation des déformations dans des structures mono- et poly-cristallines.

## Méthodologie de la thèse

La Fig. [7.2](#) présente la méthodologie suivie dans ce travail pour atteindre les objectifs généraux de ce projet de thèse, qui sont le développement d'un cadre numérique flexible capable de capter différents types d'effets de taille polycristallins et l'application de ce cadre pour étudier les phénomènes de localisation des déformations dans les structures mono- et poly-cristallines.

Une analyse bibliographique approfondie a d'abord été réalisée pour mieux comprendre les effets de taille dans les polycristaux ainsi que les techniques de modélisation utilisées pour les prédire. Sur la base de cette revue de la littérature, on peut distinguer principalement trois classes d'effets de taille : les effets de grains de premier et de second ordre et les effets de joints de grains (GB). Les théories de plasticité cristalline à gradient de déformation (SGCP) présentent des capacités intéressantes pour reproduire les deux premières classes d'effets de taille. La dernière classe peut être modélisée à l'aide d'une formulation adaptée de joints de grains (GB) qui tient compte des mécanismes d'interaction complexes entre les dislocations et les joints de grains. Un couplage entre les modèles SGCP et GB est alors nécessaire pour reproduire avec précision les principaux effets de taille polycristallins. Un tel couplage représente l'épine dorsale du cadre numérique flexible prévu. Le choix des formulations SGCP et GB à coupler peut fortement affecter l'efficacité de ce cadre et une attention particulière doit être accordée à cette tâche.

Malgré les efforts scientifiques considérables déployés pour les théories SGCP, certaines questions difficiles liées à leurs formulations théoriques doivent encore être abordées. La plupart d'entre elles concernent la définition des processus d'ordre supérieur énergétiques et dissipatifs. Les processus énergétiques sont décrits de manière pragmatique en utilisant des formes quadratiques de l'énergie de défauts. Comme l'ont souligné plusieurs auteurs (e.g., [Cordero et al., 2010](#); [Forest and Guéninchault, 2013](#)), les formes quadratiques sont inhabituelles dans les théories classiques de dislocation et peuvent être très simples pour refléter correctement la nature réelle des processus énergétiques d'ordre supérieur. D'autres formes d'énergie de défauts ont été testées, par exemple l'énergie de défauts linéaire ([Ohno and Okumura, 2007](#); [Hurtado and Ortiz, 2013](#); [Wulffinghoff et al., 2015](#)) et logarithmique ([Forest, 2013](#); [Wulffinghoff et al., 2015](#)). En fonction de la forme adoptée pour l'énergie de défauts, différents effets de taille ont été obtenus. Quant aux processus dissipatifs, dans presque tous les modèles SGCP existants, ces processus sont décrits à l'aide de mesures de déformation effective couplées impliquant les déformations plastiques et leurs gradients de manière couplée. Ce choix repose sur l'hypothèse contraignante que les processus dissipatifs dus aux déformations plastiques et à leurs gradients sont couplés. Une telle hypothèse, bien que non confirmée expérimentalement, contraint fortement le contrôle des effets dissipatifs. Dans le but de développer un modèle SGCP flexible comme partie intégrante du cadre numérique prévu, le premier objectif du présent travail de thèse est de corroborer les études existantes sur les questions SGCP. Inspiré par le travail de [Gurtin et al. \(2007\)](#), un modèle flexible de type Gurtin basé sur une énergie de défauts généralisée, avec un paramètre de contrôle d'ordre, et une hypothèse de dissipation non couplée a été développé. Une version du modèle en petites déformations a d'abord été proposée pour effectuer une analyse complète des paramètres d'ordre supérieur en l'absence des effets de grandes déformations. Ensuite, une extension aux grandes déformations a été proposée pour les problèmes impliquant des effets de grandes déformations, tels que les problèmes de localisation. Cette version a été formulée en utilisant une description entièrement lagrangienne. Les versions du modèle pour petites et grandes déformations ont été implémentées dans le code commercial d'éléments finis Abaqus/Standard via des sous-routines UEL (User-Element).

Les variantes proposées du modèle SGCP de type Gurtin en petites et grandes déformations permettent de capter les effets de taille du premier et du second ordre dans le cadre de monocristaux subissant des petites ou grandes déformations. Pour représenter les effets de GB dans les matériaux polycristallins, ces variantes doivent être couplées à des formulations de GB appropriées. Plusieurs modèles de joints de grains ont été proposés dans la littérature ([Gudmundson, 2004](#); [Fredriksson and Gudmundson, 2007](#); [Aifantis and Willis, 2005](#); [Wulffinghoff, 2017](#); [Gurtin, 2008b](#); [van Beers et al., 2013](#); [Gottschalk et al., 2016](#)). Parmi eux, le modèle de [Gurtin \(2008b\)](#) présente des capacités prometteuses pour capter différents types d'effets de taille de GB, y compris ceux dus aux orientations des grains et des joints de grains. Par conséquent, il a été choisi dans ce travail comme base pour la modélisation des effets de taille des GB. Ce modèle qui a été proposé dans le cadre des petites déformations a été implémenté dans ce travail dans Abaqus/Standard et couplé avec la version des petites déformations du modèle SGCP proposé. Pour les applications en grandes déformations, une nouvelle extension de ce modèle basée sur une description entièrement lagrangienne a été formulée et implémentée dans Abaqus/Standard. Après validation de l'implémentation du modèle, cette extension a été appliquée pour mener une étude complète sur l'influence des paramètres du modèle de GB sur la prédiction des effets de taille de GB.

Le couplage entre les modèles SGCP et GB proposés fournit un outil numérique flexible capable de capter différents types d'effets de taille dans les structures polycristallines dans le cadre de

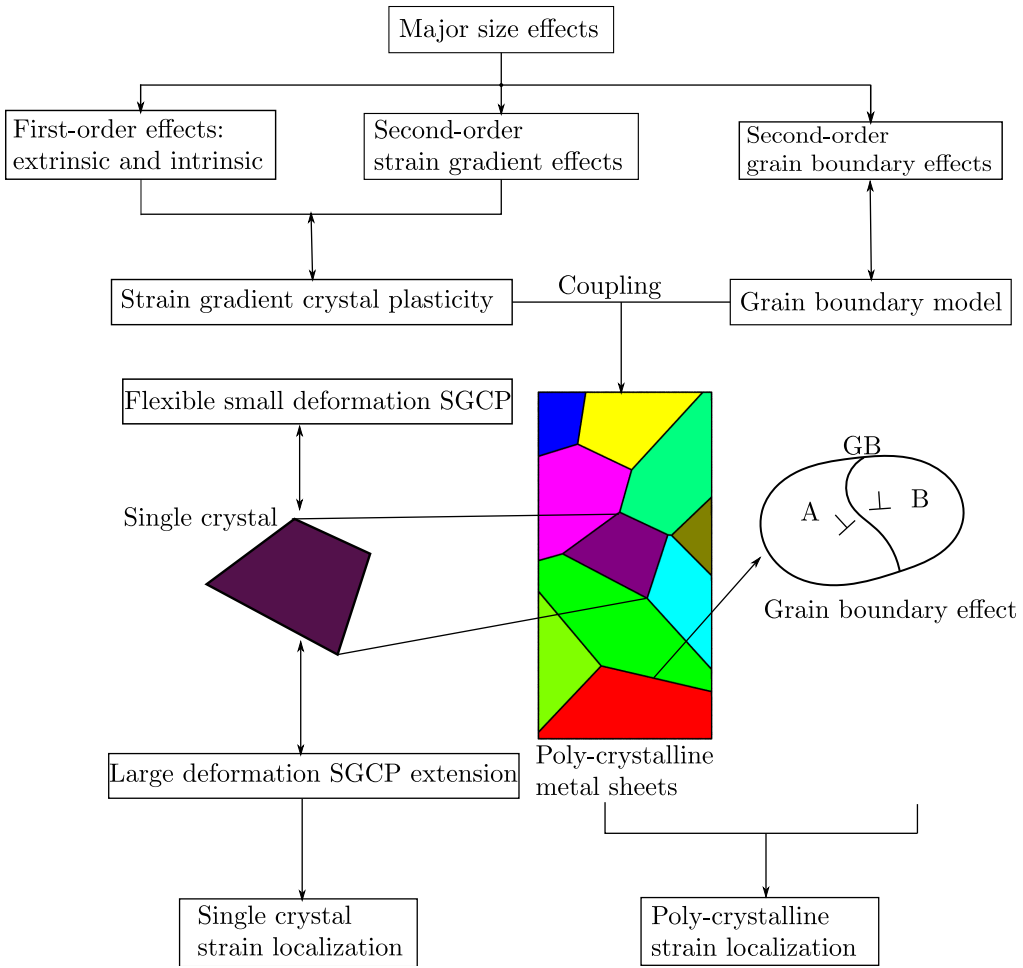


**Fig. 7.2.** Méthodologie de la thèse.

petites ou grandes déformations. Cet outil numérique a été appliqué pour faire un premier pas dans l'étude des effets de taille sur les phénomènes de localisation. Des monocristaux ont d'abord été considérés pour étudier les capacités du modèle SGCP à capturer différents types de bandes de localisation, y compris les bandes de glissement, de pliage et complexes. Ensuite, une initiation à la localisation dans des structures polycristallines a été fournie. Compte tenu du temps nécessaire à la préparation des fichiers d'entrée pour les simulations polycristallines, un outil python avancé permettant d'automatiser cette tâche a été développé. Cet outil sera utilisé dans des travaux futurs pour mener une étude complète des effets de taille sur les phénomènes de localisation et sur la prédiction de la formabilité des tôles métalliques aux petites échelles.

## Organisation de la thèse

Après l'introduction générale, les autres parties de la thèse seront organisées comme suit :

- Dans le chapitre 2 : Une revue de la littérature en lien avec les objectifs de cette thèse sera donnée. La définition et les classifications des principaux effets de taille dans les structures polycristallines seront d'abord abordées. Ensuite, quelques approches numériques courantes

utilisées pour reproduire de tels effets seront brièvement présentées et comparées. Puis, l'accent sera mis sur les théories à gradients et sur certaines questions connexes importantes, car elles sont à la base des développements de la thèse. Enfin, les progrès actuels dans l'étude des phénomènes de localisation des déformations à l'aide de ces théories seront discutés.

- Dans le chapitre 3 : Un modèle SGCP flexible en petites déformations de type Gurtin sera développé sur la base d'une énergie de défauts non quadratique généralisée et d'une hypothèse constitutive non couplée pour les processus dissipatifs. Une version bidimensionnelle du modèle proposé sera mise en œuvre et validée à l'aide d'exemples tirés de la littérature. Une évaluation systématique du modèle sera effectuée en utilisant des conditions de chargement de cisaillement proportionnel et non proportionnel.
- Une version bidimensionnelle du modèle en grandes déformations sera mise en œuvre et validée par comparaison avec des résultats en petites déformations et des résultats en grandes déformations tirés de la littérature.
- Dans le chapitre 5 : Une nouvelle extension en grandes déformations du modèle GB de [Gurtin \(2008b\)](#) sera formulée en utilisant une description entièrement lagrangienne. Ce modèle sera implémenté et couplé avec la version en grandes déformations du modèle SGCP flexible proposé. L'implémentation du modèle sera validée en comparant les résultats associés à ceux obtenus avec le modèle de [Gurtin \(2008b\)](#). Enfin, l'influence des principaux paramètres du modèle GB sera étudiée.
- Dans le chapitre 6 : Les outils numériques développés seront appliqués pour étudier la localisation des déformations dans les tôles métalliques minces mono et polycristallines. L'objectif de l'étude de la localisation des déformations dans les monocristaux est de fournir une investigation approfondie sur les capacités et les limites du modèle SGCP en grandes déformations à prédire différents types de modes de localisation. L'étude de la localisation des déformations dans les tôles métalliques minces polycristallines sera ensuite menée.
- Enfin, la thèse se terminera par plusieurs conclusions et perspectives.

# L'état de l'art

## Définition et classifications des effets de taille

D'une manière générale, les effets de taille accompagnent le changement d'échelle d'un objet et ont été découverts et décrits pour les processus de changement d'échelle ([Vollertsen, 2008](#)). Avec la demande croissante de produits miniaturisés au cours des dernières décennies, divers types d'effets de taille sont fréquemment observés au cours du processus de fabrication de ces produits. Les effets de taille peuvent être interprétés littéralement comme des déviations inattendues résultant de la modification de la dimension d'une structure. En se référant à [Vollertsen \(2008\)](#), une définition plus précise des effets de taille peut être donnée comme les déviations des valeurs intensives ou extensives extrapolées proportionnelles d'un processus qui se produisent lors de la mise à l'échelle des dimensions géométriques. Cette définition apparemment sophistiquée des effets de taille est proposée dans une perspective d'ingénierie industrielle. Pour mieux interpréter cette définition, il convient de détailler deux terminologies importantes : "valeurs intensives" et "valeurs extensives extrapolées proportionnelles". Selon [Vollertsen \(2008\)](#), les "valeurs intensives" représentent les variables qui ne changent pas lors de la modification de la taille d'une géométrie, par exemple la température. Les "valeurs extrapolées proportionnelles extensives" font référence aux variables qui changent lors de l'extrapolation proportionnelle de la taille de la géométrie, comme le contenu calorifique et la force d'inertie.

Les catégories systématiques d'effets de taille ont été proposées par [Vollertsen \(2008\)](#), notamment les effets de taille de densité, les effets de taille de forme et les effets de taille de microstructure, comme l'illustre la Fig. 7.3. Les effets de taille de densité se produisent lorsque la densité d'une géométrie est maintenue constante. Par conséquent, les caractéristiques telles que les défauts ponctuels (par exemple, les petites cavités), les défauts linéaires (par exemple, les lignes de dislocation) ou les zones d'interface (par exemple, les joints de grains) diminueront normalement dans la géométrie considérée, ce qui entraînera un renforcement et une dispersion de la contrainte d'écoulement ([Armstrong, 1961](#)). De toute évidence, la variable de densité dans cette catégorie correspond à des "valeurs intensives" comme prescrit dans la définition des effets de taille. Les effets de taille de la géométrie se produiront si la valeur d'intérêt (par exemple, les grains de surface et les grains intérieurs) dépend du rapport entre la surface totale et le volume. Ce rapport augmente tout en réduisant proportionnellement la taille de la géométrie. Un exemple typique est la diminution de la contrainte d'écoulement avec la diminution de la taille de la géométrie comme rapporté par plusieurs travaux ([Chan et al., 2011; Liu et al., 2011a](#)). La variable de forme correspond ici aux "valeurs extensives". Les effets de taille de la microstructure se produisent lorsque les caractéristiques de la microstructure (par exemple, la taille des grains ou des précipités et la rugosité de surface) restent constantes tout en diminuant la taille de la géométrie.

[Geers et al. \(2006\)](#) ont proposé une classification plus universelle des effets de taille, à savoir

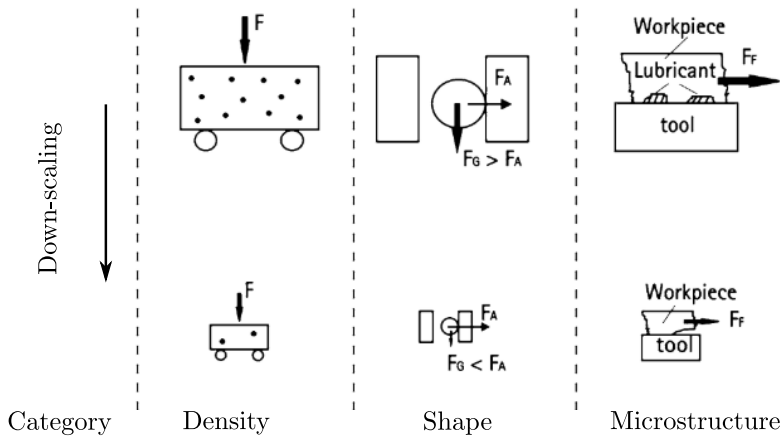


**Fig. 7.3.** Catégories d’effets de taille proposées par [Vollertsen \(2008\)](#)

les effets de premier ordre et les effets de second ordre exclusifs aux matériaux cristallins. En ce qui concerne les effets de premier ordre, ils couvrent tous les effets découlant de la nature anisotrope granulaire discrète de la microstructure. Les effets de taille de second ordre comprennent les contributions dues aux effets de courbure du réseau (par exemple, gradients de déformation, gradients de glissement, *etc.*) et aux effets de frontière (par exemple, effets de joints de grains et effets de frontières externes).

[Fu and Wang \(2021\)](#) ont classé les effets de taille en trois catégories en fonction de leurs manifestations : les effets “plus petits sont plus forts” (SS), les effets “plus petits sont plus faibles” (SW) et ceux entre SS et SW. La première, les effets SS, fait référence à l’augmentation de la propriété du matériau (par exemple, la résistance du matériau, la contrainte d’écoulement et la dureté, *etc.*) lorsque la géométrie diminue. ) lorsque la géométrie diminue. Pour les effets SW, c’est le cas inverse par rapport à SS. Les effets intermédiaires montrent une tendance variée entre SS et SW. Par exemple, [Kals \(1999\)](#) a découvert une tendance à passer des effets SW aux effets SS dans des cas de flexion d’un alliage d’aluminium.

En fait, les catégories d’effets de taille susmentionnées présentent plusieurs chevauchements. Par exemple, les effets de taille de densité de [Vollertsen \(2008\)](#) conduisent à la dispersion de la contrainte d’écoulement qui correspond aux effets de taille extrinsèques de premier ordre définis par [Geers et al. \(2006\)](#). Une manifestation des effets de taille de la forme discutée par [Vollertsen \(2008\)](#) est la diminution de la contrainte d’écoulement avec une géométrie plus petite. Elle coïncide avec l’exemple des effets de taille extrinsèques de premier ordre ([Geers et al., 2006](#)) montrant une diminution de la contrainte d’écoulement lorsque la dimension géométrique diminue. Parallèlement, elle est équivalente à la catégorie SW proposée par [Fu and Wang \(2021\)](#). Les effets de gradient de déformation considérés comme la catégorie des effets de taille de microstructure ([Vollertsen, 2008](#)) sont équivalents aux effets de second ordre ([Geers et al., 2006](#)) dus aux gradients de déformation.

En ce qui concerne les structures métalliques cristallines miniaturisées, la classification des effets de taille basée sur l’ordre ([Geers et al., 2006](#)) semble plus appropriée pour englober les différents effets de taille d’une manière organisée. Cette méthode tente de classer les effets de taille en effets d’ordre inférieur (effets locaux causés par la microstructure) et d’ordre supérieur (effets non locaux causés par les effets de gradient en plus des effets de frontières) selon les sources

générant les effets de taille. Il s'agit d'une méthode plus souple que la classification de [Fu and Wang \(2021\)](#), qui peut être considérée comme une méthode axée sur le phénomène (c'est-à-dire la classification des effets de taille en fonction du phénomène qui en résulte, comme "plus petit est plus fort" et "plus petit est plus faible"). Par conséquent, la classification des effets de taille basée sur l'ordre sera adoptée dans cette thèse et fréquemment mentionnée par la suite. Dans ce qui suit, les observations expérimentales des effets de taille sur la base de la classification de premier et de second ordre seront présentées.

## Observations expérimentales des effets de taille

### Effets de taille extrinsèques/intrinsèques de premier ordre

Selon [Geers et al. \(2006\)](#), les effets de taille de premier ordre se traduisent principalement de deux manières, à savoir les effets de taille statistiques (extrinsèques) et les effets de taille de microstructure (intrinsèques). Les effets statistiques se traduisent généralement par une diminution de la contrainte d'écoulement moyenne et une augmentation de la dispersion de la contrainte d'écoulement. La Fig. 7.4 présente un exemple de la diminution de la contrainte d'écoulement associée à la miniaturisation, à travers un essai de traction d'une feuille de CuNi18Zn20 réalisé par [Kals and Eckstein \(2000\)](#). La mesure de miniaturisation est définie par la réduction de l'épaisseur de l'échantillon  $\lambda$ , tout en gardant une taille de grain approximativement constante ( $d = 40 \mu\text{m}$ ). Il est clairement montré dans la Fig. 7.4 qu'une feuille plus mince a une contrainte d'écoulement plus faible. La diminution de la contrainte d'écoulement est généralement désignée par le phénomène "plus petit, plus faible", une caractéristique typique des effets de taille extrinsèques de premier ordre. Le phénomène "plus petit, c'est plus faible" a été largement reconnu comme étant le résultat de comportements matériels différents des grains de surface et des grains internes dus à la miniaturisation. Les grains de surface exercent moins de contraintes que les grains internes ([Miyazaki et al., 1979](#)) et ont donc un comportement de contrainte d'écoulement plus faible. Avec la miniaturisation (montrée dans la Fig. 7.4 côté droit), la proportion de grains de surface par rapport aux grains totaux augmente. Par conséquent, la contrainte d'écoulement globale, qui est composée des contributions de la surface et de l'intérieur, diminue pour une épaisseur de feuille plus fine sur la Fig. 7.4. Des essais expérimentaux similaires montrant que "plus c'est petit, plus c'est faible" peuvent également être trouvés dans des essais de traction de feuilles de matériaux différents ([Peng et al., 2007; Liu et al., 2011a](#)) et des essais de compression d'éprouvettes cylindriques ([Chan et al., 2011; Xu et al., 2015](#)) de différents diamètres.

Une autre manifestation des effets de taille statistiques (extrinsèques) de premier ordre est la dispersion de la contrainte d'écoulement. Un exemple peut être trouvé par un test de traction de feuilles d'aluminium décrit dans la Fig. 7.5. Pour chaque épaisseur de tôle de la Fig. 7.5, cinq échantillons à microstructure aléatoire et à taille de grain moyenne constante ( $100 \mu\text{m}$ ) sont adoptés. Pour les échantillons plus fins, une contrainte d'écoulement plus faible a été obtenue, ce qui indique l'effet "plus petit, plus faible". Une plus grande dispersion de la contrainte d'écoulement se produit lorsque l'épaisseur de la feuille diminue. La dispersion de la contrainte d'écoulement est la caractéristique distinctive des effets de taille extrinsèques. Avec la réduction de l'épaisseur, les grains individuels deviennent manifestes et les comportements anisotropes apparaissent évidents. L'influence de l'orientation des grains individuels devient plus significative avec moins de grains dans la section des feuilles.

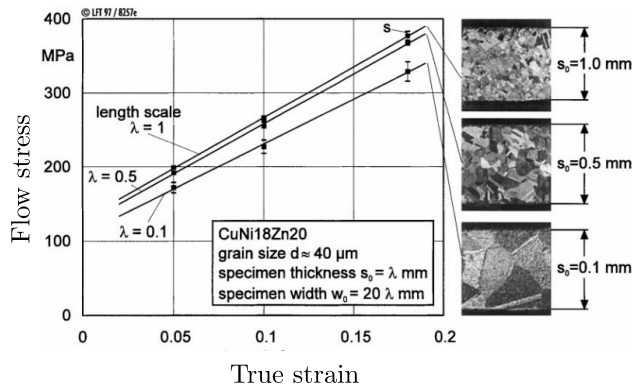


**Fig. 7.4.** Illustration des effets de taille extrinsèques de premier ordre sur le principe "plus petit, c'est plus faible" (Kals and Eckstein, 2000).

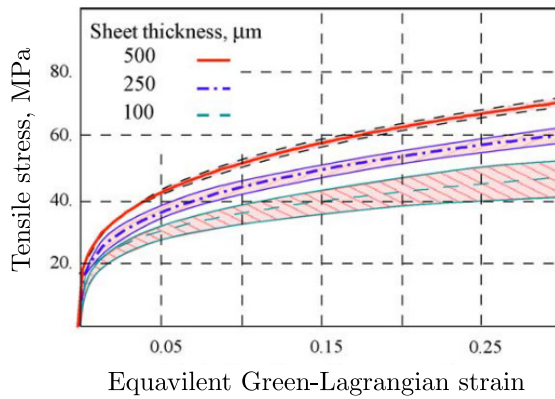


**Fig. 7.5.** Exemple illustratif des effets de la taille statistique sur la dispersion de la contrainte d'écoulement : courbes d'écoulement pour différentes épaisseurs de feuilles avec une taille de grain constante (Fülöp et al., 2006).

Les effets de taille intrinsèque de premier ordre peuvent également être appelés effets de taille de grain ou effets de taille de microstructure (Geers et al., 2006). Un exemple courant est l'augmentation de la résistance due au raffinement de la taille des grains, par exemple par un traitement thermique. Plusieurs preuves expérimentales peuvent être trouvées dans ces travaux (Kals and Eckstein, 2000; Janssen et al., 2006; Hug and Keller, 2010). Les effets d'augmentation de la résistance causés par les effets de taille intrinsèques peuvent être expliqués par l'augmentation des interactions entre dislocations à travers les joints de grains.

### Effets de taille de gradient de second ordre

Des effets de taille de gradient de second ordre se produisent avec la présence d'un gradient de déformation qui a été révélé par plusieurs expériences à petite échelle. Une expérience typique a été réalisée par Fleck et al. (1994) sur la tension et la torsion de fils de cuivre, comme le montre la Fig. 2.5. Dans les deux cas de tension et de torsion des fils de cuivre, les réponses du matériau dépendent de la taille, c'est-à-dire qu'un diamètre plus petit présente une contrainte d'écoulement et un durcissement plus importants. Les réponses du matériau en fonction de la taille sont plus

prononcées pour le chargement de torsion. Une étude similaire de torsion de fils minces a également été rapportée par Liu et al. (2012). Plusieurs expériences différentes, telles que la micro-indentation (Nix and Gao, 1998; McElhaney et al., 1998; Ma et al., 2012; Sarac et al., 2016; Dahlberg et al., 2017), la micro-flexion de feuilles minces (Stölken and Evans, 1998; Hayashi et al., 2011) et la compression de micro-piliers (Greer and Nix, 2005) ont également montré des effets de taille dus aux gradients.

Les effets de taille de second ordre dans les expériences susmentionnées pour les petites structures dimensionnelles peuvent être attribués à la présence de gradients de déformation (Fleck et al., 1994). Pendant la déformation plastique des matériaux métalliques, des dislocations sont générées, déplacées et stockées. Deux types de dislocations existent pendant le mouvement des dislocations, l'un est constitué de dislocations stockées statistiquement (SSD), qui se piègent les unes les autres de manière aléatoire, l'autre est appelé dislocations géométriquement nécessaires (GND), qui sont nécessaires pour une déformation compatible des différentes parties des matériaux cristallins (Ashby, 1970). Le concept des GND peut être expliqué par un exemple de flexion, comme illustré sur la Fig. 2.6 par une poutre pliée. En raison de la déformation plastique non uniforme, certaines dislocations sont nécessaires pour s'adapter à la courbure du réseau. Les GND sont généralement accompagnés d'une déformation plastique inhomogène conduisant à un durcissement du matériau en agissant comme des obstacles au mouvement d'autres SSD. Les GND, qui sont associés à des gradients de déformation plastique, manifestent leurs effets lorsque la longueur caractéristique de la déformation devient suffisamment petite (Gao and Huang, 2003). Ceci explique la corrélation entre "le plus petit est plus fort" dans les expériences susmentionnées et la présence de gradients de déformation.

## Techniques de modélisation numérique des effets de taille

Les effets de taille de premier et de second ordre, détaillés dans les sous-sections précédentes, sont traités comme les principaux effets de taille pour les composants miniaturisés. Il est essentiel de prendre en compte les principaux effets de taille dans le cadre constitutif afin d'obtenir des prédictions précises par des simulations numériques. Par conséquent, dans cette sous-section, les techniques de modélisation numérique associées aux effets de taille seront examinées en premier lieu. En pesant le pour et le contre concernant ces techniques, le choix des modèles numériques dans ce travail sera discuté.

### Modèles de plasticité conventionnels enrichis

Les théories de plasticité conventionnelles ne parviennent pas à prédire la dépendance aux effets de taille des réponses des matériaux à l'échelle micro, en raison de l'absence de variables dépendant de la taille. Pour remédier à cette lacune, de nombreux chercheurs se sont efforcés de prendre en compte les effets de taille en étendant les théories de plasticité conventionnelles, par exemple en ajoutant des paramètres supplémentaires associés à la taille de la géométrie. Diverses recherches ont été consacrées à la prise en compte des effets de taille en ajoutant des variables associées aux effets de taille dans les lois constitutives. Ces paramètres liés à la description des effets de taille sont généralement calibrés par des expériences à micro-échelle. Dans ce qui suit, plusieurs tentatives seront résumées.

## Couche de surface et modèle mésoscopique

Comme discuté dans 2.2.1, le phénomène "plus petit est plus faible" est dû aux différentes propriétés matérielles des grains de surface et internes dans une structure miniaturisée. De plus, le pourcentage de grains de surface dans la géométrie globale augmente avec la réduction de la géométrie. C'est pourquoi Engel and Eckstein (2002) ont proposé le concept de modèle de couche superficielle en partant de l'idée que les grains de surface libre présentent un durcissement moindre par rapport aux grains du volume intérieur, comme l'illustre la Fig. 2.7 pour une billette cylindrique.

Cependant, une des lacunes du modèle de la couche superficielle est qu'il ignore la transition entre les grains de surface et les grains intérieurs, qui est décrite de manière discontinue (c'est-à-dire la superposition mathématique de la contrainte d'écoulement des grains de surface et des grains intérieurs multipliée par leurs fractions). Pour remédier à cela, un modèle mésoscopique a été proposé par Geiger et al. (2007) qui prend en compte les effets de taille se produisant à l'échelle micro. Les influences de la taille des grains et de leur position sont prises en compte par la création d'une structure matérielle synthétique et le calcul des propriétés matérielles individuelles pour chacun des grains synthétiques.

Le modèle mésoscopique peut couvrir la plupart des caractéristiques du modèle de couche de surface d'une manière plus naturelle. De plus, les interactions entre les grains sont prises en compte. Des simulations numériques utilisant le modèle mésoscopique ont été réalisées par le biais d'un essai de refoulement à plat comme le montre la Fig. 2.8. La force de fromage moyenne prédictive par le modèle mésoscopique est en bon accord avec les résultats expérimentaux. La dispersion des facteurs de processus peut également être obtenue comme le montre la Fig. 2.8.

Bien que les méthodes susmentionnées soient capables de saisir les effets de taille, elles présentent plusieurs inconvénients. D'un point de vue général, ces modèles sont, dans une certaine mesure, construits dans un but particulier. Un autre point faible est lié à l'identification des paramètres constitutifs. Par exemple, en ce qui concerne le modèle de couche de surface, il est très compliqué et difficile d'obtenir des paramètres. Dans le travail de Li et al. (2017), une série d'essais, incluant des essais de traction et des essais de traitement d'images numériques, ont été réalisés pour déterminer les fractions des grains de surface et des grains intérieurs, les propriétés des grains de frontière et des grains intérieurs.

## Modèles de plasticité renforcée par le gradient

Dans la plasticité cristalline conventionnelle, le comportement de la microstructure sous-jacente est pris en compte. La description de la microstructure par la plasticité cristalline conventionnelle permet de saisir naturellement les effets de taille de premier ordre. L'élément central de la plasticité cristalline est la description du glissement plastique sur les systèmes de glissement individuels.

Comme mentionné dans la sous-section 2.2.2, la présence de gradients de déformation joue un rôle important pour les déformations plastiques aux petites échelles. La prise en compte de l'influence des effets de gradient de déformation devient essentielle pour la modélisation constitutive aux petites échelles. Pour inclure les effets de gradient dans les lois constitutives, des échelles de longueur internes sont nécessaires. Plusieurs modèles de plasticité à gradients, par exemple, la plasticité à gradients de déformation (Aifantis, 1984; Fleck et al., 1994; Fleck and Hutchinson, 2001; Gudmundson, 2004), la plasticité de type Cosserat (Forest et al., 1997, 2000) et les modèles micromorphes de plasticité (Forest, 2009) ont démontré leurs capacités à prédire les effets de taille

de gradients du second ordre. Les modèles de plasticité à gradients sont qualifiés de non-locaux en prenant en compte des variables non-locales, c'est-à-dire le gradient des mesures de déformation. La dimension de la mesure du gradient de déformation devient moins une unité, donc l'échelle de longueur est nécessaire pour maintenir la cohérence des dimensions.

Cependant, les modèles classiques de plasticité à gradient, c'est-à-dire les modèles de plasticité à gradient de déformation, négligent la discréétisation de la microstructure qui tend à avoir des influences significatives pour la déformation à petite échelle (effets de taille de premier ordre). La combinaison des avantages de la plasticité cristalline et de la plasticité à gradients permet de saisir les effets de taille de premier ordre et de second ordre. Il existe plusieurs modèles dans la littérature contenant les deux ingrédients (description de la microstructure et mesures du gradient de déformation), tels que la plasticité cristalline à gradient de déformation ([Gurtin, 2000](#); [Evers et al., 2004a](#); [Gurtin et al., 2007](#); [Kuroda and Tvergaard, 2008b](#)), la plasticité cristalline de Cosserat ([Forest, 1998](#); [Forest et al., 2000](#); [Forest and Sedláček, 2003](#); [Ask et al., 2018, 2020](#)), la plasticité cristalline micromorphe ([Cordero et al., 2010](#); [Wulffinghoff and Böhlke, 2012](#); [Chang et al., 2016](#); [Ling et al., 2018](#); [Scherer et al., 2019](#)).

## Choix des modèles numériques

Cette thèse vise à développer un cadre numérique complet qui puisse couvrir les principaux effets de taille, c'est-à-dire les effets de premier et de second ordre. Les contributions mentionnées ci-dessus ont fait des efforts pour décrire un ou plusieurs types d'effets de taille.

Les tentatives faites par les modèles de plasticité conventionnels augmentés de divers facteurs associés à la taille ne permettent de couvrir que la réponse du matériau dépendant de la taille, par exemple le phénomène "plus petit, plus faible". L'introduction de plusieurs facteurs associés à la taille semble être faite de manière artificielle et intentionnelle. De plus, il n'est pas pratique de procéder à l'identification des paramètres chaque fois qu'un nouveau paramètre dépendant de la taille est ajouté. Un avantage de cette approche est que ces modèles sont généralement basés sur des lois constitutives bien connues, ce qui n'est pas difficile pour les débutants.

Un progrès notable a été réalisé par le modèle de la couche superficielle qui tente de modéliser le comportement du matériau d'un point de vue plus profond que les précédents, à savoir les grains de surface et internes. Par rapport aux modèles de plasticité conventionnels améliorés, le modèle de couche de surface traite le domaine considéré comme une surface et des parties internes qui ont des comportements mécaniques différents. Malheureusement, seuls les effets de taille "plus petit est plus faible" peuvent être prédits par le modèle de couche de surface. La simple superposition des grains de surface et des grains internes multipliés par leurs pourcentages néglige les interactions entre les grains internes et les grains de surface. L'identification des paramètres dans le modèle de couche superficielle est assez peu pratique et imprécise. Par exemple, la détermination des proportions des grains de surface nécessite une technique de traitement des images numériques ([Li et al., 2017](#)).

Le modèle mésoscopique est une amélioration basée sur le modèle de couche de surface prenant en compte les transitions entre les grains de surface et les grains internes. Il peut prédire les effets de taille de premier ordre, incluant le phénomène "plus petit est plus faible" et la dispersion de la contrainte d'écoulement. Les comportements des grains individuels et leurs positions sont pris en compte par rapport au traitement des grains de surface et internes adopté dans le modèle de couche de surface. Cependant, l'identification des données est beaucoup plus compliquée que

dans le modèle de couche de surface, car chaque grain doit être traité séparément. En outre, les descriptions de la microstructure ne sont pas modélisées de manière naturelle.

Le modèle de plasticité cristalline répond à notre demande en captant les effets de taille intrinsèques et extrinsèques de premier ordre. Il relie la déformation plastique aux glissements sur les systèmes de glissement. Pour couvrir les effets de gradient de second ordre, il est couplé avec des théories de plasticité à gradients. La plasticité cristalline à gradient de déformation est un modèle typique qui peut couvrir à la fois les effets de taille dus à la microstructure sous-jacente et les effets de gradient de déformation. Par conséquent, le modèle de plasticité cristalline à gradient de déformation sera adopté comme cadre constitutif principal pour modéliser le comportement du matériau d'une structure à micro-échelle.

## Conclusions

Dans ce chapitre, l'état de l'art relatif aux objectifs de la thèse a été passé en revue. Les effets de taille sur les réponses des matériaux pour les structures miniaturisées ont un impact significatif sur les procédés de fabrication. La modélisation du comportement plastique en tenant compte des effets de taille s'avère être essentielle pour la validité des simulations numériques pour les composants miniaturisés.

La définition générale des effets de taille a été donnée et plusieurs types différents de classifications des effets de taille sont présentés. Parmi elles, la classification des effets de taille de premier et de second ordre nous fournit une catégorie plus organisée. Les effets de taille de premier ordre sont composés d'effets extrinsèques et intrinsèques provenant principalement de la microstructure sous-jacente. Pour les effets de taille de second ordre, l'un provient des gradients de déformation, et l'autre comprend les effets de joints de grains et les effets de frontières externes. Les effets de taille extrinsèques de premier ordre donnent lieu au phénomène "plus petit, c'est plus faible" et à la dispersion de la contrainte d'écoulement. Le phénomène "plus petit, est plus faible" est attribué aux grains de surface moins contraints et à une proportion accrue de grains de surface lorsque la taille de la géométrie diminue. Un autre effet lié à la microstructure est l'augmentation de la résistance qui est généralement induite par le raffinement de la taille des grains. La relation bien connue de Hall-Petch est un exemple typique de l'augmentation de la résistance liée à la taille des grains. Les effets de taille liés aux gradients de second ordre sont généralement observés lors de la présence de gradients de déformation pour les structures miniaturisées, ce qui conduit au phénomène communément observé "plus petit, plus fort" pour les expériences aux micro-échelles. Pour les matériaux polycristallins, les effets des joints de grains jouent un rôle important dans les comportements en déformation. Les joints de grains dans les matériaux polycristallins ont un impact sur les interactions des dislocations entre les grains adjacents. De plus, les influences des frontières externes ne doivent pas être négligées pour les structures miniaturisées.

Afin de prédire la déformation plastique des produits miniaturisés, les modèles numériques doivent prendre en compte les effets de taille de premier et de second ordre de manière appropriée. Les progrès actuels de la modélisation numérique des effets de taille dans les milieux continus ont été détaillés. Plusieurs tentatives ont été faites sur les modèles de plasticité conventionnels en introduisant différentes sortes de paramètres dépendant de la taille. Cette méthode est trop artificielle et non générale. Elle peut simplement prédire les effets de taille "plus petit est plus faible" parmi la catégorie de premier ordre. Par rapport à la méthode de plasticité conventionnelle améliorée,

le modèle de couche de surface tente de formuler les comportements des matériaux en modélisant respectivement les grains de surface et les grains internes. Bien qu'il semble être plus avancé que les modèles conventionnels améliorés, seul l'effet "plus petit est plus faible" peut être prédit par le modèle de couche de surface. En outre, la combinaison des grains de surface et des grains internes est effectuée de manière discontinue, c'est-à-dire une simple superposition de ces deux éléments multipliés par leurs pourcentages par rapport au volume global. Le modèle mésoscopique résout cette lacune en considérant chaque grain et en incluant les influences de ses grains voisins. Le modèle mésoscopique permet de modéliser les effets de taille de premier ordre, c'est-à-dire à la fois le "plus petit est plus faible" et la dispersion de la contrainte d'écoulement. Cependant, l'identification des paramètres du modèle mésoscopique est assez compliquée et prend beaucoup de temps, ce qui limite ses applications. Le modèle de plasticité cristalline peut naturellement couvrir les effets de taille de premier ordre grâce à sa description de la microstructure sous-jacente. Cependant, le modèle conventionnel de plasticité cristalline est formulé localement, ce qui le rend incapable de capter les effets de gradients de second ordre. Le couplage de la plasticité cristalline avec des modèles de plasticité à gradients offre une solution pour décrire à la fois les effets de taille extrinsèques/intrinsèques du premier ordre et les effets de gradients du second ordre. Par exemple, le modèle de plasticité cristalline à gradient de déformation est tout à fait adapté pour couvrir les deux effets de taille, en particulier lorsqu'il est couplé à des modèles de joints de grains. Désormais, le choix du cadre constitutif de cette thèse est déterminé, c'est-à-dire le choix du modèle de plasticité cristalline à gradient de déformation et du modèle de joints de grains associé. Ce choix permet de capter tous les effets de taille de premier et second ordre.



# Développement d'un modèle de plasticité cristalline à gradient de déformation flexible en petites déformations

## Introduction

Un modèle de plasticité cristalline à gradient de déformation flexible en petites déformations sera présenté dans ce chapitre. La théorie à gradient d'ordre supérieur et les formulations non incrémentales par rapport aux contraintes d'ordre supérieur seront utilisées. Par rapport aux théories de plasticité conventionnelles, la caractéristique la plus significative des théories de plasticité à gradient de déformation réside dans l'inclusion et la description des processus d'ordre supérieur, c'est-à-dire les processus énergétiques d'ordre supérieur formulés par l'énergie de défauts et les processus dissipatifs décrits par les fonctions de dissipation.

La formulation de l'énergie de défauts détermine les effets énergétiques d'ordre supérieur. Parmi les recherches sur l'énergie de défauts dans la littérature, plusieurs descriptions communes existent telles que l'énergie de défauts quadratique par rapport aux gradients de déformation plastique ([Gurtin et al., 2007](#); [Panteghini and Bardella, 2016](#)), l'énergie de défauts linéaire ([Ohno and Okumura, 2007](#); [Hurtado and Ortiz, 2013](#)) et l'énergie de défauts logarithmique ([Wulffinghoff et al., 2015](#)). Il est nécessaire de proposer une énergie de défauts généralisée contrôlée par un indice  $n$ . De plus, presque tous les travaux sur le sujet de l'énergie de défauts se sont limités au cas de chargements proportionnels. Il est essentiel d'étudier les réponses des matériaux dans des conditions de chargement proportionnel et non proportionnel en utilisant différents types d'énergie de défauts. Ceci devient le premier objectif de ce chapitre. Une énergie de défauts généralisée avec une forme de loi puissance contrôlée par un indice  $n$  sera développée. Les influences de l'ordre de l'énergie de défauts sous chargement proportionnel et non proportionnel seront comparées.

Les processus dissipatifs sont formulés à l'aide d'une mesure de déformation plastique effective généralisée. Cette mesure couple les déformations plastiques et leurs gradients dans divers travaux de la littérature ([Fleck and Hutchinson, 2001](#); [Gurtin et al., 2007](#); [Hutchinson, 2012](#); [Fleck et al., 2015](#); [Nelleman et al., 2017, 2018](#)). Cependant, la méthode de dissipation couplée fréquemment adoptée n'a pas été validée par des preuves expérimentales jusqu'à présent. Avec la dissipation couplée, il est difficile de traiter les sauts élastiques qui se produisent généralement au moment de la plasticité initiale ou lorsqu'une charge non proportionnelle se produit. Le deuxième objectif de ce chapitre se concentrera sur ces points. Une fonction de dissipation non couplée sera présentée en premier lieu. Avec l'aide de la dissipation non couplée, la contrainte d'ordre supérieur dépend uniquement des gradients de déformation d'ordre supérieur. Des discussions sur les sauts élastiques

seront effectuées sous chargement non proportionnel par passivation des glissements plastiques à un certain moment.

## Modèle de plasticité cristalline à gradient de déformation (SGCP)

Dans cette section, un modèle de plasticité cristalline à gradient de déformation (SGCP) de type Gurin est développé sur la base d'une énergie de défauts non quadratique généralisée et d'une dissipation non couplée, dans le cadre des petites déformations.

Les processus énergétiques sont représentés par la densité d'énergie libre  $\psi$ . Dans ce travail, la décomposition classique de  $\psi$  en une énergie de déformation élastique  $\psi_e$  et une énergie de défauts  $\psi_p$  est adoptée.  $\psi_e$  est supposée être une fonction quadratique du  $\varepsilon_e$ :

$$\psi_e(\varepsilon_e) = \frac{1}{2} \varepsilon_e : \mathbf{C} : \varepsilon_e \quad (7.1)$$

où  $\mathbf{C}$  est le tenseur d'élasticité, qui est supposé être symétrique et défini positif. En s'appuyant sur les travaux de [Gurtin et al. \(2007\)](#), on suppose que  $\psi_p$  est fonction des densités de dislocations :

$$\boldsymbol{\rho} = (\rho_{\vdash}^1, \rho_{\vdash}^2, \dots, \rho_{\vdash}^q, \rho_{\odot}^1, \rho_{\odot}^2, \dots, \rho_{\odot}^q) \quad (7.2)$$

où  $\rho_{\vdash}^{\alpha}$  et  $\rho_{\odot}^{\alpha}$  désignent respectivement les densités de dislocations de type coin et de type vis sur le système de glissement  $\alpha$ . Comme l'ont montré [Arsenlis and Parks \(1999\)](#), ces quantités peuvent être calculées comme suit :

$$\rho_{\vdash}^{\alpha} = -\mathbf{s}^{\alpha} \cdot \nabla \gamma^{\alpha}, \quad \rho_{\odot}^{\alpha} = \mathbf{l}^{\alpha} \cdot \nabla \gamma^{\alpha} \quad (7.3)$$

où  $\mathbf{l}^{\alpha}$  est la direction ligne de la distribution de dislocations définie par  $\mathbf{l}^{\alpha} = \mathbf{m}^{\alpha} \times \mathbf{s}^{\alpha}$  (" $\times$ " est l'opérateur de produit vectoriel). Cependant, contrairement aux travaux de [Gurtin et al. \(2007\)](#), dans le présent travail,  $\psi_p$  est supposé être non quadratique par rapport à ces densités. Une forme en loi puissance, avec un indice de contrôle d'ordre réglable  $n$ , est appliquée pour définir cette énergie :

$$\psi_p(\boldsymbol{\rho}) = \frac{1}{n} X_0 l_{en}^n \sum_{\alpha=1}^q [|\rho_{\vdash}^{\alpha}|^n + |\rho_{\odot}^{\alpha}|^n] \quad (7.4)$$

où  $X_0$  est une constante représentant la résistance énergétique au glissement, et  $l_{en}$  est une échelle de longueur énergétique. Pour assurer la convexité de  $\psi_p$ , l'indice énergétique de défauts  $n$  doit être supérieur ou égal à 1 ( $n \geq 1$ ). En utilisant (7.1) et (7.4), la densité d'énergie libre peut être exprimée comme suit :

$$\psi(\varepsilon_e, \boldsymbol{\rho}) = \frac{1}{2} \varepsilon_e : \mathbf{C} : \varepsilon_e + \frac{1}{n} X_0 l_{en}^n \sum_{\alpha=1}^q [|\rho_{\vdash}^{\alpha}|^n + |\rho_{\odot}^{\alpha}|^n] \quad (7.5)$$

Le tenseur des contraintes macroscopiques (énergétiques)  $\boldsymbol{\sigma}$  peut s'exprimer comme suit :

$$\boldsymbol{\sigma} = \frac{\partial \psi}{\partial \varepsilon_e} = \mathbf{C} : \varepsilon_e \quad (7.6)$$

Comme il n'y a pas de dépendance explicite de la forme supposée de  $\psi$  et les  $\gamma$ , la partie énergétique de la contrainte microscopique scalaire  $\pi_{en}^\alpha$  est nulle pour tout système de glissement  $\alpha$  :

$$\pi_{en}^\alpha = \frac{\partial \psi}{\partial \gamma^\alpha} = 0 \quad (7.7)$$

Le vecteur de contrainte microscopique énergétique  $\xi_{en}^\alpha$  sur le système de glissement  $\alpha$  peut être exprimé comme suit :

$$\xi_{en}^\alpha = \frac{\partial \psi(\varepsilon_e, \rho)}{\partial \nabla \gamma^\alpha} = X_0 l_{en}^n [|\mathbf{s}^\alpha \cdot \nabla \gamma^\alpha|^{n-2} \mathbf{s}^\alpha \otimes \mathbf{s}^\alpha + |\mathbf{l}^\alpha \cdot \nabla \gamma^\alpha|^{n-2} \mathbf{l}^\alpha \otimes \mathbf{l}^\alpha] \cdot \nabla \gamma^\alpha \quad (7.8)$$

On définit des déformations plastiques effectives indépendantes (découplées) du premier ordre et d'ordre supérieur pour chaque système de glissement  $\alpha$  ( $e_\pi^\alpha$  et  $e_\xi^\alpha$ , respectivement) comme suit :

$$\dot{e}_\pi^\alpha = |\dot{\gamma}^\alpha| = \sqrt{(\dot{\gamma}^\alpha)^2}, \quad e_\pi^\alpha = \int \dot{e}_\pi^\alpha dt \quad (7.9)$$

$$\dot{e}_\xi^\alpha = \|l_{dis} \nabla^\alpha \dot{\gamma}^\alpha\| = l_{dis} \sqrt{(\nabla^\alpha \dot{\gamma}^\alpha)^2}, \quad e_\xi^\alpha = \int \dot{e}_\xi^\alpha dt \quad (7.10)$$

où  $\nabla^\alpha$  est la projection de  $\nabla$  sur le système de glissement  $\alpha$  :

$$\nabla^\alpha \phi = (\mathbf{s}^\alpha \cdot \nabla \phi) \mathbf{s}^\alpha + (\mathbf{l}^\alpha \cdot \nabla \phi) \mathbf{l}^\alpha \quad (7.11)$$

La fonction de dissipation découplée proposée peut être exprimée comme suit :

$$\varphi(\dot{\mathbf{e}}_\pi, \mathbf{e}_\pi, \dot{\mathbf{e}}_\xi, \mathbf{e}_\xi) = \varphi_\pi(\dot{\mathbf{e}}_\pi, \mathbf{e}_\pi) + \varphi_\xi(\dot{\mathbf{e}}_\xi, \mathbf{e}_\xi) \quad (7.12)$$

avec

$$\dot{\mathbf{e}}_\pi = (\dot{e}_\pi^1, \dot{e}_\pi^2, \dots, \dot{e}_\pi^q), \quad \mathbf{e}_\pi = (e_\pi^1, e_\pi^2, \dots, e_\pi^q), \quad \dot{\mathbf{e}}_\xi = (\dot{e}_\xi^1, \dot{e}_\xi^2, \dots, \dot{e}_\xi^q), \quad \mathbf{e}_\xi = (e_\xi^1, e_\xi^2, \dots, e_\xi^q) \quad (7.13)$$

À des fins de comparaison, les expressions de  $\varphi_\pi$  et  $\varphi_\xi$  sont postulées de manière à obtenir des contraintes microscopiques dissipatives ayant des formes proches de celles proposées par [Gurtin et al. \(2007\)](#) :

$$\varphi_i(\dot{\mathbf{e}}_i, \mathbf{e}_i) = \sum_{\alpha=1}^q S_i^\alpha \frac{\dot{\gamma}_0^\alpha}{m+1} \left[ \frac{\dot{e}_i^\alpha}{\dot{\gamma}_0^\alpha} \right]^{m+1} \quad (7.14)$$

où l'indice  $i$  prend pour valeur  $\pi$  ou  $\xi$  en référence aux contraintes microscopiques dissipatives de premier ordre ou d'ordre supérieur,  $\dot{\gamma}_0^\alpha > 0$  est une vitesse de déformation constante représentative des flux d'intérêt,  $m > 0$  est une constante caractérisant la sensibilité à la vitesse du matériau considéré, et  $S_i^\alpha$  ( $i \in \{\pi, \xi\}$ ) sont des variables d'état internes ayant la dimension d'une contrainte ( $S_\pi^\alpha > 0$  et  $S_\xi^\alpha \geq 0$ ).

Sur la base des définitions ci-dessus des ingrédients de la fonctionnelle de dissipation proposée  $\varphi$ , on peut facilement vérifier que cette fonctionnelle est non négative et convexe par rapport aux

variables  $\dot{\gamma}^\alpha$  et  $\nabla\dot{\gamma}^\alpha$ , ce qui garantit a priori la satisfaction du deuxième principe de la thermodynamique (dissipation non négative). Les dérivées partielles de  $\varphi$  par rapport à  $\dot{\gamma}^\alpha$  et  $\nabla\dot{\gamma}^\alpha$  donnent les expressions de la contrainte dissipative scalaire  $\pi_{dis}^\alpha$  et du vecteur de contrainte dissipatif  $\xi_{dis}^\alpha$  sur le système de glissement  $\alpha$  :

$$\pi_{dis}^\alpha = \frac{\partial \varphi}{\partial \dot{\gamma}^\alpha} = S_\pi^\alpha \left[ \frac{\dot{e}_\pi^\alpha}{\dot{\gamma}_0^\alpha} \right]^m \frac{\dot{\gamma}^\alpha}{\dot{e}_\pi^\alpha} \quad (7.15)$$

$$\xi_{dis}^\alpha = \frac{\partial \varphi}{\partial \nabla\dot{\gamma}^\alpha} = S_\xi^\alpha l_{dis}^2 \left[ \frac{\dot{e}_\xi^\alpha}{\dot{\gamma}_0^\alpha} \right]^m \frac{\nabla^\alpha \dot{\gamma}^\alpha}{\dot{e}_\xi^\alpha} \quad (7.16)$$

Comme mentionné ci-dessus, la fonctionnelle de dissipation proposée dans ce travail  $\varphi$  conduit à des contraintes microscopiques dissipatives proches de celles postulées par [Gurtin et al. \(2007\)](#) sur la base de la règle de normalité. Ces dernières peuvent être obtenues à partir de (7.15) et (7.16) en remplaçant les déformations plastiques effectives de premier ordre et d'ordre supérieur par une déformation plastique effective couplée définie par :

$$\dot{d}^\alpha = \sqrt{(\dot{e}_\pi^\alpha)^2 + (\dot{e}_\xi^\alpha)^2}, \quad d^\alpha = \int \dot{d}^\alpha dt \quad (7.17)$$

et en remplaçant  $S_\pi^\alpha$  et  $S_\xi^\alpha$  par une seule résistance au glissement strictement positive  $S^\alpha$  calculée sur la base de  $\dot{d}^\alpha$ .

## Résultats

La Fig. 7.6 présente les courbes de contrainte-déformation pour différentes valeurs de  $n < 2$  et  $l_{en}$ , obtenues dans les conditions de chargement proportionnel et non proportionnel introduites au début de la section. En analysant uniquement la partie chargement des résultats,  $l_{en}$  semble contribuer à l'augmentation de résistance du matériau. Cette augmentation de résistance (ou renforcement du matériau caractérisé par l'augmentation de la contrainte d'écoulement) est observée dans les deux cas de chargement, proportionnel et non proportionnel. Plus la valeur de  $n$  est faible (c'est-à-dire que  $n$  s'approche de 1), plus les écarts sont importants. Dans les conditions de chargement non proportionnel considérées, les sauts élastiques obtenus à la limite d'élasticité initiale sont moins marqués que ceux obtenus dans des conditions de chargement proportionnel. De plus, lors de l'apparition de la source de chargement non proportionnel (passivation du bord supérieur), aucun saut élastique supplémentaire n'est observé, il y a seulement une courte augmentation rapide de la contrainte moyenne avec une pente beaucoup plus faible que la pente élastique (Fig. 7.6b). Comme seul le bord inférieur est passivé dès le début, des gradients de déformation plastique plus faibles se développent au sein du spécimen, ce qui explique les sauts élastiques plus faibles au moment de l'écoulement plastique initial. Après déformation, les gradients de déformation plastique continuent à se développer sur une grande partie du spécimen et leur existence avant la passivation du bord supérieur empêche l'apparition de nouveaux sauts. Si l'on considère maintenant l'ensemble des résultats lors du trajet charge-décharge, on peut noter deux caractéristiques frappantes. La première caractéristique, qui concerne à la fois les cas de chargement proportionnel et non proportionnel, est

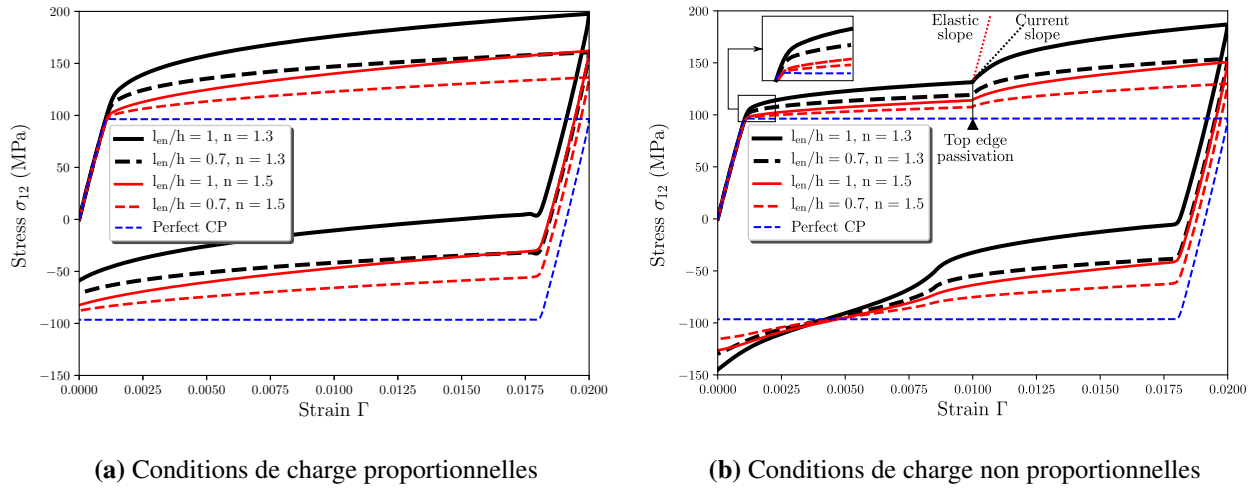


**Fig. 7.6.** Réponses contrainte-déformation dans des conditions de chargement proportionnel et non proportionnel pour différentes valeurs de l'indice d'énergie des défauts  $n$  dans la gamme  $n < 2$  et différentes valeurs de l'échelle de longueur énergétique  $l_{en}$  ( $l_{dis} = 0, H_\pi = 0$ ).

la forme concave des courbes de décharge. La deuxième caractéristique, qui concerne uniquement le cas de chargement non proportionnel, est la présence de points d'inflexion au milieu des courbes de décharge associées. Il est intéressant de noter que ces points d'inflexion semblent se produire approximativement aux mêmes états plastiques auxquels le bord supérieur a été passivé, même si aucune modification n'est apportée aux conditions de décharge.

En commençant par les conditions de chargement proportionnel, la Fig. 7.7a montre les résultats de contrainte-déformation associés à différentes valeurs de  $S_{\xi_0}$ , avec  $l_{dis} = h$  et  $H_\xi = 100$  MPa. À  $l_{dis}$  fixe, les sauts élastiques à la limite d'élasticité initiale sont largement contrôlés par  $S_{\xi_0}$ . Plus ce paramètre est petit, plus les sauts sont petits, qui peuvent également être supprimés en fixant  $S_{\xi_0} = 0$  (en pratique, une petite valeur doit être utilisée au lieu de 0 pour éviter des pas de temps trop petits pour la convergence). En utilisant  $S_{\xi_0} = 0,01$  MPa, aucun saut élastique apparent n'est obtenu à la limite d'élasticité initiale. Ceci est conforme aux résultats de Fleck et al. (2015) et peut être expliqué par des contraintes dissipatives d'ordre supérieur nulles (presque nulles)  $\xi_{dis}^\alpha$  au début de la déformation. Il convient de rappeler qu'avec l'hypothèse d'une dissipation non couplée, les contraintes dissipatives d'ordre supérieur  $\xi_{dis}^\alpha$  ne dépendent que des gradients de glissement plastique et de leurs taux, et qu'elles continuent à être nulles après toute déformation plastique uniforme. Par conséquent, le modèle proposé permet d'éviter les sauts élastiques non seulement au moment de l'élasticité initiale mais aussi après toute déformation plastique uniforme.

En ce qui concerne les conditions de chargement non proportionnel, la Fig. 7.7b présente les résultats correspondants obtenus en utilisant différentes valeurs de  $S_{\xi_0}$ , avec  $l_{dis} = h$  et  $H_\xi = 100$  MPa. Cette figure montre que, contrairement à  $l_{en}$ , l'échelle de longueur dissipative  $l_{dis}$  peut conduire à des sauts élastiques non seulement au niveau du seuil d'écoulement initial mais aussi au niveau de la passivation du bord supérieur. Pour  $S_{\xi_0}$  non nul, les sauts observés à la limite élastique initiale dans des conditions de chargement proportionnel, avec les deux bords passivés dès le début, sont divisés en deux parties. Une partie se produit à la limite d'élasticité initiale, où seul le bord inférieur est passivé ; et l'autre partie se produit à la passivation du bord supérieur. Pour un  $S_{\xi_0}$

nul (ou presque nul), aucun saut élastique apparent n'est observé, ni à la limite d'élasticité initiale, ni à l'apparition de la source de chargement non proportionnelle. Si l'absence de sauts élastiques à la limite d'élasticité initiale s'explique de la même manière que précédemment, leur absence à la passivation du bord supérieur est plus difficile à expliquer. En effet, dans les conditions de chargement non proportionnel considérées, des déformations plastiques non uniformes se développent au sein du spécimen étudié avant la passivation du bord supérieur, rendant les résistances au glissement d'ordre supérieur actuelles  $S_\xi^\alpha$  (puis  $\xi_{dis}^\alpha$ ) en évolution au sein du spécimen étudié. Pour mieux expliquer l'absence de sauts élastiques dans ce cas, les termes de sensibilité à la vitesse de déformation, qui ne servent qu'à la régularisation, seront ignorés par la suite. Dans la limite d'un écoulement plastique indépendant de la vitesse, l'absence de sauts élastiques lors de l'apparition d'une source de chargement non proportionnelle se traduit par l'existence de taux de glissement plastique non nuls  $\dot{\gamma}^\alpha$  qui satisfont les équations d'équilibre microscopique. En supposant, pour simplifier, que les conditions aux limites sont telles que soit  $\dot{\gamma}^\alpha = 0$ , soit  $\chi^\alpha = 0$  à la frontière, en l'absence de contraintes énergétiques d'ordre supérieur, ces équations peuvent être écrites, sous forme faible, comme :

$$G_\gamma = \sum_{\alpha=1}^q \int_V [(|\tau^\alpha| - S_\pi^\alpha) \dot{e}_\pi^\alpha - S_\xi^\alpha \dot{e}_\xi^\alpha] dv = 0 \quad (7.18)$$

Pour que cette expression ait des solutions  $\dot{\gamma}^\alpha$  non nulles lors de l'apparition d'une source de chargement non proportionnel, cette dernière ne doit pas modifier significativement le rapport entre  $\dot{e}_\pi^\alpha$  et  $\dot{e}_\xi^\alpha$  dans les régions où les contraintes dissipatives d'ordre supérieur  $\xi_{dis}^\alpha$  sont activées ( $S_\xi^\alpha \neq 0$ ). Sinon, le flux plastique est interrompu jusqu'à ce que les cissions critiques résolues  $\tau^\alpha$  (évoluant de manière élastique) atteignent des valeurs suffisantes pour compenser les variations disproportionnées entre les termes de (7.18). En ne passivant que le bord inférieur, les gradients de déformation plastique ne se développent que dans la moitié inférieure du spécimen étudié. En utilisant  $S_{\xi 0} = 0$ , après déformation, les contraintes  $\xi_{dis}^\alpha$  sont continuellement activées (à partir de 0) dans cette partie du spécimen et restent inactives autrement. L'apparition de la passivation du bord supérieur modifie les distributions de glissement plastique uniquement dans la moitié supérieure du spécimen étudié, où les contraintes  $\xi_{dis}^\alpha$  ne sont pas encore activées. Ceci explique l'absence de sauts élastiques à la passivation de ce bord.

## Conclusion

Un modèle flexible de plasticité cristalline à gradient de déformation (SGCP) de type Gurin a été développé, basé sur une énergie de défauts non quadratique et une dissipation non couplée. Les contraintes microscopiques énergétiques (récupérables) et dissipatives (non récupérables) sont prises en compte dans ce modèle. Les contraintes microscopiques énergétiques d'ordre supérieur sont déduites d'une énergie de défauts généralisée de type puissance, avec un indice de contrôle d'ordre n ajustable. Cette forme d'énergie de défauts est proposée pour étudier l'interaction entre la forme de cette énergie et les effets d'échelle de longueur énergétique dans des conditions de chargements proportionnel et non proportionnel. Les contraintes microscopiques dissipatives sont déduites d'une fonction de dissipation non couplée, qui est exprimée comme une somme de deux fonctions séparées de mesures de déformation plastique effective de premier ordre et d'ordre supérieur.

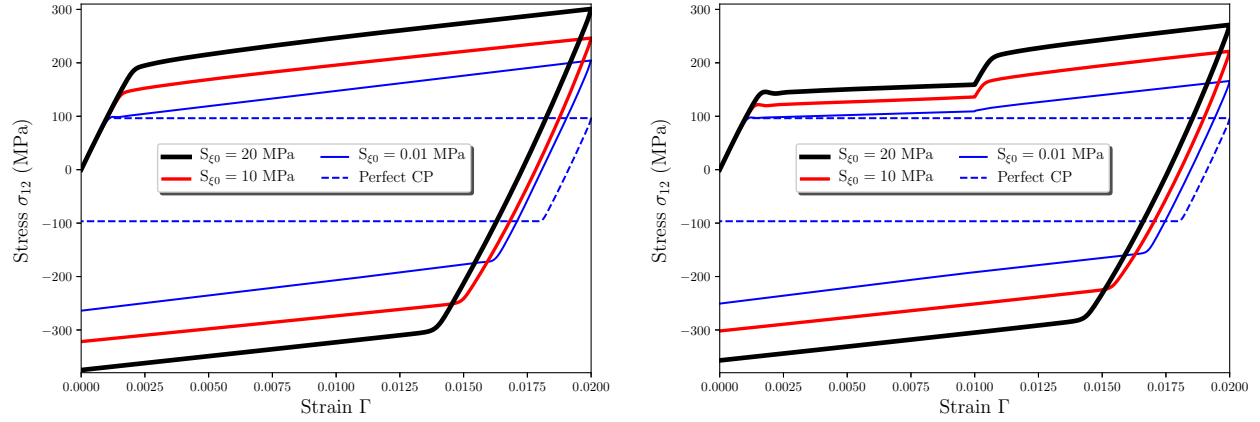


**Fig. 7.7.** Influence de la résistance initiale au glissement dissipatif d'ordre supérieur  $S_{\xi 0}$  sur l'écart élastique dans des conditions de chargement proportionnel et non proportionnel ( $l_{en} = 0$ ,  $l_{dis} = h$ ,  $H_{\pi} = 0$ ,  $H_{\xi} = 100$  MPa).

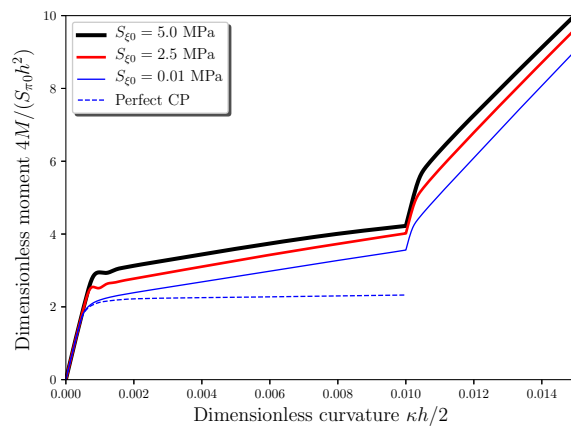


**Fig. 7.8.** Influence de la résistance initiale au glissement d'ordre supérieur  $S_{\xi 0}$  sur la réponse moment-courbure de la bande considérée en flexion pure avec des conditions de microflexion, suivie d'une passivation des bords supérieurs et inférieurs et d'une flexion continue ( $l_{en} = 0$ ,  $l_{dis} = h$ ,  $H_{\pi} = 0$ ,  $H_{\xi} = 100$  MPa).

En commençant par les effets d'échelle de longueur énergétique, il a été constaté que ces effets dépendent de la valeur de l'indice de contrôle d'ordre  $n$  et des conditions de chargement. Deux cas peuvent être distingués :  $n < 2$  et  $n \geq 2$ . Dans le domaine de  $n < 2$ , l'échelle de longueur énergétique  $l_{en}$  conduit à un écrouissage cinématique non linéaire inhabituel, ce qui entraîne une augmentation apparente de la limite d'élasticité (augmentation de résistance) sous chargement monotone. À partir de  $n = 2$ , quel que soit le type de chargement,  $l_{en}$  n'a d'influence que sur la vitesse de durcissement (d'écrouissage) après la limite d'élasticité mais pas sur l'augmentation de résistance du matériau, comme cela est largement reconnu dans la littérature.

Concernant les aspects de dissipation, en termes de réponse contrainte-déformation, l'hypothèse d'une dissipation non couplée n'a pas d'impact significatif. L'avantage de l'utilisation de la dissipation non couplée est le contrôle flexible de certains effets dissipatifs importants, tels que les sauts élastiques qui peuvent facilement être contrôlés en faisant varier la résistance au glissement d'ordre supérieur initiale  $S_{\xi_0}$ . En annulant ce dernier paramètre, on peut obtenir une variante du modèle proposé permettant de supprimer ces sauts dans certaines circonstances, par exemple au moment de l'élasticité initiale ou, d'une manière générale, lorsqu'une source de chargement non proportionnel ne fait pas varier de manière significative les gradients de glissement plastique dans les régions où les contraintes dissipatives d'ordre supérieur sont activées.

Bien qu'il soit encore tôt pour confirmer quels mécanismes aux petites échelles doivent être considérés pour reproduire correctement le comportement aux petites échelles des matériaux réels, le modèle proposé, avec ses parties énergétique et dissipative, offre une grande flexibilité dans le suivi de la majeure partie de ces mécanismes. Cela rend la tâche de passer de l'un à l'autre relativement facile.

# Extension aux grandes déformations du modèle de plasticité cristalline flexible à gradient de déformation

## Introduction

L'objectif de cette thèse est de développer un ensemble d'outils numériques adaptés aux études de localisation des déformations. Le phénomène de localisation des déformations implique une déformation plastique sévère et des effets significatifs de grandes déformations, par exemple, des effets géométriques et des effets de rotation du réseau. Par conséquent, un cadre constitutif de grandes déformations est essentiel pour capter correctement les phénomènes de localisation des déformations. À cette fin, le modèle SGCP en petites déformations proposé dans le précédent chapitre, basé sur une énergie de défauts non quadratique et une hypothèse de dissipation non couplée, est étendu au cadre des grandes déformations.

## Modèle SGCP en grandes déformations

Dans cette section, le modèle SGCP en petites déformations, basé sur l'énergie de défauts généralisée et la dissipation non couplée, est étendu au cadre des grandes déformations. Le modèle en grandes déformations est formulé relativement à la configuration de référence afin de simplifier son implémentation numérique.

Dans le cadre des grandes déformations, la cinématique élasto-plastique est décrite par la décomposition de Kröner-Lee du gradient de transformation  $\mathbf{F}$  ([Kröner, 1959](#); [Lee, 1964](#)) comme le montre la Fig. 7.9 :

$$\mathbf{F} = \mathbf{F}^e \mathbf{F}^p \quad (7.19)$$

où  $\mathbf{F}^e$  représente la distorsion élastique incluant l'étirement et la rotation du réseau et  $\mathbf{F}^p$  représente la distorsion plastique due à la déformation plastique causée par l'écoulement des défauts. L'incompressibilité plastique est également supposée avec  $\det(\mathbf{F}^p) = 1$ .

Comme le montre la Fig. 7.9, le treillis non déformé réside dans les configurations intermédiaires. Cependant, de nombreux travaux adoptent l'hypothèse que le treillis non déformé se trouve dans la configuration de référence, c'est-à-dire l'espace matériel ([Ling, 2018](#); [Marano, 2019](#)). Ceci n'est pas correct, comme le soutiennent [Gurtin et al. \(2010\)](#) : un flux de dislocations implique

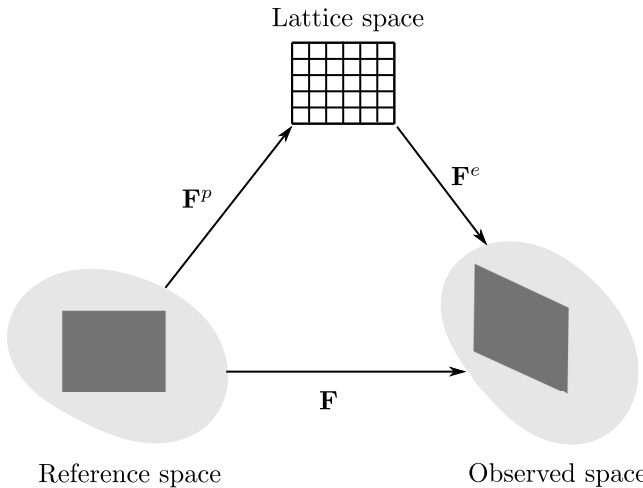


**Fig. 7.9.** Illustration de la décomposition multiplicative du gradient de déformation : Décomposition de Kröner-Lee ([Kröner, 1959](#); [Lee, 1964](#)).

un flux de matière par rapport au treillis non déformé, les vecteurs du treillis ne peuvent pas être matériels<sup>1</sup>. Dans ce travail, nous adoptons la notion proposée par [Gurtin et al. \(2010\)](#).

Considérant (7.19), le tenseur du gradient de vitesse peut être écrit comme :

$$\mathbf{L} = \dot{\mathbf{F}}\mathbf{F}^{-1} = \mathbf{L}^e + \mathbf{F}^e\mathbf{L}^p\mathbf{F}^{e-1} \quad (7.20)$$

avec les tenseurs de taux de distorsion élastique et plastique  $\mathbf{L}^e$  et  $\mathbf{L}^p$  définis par :

$$\mathbf{L}^e = \dot{\mathbf{F}}^e\mathbf{F}^{-e} \quad \text{and} \quad \mathbf{L}^p = \dot{\mathbf{F}}^p\mathbf{F}^{p-1} \quad (7.21)$$

L'hypothèse du monocristal exige que le tenseur  $\mathbf{L}^p$  soit régi par les taux de glissement sur les systèmes de glissement individuels. Ces systèmes sont définis dans l'espace intermédiaire, également appelé treillis ou espace structurel. Dans cet espace, la direction du glissement et la direction de la normale au plan de glissement associées à un système de glissement  $\alpha$ , respectivement notées  $\mathbf{s}^\alpha$  et  $\mathbf{m}^\alpha$ , sont des vecteurs constants du réseau :

$$\mathbf{s}^\alpha \cdot \mathbf{m}^\alpha = 0 \quad \text{and} \quad |\mathbf{s}^\alpha| = |\mathbf{m}^\alpha| = 1 \quad (7.22)$$

Ces vecteurs, ainsi que le vecteur directionnel de glissement ( $\mathbf{l}^\alpha = \mathbf{m}^\alpha \wedge \mathbf{s}^\alpha$ ), sont exprimés dans la configuration de référence comme suit ([Gurtin, 2006](#)) :

$$\mathbf{s}_r^\alpha = \mathbf{F}^{p-1}\mathbf{s}^\alpha, \quad \mathbf{m}_r^\alpha = \mathbf{F}^{pT}\mathbf{m}^\alpha, \quad \mathbf{l}_r^\alpha = \mathbf{F}^{p-1}\mathbf{l}^\alpha \quad (7.23)$$

En utilisant l'hypothèse du monocristal, le tenseur de taux de distorsion plastique  $\mathbf{L}^p$  peut être écrit dans l'espace intermédiaire comme suit :

$$\mathbf{L}^p = \sum_{\alpha=1}^q \dot{\gamma}^\alpha \mathbb{S}^\alpha \quad (7.24)$$

---

<sup>1</sup>Pour des explications plus détaillées, voir [Gurtin et al. \(2010\)](#), section 91.2.

où  $\mathbb{S}^\alpha = \mathbf{s}^\alpha \otimes \mathbf{m}^\alpha$  désigne le tenseur de Schmid associé au système de glissement  $\alpha$ ,  $\dot{\gamma}^\alpha$  représente le taux de glissement plastique sur ce système, et  $q$  est le nombre de systèmes de glissement. Par souci de cohérence avec le modèle SGCP en petites déformations proposé par [Jebahi et al. \(2020\)](#), le même symbole ( $\dot{\gamma}^\alpha$ ) est utilisé pour désigner le taux de glissement plastique sur le système de glissement  $\alpha$ . Cependant, dans le cadre des grandes déformations,  $\dot{\gamma}^\alpha$  ne peut pas être interprété comme la dérivée temporelle matérielle d'une variable de champ physiquement significative  $\gamma^\alpha$ . En effet, les glissements (en tant que champs sur des systèmes de glissement individuels) ne sont pas en général des quantités bien définies d'un point de vue physique ([Gurtin, 2008b](#)).

L'énergie libre consiste en une énergie de déformation élastique  $\Psi^e$  et une énergie de défaut  $\Psi^\rho$ . En s'appuyant sur les travaux de [Gurtin \(2008b\)](#), on suppose que  $\Psi^\rho$  est fonction des densités de dislocations :

$$\boldsymbol{\rho} = \{\rho_{\vdash}^1 \cdots \rho_{\vdash}^q, \rho_{\odot}^1 \cdots \rho_{\odot}^q\}$$

où  $\rho_{\vdash}^\alpha$  et  $\rho_{\odot}^\alpha$  sont respectivement les densités de dislocations de type coin et de type vis associées au système de glissement  $\alpha$ , qui sont respectivement définies par :

$$\dot{\rho}_{\vdash}^\alpha = -\mathbf{s}^\alpha \cdot \mathbf{grad}_\#(\dot{\gamma}^\alpha) \quad \text{and} \quad \dot{\rho}_{\odot}^\alpha = \mathbf{l}^\alpha \cdot \mathbf{grad}_\#(\dot{\gamma}^\alpha) \quad (7.25)$$

Ces densités sont en unités de  $length^{-1}$  et peuvent être positives ou négatives. En gardant à l'esprit les équations (7.23), on peut facilement démontrer que :

$$\dot{\rho}_{\vdash}^\alpha = -\mathbf{s}_r^\alpha \cdot \mathbf{grad}_X(\dot{\gamma}^\alpha) \quad \text{and} \quad \dot{\rho}_{\odot}^\alpha = \mathbf{l}_r^\alpha \cdot \mathbf{grad}_X(\dot{\gamma}^\alpha) \quad (7.26)$$

L'énergie de déformation élastique  $\Psi^e$  est supposée être une forme quadratique de  $\mathbf{E}^e$  :

$$\Psi^e = \frac{1}{2} \mathbf{E}^e : \mathbb{C} : \mathbf{E}^e$$

où  $\mathbb{C}$  est un tenseur d'élasticité symétrique et défini positif. Sous forme de taux, cette quantité peut être écrite comme suit :

$$\dot{\Psi}^e = \frac{\partial \Psi^e}{\partial \mathbf{E}^e} : \dot{\mathbf{E}}^e \quad (7.27)$$

Une énergie de défauts généralisée de type loi puissance avec un indice de contrôle d'ordre  $n$  ajustable est adoptée dans ce travail :

$$\Psi^\rho = \frac{1}{n} X_0 l_{en}^n \sum_{\alpha=1}^q (|\rho_{\vdash}^\alpha|^n + |\rho_{\odot}^\alpha|^n) \quad (7.28)$$

où  $X_0$  est une constante représentant la résistance énergétique au glissement, et  $l_{en}$  est une échelle de longueur énergétique. Pour assurer la convexité de  $\Psi^\rho$ , l'indice énergétique de défaut  $n$  doit être supérieur ou égal à 1 ( $n \geq 1$ ). Sa forme de taux est donnée par :

$$\begin{aligned} \dot{\Psi}^\rho &= \sum_{\alpha=1}^q \left( \frac{\partial \Psi^\rho}{\partial \rho_{\vdash}^\alpha} \dot{\rho}_{\vdash}^\alpha + \frac{\partial \Psi^\rho}{\partial \rho_{\odot}^\alpha} \dot{\rho}_{\odot}^\alpha \right) \\ &= X_0 l_{en}^n \sum_{\alpha=1}^q \left( -|\rho_{\vdash}^\alpha|^{n-2} \rho_{\vdash}^\alpha \mathbf{s}_r^\alpha + |\rho_{\odot}^\alpha|^{n-2} \rho_{\odot}^\alpha \mathbf{l}_r^\alpha \right) \cdot \mathbf{grad}_X(\dot{\gamma}^\alpha) \end{aligned} \quad (7.29)$$

L'écart à l'équilibre local de l'énergie libre peut être réécrit comme suit :

$$\left( \frac{\partial \Psi^e}{\partial \mathbf{E}^e} - \mathbf{S}^e \right) : \dot{\mathbf{E}}^e + \sum_{\alpha=1}^q \left[ X_0 l_{en}^n \left( -|\rho_{\vdash}^{\alpha}|^{n-2} \rho_{\vdash}^{\alpha} \mathbf{s}_r^{\alpha} + |\rho_{\odot}^{\alpha}|^{n-2} \rho_{\odot}^{\alpha} \mathbf{l}_r^{\alpha} \right) - \boldsymbol{\xi}^{\alpha} \right] \cdot \mathbf{grad}_X(\dot{\gamma}^{\alpha}) - \sum_{\alpha=1}^q \pi^{\alpha} \dot{\gamma}^{\alpha} \leq 0$$

Dans ce qui suit, on suppose que le  $\mathbf{S}^e$  est entièrement énergétique, que  $\pi^{\alpha}$  est entièrement dissipatif et que le est divisé en parties énergétique et dissipative :

$$\mathbf{S}^e = \frac{\partial \Psi^e}{\partial \mathbf{E}^e}, \quad \pi^{\alpha} = \pi_{dis}^{\alpha}, \quad \text{and} \quad \boldsymbol{\xi}^{\alpha} = \boldsymbol{\xi}_{en}^{\alpha} + \boldsymbol{\xi}_{dis}^{\alpha}$$

Les lois constitutives énergétiques peuvent alors être obtenues :

$$\begin{aligned} \mathbf{S}^e &= \mathbb{C} : \mathbf{E}^e \\ \boldsymbol{\xi}_{en}^{\alpha} &= X_0 l_{en}^n \left( -|\rho_{\vdash}^{\alpha}|^{n-2} \rho_{\vdash}^{\alpha} \mathbf{s}_r^{\alpha} + |\rho_{\odot}^{\alpha}|^{n-2} \rho_{\odot}^{\alpha} \mathbf{l}_r^{\alpha} \right) \end{aligned} \quad (7.30)$$

Il peut être vérifié à partir de (7.30)<sub>2</sub> que la contrainte microscopique énergétique  $\boldsymbol{\xi}_{en}^{\alpha}$  est tangente au  $\alpha^{ième}$  plan de glissement. Utilisant (7.30), l'inégalité de dissipation devient :

$$\sum_{\alpha=1}^q (\pi_{dis}^{\alpha} \dot{\gamma}^{\alpha} + \boldsymbol{\xi}_{dis}^{\alpha} \cdot \mathbf{grad}_X(\dot{\gamma}^{\alpha})) \geq 0 \quad (7.31)$$

$\boldsymbol{\xi}_{dis}^{\alpha}$  caractérise les forces microscopiques dissipatives associées à l'évolution des dislocations dans le  $\alpha^{ième}$  plan de glissement. Le mouvement de ces dislocations étant tangent à ce plan,  $\boldsymbol{\xi}_{dis}^{\alpha}$  doit également être tangentielle. Par conséquent, sans perte de généralité, le terme de gradient dans (7.31) peut être remplacé par le gradient tangentiel correspondant défini par :

$$\mathbf{grad}_X^{\alpha}(\dot{\gamma}^{\alpha}) = (\mathbf{I} - \bar{\mathbf{m}}_r^{\alpha} \otimes \bar{\mathbf{m}}_r^{\alpha}) \cdot \mathbf{grad}_X(\dot{\gamma}^{\alpha}), \quad \text{with} \quad \bar{\mathbf{m}}_r^{\alpha} = \frac{\mathbf{m}_r^{\alpha}}{|\mathbf{m}_r^{\alpha}|}$$

Cela donne :

$$\sum_{\alpha=1}^q (\pi_{dis}^{\alpha} \dot{\gamma}^{\alpha} + \boldsymbol{\xi}_{dis}^{\alpha} \cdot \mathbf{grad}_X^{\alpha}(\dot{\gamma}^{\alpha})) \geq 0 \quad (7.32)$$

Des mesures de déformation plastique effective non couplées sont utilisées pour décrire les effets dissipatifs de premier ordre et d'ordre supérieur. Ces mesures, qui sont appelées ci-après mesures de premier ordre et d'ordre supérieur, sont respectivement définies par :

$$\begin{aligned} \dot{e}_{\pi}^{\alpha} &= |\dot{\gamma}^{\alpha}|, \quad e_{\pi}^{\alpha} = \int \dot{e}_{\pi}^{\alpha} dt \\ \dot{e}_{\xi}^{\alpha} &= l_{dis} \|\mathbf{grad}_X^{\alpha}(\dot{\gamma}^{\alpha})\|, \quad e_{\xi}^{\alpha} = \int \dot{e}_{\xi}^{\alpha} dt \end{aligned}$$

où  $l_{dis}$  est l'échelle de longueur interne dissipative. Pour assurer une dissipation positive, les contraintes dissipatives scalaires et vectorielles associées au système de glissement  $\alpha$  sont prises comme suit :

$$\pi_{dis}^{\alpha} = S_{\pi}^{\alpha} \left( \frac{\dot{e}_{\pi}^{\alpha}}{\dot{\gamma}_0^{\alpha}} \right)^m \frac{\dot{\gamma}^{\alpha}}{\dot{e}_{\pi}^{\alpha}} \quad (7.33)$$

$$\xi_{dis}^{\alpha} = S_{\xi}^{\alpha} l_{dis}^2 \left( \frac{\dot{e}_{\xi}^{\alpha}}{\dot{\gamma}_0^{\alpha}} \right)^m \frac{\text{grad}_X^{\alpha}(\dot{\gamma}^{\alpha})}{\dot{e}_{\xi}^{\alpha}} \quad (7.34)$$

où  $\dot{\gamma}_0^{\alpha} > 0$  est une vitesse de déformation constante représentative des flux d'intérêt,  $m > 0$  est une constante caractérisant la sensibilité à la vitesse du matériau considéré, et  $S_i^{\alpha}$  ( $i \in \{\pi, \xi\}$ ) sont des variables d'état internes ayant la dimension d'une contrainte ( $S_{\pi}^{\alpha} > 0$  and  $S_{\xi}^{\alpha} \geq 0$ ). Ces variables sont appelées ci-après résistances au glissement dissipatif.

## Résultats

La Fig. 7.10 compare les résultats obtenus en utilisant le présent modèle en grandes déformations avec ceux obtenus en utilisant le modèle en petites déformations, pour différents paramètres énergétiques et dissipatifs. Les courbes en trait plein correspondent aux résultats en grandes déformations et celles avec des marqueurs correspondent à ceux en petites déformations. À des fins de comparaison, les résultats obtenus en utilisant la plasticité cristalline conventionnelle en petites déformations et en grandes déformations sans durcissement ( $H_{\pi} = 0$ ) sont également présentés dans la Fig. 7.10 (courbes nommées "Perfect CP"). On peut voir que les réponses contrainte-déformation obtenues en utilisant la formulation en grandes déformations montrent un très bon accord avec celles obtenues en utilisant la formulation en petites déformations. Notez que les courbes de contrainte-déformation obtenues en utilisant  $n = 1.7$  présentent des points d'inflexion, reflétant l'écrouissage cinématique non linéaire de type III (KIII) d'[Asaro \(1975\)](#). D'autres discussions sur ce type de durcissement peuvent être trouvées dans [Wulffinghoff et al. \(2015\)](#), [El-Naaman et al. \(2019\)](#) et [Jebahi et al. \(2020\)](#). En appliquant un faible chargement de cisaillement, les effets géométriques non linéaires sont insignifiants. Dans ce cas, les formulations en petites déformations et en grandes déformations doivent conduire à des résultats similaires, ce qui est le cas selon la Fig. 7.10. Ceci valide les capacités du modèle en grandes déformations implémenté à reproduire correctement les effets énergétiques et dissipatifs, au moins dans la gamme de chargement de cisaillement prescrite.

Afin d'examiner l'efficacité de l'implémentation du présent modèle en ce qui concerne les effets géométriques non linéaires, l'exemple de cisaillement simple de [Kuroda and Tvergaard \(2008a\)](#) qui implique une charge de cisaillement importante est reproduit dans ce travail. Dans cet exemple, le même échantillon géométrique que dans la Fig. 4.3 est utilisé, avec un chargement de cisaillement imposé  $\Gamma = 0.24$ . L'indice d'énergie de défauts et l'échelle de longueur dissipative sont fixés à  $n = 2$  et  $l_{dis} = 0$ , respectivement. Avec ces choix, le présent modèle en grandes déformations est équivalent à celui de [Kuroda and Tvergaard \(2008a\)](#), dans lequel seule la contrainte de retour énergétique est considérée. La Fig. 7.11 compare les résultats du présent modèle avec ceux obtenus par [Kuroda and Tvergaard \(2008a\)](#) pour deux valeurs de l'échelle de longueur énergétique  $l_{en}$ . Un très bon accord entre les résultats est obtenu, quelle que soit la valeur de  $l_{en}$ . Cela montre la capacité de l'implémentation du modèle actuel à reproduire correctement les effets de grandes déformations. Comme on peut le voir sur la Fig. 7.11a, dans la gamme des petites déformations de cisaillement, jusqu'à approximativement  $\Gamma = 0.025$ , les effets géométriques non linéaires sont insignifiants et la contrainte de cisaillement  $\sigma_{12}$  augmente presque linéairement avec  $\Gamma$  après déformation. Au-delà d'environ  $\Gamma = 0.025$ , la dépendance non linéaire entre la contrainte et la déformation prend place

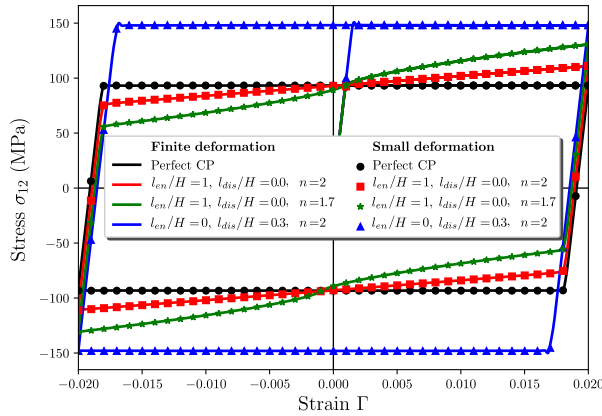


**Fig. 7.10.** Résultats des charges de petit cisaillement pour différents paramètres énergétiques et dissipatifs : comparaison entre le modèle de petite déformation et le modèle de déformation finie.

et devient plus remarquable à des déformations plus importantes, en raison des effets géométriques non linéaires. La Fig. 7.11 présente les distributions des variables plastiques totales  $\gamma^\alpha$  associées aux systèmes de glissement considérés le long de la direction  $x_2$ , telles qu’elles ont été obtenues en utilisant le présent modèle et celui de Kuroda and Tvergaard (2008a). Comme on le voit, les effets géométriques non linéaires entraînent une évolution asymétrique de ces variables, malgré la symétrie initiale des systèmes de glissement par rapport à la direction de chargement. Une déviation claire entre les profils  $\gamma^1$  et  $\gamma^2$ , qui coïncident avec ceux obtenus par Kuroda and Tvergaard (2008a), est observée. Une telle déviation a également été rapportée par Bittencourt (2018) en utilisant un problème similaire de cisaillement simple sous un chargement monotone de grand cisaillement. Il peut être expliqué par une augmentation apparente du durcissement dans un système et une diminution apparente du durcissement dans l’autre système en raison des effets de rotation du réseau (Kuroda and Tvergaard, 2008a; Bittencourt, 2018).

## Conclusions

Un objectif important, qui sera abordé dans les chapitres suivants de la thèse, est d’étudier les capacités et les limites de la plasticité cristalline à gradient de déformation (SGCP) pour modéliser les phénomènes de localisation de déformation dans les monocristaux. A cette fin, un modèle SGCP en grandes déformations de type Gurtin a été proposé en étendant la version SGCP en petites déformations basée sur l’énergie de défauts généralisée et la dissipation non couplée. Ce modèle a été formulé dans la configuration de référence, en supposant que les taux de glissement plastique individuels sur les systèmes de glissement sont des variables indépendantes. Une version bidimensionnelle simplifiée de ce modèle a été mise en œuvre dans le code commercial d’éléments finis Abaqus/Standard par le biais d’un sous-programme UEL (User-ELement). Pour valider l’implémentation du modèle, celui-ci a été appliqué pour simuler un problème de cisaillement simple d’une couche contrainte dans des conditions de déformation plane. La couche considérée a d’abord été soumise à une petit chargement de cisaillement, permettant une comparaison avec la version du modèle en petites déformations. Cette comparaison avait pour but

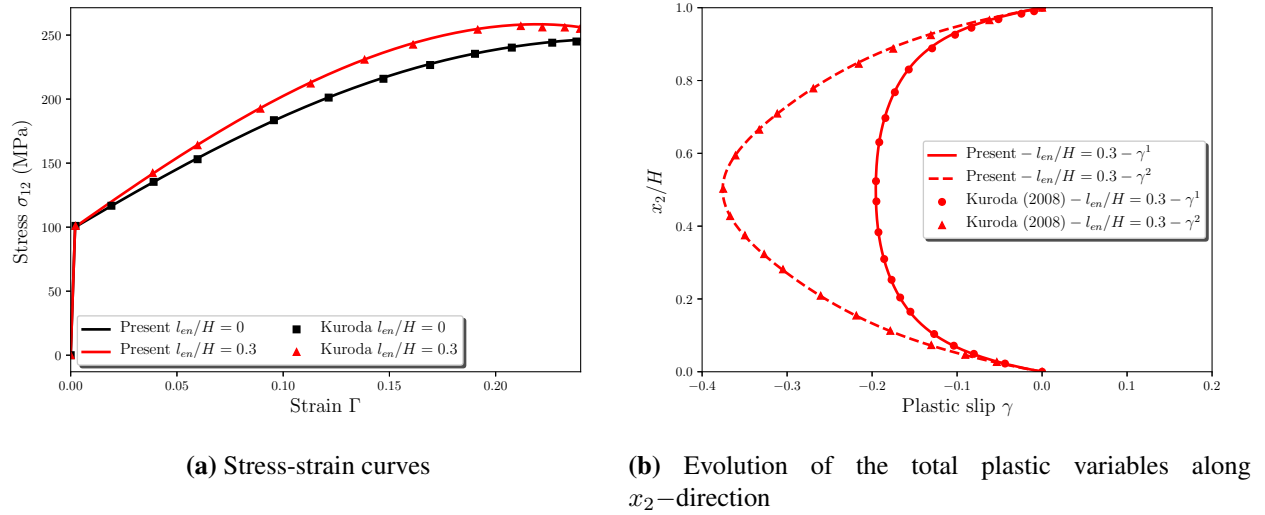


**Fig. 7.11.** Résultats des charges de grand cisaillement : comparaison entre le présent modèle et le modèle de [Kuroda and Tvergaard \(2008a\)](#) pour différentes valeurs de  $l_{en}/H$ .

d'évaluer l'efficacité du modèle à reproduire différents effets de taille énergétiques et dissipatifs, pour lesquels les résultats de grandes déformations ne sont pas disponibles dans la littérature. Un chargement de cisaillement important est ensuite appliqué pour un cas particulier d'énergie de défauts quadratique ( $n = 2$ ) sans dissipation d'ordre supérieur ( $l_{dis} = 0$ ). Pour ce cas, le modèle proposé est équivalent au modèle de ([Kuroda and Tvergaard, 2008a](#)), pour lequel des résultats en grandes déformations sont disponibles. Ces résultats ont été utilisés pour évaluer la capacité du modèle proposé à prédire correctement les effets des grandes déformations. Pour les deux cas de chargement, les résultats obtenus avec le modèle proposé sont en très bon accord avec ceux de référence.



# Développement d'un modèle de joints de grains en grandes déformations

## Introduction

Le modèle SGCP en grandes déformations permet de capturer les effets de taille de premier et de second ordre dans les monocristaux. L'application de ce modèle pour prédire les effets de taille dans les structures polycristallines n'est possible que dans les cas limites de conditions de joints de grains (GB) micro-libre (totalement transparents) et micro-dur (totalement opaques). Cependant, ces cas limites sont beaucoup trop simplifiés pour reproduire avec précision les contributions des GB au comportement global des structures polycristallines. En effet, les interactions des dislocations à travers les joints de grains (GBs) peuvent avoir des formes beaucoup plus complexes, incluant les empilements de dislocations, l'absorption, la transmission et la réflexion, etc. ([Bayerschen et al., 2016](#)). Avec la diminution de la taille, les proportions des GB deviennent plus importantes et leurs contributions au comportement global du matériau doivent être traitées avec précision. Cette préoccupation a motivé le travail du présent chapitre qui vise à mettre en lumière la modélisation des comportements des GB dans un contexte de grandes déformations.

Plusieurs travaux relatifs aux GB ont été réalisés et divers modèles de GB ont été développés dans la littérature ([Cermelli and Gurtin, 2002](#); [Gudmundson, 2004](#); [Aifantis and Willis, 2005](#); [Aifantis et al., 2006](#); [Fredriksson and Gudmundson, 2007](#); [Wulfinghoff et al., 2013](#); [Bayerschen et al., 2015](#); [Wulfinghoff, 2017](#)). Les premiers modèles de GB ont été formulés dans le cadre de petites déformations basées sur des lois constitutives phénoménologiques simplifiées ignorant les orientations cristallographiques aux interfaces entre les grains. Ces modèles ont été appliqués avec succès pour reproduire certains phénomènes de GB importants, par exemple le durcissement dû aux GB. Une extension de ces modèles pour prendre en compte les caractéristiques cristallographiques peut être trouvée dans l'article emblématique de [Gurtin \(2008b\)](#) où désorientation des grains et l'orientation des joints de grains sont considérés. Cet article a montré l'importance de la prise en compte de ces caractéristiques et a motivé les travaux ultérieurs sur le sujet. [van Beers et al. \(2013\)](#) ont proposé un modèle de GB dans le cadre de l'approche SGCP en petites déformations d'[Evers et al. \(2004a\)](#) basé sur les vecteurs de glissement normaux de l'interface pour mesurer le désajustement de GB. Il a été démontré par la suite que cette manière de décrire le désajustement de GB est équivalente à celle proposée par [Gurtin \(2008b\)](#) dans le cadre de restrictions planaires. En se basant sur le cadre de la plasticité d'ordre supérieur (SGP), [Voyiadjis et al. \(2014\)](#) ont proposé une approche de GB généralisée en petites déformations qui tient compte du stockage d'énergie au niveau du GB dû à l'empilement des dislocations et de la dissipation d'énergie causée par le transfert des dislocations à travers le joint de grain.

Dans le cadre des grandes déformations, de nombreux modèles de GB ont été développés (Wulffinghoff et al., 2013; Bayerschen et al., 2015; McBride et al., 2016; Alipour et al., 2019; Peng et al., 2019; Alipour et al., 2020). Cependant, seuls quelques-uns incluent une description cristallographique qui est nécessaire pour prédire avec précision les contributions des GB aux petites échelles. McBride et al. (2016) ont proposé une extension aux grandes déformations du modèle de Gurtin (2008b) utilisant le tenseur de taux de distorsion plastique  $L^p$  pour décrire le décalage entre les grains adjacents. Ce modèle a été formulé en utilisant la description eulérienne qui n'est pas largement utilisée dans le contexte des continus à gradient de déformation. Peng et al. (2019) ont développé un modèle de GB en grandes déformations utilisant le même tenseur  $L^p$  pour décrire le mismatch de GB. Le modèle a été formulé dans la configuration lagrangienne en utilisant une hypothèse simplificatrice selon laquelle le réseau non déformé réside dans l'espace (matériel) de référence et non dans l'espace structurel. Cependant, cette hypothèse n'est pas pertinente d'un point de vue physique, comme l'indiquent Gurtin et al. (2010). En effet, un flux de dislocations implique un flux de matière par rapport au réseau non déformé (les vecteurs du réseau ne peuvent pas être matériels). Bien que la description lagrangienne soit largement utilisée dans le contexte de la plasticité à gradient de déformation, il existe dans la littérature très peu de variantes de modèles de GB en grandes déformations basés sur cette description avec des considérations cristallographiques. Le modèle proposé par Alipour et al. (2020) est l'un des rares modèles pouvant être cité dans ce contexte. Cependant, ce modèle ne peut prendre en compte que la désorientation entre les grains en ignorant les effets dus à l'orientation des joints de grains. Inspiré par le travail de Gurtin (2008b), le présent chapitre vise à développer un modèle de GB en grandes déformations qui prend en compte les effets cristallographiques dus à la fois aux orientations des grains et des joints de grains dans un cadre entièrement lagrangien.

## Formulation théorique

La présente section détaille une nouvelle formulation d'un modèle de GB en grandes déformations proposé dans un cadre entièrement lagrangien. Ce modèle sera utilisé pour décrire l'interaction entre les grains en considérant les orientations cristallographiques aux joints de grains. Le comportement à l'intérieur de chaque grain est décrit en utilisant le modèle SGCP développé dans le cadre des grandes déformations.

Considérons un domaine composé de deux grains A et B séparés par un joint de grain  $\mathcal{G}$  (Fig. 7.12). Dans la configuration de référence, le vecteur normal unitaire de la surface externe est noté  $\mathbf{n}_{t_r}$ . De plus, les vecteurs normaux unitaires extérieurs associés aux grains A et B au joint des grains  $\mathcal{G}$  sont respectivement désignés par  $\mathbf{n}_{A_r}$  et  $\mathbf{n}_{B_r}$ . Soit  $\mathbf{n}_{GB_r}$  le vecteur normal unitaire au joint de grain  $\mathcal{G}$  dirigé vers l'extérieur du grain A :

$$\mathbf{n}_{GB_r} = \mathbf{n}_{A_r} = -\mathbf{n}_{B_r} \quad (7.35)$$

Étant donné un champ arbitraire  $\phi$  dans le domaine considéré, ce champ est supposé être régulier dans chaque grain et continu jusqu'à la limite du grain  $\mathcal{G}$  depuis l'un ou l'autre grain. Le saut de  $\phi$  à travers  $\mathcal{G}$  est donné par :

$$\mathbb{G} = [\phi] = \phi_B - \phi_A \quad (7.36)$$

Le choix du champ  $\phi$  pour contrôler l'interaction entre les grains représente la principale différence entre les modèles de GB existants.

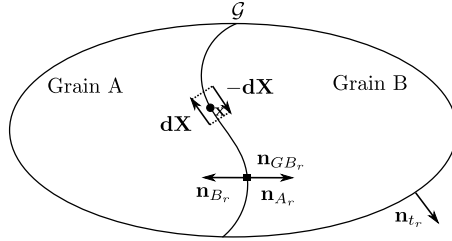


**Fig. 7.12.** Un domaine constitué de deux grains A et B séparés par un joint de grain  $\mathcal{G}$  dans la configuration de référence.

En suivant une approche similaire à celle de [Gurtin et al. \(2010\)](#), une contrepartie en grandes déformations de (5.3) est développée ci-après dans un cadre entièrement lagrangien. Dans la présente formulation de GB, le réseau est supposé être défini dans la configuration structurelle telle que largement reconnue dans la littérature. Considérons un point arbitraire  $\mathbf{X}$  sur le joint de grain  $\mathcal{G}$  et un vecteur ligne arbitraire  $d\mathbf{X}$  en ce point tangent à  $\mathcal{G}$ . Soit  $d\Gamma$  un circuit infinitésimal constitué de  $d\mathbf{X}$  dans le grain A et  $-d\mathbf{X}$  dans le grain B (Fig. 7.12). Le vecteur de burgers associé à  $d\Gamma$  peut être défini en grandes déformations comme ([Cermelli and Gurtin, 2001](#)) :

$$\mathbf{b}_r(d\Gamma) = \int_{d\Gamma} \mathbf{F}^p d\mathbf{X} = \int_{dS_\Gamma} \text{Curl}(\mathbf{F}^p)^T \mathbf{n}_r d\mathbf{X} \quad (7.37)$$

où  $dS_\Gamma$  est un élément de surface délimité par  $d\Gamma$ . Notez que  $\text{Curl}(\mathbf{F}^p)^T = \mathbf{0}$  pour toute déformation plastique compatible (c'est-à-dire le gradient d'un champ vectoriel). Ce tenseur fournit une mesure de l'incompatibilité de la déformation plastique. Avec le circuit infinitésimal considéré, la relation suivante peut être obtenue :

$$\int_{d\Gamma} \mathbf{F}^p d\mathbf{X} = -[\mathbf{F}_B^p - \mathbf{F}_A^p] \cdot d\mathbf{X} = -[\llbracket \mathbf{F}^p \rrbracket] \cdot d\mathbf{X} \quad (7.38)$$

Puisque le vecteur  $d\mathbf{X}$  est tangent à  $\mathcal{G}$ , il peut être remplacé par sa projection sur  $\mathcal{G}$  sans perte de généralité :

$$-\llbracket \mathbf{F}^p \rrbracket d\mathbf{X} = -\llbracket \mathbf{F}^p \rrbracket (\mathbf{I} - \mathbf{n}_{GB_r} \otimes \mathbf{n}_{GB_r}) d\mathbf{X} \quad (7.39)$$

L'équation ci-dessus peut encore être reformulée en utilisant la relation d'identité suivante :

$$\mathbf{I} - \mathbf{n}_{GB_r} \otimes \mathbf{n}_{GB_r} = -(\mathbf{n}_{GB_r} \times)(\mathbf{n}_{GB_r} \times) \quad (7.40)$$

ce qui donne :

$$-\llbracket \mathbf{F}^p \rrbracket d\mathbf{X} = \llbracket \mathbf{F}^p \rrbracket (\mathbf{n}_{GB_r} \times)(\mathbf{n}_{GB_r} \times) d\mathbf{X} = (\llbracket \mathbf{F}^p \rrbracket (\mathbf{n}_{GB_r} \times)) (\mathbf{n}_{GB_r} \times d\mathbf{X}) \quad (7.41)$$

Notez que  $-\mathbf{n}_{GB_r} \times d\mathbf{X}$  représente un élément de surface dirigé orthogonalement à  $dS_\Gamma$  (élément de surface délimité par  $d\Gamma$ ) et tangent au joint de grain. Le signe moins est ajouté pour obtenir une direction normale à droite par rapport à l'orientation de  $d\Gamma$  (Fig. 7.12). Le tenseur défini par :

$$\mathbb{G} = \llbracket \mathbf{F}^p \rrbracket (\mathbf{n}_{GB_r} \times) \quad (7.42)$$

peut être considéré comme une généralisation de (5.3) en grandes déformations. Ce tenseur sera appelé ci-après tenseur de Burgers du GB. Sa forme en taux qui est définie par :

$$\dot{\mathbb{G}} = \llbracket \dot{\mathbf{F}}^p \rrbracket (\mathbf{n}_{GBr} \times) \quad (7.43)$$

peut être interprétée comme le flux du vecteur de Burgers sortant du joint de grain  $\mathcal{G}$  à partir des grains ou également comme la production du vecteur de Burgers à l'intérieur du joint de grain.  $\dot{\mathbb{G}}$  fournit une mesure de type taux de l'inadéquation cinématique et géométrique au niveau du joint de grain en grandes déformations et sera utilisé dans la suite pour développer un modèle de GB en grandes déformations basé sur la description lagrangienne. Comme dans [Gurtin \(2008b\)](#), ce modèle est basé sur l'hypothèse qu'aucun saut de déplacement ne se produit aux joints de grains, c'est-à-dire qu'il n'y a pas de glissement ou d'ouverture des joints de grains. Pour les modèles de GB impliquant le glissement de GB couplé au cadre de plasticité à gradient de déformation, le lecteur peut se référer aux travaux de [Cermelli and Gurtin \(2002\)](#) et [Gurtin and Anand \(2008\)](#).

La présente sous-section se concentre sur la formulation des lois constitutives au niveau du joint de grain. L'énergie libre provenant du GB est supposée être une fonction quadratique du tenseur de Burgers donnée par (7.42) :

$$\Psi_{GB} = \Psi_{GB}(\mathbb{G}) = \frac{1}{2} \kappa \|\mathbb{G}\|^2 \quad (7.44)$$

où  $\kappa > 0$  est une constante matériau pour le joint de grain. Sous la forme de taux, cette énergie peut s'écrire :

$$\dot{\Psi}_{GB} = \frac{\partial \Psi_{GB}}{\partial \mathbb{G}} : \dot{\mathbb{G}} \quad (7.45)$$

En substituant (7.45) dans (5.24), le déséquilibre local d'énergie libre du GB devient :

$$\left( \mathbb{K} - \frac{\partial \Psi_{GB}}{\partial \mathbb{G}} \right) : \dot{\mathbb{G}} \geq 0 \quad (7.46)$$

Afin de modéliser les effets énergétiques et dissipatifs au niveau des GB, on suppose que  $\mathbb{K}$  est divisé en parties énergétique et dissipative ( $\mathbb{K} = \mathbb{K}_{en} + \mathbb{K}_{dis}$ ).  $\mathbb{K}_{en}$  peut être obtenu comme suit :

$$\mathbb{K}_{en} = \frac{\partial \Psi_{GB}}{\partial \mathbb{G}} = \kappa \mathbb{G} \quad (7.47)$$

ce qui conduit à l'inégalité de dissipation du GB réduite suivante :

$$\mathcal{D} = \mathbb{K}_{dis} : \dot{\mathbb{G}} \geq 0 \quad (7.48)$$

Pour modéliser la force de GB dissipative, on introduit une défectuosité du GB cumulée définie par  $\dot{\Delta} = \|\dot{\mathbb{G}}\|$ , représentant l'imperméabilité des GB au flux du vecteur de Burgers. Inspiré par ([Gurtin and Needleman, 2005](#); [Gurtin, 2008b](#)), la force dissipative des GB est supposée être décrite comme suit :

$$\mathbb{K}_{dis} = S_{GB} \left\| \frac{\dot{\mathbb{G}}}{\dot{\mathbb{G}}_0} \right\|^d \frac{\dot{\mathbb{G}}}{\|\dot{\mathbb{G}}\|} \quad (7.49)$$

où  $S_{GB} > 0$  représente une fonction dissipative de durcissement au niveau des GB,  $d > 0$  un paramètre de sensibilité pour les GB, et  $\dot{\mathbb{G}}_0 > 0$  est une vitesse de référence scalaire du tenseur de Burgers au niveau des GB. Pour modéliser le durcissement des GB, on suppose que  $S_{GB}$  évolue selon la formule suivante :

$$\dot{S}_{GB} = H_{GB} \left\| \dot{\mathbb{G}} \right\| \quad \text{with} \quad S_{GB}(0) = S_{GB_0} \geq 0 \quad (7.50)$$

avec  $H_{GB}$  module de durcissement des GB et  $S_{GB_0}$  la résistance initiale à la défectuosité du joint de grain.

L'équation de base impliquée dans la théorie proposée, considérant à la fois les grains massifs et les joints de grains, peut être résumée comme suit :

- équations cinématiques :

$$\mathbf{F} = \mathbf{F}^e \mathbf{F}^p, \quad \mathbf{L}^p = \sum_{\alpha} \dot{\gamma}^{\alpha} \mathbb{S}^{\alpha}$$

$$\mathbb{G} = [\![\mathbf{F}^p]\!] (\mathbf{n}_{GB_r} \times)$$

- les équations d'équilibre macroscopiques avec les conditions aux limites macroscopiques :

$$\begin{aligned} \operatorname{div}_X(\mathbf{P}) &= \mathbf{0} && \text{in } V_0 \\ \mathbf{P} \mathbf{n}_{t_r} &= \mathbf{t} && \text{on } S_0 \end{aligned} \quad (7.51)$$

- les équations d'équilibre microscopiques ainsi que les conditions aux limites et d'interface microscopiques :

$$\begin{aligned} \operatorname{div}_X(\boldsymbol{\xi}^{\alpha}) + \tau^{\alpha} - \pi^{\alpha} &= 0 && \text{in } V_0 \\ \boldsymbol{\xi}^{\alpha} \cdot \mathbf{n}_{t_r} &= \chi^{\alpha} && \text{on } S_0 \\ \boldsymbol{\xi}_B^{\alpha} \cdot \mathbf{n}_{GB_r} &= \mathbb{K} : [\mathbb{S}_B^{\alpha} \mathbf{F}_B^p (\mathbf{n}_{GB_r} \times)] && \text{on } S_{GB} \\ \boldsymbol{\xi}_A^{\alpha} \cdot \mathbf{n}_{GB_r} &= \mathbb{K} : [\mathbb{S}_A^{\alpha} \mathbf{F}_A^p (\mathbf{n}_{GB_r} \times)] && \text{on } S_{GB} \end{aligned}$$

- équations constitutives dans les grains massifs :

$$\begin{aligned} \mathbf{S}^e &= \mathbb{C} : \mathbf{E}^e \\ \pi_{dis}^{\alpha} &= S_{\pi}^{\alpha} \left( \frac{\dot{e}_{\pi}^{\alpha}}{\dot{\gamma}_0^{\alpha}} \right)^m \frac{\dot{\gamma}^{\alpha}}{\dot{e}^{\alpha}} \\ \boldsymbol{\xi}_{en}^{\alpha} &= X_0 l_{en}^n \left( -|\rho_{\perp}^{\alpha}|^{n-2} \rho_{\perp}^{\alpha} \mathbf{s}_r^{\alpha} + |\rho_{\odot}^{\alpha}|^{n-2} \rho_{\odot}^{\alpha} \mathbf{l}_r^{\alpha} \right) \\ \boldsymbol{\xi}_{dis}^{\alpha} &= S_{\xi}^{\alpha} l_{dis}^2 \left( \frac{\dot{e}_{\xi}^{\alpha}}{\dot{\gamma}_0^{\alpha}} \right)^m \frac{\underline{\operatorname{grad}}_X^{\alpha}(\dot{\gamma}^{\alpha})}{\dot{e}^{\alpha}} \end{aligned}$$

- équations constitutives au niveau du GB :

$$\mathbb{K}_{en} = \kappa \mathbb{G}$$

$$\mathbb{K}_{dis} = S_{GB} \left\| \frac{\dot{\mathbb{G}}}{\dot{\mathbb{G}}_0} \right\|^d \frac{\dot{\mathbb{G}}}{\left\| \dot{\mathbb{G}} \right\|}, \quad \dot{S}_{GB} = H_{GB} \left\| \dot{\mathbb{G}} \right\|$$

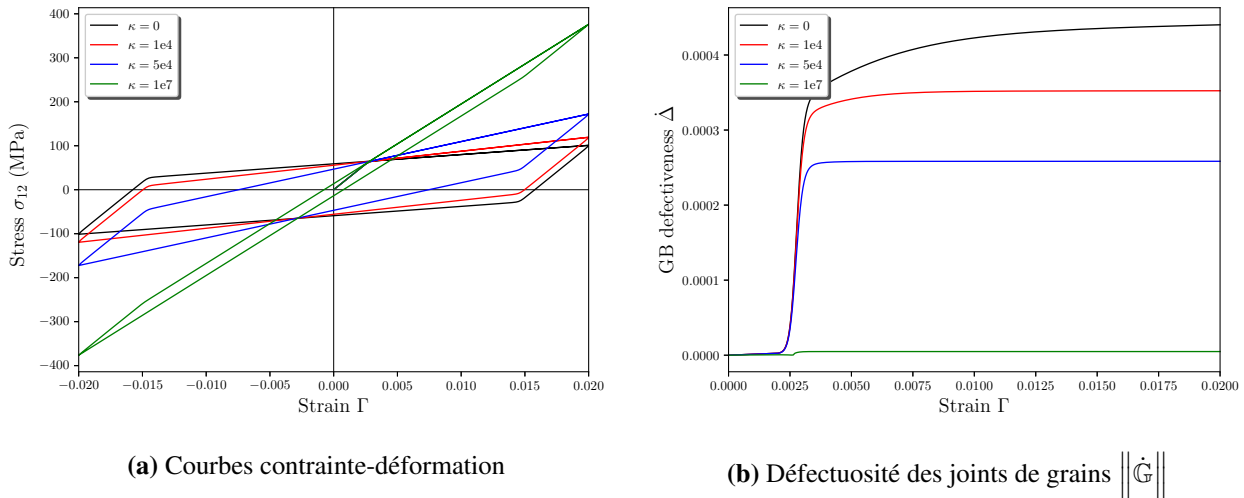


**Fig. 7.13.** Influence du seul paramètre énergétique GB  $\kappa$  sous chargement cyclique ( $l_{en}/W = 10$ ,  $S_{GB_0} = 0$ ,  $H_{GB} = 0$ ).

## Résultats numériques

L'influence des paramètres des GB énergétiques et dissipatifs est illustrée pour un chargement de cisaillement cyclique dans les Figs. 7.13 et 7.14, respectivement. Comme le montre la Fig. 7.13a, le coefficient énergétique du GB  $\kappa$  entraîne un écrouissage cinématique et n'influence que la pente de l'écrouissage après déformation. Quelle que soit la valeur de  $\kappa$ , aucun effet sur la limite d'écoulement initiale n'est observé. Cependant, une plus grande valeur de  $\kappa$  conduit à une pente d'écrouissage cinématique plus raide. L'analyse des courbes  $\|\dot{G}\|$  ne montre aucune influence de  $\kappa$  sur l'activation du GB (Fig. 7.13b). Après l'activation des GB,  $\|\dot{G}\|$  présente une évolution en forme de plateau pour laquelle la valeur maximale diminue avec l'augmentation de  $\kappa$ . Le cas de  $\kappa = 1e7$  N/mm représente des GB presque micro-durs avec une défectuosité des GB insignifiante ( $\|\dot{G}\| \approx 0$ ).

La Fig. 7.14 montre les influences des effets dissipatifs du GB  $S_{GB}$  sans le coefficient de durcissement  $H_{GB}$  sous chargement de cisaillement cyclique. Les courbes contrainte-déformation de la Fig. 7.14a montrent un écrouissage isotrope évident. Une plus grande résistance initiale des GB  $S_{GB_0}$  retardé l'activation des interactions entre dislocations à travers les GB, conduisant à un durcissement renforcé. Cette activation retardée peut également être trouvée dans l'évolution de la défectuosité des GB de la Fig. 7.14b. Après l'activation des GB, la défectuosité de la Fig. 7.14b a atteint un niveau identique. Il s'agit d'une caractéristique intéressante par rapport aux effets de l'activation de GB qui modifie uniquement les flux de dislocation à travers les GB. Des effets de joints de grains énergétiques et dissipatifs similaires peuvent également être trouvés dans van Beers et al. (2013) et Peng et al. (2019).

Une plaque carrée polycristalline composée de grains distribués de façon aléatoire est représentée sur la Fig. 7.15. Dans chaque grain, on considère deux systèmes de glissement avec un angle  $\theta = 60^\circ$  entre eux.

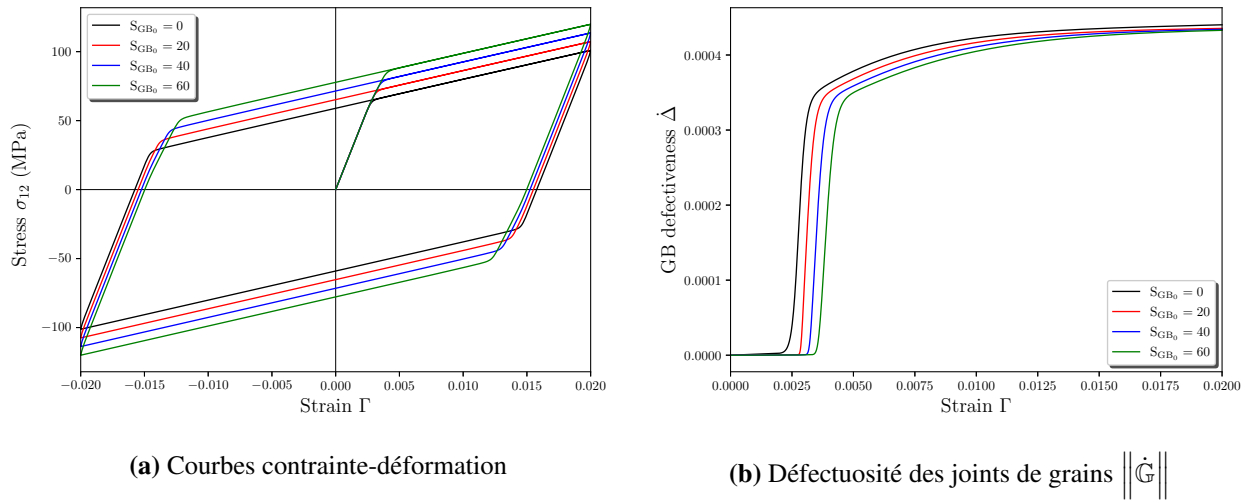


**Fig. 7.14.** Influence du seul paramètre dissipatif  $S_{GB_0}$  sous chargement cyclique ( $l_{en}/W = 10, \kappa = 0, H_{GB} = 0$ ).

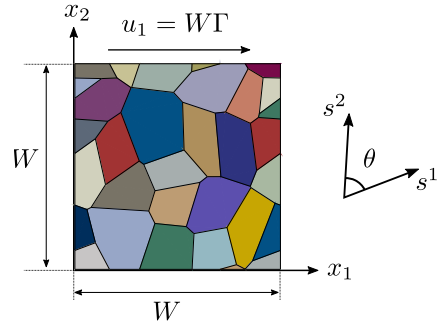


**Fig. 7.15.** Une plaque carrée polycristalline dont les grains sont répartis de manière aléatoire et qui présente deux systèmes de glissement dans chaque grain.

La Fig. 7.16a présente les réponses contrainte-déformation pour différentes tailles géométriques  $W$  sous chargement cyclique proportionnel et non proportionnel. Des effets de taille évidents peuvent être observés pour une taille de géométrie  $W$  plus petite en termes de limite d'écoulement initial et de pente d'écrouissage. La Fig. 7.16b montre la limite d'écoulement initial en fonction de l'inverse de la taille de la géométrie  $W$ . Une relation linéaire entre la limite d'écoulement initial et l'inverse de la taille de la géométrie  $1/W$  a été trouvée. Il est intéressant de noter qu'en appliquant une passivation sur les bords supérieur et inférieur, seule une augmentation du durcissement est détectée, sans apparition de "sauts élastiques". Il est utile de rappeler qu'en utilisant presque toutes les approches SGCP existantes, incluant la dissipation d'ordre supérieur thermodynamiquement cohérente dans un monocristal, l'étape de passivation est accompagnée de la formation d'un saut élastique. Ce résultat pourrait être intéressant d'un point de vue physique car il peut renforcer l'hypothèse que les sauts élastiques ne sont pas physiques, ce qui fait l'objet d'une discussion approfondie au sein de la communauté de la plasticité à gradient de déformation.

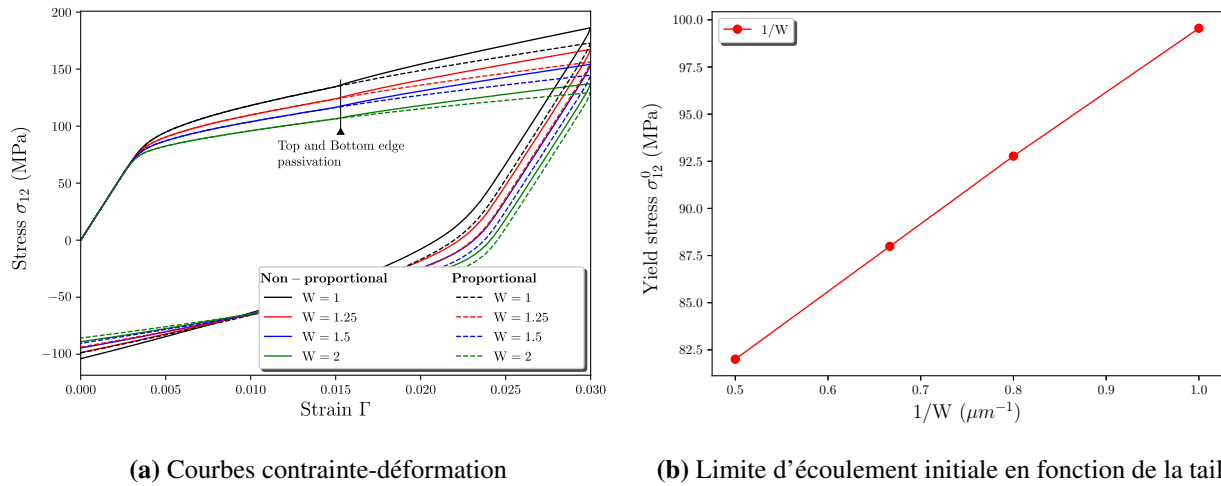


**Fig. 7.16.** Réponses contrainte-déformation d'une plaque polycristalline sous chargement cyclique non proportionnel et proportionnel avec des paramètres constitutifs GB dissipatifs pour différentes tailles géométriques ( $l_{en} = 10$ ,  $\kappa = 0$ ,  $S_{GB} = 5$ ,  $H_{GB} = 0$ ).

## Conclusions

La nouveauté de ce travail réside dans le développement d'un modèle de joints de grains de type Gurin (Gurtin, 2008b) dans un cadre de grandes déformations. Ce modèle propose un tenseur de Burgers de joint de grain décrit à l'aide de la distorsion plastique  $\mathbf{F}^p$  dans un cadre de grandes déformations, qui peut être considéré comme la contrepartie du tenseur de Burgers en petites déformations proposé par (Gurtin, 2008b) avec la distorsion plastique  $\mathbf{H}^p$  de la théorie des petites déformations. Sur la base du tenseur de Burgers du joint de grain en grandes déformations proposé, les forces microscopiques énergétiques et dissipatives du joint de grain sont formulées. Le tenseur de Burgers du joint de grain proposé est formulé dans la configuration de référence, ce qui facilite sa mise en œuvre numérique.

Le modèle de joint de grain proposé est mis en œuvre dans le logiciel commercial de calcul par éléments finis Abaqus/Standard par le biais d'un sous-programme UEL (User-Element) en introduisant un élément d'épaisseur nulle pour les GB. À des fins de comparaison, le modèle de joint de grain en petites déformations de [Gurtin \(2008b\)](#) est également mis en œuvre. De plus, le modèle SGCP-UEL en petites déformations du travail précédent des auteurs ([Jebahi et al., 2020](#)) est également utilisé pour comparaison. Les résultats d'un cas de cisaillement bi-cristallin périodique montrent que les courbes de contrainte-déformation sont presque identiques dans la plage des petites déformations tout en se différenciant dans la plage des grandes déformations, en raison des effets de rotation du réseau. En termes de défectuosité des joints de grains, les cadres des petites ou grandes déformations , que ce soit pour les grains massifs ou pour les GB, présentent des différences. Ce travail a mis en évidence pour la première fois les différences entre les modèles de joints de grains en petites et grandes déformations.

Le modèle de joint de grain en grandes déformations est ensuite évalué via le bi-cristal périodique sous chargement cyclique en termes des propriétés énergétiques et dissipatives du joint de grain, la désorientation du grain et l'orientation du joint de grain. Les résultats de l'évaluation sont

cohérents avec certains travaux existants tels que [van Beers et al. \(2013\)](#) et [Peng et al. \(2019\)](#) sur les réponses de contrainte-déformation. Cependant, certaines différences apparaissent concernant la défectuosité du joint de grain en raison de la formulation distincte du modèle proposé. Par un cas simple de cisaillement d'une plaque polycristalline sous chargement cyclique, les influences des propriétés dissipatives des joints de grains sont montrées. Le durcissement dissipatif des joints de grains conduit à une caractéristique d'écrouissage isotrope notable sous chargement cyclique.



# Application à la localisation de la déformation dans les tôles métalliques mono et polycristallines

## Introduction

Plusieurs travaux étudiant la localisation de la déformation dans des monocristaux subissant des glissements simples et multiples peuvent être trouvés dans la littérature (Rice, 1976; Asaro and Rice, 1977; Needleman and Tvergaard, 1992; Forest, 1998; Marano et al., 2019, 2021). En utilisant des systèmes de glissement multiples, il a été démontré que la localisation de la déformation peut se produire le long de bandes de cisaillement étroites, qui peuvent être orientées arbitrairement par rapport aux directions cristallographiques initiales (Rice, 1976; Needleman and Tvergaard, 1992; Kuroda, 2011). Dans le cas d'un système de glissement unique, deux types de bandes de cisaillement, connues sous le nom de bandes de glissement et de bandes de pliage, peuvent avoir lieu (Asaro and Rice, 1977).

En raison du manque d'échelle(s) de longueur interne(s), les théories conventionnelles de plasticité cristalline ne sont pas en mesure de capturer correctement les bandes de localisation. Comme alternative, Forest (1998) a appliqué une théorie de plasticité monocristalline de Cosserat en petites déformations pour étudier la formation de bandes de glissement et de pliage dans les monocristaux. Comme l'a montré l'auteur, cette théorie permet de régulariser les bandes de pliage qui auront une épaisseur finie. Cependant, elle ne régularise pas les bandes de glissement qui ne sont pas nécessairement associées à la courbure du réseau (Forest, 1998; Forest et al., 2001). Bien que peu étudiées dans la littérature, les théories SGCP, qui sont classiquement basées sur les densités GND, devraient également présenter des difficultés pour régulariser les bandes de glissement idéalisées. En effet, un gradient de glissement le long de la normale aux plans de glissement n'entraîne pas le stockage de GNDs. Récemment, Ling et al. (2018) ont proposé un modèle de plasticité cristalline micromorphe en grandes déformations qui est capable de régulariser à la fois les bandes de pliage et de glissement. L'application de ce modèle à la localisation de la déformation dans des monocristaux présentant un système de glissement a mis en évidence un comportement de localisation complexe avec une compétition entre les bandes de coude et de glissement. La capacité des théories SGCP à prédire un tel comportement complexe n'a pas encore été explorée.

Le présent chapitre a pour but de fournir une étude approfondie des capacités et des limites du modèle SGCP en grandes déformations proposé pour prédire différents types de modes de localisation dans les monocristaux. Une attention particulière sera accordée à la capacité d'un tel modèle à reproduire le comportement de localisation complexe rencontré en considérant un sys-

tème de glissement unique. L'influence des effets énergétiques et dissipatifs sur ce comportement sera également discutée. Dans un deuxième temps, la localisation des déformations dans des tôles métalliques polycristallines sera étudiée.

## Application à la localisation de la déformation dans les monocristaux

Avant d'appliquer le modèle SGCP implémenté pour étudier des phénomènes de localisation complexes, la présente partie vise à examiner sa capacité à capter différents types de bandes de localisation, incluant les bandes de glissement et de pliage idéalisées ainsi que les bandes de cisaillement générales (c'est-à-dire sans orientation particulière par rapport aux directions cristallographiques initiales).

### Cisaillement simple avec un seul système de glissement : régularisation des bandes de glissement/de pliage idéalisées

Dans le cas d'un glissement horizontal, la Fig. 7.17 présente les résultats associés en termes de courbes de contrainte-déformation et de distributions de la variable scalaire plastique  $\gamma$  le long de la direction  $x_2$  pour différents raffinements de maillage. Bien que ces résultats soient obtenus en considérant uniquement les effets énergétiques d'ordre supérieur ( $l_{en}/H = 0.1$  et  $l_{dis} = 0$ ), il a été vérifié que l'activation des effets dissipatifs d'ordre supérieur ( $l_{dis} \neq 0$ ) ne les affecte pas. Le modèle SGCP n'a pas permis de régulariser la bande de glissement idéalisée obtenue, qui présente une dépendance vis-à-vis du maillage. Comme on peut le voir sur la Fig. 7.17b, la largeur de la bande obtenue est déterminée par le raffinement du maillage et diminue avec l'augmentation du nombre d'éléments finis. Pour la configuration de glissement considérée, le présent modèle SGCP se comporte comme un modèle de plasticité cristalline classique. En effet, les gradients de glissement dans la direction normale au plan de glissement ne correspondent pas aux GNDs (Forest, 1998; Gurtin et al., 2007; Gurtin, 2008a). Par conséquent, aucun effet de taille n'est prévu par les théories SGCP basées sur les GND pour le développement de tels gradients de glissement normaux. C'est également le cas pour les théories de plasticité cristalline de Cosserat dans lesquelles les effets de taille sont uniquement déclenchés par la courbure du réseau (Forest, 1998).

La Fig. 7.18 présente les résultats de cisaillement associés au cas de glissement vertical en termes de réponses contrainte-déformation et de distributions de la variable scalaire plastique  $\gamma$  le long de la direction  $x_2$  pour différents raffinements de maillage. En utilisant un maillage suffisamment fin, la réponse contrainte-déformation devient presque indépendante du maillage (Fig. 7.18a). Notez que l'inversion de pente et la forme en plateau observées sur les courbes de contrainte-déformation au-delà de  $\Gamma = 0.008$  sont dues à la compétition entre l'adoucissement causé par un  $H_\pi$  négatif et le durcissement causé par des effets énergétiques d'ordre supérieur ( $l_{en} \neq 0$ ). Comme le montre la Fig. 7.18b, on obtient des bandes de plissement épaisses qui s'étendent sur plusieurs éléments finis. Pour un maillage relativement fin, l'épaisseur de ces bandes est presque insensible au maillage.

Comme pour les modèles de plasticité cristalline de (Forest, 1998), le modèle SGCP proposé permet de simuler, sans dépendance au maillage, des bandes de glissement qui impliquent des gradients de glissement dans la direction du glissement. En revanche, il ne parvient pas à régulariser

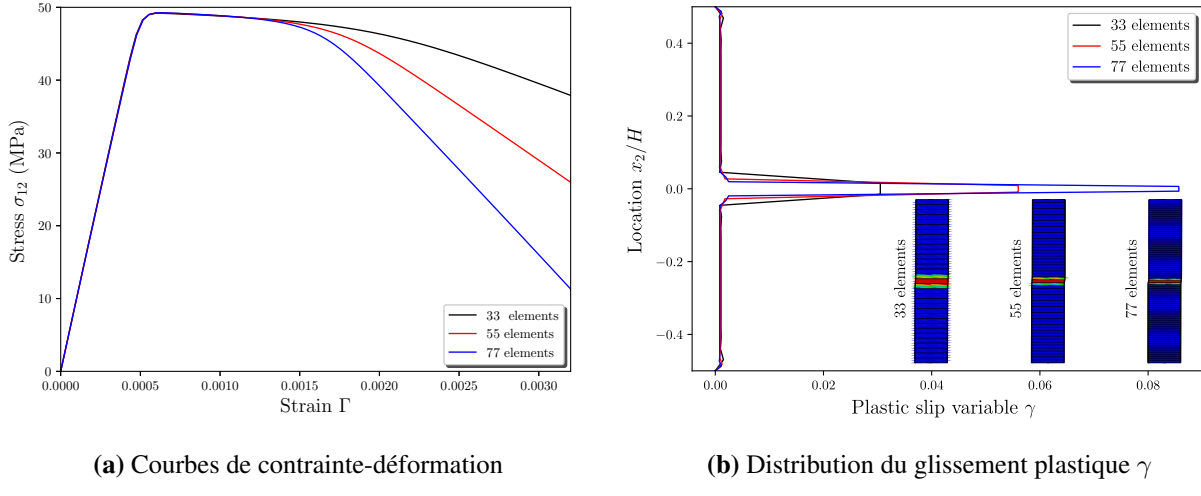


**Fig. 7.17.** Courbes de contrainte-déformation et distributions de la variable scalaire plastique  $\gamma$  le long de la direction  $x_2$  dans le cas d'un glissement horizontal à  $\Gamma = 0.0032$  pour différents raffinements de maillage ( $l_{en}/H = 0.1$ ,  $l_{dis} = 0$ ,  $H_\pi = -500$  MPa,  $n = 2$ ).

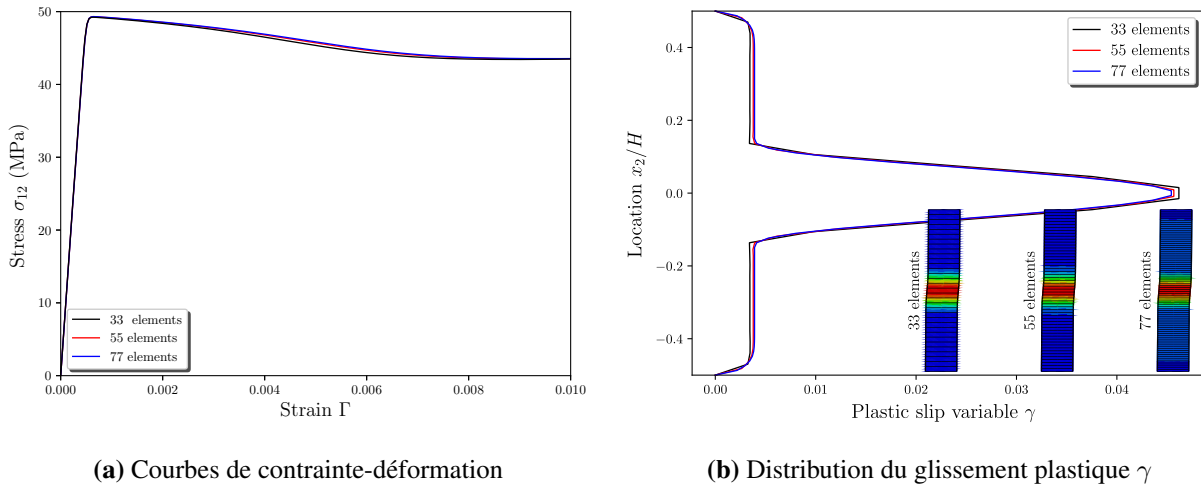


**Fig. 7.18.** Courbes de contrainte-déformation et distributions de la variable scalaire plastique  $\gamma$  le long de la direction  $x_2$  dans le cas d'un glissement vertical à  $\Gamma = 0.01$  pour différents raffinements de maillage ( $l_{en}/H = 0.1$ ,  $l_{dis} = 0$ ,  $H_\pi = -500$  MPa,  $n = 2$ ).

les bandes de glissement idéalisées qui ne sont pas accompagnées du développement de GNDs. Cependant, les conditions de glissement idéalisées utilisées pour obtenir ces dernières bandes ne sont pas couramment rencontrées dans la déformation réelle des matériaux. La sous-section suivante discute de la capacité du présent modèle SGCP à capturer correctement la localisation des déformations dans le cadre d'un problème plus pratique, pour lequel les bandes de cisaillement n'ont pas nécessairement des orientations particulières par rapport aux directions cristallographiques initiales.

## Tension uniaxiale avec deux systèmes de glissement : régularisation des bandes de localisation générales

La Fig. 7.19 présente les résultats associés en termes de courbes de contrainte-déformation nominales et de distributions de variables de glissement plastique cumulé le long de la direction  $x_2$  pour différents raffinements de maillage. La contrainte nominale est calculée comme la force de réaction  $F$  sur le bord supérieur sur la largeur initiale  $W_0$  de la partie de plaque étudiée (l'épaisseur est supposée être 1) et la déformation nominale comme le rapport entre l'allongement  $\Delta L$  et la longueur initiale  $L_0$ . Les valeurs de  $\gamma_{acc}$  dans la Fig. 7.19b sont déterminées aux nœuds appartenant à la ligne centrale de la partie étudiée de la plaque. La Fig. 7.20 présente les maillages déformés et les contours de la variable de glissement plastique cumulé  $\gamma_{acc}$  pour différents raffinements de maillages. Concernant la réponse contrainte-déformation nominale, la convergence des maillages est obtenue dès qu'un maillage suffisamment fin est appliqué (Fig. 7.19a). En termes de localisation de la déformation, il semble que des maillages plus fins conduisent à une plus grande valeur de pic  $\gamma_{acc}$  dans la bande de cisaillement obtenue. Cependant, cette bande présente une largeur finie qui converge vers une valeur intrinsèque couvrant plusieurs éléments finis. D'après la Fig. 7.20, cette bande est orientée selon un angle d'environ  $54^\circ$  par rapport à la direction  $x_1$ , ce qui est légèrement inférieur à l'angle de la première direction de glissement ( $\theta_1 = 60^\circ$ ). Ceci est en accord avec la bifurcation et les résultats numériques de Kuroda (2011). En utilisant une configuration similaire de systèmes de glissement activés avec  $\theta_1 = 54.7^\circ$ , ces auteurs ont montré que la localisation des déformations se produit le long d'une ligne inclinée à environ  $49^\circ$  de la direction  $x_1$ . Pour mieux analyser les résultats obtenus, la rotation du réseau est approximée sur la base de la décomposition polaire du gradient de transformation élastique :  $\mathbf{F}^e = \mathbf{R}^e \mathbf{U}^e$ , où  $\mathbf{R}^e$  et  $\mathbf{U}^e$  sont respectivement les tenseurs de rotation élastique et d'étirement élastique. En négligeant la distorsion élastique décrite par  $\mathbf{U}^e$ ,  $\mathbf{R}^e$  peut être interprété comme la rotation du réseau et l'angle correspondant  $\theta$  est calculé en utilisant :

$$\theta = \arccos \left[ \frac{1}{2} (\text{tr } \mathbf{R}^e - 1) \right] \quad (7.52)$$

Le signe de l'angle est déterminé en considérant le signe des termes hors diagonale de  $\mathbf{R}^e$ . Ce faisant, on constate que la localisation de la déformation est accompagnée d'une rotation du réseau d'environ  $-5.5^\circ$ . Par conséquent, la bande de localisation obtenue dans la partie considérée de la plaque n'est pas une bande de glissement idéalisée, car elle est associée à la courbure du réseau, ce qui explique sa régularisation par le présent modèle SGCP. Cependant, la bande obtenue pourrait être considérée comme une bande de glissement puisqu'elle est presque parallèle à la première direction de glissement tournée à l'intérieur de la bande ( $60^\circ - 5.5^\circ = 54.5^\circ$ ).

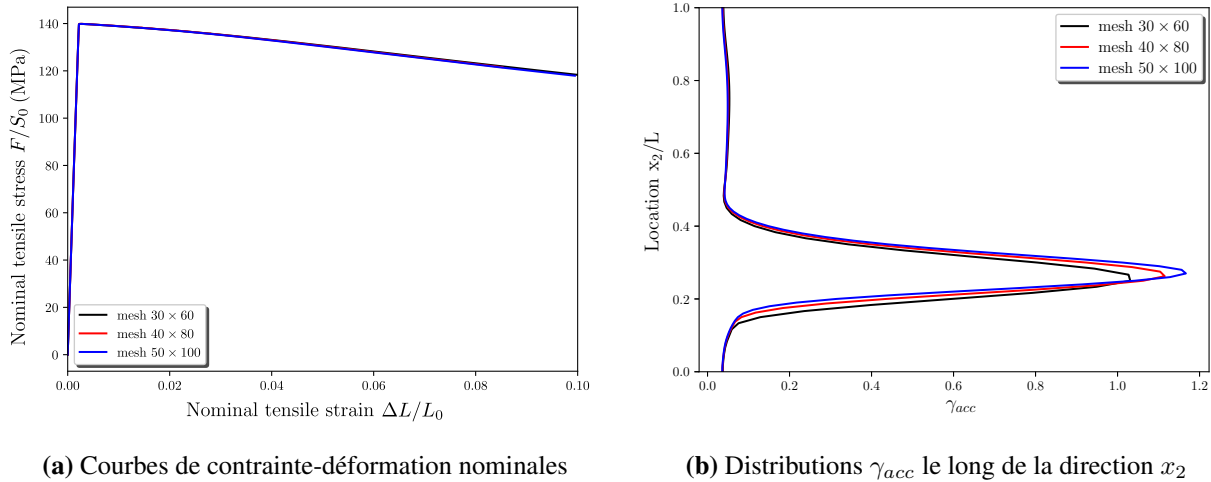


**Fig. 7.19.** Courbes de contrainte-déformation nominales et distributions des variables de glissement plastique cumulé le long de la direction  $x_2$  à la déformation nominale  $\Delta L/L_0 = 0.1$  pour différents raffinements de maillage ( $l_{en}/W = 0.2$ ,  $l_{dis} = 0$ ,  $H_\pi = -500$  MPa).

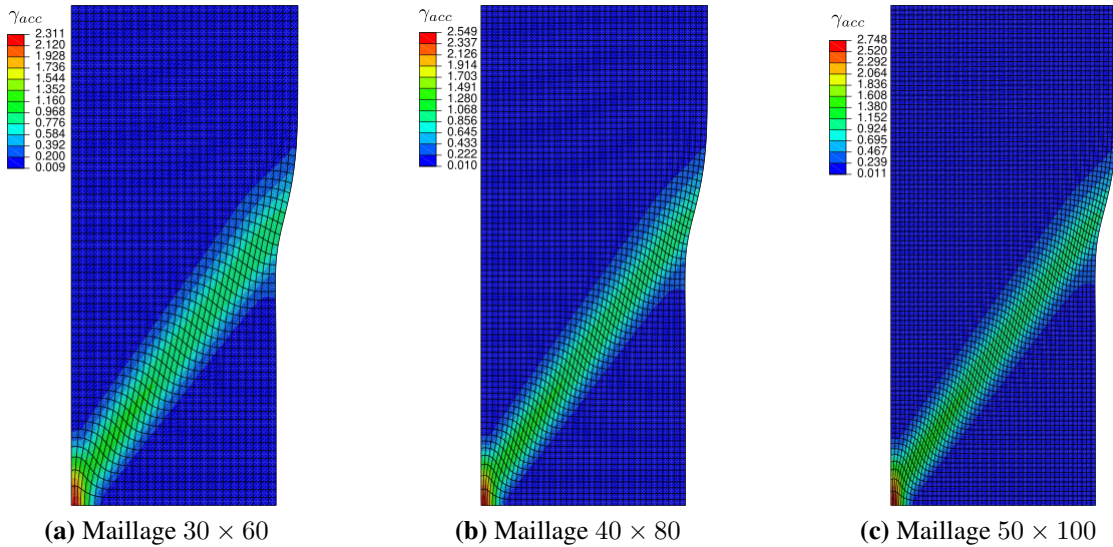


**Fig. 7.20.** Maillages déformés et contours de la variable de glissement plastique cumulé  $\gamma_{acc}$  à la déformation nominale  $\Delta L/L_0 = 0.1$  pour différents raffinements de maillage ( $l_{en}/W = 0.2$ ,  $l_{dis} = 0$ ,  $H_\pi = -500$  MPa).

Bien que les théories SGCP basées sur les GND ne parviennent pas à régulariser les bandes de glissement idéalisées, la présente étude montre qu’elles sont capables de régulariser les bandes de localisation générales. La sous-section suivante vise à étudier la capacité de ces théories à capter correctement des comportements de localisation complexes avec une compétition entre les bandes de pliage et de glissement.

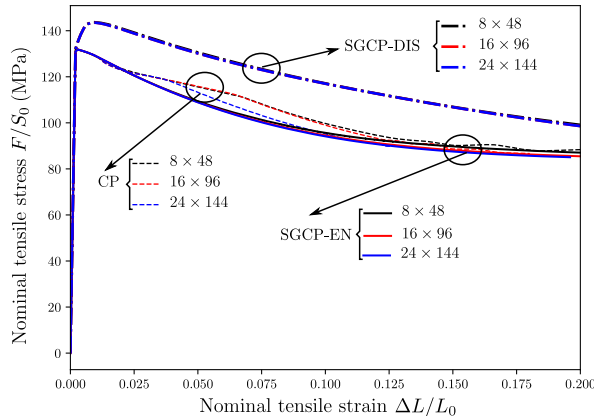


**Fig. 7.21.** Résultats de traction uniaxiale obtenus en utilisant la CP conventionnelle ( $l_{en} = l_{dis} = 0$ ), la SGCP incluant seulement les effets énergétiques d'ordre supérieur (SGCP-EN:  $l_{en}/W = 0.25$ ,  $l_{dis} = 0$ ) et SGCP incluant uniquement les effets dissipatifs d'ordre supérieur (SGCP-DIS:  $l_{en} = 0$ ,  $l_{dis}/W = 0.25$ ) pour différentes maillages, avec  $S_{\xi 0} = 60.84 \text{ MPa}$  et  $H_{\xi} = 0$ .

### Étude des modes de localisation dans les monocristaux soumis à un glissement simple

Pour vérifier la capacité de régularisation de maillage du modèle SGCP actuel en ce qui concerne la réponse contrainte-déformation, différents raffinements de maillage sont considérés :  $8 \times 48$ ,  $16 \times 96$  et  $24 \times 144$  mailles. La Fig. 7.21 présente les résultats associés obtenus en utilisant différentes configurations constitutives. Dans cette figure, les courbes CP, SGCP-EN et SGCP-DIS sont respectivement associées à la CP conventionnelle ( $l_{en} = l_{dis} = 0$ ), à la SGCP incluant uniquement les effets énergétiques d'ordre supérieur ( $l_{en}/W = 0.25$  et  $l_{dis}/W = 0$ ) et à la SGCP incluant uniquement les effets dissipatifs d'ordre supérieur ( $l_{en}/W = 0$  et  $l_{dis}/W = 0.25$ ). Pour la plasticité cristalline conventionnelle, les résultats dépendent fortement du maillage et présentent des oscillations parasites. Des résultats similaires ont été obtenus par Ling et al. (2018). L'activation des effets d'ordre supérieur, quelle que soit leur nature énergétique ou dissipative, permet de surmonter ces difficultés de maillage. Aucune oscillation parasite n'est observée pour les résultats associés aux cas SGCP-EN et SGCP-DIS. De plus, la convergence du maillage est obtenue pour les deux cas dès qu'un maillage suffisamment raffiné est utilisé. Les résultats associés aux maillages  $16 \times 96$  et  $24 \times 144$  sont en accord très étroit pour ces deux cas. L'augmentation apparente de la limite d'élasticité obtenue pour le cas SGCP-DIS est due aux effets d'augmentation de résistance induite par l'échelle de longueur dissipative  $l_{dis}$ , comme largement reconnu dans la littérature (Gurtin et al., 2007; Jebahi et al., 2020). Dans les sous-sections suivantes, la plaque considérée est discrétisée à l'aide d'un maillage de  $24 \times 144$ .

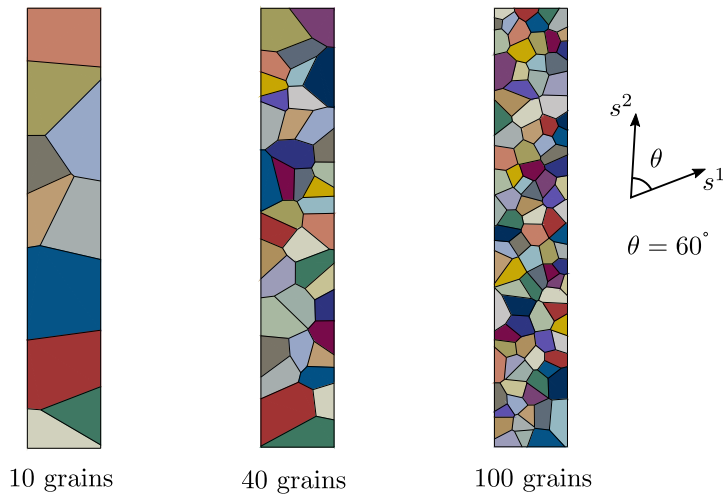


**Fig. 7.22.** Plaque polycristalline constituée de trois différents nombres de grains avec deux systèmes de glissement dans chaque grain.

## Application à la localisation des déformations dans les polycristaux

Dans la section précédente, nous avons mené une étude approfondie de plusieurs problèmes liés à la localisation des déformations dans les monocristaux en utilisant le cadre constitutif développé. La validité et l'efficacité ont été bien démontrées par une série d'exemples numériques. À cette fin, trois plaques polycristallines avec différents nombres de grains générés par tesselation de Voronoï seront utilisées comme indiqué sur la Fig. 7.22. Deux systèmes de glissement avec  $60^\circ$  entre eux sont activés dans chaque grain avec une orientation aléatoire.

### Effets de taille induits par les grains

Afin d'illustrer les effets de taille induits uniquement par les grains, on adopte la condition de GB micro-libre ( $\kappa = 0$ ,  $S_{GB_0} = 0$ ,  $H_{GB} = 0$ ). Un cas conventionnel de CP ( $l_{en} = l_{dis} = 0$ ) est présenté en premier lieu. Pour commencer, les influences de la désorientation des grains sur les réponses polycristallines sont réalisées en définissant cinq ensembles différents de distribution aléatoire pour chaque plaque, en utilisant les paramètres constitutifs CP conventionnels. La Fig. 7.23 présente les courbes de contrainte-déformation nominales en utilisant cinq orientations de grains aléatoires différentes. Notez que l'orientation aléatoire des grains a été générée par une fonction aléatoire. On peut constater que, par exemple dans la Fig. 7.23a, les courbes de contrainte-déformation nominales diffèrent les unes des autres en termes de désorientation différente, ce qui correspond à ce que l'on appelle les effets de taille extrinsèques de premier ordre, c'est-à-dire la dispersion des contraintes d'écoulement. Des résultats similaires ont également été rapportés dans plusieurs travaux (Geers et al., 2006; Yalçinkaya et al., 2018). Cependant, aucun de ces travaux n'inclut l'adoucissement accompagné de la localisation des déformations. En se concentrant sur les réponses de contrainte-déformation dans la plage de déformation inférieure à 0.05 pour les trois cas, la dispersion des courbes de contrainte-déformation devient moins évidente avec l'augmentation du nombre de grains, ce qui représente une caractéristique moins anisotrope due à la microstructure.

Avec l'augmentation de la déformation après 0.05, la contrainte nominale diminue constamment, ce qui signifie que la localisation de la déformation s'intensifie. On peut voir que même dans la Fig. 7.23c, il existe toujours une dispersion des courbes de contrainte-déformation à la fin du chargement. Cela est dû au fait qu'il y a moins de grains dans la direction horizontale que dans la direction verticale, comme le montre la Fig. 7.22.

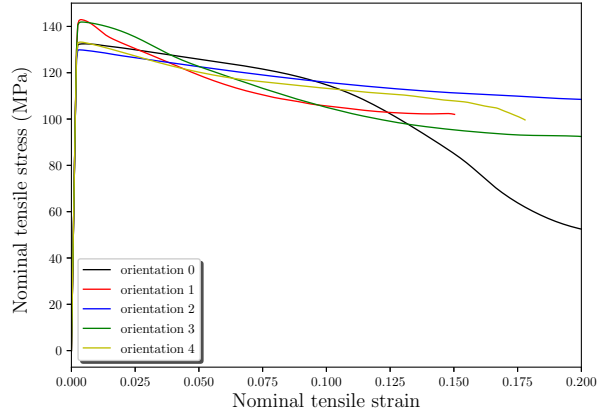
Ensuite, les effets de gradient d'ordre supérieur sont activés en introduisant des échelles de longueur internes énergétiques/dissipatives pour une plaque avec 40 grains et une numérotation de l'orientation des grains "0". En outre, la condition de GB micro-libre est toujours adoptée. La Fig. 7.24 montre les réponses traction-déformation nominales en utilisant différentes échelles de longueur d'ordre supérieur énergétiques ( $l_{dis} = 0$ ) et dissipatives ( $l_{en} = 0, S_{\xi 0} = 60.84 \text{ MPa}, H_{\xi} = 60.84 \text{ MPa}$ ). Par rapport aux exemples monocristallins présentés dans Fig. 6.10, les influences présentent des différences significatives pour les réponses polycristallines. Comme l'illustre la Fig. 7.24a, une échelle de longueur énergétique plus grande  $l_{en}$  augmente non seulement le durcissement mais affecte également le début de la chute de contrainte, c'est-à-dire le signe de la localisation de la déformation. L'exemple monocristallin de la Fig. 6.10a présente uniquement l'influence du durcissement dû à l'échelle de longueur énergétique  $l_{en}$ . Il convient de noter que la comparaison entre les exemples monocristallins et polycristallins n'est faite que d'un point de vue qualitatif. En ce qui concerne les cas dissipatifs dans la Fig. 7.24b, la limite d'élasticité varie pour différentes échelles de longueur dissipatives  $l_{dis}$ . Il semble que le début de la localisation ne change pas en fonction des différentes  $l_{dis}$ . Les courbes de contrainte-déformation avec  $l_{dis}$  non nulle se comportent comme des courbes translatées, ce qui est similaire à celles des exemples de monocristaux dans la Fig. 6.12a.

En résumé, la réponse d'un matériau polycristallin est plus compliquée que celle d'un monocristal en raison de divers comportements de glissement distincts dans chaque grain. Plusieurs exemples dans cette partie ont démontré la capacité de capter la réponse des matériaux polycristallins dans le cadre développé. Dans ce qui suit, les effets de joints de grains seront pris en compte par le modèle de joints de grains proposé.

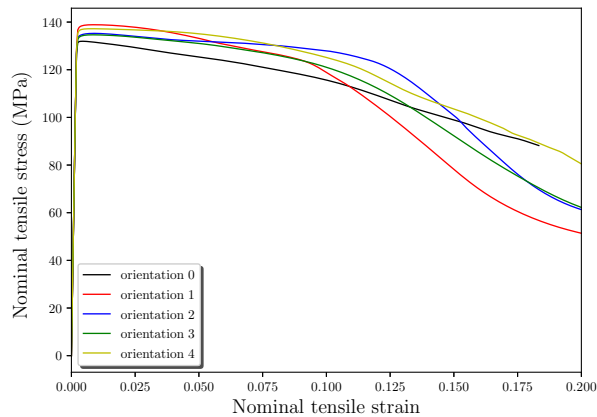
## Effets énergétiques/dissipatifs des joints de grains

Une caractéristique distinctive du présent cadre constitutif est la capacité de capter les comportements des joints de grains. Cette sous-section a pour but de fournir plusieurs exemples pour montrer les effets des joints de grains dans les problèmes de localisation des déformations. Seuls les effets énergétiques d'ordre supérieur sont activés pour chaque exemple ( $l_{en}/W = 0.25, l_{dis} = 0$ ). La Fig. 7.25 montre les courbes de contrainte-déformation nominales avec uniquement des effets GB énergétiques ( $S_{GB0} = 0, H_{GB} = 0$ ) et uniquement des effets GB dissipatifs ( $\kappa = 0, H_{GB} = 0$ ). On peut constater sur la Fig. 7.25a qu'un coefficient énergétique GB plus grand  $\kappa$  conduit à un écrouissage plus important. En outre, la chute approximative de la contrainte de traction est associée au coefficient énergétique GB  $\kappa$ , c'est-à-dire qu'un plus grand  $\kappa$  entraîne un début plus précoce de la chute de contrainte. En ce qui concerne l'influence de la résistance dissipative GB initiale  $S_{GB0}$ , des valeurs plus grandes augmentent la limite d'élasticité comme le montre 7.25b.

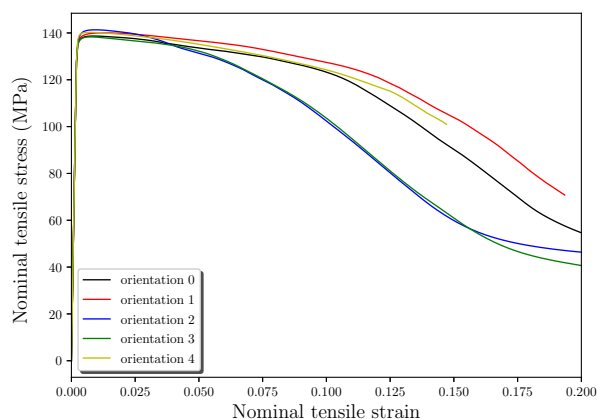
Les contours déformés du glissement plastique cumulé  $\gamma_{acc}$  à la fin du chargement pour les paramètres GB énergétiques et dissipatifs sont présentés dans la Fig. 7.26. Il est évident que les paramètres GB affectent significativement la position de la localisation finale. Par exemple, en se concentrant sur le coefficient énergétique GB  $\kappa$ , le motif de localisation à la fin du chargement s'est



(a) 10 grains



(b) 40 grains



(c) 100 grains

**Fig. 7.23.** Courbes de contrainte-déformation nominales utilisant la CP conventionnelle ( $l_{en} = l_{dis} = 0$ ) avec des orientations de grains aléatoires adoptant des conditions de GB micro-libre ( $\kappa = 0, S_{GB_0} = 0, H_{GB} = 0$ ) pour différents nombres de grains.

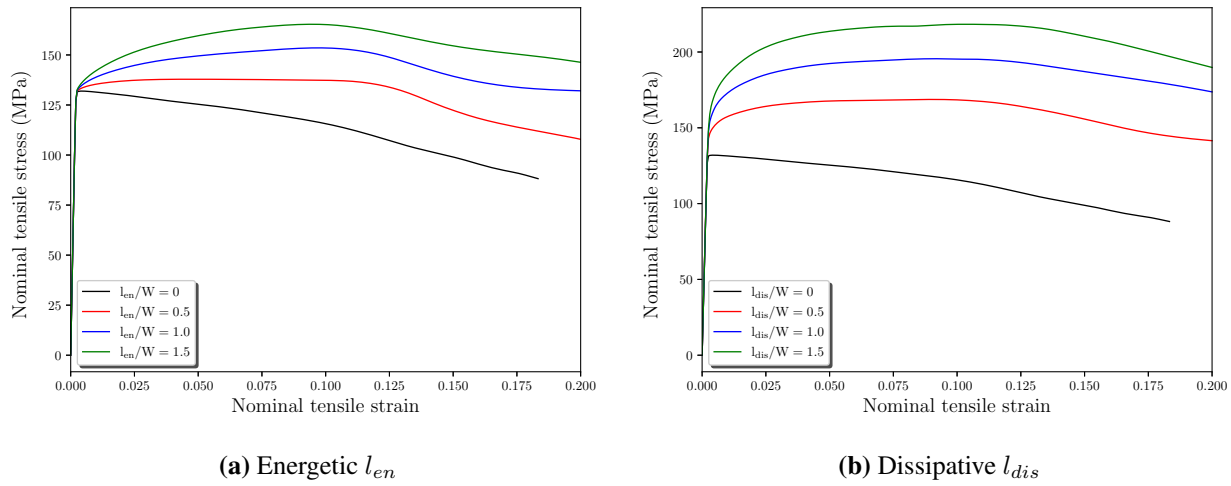


**Fig. 7.24.** Influence des effets énergétiques d'ordre supérieur ( $l_{dis} = 0$ ) et dissipatifs ( $l_{en} = 0, S_{\xi 0} = 60.84 \text{ MPa}, H_{\xi} = 60.84 \text{ MPa}$ ) sur les réponses nominales traction-déformation avec une condition de GB micro-libre ( $\kappa = 0, S_{GB_0} = 0, H_{GB} = 0$ ) pour une plaque à 40 grains avec une orientation de grain "0".

déplacé pour  $\kappa = 1e4 \text{ N m}^{-1}$  comparé à  $\kappa = 1e2 \text{ N m}^{-1}$  comme on le voit sur la Fig. 7.26. Ce résultat intéressant souligne la nécessité de modéliser le comportement des joints de grains pour les structures miniaturisées en termes d'études de localisation des déformations.

## Effets de taille globaux prédicts par le cadre constitutif

Les effets de taille de premier et de second ordre peuvent intervenir pendant la déformation des structures miniaturisées. Par conséquent, un exemple considérant les effets de taille globaux sera présenté ici, qui vise à démontrer la capacité du cadre constitutif actuel à les capter de manière aussi complète que possible. À titre d'exemple, les paramètres du cristal massif pour les effets d'ordre supérieur seront choisis comme suit:  $l_{en} = l_{dis} = 2 \mu\text{m}$ ,  $S_{\xi 0} = 60.84 \text{ MPa}$ ,  $H_{\xi} = 60.84 \text{ MPa}$ . Le modèle de GB adopte les paramètres suivants:  $\kappa = 1e2 \text{ N m}^{-1}$ ,  $S_{GB_0} = 5 \text{ N m}^{-1}$ ,  $H_{GB} = 1e3 \text{ N m}^{-1}$ . Il convient de noter que ces paramètres constitutifs ne se rapportent pas nécessairement à des matériaux spécifiques, mais uniquement à des fins de démonstration. La Fig. 7.27 présente les réponses traction-déformation nominales utilisant ces paramètres constitutifs mesurés par différentes tailles géométriques  $W$ . Les différentes mesures par  $W$  représentent une mise à l'échelle proportionnelle de la plaque polycristalline dans toutes les dimensions. Les effets de taille, "plus petit, est plus fort", peuvent être clairement reflétés par des courbes de contraintes plus élevées avec des tailles géométriques  $W$  plus petites.

Pour présenter la relation entre la localisation des déformations et la taille de la géométrie, les points critiques (le début de la localisation des déformations par rapport au critère de force maximum) sont déterminés de manière approximative sur la Fig. 7.27 et les déformations et contraintes critiques correspondantes sont obtenues. Les variables critiques (contraintes et déformations nominales) sont représentées sur la Fig. 7.28 en fonction de  $1/W$ . La contrainte critique nominale présente une relation presque linéaire par rapport à  $1/W$  comme illustré dans la Fig. , ce qui est le

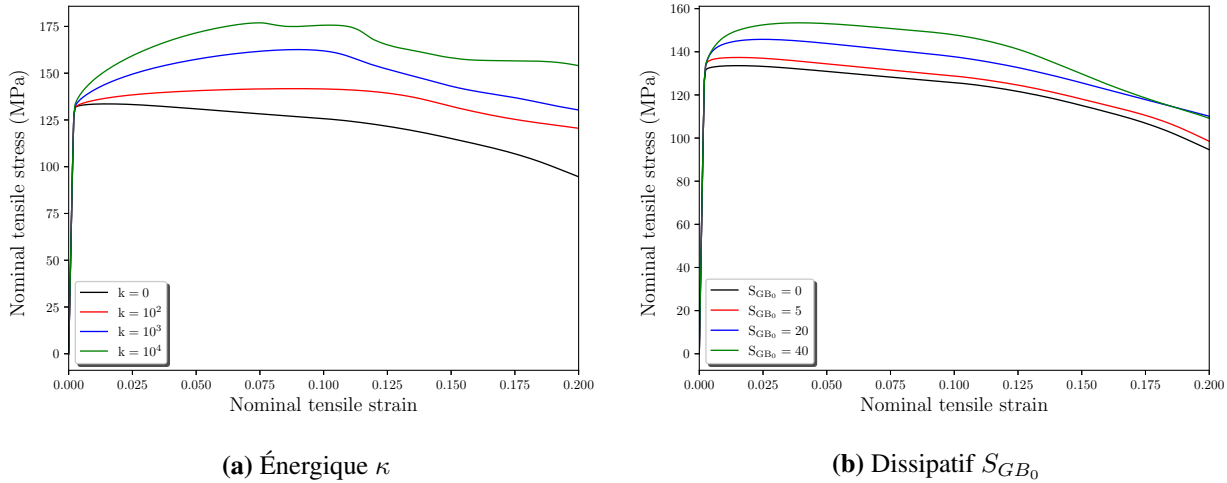


**Fig. 7.25.** Influence des effets énergétiques ( $S_{GB_0} = 0, H_{GB} = 0$ ) et dissipatifs ( $\kappa = 0, H_{GB} = 0$ ) de GB sur les réponses traction-déformation nominales avec seulement des effets énergétiques d'ordre supérieur ( $l_{en}/W = 0.25, l_{dis} = 0$ ) dans les cristaux massifs pour une plaque à 40 grains avec une orientation de grain "0".

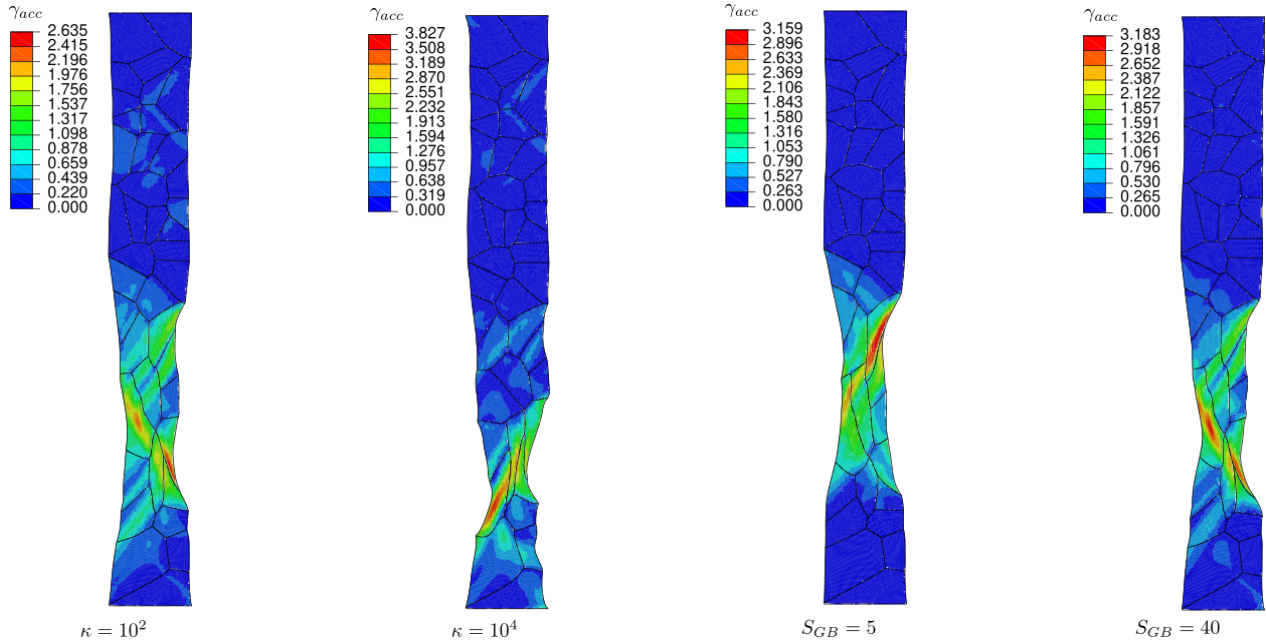


**Fig. 7.26.** Contours déformés de la variable de glissement plastique cumulé  $\gamma_{acc}$  à la fin du chargement en utilisant différents coefficients énergétiques GB  $\kappa$  ( $S_{GB} = 0, H_{GB} = 0, l_{en}/W = 0.25, l_{dis} = 0$ ) et résistance initiale dissipative  $S_{GB_0}$  ( $\kappa = 0, H_{GB} = 0, l_{en}/W = 0.25, l_{dis} = 0$ ) pour une plaque à 40 grains avec une orientation de grain "0".

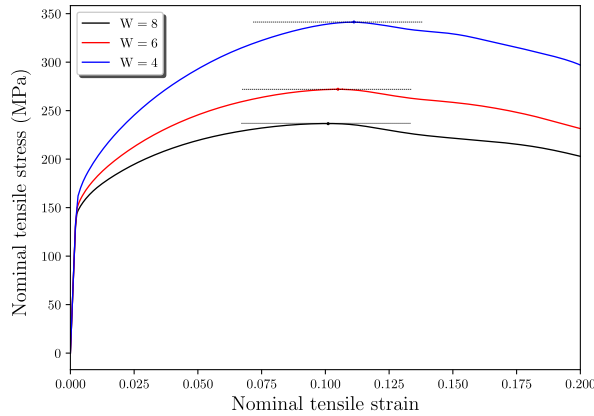


**Fig. 7.27.** Exemple illustratif des effets de taille globaux pour différentes tailles de géométrie  $W$  en termes de courbes de contrainte-déformation nominales utilisant les paramètres constitutifs SGCP ( $l_{en} = l_{dis} = 2 \mu\text{m}$ ,  $S_{\xi 0} = 60.84 \text{ MPa}$ ,  $H_{\xi} = 60.84 \text{ MPa}$ ) dans la masse et les paramètres GB ( $\kappa = 1e2 \text{ N m}^{-1}$ ,  $S_{GB_0} = 5 \text{ N m}^{-1}$ ,  $H_{GB} = 1e3 \text{ N m}^{-1}$ ).

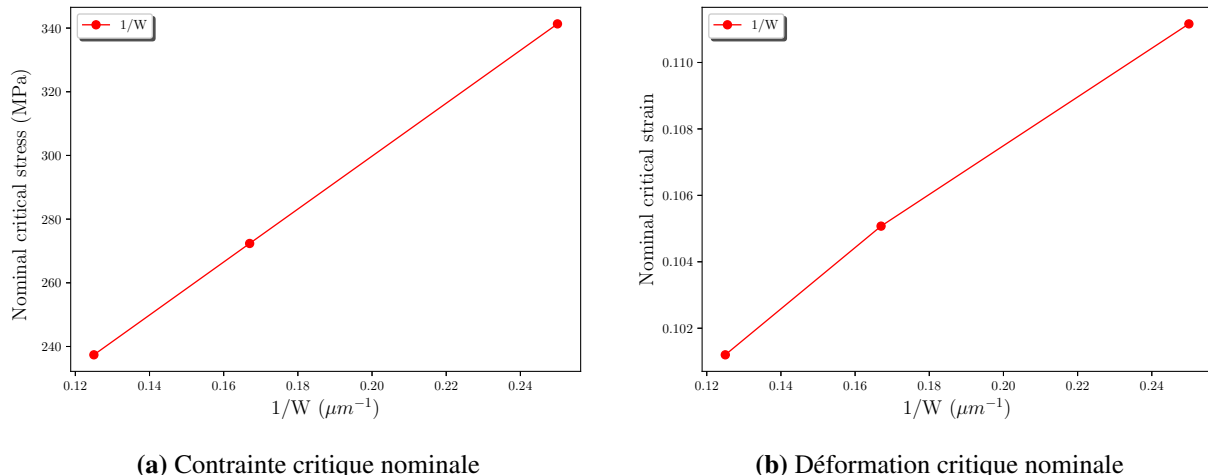


**Fig. 7.28.** Relation entre la contrainte et la déformation critiques nominales au début de la localisation des déformations par rapport à l'inverse de la dimension horizontale de la géométrie  $1/W$  en utilisant à la fois les paramètres SGCP ( $l_{en} = l_{dis} = 2 \mu\text{m}$ ,  $S_{\xi 0} = 60.84 \text{ MPa}$ ,  $H_{\xi} = 60.84 \text{ MPa}$ ) et les paramètres GB ( $\kappa = 1e2 \text{ N m}^{-1}$ ,  $S_{GB_0} = 5 \text{ N m}^{-1}$ ,  $H_{GB} = 1e3 \text{ N m}^{-1}$ ).

même cas pour la limite d'élasticité présentée dans la Fig. 7.16b. La déformation critique nominale ne présente pas une forme linéaire en fonction de  $1/W$  de manière rigoureuse. Pourtant, elle indique à travers la Fig. 7.28a qu'une taille géométrique plus petite retarde le début de la localisation. En fait, les points de la Fig. 7.28b représentent des points d'un trajet de chargement spécifique dans une courbe limite de formage. Les travaux futurs se concentreront sur les effets de taille sur les courbes limites de formage en utilisant le cadre constitutif développé.

## Conclusions

Le présent chapitre s'est concentré sur l'application de l'outil numérique SGCP-GB à déformation finie pour étudier les phénomènes de localisation dans les structures mono- et poly-cristallines. Les capacités du modèle SGCP de déformation finie proposé à régulariser différents types de bandes de localisation ont d'abord été revues à l'aide de plusieurs tests de localisation élémentaires. Il a été montré que seules les bandes de glissement idéalisées, qui ne sont pas très courantes dans les problèmes réels, ne peuvent pas être régularisées par le modèle appliqué. Cela est dû au fait que les gradients de glissement dans la direction normale au plan de glissement ne correspondent pas aux GND et qu'aucun effet de taille n'est prévu pour le développement de tels gradients de glissement normaux. En ce qui concerne les bandes de glissement idéalisées, le présent modèle SGCP se comporte comme un modèle conventionnel de plasticité cristalline. C'est également le cas des modèles de plasticité cristalline de Cosserat dans lesquels les effets de taille ne sont déclenchés que par la courbure du réseau (Forest, 1998).

Les bonnes capacités du modèle SGCP à traiter les bandes de localisation générales ont motivé l'application de ce modèle pour étudier le comportement de localisation complexe avec compétition entre les bandes de glissement et de pliage, qui est rencontré dans les monocristaux subissant un glissement unique. Ce comportement a déjà été étudié par Ling et al. (2018) en utilisant une approche micromorphique réduite. À cette fin, un problème de tension uniaxiale d'une plaque monocristalline présentant un système de glissement unique a été simulé à l'aide du présent modèle SGCP. Différentes configurations constitutives, y compris des effets énergétiques d'ordre purement supérieur et des effets dissipatifs d'ordre purement supérieur, sont considérées. Des simulations utilisant la plasticité cristalline conventionnelle (CCP) ont également été réalisées à des fins de comparaison. Les résultats associés à ces dernières simulations montrent une pathologie de dépendance vis-à-vis des mailles. Il a été démontré que cette pathologie peut être éliminée en incluant des effets d'ordre supérieur, soit énergétiques, soit dissipatifs. Selon la nature des effets d'ordre supérieur, différents comportements de localisation ont été obtenus. L'application d'effets énergétiques d'ordre supérieur donne lieu à un comportement de localisation avec une compétition entre les bandes de glissement et de pliage. Les résultats obtenus sont en bon accord avec ceux obtenus par Ling et al. (2018) en utilisant l'approche micromorphique. L'application d'effets dissipatifs d'ordre supérieur avec une résistance initiale au glissement d'ordre supérieur non nulle conduit à un comportement de localisation qui est dominé de manière écrasante par les bandes de glissement, bien que l'analyse de la rotation du réseau pendant la localisation montre la coexistence du vrillage.

Après l'application du modèle SGCP pour capturer les phénomènes de localisation dans les monocristaux, ce modèle ainsi que le modèle GB ont été appliqués pour étudier les effets de taille sur la réponse de localisation des structures polycristallines. Les caractéristiques intéressantes du cadre numérique SGCP-GB pour capturer différents types d'effets de taille de premier et de second ordre sur les phénomènes de localisation polycristallins ont été démontrées par cette étude. Il a été démontré que les effets énergétiques d'ordre supérieur (à la fois dans les grains et aux limites des grains) agissent comme des accélérateurs de la localisation de la déformation. Au contraire, les effets dissipatifs d'ordre supérieur ont tendance à retarder ce phénomène.



# Conclusions et perspectives

## Conclusions

La forte demande de produits miniaturisés a motivé de nombreuses recherches visant à la fabrication précise de produits de haute qualité à petite échelle. Parmi ces travaux, la modélisation du comportement des matériaux aux petites échelles est devenue un sujet d'actualité en raison de l'apparition de ce que l'on appelle les effets de taille avec la miniaturisation. Comparée aux études expérimentales concernant les effets de taille, l'analyse par modélisation numérique réduit considérablement les coûts et améliore effectivement l'efficacité. Par conséquent, les modèles numériques qui peuvent couvrir les effets de taille dans une perspective globale sont fortement recherchés. Orientée vers la demande de modélisation numérique pour les produits miniaturisés, cette thèse vise à développer un ensemble d'outils numériques qui peuvent considérer plusieurs effets de taille communs. Pour atteindre cet objectif, les aspects suivants ont été étudiés.

Un panorama de plusieurs aspects importants de cette thèse a été présenté dans le chapitre 2. Tout d'abord, une description complète des effets de taille est résumée à partir de la définition, la classification et la manifestation. Dans le cadre de cette thèse, les effets de taille représentent le comportement du matériau dépendant de la taille lors du changement de taille de la géométrie. La classification des effets de taille basée sur l'ordre est adoptée en raison de sa clarté. Les effets de taille de premier ordre sont composés d'effets extrinsèques et intrinsèques provenant de la microstructure sous-jacente, tandis que les effets de taille de second ordre sont causés par les gradients de déformation et les effets de frontière. Ce sont les principaux effets de taille que ce travail tente de couvrir dans un ensemble de modèles numériques. Les principaux effets de taille ont plusieurs manifestations significatives, par exemple, "plus petit est plus faible", "plus petit est plus fort" et la dispersion des contraintes d'écoulement, etc. Dans un deuxième temps, une revue des travaux récents sur la modélisation des effets de taille a été effectuée. Parmi plusieurs modèles numériques, le modèle de plasticité cristalline à gradient de déformation (SGCP) couplé au modèle de joints de grains (GB) est le plus approprié en termes de capture des effets de taille de premier et de second ordre. Ensuite, une revue des modèles SGCP et GB est proposée. En ce qui concerne les théories SGCP, deux questions restent ouvertes, à savoir la description de l'énergie de défauts et des processus de dissipation. Pour les modèles GB permettant de prendre en compte les effets de la désorientation des grains et de l'orientation des GB, peu sont destinés au cadre des grandes déformations. Par conséquent, ces considérations seront des sujets de recherche dans ce travail.

Dans le chapitre 3, un modèle SGCP flexible en petites déformations a été proposé. Ce modèle est basé sur une théorie SGCP de type Gurtin ([Gurtin et al., 2007](#)) avec de nouvelles caractéristiques pour l'énergie de défauts non quadratique généralisée et l'hypothèse constitutive non couplée pour les processus dissipatifs. Une énergie de défauts en loi puissance, avec un indice de contrôle

d'ordre  $n$  ajustable, est proposée pour fournir une étude complète des effets d'échelle de longueur énergétique dans des conditions de chargement proportionnel et non proportionnel. Les résultats de cette étude révèlent des effets très différents de l'échelle de longueur énergétique, en fonction de la valeur de  $n$  et du type de chargement. Pour  $n \geq 2$ , quel que soit le type de chargement, l'échelle de longueur énergétique n'a qu'une influence sur la vitesse du durcissement cinématique classique, comme indiqué dans plusieurs travaux de type SGCP. Cependant, dans la gamme de  $n < 2$ , ce paramètre conduit à des effets de durcissement cinématique non linéaires inhabituels avec des points d'inflexion dans la réponse mécanique macroscopique, résultant en une augmentation apparente de la limite d'élasticité sous chargement monotone. Des effets plus complexes, avec des points d'inflexion supplémentaires, sont obtenus dans des conditions de chargement non proportionnel, révélant de nouveaux effets mémoire de l'histoire du chargement liés à l'échelle de la longueur énergétique. En ce qui concerne la dissipation, pour rendre les effets dissipatifs plus facilement contrôlables, les processus dissipatifs dus aux déformations plastiques et à leurs gradients sont supposés être découplés. Des formulations distinctes, exprimées à l'aide de différentes mesures de déformation plastique effective, sont proposées pour décrire ces processus. Les résultats obtenus à l'aide de ces formulations montrent la grande flexibilité du modèle proposé pour contrôler certains effets dissipatifs majeurs, tels que les sauts élastiques. Une manière simple de supprimer ces sauts dans certaines conditions de chargement non proportionnel est fournie. L'application des formulations découpées proposées pour simuler la réponse mécanique d'un spécimen cisaillé a conduit à une prédiction précise des distributions de déformation plastique, qui se comparent très favorablement à celles prédictes par la mécanique des dislocations discrètes.

Dans le chapitre 4, le modèle SGCP flexible en petites déformations est étendu aux grandes déformations. L'extension aux grandes déformations est destinée à d'autres applications, notamment l'analyse de la localisation des déformations, qui implique généralement des déformations plastiques sévères. Les équations constitutives de la version en grandes déformations sont développées dans la configuration de référence pour faciliter la mise en œuvre numérique. Sur la base de la cinématique de la décomposition de Kröner-Lee de la déformation plastique, les lois constitutives en grandes déformations sont formulées. Une version bidimensionnelle du modèle SGCP flexible a été résumée et implémentée numériquement. Pour valider l'implémentation numérique, il est d'abord appliqué à un problème de cisaillement simple dans une gamme de petites déformations pour l'évaluer systématiquement par rapport aux résultats de la version pour petites déformations du chapitre 3. Ensuite, le modèle est soumis à de grandes déformations et comparé à plusieurs résultats de la littérature pour examiner sa capacité à capter les effets géométriques. Les résultats en grandes déformations de ce chapitre ont montré un bon accord avec les résultats de référence en petites et grandes déformations, qui ont été obtenus soit dans les précédents chapitres, soit dans la littérature.

Dans le chapitre 5, l'accent mis sur la modélisation des effets de taille dans un cristal massif s'est déplacé vers les joints de grains. Un modèle de GB en grandes déformations, qui peut naturellement se coupler avec le modèle SGCP flexible en grandes déformations, a été proposé. La nouveauté du modèle GB proposé réside dans la mesure de la désadaptation GB par rapport aux modèles existants dans la littérature. Une description du tenseur de Burgers du GB, analogue à son homologue dans les grains massifs, a été proposée et employée comme mesure primaire de l'inadéquation du GB. Des processus de GB énergétiques et dissipatifs sont proposés sur la base du décalage de GB. De plus, les influences de la désorientation des grains et de l'orientation des GB sont introduites dans les lois constitutives des GB à l'aide de la mesure des GB proposée. Basé

sur le cadre des grandes déformations SGCP pour le cristal massif, le modèle GB est mis en œuvre en introduisant un élément d'épaisseur zéro pour le GB. Le modèle GB est bien validé par comparaison avec les résultats de la littérature. C'est la première fois qu'une comparaison entre les modèles GB en petites et grandes déformations est présentée dans ce travail. Le modèle est ensuite évalué systématiquement par un exemple de cisaillement simple périodique bi-cristallin. Les influences des paramètres constitutifs des GB montrent un bon accord qualitatif par rapport aux travaux existants.

Dans le chapitre 6, l'ensemble du cadre numérique composé par le modèle SGCP flexible en grandes déformations et le modèle de GB proposé est utilisé pour étudier les problèmes de localisation des déformations dans les tôles monocrystallines et polycristallines. Pour avoir une compréhension approfondie des différents modes de localisation, un exemple monocrystallin est adopté pour montrer les capacités et les limites du modèle SGCP en grandes déformations dans le traitement des problèmes de localisation des déformations. Dans un exemple de cisaillement simple, il a été prouvé que le modèle SGCP en grandes déformations permet la régularisation des bandes de localisation générales. Seules les bandes de glissement idéalisées ne peuvent pas être régularisées par le présent modèle, qui ne sont d'ailleurs pas très courantes dans la déformation réelle des matériaux. Le modèle est ensuite appliqué à une traction uniaxiale d'une plaque monocrystalline pour étudier les modes de localisation complexes, ce qui est fait ici pour la première fois en utilisant un modèle SGCP. Différentes configurations constitutives ont été réalisées telles que la plasticité cristalline conventionnelle (CP), uniquement les effets énergétiques d'ordre supérieur et uniquement les effets dissipatifs d'ordre supérieur. La PC conventionnelle a prédit des résultats dépendant du maillage en termes de réponses contrainte-déformation, tandis qu'ils ont été régularisés à l'aide d'échelles de longueur internes (énergétiques ou dissipatives). L'évolution et la compétition des bandes de glissement et de pliage ont été révélées dans ces paramètres constitutifs. La bonne capacité du modèle SGCP en grandes déformations à prédire le comportement de déformation pour les monocristaux a posé une base fiable lors du couplage avec le modèle de GB. L'exemple de la traction uniaxiale monocrystalline est ensuite étendu au cas polycristallin en utilisant la tessellation de Voronoï. La capacité du modèle SGCP couplé au modèle de GB a été vérifiée en activant différents paramètres constitutifs. Il a été démontré que l'outil numérique composé du modèle SGCP en grandes déformations et du modèle de GB est capable de capter les principaux effets de taille.

## Perspectives et travaux futurs

Cette thèse avait pour but de développer un ensemble d'outils numériques qui peuvent couvrir les principaux effets de taille pour les produits miniaturisés, spécialisés dans l'étude du phénomène de localisation des déformations dans les structures mono et poly-cristallines. Le développement de l'outil numérique est composé par les contributions de chaque chapitre. Plusieurs perspectives réalisables émergent dans chaque chapitre et peuvent être étudiées dans des travaux futurs.

Les principaux effets de taille détaillés dans le chapitre 2 peuvent être considérés comme des effets d'origine interne. Par exemple, les effets de taille extrinsèques/intrinsèques de premier ordre sont dus à la microstructure sous-jacente des matériaux qui peuvent être considérés comme des sources internes. Les effets de gradient de second ordre sont causés par les gradients de déformation qui sont liés à l'accumulation de GND à l'intérieur des matériaux. Les effets de joints de grains appartiennent évidemment à cette catégorie. Avec la diminution de la taille de la géométrie, le rap-

port surface libre/volume augmente également. Ici, la surface libre se réfère à celles qui n'imposent pas de conditions limites externes. Dans cette thèse, les surfaces libres sont considérées comme exemptes de dislocations, représentant des dépenses d'énergie microscopiques nulles. Cependant, plusieurs expériences (Shan et al., 2008; Oh et al., 2009) montrent que les surfaces peuvent également agir comme, par exemple, des sources et des puits de dislocations qui sont similaires aux joints de grains. Cela conduit à une dépense d'énergie (travail) microscopique supplémentaire due à ces interactions de dislocations avec les surfaces. Par conséquent, les effets de surface sont aussi importants que les effets de taille de premier et de second ordre qui doivent être pris en compte dans les lois constitutives. Très récemment, Peng and Huang (2015, 2017) ont proposé des modèles constitutifs captant les effets de surface énergétiques et dissipatifs, dans le cadre de la théorie SGCP. Il a été rapporté que les effets de surface influencent significativement le comportement plastique. Motivés par leurs travaux (Peng and Huang, 2015, 2017), un travail futur prometteur pourrait se concentrer sur l'enrichissement du cadre numérique développé pour couvrir les effets de surface.

Comme mentionné dans le chapitre 3, le contrôle flexible des "sauts élastiques" est devenu une question ouverte dans les théories de plasticité à gradient de déformation pour les types non-incrémentaux. Cette thèse tente de contrôler les sauts élastiques en proposant un processus de dissipation découplé. Inspiré par les recherches sur les problèmes de sauts élastiques en utilisant des exemples de chargement non proportionnel, une autre solution possible a été proposée. Il est bien connu que la déformation totale  $\varepsilon$  peut être décomposée de manière additive en une partie élastique  $\varepsilon_e$  et une partie plastique  $\varepsilon_p$  dans un cadre de déformation infinitésimale. On pense que cette décomposition est susceptible de s'appliquer à une déformation d'ordre supérieur, c'est-à-dire au gradient de glissement plastique  $\nabla\gamma$ . L'idée de la décomposition de la déformation d'ordre supérieur peut être utile pour contrôler les sauts élastiques sous un chargement non proportionnel. Il est à noter que très récemment, une série de résultats expérimentaux et d'équipements ont été rapportés par Hua et al. (2021). Cependant, le chargement non-proportionnel n'a pas été rapporté. D'autres méthodes numériques, telles que la dynamique des dislocations discrètes (DDD), sont également utiles pour comprendre le mécanisme du phénomène de sauts élastiques. L'idée d'une décomposition de la déformation d'ordre supérieur peut être étudiée dans des travaux futurs.

Comme indiqué au chapitre 4, il existe deux méthodes de modélisation numérique des SGCP, à savoir la méthode  $\rho$  et la méthode  $\gamma$ . La différence entre ces deux méthodes de modélisation réside dans la sélection des variables d'état primaires. Klusemann et al. (2012) ont signalé que les deux modèles prédisent généralement des résultats presque identiques pour les monocristaux dans le cadre des petites déformations. Les différences apparaissent près des frontières en raison de la façon dont les conditions aux limites sont imposées par les deux formulations. Cependant, il n'existe aucune étude associée dans la littérature dans le cadre des grandes déformations. En outre, on se demande légitimement si ces deux méthodes conduiront à des différences pour le modèle de GB (la modélisation GB par la méthode  $\rho$  peut être trouvée dans van Beers et al. (2013); Peng et al. (2019) et par la méthode  $\gamma$  dans Özdemir and Yalçinkaya (2014); Gottschalk et al. (2016); Yalçinkaya et al. (2018)). Fortement motivé par cette idée, le modèle SGCP actuel en grandes déformations couplé au modèle de GB sera mis en œuvre en utilisant la méthode  $\rho$  dans les travaux futurs.

Le modèle de GB proposé au chapitre 5 suppose une dépense d'énergie (travail) nulle dans les sauts de déplacement à travers les GB, c'est-à-dire que le déplacement est supposé être continu à travers les GB. En fait, lors d'une déformation plastique sévère dans le cas d'une grande déformation, le glissement et l'ouverture des GB sont susceptibles de se produire. Le présent modèle de

GB en grandes déformations peut introduire ces effets de manière efficace. Plusieurs modèles connexes incluant le glissement des GB peuvent être trouvés dans [Gurtin \(2008b\)](#) et [Gurtin and Anand \(2008\)](#). Des extensions beaucoup plus complexes, telles que l'ouverture des GB, nécessitent une technique de zone cohésive ([Shawish et al., 2013; Rezaei et al., 2020](#)).

L'exemple d'une plaque polycristalline dans le chapitre 6 montre la capacité de l'outil numérique à décrire les effets de taille concernés. Cependant, une extension tridimensionnelle est fortement requise, ce qui facilitera son application à des exemples d'ingénierie réels. Un autre travail prometteur se concentrera sur la prédiction des diagrammes de limite de formage (FLD) en utilisant le modèle SGCP et GB, qui permet de capturer les influences des effets de taille majeurs sur la limite de ductilité des tôles métalliques fines.



# **Part III**

## **Appendices**



# Appendix A

## Numerical aspects of small deformation SGCP

In this appendix, a detailed numerical implementation of small deformation SGCP will be presented. In the second section A.2, degrees of freedom (DOF) and interpolation functions are presented. Detailed information on how DOF are arranged in the UEL is provided. This directly determines the corresponding interpolation functions. In section A.3, the widely-used regularization function for the viscoplastic function in gradient plasticity is introduced. In section A.4, a detailed presentation of calculation of tangent matrices is given. In the last section A.5, the shape functions and integration scheme used in the small deformation example are illustrated.

### A.1 Overview of the implementation

The small deformation SGCP model proposed in chapter 3 will be implemented through a UEL subroutine in Abaqus. Generally speaking, the implementation of any constitutive theories by using a UEL subroutine requires two steps, as shown in Fig. A.1:

- From a theoretical viewpoint, the governing equations and corresponding constitutive equations are needed.
- From a numerical viewpoint, the calculation of variables is needed by the UEL.

With the help of the weak forms in (3.71), the calculations performed by the UEL part will be detailed in this chapter.

### A.2 Degrees of freedom and interpolation functions

The nodal degrees of freedom (DOF) are arranged in this work as:

$$\begin{aligned}\underline{U} &= [U_1^1 \ \dots \ U_1^{nn} \ U_2^1 \ \dots \ U_2^{nn} \ U_3^1 \ \dots \ U_3^{nn}]^T \\ \underline{\Gamma} &= [\Gamma_1^1 \ \dots \ \Gamma_1^{nn} \ \dots \ \Gamma_q^1 \ \dots \ \Gamma_q^{nn}]^T\end{aligned}\tag{A.1}$$

with  $nn$  representing the number of nodes of an element and  $q$  the number of slip systems. It should be noted that for nodal DOF, capital letters ( $U_1$  for example) are used, while lower-case letters (e.g.,

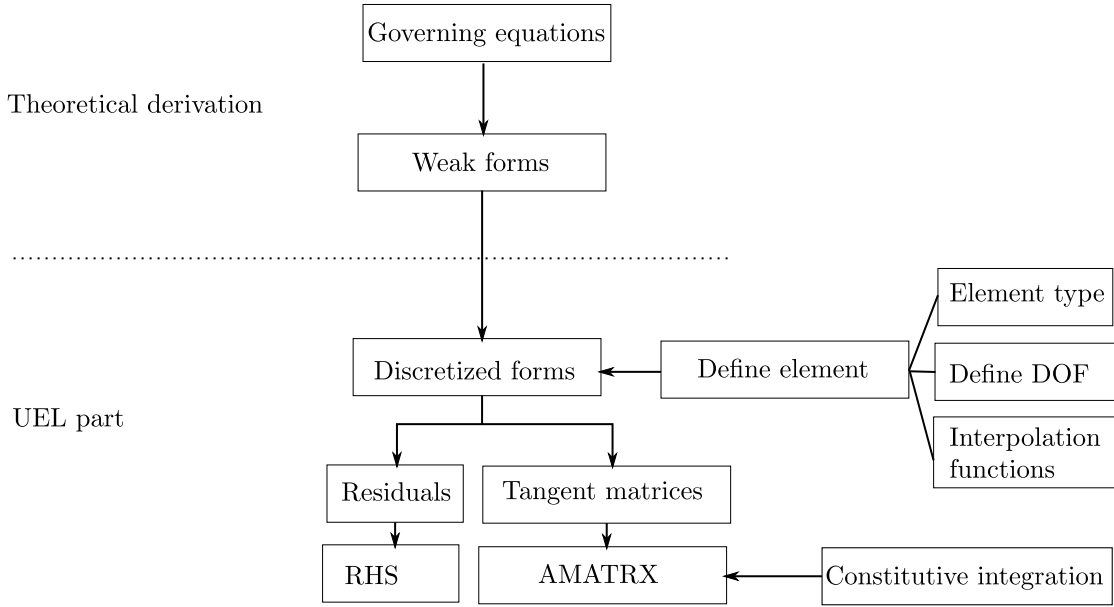


**Fig. A.1.** Flow chart of numerical implementation.

$u_1$ ) are used for DOF in the element. As long as the arrangement of DOF has been prescribed, the interpolation functions associated with nodal DOF should be figured out. In what follows, these functions will be presented in matrix forms.

## Displacement interpolation

Denoting the displacement field  $\mathbf{u}$  in a representative element, it can be interpolated from nodal values  $\mathbf{U}$  through the approximation as:

$$\mathbf{u} = \sum_{k=1}^{nn} N_k(\xi) \mathbf{U}^k \quad (\text{A.2})$$

where  $N_k(\xi)$  represents the shape function for node  $k$  of the element with local reference coordinates  $\xi = (\xi_1, \xi_2, \xi_3)$  and  $\mathbf{U}$  is the vector form of nodal displacements. The displacement approximation can be expressed in a matrix form following the arrangement of displacement (A.1) as:

$$\begin{bmatrix} u_1 \\ u_2 \\ u_3 \end{bmatrix} = \begin{bmatrix} N^1 & \dots & N^{nn} & 0 & \dots & 0 & 0 & \dots & 0 \\ 0 & \dots & 0 & N^1 & \dots & N^{nn} & 0 & \dots & 0 \\ 0 & \dots & 0 & 0 & \dots & 0 & N^1 & \dots & N^{nn} \end{bmatrix} \begin{bmatrix} U_1^1 \\ \vdots \\ U_1^{nn} \\ U_2^1 \\ \vdots \\ U_2^{nn} \\ U_3^1 \\ \vdots \\ U_3^{nn} \end{bmatrix} \quad (\text{A.3})$$

and a more compact expression reads

$$\underline{u} = \underline{\underline{N}}_u \underline{U}. \quad (\text{A.4})$$

The shape functions used in the small deformation example can be found in section [A.5](#).

## Plastic slip fields interpolation

Similarly, the plastic slip fields  $\gamma$  can be interpolated from nodal values as:

$$\gamma = \sum_{k=1}^{nn} N_k(\xi) \Gamma^k \quad (\text{A.5})$$

and the corresponding matrix form gives:

$$\begin{bmatrix} \gamma_1 \\ \vdots \\ \gamma_q \end{bmatrix} = \begin{bmatrix} N^1 & \dots & N^{nn} & 0 \dots 0 & 0 & \dots & 0 \\ \vdots & & \vdots & \vdots & \vdots & & \vdots \\ 0 & \dots & 0 & 0 \dots 0 & N^1 & \dots & N^{nn} \end{bmatrix} \begin{bmatrix} \Gamma_1^1 \\ \vdots \\ \Gamma_1^{nn} \\ \vdots \\ \Gamma_q^1 \\ \vdots \\ \Gamma_q^{nn} \end{bmatrix} \quad (\text{A.6})$$

or

$$\underline{\gamma} = \underline{\underline{N}}_\gamma \underline{\Gamma} \quad (\text{A.7})$$

## Strain field interpolation

The strain filed  $\varepsilon$  is calculated as:

$$\varepsilon = \frac{1}{2} [\nabla \mathbf{u} + (\nabla \mathbf{u})^T]. \quad (\text{A.8})$$

Therefore, it is necessary to figure out the interpolation of the displacement gradient tensor  $\nabla \mathbf{u}$  from nodal values. The displacement gradient is calculated by differentiating [\(A.2\)](#) with respect to the reference configuration:

$$\nabla \mathbf{u} = \sum_{k=1}^{nn} \frac{\partial N_k(\xi)}{\partial \mathbf{X}} \mathbf{U}^k \quad (\text{A.9})$$

with  $\mathbf{X}$  a point in the reference configuration. The derivative  $\frac{\partial N_k(\xi)}{\partial \mathbf{X}}$  can be rewritten with respect to local coordinates as:

$$\begin{aligned} \frac{\partial N_k(\xi)}{\partial \mathbf{X}} &= \frac{\partial N_k(\xi)}{\partial \xi} \frac{\partial \xi}{\partial \mathbf{X}} \\ &= \frac{\partial N_k(\xi)}{\partial \xi} \left( \frac{\partial \mathbf{X}}{\partial \xi} \right)^{-1} \end{aligned}$$

where the derivative  $\frac{\partial \mathbf{X}}{\partial \xi}$  is the Jacobian which relates variables in the material configuration to those in the local reference coordinate system. In matrix form, the derivative  $\frac{\partial N_k(\xi)}{\partial \mathbf{X}}$  can be expressed as:

$$\begin{bmatrix} \frac{\partial N^1}{\partial X_1} & \dots & \frac{\partial N^{nn}}{\partial X_1} \\ \frac{\partial N^1}{\partial X_2} & \dots & \frac{\partial N^{nn}}{\partial X_2} \\ \frac{\partial N^1}{\partial X_3} & \dots & \frac{\partial N^{nn}}{\partial X_3} \\ \frac{\partial N^1}{\partial X_1} & \dots & \frac{\partial N^{nn}}{\partial X_1} \\ \frac{\partial N^1}{\partial X_3} & \dots & \frac{\partial N^{nn}}{\partial X_3} \end{bmatrix} = [J]^{-1} \begin{bmatrix} \frac{\partial N^1}{\partial \xi_1} & \dots & \frac{\partial N^{nn}}{\partial \xi_1} \\ \frac{\partial N^1}{\partial \xi_2} & \dots & \frac{\partial N^{nn}}{\partial \xi_2} \\ \frac{\partial N^1}{\partial \xi_3} & \dots & \frac{\partial N^{nn}}{\partial \xi_3} \\ \frac{\partial N^1}{\partial \xi_1} & \dots & \frac{\partial N^{nn}}{\partial \xi_1} \\ \frac{\partial N^1}{\partial \xi_3} & \dots & \frac{\partial N^{nn}}{\partial \xi_3} \end{bmatrix}$$

with Jacobian matrix

$$[J] = \begin{bmatrix} \frac{\partial X_1}{\partial \xi_j} \\ \frac{\partial X_2}{\partial \xi_j} \\ \frac{\partial X_3}{\partial \xi_j} \end{bmatrix} = \begin{bmatrix} \frac{\partial X_1}{\partial \xi_1} & \frac{\partial X_2}{\partial \xi_1} & \frac{\partial X_3}{\partial \xi_1} \\ \frac{\partial X_1}{\partial \xi_2} & \frac{\partial X_2}{\partial \xi_2} & \frac{\partial X_3}{\partial \xi_2} \\ \frac{\partial X_1}{\partial \xi_3} & \frac{\partial X_2}{\partial \xi_3} & \frac{\partial X_3}{\partial \xi_3} \end{bmatrix} = \begin{bmatrix} \frac{\partial N^1}{\partial \xi_1} & \dots & \frac{\partial N^{nn}}{\partial \xi_1} \\ \frac{\partial N^1}{\partial \xi_2} & \dots & \frac{\partial N^{nn}}{\partial \xi_2} \\ \frac{\partial N^1}{\partial \xi_3} & \dots & \frac{\partial N^{nn}}{\partial \xi_3} \end{bmatrix} \begin{bmatrix} X_1^1 & X_2^1 & X_3^1 \\ \vdots & \vdots & \vdots \\ X_1^{nn} & X_2^{nn} & X_3^{nn} \end{bmatrix}$$

Therefore, the displacement gradient can be arranged as:

$$\begin{bmatrix} u_{1,1} & u_{1,2} & u_{1,3} \\ u_{2,1} & u_{2,2} & u_{2,3} \\ u_{3,1} & u_{3,2} & u_{3,3} \end{bmatrix} = \begin{bmatrix} \frac{\partial N^1}{\partial X_1} & \dots & \frac{\partial N^{nn}}{\partial X_1} \\ \frac{\partial N^1}{\partial X_2} & \dots & \frac{\partial N^{nn}}{\partial X_2} \\ \frac{\partial N^1}{\partial X_3} & \dots & \frac{\partial N^{nn}}{\partial X_3} \end{bmatrix} \begin{bmatrix} U_1^1 & U_2^1 & U_3^1 \\ \vdots & \vdots & \vdots \\ U_1^{nn} & U_2^{nn} & U_3^{nn} \end{bmatrix}$$

Then, the strain field  $\boldsymbol{\varepsilon}$  can be calculated following (A.8) as<sup>1</sup>:

$$\begin{bmatrix} \varepsilon_{11} \\ \varepsilon_{22} \\ \varepsilon_{33} \\ 2\varepsilon_{12} \\ 2\varepsilon_{13} \\ 2\varepsilon_{23} \end{bmatrix} = \begin{bmatrix} \frac{\partial N^1}{\partial X_1} & \dots & \frac{\partial N^{nn}}{\partial X_1} & 0 & \dots & 0 & 0 & \dots & 0 \\ 0 & \dots & 0 & \frac{\partial N^1}{\partial X_2} & \dots & \frac{\partial N^{nn}}{\partial X_2} & 0 & \dots & 0 \\ 0 & \dots & 0 & 0 & \dots & 0 & \frac{\partial N^1}{\partial X_3} & \dots & \frac{\partial N^{nn}}{\partial X_3} \\ \frac{\partial N^1}{\partial X_2} & \dots & \frac{\partial N^{nn}}{\partial X_2} & \frac{\partial N^1}{\partial X_1} & \dots & \frac{\partial N^{nn}}{\partial X_1} & 0 & \dots & 0 \\ \frac{\partial N^1}{\partial X_3} & \dots & \frac{\partial N^{nn}}{\partial X_3} & 0 & \dots & 0 & \frac{\partial N^1}{\partial X_1} & \dots & \frac{\partial N^{nn}}{\partial X_1} \\ 0 & \dots & 0 & \frac{\partial N^1}{\partial X_3} & \dots & \frac{\partial N^{nn}}{\partial X_3} & \frac{\partial N^1}{\partial X_2} & \dots & \frac{\partial N^{nn}}{\partial X_2} \end{bmatrix} \begin{bmatrix} U_1^1 \\ \vdots \\ U_1^{nn} \\ U_2^1 \\ \vdots \\ U_2^{nn} \\ U_3^1 \\ \vdots \\ U_3^{nn} \end{bmatrix} \quad (\text{A.10})$$

or

$$\underline{\underline{\varepsilon}} = \underline{\underline{B}}_u \underline{\underline{U}} \quad (\text{A.11})$$

<sup>1</sup>The arrangement of strain components strictly follows the voigt convention which is commonly acknowledged in numerical implementation of small deformation plasticity models. Note that engineering shear strain is adopted in this work, e.g.,  $\gamma_{12} = 2\varepsilon_{12}$

## Gradient of plastic slips interpolation

Following (A.5), the gradient of plastic slips can be calculated as:

$$\nabla \gamma = \sum_{k=1}^{nn} \frac{\partial N_k(\xi)}{\partial \mathbf{X}} \Gamma^k \quad (\text{A.12})$$

Then, a matrix form can be expressed as:

$$\begin{bmatrix} \gamma_{1,1} \\ \gamma_{1,2} \\ \gamma_{1,3} \\ \vdots \\ \gamma_{q,1} \\ \gamma_{q,2} \\ \gamma_{q,3} \end{bmatrix} = \begin{bmatrix} \frac{\partial N^1}{\partial X_1} & \cdots & \frac{\partial N^{nn}}{\partial X_1} & \cdots & 0 & \cdots & 0 \\ \frac{\partial N^1}{\partial X_2} & \cdots & \frac{\partial N^{nn}}{\partial X_2} & \cdots & 0 & \cdots & 0 \\ \frac{\partial N^1}{\partial X_3} & \cdots & \frac{\partial N^{nn}}{\partial X_3} & \cdots & 0 & \cdots & 0 \\ \vdots & \cdots & \vdots & \ddots & \vdots & \cdots & \vdots \\ 0 & \cdots & 0 & \cdots & \frac{\partial N^1}{\partial X_1} & \cdots & \frac{\partial N^{nn}}{\partial X_1} \\ 0 & \cdots & 0 & \cdots & \frac{\partial N^1}{\partial X_2} & \cdots & \frac{\partial N^{nn}}{\partial X_2} \\ 0 & \cdots & 0 & \cdots & \frac{\partial N^1}{\partial X_3} & \cdots & \frac{\partial N^{nn}}{\partial X_3} \end{bmatrix} \begin{bmatrix} \Gamma_1^1 \\ \vdots \\ \Gamma_1^{nn} \\ \vdots \\ \Gamma_q^1 \\ \vdots \\ \Gamma_q^{nn} \end{bmatrix} \quad (\text{A.13})$$

or

$$\underline{\nabla \gamma} = \underline{\underline{B}_\gamma} \underline{\Gamma} \quad (\text{A.14})$$

## A.3 Regularization function

The viscoplastic-like function in dissipative constitutive equations (as shown in (3.70) in small deformation SGCP model) takes the form:

$$R(\dot{e}_\pi^\alpha) = \left[ \frac{\dot{e}_\pi^\alpha}{\dot{\gamma}_0^\alpha} \right]^m, \quad R(\dot{e}_\xi^\alpha) = \left[ \frac{\dot{e}_\xi^\alpha}{\dot{\gamma}_0^\alpha} \right]^m$$

with

$$\dot{e}_\pi^\alpha = |\dot{\gamma}^\alpha|, \quad \dot{e}_\xi^\alpha = \|l_{dis} \nabla^\alpha \dot{\gamma}^\alpha\|.$$

Without regularization, the derivative related to these components will lead to infinite values, making the overall tangent stiffness matrix ill-conditioned. Taking lower-order function  $R(\dot{e}_\pi^\alpha)$  as an example, the derivative with respect to  $\dot{\gamma}^\alpha$  can be expressed as:

$$\begin{aligned} \frac{\partial R(\dot{e}_\pi^\alpha)}{\partial \dot{\gamma}^\alpha} &= \frac{m}{\dot{\gamma}_0^\alpha} \left[ \frac{\dot{e}_\pi^\alpha}{\dot{\gamma}_0^\alpha} \right]^{m-1} \frac{\dot{\gamma}^\alpha}{\dot{e}_\pi^\alpha} \\ &= \frac{m}{\dot{\gamma}_0^\alpha} \left[ \frac{\dot{e}_\pi^\alpha}{\dot{\gamma}_0^\alpha} \right]^{m-1} \operatorname{sgn}(\dot{\gamma}^\alpha) \end{aligned}$$

Note that the range of the rate sensitivity parameter is  $0 < m \leq 1$ . The initial value of  $\dot{\gamma}^\alpha$  tends to be 0 leading to an infinite  $\left[ \frac{\dot{e}_\pi^\alpha}{\dot{\gamma}_0^\alpha} \right]^{m-1}$ , and thus infinite values of  $K_{\gamma\gamma}$  in the overall tangent matrix. The infinite  $K_{\gamma\gamma}$  yields infinitesimal solutions of  $\gamma$  field, leading to an eternal state of elasticity. To overcome this ill-conditioned form of small values of  $\dot{\gamma}^\alpha$ , a regularization function should be developed. Various forms of regularization functions can be found in [Panteghini and Bardella \(2016\)](#); [Fuentes-Alonso and Martínez-Pañeda \(2020\)](#). Inspired by these formulations, this work adopts the regularization function as follows:

$$R(e_\eta^\alpha) = \begin{cases} \frac{\dot{e}_\eta^\alpha}{\omega \dot{\gamma}_0^\alpha} & \text{if } \dot{e}_\eta^\alpha \leq \dot{\gamma}_* \\ \left( \frac{e_\eta^\alpha - \Phi}{\dot{\gamma}_0} \right)^m & \text{if } \dot{e}_\eta^\alpha > \dot{\gamma}_* \end{cases} \quad (\text{A.15})$$

where  $\omega$  is a parameter of regularization,  $\dot{e}_\eta^\alpha$  could be  $\dot{e}_\pi^\alpha$  (for  $\pi_{dis}^\alpha$ ) or  $\dot{e}_\xi^\alpha$  (for  $\xi_{dis}^\alpha$ ) and  $\eta \in (\pi, \xi)$ .

These two parameters should be determined such that equation (A.15) should always be satisfied with  $C^1$  continuous condition, *i.e.*, there is a smooth transition between the two parts. With  $C^1$  continuity condition, it yields

$$\begin{cases} \frac{\dot{e}_\eta^\alpha}{\omega \dot{\gamma}_0^\alpha} = \left( \frac{e_\eta^\alpha - \Phi}{\dot{\gamma}_0} \right)^m, & \text{at } \dot{e}_\eta^\alpha = \dot{\gamma}_* \\ \left( \frac{\dot{e}_\eta^\alpha}{\omega \dot{\gamma}_0^\alpha} \right)' = \left\{ \left( \frac{e_\eta^\alpha - \Phi}{\dot{\gamma}_0} \right)^m \right\}', & \text{at } \dot{e}_\eta^\alpha = \dot{\gamma}_* \end{cases} \quad (\text{A.16})$$

Therefore, we have:

$$\begin{cases} \frac{\dot{\gamma}_*}{\omega \dot{\gamma}_0^\alpha} = \left( \frac{\dot{\gamma}_* - \Phi}{\dot{\gamma}_0} \right)^m \\ \frac{1}{\omega \dot{\gamma}_0^\alpha} = \frac{m}{\dot{\gamma}_0} \left( \frac{\dot{\gamma}_* - \Phi}{\dot{\gamma}_0} \right)^{m-1} \end{cases} \quad (\text{A.17})$$

By equation (A.17), the following equation can be obtained

$$\Phi = \dot{\gamma}_* (1 - m) \quad (\text{A.18})$$

Substituting (A.18) into (A.17),  $\dot{\gamma}_*$  can be expressed as

$$\dot{\gamma}_* = \frac{\dot{\gamma}_0}{m} \left( \frac{1}{\omega m} \right)^{\frac{1}{m-1}} \quad (\text{A.19})$$

The derivatives can be calculated as

$$\frac{\partial R(\dot{e}_\eta^\alpha)}{\partial \dot{e}_\eta^\alpha} = \begin{cases} \frac{1}{\omega \dot{\gamma}_0^\alpha} & \text{if } \dot{e}_\eta^\alpha \leq \dot{\gamma}_* \\ \frac{m}{\dot{\gamma}_0} \left( \frac{\dot{e}_\eta^\alpha - \Phi}{\dot{\gamma}_0} \right)^{m-1} & \text{if } \dot{e}_\eta^\alpha > \dot{\gamma}_* \end{cases} \quad (\text{A.20})$$

These formulations will be used in the calculation of tangent matrices in the following.

## A.4 Tangent matrices

The residuals for small deformation SGCP are written as (taken from (3.74)):

$$\begin{aligned}\underline{R}_u^e &= \int_{\mathcal{V}^e} \underline{\underline{B}}_u^T \underline{\sigma} dv - \int_{\mathcal{S}_t^e} \underline{\underline{N}}_u^T \underline{t} ds = 0 \\ \underline{R}_\gamma^e &= \int_{\mathcal{V}^e} \underline{\underline{B}}_\gamma^T \underline{\xi} dv + \int_{\mathcal{V}^e} \underline{\underline{N}}_\gamma^T \underline{\pi} dv - \int_{\mathcal{V}^e} \underline{\underline{N}}_\gamma^T \underline{\tau} dv - \int_{\mathcal{S}_\chi^e} \underline{\underline{N}}_\gamma^T \underline{\chi} ds = 0\end{aligned}\quad (\text{A.21})$$

Considering null power expenditure on the boundary ( $\int_{\mathcal{S}_t^e} \underline{\underline{N}}_u^T \underline{t} ds = 0$ ,  $\int_{\mathcal{S}_\chi^e} \underline{\underline{N}}_\gamma^T \underline{\chi} ds = 0$ ), the tangent stiffness can be calculated as:

$$\begin{aligned}\underline{K}_{uu}^e &= \frac{\partial \underline{R}_u^e}{\partial \underline{U}^e} \\ &= \int_{\mathcal{V}^e} \underline{\underline{B}}_u^T \frac{\partial \underline{\sigma}}{\partial \underline{\varepsilon}} \frac{\partial \underline{\varepsilon}}{\partial \underline{U}^e} dv \\ &= \int_{\mathcal{V}^e} \underline{\underline{B}}_u^T \frac{\partial \underline{\sigma}}{\partial \underline{\varepsilon}} \underline{\underline{B}}_u dv\end{aligned}\quad (\text{A.22})$$

$$\begin{aligned}\underline{K}_{u\gamma}^e &= \frac{\partial \underline{R}_u^e}{\partial \underline{\Gamma}^e} \\ &= \int_{\mathcal{V}^e} \underline{\underline{B}}_u^T \frac{\partial \underline{\sigma}}{\partial \underline{\gamma}} \frac{\partial \underline{\gamma}}{\partial \underline{\Gamma}^e} dv \\ &= \int_{\mathcal{V}^e} \underline{\underline{B}}_u^T \frac{\partial \underline{\sigma}}{\partial \underline{\gamma}} \underline{\underline{N}}_\gamma dv\end{aligned}\quad (\text{A.23})$$

$$\begin{aligned}\underline{\underline{K}}_{\gamma u}^e &= \frac{\partial \underline{R}_u^e}{\partial \underline{U}^e} \\ &= - \int_{\mathcal{V}^e} \underline{\underline{N}}_\gamma^T \frac{\partial \underline{\tau}}{\partial \underline{\varepsilon}} \frac{\partial \underline{\varepsilon}}{\partial \underline{U}^e} dv \\ &= - \int_{\mathcal{V}^e} \underline{\underline{N}}_\gamma^T \frac{\partial \underline{\tau}}{\partial \underline{\varepsilon}} \underline{\underline{B}}_u dv\end{aligned}\quad (\text{A.24})$$

$$\begin{aligned}\underline{\underline{K}}_{\gamma\gamma}^e &= \frac{\partial \underline{R}_\gamma^e}{\partial \underline{\Gamma}^e} \\ &= \int_{\mathcal{V}^e} \underline{\underline{B}}_\gamma^T \frac{\partial \underline{\xi}}{\partial \underline{\nabla\gamma}} \frac{\partial \underline{\nabla\gamma}}{\partial \underline{\Gamma}^e} dv + \int_{\mathcal{V}^e} \underline{\underline{N}}_\gamma^T \frac{\partial \underline{\pi}}{\partial \underline{\gamma}} \frac{\partial \underline{\gamma}}{\partial \underline{\Gamma}^e} dv - \int_{\mathcal{V}^e} \underline{\underline{N}}_\gamma^T \frac{\partial \underline{\tau}}{\partial \underline{\gamma}} \frac{\partial \underline{\gamma}}{\partial \underline{\Gamma}^e} dv \\ &= \int_{\mathcal{V}^e} \underline{\underline{B}}_\gamma^T \frac{\partial \underline{\xi}}{\partial \underline{\nabla\gamma}} \underline{\underline{B}}_\gamma^T dv + \int_{\mathcal{V}^e} \underline{\underline{N}}_\gamma^T \frac{\partial \underline{\pi}}{\partial \underline{\gamma}} \underline{\underline{N}}_\gamma dv - \int_{\mathcal{V}^e} \underline{\underline{N}}_\gamma^T \frac{\partial \underline{\tau}}{\partial \underline{\gamma}} \underline{\underline{N}}_\gamma dv\end{aligned}\quad (\text{A.25})$$

These derivatives in the tangent matrices will be illustrated as follows.

**Derivative**  $\frac{\partial \underline{\sigma}}{\partial \underline{\varepsilon}}$

The stress-strain constitutive relation reads:

$$\boldsymbol{\sigma} = \mathbf{C} : (\boldsymbol{\varepsilon} - \boldsymbol{\varepsilon}_p). \quad (\text{A.26})$$

Then the derivative is:

$$\frac{\partial \boldsymbol{\sigma}}{\partial \boldsymbol{\varepsilon}} = \mathbf{C} \quad (\text{A.27})$$

where  $\mathbf{C}$  is the elasticity tensor. The above can be rewritten in matrix form as:

$$\begin{bmatrix} \sigma_{11} \\ \sigma_{22} \\ \sigma_{33} \\ \sigma_{23} \\ \sigma_{13} \\ \sigma_{12} \end{bmatrix} = \begin{bmatrix} \lambda + 2\mu & \lambda & \lambda & 0 & 0 & 0 \\ \lambda & \lambda + 2\mu & \lambda & 0 & 0 & 0 \\ \lambda & \lambda & \lambda + 2\mu & 0 & 0 & 0 \\ 0 & 0 & 0 & \mu & 0 & 0 \\ 0 & 0 & 0 & 0 & \mu & 0 \\ 0 & 0 & 0 & 0 & 0 & \mu \end{bmatrix} \begin{bmatrix} \varepsilon_{11}^e \\ \varepsilon_{22}^e \\ \varepsilon_{33}^e \\ 2\varepsilon_{23}^e \\ 2\varepsilon_{13}^e \\ 2\varepsilon_{12}^e \end{bmatrix}, \underline{\sigma} = \underline{\underline{C}} \underline{\varepsilon}^e \quad (\text{A.28})$$

with  $\lambda$  and  $\mu$  lame constants. Finally, the matrix form gives:

$$\frac{\partial \underline{\sigma}}{\partial \underline{\varepsilon}} = \underline{\underline{C}} \quad (\text{A.29})$$

**Derivative**  $\frac{\partial \underline{\sigma}}{\partial \underline{\gamma}}$

Plastic strain can be calculated as (taken from (3.4)):

$$\boldsymbol{\varepsilon}_p = \sum_{\alpha=1}^q \gamma^\alpha \mathbf{P}^\alpha \quad (\text{A.30})$$

where  $\mathbf{P}^\alpha$  is the symmetrized Schmid tensor associated with slip system  $\alpha$ :

$$\mathbf{P}^\alpha = \frac{1}{2} (\mathbf{s}^\alpha \otimes \mathbf{m}^\alpha + \mathbf{m}^\alpha \otimes \mathbf{s}^\alpha) \quad (\text{A.31})$$

Therefore, the derivative with respect to slip system  $\alpha$  can be calculated as:

$$\begin{aligned} \frac{\partial \boldsymbol{\sigma}}{\partial \gamma^\alpha} &= \frac{\partial}{\partial \gamma^\alpha} [\mathbf{C} : (\boldsymbol{\varepsilon} - \boldsymbol{\varepsilon}_p)] \\ &= -\mathbf{C} : \frac{\partial \boldsymbol{\varepsilon}_p}{\partial \gamma^\alpha} \\ &= -\mathbf{C} : \mathbf{P}^\alpha \end{aligned} \quad (\text{A.32})$$

which is a second-order tensor. The above can be rewritten in matrix form. For plastic strain tensor  $\underline{\varepsilon}_p$ , its matrix form gives:

$$\underline{\varepsilon}_p = \begin{bmatrix} \varepsilon_p^{11} \\ \varepsilon_p^{22} \\ \varepsilon_p^{33} \\ 2\varepsilon_p^{23} \\ 2\varepsilon_p^{13} \\ 2\varepsilon_p^{12} \end{bmatrix} = \sum_{\alpha=1}^q \gamma^\alpha \underline{P}^\alpha = \gamma^1 \underline{P}^1 + \cdots + \gamma^q \underline{P}^q = \underbrace{\begin{bmatrix} \underline{P}^1 & \cdots & \underline{P}^q \end{bmatrix}}_{\underline{\underline{P}}} \begin{bmatrix} \gamma^1 \\ \vdots \\ \gamma^q \end{bmatrix} \quad (\text{A.33})$$

with

$$\underline{P}^\alpha = \begin{bmatrix} s_1^\alpha m_1^\alpha \\ s_2^\alpha m_2^\alpha \\ s_3^\alpha m_3^\alpha \\ s_1^\alpha m_2^\alpha + s_2^\alpha m_1^\alpha \\ s_1^\alpha m_3^\alpha + s_3^\alpha m_1^\alpha \\ s_2^\alpha m_3^\alpha + s_3^\alpha m_2^\alpha \end{bmatrix} \quad (\text{A.34})$$

Then,  $\underline{\varepsilon}_p$  can be assembled as:

$$\underline{\varepsilon}_p = \underline{\underline{P}} \underline{\gamma} \quad (\text{A.35})$$

Finally, the derivative in matrix form is:

$$\frac{\partial \underline{\sigma}}{\partial \underline{\gamma}} = -\underline{\underline{C}} \underline{\underline{P}} \quad (\text{A.36})$$

where  $\underline{\underline{C}}$  follows its form defined in (A.28).

**Derivative**  $\frac{\partial \underline{\tau}}{\partial \underline{\varepsilon}}$

Resolved shear stress on slip system  $\alpha$  is calculated as:

$$\tau^\alpha = \boldsymbol{\sigma} : (\mathbf{s}^\alpha \otimes \mathbf{m}^\alpha) \quad (\text{A.37})$$

Then, the derivative:

$$\begin{aligned} \frac{\partial \underline{\tau}}{\partial \underline{\varepsilon}} &= \frac{\partial}{\partial \underline{\varepsilon}} [\boldsymbol{\sigma} : (\mathbf{s}^\alpha \otimes \mathbf{m}^\alpha)] \\ &= \frac{\partial \boldsymbol{\sigma}}{\partial \underline{\varepsilon}} : (\mathbf{s}^\alpha \otimes \mathbf{m}^\alpha) \\ &= \mathbf{C} : (\mathbf{s}^\alpha \otimes \mathbf{m}^\alpha) \end{aligned} \quad (\text{A.38})$$

The above can be rewritten in matrix form. Considering resolved shear stress  $\tau^\alpha$  for slip system  $\alpha$ :

$$\begin{aligned} \tau^\alpha &= \begin{bmatrix} \sigma_{11} & \sigma_{12} & \sigma_{13} \\ \sigma_{21} & \sigma_{22} & \sigma_{23} \\ \sigma_{31} & \sigma_{32} & \sigma_{33} \end{bmatrix} : \begin{bmatrix} s_1^\alpha m_1^\alpha & s_1^\alpha m_2^\alpha & s_1^\alpha m_3^\alpha \\ s_2^\alpha m_1^\alpha & s_2^\alpha m_2^\alpha & s_2^\alpha m_3^\alpha \\ s_3^\alpha m_1^\alpha & s_3^\alpha m_2^\alpha & s_3^\alpha m_3^\alpha \end{bmatrix} \\ &= \begin{bmatrix} \sigma_{11} & \sigma_{12} & \sigma_{13} \\ \sigma_{12} & \sigma_{22} & \sigma_{23} \\ \sigma_{13} & \sigma_{23} & \sigma_{33} \end{bmatrix} : \begin{bmatrix} s_1^\alpha m_1^\alpha & s_1^\alpha m_2^\alpha & s_1^\alpha m_3^\alpha \\ s_2^\alpha m_1^\alpha & s_2^\alpha m_2^\alpha & s_2^\alpha m_3^\alpha \\ s_3^\alpha m_1^\alpha & s_3^\alpha m_2^\alpha & s_3^\alpha m_3^\alpha \end{bmatrix} \end{aligned}$$

Using the symmetry property of Cauchy stress tensor, it can be rewritten as:

$$\begin{aligned}\tau^\alpha &= \begin{bmatrix} s_1^\alpha m_1^\alpha & s_2^\alpha m_2^\alpha & s_3^\alpha m_3^\alpha & s_1^\alpha m_2^\alpha + s_2^\alpha m_1^\alpha & s_1^\alpha m_3^\alpha + s_3^\alpha m_1^\alpha & s_2^\alpha m_3^\alpha + s_3^\alpha m_2^\alpha \end{bmatrix} \begin{bmatrix} \sigma_{11} \\ \sigma_{22} \\ \sigma_{33} \\ \sigma_{23} \\ \sigma_{13} \\ \sigma_{12} \end{bmatrix} \\ &= \underline{\underline{P}}^{\alpha T} \underline{\underline{\sigma}}\end{aligned}$$

where  $\underline{\underline{P}}^\alpha$  is defined in (A.34). Matrix formulation reads:

$$\underline{\underline{\tau}} = \begin{bmatrix} \tau^1 \\ \vdots \\ \tau^q \end{bmatrix} = \begin{bmatrix} \underline{\underline{P}}^{1T} \\ \vdots \\ \underline{\underline{P}}^{qT} \end{bmatrix} \begin{bmatrix} \sigma_{11} \\ \sigma_{22} \\ \sigma_{33} \\ \sigma_{23} \\ \sigma_{13} \\ \sigma_{12} \end{bmatrix} = \underline{\underline{\underline{P}}}^T \underline{\underline{\sigma}}$$

Therefore,

$$\frac{\partial \underline{\underline{\tau}}}{\partial \underline{\underline{\varepsilon}}} = \underline{\underline{\underline{P}}}^T \frac{\partial \underline{\underline{\sigma}}}{\partial \underline{\underline{\varepsilon}}} = \underline{\underline{\underline{P}}}^T \underline{\underline{\underline{C}}}$$

**Derivative**  $\frac{\partial \underline{\underline{\tau}}}{\partial \underline{\underline{\gamma}}}$

The derivative can be calculated as:

$$\begin{aligned}\frac{\partial \underline{\underline{\tau}}}{\partial \underline{\underline{\gamma}}^\alpha} &= \frac{\partial}{\partial \underline{\underline{\gamma}}^\alpha} [\underline{\underline{\sigma}} : (\underline{\underline{s}}^\alpha \otimes \underline{\underline{m}}^\alpha)] \\ &= \frac{\partial \underline{\underline{\sigma}}}{\partial \underline{\underline{\gamma}}^\alpha} : (\underline{\underline{s}}^\alpha \otimes \underline{\underline{m}}^\alpha)\end{aligned}$$

Substituting (A.32), it can be rewritten as:

$$\frac{\partial \underline{\underline{\tau}}}{\partial \underline{\underline{\gamma}}^\alpha} = -\underline{\underline{\mathbf{C}}} : \underline{\underline{\mathbf{P}}}^\alpha : (\underline{\underline{s}}^\alpha \otimes \underline{\underline{m}}^\alpha) \quad (\text{A.39})$$

Using matrix form, it reads:

$$\begin{aligned}\frac{\partial \underline{\underline{\tau}}}{\partial \underline{\underline{\gamma}}} &= \frac{\partial}{\partial \underline{\underline{\gamma}}} (\underline{\underline{\underline{P}}}^T \underline{\underline{\sigma}}) \\ &= \underline{\underline{\underline{P}}}^T \frac{\partial \underline{\underline{\sigma}}}{\partial \underline{\underline{\gamma}}} = -\underline{\underline{\underline{P}}}^T \underline{\underline{\underline{C}}} \underline{\underline{\underline{P}}}\end{aligned} \quad (\text{A.40})$$

$$\mathbf{Derivative} \frac{\partial \underline{\xi}}{\partial \underline{\nabla \gamma}}$$

The microscopic stress  $\underline{\xi}$  has energetic and dissipative parts:

$$\underline{\xi} = \underline{\xi}_{en} + \underline{\xi}_{dis}$$

Energetic part  $\underline{\xi}_{en}^\alpha$  is calculated as (taken from (7.8)):

$$\underline{\xi}_{en}^\alpha = X_0 l_{en}^n |\mathbf{s}^\alpha \cdot \nabla \gamma^\alpha|^{n-2} \mathbf{s}^\alpha \otimes \mathbf{s}^\alpha \nabla \gamma^\alpha + X_0 l_{en}^n |\mathbf{l}^\alpha \cdot \nabla \gamma^\alpha|^{n-2} \mathbf{l}^\alpha \otimes \mathbf{l}^\alpha \nabla \gamma^\alpha \quad (\text{A.41})$$

The derivative yields:

$$\begin{aligned} \frac{\partial \underline{\xi}_{en}^\alpha}{\partial \nabla \gamma^\beta} &= \delta_{\alpha\beta} X_0 l_{en}^n \left[ \frac{\partial (|\mathbf{s}^\alpha \cdot \nabla \gamma^\alpha|^{n-2})}{\partial \nabla \gamma^\alpha} [\mathbf{s}^\alpha \otimes \mathbf{s}^\alpha] \nabla \gamma^\alpha + |\mathbf{s}^\alpha \cdot \nabla \gamma^\alpha|^{n-2} [\mathbf{s}^\alpha \otimes \mathbf{s}^\alpha] \mathbf{I} \right] \\ &\quad + \delta_{\alpha\beta} X_0 l_{en}^n \left[ \frac{\partial (|\mathbf{l}^\alpha \cdot \nabla \gamma^\alpha|^{n-2})}{\partial \nabla \gamma^\alpha} [\mathbf{l}^\alpha \otimes \mathbf{l}^\alpha] \nabla \gamma^\alpha + |\mathbf{l}^\alpha \cdot \nabla \gamma^\alpha|^{n-2} [\mathbf{l}^\alpha \otimes \mathbf{l}^\alpha] \mathbf{I} \right] \end{aligned} \quad (\text{A.42})$$

with

$$\frac{\partial (|\mathbf{s}^\alpha \cdot \nabla \gamma^\alpha|^{n-2})}{\partial \nabla \gamma^\alpha} = (n-2) |\mathbf{s}^\alpha \cdot \nabla \gamma^\alpha|^{n-3} \mathbf{s}^\alpha \quad (\text{A.43})$$

$$\frac{\partial (|\mathbf{l}^\alpha \cdot \nabla \gamma^\alpha|^{n-2})}{\partial \nabla \gamma^\alpha} = (n-2) |\mathbf{l}^\alpha \cdot \nabla \gamma^\alpha|^{n-3} \mathbf{l}^\alpha \quad (\text{A.44})$$

$$\delta_{\alpha\beta} = \begin{cases} 0 & \text{if } \alpha \neq \beta \\ 1 & \text{if } \alpha = \beta \end{cases} \quad (\text{A.45})$$

Substituting (A.43) and (A.44) into (A.42) we obtain:

$$\frac{\partial \underline{\xi}_{en}^\alpha}{\partial \nabla \gamma^\beta} = \delta_{\alpha\beta} X_0 l_{en}^n (n-1) [|\mathbf{s}^\alpha \cdot \nabla \gamma^\alpha|^{n-2} (\mathbf{s}^\alpha \otimes \mathbf{s}^\alpha) + |\mathbf{l}^\alpha \cdot \nabla \gamma^\alpha|^{n-2} (\mathbf{l}^\alpha \otimes \mathbf{l}^\alpha)] \quad (\text{A.46})$$

For dissipative part  $\underline{\xi}_{dis}$ :

$$\underline{\xi}_{dis}^\alpha = S_\xi^\alpha l_{dis}^2 R(\dot{e}_\xi^\alpha) \frac{\nabla^\alpha \dot{\gamma}^\alpha}{\dot{e}_\xi^\alpha}$$

with

$$S_{\xi_{n+1}}^\alpha = S_{\xi_n}^\alpha + \dot{S}_\xi^\alpha \Delta t, \quad \dot{S}_\xi^\alpha = \sum_{\beta=1}^q h_\xi^{\alpha\beta} (S_\xi^\beta) \dot{e}_\xi^\beta$$

$$\dot{e}_\xi^\alpha = \|l_{dis} \nabla^\alpha \dot{\gamma}^\alpha\|$$

$$\begin{aligned}\nabla^\alpha \dot{\gamma}^\alpha &= (\mathbf{s}^\alpha \cdot \nabla \dot{\gamma}^\alpha) \mathbf{s}^\alpha + (\mathbf{l}^\alpha \cdot \nabla \dot{\gamma}^\alpha) \mathbf{l}^\alpha \\ &= (\mathbf{s}^\alpha \otimes \mathbf{s}^\alpha) \nabla \dot{\gamma}^\alpha + (\mathbf{l}^\alpha \otimes \mathbf{l}^\alpha) \nabla \dot{\gamma}^\alpha\end{aligned}\quad (\text{A.47})$$

Then the dissipative part derivative can be converted into:

$$\begin{aligned}\frac{\partial \underline{\xi}_{dis}^\alpha}{\partial \nabla \dot{\gamma}^\beta} &= \frac{\partial \underline{\xi}_{dis}^\alpha}{\partial \nabla \dot{\gamma}^\beta} \frac{1}{\Delta t} \\ \frac{\partial \underline{\xi}_{dis}^\alpha}{\partial \nabla \dot{\gamma}^\beta} &= \underbrace{\frac{\partial S_\xi^\alpha}{\partial \nabla \dot{\gamma}^\beta} l_{dis}^2 R(\dot{e}_\xi^\alpha)}_{\text{I}} \frac{\nabla^\alpha \dot{\gamma}^\alpha}{\dot{e}_\xi^\alpha} + \underbrace{S_\xi^\alpha l_{dis}^2 \frac{\partial R(\dot{e}_\xi^\alpha)}{\partial \nabla \dot{\gamma}^\beta} \frac{\nabla^\alpha \dot{\gamma}^\alpha}{\dot{e}_\xi^\alpha}}_{\text{II}} + \underbrace{S_\xi^\alpha l_{dis}^2 R(\dot{e}_\xi^\alpha) \frac{\partial}{\partial \nabla \dot{\gamma}^\beta} \left( \frac{\nabla^\alpha \dot{\gamma}^\alpha}{\dot{e}_\xi^\alpha} \right)}_{\text{III}}\end{aligned}\quad (\text{A.48})$$

For derivative in I:

$$\begin{aligned}\frac{\partial S_\xi^\alpha}{\partial \nabla \dot{\gamma}^\beta} &= \frac{\partial S_\xi^\alpha}{\partial \dot{e}_\xi^\beta} \frac{\partial \dot{e}_\xi^\beta}{\partial \nabla \dot{\gamma}^\beta} \\ &= \Delta t H^{\alpha\beta} \frac{\partial \dot{e}_\xi^\beta}{\partial \nabla \dot{\gamma}^\beta}\end{aligned}\quad (\text{A.49})$$

$$\begin{aligned}\frac{\partial \dot{e}_\xi^\beta}{\partial \nabla \dot{\gamma}^\beta} &= \frac{\partial \dot{e}_\xi^\beta}{\partial \nabla^\beta \dot{\gamma}^\beta} \frac{\partial \nabla^\beta \dot{\gamma}^\beta}{\partial \nabla \dot{\gamma}^\beta} \\ &= l_{dis}^2 \frac{\nabla^\beta \dot{\gamma}^\beta}{\dot{e}_\xi^\beta} \frac{\partial \nabla^\beta \dot{\gamma}^\beta}{\partial \nabla \dot{\gamma}^\beta}\end{aligned}\quad (\text{A.50})$$

$$\frac{\partial \nabla^\beta \dot{\gamma}^\beta}{\partial \nabla \dot{\gamma}^\beta} = \mathbf{s}^\beta \otimes \mathbf{s}^\beta + \mathbf{l}^\beta \otimes \mathbf{l}^\beta \quad (\text{A.51})$$

For derivative in II:

$$\frac{\partial R(\dot{e}_\xi^\alpha)}{\partial \nabla \dot{\gamma}^\beta} = \delta_{\alpha\beta} \frac{\partial R(\dot{e}_\xi^\alpha)}{\partial \dot{e}_\xi^\alpha} \frac{\partial \dot{e}_\xi^\alpha}{\partial \nabla \dot{\gamma}^\alpha} \quad (\text{A.52})$$

For derivative in III:

$$\begin{aligned}\frac{\partial}{\partial \nabla \dot{\gamma}^\beta} \left( \frac{\nabla^\alpha \dot{\gamma}^\alpha}{\dot{e}_\xi^\alpha} \right) &= \frac{1}{\dot{e}_\xi^\alpha} \frac{\partial \nabla^\alpha \dot{\gamma}^\alpha}{\partial \nabla \dot{\gamma}^\beta} - \frac{\nabla^\alpha \dot{\gamma}^\alpha}{(\dot{e}_\xi^\alpha)^2} \frac{\partial \dot{e}_\xi^\alpha}{\partial \nabla \dot{\gamma}^\beta} \\ &= \delta_{\alpha\beta} \frac{1}{\dot{e}_\xi^\alpha} \frac{\partial \nabla^\alpha \dot{\gamma}^\alpha}{\partial \nabla \dot{\gamma}^\alpha} - \delta_{\alpha\beta} \frac{\nabla^\alpha \dot{\gamma}^\alpha}{(\dot{e}_\xi^\alpha)^2} \frac{\partial \dot{e}_\xi^\alpha}{\partial \nabla \dot{\gamma}^\alpha}\end{aligned}\quad (\text{A.53})$$

Noting  $\frac{\partial \underline{\xi}}{\partial \nabla \dot{\gamma}}$  as  $\underline{\underline{C}}_\xi^{\alpha\beta}$  for brevity, the matrix form can be detailed as:

$$\frac{\partial \underline{\xi}}{\partial \nabla \dot{\gamma}} = \underline{\underline{C}}_\xi^{\alpha\beta} = \begin{bmatrix} C_\xi^{11} & \cdots & C_\xi^{1q} \\ \vdots & \ddots & \vdots \\ C_\xi^{q1} & \cdots & C_\xi^{qq} \end{bmatrix} \quad (\text{A.54})$$

with each component  $C_{\xi}^{\alpha\beta}$  which has been calculated in (A.46) and (A.48):

$$C_{\xi}^{\alpha\beta} = \frac{\partial \xi_{en}^{\alpha}}{\partial \nabla \gamma^{\beta}} + \frac{\partial \xi_{dis}^{\alpha}}{\partial \nabla \dot{\gamma}^{\beta}} \frac{1}{\Delta t} \quad (\text{A.55})$$

**Derivative**  $\frac{\partial \underline{\pi}}{\partial \underline{\gamma}}$

The microscopic stress  $\pi_{dis}$  has the following form:

$$\pi_{dis}^{\alpha} = S_{\pi}^{\alpha} R(\dot{e}_{\pi}^{\alpha}) \frac{\dot{\gamma}^{\alpha}}{\dot{e}_{\pi}^{\alpha}} \quad (\text{A.56})$$

with

$$S_{\pi_{n+1}}^{\alpha} = S_{\pi_n}^{\alpha} + \dot{S}_{\pi}^{\alpha} \Delta t, \quad \dot{S}_{\pi}^{\alpha} = \sum_{\beta=1}^q h_{\pi}^{\alpha\beta} (S_{\pi}^{\beta}) \dot{e}_{\pi}^{\beta}$$

$$\dot{e}_{\pi}^{\alpha} = |\dot{\gamma}^{\alpha}| = \sqrt{(\dot{\gamma}^{\alpha})^2}$$

The derivative  $\frac{\partial \pi^{\alpha}}{\partial \gamma^{\beta}}$  can be calculated with respect to rate of plastic slips as:

$$\frac{\partial \pi^{\alpha}}{\partial \gamma^{\beta}} = \frac{\partial \pi^{\alpha}}{\partial \dot{\gamma}^{\beta}} \frac{1}{\Delta t}$$

Hence, the derivative has the form:

$$\frac{\partial \pi_{dis}^{\alpha}}{\partial \dot{\gamma}^{\beta}} = \underbrace{\frac{\partial S_{\pi}^{\alpha}}{\partial \dot{e}_{\pi}^{\beta}} R(\dot{e}_{\pi}^{\alpha}) \frac{\dot{\gamma}^{\alpha}}{\dot{e}_{\pi}^{\alpha}}}_{\text{I}} + \underbrace{S_{\pi}^{\alpha} \frac{\partial R(\dot{e}_{\pi}^{\alpha})}{\partial \dot{\gamma}^{\beta}} \frac{\dot{\gamma}^{\alpha}}{\dot{e}_{\pi}^{\alpha}}}_{\text{II}} + \underbrace{S_{\pi}^{\alpha} R(\dot{e}_{\pi}^{\alpha}) \frac{\partial}{\partial \dot{\gamma}^{\beta}} \left( \frac{\dot{\gamma}^{\alpha}}{\dot{e}_{\pi}^{\alpha}} \right)}_{\text{III}}$$

with derivative in I:

$$\frac{\partial S_{\pi}^{\alpha}}{\partial \dot{e}_{\pi}^{\beta}} = \frac{\partial S_{\pi}^{\alpha}}{\partial \dot{e}_{\pi}^{\beta}} \frac{\partial \dot{e}_{\pi}^{\beta}}{\partial \dot{\gamma}^{\beta}} = H^{\alpha\beta} \frac{\dot{\gamma}^{\beta}}{\dot{e}_{\pi}^{\beta}} \Delta t \quad (\text{A.57})$$

derivative in II:

$$\begin{aligned} \frac{\partial R(\dot{e}_{\pi}^{\alpha})}{\partial \dot{\gamma}^{\beta}} &= \delta_{\alpha\beta} \frac{\partial R(\dot{e}_{\pi}^{\alpha})}{\partial \dot{e}_{\pi}^{\alpha}} \frac{\partial \dot{e}_{\pi}^{\alpha}}{\partial \dot{\gamma}^{\beta}} \\ &= \delta_{\alpha\beta} \frac{\partial R(\dot{e}_{\pi}^{\alpha})}{\partial \dot{e}_{\pi}^{\alpha}} \frac{\dot{\gamma}^{\alpha}}{\dot{e}_{\pi}^{\alpha}} \end{aligned} \quad (\text{A.58})$$

derivative in III:

$$\frac{\partial}{\partial \dot{\gamma}^{\beta}} \left( \frac{\dot{\gamma}^{\alpha}}{\dot{e}_{\pi}^{\alpha}} \right) = 0. \quad (\text{A.59})$$

Therefore,

$$\begin{aligned}\frac{\partial \pi_{dis}^{\alpha}}{\partial \dot{\gamma}^{\beta}} &= \left[ H^{\alpha\beta} \frac{\dot{\gamma}^{\beta}}{\dot{e}_{\pi}^{\beta}} \Delta t \right] R(\dot{e}_{\pi}^{\alpha}) \frac{\dot{\gamma}^{\alpha}}{\dot{e}_{\pi}^{\alpha}} + S_{\pi}^{\alpha} \left[ \delta_{\alpha\beta} \frac{\partial R(\dot{e}_{\pi}^{\alpha})}{\partial \dot{e}_{\pi}^{\alpha}} \frac{\dot{\gamma}^{\alpha}}{\dot{e}_{\pi}^{\alpha}} \right] \frac{\dot{\gamma}^{\alpha}}{\dot{e}_{\pi}^{\alpha}} \\ &= H^{\alpha\beta} R(\dot{e}_{\pi}^{\alpha}) \frac{\dot{\gamma}^{\beta} \dot{\gamma}^{\alpha}}{\dot{e}_{\pi}^{\beta} \dot{e}_{\pi}^{\alpha}} \Delta t + \delta_{\alpha\beta} S_{\pi}^{\alpha} \frac{\partial R(\dot{e}_{\pi}^{\alpha})}{\partial \dot{e}_{\pi}^{\alpha}}\end{aligned}$$

Finally:

$$\begin{aligned}\frac{\partial \pi^{\alpha}}{\partial \underline{\gamma}^{\beta}} &= \left[ H^{\alpha\beta} R(\dot{e}_{\pi}^{\alpha}) \frac{\dot{\gamma}^{\beta} \dot{\gamma}^{\alpha}}{\dot{e}_{\pi}^{\beta} \dot{e}_{\pi}^{\alpha}} \Delta t + \delta_{\alpha\beta} S_{\pi}^{\alpha} \frac{\partial R(\dot{e}_{\pi}^{\alpha})}{\partial \dot{e}_{\pi}^{\alpha}} \right] \frac{1}{\Delta t} \\ &= H^{\alpha\beta} R(\dot{e}_{\pi}^{\alpha}) \frac{\dot{\gamma}^{\beta} \dot{\gamma}^{\alpha}}{\dot{e}_{\pi}^{\beta} \dot{e}_{\pi}^{\alpha}} + \delta_{\alpha\beta} S_{\pi}^{\alpha} \frac{\partial R(\dot{e}_{\pi}^{\alpha})}{\partial \dot{e}_{\pi}^{\alpha}} \frac{1}{\Delta t}\end{aligned}\tag{A.60}$$

Noting  $\frac{\partial \underline{\pi}}{\partial \underline{\gamma}}$  as  $C_{\pi}^{\alpha\beta}$  for brevity, the matrix form can be detailed as:

$$\frac{\partial \underline{\pi}}{\partial \underline{\gamma}} = \underline{\underline{C}}_{\pi}^{\alpha\beta} = \begin{bmatrix} C_{\pi}^{11} & \cdots & C_{\pi}^{1q} \\ \vdots & \ddots & \vdots \\ C_{\pi}^{q1} & \cdots & C_{\pi}^{qq} \end{bmatrix}$$

with each component  $C_{\pi}^{\alpha\beta}$  calculated by (A.60).

## Summary

The tangent matrices can be rewritten as:

$$\underline{\underline{K}}_{uu}^e = \int_{\mathcal{V}^e} \underline{\underline{B}}_u^T \underline{\underline{C}} \underline{\underline{B}}_u dv\tag{A.61}$$

$$\underline{\underline{K}}_{u\underline{\gamma}}^e = - \int_{\mathcal{V}^e} \underline{\underline{B}}_u^T \underline{\underline{C}} \underline{\underline{P}} \underline{\underline{N}}_{\gamma} dv\tag{A.62}$$

$$\underline{\underline{K}}_{\gamma u}^e = - \int_{\mathcal{V}^e} \underline{\underline{N}}_{\gamma}^T \underline{\underline{P}}^T \underline{\underline{C}} \underline{\underline{B}}_u dv\tag{A.63}$$

$$\underline{\underline{K}}_{\gamma\gamma}^e = \int_{\mathcal{V}^e} \underline{\underline{B}}_{\gamma}^T \underline{\underline{C}}_{\xi}^{\alpha\beta} \underline{\underline{B}}_{\gamma}^T dv + \int_{\mathcal{V}^e} \underline{\underline{N}}_{\gamma}^T \underline{\underline{C}}_{\pi}^{\alpha\beta} \underline{\underline{N}}_{\gamma} dv + \int_{\mathcal{V}^e} \underline{\underline{N}}_{\gamma}^T \underline{\underline{P}}^T \underline{\underline{C}} \underline{\underline{P}} \underline{\underline{N}}_{\gamma} dv\tag{A.64}$$

and associated residuals as:

$$\underline{R}_u^e = \int_{\mathcal{V}^e} \underline{\underline{B}}_u^T \underline{\sigma} dv\tag{A.65}$$

$$\underline{R}_{\gamma}^e = \int_{\mathcal{V}^e} \underline{\underline{B}}_{\gamma}^T \underline{\xi} dv + \int_{\mathcal{V}^e} \underline{\underline{N}}_{\gamma}^T \underline{\pi} dv - \int_{\mathcal{V}^e} \underline{\underline{N}}_{\gamma}^T \underline{\underline{P}}^T \underline{\sigma} dv\tag{A.66}$$

## A.5 Shape functions for small deformation example

The small deformation SGCP model has been implemented using an eight-noded plane strain element as shown in Fig. A.2. The shape functions are as follows:

$$\left\{ \begin{array}{l} N_1 = \frac{1}{4}(1-\xi)(1-\eta)(-\xi-\eta-1) \\ N_2 = \frac{1}{4}(1+\xi)(1-\eta)(+\xi-\eta-1) \\ N_3 = \frac{1}{4}(1+\xi)(1+\eta)(+\xi+\eta-1) \\ N_4 = \frac{1}{4}(1-\xi)(1+\eta)(-\xi+\eta-1) \\ N_5 = \frac{1}{2}(1-\eta)(1+\xi)(1-\xi) \\ N_6 = \frac{1}{2}(1+\xi)(1+\eta)(1-\eta) \\ N_7 = \frac{1}{2}(1+\eta)(1+\xi)(1-\xi) \\ N_8 = \frac{1}{2}(1-\xi)(1+\eta)(1-\eta) \end{array} \right. \quad (\text{A.67})$$

For Gauss integration scheme, nine integration points with natural coordinates  $(\xi, \eta)$  and weighting factors  $W_p$  are adopted as listed in A.1.

Number	$\xi$	$\eta$	$W_p$
1	$-\sqrt{3/5}$	$-\sqrt{3/5}$	$25/81$
2	0	$-\sqrt{3/5}$	$40/81$
3	$+\sqrt{3/5}$	$-\sqrt{3/5}$	$25/81$
4	$-\sqrt{3/5}$	0	$40/81$
5	0	0	$64/81$
6	$+\sqrt{3/5}$	0	$40/81$
7	$-\sqrt{3/5}$	$+\sqrt{3/5}$	$25/81$
8	0	$+\sqrt{3/5}$	$40/81$
9	$+\sqrt{3/5}$	$+\sqrt{3/5}$	$25/81$

**Tab. A.1.** Gauss points for quadratic quadrilateral element.

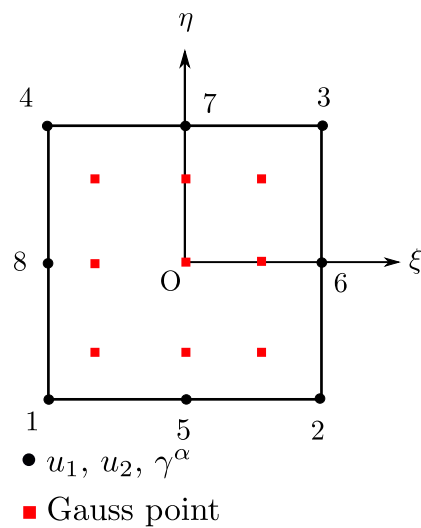


**Fig. A.2.** The quadratic quadrilateral element with natural coordinates.

# Appendix B

## Numerical aspects of large deformation SGCP

In this appendix, numerical implementation details are presented. This appendix shares several parts with small deformation appendix. In section B.1, arrangement of degrees of freedom and interpolation functions are first introduced. Regularization function of the viscoplastic function is consistent with that in small deformation, hence it is not presented in this appendix. In section B.2, calculations of tangent matrices are presented in detail. These formulations are quite different and complicated compared to those in small deformation, due to the multiplicative decomposition in finite deformation. Finally, shape functions used in the finite deformation example are presented in section B.3.

### B.1 Degrees of freedom and interpolation functions

The same type of arrangement for DOF as defined in (A.1) is employed for finite deformation implementation. In small deformation implementation, most of the tensor variables are symmetric. Therefore, voigt notation is adopted. For instance, Cauchy stress tensor  $\sigma$  can be expressed as:

$$\boldsymbol{\sigma} = \begin{bmatrix} \sigma_{11} & \sigma_{12} & \sigma_{13} \\ \sigma_{21} & \sigma_{22} & \sigma_{23} \\ \sigma_{31} & \sigma_{32} & \sigma_{33} \end{bmatrix} \implies \underline{\sigma} = [\sigma_{11} \ \sigma_{22} \ \sigma_{33} \ \sigma_{23} \ \sigma_{13} \ \sigma_{12}]^T$$

However, it is not the same case as for finite deformation implementation in the reference configuration. Therefore, it is necessary to define how unsymmetrical tensor variables are stored as vector forms. In this thesis, a tensor  $\mathbf{A}$ , whether symmetric or unsymmetrical in finite deformation implementation processes, is arranged as:

$$\mathbf{A} = \begin{bmatrix} A_{11} & A_{12} & A_{13} \\ A_{21} & A_{22} & A_{23} \\ A_{31} & A_{32} & A_{33} \end{bmatrix} \implies \underline{\mathbf{A}} = [A_{11} \ A_{22} \ A_{33} \ A_{12} \ A_{23} \ A_{31} \ A_{21} \ A_{32} \ A_{13}]^T$$

Displacement gradient tensor  $\nabla \mathbf{u}$ , deformation gradient tensor  $\mathbf{F}$ , the first Piola-Kirchhoff stress tensor  $\mathbf{P}$  and derivatives derived with these variables will strictly follow this arrangement. In addition, fourth-order tensor is also frequently used in the following. In this work, a fourth-order

tensor can be re-arranged in a matrix form. For instance, a fourth-order tensor  $\mathbb{C}$  whose components are named as  $C_{ijkl}$  can be re-arranged in a matrix form as follows:

$$\mathbb{C} = \begin{bmatrix} C_{1111} & C_{1122} & C_{1133} & C_{1112} & C_{1123} & C_{1131} & C_{1121} & C_{1132} & C_{1113} \\ C_{2211} & \ddots & & & & & & & \\ C_{3311} & & \ddots & & & & & & \\ C_{1211} & & & \ddots & & & & & \\ C_{2311} & & & & \ddots & & & & \\ C_{3111} & & & & & \ddots & & & \\ C_{2111} & & & & & & \ddots & & \\ C_{3211} & & & & & & & \ddots & \\ C_{1311} & & & & & & & & \ddots \end{bmatrix} \quad (\text{B.1})$$

## Displacement gradient interpolation function

Displacement gradient vector form can be expressed as:

$$\underline{\nabla u} = [ u_{1,1} \ u_{2,2} \ u_{3,3} \ u_{1,2} \ u_{2,3} \ u_{3,1} \ u_{2,1} \ u_{3,2} \ u_{1,3} ]^T$$

Then a detailed form of displacement gradient interpolation can be expressed as:

$$\begin{bmatrix} u_{1,1} \\ u_{2,2} \\ u_{3,3} \\ u_{1,2} \\ u_{2,3} \\ u_{3,1} \\ u_{2,1} \\ u_{3,2} \\ u_{1,3} \end{bmatrix} = \begin{bmatrix} \frac{\partial N^1}{\partial X_1} & \dots & \frac{\partial N^{nn}}{\partial X_1} & 0 & \dots & 0 & 0 & \dots & 0 \\ 0 & \dots & 0 & \frac{\partial N^1}{\partial X_2} & \dots & \frac{\partial N^{nn}}{\partial X_2} & 0 & \dots & 0 \\ 0 & \dots & 0 & 0 & \dots & 0 & \frac{\partial N^1}{\partial X_3} & \dots & \frac{\partial N^{nn}}{\partial X_3} \\ \frac{\partial N^1}{\partial X_2} & \dots & \frac{\partial N^{nn}}{\partial X_2} & 0 & \dots & 0 & 0 & \dots & 0 \\ 0 & \dots & 0 & \frac{\partial N^1}{\partial X_3} & \dots & \frac{\partial N^{nn}}{\partial X_3} & 0 & \dots & 0 \\ 0 & \dots & 0 & 0 & \dots & 0 & \frac{\partial N^1}{\partial X_1} & \dots & \frac{\partial N^{nn}}{\partial X_1} \\ 0 & \dots & 0 & \frac{\partial N^1}{\partial X_1} & \dots & \frac{\partial N^{nn}}{\partial X_1} & 0 & \dots & 0 \\ 0 & \dots & 0 & 0 & \dots & 0 & \frac{\partial N^1}{\partial X_2} & \dots & \frac{\partial N^{nn}}{\partial X_2} \\ \frac{\partial N^1}{\partial X_3} & \dots & \frac{\partial N^{nn}}{\partial X_3} & 0 & \dots & 0 & 0 & \dots & 0 \end{bmatrix} \begin{bmatrix} U_1^1 \\ \vdots \\ U_1^{nn} \\ U_2^1 \\ \vdots \\ U_2^{nn} \\ U_3^1 \\ \vdots \\ U_3^{nn} \end{bmatrix} \quad (\text{B.2})$$

$$\underline{\nabla u} = \underline{\underline{B}}_u \underline{U} \quad (\text{B.3})$$

Interpolation functions  $\underline{\underline{N}}_u$ ,  $\underline{\underline{N}}_\gamma$  and  $\underline{\underline{B}}_\gamma$  remain identical to their expressions for small deformation.

## Deformation gradient

The deformation gradient is given by:

$$\underline{\mathbf{F}} = \frac{\partial \mathbf{x}}{\partial \underline{\mathbf{X}}} = \underline{\nabla} \mathbf{u} + \underline{\mathbf{I}} \quad (\text{B.4})$$

The vector form for the deformation gradient  $\underline{F}$  is arranged as:

$$\underline{F} = [ F_{11} \ F_{22} \ F_{33} \ F_{12} \ F_{23} \ F_{31} \ F_{21} \ F_{32} \ F_{13} ]^T$$

Then, it can be written as:

$$\underline{F} = \underline{\underline{B}}_u \underline{U} + \underline{\underline{I}}$$

with  $\underline{\underline{I}}$  a vector form of identity tensor.

## B.2 Tangent matrices

The residuals in finite deformation SGCP:

$$\begin{aligned} \underline{R}_u^e &= \int_{V_{e0}} \underline{\underline{B}}_u^T \underline{P} dv - \int_{S_{e0}^t} \underline{\underline{N}}_u^T \underline{t} ds = 0 \\ \underline{R}_\gamma^e &= \int_{V_{e0}} \underline{\underline{B}}_\gamma^T \underline{\xi} dv + \int_{V_{e0}} \underline{\underline{N}}_\gamma^T \underline{\pi} dv - \int_{V_{e0}} \underline{\underline{N}}_\gamma^T \underline{\tau} dv - \int_{S_{e0}^\chi} \underline{\underline{N}}_\gamma^T \underline{\chi} ds = 0 \end{aligned} \quad (\text{B.5})$$

Considering null power expenditure on the boundary, the tangent matrices yield:

$$\begin{aligned} \underline{\underline{K}}_{uu} &= \frac{\partial \underline{R}_u^e}{\partial \underline{U}^e} \\ &= \int_{V_{e0}} \underline{\underline{B}}_u^T \frac{\partial \underline{P}}{\partial \underline{F}} \frac{\partial \underline{F}}{\partial \underline{U}} dv \\ &= \int_{V_{e0}} \underline{\underline{B}}_u^T \frac{\partial \underline{P}}{\partial \underline{F}} \underline{\underline{B}}_u dv \end{aligned} \quad (\text{B.6})$$

$$\begin{aligned} \underline{\underline{K}}_{u\gamma} &= \frac{\partial \underline{R}_u^e}{\partial \underline{\Gamma}^e} \\ &= \int_{V_{e0}} \underline{\underline{B}}_u^T \frac{\partial \underline{P}}{\partial \underline{\gamma}} \frac{\partial \underline{\gamma}}{\partial \underline{\Gamma}} dv \\ &= \int_{V_{e0}} \underline{\underline{B}}_u^T \frac{\partial \underline{P}}{\partial \underline{\gamma}} \underline{\underline{N}}_\gamma dv \end{aligned} \quad (\text{B.7})$$

$$\begin{aligned} \underline{\underline{K}}_{\gamma u} &= \frac{\partial \underline{R}_\gamma^e}{\partial \underline{U}^e} \\ &= - \int_{V_{e0}} \underline{\underline{N}}_\gamma^T \frac{\partial \underline{\tau}}{\partial \underline{F}} \frac{\partial \underline{F}}{\partial \underline{U}} dv \\ &= - \int_{V_{e0}} \underline{\underline{N}}_\gamma^T \frac{\partial \underline{\tau}}{\partial \underline{F}} \underline{\underline{B}}_u dv \end{aligned} \quad (\text{B.8})$$

$$\begin{aligned}
\underline{\underline{K}}_{\gamma\gamma} &= \frac{\partial \underline{\underline{R}}_{\gamma}^e}{\partial \underline{\underline{\Gamma}}^e} \\
&= \int_{V_{e0}} \underline{\underline{B}}_{\gamma}^T \frac{\partial \underline{\xi}}{\partial \underline{\nabla}_{\gamma}} \frac{\partial \underline{\nabla}_{\gamma}}{\partial \underline{\underline{\Gamma}}} dv + \int_{V_{e0}} \underline{\underline{N}}_{\gamma}^T \frac{\partial \underline{\pi}}{\partial \underline{\gamma}} \frac{\partial \underline{\gamma}}{\partial \underline{\underline{\Gamma}}} dv - \int_{V_{e0}} \underline{\underline{N}}_{\gamma}^T \frac{\partial \underline{\tau}}{\partial \underline{\gamma}} \frac{\partial \underline{\gamma}}{\partial \underline{\underline{\Gamma}}} dv \\
&= \int_{V_{e0}} \underline{\underline{B}}_{\gamma}^T \frac{\partial \underline{\xi}}{\partial \underline{\nabla}_{\gamma}} \underline{\underline{B}}_{\gamma} dv + \int_{V_{e0}} \underline{\underline{N}}_{\gamma}^T \frac{\partial \underline{\pi}}{\partial \underline{\gamma}} \underline{\underline{N}}_{\gamma} dv - \int_{V_{e0}} \underline{\underline{N}}_{\gamma}^T \frac{\partial \underline{\tau}}{\partial \underline{\gamma}} \underline{\underline{N}}_{\gamma} dv
\end{aligned} \tag{B.9}$$

Before preparation of derivatives in the tangent matrices, several tensor operations are defined.

Dyad function:

$$\underline{\underline{C}} = \underline{\underline{A}} \otimes \underline{\underline{B}}, \quad C_{ijkl} = A_{ij} B_{kl} \tag{B.10}$$

Top dyad function:

$$\underline{\underline{C}} = \underline{\underline{A}} \bar{\otimes} \underline{\underline{B}}, \quad C_{ijkl} = A_{ik} B_{jl} \tag{B.11}$$

Bottom dyad function:

$$\underline{\underline{C}} = \underline{\underline{A}} \otimes \underline{\underline{B}}, \quad C_{ijkl} = A_{il} B_{jk} \tag{B.12}$$

Tensor contraction:

$$\underline{\underline{C}} = \underline{\underline{A}} : \underline{\underline{B}}, \quad C_{ij} = A_{ijkl} B_{kl} \tag{B.13}$$

**Derivative**  $\frac{\partial P}{\partial F}$

To calculate this derivative, the relation between  $P$  and  $F$  should be figured out. The first Piola-Kirchhoff stress tensor gives the relation:

$$\mathbf{P} = J \boldsymbol{\sigma} \mathbf{F}^{T-1}. \tag{B.14}$$

By pulling back Cauchy stress from the current configuration to the reference configuration, it gives the relation:

$$\mathbf{S} = J \mathbf{F}^{-1} \boldsymbol{\sigma} \mathbf{F}^{-T}. \tag{B.15}$$

By pushing forward  $\mathbf{S}^e$  to the current configuration, it gives:

$$\boldsymbol{\sigma} = J^{-1} \mathbf{F}^e \mathbf{S}^e \mathbf{F}^{eT}$$

The above relations yields:

$$\mathbf{P} = \mathbf{F} \mathbf{S}, \quad \mathbf{S} = \mathbf{F}^{p-1} \mathbf{S}^e \mathbf{F}^{p-T} \tag{B.16}$$

Therefore, the derivative calculated with tensor notations can be written as:

$$\frac{\partial \mathbf{P}}{\partial \mathbf{F}} = \frac{\partial}{\partial \mathbf{F}} (\mathbf{F} \mathbf{S}) + \frac{\partial}{\partial \mathbf{S}} (\mathbf{F} \mathbf{S}) : \frac{\partial \mathbf{S}}{\partial \mathbf{C}} : \frac{\partial \mathbf{C}}{\partial \mathbf{F}}$$

with<sup>1</sup>

$$\begin{aligned}\frac{\partial}{\partial \mathbf{F}} (\mathbf{FS}) &= \frac{\partial}{\partial F_{kl}} (F_{im} S_{mj}) \\ &= \delta_{ik} \delta_{ml} S_{mj} \\ &= \delta_{ik} S_{jm} \delta_{ml} \\ &= \mathbf{I} \overline{\otimes} \mathbf{S}\end{aligned}\tag{B.17}$$

$$\begin{aligned}\frac{\partial}{\partial \mathbf{S}} (\mathbf{FS}) &= \frac{\partial}{\partial S_{kl}} (F_{im} S_{mj}) \\ &= F_{im} \delta_{mk} \delta_{jl} \\ &= (F_{im} \delta_{mk}) \delta_{jl} \\ &= \mathbf{F} \overline{\otimes} \mathbf{I}\end{aligned}\tag{B.18}$$

$$\begin{aligned}\frac{\partial \mathbf{C}}{\partial \mathbf{F}} &= \frac{\partial}{\partial \mathbf{F}} (\mathbf{F}^T \mathbf{F}) \\ &= \frac{\partial}{\partial F_{kl}} (F_{mi} F_{mj}) \\ &= (\delta_{mk} \delta_{il} F_{mj} + F_{mi} \delta_{mk} \delta_{jl}) \\ &= (\delta_{il} F_{jm}^T \delta_{mk} + F_{im}^T \delta_{mk} \delta_{jl}) \\ &= (\mathbf{I} \underline{\otimes} \mathbf{F}^T + \mathbf{F}^T \overline{\otimes} \mathbf{I}).\end{aligned}\tag{B.19}$$

It can be rewritten as:

$$\frac{\partial \mathbf{P}}{\partial \mathbf{F}} = \mathbf{I} \overline{\otimes} \mathbf{S} + \mathbf{F} \overline{\otimes} \mathbf{I} : \frac{\partial \mathbf{S}}{\partial \mathbf{C}} : (\mathbf{I} \underline{\otimes} \mathbf{F}^T + \mathbf{F}^T \overline{\otimes} \mathbf{I})\tag{B.20}$$

Equation (B.20) is a general derivative for  $\mathbf{P}$  with respect to  $\mathbf{F}$ . When using different elastic constitutive models (*e.g.*, Neo-Hookean, Saint Venant–Kirchhoff, *etc.*), only the term  $\frac{\partial \mathbf{S}}{\partial \mathbf{C}}$  varies. In this work, the elastic constitutive model is expressed as:

$$\left\{ \begin{array}{lcl} \mathbf{S}^e & = & \mathbb{C} : \frac{1}{2} (\mathbf{C}^e - \mathbf{I}) \\ \mathbf{C} & = & \mathbf{F}^{p^T} \mathbf{C}^e \mathbf{F}^p \\ \mathbf{S} & = & \mathbf{F}^{p^{-1}} \mathbf{S}^e \mathbf{F}^{p^{-T}} \end{array} \right.\tag{B.21}$$

Then, the term  $\frac{\partial \mathbf{S}}{\partial \mathbf{C}}$  can be obtained as:

$$\frac{\partial \mathbf{S}}{\partial \mathbf{C}} = \frac{\partial \mathbf{S}}{\partial \mathbf{S}^e} : \frac{\partial \mathbf{S}^e}{\partial \mathbf{C}^e} : \frac{\partial \mathbf{C}^e}{\partial \mathbf{C}}$$

---

<sup>1</sup>Note that, index notations are frequently used to calculate derivatives involved with tensors hereafter.

with

$$\begin{aligned}
\frac{\partial \mathbf{S}}{\partial \mathbf{S}^e} &= \frac{\partial F_{im}^{p^{-1}} S_{mn}^e F_{nj}^{-T}}{\partial S_{kl}^e} \\
&= F_{im}^{p^{-1}} \delta_{mk} \delta_{nl} F_{nj}^{-T} \\
&= \left( F_{im}^{p^{-1}} \delta_{mk} \right) \left( F_{jn}^{-1} \delta_{nl} \right) \\
&= \mathbf{F}^{p^{-1}} \overline{\otimes} \mathbf{F}^{p^{-1}}
\end{aligned} \tag{B.22}$$

$$\begin{aligned}
\frac{\partial \mathbf{S}^e}{\partial \mathbf{C}^e} &= \frac{\partial}{\partial \mathbf{C}^e} \left( \mathbb{C} : \frac{1}{2} (\mathbf{C}^e - \mathbf{I}) \right) \\
&= \frac{1}{2} \frac{\partial}{\partial \mathbf{C}^e} (\mathbb{C} : \mathbf{C}^e) \\
&= \frac{1}{2} \mathbb{C}
\end{aligned} \tag{B.23}$$

$$\begin{aligned}
\frac{\partial \mathbf{C}^e}{\partial \mathbf{C}} &= \frac{\partial}{\partial C_{kl}} \left( F_{im}^{p^{-T}} C_{mn} F_{nj}^{p^{-1}} \right) \\
&= F_{im}^{p^{-T}} \delta_{mk} \delta_{nl} F_{nj}^{p^{-1}} \\
&= \left( F_{im}^{p^{-T}} \delta_{mk} \right) \left( F_{jn}^{p^{-1}} \delta_{nl} \right) \\
&= \mathbf{F}^{p^{-T}} \overline{\otimes} \mathbf{F}^{p^{-T}}
\end{aligned} \tag{B.24}$$

To summarize, the term  $\frac{\partial \mathbf{S}}{\partial \mathbf{C}}$  can be rewritten as:

$$\frac{\partial \mathbf{S}}{\partial \mathbf{C}} = \left( \mathbf{F}^{p^{-1}} \overline{\otimes} \mathbf{F}^{p^{-1}} \right) : \left( \frac{1}{2} \mathbb{C} \right) : \left( \mathbf{F}^{p^{-T}} \overline{\otimes} \mathbf{F}^{p^{-T}} \right) \tag{B.25}$$

Finally, the derivative  $\frac{\partial \mathbf{P}}{\partial \mathbf{F}}$  is:

$$\frac{\partial \mathbf{P}}{\partial \mathbf{F}} = \mathbf{I} \overline{\otimes} \mathbf{S} + (\mathbf{F} \overline{\otimes} \mathbf{I}) : \left( \mathbf{F}^{p^{-1}} \overline{\otimes} \mathbf{F}^{p^{-1}} \right) : \left( \frac{1}{2} \mathbb{C} \right) : \left( \mathbf{F}^{p^{-T}} \overline{\otimes} \mathbf{F}^{p^{-T}} \right) : (\mathbf{I} \underline{\otimes} \mathbf{F}^T + \mathbf{F}^T \overline{\otimes} \mathbf{I}) \tag{B.26}$$

Equation (B.26) presents the derivative  $\frac{\partial \mathbf{P}}{\partial \mathbf{F}}$  calculated by tensor components. In fact, its matrix form  $\frac{\partial \underline{\mathbf{P}}}{\partial \underline{\mathbf{F}}}$  will be assembled into (B.6). Therefore, it is of vital importance to develop and rearrange the tensor form into matrix form, which strictly corresponds to interpolation functions. During calculations in the UEL for (B.26), tensor variables are used to obtain the derivative  $\frac{\partial \mathbf{P}}{\partial \mathbf{F}}$  in a tensor form. It is clear that the derivative has an order of four. Special attention should be paid to the elasticity tensor  $\mathbb{C}$  for its tensor form. Bearing in mind the classical elasticity relations:

$$\boldsymbol{\sigma} = \mathbb{C} : \boldsymbol{\varepsilon}, \quad \boldsymbol{\sigma} = 2\mu \boldsymbol{\varepsilon} + \lambda \text{Tr}(\boldsymbol{\varepsilon}) \mathbf{I} \tag{B.27}$$

the elasticity relation in finite deformation reads:

$$\mathbf{S}^e = \mathbb{C} : \mathbf{E}^e, \quad \mathbf{S}^e = 2\mu \mathbf{E}^e + \lambda \text{Tr}(\mathbf{E})^e \mathbf{I} \quad (\text{B.28})$$

Expanding the above equation in a matrix form, it gives:

$$\begin{bmatrix} S_{11}^e \\ S_{22}^e \\ S_{33}^e \\ S_{12}^e \\ S_{23}^e \\ S_{31}^e \\ S_{21}^e \\ S_{32}^e \\ S_{13}^e \end{bmatrix} = \begin{bmatrix} \lambda + 2\mu & \lambda & \lambda & 0 & 0 & 0 & 0 & 0 & 0 \\ \lambda & \lambda + 2\mu & \lambda & 0 & 0 & 0 & 0 & 0 & 0 \\ \lambda & \lambda & \lambda + 2\mu & 0 & 0 & 0 & 0 & 0 & 0 \\ 0 & 0 & 0 & 2\mu & 0 & 0 & 0 & 0 & 0 \\ 0 & 0 & 0 & 0 & 2\mu & 0 & 0 & 0 & 0 \\ 0 & 0 & 0 & 0 & 0 & 2\mu & 0 & 0 & 0 \\ 0 & 0 & 0 & 0 & 0 & 0 & 2\mu & 0 & 0 \\ 0 & 0 & 0 & 0 & 0 & 0 & 0 & 2\mu & 0 \\ 0 & 0 & 0 & 0 & 0 & 0 & 0 & 0 & 2\mu \end{bmatrix} \begin{bmatrix} E_{11}^e \\ E_{22}^e \\ E_{33}^e \\ E_{12}^e \\ E_{23}^e \\ E_{31}^e \\ E_{21}^e \\ E_{32}^e \\ E_{13}^e \end{bmatrix} \quad (\text{B.29})$$

$$\underline{\mathbf{S}}^e = \underline{\mathbb{C}} \underline{\mathbf{E}}^e$$

Referring to (B.29) and following the transformation between fourth-order tensor and its matrix form, the elastic modulus tensor can be assembled. When assembling the fourth-order tensor  $\mathbb{C}$ , the subscripts in (B.29) should be strictly followed. For instance,  $\mathbb{C}(1, 1, 1, 1) = C_{1111} = \lambda + 2\mu$  and so on. In the meantime, the derivative  $\frac{\partial \underline{\mathbf{P}}}{\partial \underline{\mathbf{F}}}$  yields a fourth-order tensor. Following the transformation in (B.1), it can be re-arranged into matrix form  $\frac{\partial \underline{\mathbf{P}}}{\partial \underline{\mathbf{F}}}$ .

**Derivative**  $\frac{\partial \underline{\mathbf{P}}}{\partial \underline{\gamma}}$

To calculate this derivative, the following relations are needed:

$$\begin{cases} \mathbf{P} = \mathbf{FS} \\ \mathbf{S} = \mathbf{F}^{p-1} \mathbf{S}^e \mathbf{F}^{p-T} \end{cases} \quad (\text{B.30})$$

The derivative with respect to slip system  $\alpha$  can be obtained as:

$$\begin{aligned} \frac{\partial \underline{\mathbf{P}}}{\partial \underline{\gamma}^\alpha} &= \frac{\partial \underline{\mathbf{P}}}{\partial \underline{\mathbf{S}}} : \frac{\partial \underline{\mathbf{S}}}{\partial \underline{\gamma}^\alpha} \\ &= \frac{\partial \underline{\mathbf{P}}}{\partial \underline{\mathbf{S}}} : \frac{\partial \underline{\mathbf{S}}}{\partial \underline{\mathbf{S}}^e} : \frac{\partial \underline{\mathbf{S}}^e}{\partial \underline{\mathbf{F}}^e} : \frac{\partial \underline{\mathbf{F}}^e}{\partial \underline{\gamma}^\alpha} \end{aligned}$$

with

$$\begin{aligned} \frac{\partial \underline{\mathbf{P}}}{\partial \underline{\mathbf{S}}} &= \frac{\partial}{\partial S_{kl}} (F_{im} S_{mj}) \\ &= F_{im} \delta_{mk} \delta_{jl} \\ &= \mathbf{F} \otimes \mathbf{I} \end{aligned} \quad (\text{B.31})$$

$$\begin{aligned}\frac{\partial \mathbf{S}^e}{\partial \mathbf{F}^e} &= \frac{\partial \mathbf{S}^e}{\partial \mathbf{C}^e} : \frac{\partial \mathbf{C}^e}{\partial \mathbf{F}^e} \\ &= \frac{1}{2} \mathbb{C} : (\mathbf{I} \underline{\otimes} \mathbf{F}^{eT} + \mathbf{F}^{eT} \overline{\otimes} \mathbf{I})\end{aligned}\quad (\text{B.32})$$

$$\begin{aligned}\frac{\partial \mathbf{F}^e}{\partial \gamma^\alpha} &= \frac{\partial \mathbf{F}^e}{\partial \mathbf{F}^{p-1}} : \frac{\partial \mathbf{F}^{p-1}}{\partial \gamma^\alpha} \\ &= \frac{\partial (\mathbf{F} \mathbf{F}^{p-1})}{\partial \mathbf{F}^{p-1}} : \frac{\partial \mathbf{F}^{p-1}}{\partial \gamma^\alpha} \\ &= (\mathbf{F} \overline{\otimes} \mathbf{I}) : \frac{\partial \mathbf{F}^{p-1}}{\partial \gamma^\alpha}\end{aligned}\quad (\text{B.33})$$

The last term in (B.33) will be calculated based on equation (4.41):

$$\begin{aligned}\mathbf{F}_{n+1}^{p-1} &= \mathbf{F}_n^{p-1} \text{uni} \underbrace{\left( \mathbf{I} - \sum_{\alpha=1}^q \Delta \gamma^\alpha \mathbb{S}^\alpha \right)}_{\mathbf{n}} \\ &= \mathbf{F}_n^{p-1} \text{uni}(\mathbf{n})\end{aligned}$$

then it yields

$$\begin{aligned}\frac{\partial \mathbf{F}_{n+1}^{p-1}}{\partial \gamma_{n+1}^\alpha} &= \mathbf{F}_n^{p-1} \frac{\partial [\text{uni}(\mathbf{n})]}{\partial \mathbf{n}} \frac{\partial \mathbf{n}}{\partial \gamma_{n+1}^\alpha} \\ &= \mathbf{F}_n^{p-1} \left\{ \frac{1}{\det(\mathbf{n})^{1/3}} \left[ \mathbf{I} \overline{\otimes} \mathbf{I} - \frac{1}{3} [\mathbf{n}] \otimes [\mathbf{n}] \right] \right\} \left[ \frac{\partial (\mathbf{I} - \sum_\alpha (\gamma_{n+1}^\alpha - \gamma_n^\alpha) \mathbb{S}^\alpha)}{\partial \gamma_{n+1}^\alpha} \right] \\ &= -\mathbf{F}_n^{p-1} \left\{ \frac{1}{\det(\mathbf{n})^{1/3}} \left[ \mathbf{I} \overline{\otimes} \mathbf{I} - \frac{1}{3} [\mathbf{n}] \otimes [\mathbf{n}] \right] \right\} \mathbb{S}^\alpha\end{aligned}\quad (\text{B.34})$$

This derivative (B.34) is quite useful even in the GB modeling. The derivative  $\frac{\partial \mathbf{P}}{\partial \gamma^\alpha}$  can be written as:

$$\frac{\partial \mathbf{P}}{\partial \gamma^\alpha} = (\mathbf{F} \overline{\otimes} \mathbf{I}) : (\mathbf{F}^{p-1} \overline{\otimes} \mathbf{F}^{p-1}) : \frac{1}{2} \mathbb{C} : (\mathbf{I} \underline{\otimes} \mathbf{F}^{eT} + \mathbf{F}^{eT} \overline{\otimes} \mathbf{I}) : (\mathbf{F} \overline{\otimes} \mathbf{I}) : \frac{\partial \mathbf{F}^{p-1}}{\partial \gamma^\alpha} \quad (\text{B.35})$$

**Derivative**  $\frac{\partial \underline{\tau}}{\partial \underline{F}}$

Recall that:

$$\begin{aligned}\underline{\tau}^\alpha &= \mathbf{C}^e \mathbf{S}^e : \mathbb{S}^\alpha \\ &= \mathbf{M}^e : \mathbb{S}^\alpha\end{aligned}$$

the derivative  $\frac{\partial \tau^\alpha}{\partial \mathbf{F}}$  can be obtained as:

$$\frac{\partial \tau^\alpha}{\partial \mathbf{F}} = \frac{\partial \tau^\alpha}{\partial \mathbf{M}^e} : \frac{\partial \mathbf{M}^e}{\partial \mathbf{C}^e} : \frac{\partial \mathbf{C}^e}{\partial \mathbf{F}^e} : \frac{\partial \mathbf{F}^e}{\partial \mathbf{F}}$$

with

$$\frac{\partial \tau^\alpha}{\partial \mathbf{M}^e} = \mathbb{S}^\alpha$$

$$\frac{\partial \mathbf{M}^e}{\partial \mathbf{C}^e} = \mathbf{I} \overline{\otimes} \mathbf{S}^e + \frac{1}{2} (\mathbf{C}^e \overline{\otimes} \mathbf{I}) : \mathbb{C}$$

$$\frac{\partial \mathbf{C}^e}{\partial \mathbf{F}^e} = \mathbf{I} \underline{\otimes} \mathbf{F}^{e^T} + \mathbf{F}^{e^T} \overline{\otimes} \mathbf{I}$$

$$\begin{aligned} \frac{\partial \mathbf{F}^e}{\partial \mathbf{F}} &= \left( \frac{\partial \mathbf{F} \mathbf{F}^{p^{-1}}}{\partial \mathbf{F}} \right)_{ijkl} \\ &= \frac{\partial (F_{im} F_{mj}^{p^{-1}})}{\partial F_{kl}} \\ &= F_{mj}^{p^{-1}} \delta_{ik} \delta_{ml} \\ &= \delta_{ik} F_{jm}^{p^{-T}} \delta_{ml} \\ &= \delta_{ik} \left( \mathbf{F}^{p^{-T}} \mathbf{I} \right)_{jl} \\ &= \mathbf{I} \overline{\otimes} \mathbf{F}^{p^{-T}} \end{aligned}$$

The derivative  $\frac{\partial \tau^\alpha}{\partial \mathbf{F}}$  can be assembled as:

$$\frac{\partial \tau^\alpha}{\partial \mathbf{F}} = \mathbb{S}^\alpha : \left[ \mathbf{I} \overline{\otimes} \mathbf{S}^e + \frac{1}{2} (\mathbf{C}^e \overline{\otimes} \mathbf{I}) : \mathbb{C} \right] : \left( \mathbf{I} \underline{\otimes} \mathbf{F}^{e^T} + \mathbf{F}^{e^T} \overline{\otimes} \mathbf{I} \right) : \left( \mathbf{I} \overline{\otimes} \mathbf{F}^{p^{-T}} \right) \quad (\text{B.36})$$

**Derivative**  $\frac{\partial \tau}{\partial \underline{\gamma}}$

It can be calculated as:

$$\frac{\partial \tau^\alpha}{\partial \underline{\gamma}^\alpha} = \frac{\partial \tau^\alpha}{\partial \mathbf{F}^e} : \frac{\partial \mathbf{F}^e}{\partial \mathbf{F}^p} : \frac{\partial \mathbf{F}^p}{\partial \underline{\gamma}^\alpha}$$

with

$$\frac{\partial \tau^\alpha}{\partial \mathbf{F}^e} = \frac{\partial \tau^\alpha}{\partial \mathbf{M}^e} : \frac{\partial \mathbf{M}^e}{\partial \mathbf{C}^e} : \frac{\partial \mathbf{C}^e}{\partial \mathbf{F}^e}$$

$$\begin{aligned}
\frac{\partial \mathbf{F}^e}{\partial \mathbf{F}^p} &= \left( \frac{\partial \mathbf{F} \mathbf{F}^{p^{-1}}}{\partial \mathbf{F}^p} \right)_{ijkl} \\
&= \frac{\partial F_{im} F_{mj}^{p^{-1}}}{\partial F_{kl}} \\
&= F_{im} \left( -F_{mk}^{p^{-1}} F_{lj}^{p^{-1}} \right) \\
&= \left( -F_{im} F_{mk}^{p^{-1}} \right) F_{lj}^{p^{-1}} \\
&= -\left( \mathbf{F} \mathbf{F}^{p^{-1}} \right)_{ik} F_{jl}^{p^{-1}} \\
&= -\mathbf{F}^e \overline{\otimes} \mathbf{F}^{p^{-T}}
\end{aligned}$$

$$\begin{aligned}
\frac{\partial \mathbf{F}^p}{\partial \gamma^\alpha} &= \frac{\partial \mathbf{F}^p}{\partial \mathbf{F}^{p^{-1}}} : \frac{\partial \mathbf{F}^{p^{-1}}}{\partial \gamma^\alpha} \\
&= \left( -\mathbf{F}^p \overline{\otimes} \mathbf{F}^{p^T} \right) : \frac{\partial \mathbf{F}^{p^{-1}}}{\partial \gamma^\alpha}
\end{aligned}$$

It can be assembled as:

$$\frac{\partial \tau^\alpha}{\partial \gamma^\alpha} = \mathbb{S}^\alpha : \left[ \mathbf{I} \overline{\otimes} \mathbf{S}^e + \frac{1}{2} (\mathbf{C}^e \overline{\otimes} \mathbf{I}) : \mathbb{C} \right] : (\mathbf{I} \underline{\otimes} \mathbf{F}^{eT} + \mathbf{F}^{eT} \overline{\otimes} \mathbf{I}) : (\mathbf{F}^e \overline{\otimes} \mathbf{F}^{p-T}) : (\mathbf{F}^p \overline{\otimes} \mathbf{F}^{pT}) : \frac{\partial \mathbf{F}^{p^{-1}}}{\partial \gamma^\alpha} \quad (\text{B.37})$$

**Derivative**  $\frac{\partial \underline{\pi}}{\partial \underline{\gamma}}$

This derivative is the same as calculated in small deformation SGCP in (A.60).

**Derivative**  $\frac{\partial \underline{\xi}}{\partial \underline{\nabla \gamma}}$

To calculate this derivative, the formulation of  $\underline{\xi}$  is listed as:

$$\begin{cases} \underline{\xi}_{en}^\alpha &= X_0 l_{en}^n (-|\rho_r^\alpha|^{n-2} \rho_r^\alpha \mathbf{s}_r^\alpha + |\rho_r^\alpha|_\odot^{n-2} \rho_\odot^\alpha \mathbf{l}_r^\alpha) \\ \underline{\xi}_{dis}^\alpha &= S_\xi^\alpha l_{dis}^2 R(\dot{\epsilon}_\eta^\alpha) \frac{\nabla^\alpha \dot{\gamma}^\alpha}{\dot{\epsilon}_\xi^\alpha} \end{cases}$$

with

$$\rho_{\vdash n+1}^\alpha = \rho_{\vdash n}^\alpha + \dot{\rho}_{\vdash}^\alpha \Delta t, \quad \rho_{\odot n+1}^\alpha = \rho_{\odot n}^\alpha + \dot{\rho}_\odot^\alpha \Delta t$$

$$\dot{\rho}_{\vdash}^\alpha = -\mathbf{s}_r^\alpha \cdot \nabla \nu^\alpha, \quad \dot{\rho}_\odot^\alpha = \mathbf{l}_r^\alpha \cdot \nabla \nu^\alpha$$

$$S_{\xi n+1}^\alpha = S_{\xi n}^\alpha + \dot{S}_\xi^\alpha \Delta t, \quad \dot{S}_\xi^\alpha = \sum_{\beta=1}^q h_\xi^{\alpha\beta} \left( S_\xi^\beta \right) \dot{\epsilon}_\xi^\beta$$

$$\dot{e}_\xi^\alpha = \|l_{dis} \nabla^\alpha \dot{\gamma}^\alpha\|$$

$$\begin{aligned}\nabla^\alpha \dot{\gamma}^\alpha &= (\bar{\mathbf{s}}_r^\alpha \cdot \nabla \dot{\gamma}^\alpha) \bar{\mathbf{s}}_r^\alpha + (\bar{\mathbf{l}}_r^\alpha \cdot \nabla \dot{\gamma}^\alpha) \bar{\mathbf{l}}_r^\alpha \\ &= (\mathbf{s}_r^\alpha \cdot \nabla \dot{\gamma}^\alpha) \mathbf{s}_r^\alpha / |\mathbf{s}_r^\alpha|^2 + (\mathbf{l}_r^\alpha \cdot \nabla \dot{\gamma}^\alpha) \mathbf{l}_r^\alpha / |\mathbf{l}_r^\alpha|^2\end{aligned}$$

Hence, the energetic tangent is:

$$\frac{\partial \boldsymbol{\xi}_{en}^\alpha}{\partial \nabla \dot{\gamma}^\beta} = \Delta t \delta_{\alpha\beta} (n-1) X_0 l_{en}^n \left[ |\rho_\vdash^\alpha|^{n-2} (\mathbf{s}_r^\alpha \otimes \mathbf{s}_r^\alpha) + |\rho_\odot^\alpha|^{n-2} (\mathbf{l}_r^\alpha \otimes \mathbf{l}_r^\alpha) \right]$$

The dissipative tangent can be calculated by three parts as:

$$\frac{\partial \boldsymbol{\xi}_{dis}^\alpha}{\partial \nabla \dot{\gamma}^\beta} = \underbrace{\frac{\partial S_\xi^\alpha}{\partial \nabla \dot{\gamma}^\beta} l_{dis}^2 R(\dot{e}_\eta^\alpha)}_{\text{I}} \frac{\nabla^\alpha \dot{\gamma}^\alpha}{\dot{e}_\xi^\alpha} + \underbrace{S_\xi^\alpha l_{dis}^2 \frac{\partial R(\dot{e}_\eta^\alpha)}{\partial \nabla \dot{\gamma}^\beta} \frac{\nabla^\alpha \dot{\gamma}^\alpha}{\dot{e}_\xi^\alpha}}_{\text{II}} + \underbrace{S_\xi^\alpha l_{dis}^2 R(\dot{e}_\eta^\alpha) \frac{\partial}{\partial \nabla \dot{\gamma}^\beta} \left( \frac{\nabla^\alpha \dot{\gamma}^\alpha}{\dot{e}_\xi^\alpha} \right)}_{\text{III}}$$

with derivative in I:

$$\frac{\partial S_\xi^\alpha}{\partial \nabla \dot{\gamma}^\beta} = \frac{\partial S_\xi^\alpha}{\partial \dot{e}_\xi^\beta} \frac{\partial \dot{e}_\xi^\beta}{\partial \nabla \dot{\gamma}^\beta} = \Delta t H^{\alpha\beta} \frac{\partial \dot{e}_\xi^\beta}{\partial \nabla \dot{\gamma}^\beta} \quad (\text{B.38})$$

derivative in II:

$$\frac{\partial R(\dot{e}_\eta^\alpha)}{\partial \nabla \dot{\gamma}^\beta} = \delta_{\alpha\beta} \frac{\partial R(\dot{e}_\eta^\alpha)}{\partial \dot{e}_\xi^\alpha} \frac{\partial \dot{e}_\xi^\alpha}{\partial \nabla \dot{\gamma}^\alpha} \quad (\text{B.39})$$

$$\begin{aligned}\frac{\partial \dot{e}_\xi^\beta}{\partial \nabla \dot{\gamma}^\beta} &= \frac{\partial}{\partial \nabla \dot{\gamma}^\beta} \left( l_{dis} \sqrt{(\nabla^\beta \dot{\gamma}^\beta)^2} \right) \\ &= l_{dis}^2 \frac{\nabla^\beta \dot{\gamma}^\beta}{\dot{e}_\xi^\beta} \frac{\partial \nabla^\beta \dot{\gamma}^\beta}{\partial \nabla \dot{\gamma}^\beta}\end{aligned}$$

$$\frac{\partial \nabla^\beta \dot{\gamma}^\beta}{\partial \nabla \dot{\gamma}^\beta} = \frac{\mathbf{s}_r^\beta \otimes \mathbf{s}_r^\beta}{|\mathbf{s}_r^\beta|^2} + \frac{\mathbf{l}_r^\beta \otimes \mathbf{l}_r^\beta}{|\mathbf{l}_r^\beta|^2}$$

derivative in III:

$$\begin{aligned}\frac{\partial}{\partial \nabla \dot{\gamma}^\beta} \left( \frac{\nabla^\alpha \dot{\gamma}^\alpha}{\dot{e}_\xi^\alpha} \right) &= \frac{1}{\dot{e}_\xi^\alpha} \frac{\partial \nabla^\alpha \dot{\gamma}^\alpha}{\partial \nabla \dot{\gamma}^\beta} - \frac{\nabla^\alpha \dot{\gamma}^\alpha}{(\dot{e}_\xi^\alpha)^2} \frac{\partial \dot{e}_\xi^\alpha}{\partial \nabla \dot{\gamma}^\beta} \\ &= \delta_{\alpha\beta} \frac{1}{\dot{e}_\xi^\alpha} \frac{\partial \nabla^\alpha \dot{\gamma}^\alpha}{\partial \nabla \dot{\gamma}^\alpha} - \delta_{\alpha\beta} \frac{\nabla^\alpha \dot{\gamma}^\alpha}{(\dot{e}_\xi^\alpha)^2} \frac{\partial \dot{e}_\xi^\alpha}{\partial \nabla \dot{\gamma}^\alpha}\end{aligned}$$

### B.3 Shape functions

As shown in Fig. 4.2, eight-noded (quadratic) interpolation of  $\mathbf{u}$ , four-noded (linear) interpolation of  $\gamma^\alpha$  and  $2 \times 2$  Gauss integration are adopted. For displacement fields  $\mathbf{u}$ , the shape functions are:

$$\left\{ \begin{array}{l} N_1 = \frac{1}{4}(1-\xi)(1-\eta)(-\xi-\eta-1) \\ N_2 = \frac{1}{4}(1+\xi)(1-\eta)(+\xi-\eta-1) \\ N_3 = \frac{1}{4}(1+\xi)(1+\eta)(+\xi+\eta-1) \\ N_4 = \frac{1}{4}(1-\xi)(1+\eta)(-\xi+\eta-1) \\ N_5 = \frac{1}{2}(1-\eta)(1+\xi)(1-\xi) \\ N_6 = \frac{1}{2}(1+\xi)(1+\eta)(1-\eta) \\ N_7 = \frac{1}{2}(1+\eta)(1+\xi)(1-\xi) \\ N_8 = \frac{1}{2}(1-\xi)(1+\eta)(1-\eta) \end{array} \right. \quad (\text{B.40})$$

For plastic slip field  $\gamma^\alpha$ , the shape functions are as follows:

$$\left\{ \begin{array}{l} N_1 = \frac{1}{4}(1-\xi)(1-\eta) \\ N_2 = \frac{1}{4}(1+\xi)(1-\eta) \\ N_3 = \frac{1}{4}(1+\xi)(1+\eta) \\ N_4 = \frac{1}{4}(1-\xi)(1+\eta) \end{array} \right. \quad (\text{B.41})$$

The four integration points are listed in B.1

Number	$\xi$	$\eta$	$W_p$
1	$-\sqrt{1/3}$	$-\sqrt{1/3}$	1.0
2	$+\sqrt{1/3}$	$-\sqrt{1/3}$	1.0
3	$+\sqrt{1/3}$	$+\sqrt{1/3}$	1.0
4	$-\sqrt{1/3}$	$+\sqrt{1/3}$	1.0

**Tab. B.1.** Gauss points for element in finite deformation example.

# Appendix C

## Numerical aspects of grain boundary modeling

This appendix introduces several details about GB modeling. In section C.1, an illustrative derivation of GB mismatch proposed by Peng et al. (2019) has been presented. As shown in this derivation, the GB mismatch proposed by Peng et al. (2019) has similarities with the classical one of Gurtin (2008b). Section C.2 presents the regularization function with respect to the viscoplastic term in dissipative constitutive laws of the GB model. Then, the calculations of tangent matrices contributed by GB power expenditure will be given in section C.3. The shape functions used in the GB element are presented in the last section C.4.

### C.1 Derivation of grain boundary mismatch of Peng et al. (2019)

The rate of the density of the residual GB defects as proposed by Peng et al. (2019) in the lattice configuration reads:

$$\dot{\mathbb{G}}_{AB}^{\alpha\beta} = -\dot{\gamma}_{AB}^{\alpha\beta} \mathbf{M}_{AB}^{\alpha\beta} \quad (\text{C.1})$$

with

$$\mathbf{M}_{AB}^{\alpha\beta} = \left[ \mathbf{s}_A^\alpha \otimes [\mathbf{m}_A^\alpha \times \mathbf{n}_A] + D_{AB}^{\alpha\beta} \mathbf{s}_B^\beta \otimes [\mathbf{m}_B^\alpha \times \mathbf{n}_B] \right] \quad (\text{C.2})$$

The rate form variable  $\dot{\gamma}_{AB}^{\alpha\beta}$  relates plastic slip rates in grain A and B and yields the relation defined by Peng et al. (2019) as:

$$\dot{\gamma}_A^\alpha = \sum_\beta \dot{\gamma}_{AB}^{\alpha\beta}, \quad \dot{\gamma}_B^\beta = \sum_\alpha D_{AB}^{\alpha\beta} \dot{\gamma}_{AB}^{\alpha\beta} \quad (\text{C.3})$$

Summing up all slip systems  $\alpha$  in grain A and  $\beta$  in B at the grain boundary yields the Burgers tensor  $\dot{\mathbb{G}}_{\text{Peng}}$  as:

$$\begin{aligned}\dot{\mathbb{G}}_{\text{Peng}} &= \sum_{\alpha, \beta} \dot{\mathbb{G}}_{AB}^{\alpha\beta} \\ &= - \sum_{\alpha, \beta} \left\{ \dot{\gamma}_{AB}^{\alpha\beta} \mathbf{s}_A^\alpha \otimes [\mathbf{m}_A^\alpha \times \mathbf{n}_A] + D_{AB}^{\alpha\beta} \dot{\gamma}_{AB}^{\alpha\beta} \mathbf{s}_B^\beta \otimes [\mathbf{m}_B^\beta \times \mathbf{n}_B] \right\}\end{aligned}$$

Considering grain boundary normal relation in (7.35) which is also valid in the intermediate configuration, it can be rewritten as:

$$\dot{\mathbb{G}}_{\text{Peng}} = - \sum_{\alpha, \beta} \dot{\gamma}_{AB}^{\alpha\beta} \mathbf{s}_A^\alpha \otimes [\mathbf{m}_A^\alpha \times \mathbf{n}_A] - \sum_{\alpha, \beta} D_{AB}^{\alpha\beta} \dot{\gamma}_{AB}^{\alpha\beta} \mathbf{s}_B^\beta \otimes [\mathbf{m}_B^\beta \times \mathbf{n}_B]$$

Reformulating by summing each slip system one by another, it gives:

$$\dot{\mathbb{G}}_{\text{Peng}} = - \sum_{\alpha} \sum_{\beta} \dot{\gamma}_{AB}^{\alpha\beta} \mathbf{s}_A^\alpha \otimes [\mathbf{m}_A^\alpha \times \mathbf{n}_{GB}] + \sum_{\beta} \sum_{\alpha} D_{AB}^{\alpha\beta} \dot{\gamma}_{AB}^{\alpha\beta} \mathbf{s}_B^\beta \otimes [\mathbf{m}_B^\beta \times \mathbf{n}_{GB}]$$

Using (C.3), it can be rewritten as:

$$\begin{aligned}\dot{\mathbb{G}}_{\text{Peng}} &= - \sum_{\alpha} \dot{\gamma}_A^\alpha \mathbf{s}_A^\alpha \otimes [\mathbf{m}_A^\alpha \times \mathbf{n}_{GB}] + \sum_{\beta} \dot{\gamma}_B^\beta \mathbf{s}_B^\beta \otimes [\mathbf{m}_B^\beta \times \mathbf{n}_{GB}] \\ &= - \underbrace{\sum_{\alpha} \dot{\gamma}_A^\alpha \mathbf{s}_A^\alpha \otimes \mathbf{m}_A^\alpha (\mathbf{n}_{GB} \times)}_{\mathbf{L}_A^p} + \underbrace{\sum_{\beta} \dot{\gamma}_B^\beta \mathbf{s}_B^\beta \otimes \mathbf{m}_B^\beta (\mathbf{n}_{GB} \times)}_{\mathbf{L}_B^p}\end{aligned}$$

Finally,

$$\dot{\mathbb{G}}_{\text{Peng}} = \llbracket \mathbf{L}^p \rrbracket (\mathbf{n}_{GB} \times)$$

## C.2 Regularization function

In GB dissipative constitutive formulations, a viscoplastic function with respect to  $\|\dot{\mathbb{G}}\|$  has been adopted, which is consistent with that used in small and large bulk crystal formulated in SGCP model. Similarly, a regularization function  $R(\|\dot{\mathbb{G}}\|)$  is also needed for  $\|\frac{\dot{\mathbb{G}}}{\mathbb{G}_0}\|^q$  defined as:

$$R(\|\dot{\mathbb{G}}\|) = \begin{cases} \frac{\|\dot{\mathbb{G}}\|}{\omega \mathbb{G}_0} & \text{if } \|\dot{\mathbb{G}}\| \leq c \\ \left( \frac{\|\dot{\mathbb{G}}\| - \Phi}{\mathbb{G}_0} \right)^q & \text{if } \|\dot{\mathbb{G}}\| > c \end{cases} \quad (\text{C.4})$$

with

$$\Phi = c(1 - q)$$

$$c = \frac{1}{q} \left( \frac{1}{\omega q} \right)^{\frac{1}{q-1}}$$

where  $\omega$  is a parameter of regularization. The derivative with respect to  $\|\dot{\mathbb{G}}\|$  can be calculated as:

$$\frac{\partial R(\|\dot{\mathbb{G}}\|)}{\partial \|\dot{\mathbb{G}}\|} = \begin{cases} \frac{1}{\omega \mathbb{G}_0} & \text{if } \|\dot{\mathbb{G}}\| \leq c \\ \frac{q}{\mathbb{G}_0} \left( \frac{\|\dot{\mathbb{G}}\| - \Phi}{\mathbb{G}_0} \right)^{q-1} & \text{if } \|\dot{\mathbb{G}}\| > c \end{cases} \quad (\text{C.5})$$

These formulations will be recalled in the calculations of tangent matrices.

### C.3 Tangent matrices

The residuals for the grain boundary can be written:

$$\underline{R}_{\gamma_{GB}}^e = \int_{S_{GB}} \underline{\underline{N}}_{\gamma_B}^T \cdot \underline{\underline{\Pi}}_B - \underline{\underline{N}}_{\gamma_A}^T \cdot \underline{\underline{\Pi}}_A ds = \underline{0}$$

Therefore, the tangent matrices take the form:

$$\begin{aligned} \underline{\underline{K}}_{\gamma_{GB}}^e &= \frac{\partial \underline{R}_{\gamma_{GB}}^e}{\partial \Gamma} \\ &= \int_{S_{GB}} \underline{\underline{N}}_{\gamma_B}^T \frac{\partial \underline{\underline{\Pi}}_B}{\partial \Gamma} - \underline{\underline{N}}_{\gamma_A}^T \frac{\partial \underline{\underline{\Pi}}_A}{\partial \Gamma} ds_{R_{\gamma_{GB}}^e} \\ &= \int_{S_{GB}} \underline{\underline{N}}_{\gamma_B}^T \left( \frac{\partial \underline{\underline{\Pi}}_B}{\partial \underline{\gamma}_B} \underline{\underline{N}}_{\gamma_B} + \frac{\partial \underline{\underline{\Pi}}_B}{\partial \underline{\gamma}_A} \underline{\underline{N}}_{\gamma_B} \right) - \underline{\underline{N}}_{\gamma_A}^T \left( \frac{\partial \underline{\underline{\Pi}}_A}{\partial \underline{\gamma}_A} \underline{\underline{N}}_{\gamma_A} + \frac{\partial \underline{\underline{\Pi}}_A}{\partial \underline{\gamma}_B} \underline{\underline{N}}_{\gamma_B} \right) ds_{R_{\gamma_{GB}}^e} \end{aligned}$$

For clarity,  $\underline{\underline{\Pi}}_A^\alpha$  and  $\underline{\underline{\Pi}}_B^\alpha$  can be rewritten as:

$$\underline{\underline{\Pi}}_A^\alpha = \underbrace{\mathbb{N}_A^\alpha : \mathbb{K}_{en}}_{\Pi_{A,en}^\alpha} + \underbrace{\mathbb{N}_A^\alpha : \mathbb{K}_{dis}}_{\Pi_{A,dis}^\alpha} \quad \underline{\underline{\Pi}}_B^\alpha = \underbrace{\mathbb{N}_B^\alpha : \mathbb{K}_{en}}_{\Pi_{B,en}^\alpha} + \underbrace{\mathbb{N}_B^\alpha : \mathbb{K}_{dis}}_{\Pi_{B,dis}^\alpha} \quad (\text{C.6})$$

**Derivative**  $\frac{\partial \underline{\underline{\Pi}}_A}{\partial \underline{\gamma}_A}$

The general form  $\frac{\partial \Pi_A^\alpha}{\partial \gamma_A^\beta}$  can be divided into:

$$\frac{\partial \Pi_A^\alpha}{\partial \gamma_A^\beta} = \frac{\partial \Pi_{A,en}^\alpha}{\partial \gamma_A^\beta} + \frac{\partial \Pi_{A,dis}^\alpha}{\partial \gamma_A^\beta}$$

The energetic and dissipative contributions give:

$$\frac{\partial \Pi_{A,en}^\alpha}{\partial \gamma_A^\beta} = \frac{\partial}{\partial \gamma_A^\beta} (\mathbb{N}_A^\alpha : \mathbb{K}_{en}) + \mathbb{N}_A^\alpha : \frac{\partial}{\partial \gamma_A^\beta} (\mathbb{K}_{en})$$

$$\frac{\partial \Pi_{A_{dis}}^{\alpha}}{\partial \gamma_A^{\beta}} = \frac{\partial}{\partial \gamma_A^{\beta}} (\mathbb{N}_A^{\alpha}) : \mathbb{K}_{dis} + \mathbb{N}_A^{\alpha} : \frac{\partial}{\partial \gamma_A^{\beta}} (\mathbb{K}_{dis})$$

with

$$\frac{\partial}{\partial \gamma_A^{\beta}} (\mathbb{N}_A^{\alpha}) = \mathbb{S}_A^{\alpha} \frac{\partial \mathbf{F}_A^p}{\partial \gamma_A^{\beta}} (\mathbf{n}_{GB_r} \times)$$

$$\frac{\partial}{\partial \gamma_A^{\beta}} (\mathbb{K}_{en}) = -\kappa \left( \frac{\partial \mathbf{F}_A^p}{\partial \gamma_A^{\beta}} \right) (\mathbf{n}_{GB_r} \times)$$

The derivatives  $\frac{\partial \mathbf{F}_A^p}{\partial \gamma_A^{\beta}}$  can be calculated by (B.34).

**Derivative**  $\frac{\partial \underline{\Pi}_A}{\partial \underline{\gamma}_B}$

This derivative  $\frac{\partial \underline{\Pi}_A}{\partial \underline{\gamma}_B}$  yields:

$$\frac{\partial \underline{\Pi}_A}{\partial \underline{\gamma}_B} = \frac{\partial \Pi_{A_{en}}^{\alpha}}{\partial \gamma_B^{\beta}} + \frac{\partial \Pi_{A_{dis}}^{\alpha}}{\partial \gamma_B^{\beta}}$$

The energetic and dissipative contributions give:

$$\frac{\partial \Pi_{A_{en}}^{\alpha}}{\partial \gamma_B^{\beta}} = \frac{\partial}{\partial \gamma_B^{\beta}} (\mathbb{N}_A^{\alpha}) : \mathbb{K}_{en} + \mathbb{N}_A^{\alpha} : \frac{\partial}{\partial \gamma_B^{\beta}} (\mathbb{K}_{en})$$

$$\frac{\partial \Pi_{A_{dis}}^{\alpha}}{\partial \gamma_B^{\beta}} = \frac{\partial}{\partial \gamma_B^{\beta}} (\mathbb{N}_A^{\alpha}) : \mathbb{K}_{dis} + \mathbb{N}_A^{\alpha} : \frac{\partial}{\partial \gamma_B^{\beta}} (\mathbb{K}_{dis})$$

with

$$\frac{\partial}{\partial \gamma_B^{\beta}} (\mathbb{N}_A^{\alpha}) = 0$$

$$\frac{\partial}{\partial \gamma_B^{\beta}} (\mathbb{K}_{en}) = \kappa \left( \frac{\partial \mathbf{F}_B^p}{\partial \gamma_B^{\beta}} \right) (\mathbf{n}_{GB_r} \times)$$

**Derivative**  $\frac{\partial \underline{\Pi}_B}{\partial \underline{\gamma}_A}$

This derivative gives:

$$\frac{\partial \underline{\Pi}_B}{\partial \underline{\gamma}_A} = \frac{\partial \Pi_{B_{en}}^{\alpha}}{\partial \gamma_A^{\beta}} + \frac{\partial \Pi_{B_{dis}}^{\alpha}}{\partial \gamma_A^{\beta}}$$

The energetic and dissipative contributions give:

$$\begin{aligned}\frac{\partial \Pi_{B_{en}}^{\alpha}}{\partial \gamma_A^{\beta}} &= \frac{\partial}{\partial \gamma_A^{\beta}} (\mathbb{N}_B^{\alpha}) : \mathbb{K}_{en} + \mathbb{N}_B^{\alpha} : \frac{\partial}{\partial \gamma_A^{\beta}} (\mathbb{K}_{en}) \\ \frac{\partial \Pi_{B_{dis}}^{\alpha}}{\partial \gamma_A^{\beta}} &= \frac{\partial}{\partial \gamma_A^{\beta}} (\mathbb{N}_B^{\alpha}) : \mathbb{K}_{dis} + \mathbb{N}_B^{\alpha} : \frac{\partial}{\partial \gamma_A^{\beta}} (\mathbb{K}_{dis})\end{aligned}$$

with

$$\begin{aligned}\frac{\partial}{\partial \gamma_A^{\beta}} (\mathbb{N}_B^{\alpha}) &= 0 \\ \frac{\partial}{\partial \gamma_A^{\beta}} (\mathbb{K}_{en}) &= -\kappa \left( \frac{\partial \mathbf{F}_A^p}{\partial \gamma_A^{\beta}} \right) (\mathbf{n}_{GB_r} \times)\end{aligned}$$

**Derivative**  $\frac{\partial \underline{\Pi}_B}{\partial \underline{\gamma}_B}$

The derivative gives:

$$\frac{\partial \Pi_B^{\alpha}}{\partial \gamma_B^{\beta}} = \frac{\partial \Pi_{B_{en}}^{\alpha}}{\partial \gamma_B^{\beta}} + \frac{\partial \Pi_{B_{dis}}^{\alpha}}{\partial \gamma_B^{\beta}}$$

The energetic and dissipative contributions give:

$$\begin{aligned}\frac{\partial \Pi_{B_{en}}^{\alpha}}{\partial \gamma_B^{\beta}} &= \frac{\partial}{\partial \gamma_B^{\beta}} (\mathbb{N}_B^{\alpha}) : \mathbb{K}_{en} + \mathbb{N}_B^{\alpha} : \frac{\partial}{\partial \gamma_B^{\beta}} (\mathbb{K}_{en}) \\ \frac{\partial \Pi_{B_{dis}}^{\alpha}}{\partial \gamma_B^{\beta}} &= \frac{\partial}{\partial \gamma_B^{\beta}} (\mathbb{N}_B^{\alpha}) : \mathbb{K}_{dis} + \mathbb{N}_B^{\alpha} : \frac{\partial}{\partial \gamma_B^{\beta}} (\mathbb{K}_{dis})\end{aligned}$$

with

$$\begin{aligned}\frac{\partial}{\partial \gamma_B^{\beta}} (\mathbb{N}_B^{\alpha}) &= \mathbb{S}_B^{\alpha} \frac{\partial \mathbf{F}_B^p}{\partial \gamma_B^{\beta}} (\mathbf{n}_{GB_r} \times) \\ \frac{\partial}{\partial \gamma_B^{\beta}} (\mathbb{K}_{en}) &= \kappa \left( \frac{\partial \mathbf{F}_B^p}{\partial \gamma_B^{\beta}} \right) (\mathbf{n}_{GB_r} \times)\end{aligned}$$

**Shared derivative**  $\frac{\partial}{\partial \gamma_A^{\beta}} (\mathbb{K}_{dis})$  **and**  $\frac{\partial}{\partial \gamma_B^{\beta}} (\mathbb{K}_{dis})$

Considering the derivative  $\frac{\partial}{\partial \gamma_A^{\beta}} (\mathbb{K}_{dis})$  which can be treated as derivative of dissipative GB microscopic force  $\mathbb{K}_{dis}$  with respect to state variable from grain A, it can be calculated as:

$$\frac{\partial}{\partial \gamma_A^{\beta}} (\mathbb{K}_{dis}) = \frac{1}{\Delta t} \frac{\partial}{\partial \dot{\gamma}_A^{\beta}} (\mathbb{K}_{dis}) \quad (C.7)$$

$$\frac{\partial}{\partial \dot{\gamma}_A^\beta} (\mathbb{K}_{dis}) = \underbrace{\frac{\partial S_{GB}}{\partial \dot{\gamma}_A^\beta} R(\|\dot{\mathbf{G}}\|) \frac{\dot{\mathbf{G}}}{\|\dot{\mathbf{G}}\|}}_{\text{I}} + \underbrace{S_{GB} \frac{\partial}{\partial \dot{\gamma}_A^\beta} [R(\|\dot{\mathbf{G}}\|)] \frac{\dot{\mathbf{G}}}{\|\dot{\mathbf{G}}\|}}_{\text{II}} + \underbrace{S_{GB} R(\|\dot{\mathbf{G}}\|) \frac{\partial}{\partial \dot{\gamma}_A^\beta} \left( \frac{\dot{\mathbf{G}}}{\|\dot{\mathbf{G}}\|} \right)}_{\text{III}}$$

with derivative in item I:

$$\begin{aligned} \frac{\partial S_{GB}}{\partial \dot{\gamma}_A^\beta} &= \frac{\partial S_{GB}}{\partial \|\dot{\mathbf{G}}\|} \frac{\partial \|\dot{\mathbf{G}}\|}{\partial \dot{\gamma}_A^\beta} \\ &= \Delta t H_{GB} \frac{\partial \|\dot{\mathbf{G}}\|}{\partial \dot{\gamma}_A^\beta} \end{aligned} \quad (\text{C.8})$$

$$\begin{aligned} \frac{\partial \|\dot{\mathbf{G}}\|}{\partial \dot{\gamma}_A^\beta} &= \frac{\partial \|\dot{\mathbf{G}}\|}{\partial \dot{\mathbf{G}}} : \frac{\partial \dot{\mathbf{G}}}{\partial \dot{\gamma}_A^\beta} \\ &= \frac{\dot{\mathbf{G}}}{\|\dot{\mathbf{G}}\|} : \left( -\frac{\partial \mathbf{F}_A^p}{\partial \dot{\gamma}_A^\beta} (\mathbf{n}_{GB_r} \times) \right) \end{aligned} \quad (\text{C.9})$$

derivative in item II:

$$\frac{\partial}{\partial \dot{\gamma}_A^\beta} [R(\|\dot{\mathbf{G}}\|)] = \frac{\partial R(\|\dot{\mathbf{G}}\|)}{\partial \|\dot{\mathbf{G}}\|} \frac{\partial \|\dot{\mathbf{G}}\|}{\partial \dot{\gamma}_A^\beta}$$

derivative in item III:

$$\begin{aligned} \frac{\partial}{\partial \dot{\gamma}_A^\beta} \left( \frac{\dot{\mathbf{G}}}{\|\dot{\mathbf{G}}\|} \right) &= \frac{\partial \dot{\mathbf{G}}}{\partial \dot{\gamma}_A^\beta} \|\dot{\mathbf{G}}\|^{-1} + \dot{\mathbf{G}} \frac{\partial}{\partial \dot{\gamma}_A^\beta} (\|\dot{\mathbf{G}}\|^{-1}) \\ &= \frac{\partial \dot{\mathbf{G}}}{\partial \dot{\gamma}_A^\beta} \|\dot{\mathbf{G}}\|^{-1} - \frac{\dot{\mathbf{G}}}{\|\dot{\mathbf{G}}\|^2} \frac{\partial \|\dot{\mathbf{G}}\|}{\partial \dot{\gamma}_A^\beta} \end{aligned} \quad (\text{C.10})$$

For the derivative of dissipative GB microscopic force  $\mathbb{K}_{dis}$  with respect to state variable from grain B, namely,  $\frac{\partial}{\partial \dot{\gamma}_B^\beta} (\mathbb{K}_{dis})$ , it only needs to replace the subscript “A” with “B” in equation (C.7) and its associated ones (C.8), (C.10) and (C.9) except for the following term:

$$\frac{\partial \dot{\mathbf{G}}}{\partial \dot{\gamma}_B^\beta} = \frac{\partial \mathbf{F}_B^p}{\partial \dot{\gamma}_B^\beta} (\mathbf{n}_{GB_r} \times)$$

## C.4 Shape functions

One dimensional line element with two nodes is adopted for GB element. The shape functions are as follows:

$$\begin{cases} N_1 &= 0.5(1-\xi) \\ N_2 &= 0.5(1+\xi) \end{cases}$$

Two integration points are used for the GB element with coordinates and weighting factors as follows:

Number	$\xi$	$W_p$
1	$-\sqrt{1/3}$	1.0
2	$+\sqrt{1/3}$	1.0

**Tab. C.1.** Gauss points for one-dimensional line element in finite deformation example.



# Bibliography

- Acharya, A., Bassani, J.L., 2000. Lattice incompatibility and a gradient theory of crystal plasticity. *J. Mech. Phys. Solids* 48, 1565–1595.
- Acharya, A., Bassani, J.L., Beau@doin, A., 2003. Geometrically necessary dislocations, hardening, and a simple gradient theory of crystal plasticity. *Scr. Mater.* 48, 167–172.
- Acharya, A., Tang, H., Saigal, S., Bassani, J.L., 2004. On boundary conditions and plastic strain-gradient discontinuity in lower-order gradient plasticity. *J. Mech. Phys. Solids* 52, 1793–1826.
- Aifantis, E.C., 1984. on the Microstructural Origin of Certain Inelastic Models. *Am. Soc. Mech. Eng.* 106.
- Aifantis, E.C., 1987. The physics of plastic deformation. *Int. J. Plast.* 3, 211–247.
- Aifantis, E.C., 1996. Non-linearity, periodicity and patterning in plasticity and fracture. *Int. J. Non. Linear. Mech.* 31, 797–809.
- Aifantis, E.C., 1999. Strain gradient interpretation of size effects. *Int. J. Fract.* 95, 299–314.
- Aifantis, K.E., Soer, W.A., De Hosson, J.T.M., Willis, J.R., 2006. Interfaces within strain gradient plasticity: Theory and experiments. *Acta Mater.* 54, 5077–5085.
- Aifantis, K.E., Willis, J.R., 2005. The role of interfaces in enhancing the yield strength of composites and polycrystals. *J. Mech. Phys. Solids* 53, 1047–1070.
- Alipour, A., Reese, S., Svendsen, B., Wulffinghoff, S., 2020. A grain boundary model considering the grain misorientation within a geometrically nonlinear gradient-extended crystal viscoplasticity theory. *Proc. R. Soc. A Math. Phys. Eng. Sci.* 476, 20190581.
- Alipour, A., Reese, S., Wulffinghoff, S., 2019. A grain boundary model for gradient-extended geometrically nonlinear crystal plasticity: Theory and numerics. *Int. J. Plast.* 118, 17–35.
- Armstrong, R., Codd, I., Douthwaite, R.M., Petch, N.J., 1962. The plastic deformation of polycrystalline aggregates. *Philos. Mag.* 7, 45–58.
- Armstrong, R.W., 1961. On size effects in polycrystal plasticity. *J. Mech. Phys. Solids* 9, 196–199.
- Arsenlis, A., Parks, D.M., 1999. Crystallographic aspects of geometrically-necessary and statistically-stored dislocation density. *Acta Mater.* 47, 1597–1611.

- Asaro, R.J., 1975. Elastic-plastic memory and kinematic-type hardening. *Acta Metall.* 23, 1255–1265.
- Asaro, R.J., Rice, J.R., 1977. Strain localization in ductile single crystals. *J. Mech. Phys. Solids* 25, 309–338.
- Ashby, M.F., 1970. The deformation of plastically non-homogeneous materials. *Philos. Mag.* 21, 399–424.
- Ask, A., Forest, S., Appolaire, B., Ammar, K., 2020. Microstructure evolution in deformed polycrystals predicted by a diffuse interface Cosserat approach. *Adv. Model. Simul. Eng. Sci.* 7.
- Ask, A., Forest, S., Appolaire, B., Ammar, K., Salman, O.U., 2018. A Cosserat crystal plasticity and phase field theory for grain boundary migration. *J. Mech. Phys. Solids* 115, 167–194.
- Bardella, L., 2010. Size effects in phenomenological strain gradient plasticity constitutively involving the plastic spin. *Int. J. Eng. Sci.* 48, 550–568.
- Bardella, L., Panteghini, A., 2015. Modelling the torsion of thin metal wires by distortion gradient plasticity. *J. Mech. Phys. Solids* 78, 467–492.
- Bassani, J.L., 2001. Incompatibility and a simple gradient theory of plasticity. *J. Mech. Phys. Solids* 49, 1983–1996.
- Bayerschen, E., Böhlke, T., 2016. Power-law defect energy in a single-crystal gradient plasticity framework: a computational study. *Comput. Mech.* 58, 13–27.
- Bayerschen, E., McBride, A.T., Reddy, B.D., Böhlke, T., 2016. Review on slip transmission criteria in experiments and crystal plasticity models. *J. Mater. Sci.* 51, 2243–2258.
- Bayerschen, E., Stricker, M., Wulffinghoff, S., Weygand, D., Böhlke, T., 2015. Equivalent plastic strain gradient plasticity with grain boundary hardening and comparison to discrete dislocation dynamics. *Proc. R. Soc. A Math. Phys. Eng. Sci.* 471, 20150388.
- Bayley, C.J., Brekelmans, W.A., Geers, M.G., 2006. A comparison of dislocation induced back stress formulations in strain gradient crystal plasticity. *Int. J. Solids Struct.* 43, 7268–7286.
- van Beers, P., McShane, G., Kouznetsova, V., Geers, M., 2013. Grain boundary interface mechanics in strain gradient crystal plasticity. *J. Mech. Phys. Solids* 61, 2659–2679.
- Berbenni, S., Taupin, V., Lebensohn, R.A., 2020. A fast Fourier transform-based mesoscale field dislocation mechanics study of grain size effects and reversible plasticity in polycrystals. *J. Mech. Phys. Solids* 135, 1–23.
- Bittencourt, E., 2018. On the effects of hardening models and lattice rotations in strain gradient crystal plasticity simulations. *Int. J. Plast.* 108, 169–185.
- Bittencourt, E., 2019. Interpretation of the size effects in micropillar compression by a strain gradient crystal plasticity theory. *Int. J. Plast.* 116, 280–296.

- Bittencourt, E., Needleman, A., Gurtin, M.E., Van der Giessen, E., 2003. A comparison of nonlocal continuum and discrete dislocation plasticity predictions. *J. Mech. Phys. Solids* 51, 281–310.
- Borg, U., 2007. Strain gradient crystal plasticity effects on flow localization. *Int. J. Plast.* 23, 1400–1416.
- Carlsson, K., Runesson, K., Larsson, F., Ekh, M., 2017. A comparison of the primal and semi-dual variational formats of gradient-extended crystal inelasticity. *Comput. Mech.* 60, 531–548.
- Cermelli, P., Gurtin, M.E., 2001. On the characterization of geometrically necessary dislocations in finite plasticity. *J. Mech. Phys. Solids* 49, 1539–1568.
- Cermelli, P., Gurtin, M.E., 2002. Geometrically necessary dislocations in viscoplastic single crystals and bicrystals undergoing small deformations. *Int. J. Solids Struct.* 39, 6281–6309.
- Chan, W.L., Fu, M.W., Lu, J., 2011. The size effect on micro deformation behaviour in micro-scale plastic deformation. *Mater. Des.* 32, 198–206.
- Chang, H.J., Cordero, N.M., Déprés, C., Fivel, M., Forest, S., 2016. Micromorphic crystal plasticity versus discrete dislocation dynamics analysis of multilayer pile-up hardening in a narrow channel. *Arch. Appl. Mech.* 86, 21–38.
- Chen, X.X., Ngan, A.H., 2011. Specimen size and grain size effects on tensile strength of Ag microwires. *Scr. Mater.* 64, 717–720.
- Chtourou, R., Leconte, N., Zouari, B., Chaari, F., Markiewicz, E., Langrand, B., 2017. Macro-modeling of spot weld strength and failure: Formulation and identification procedure based on pure and mixed modes of loading. *Eng. Comput. (Swansea, Wales)* 34, 941–959.
- Considère, A., 1885. *Ann Ponts Chaussee*, 9, 574–775.
- Cordero, N.M., Forest, S., Busso, E.P., Berbenni, S., Cherkaoui, M., 2012. Grain size effects on plastic strain and dislocation density tensor fields in metal polycrystals. *Comput. Mater. Sci.* 52, 7–13.
- Cordero, N.M., Gaubert, A., Forest, S., Busso, E.P., Gallerneau, F., Kruch, S., 2010. Size effects in generalised continuum crystal plasticity for two-phase laminates. *J. Mech. Phys. Solids* 58, 1963–1994.
- Dahlberg, C.F., Saito, Y., Öztop, M.S., Kysar, J.W., 2017. Geometrically necessary dislocation density measurements at a grain boundary due to wedge indentation into an aluminum bicrystal. *J. Mech. Phys. Solids* 105, 131–149.
- Di Gioacchino, F., Quinta Da Fonseca, J., 2015. An experimental study of the polycrystalline plasticity of austenitic stainless steel. *Int. J. Plast.* 74, 92–109.
- Duan, X.J., Jain, M.K., Bruhis, M., Wilkinson, D.S., 2005. Experimental and Numerical Study of Intense Shear Banding for Al-Alloy under Uniaxial Tension. *Adv. Mater. Res.* 6-8, 737–744.
- Ekh, M., Grymer, M., Runesson, K., Svedberg, T., 2007. Gradient crystal plasticity as part of the computational modelling of polycrystals. *Int. J. Numer. Methods Eng.* .

- El-Naaman, S.A., Nielsen, K.L., Niordson, C.F., 2016. On modeling micro-structural evolution using a higher order strain gradient continuum theory. *Int. J. Plast.* 76, 285–298.
- El-Naaman, S.A., Nielsen, K.L., Niordson, C.F., 2019. An investigation of back stress formulations under cyclic loading. *Mech. Mater.* 130, 76–87.
- Engel, U., Eckstein, R., 2002. Microforming - From basic research to its realization. *J. Mater. Process. Technol.* 125-126, 35–44.
- Erdle, H., Böhlke, T., 2017. A gradient crystal plasticity theory for large deformations with a discontinuous accumulated plastic slip. *Comput. Mech.* 60, 923–942.
- Evers, L.P., Brekelmans, W.A., Geers, M.G., 2004a. Non-local crystal plasticity model with intrinsic SSD and GND effects. *J. Mech. Phys. Solids* 52, 2379–2401.
- Evers, L.P., Brekelmans, W.A., Geers, M.G., 2004b. Scale dependent crystal plasticity framework with dislocation density and grain boundary effects. *Int. J. Solids Struct.* 41, 5209–5230.
- Evers, L.P., Parks, D.M., Brekelmans, W.A., Geers, M.G., 2002. Crystal plasticity model with enhanced hardening by geometrically necessary dislocation accumulation. *J. Mech. Phys. Solids* 50, 2403–2424.
- Fleck, N.A., Hutchinson, J.W., 1997. Strain Gradient Plasticity. *Adv. Appl. Mech.* 33, 295–361.
- Fleck, N.A., Hutchinson, J.W., 2001. A reformulation of strain gradient plasticity. *J. Mech. Phys. Solids*.
- Fleck, N.A., Hutchinson, J.W., Willis, J.R., 2014. Strain gradient plasticity under non-proportional loading. *Proc. R. Soc. A Math. Phys. Eng. Sci.* 470.
- Fleck, N.A., Hutchinson, J.W., Willis, J.R., 2015. Guidelines for constructing strain gradient plasticity theories. *J. Appl. Mech. Trans. ASME* 82, 1–10.
- Fleck, N.A., Muller, G.M., Ashby, M.F., Hutchinson, J.W., 1994. Strain gradient plasticity: Theory and experiment. *Acta Metall. Mater.* 42, 475–487.
- Fleck, N.A., Willis, J.R., 2009. A mathematical basis for strain-gradient plasticity theory-Part I: Scalar plastic multiplier. *J. Mech. Phys. Solids* 57, 161–177.
- Fleck, N.A., Willis, J.R., 2015. Strain gradient plasticity: energetic or dissipative? *Acta Mech. Sin. Xuebao* 31, 465–472.
- Forest, S., 1998. Modeling slip, kink and shear banding in classical and generalized single crystal plasticity. *Acta Mater.* 46, 3265–3281.
- Forest, S., 2009. Micromorphic approach for gradient elasticity, viscoplasticity, and damage. *J. Eng. Mech.* 135, 117–131.
- Forest, S., 2011. Strain Localization Phenomena in Generalized Single Crystal Plasticity. *J. Mech. Behav. Mater.* 11, 45–50.

- Forest, S., 2013. Questioning size effects as predicted by strain gradient plasticity. *J. Mech. Behav. Mater.* 22, 101–110.
- Forest, S., Aifantis, E.C., 2010. Some links between recent gradient thermo-elasto-plasticity theories and the thermomechanics of generalized continua. *Int. J. Solids Struct.* 47, 3367–3376.
- Forest, S., Barbe, F., Cailletaud, G., 2000. Cosserat modelling of size effects in the mechanical behaviour of polycrystals and multi-phase materials. *Int. J. Solids Struct.* 37, 7105–7126.
- Forest, S., Boubidi, P., Sievert, R., 2001. Strain localization patterns at a crack tip in generalized single crystal plasticity. *Scr. Mater.* 44, 953–958.
- Forest, S., Cailletaud, G., 1995. Strain localization in single crystals : bifurcation analysis, effects of boundaries and interfaces.
- Forest, S., Cailletaud, G., Sievert, R., 1997. A Cosserat theory for elastoviscoplastic single crystals at finite deformation. *Arch. Mech.* 49, 705–736.
- Forest, S., Guéninchault, N., 2013. Inspection of free energy functions in gradient crystal plasticity. *Acta Mech. Sin. Xuebao* 29, 763–772.
- Forest, S., Lorentz, E., 2004. Localization phenomena and regularization methods. *Local Approach to Fract.* 1, 311–371.
- Forest, S., Sedláček, R., 2003. Plastic slip distribution in two-phase laminate microstructures: Dislocation-based versus generalized-continuum approaches. *Philos. Mag.* 83, 245–276.
- Fredriksson, P., Gudmundson, P., 2007. Modelling of the interface between a thin film and a substrate within a strain gradient plasticity framework. *J. Mech. Phys. Solids*.
- Fu, M.W., Wang, J.L., 2021. Size effects in multi-scale materials processing and manufacturing. *Int. J. Mach. Tools Manuf.* 167.
- Fuentes-Alonso, S., Martínez-Pañeda, E., 2020. Fracture in distortion gradient plasticity. *Int. J. Eng. Sci.* 156, 103369.
- Fülöp, T., Brekelmans, W.A., Geers, M.G., 2006. Size effects from grain statistics in ultra-thin metal sheets. *J. Mater. Process. Technol.* 174, 233–238.
- Gao, H., Huang, Y., 2003. Geometrically necessary dislocation and size-dependent plasticity. *Scr. Mater.* 48, 113–118.
- Geers, M.G., Brekelmans, W.A., Janssen, P.J., 2006. Size effects in miniaturized polycrystalline FCC samples: Strengthening versus weakening. *Int. J. Solids Struct.* 43, 7304–7321.
- Geiger, M., Geißdörfer, S., Engel, U., 2007. Mesoscopic model: advanced simulation of micro-forming processes. *Prod. Eng.* 1, 79–84.
- Germain, P., 1973. The Method of Virtual Power in Continuum Mechanics. Part 2: Microstructure. *SIAM J. Appl. Math.* 25, 556–575.

- Gottschalk, D., McBride, A., Reddy, B.D., Javili, A., Wriggers, P., Hirschberger, C.B., 2016. Computational and theoretical aspects of a grain-boundary model that accounts for grain misorientation and grain-boundary orientation. *Comput. Mater. Sci.* 111, 443–459.
- Greer, J.R., Nix, W.D., 2005. Size dependence of mechanical properties of gold at the sub-micron scale. *Appl. Phys. A Mater. Sci. Process.* 80, 1625–1629.
- Groma, I., Csikor, F.F., Zaiser, M., 2003. Spatial correlations and higher-order gradient terms in a continuum description of dislocation dynamics. *Acta Mater.* 51, 1271–1281.
- Gudmundson, P., 2004. A unified treatment of strain gradient plasticity. *J. Mech. Phys. Solids* 52, 1379–1406.
- Gurtin, M.E., 2000. On the plasticity of single crystals: Free energy, microforces, plastic-strain gradients. *J. Mech. Phys. Solids* 48, 989–1036.
- Gurtin, M.E., 2002. A gradient theory of single-crystal viscoplasticity that accounts for geometrically necessary dislocations. *J. Mech. Phys. Solids* 50, 5–32.
- Gurtin, M.E., 2004. A gradient theory of small-deformation isotropic plasticity that accounts for the Burgers vector and for dissipation due to plastic spin. *J. Mech. Phys. Solids* 52, 2545–2568.
- Gurtin, M.E., 2006. The Burgers vector and the flow of screw and edge dislocations in finite-deformation single-crystal plasticity. *J. Mech. Phys. Solids* 54, 1882–1898.
- Gurtin, M.E., 2008a. A finite-deformation, gradient theory of single-crystal plasticity with free energy dependent on densities of geometrically necessary dislocations. *Int. J. Plast.* 24, 702–725.
- Gurtin, M.E., 2008b. A theory of grain boundaries that accounts automatically for grain misorientation and grain-boundary orientation. *J. Mech. Phys. Solids* 56, 640–662.
- Gurtin, M.E., 2010. A finite-deformation, gradient theory of single-crystal plasticity with free energy dependent on the accumulation of geometrically necessary dislocations. *Int. J. Plast.* 26, 1073–1096.
- Gurtin, M.E., Anand, L., 2008. Nanocrystalline grain boundaries that slip and separate: A gradient theory that accounts for grain-boundary stress and conditions at a triple-junction. *J. Mech. Phys. Solids* 56, 184–199.
- Gurtin, M.E., Anand, L., 2009. Thermodynamics applied to gradient theories involving the accumulated plastic strain: The theories of Aifantis and Fleck and Hutchinson and their generalization. *J. Mech. Phys. Solids* 57, 405–421.
- Gurtin, M.E., Anand, L., Lele, S.P., 2007. Gradient single-crystal plasticity with free energy dependent on dislocation densities. *J. Mech. Phys. Solids* 55, 1853–1878.
- Gurtin, M.E., Fried, E., Anand, L., 2010. *The Mechanics and Thermodynamics of Continua*. Cambridge University Press, Cambridge.

- Gurtin, M.E., Needleman, A., 2005. Boundary conditions in small-deformation, single-crystal plasticity that account for the Burgers vector. *J. Mech. Phys. Solids* 53, 1–31.
- Gurtin, M.E., Ohno, N., 2011. A gradient theory of small-deformation, single-crystal plasticity that accounts for GND-induced interactions between slip systems. *J. Mech. Phys. Solids* 59, 320–343.
- Gurtin, M.E., Reddy, B.D., 2016. Some issues associated with the intermediate space in single-crystal plasticity. *J. Mech. Phys. Solids* 95, 230–238.
- Hayashi, I., Sato, M., Kuroda, M., 2011. Strain hardening in bent copper foils. *J. Mech. Phys. Solids* 59, 1731–1751.
- Hill, R., 1952. On discontinuous plastic states, with special reference to localized necking in thin sheets. *J. Mech. Phys. Solids* 1, 19–30.
- Hua, F., Liu, D., Li, Y., He, Y., Dunstan, D.J., 2021. On energetic and dissipative gradient effects within higher-order strain gradient plasticity: Size effect, passivation effect, and Bauschinger effect. *Int. J. Plast.* 141, 102994.
- Huang, Y., Qu, S., Hwang, K.C., Li, M., Gao, H., 2004. A conventional theory of mechanism-based strain gradient plasticity. *Int. J. Plast.* 20, 753–782.
- Hug, E., Keller, C., 2010. Intrinsic effects due to the reduction of thickness on the mechanical behavior of nickel polycrystals. *Metall. Mater. Trans. A Phys. Metall. Mater. Sci.* 41, 2498–2506.
- Hug, E., Keller, C., Habraken, A.M., 2014. Impact of metallurgical size effects on plasticity of thin metallic materials, in: *Mater. Sci. Forum*, Trans Tech Publications Ltd. pp. 2290–2295.
- Hurtado, D.E., Ortiz, M., 2013. Finite element analysis of geometrically necessary dislocations in crystal plasticity. *Int. J. Numer. Methods Eng.* 93, 66–79.
- Hutchinson, J.W., 2012. Generalizing J2 flow theory: Fundamental issues in strain gradient plasticity. *Acta Mech. Sin. Xuebao* 28, 1078–1086.
- Janssen, P.J., de Keijser, T.H., Geers, M.G., 2006. An experimental assessment of grain size effects in the uniaxial straining of thin Al sheet with a few grains across the thickness. *Mater. Sci. Eng. A* 419, 238–248.
- Jebahi, M., Cai, L., Abed-Meraim, F., 2020. Strain gradient crystal plasticity model based on generalized non-quadratic defect energy and uncoupled dissipation. *Int. J. Plast.* 126, 102617.
- Jebahi, M., Forest, S., 2021. Scalar-based strain gradient plasticity theory to model size-dependent kinematic hardening effects. *Contin. Mech. Thermodyn.* , 1–23.
- Kalidindi, S.R., Bronkhorst, C.A., Anand, L., 1992. Crystallographic texture evolution in bulk deformation processing of FCC metals. *J. Mech. Phys. Solids* 40, 537–569.
- Kals, R.T.A., 1999. Fundamentals on the Miniaturization of Sheet Metal Working Processes: Bericht Aus Dem Lehrstuhl Für Fertigungstechnologie.

- Kals, T.A., Eckstein, R., 2000. Miniaturization in sheet metal working. *J. Mater. Process. Technol.* 103, 95–101.
- Kazantseva, N.V., Pilyugin, V.P., Danilov, S.E., Kolosov, V.Y., 2015. Effect of severe plastic deformation on the structure and crystal-lattice distortions in the Ni<sub>3</sub>(Al,X) (X = Ti, Nb) intermetallic compound. *Physics of Metals and Metallography* 116, 501–508.
- Keller, C., Habraken, A.M., Duchene, L., 2012a. Finite element investigation of size effects on the mechanical behavior of nickel single crystals. *Mater. Sci. Eng. A* 550, 342–349.
- Keller, C., Hug, E., Habraken, A.M., Duchene, L., 2012b. Finite element analysis of the free surface effects on the mechanical behavior of thin nickel polycrystals. *Int. J. Plast.* 29, 155–172.
- Keller, C., Hug, E., Habraken, A.M., Duchêne, L., 2015. Effect of stress path on the miniaturization size effect for nickel polycrystals. *Int. J. Plast.* 64, 26–39.
- Kiener, D., Motz, C., Grosinger, W., Weygand, D., Pippan, R., 2010. Cyclic response of copper single crystal micro-beams. *Scr. Mater.* 63, 500–503.
- Kim, G.Y., Ni, J., Koç, M., 2007. Modeling of the size effects on the behavior of metals in microscale deformation processes. *J. Manuf. Sci. Eng. Trans. ASME* 129, 470–476.
- Klusemann, B., Bargmann, S., Svendsen, B., 2012. Two models for gradient inelasticity based on non-convex energy. *Comput. Mater. Sci.* 64, 96–100.
- Kröner, E., 1959. Allgemeine Kontinuumstheorie der Versetzungen und Eigenspannungen. *Arch. Ration. Mech. Anal.* .
- Kuroda, M., 2011. On large-strain finite element solutions of higher-order gradient crystal plasticity. *Int. J. Solids Struct.* 48, 3382–3394.
- Kuroda, M., Needleman, A., 2019. Nonuniform and localized deformation in single crystals under dynamic tensile loading. *J. Mech. Phys. Solids* 125, 347–359.
- Kuroda, M., Tvergaard, V., 2008a. A finite deformation theory of higher-order gradient crystal plasticity. *J. Mech. Phys. Solids* 56, 2573–2584.
- Kuroda, M., Tvergaard, V., 2008b. On the formulations of higher-order strain gradient crystal plasticity models. *J. Mech. Phys. Solids* 56, 1591–1608.
- Lai, X., Peng, L., Hu, P., Lan, S., Ni, J., 2008. Material behavior modelling in micro/meso-scale forming process with considering size/scale effects. *Comput. Mater. Sci.* 43, 1003–1009.
- Lee, E.H., 1964. Elastic-plastic deformation at finite strains. *J. Appl. Mech. Trans. ASME* 36, 1–6.
- Lei, C., Deng, X., Li, X., Wang, Z., Wang, G., Misra, R.D., 2016. Mechanical properties and strain hardening behavior of phase reversion-induced nano/ultrafine Fe-17Cr-6Ni austenitic structure steel. *J. Alloys Compd.* 689, 718–725.
- Leu, D.K., 2009. Modeling of size effect on tensile flow stress of sheet metal in microforming. *J. Manuf. Sci. Eng. Trans. ASME* 131, 0110021–0110028.

- Leu, D.K., 2015. Distinguishing micro-scale from macro-scale tensile flow stress of sheet metals in microforming. *Mater. Des.* 87, 773–779.
- Li, W.T., Fu, M.W., Shi, S.Q., 2017. Study of deformation and ductile fracture behaviors in micro-scale deformation using a combined surface layer and grain boundary strengthening model. *Int. J. Mech. Sci.* 131-132, 924–937.
- Ling, C., 2018. Modeling the intragranular ductile fracture of irradiated steels . Effects of crystal anisotropy and strain gradient .
- Ling, C., Forest, S., Besson, J., Tanguy, B., Latourte, F., 2018. A reduced micromorphic single crystal plasticity model at finite deformations. Application to strain localization and void growth in ductile metals. *Int. J. Solids Struct.* 134, 43–69.
- Liu, D., He, Y., Dunstan, D.J., Zhang, B., Gan, Z., Hu, P., Ding, H., 2013. Toward a further understanding of size effects in the torsion of thin metal wires: An experimental and theoretical assessment. *Int. J. Plast.* 41, 30–52.
- Liu, D., He, Y., Tang, X., Ding, H., Hu, P., Cao, P., 2012. Size effects in the torsion of microscale copper wires: Experiment and analysis. *Scr. Mater.* 66, 406–409.
- Liu, J.G., Fu, M.W., Lu, J., Chan, W.L., 2011a. Influence of size effect on the springback of sheet metal foils in micro-bending. *Comput. Mater. Sci.* 50, 2604–2614.
- Liu, Z.L., Zhuang, Z., Liu, X.M., Zhao, X.C., Zhang, Z.H., 2011b. A dislocation dynamics based higher-order crystal plasticity model and applications on confined thin-film plasticity. *Int. J. Plast.* 27, 201–216.
- Lubarda, V.a., 2007. Elastoplasticity Theory.
- Ma, Z.S., Zhou, Y.C., Long, S.G., Lu, C., 2012. On the intrinsic hardness of a metallic film/substrate system: Indentation size and substrate effects. *Int. J. Plast.* 34, 1–11.
- Marano, A., 2019. Numerical simulation of strain localization in irradiated polycrystals. Theses. Université Paris sciences et lettres.
- Marano, A., Gélibert, L., Forest, S., 2019. Intragranular localization induced by softening crystal plasticity: Analysis of slip and kink bands localization modes from high resolution FFT-simulations results. *Acta Mater.* 175, 262–275.
- Marano, A., Lionel, G., Gélibert, L., Forest, S., 2021. FFT-based simulations of slip and kink bands formation in 3D polycrystals: Influence of strain gradient crystal plasticity. *J. Mech. Phys. Solids*, 104295.
- Martínez-Pañeda, E., del Busto, S., Betegón, C., 2017. Non-local plasticity effects on notch fracture mechanics. *Theor. Appl. Fract. Mech.* 92, 276–287.
- Martínez-Pañeda, E., Deshpande, V.S., Niordson, C.F., Fleck, N.A., 2019. The role of plastic strain gradients in the crack growth resistance of metals. *J. Mech. Phys. Solids* 126, 136–150.

- Martínez-Pañeda, E., Niordson, C.F., Bardella, L., 2016. A finite element framework for distortion gradient plasticity with applications to bending of thin foils. *Int. J. Solids Struct.* 96, 288–299.
- McBride, A.T., Gottschalk, D., Reddy, B.D., Wriggers, P., Javili, A., 2016. Computational and theoretical aspects of a grain-boundary model at finite deformations. *Tech. Mech.* 36, 102–119.
- McElhaney, K.W., Vlassak, J.J., Nix, W.D., 1998. Determination of indenter tip geometry and indentation contact area for depth-sensing indentation experiments. *J. Mater. Res.* 13, 1300–1306.
- Meng, B., Fu, M.W., 2015. Size effect on deformation behavior and ductile fracture in microforming of pure copper sheets considering free surface roughening. *Mater. Des.* 83, 400–412.
- Miyazaki, S., Fujita, H., Hiraoka, H., 1979. Effect of specimen size on the flow stress of rod specimens of polycrystalline CuAl alloy. *Scr. Metall.* 13, 447–449.
- Molotnikov, A., Lapovok, R., Davies, C.H., Cao, W., Estrin, Y., 2008. Size effect on the tensile strength of fine-grained copper. *Scr. Mater.* 59, 1182–1185.
- Motz, C., Schöberl, T., Pippan, R., 2005. Mechanical properties of micro-sized copper bending beams machined by the focused ion beam technique. *Acta Mater.* 53, 4269–4279.
- Needleman, A., 1988. Material rate dependence and mesh sensitivity in localization problems. *Comput. Methods Appl. Mech. Eng.* 67, 69–85.
- Needleman, A., Tvergaard, V., 1992. Analyses of plastic flow localization in metals. *Appl. Mech. Rev.* 45, S3–S18.
- Nellemann, C., Niordson, C.F., Nielsen, K.L., 2017. An incremental flow theory for crystal plasticity incorporating strain gradient effects. *Int. J. Solids Struct.* 110-111, 239–250.
- Nellemann, C., Niordson, C.F., Nielsen, K.L., 2018. Hardening and strengthening behavior in rate-independent strain gradient crystal plasticity. *Eur. J. Mech. A/Solids* 67, 157–168.
- Niordson, C.F., Hutchinson, J.W., 2003. On lower order strain gradient plasticity theories. *Eur. J. Mech. A/Solids* 22, 771–778.
- Niordson, C.F., Redanz, P., 2004. Size-effects in plane strain sheet-necking. *J. Mech. Phys. Solids* 52, 2431–2454.
- Nix, W.D., Gao, H., 1998. Indentation size effects in crystalline materials: A law for strain gradient plasticity. *J. Mech. Phys. Solids* 46, 411–425.
- Oh, S.H., Legros, M., Kiener, D., Dehm, G., 2009. In situ observation of dislocation nucleation and escape in a submicrometre aluminium single crystal. *Nat. Mater.* 8, 95–100.
- Ohno, N., Okumura, D., 2007. Higher-order stress and grain size effects due to self-energy of geometrically necessary dislocations. *J. Mech. Phys. Solids* 55, 1879–1898.
- Ohno, N., Okumura, D., Shibata, T., 2008. Grain-size dependent yield behavior under loading, unloading and reverse loading. *Int. J. Mod. Phys. B* 22, 5937–5942.

- Orowan, E., 1942. A TYPE OF PLASTIC DEFORMATION NEW IN METALS. *Nature* 149, 643–644.
- Özdemir, I., Yalçinkaya, T., 2014. Modeling of dislocation-grain boundary interactions in a strain gradient crystal plasticity framework. *Comput. Mech.* 54, 255–268.
- Özdemir, Ä., Yalçinkaya, T., 2016. Strain Gradient Crystal Plasticity: Intragranular Microstructure Formation, in: Handb. Nonlocal Contin. Mech. Mater. Struct.. Springer International Publishing, Cham, pp. 1–29.
- Panteghini, A., Bardella, L., 2016. On the Finite Element implementation of higher-order gradient plasticity, with focus on theories based on plastic distortion incompatibility. *Comput. Methods Appl. Mech. Eng.* 310, 840–865.
- Panteghini, A., Bardella, L., Niordson, C.F., 2019. A potential for higher-order phenomenological strain gradient plasticity to predict reliable response under non-proportional loading. *Proc. R. Soc. A Math. Phys. Eng. Sci.* 475, 20190258.
- Peirce, D., Asaro, R.J., Needleman, A., 1982. An analysis of nonuniform and localized deformation in ductile single crystals. *Acta Metall.* 30, 1087–1119.
- Peirce, D., Asaro, R.J., Needleman, A., 1983. Material rate dependence and localized deformation in crystalline solids. *Acta Metall.* 31, 1951–1976.
- Peng, L., Liu, F., Ni, J., Lai, X., 2007. Size effects in thin sheet metal forming and its elastic-plastic constitutive model. *Mater. Des.* 28, 1731–1736.
- Peng, X.L., Huang, G.Y., 2015. Modeling dislocation absorption by surfaces within the framework of strain gradient crystal plasticity. *Int. J. Solids Struct.* 72, 98–107.
- Peng, X.L., Huang, G.Y., 2017. Effect of dislocation absorption by surfaces on strain hardening of single crystalline thin films. *Arch. Appl. Mech.* 87, 1333–1345.
- Peng, X.L., Huang, G.Y., Bargmann, S., 2019. Gradient Crystal Plasticity: A Grain Boundary Model for Slip Transmission. *Materials (Basel)*. 12, 3761.
- Peng, X.L., Husser, E., Huang, G.Y., Bargmann, S., 2018. Modeling of surface effects in crystalline materials within the framework of gradient crystal plasticity. *J. Mech. Phys. Solids* 112, 508–522.
- Pouriayevali, H., Xu, B., 2015. A Hardening Description based on a Finite-Deformation Gradient Crystal Plasticity Model: Formulation and Numerical Implementation. *Pamm* 15, 343–344.
- Pouriayevali, H., Xu, B.X., 2017. A study of gradient strengthening based on a finite-deformation gradient crystal-plasticity model. *Contin. Mech. Thermodyn.* 29, 1–24.
- Ran, J.Q., Fu, M.W., Chan, W.L., 2013. The influence of size effect on the ductile fracture in micro-scaled plastic deformation. *Int. J. Plast.* 41, 65–81.

- Reddy, B.D., 2011. The role of dissipation and defect energy in variational formulations of problems in strain-gradient plasticity. Part 1: Polycrystalline plasticity. *Contin. Mech. Thermodyn.* 23, 527–549.
- Rezaei, S., Rezaei Mianroodi, J., Khaledi, K., Reese, S., 2020. A nonlocal method for modeling interfaces: Numerical simulation of decohesion and sliding at grain boundaries. *Comput. Methods Appl. Mech. Eng.* 362, 112836.
- Rice, J.R., 1976. The localization of plastic deformation. 14th Int. Congr. Theoretical Appl. Mech. , 207–220.
- Sarac, A., Oztop, M.S., Dahlberg, C.F., Kysar, J.W., 2016. Spatial distribution of the net Burgers vector density in a deformed single crystal. *Int. J. Plast.* 85, 110–129.
- Scherer, J.M., Besson, J., Forest, S., Hure, J., Tanguy, B., 2019. Strain gradient crystal plasticity with evolving length scale: Application to voided irradiated materials. *Eur. J. Mech. A/Solids* 77, 103768.
- Scherer, J.M., Phalke, V., Besson, J., Forest, S., Hure, J., Tanguy, B., 2020. Lagrange multiplier based vs micromorphic gradient-enhanced rate-(in)dependent crystal plasticity modelling and simulation. *Comput. Methods Appl. Mech. Eng.* 372, 113426.
- Shan, Z.W., Mishra, R.K., Syed Asif, S.A., Warren, O.L., Minor, A.M., 2008. Mechanical annealing and source-limited deformation in submicrometre- diameter Nicrystals. *Nat. Mater.* 7, 115–119.
- Shawish, S.E., Cizelj, L., Simonovski, I., 2013. Modeling grain boundaries in polycrystals using cohesive elements: Qualitative and quantitative analysis. *Nucl. Eng. Des.* 261, 371–381.
- Shu, J.Y., Fleck, N.A., 1999. Strain gradient crystal plasticity: Size-dependent deformation of bicrystals. *J. Mech. Phys. Solids* .
- Shu, J.Y., Fleck, N.A., Van Der Giessen, E., Needleman, A., 2001. Boundary layers in constrained plastic flow: Comparison of nonlocal and discrete dislocation plasticity. *J. Mech. Phys. Solids* 49, 1361–1395.
- Sluys, L.J., Estrin, Y., 2000. Analysis of shear banding with a dislocation based gradient plasticity model. *Int. J. Solids Struct.* 37, 7127–7142.
- Song, Y., Voyatzis, G.Z., 2020. Strain gradient finite element model for finite deformation theory: size effects and shear bands. *Comput. Mech.* 65, 1219–1246.
- Stölken, J.S., Evans, A.G., 1998. A microbend test method for measuring the plasticity length scale. *Acta Mater.* 46, 5109–5115.
- Stoltz, R.E., Pelloux, R.M., 1976. The Bauschinger effect in precipitation strengthened aluminum alloys. *Metall. Trans. A* 7, 1295–1306.
- Taillard, R., Pineau, A., 1982. Room temperature tensile properties of Fe-19wt.alloys precipitation hardened by the intermetallic compound NiAl. *Mater. Sci. Eng.* 56, 219–231.

- Takagi, K., Mayama, T., Mine, Y., Chiu, Y.L., Takashima, K., 2019. Extended ductility due to kink band formation and growth under tensile loading in single crystals of Mg-Zn-Y alloy with 18R-LPSO structure. *J. Alloys Compd.* 806, 1384–1393.
- Tsagrakis, I., Konstantinidis, A., Aifantis, E.C., 2003. Strain gradient and wavelet interpretation of size effects in yield and strength, in: *Mech. Mater.*, Elsevier, pp. 733–745.
- Vollertsen, F., 2008. Categories of size effects. *Prod. Eng.* 2, 377–383.
- Vollertsen, F., Schulze Niehoff, H., Hu, Z., 2006. State of the art in micro forming. *Int. J. Mach. Tools Manuf.* 46, 1172–1179.
- Voyiadjis, G.Z., Deliktaş, B., 2009a. Formulation of strain gradient plasticity with interface energy in a consistent thermodynamic framework. *Int. J. Plast.* 25, 1997–2024.
- Voyiadjis, G.Z., Deliktaş, B., 2009b. Mechanics of strain gradient plasticity with particular reference to decomposition of the state variables into energetic and dissipative components. *Int. J. Eng. Sci.* 47, 1405–1423.
- Voyiadjis, G.Z., Faghihi, D., Zhang, Y., 2014. A theory for grain boundaries with strain-gradient plasticity. *Int. J. Solids Struct.* 51, 1872–1889.
- Wang, C., Wang, C., Guo, B., Shan, D., Huang, G., 2013. Size effect on flow stress in uniaxial compression of pure nickel cylinders with a few grains across thickness. *Mater. Lett.* 106, 294–296.
- Werner, E., Prantl, W., 1990. Slip transfer across grain and phase boundaries. *Acta Metall. Mater.* 38, 533–537.
- Wulffinghoff, S., 2017. A generalized cohesive zone model and a grain boundary yield criterion for gradient plasticity derived from surface- and interface-related arguments. *Int. J. Plast.* 92, 57–78.
- Wulffinghoff, S., Bayerschen, E., Böhlke, T., 2013. A gradient plasticity grain boundary yield theory. *Int. J. Plast.* 51, 33–46.
- Wulffinghoff, S., Böhlke, T., 2012. Equivalent plastic strain gradient enhancement of single crystal plasticity: theory and numerics. *Proc. R. Soc. A Math. Phys. Eng. Sci.* 468, 2682–2703.
- Wulffinghoff, S., Böhlke, T., 2013. Equivalent plastic strain gradient crystal plasticity - Enhanced power law subroutine. *GAMM Mitteilungen* 36, 134–148.
- Wulffinghoff, S., Böhlke, T., 2015. Gradient crystal plasticity including dislocation-based work-hardening and dislocation transport. *Int. J. Plast.* 69, 152–169.
- Wulffinghoff, S., Forest, S., Böhlke, T., 2015. Strain gradient plasticity modeling of the cyclic behavior of laminate microstructures. *J. Mech. Phys. Solids* 79, 1–20.
- Xu, J., Li, J., Shi, L., Shan, D., Guo, B., 2015. Effects of temperature, strain rate and specimen size on the deformation behaviors at micro/meso-scale in ultrafine-grained pure Al. *Mater. Charact.* 109, 181–188.

- Yalçinkaya, T., Demirci, A., Simonovski, I., Özdemir, I., 2017. Micromechanical Modelling of Size Effects in Microforming. *Procedia Eng.* 207, 998–1003.
- Yalçinkaya, T., Özdemir, Ä., Simonovski, I., 2018. Micromechanical modeling of intrinsic and specimen size effects in microforming. *Int. J. Mater. Form.* 11, 729–741.
- Yun, W., Peilong, D., Zhenying, X., Hua, Y., Jiangping, W., Jingjing, W., 2010. A constitutive model for thin sheet metal in micro-forming considering first order size effects. *Mater. Des.* 31, 1010–1014.
- Zbib, H.M., Aifantis, E.C., 1988. On the structure and width of shear bands. *Scr. Metall.* 22, 703–708.
- Zbib, H.M., Aifantis, E.C., 2003. Size effects and length scales in gradient plasticity and dislocation dynamics. *Scr. Mater.* 48, 155–160.
- Zhang, M., Bridier, F., Villechaise, P., Mendez, J., McDowell, D.L., 2010. Simulation of slip band evolution in duplex Ti-6Al-4V. *Acta Mater.* 58, 1087–1096.

# Lei CAI

## Plasticité cristalline à gradients dans le cadre des grandes déformations pour modéliser les effets de taille dans les composants miniaturisés : Application à la localisation de la déformation dans les tôles métalliques mono- et poly-cristallines

### Résumé

Au cours des dernières décennies, les développements significatifs de la microélectronique et des systèmes micro-électromécaniques (MEMS) ont conduit à une augmentation spectaculaire de la demande en produits miniaturisés. Au cours des processus de miniaturisation, les propriétés mécaniques ne sont plus indépendantes de la taille, ce qui entraîne ce que l'on appelle les effets de taille, qui peuvent influencer les paramètres des matériaux et des processus et doivent être soigneusement pris en compte. Le présent travail de thèse vise à proposer un outil numérique flexible pour modéliser les effets de taille dans les composants polycristallins miniaturisés. Pour modéliser différents types d'effets de taille polycristallins, l'outil numérique proposé consiste en un couplage entre la théorie de plasticité cristalline à gradients de déformation (SGCP) et la modélisation de joints de grains (GB). Dans le cadre de ce couplage, un modèle flexible de type Gurtin basé sur l'approche de Gurtin (2007) a été développé. Une version en petites déformations de ce modèle a d'abord été proposée pour étudier l'influence des paramètres impliqués sur la prédiction des effets de taille en l'absence d'effets de grandes déformations. Une extension aux grandes déformations a ensuite été proposée pour permettre des applications en grandes déformations. Pour capter les effets de taille dus aux joints de grains, une extension aux grandes déformations du modèle GB proposé par Gurtin (2008) a été effectuée dans un cadre entièrement lagrangien tenant compte de la distorsion plastique du réseau. Comme application, l'outil numérique proposé a été utilisé pour faire un premier pas vers la modélisation des effets de taille sur les modes de localisation dans les structures mono- et poly-cristallines. Cet outil numérique sera utilisé à l'avenir pour modéliser les effets de taille sur la formabilité des tôles métalliques ultra-minces.

**Mots clés :** Effets de taille, plasticité cristalline à gradients de déformation, joint de grain, localisation de la déformation.

### Résumé en anglais

Over the past few decades, the significant developments in micro-electronics and micro-electro-mechanical systems (MEMS) has led to a dramatically increasing demand for miniaturized products. During miniaturization processes, the mechanical properties are no longer size-independent leading to the so-called size effects, which may influence both material and process parameters and must be carefully considered. The present PhD work aims at proposing a flexible numerical tool to model size effects within miniaturized polycrystalline components. To model different kinds of poly-crystal size effects, the proposed numerical tool consists in a coupling between strain gradient crystal plasticity (SGCP) and grain boundary (GB) theories. As a part of this coupling, a flexible Gurtin-type model based on Gurtin (2007) approach was developed. A small deformation version of this model was first proposed to investigate the influence of the involved parameters on the prediction of size effects in the absence of large strain effects. A finite deformation extension was then proposed allowing for large strain applications. The implemented SGCP model allows for predicting first- and second-order effects within grains. To capture size effects due to grain boundaries, a finite deformation extension of the GB model proposed by Gurtin (2008) was performed within fully Lagrangian framework accounting for plastic lattice distortion. As an application, the proposed numerical tool was applied to take a first step towards the modeling of size effects on the localization modes within single- and poly-crystalline structures. This numerical tool will be used in future to model size effects on the formability of ultra-thin sheet metals.

**Keywords:** Size effects, strain gradient crystal plasticity, grain boundary, strain localization.